



UNIVERSITY OF THE
WITWATERSRAND,
JOHANNESBURG



Research Project Dissertation

Solar-Powered Evaporative Cooler For Fruits And Vegetables In Developing Countries

Edward Rycroft

Student Number: 1478715

Supervisor: Dr. H. Roohani

Course: MECN8006A

A research project dissertation submitted to the Faculty of Engineering and the Built Environment at the University of the Witwatersrand, Johannesburg, in fulfilment of the requirements for completing the degree of a Master of Science in Engineering (Mechanical).

Johannesburg, January 2022

DECLARATION

I declare that this dissertation is my own unaided work, except where otherwise explicitly acknowledged. It is being submitted in fulfilment of the requirements for completing the degree of a Master of Science in Engineering (Mechanical) at the University of the Witwatersrand, Johannesburg.

I also hereby declare the following:

- I confirm that this project has not been submitted before for any other course requirement, examination, or degree at any other university or tertiary educational institution.
- I am aware that plagiarism (the use of work created by someone else without their permission and/or without acknowledging the original source) is wrong.
- I have followed the required conventions in referencing the thoughts and ideas of others.
- I understand that the University of the Witwatersrand, Johannesburg, may take disciplinary action against me if it can be shown that this project is not my own unaided work or that I have failed to acknowledge the sources of the ideas or words in my writing of this project.
- I have completed this project while employed by Defy Appliances as a Graduate Engineer. With regards to dissemination, background intellectual property, and restrictions concerning third party rights, please refer to the Terms And Conditions as set out in the Framework Agreement between Defy Appliances and the University of the Witwatersrand, Johannesburg.

Signed this 30th day of January 2022.

A handwritten signature in black ink, appearing to read 'E. Rycroft', written in a cursive style.

Edward Rycroft

Student No. 1478715

ABSTRACT

An investigation was undertaken into the potential of evaporative cooling using forced convection for the short-term storage of fruits and vegetables on a scale which was manually transportable by a single person and used a self-contained photovoltaic system. Previous research and existing products have primarily focused on the use of evaporative cooling with natural convection and there has been minimal evaluation of the possible improvements in performance realised with forced convection. Furthermore, food insecurity in developing countries is extensive with many cases of severe undernourishment due to the spoilage of the available food, where an affordable solution under €45 to control wastage through preservation could be transformative in promoting healthier societies. With the aim of achieving a cooling effect with a temperature decrease of at least 11°C and relative humidity increase of at least 35%, a prototype of 6.62kg and 585mm by 405mm by 360mm was designed through analytical calculations and numerical simulations using a radial fan for optimal operation at ambient temperatures above 32°C and ambient relative humidities below 50%. Under practical experimentation in Johannesburg, South Africa, with a solar panel of 6.0W, the prototype was able to achieve the desired performance in 81.9% of the relevant periods using cotton ring spun and polyester for the cooling pad. This was complemented with an increase in shelf life by 88.3% on average for a sample of fruits and vegetables stored within the internal volume of 45L compared to an identical sample stored externally. For further optimisation, a thermoelectric module was incorporated with an additional solar panel of 7.0W. This enhancement resulted in an improved performance minimising the temperature fluctuations to 1°C for each 3.5°C fluctuation in ambient temperature on average, compared to the previous results of 1°C for each 2.4°C fluctuation in ambient temperature on average, at the expense of an unsatisfactory increase in costs of 83.8%. Overall, the performance was successfully promising and it is recommended for further practical experimentation under more extreme environmental conditions.

ACKNOWLEDGEMENTS

Firstly, I would like to express my sincere appreciation to Dr. Hamed Roohani for his encouraging and brilliant guidance, suggestions, and assistance as my supervisor throughout the progression of this project. Secondly, I would like to convey my genuine gratitude towards Defy Appliances for their invaluable sponsoring and contributions towards this endeavour with regards to advice, funding, resources, and facilities throughout the course of this project - especially Sameer Ramnarain as an understanding colleague and mentor. Finally, I would like to earnestly thank my parents, family, friends, and teachers for their constant and immeasurable support throughout my life.

LIST OF CONTENTS

Declaration	i
Abstract	ii
Acknowledgements	iii
List Of Contents	iv
List Of Figures	viii
List Of Tables	xiv
List Of Symbols	xvi
1 Introduction	1
1.1 Background	1
1.1.1 Developing Countries Food Security	1
1.1.2 Geographical Considerations	3
1.1.3 Fruit And Vegetable Physiology	4
1.1.4 Fruit And Vegetable Preservation	9
1.1.5 Conventional Refrigeration	12
1.1.6 Promising Alternative Technologies	15
1.2 Motivation	16
1.3 Research Question	17
1.4 Initial Task Statement	17
2 Literature Review	19
2.1 Environmental Conditions	19
2.1.1 Temperature And Relative Humidity	20
2.1.2 Incoming Solar Radiation	21
2.2 User Ergonomics	23
2.3 Psychrometry	24
2.3.1 Work, Heat, And Energy	24
2.3.2 Pressure-Volume-Temperature Relationships	26
2.3.3 Ideal Gas Idealisation	27
2.3.4 Psychrometric Applications	28
2.3.5 Air And Water Properties	30
2.4 Heat Transfer	30
2.4.1 Conduction	30
2.4.2 Convection	32
2.4.2.1 Analytical Considerations	32
2.4.2.2 Internal Flows	37

2.4.3	Radiation	39
2.4.4	Resistance And Overall Heat Transfer	41
2.5	Evaporative Cooling	42
2.5.1	Basic Process Model	42
2.5.2	Conventional Cooling Pads	47
2.5.3	Forced Air Flow	50
2.5.3.1	Performance Characteristics	51
2.5.3.2	Driving Electric Motor	53
2.6	Solar Power And Photovoltaic Systems	55
2.6.1	Photovoltaic Effect	56
2.6.2	Construction And Performance	56
2.6.3	Energy Storage Components	59
2.7	Existing Products	60
2.7.1	Traditional Cooler	60
2.7.2	Zeer Pot	62
2.7.3	Bosch FreshBox	65
2.7.4	Fenik Yuma Cooler	66
2.7.5	Wakati One	67
2.7.6	Building Air Conditioning	69
2.8	Thermoelectric Cooling	71
3	Project Objectives	74
3.1	Defined Task Statement	74
3.2	Desired Specifications	75
3.2.1	Overall Requirements	75
3.2.2	Overall Constraints	76
3.2.3	Concept Criteria	77
4	Project Methodology	78
5	Analysis Development	81
5.1	Provisional User Considerations	81
5.2	Preliminary Concept Generation	82
5.2.1	Criteria Weighting	82
5.2.2	Inlet Concepts	84
5.2.3	Outlet Concepts	86
5.3	Initial Analytical Analysis	87
5.3.1	Fundamental Assumptions	87

5.3.2	Evaporative Cooling Effect	90
5.3.3	Air Flow Properties	93
5.4	Flow Simulation Analysis	96
5.4.1	Design Inception	96
5.4.2	Basic Analytical Predictions	97
5.4.3	Theoretical Background	98
5.4.4	Model Configuration	101
5.4.5	Base Setup And Results	103
5.5	Flow Optimisations	111
5.5.1	Blade Outlet Angle	111
5.5.2	Blade Quantity Count	116
5.5.3	Blade Inclination Angle	120
5.5.4	Blade Breadth	124
5.5.5	Channel Width	127
5.5.6	Corner Bend Radius	131
5.6	Cooling Pad	134
5.6.1	Material Types	134
5.6.2	Practical Comparison	136
5.7	Water Supply Layout	139
5.8	External Insulation	140
5.9	Structural Strength	141
5.9.1	Design Inception	142
5.9.2	Basic Analytical Predictions	142
5.9.3	Theoretical Background	144
5.9.4	Model Configuration	147
5.9.5	Base Setup And Results	149
6	Practical Experimentation	153
6.1	Electronic Components	153
6.1.1	Solar Panel	153
6.1.2	Energy Storage	154
6.1.3	Power Management Module	155
6.1.4	Radial Fan Motor	156
6.2	Structure Construction	158
6.3	Cost Analysis	159
6.3.1	Electronic Costs	160

6.3.2	Material Costs	162
6.4	Monitoring Equipment	162
6.4.1	Properties Measurement	162
6.4.2	Microcontroller And Data	164
6.5	Data And Results	164
6.5.1	Energy Storage Factors	165
6.5.2	Cotton Ring Spun Results	166
6.5.3	Polyester Results	171
6.5.4	Fruits And Vegetables Results	176
6.6	Discussion	194
7	Performance Enhancement	199
7.1	Electronic Components	199
7.1.1	Additional Solar Panels	199
7.1.2	Thermoelectric Module	200
7.2	Cost Analysis	201
7.3	Data And Results	201
7.4	Discussion	206
8	Conclusions And Recommendations	209
	List Of References	213
A	Additional Resources	229
B	Auxiliary Resources	229
C	Collaboration Disclaimer	229

LIST OF FIGURES

1.1	Estimations of individuals in the total population classified as undernourished	2
1.2	Assessment of the global number of people living in poverty	3
1.3	Examples of the effect of temperature on respiration for selected fruits and vegetables ...	8
1.4	Microscopic structure of the skin of most fruits and vegetables	8
1.5	Examples of the effect of temperature on shelf life for selected fruits and vegetables	9
1.6	Schematic of the processes for a vapour-compression cycle	13
1.7	Schematic of the processes for a vapour-absorption cycle	14
2.1	Average surface air temperature during the day for each month in 2019	20
2.2	Average surface relative humidity during the day for each month in 2019	21
2.3	Average solar insolation during the day for each month in 2019	22
2.4	Overall dimensions of a male and female for 2.5th, 50th, and 97.5th percentiles	23
2.5	Relationship between pressure, specific volume, and temperature	26
2.6	Example of a psychrometric chart with axes for reading various properties	29
2.7	Simplification of conduction and example through a plane wall	31
2.8	Variation in thermal conductivity for changes in temperature for selected substances	31
2.9	Development of the velocity, thermal, and concentration boundary layers	34
2.10	Velocity and thermal boundary layers for a flow within a circular duct	37
2.11	Example of a body emitting and absorbing radiation to and from the surroundings	39
2.12	Propagation of insolation from the Sun through space towards the Earth	41
2.13	Variation in heat of evaporation for changes in temperature for selected substances	43
2.14	Simplification of evaporative cooling considering molecular interactions	43
2.15	Illustration of evaporative cooling with moist air flow through a soaked pad	44
2.16	Example of a psychrometric chart for moist air undergoing evaporative cooling	46
2.17	Selected samples of common materials used for convectional pads	48
2.18	Capillarity in a cylindrical tube and simplification of capillarity between the fibres	49
2.19	Difference in basic fan construction transitioning from radial flow to axial flow	51
2.20	Velocity triangles along the fan blades for a radial flow and axial flow	51
2.21	Comparison between the profile of blades for a radial fan and axial fan	53
2.22	Comparison between the construction of brushed and brushless direct current motors	54
2.23	Typical variation in current, torque, power and efficiency for direct current motors	55
2.24	Effect of friction and other losses on the head rise over a fan with flow rate	55
2.25	Performance of p-n junctions in photovoltaic cells with different constructions	57

2.26	Construction of a photovoltaic cell with mono-crystalline and multi-crystalline silicon ...	58
2.27	Variation in current and voltage for changes in light intensity and temperature	58
2.28	Construction of an electro-chemical battery and electro-chemical capacitor	60
2.29	Schematic and graphic of the evaporative cooling utilised by a Zeer Pot	62
2.30	Representative results for an evaporative cooling design similar to a Zeer Pot	64
2.31	Graphic of a MittiCool with assemblies of the first version and second version	64
2.32	Graphic of a FreshBox with assumed materials and assembly for the construction	65
2.33	Graphic of a Yuma with assumed materials and assembly for the construction	67
2.34	Graphic of a Wakati One with the micro-climate device and assembly	68
2.35	Photographs of vegetables which were stored inside and outside of the Wakati One	68
2.36	Comparison between direct and indirect evaporative cooling for buildings	69
2.37	Arrangement of a wet surface heat exchanger with a counter-flow example	70
2.38	Illustration of a thermoelectric module with a cold and hot plate	71
2.39	Variation in the temperature, intensity of insolation, and coefficient of performance	73
5.1	Proportions for the torso of an average male and female with extended arms	81
5.2	Examples for the torso of an average male and female carrying a box	82
5.3	Illustration of the concepts for the combination of fan type and cooling pad	84
5.4	Illustration of the concepts for the combination of the channels and exhaust	86
5.5	Internal layout of the design for the analytical analysis	90
5.6	Variation of the convection coefficients with temperature for velocity	92
5.7	Variation of the enclosure temperature with dry-bulb temperature for velocity	92
5.8	Variation of the outlet temperature with inlet temperature for efficiency at 0m	94
5.9	Variation of the outlet temperature with inlet temperature for efficiency at 1700m	95
5.10	Geometry layout for the initial generation of the backward-curved blade profile	97
5.11	Experimental recommendations for the number of blades for the outlet angle	97
5.12	Velocity profile through backward-curved blades and sections of the channels	98
5.13	Example of random fluctuations in velocity about an average for turbulent flow	99
5.14	Typical characteristics of the velocity profile for a turbulent boundary layer	99
5.15	Radial fan and basic enclosure to construct the model for the CFD analysis	102
5.16	Examples of the initial meshes with cross-sections of the top, front, and isometric	106
5.17	Changes in the scaled residuals and properties for the initial meshes	109
5.18	Velocity and pressure contours for the initial model considering the medium mesh	110
5.19	Modifications applied to the model to include a grill at the inlet and outlet	111
5.20	Example of the model with an outlet angle of 35°, 50°, and 65°	112

5.21	Contours for an outlet angle of 35° using a quantity of 12 blades, inclination angle of 0°, breadth of 20mm, channel width of 15mm, and corner radius of 25mm	113
5.22	Contours for an outlet angle of 50° using a quantity of 12 blades, inclination angle of 0°, breadth of 20mm, channel width of 15mm, and corner radius of 25mm	114
5.23	Contours for an outlet angle of 65° using a quantity of 12 blades, inclination angle of 0°, breadth of 20mm, channel width of 15mm, and corner radius of 25mm	115
5.24	Example of the model with a quantity of 10, 12, and 14 blades	117
5.25	Contours for a quantity of 10 blades using an outlet angle of 50°, inclination angle of 0°, breadth of 20mm, channel width of 15mm, and corner radius of 25mm	118
5.26	Contours for a quantity of 14 blades using an outlet angle of 50°, inclination angle of 0°, breadth of 20mm, channel width of 15mm, and corner radius of 25mm	119
5.27	Example of the model with an inclination angle of 0°, 10°, and 20°	120
5.28	Contours for an inclination angle of 10° using an outlet angle of 50°, quantity of 14 blades, breadth of 20mm, channel width of 15mm, and corner radius of 25mm	121
5.29	Contours for an inclination angle of 20° using an outlet angle of 50°, quantity of 14 blades, breadth of 20mm, channel width of 15mm, and corner radius of 25mm	122
5.30	Example of the model with a breadth of 20mm, 30mm, and 40mm	124
5.31	Contours for a breadth of 30mm using an outlet angle of 50°, quantity of 14 blades, inclination angle of 0°, channel width of 15mm, and corner radius of 25mm	125
5.32	Contours for a breadth of 40mm using an outlet angle of 50°, quantity of 14 blades, inclination angle of 0°, channel width of 15mm, and corner radius of 25mm	126
5.33	Contours for a channel width of 20mm and breadth of 20mm using an outlet angle of 50°, quantity of 14 blades, inclination angle of 0°, and corner radius of 25mm	128
5.34	Contours for a channel width of 20mm and breadth of 30mm using an outlet angle of 50°, quantity of 14 blades, inclination angle of 0°, and corner radius of 25mm	129
5.35	Contours for a channel width of 20mm and breadth of 40mm using an outlet angle of 50°, quantity of 14 blades, inclination angle of 0°, and corner radius of 25mm	130
5.36	Example of the model with a corner radius of 40mm	132
5.37	Contours for a corner radius of 40mm using an outlet angle of 50°, quantity of 14 blades, inclination angle of 0°, breadth of 20mm, and channel width of 15mm	133
5.38	Samples of the selected materials used for deciding the fabric of the cooling pad	135
5.39	Practical test of the best material for wicking, distributing, and retaining water	136
5.40	Illustration of the uniform distribution and irregular distribution with branches	138
5.41	Dimensions of the water supply using a reservoir	139

5.42	Layout of the water supply using a reservoir	139
5.43	Basic layout of the insulation to minimise the effects from insolation	141
5.44	Layout of the structure through the centre of the enclosure	142
5.45	Simplified cross-section plane through the middle of the enclosure	144
5.46	Illustration of the equilibrium conditions for an element shown in each direction	146
5.47	Structure of the enclosure to construct the model for the FEA analysis	148
5.48	Example of a linear and quadratic tetrahedral element	148
5.49	Examples of the initial mesh with cross-sections of various views	149
5.50	Convergence of maximum displacement within 2% through refinement of the mesh	150
5.51	Convergence of maximum stress within 2% through refinement of the mesh	150
5.52	Contours of displacement with deformation scaled, reflective mirroring to display the whole enclosure, and highlights of the critical regions and positions of interest	151
5.53	Contours of stress with deformation scaled, reflective mirroring to display the whole enclosure, and highlights of the critical regions and positions of interest	151
5.54	Contours of safety factor with deformation scaled, reflective mirroring to display the whole enclosure, and highlights of the critical regions and positions of interest	152
6.1	Interactions between the electronic components	153
6.2	Front and back photographs of the 0.50A 12V 6.0W generic solar panel	154
6.3	Photographs of the lithium-ion 14500 battery and 26650 battery	155
6.4	Photograph of the DFRobot Solar Power Manager SKU DFR0535	155
6.5	Photograph of the original axial Sunon MFC0251V2-0000-A99	157
6.6	Performance curve for the original axial Sunon MFC0251V2-0000-A99	157
6.7	Timing for the polarity of the stator based on the position of the rotor	157
6.8	Rendering of the construction of the overall assembly	158
6.9	Photographs of the construction of the assembled prototype	159
6.10	Top and bottom photographs of the Waveshare Solar Management Module 16120	161
6.11	Top and bottom photographs of the MT3608 boost voltage regulator	161
6.12	Photographs of the DHT22 for measuring temperature and relative humidity	163
6.13	Locations of the DHT22 for measuring temperature and relative humidity	163
6.14	Photograph and connections of the Arduino Uno Revision 3 for recording data	164
6.15	Satellite photographs and insolation between 11 Feb. and 16 Feb. 2021	167
6.16	Measurements of temperature using cotton from 11 Feb. to 16 Feb. 2021	168
6.17	Measurements of relative humidity using cotton from 11 Feb. to 16 Feb. 2021	168
6.18	Differences in temperature using cotton from 11 Feb. to 16 Feb. 2021	169

6.19	Differences in relative humidity using cotton from 11 Feb. to 16 Feb. 2021	169
6.20	Satellite photographs and insolation between 17 Feb. and 22 Feb. 2021	172
6.21	Measurements of temperature using polyester from 17 Feb. to 22 Feb. 2021	173
6.22	Measurements of relative humidity using polyester from 17 Feb. to 22 Feb. 2021	173
6.23	Differences in temperature using polyester from 17 Feb. to 22 Feb. 2021	174
6.24	Differences in relative humidity using polyester from 17 Feb. to 22 Feb. 2021	174
6.25	Photographs of the fruits and vegetables stored in the surroundings and enclosure	176
6.26	Satellite photographs and insolation between 23 Feb. and 1 Mar. 2021	178
6.27	Measurements of temperature using fruits and vegetables from 23 Feb. to 1 Mar. 2021 ..	179
6.28	Measurements of humidity using fruits and vegetables from 23 Feb. to 1 Mar. 2021	179
6.29	Differences in temperature using fruits and vegetables from 23 Feb. to 1 Mar. 2021	180
6.30	Differences in humidity using fruits and vegetables from 23 Feb. to 1 Mar. 2021	180
7.1	Interactions between the additional solar panels and thermoelectric module	199
7.2	Front and back photographs of the 0.5833A 6V 3.5W generic solar panel	200
7.3	Photographs of the TEC1-12706, heat sink, and location at the back of the enclosure	200
7.4	Performance curves for the TEC1-12706 thermoelectric module	201
7.5	Satellite photographs and insolation between 2 Mar. and 5 Mar. 2021	202
7.6	Measurements of temperature using thermoelectric module from 2 Mar. to 5 Mar. 2021 ..	203
7.7	Measurements of humidity using thermoelectric module from 2 Mar. to 5 Mar. 2021	203
7.8	Differences in temperature using thermoelectric module from 2 Mar. to 5 Mar. 2021	204
7.9	Differences in humidity using thermoelectric module from 2 Mar. to 5 Mar. 2021	204
A.1	Average surface air temperature during the night for each month in 2019	232
A.2	Average surface relative humidity during the night for each month in 2019	232
A.3	Psychrometric chart for an altitude of 1700m and atmospheric pressure of 82.50kPa	233
B.1	Convergence for an outlet of 35°, 50°, and 65° using a quantity of 12 blades, inclination of 0°, breadth of 20mm, channel thickness of 15mm, and corner radius of 25mm	234
B.2	Convergence for a quantity of 10, 12, and 14 blades using an outlet of 50°, inclination of 0°, breadth of 20mm, channel thickness of 15mm, and corner radius of 25mm	235
B.3	Convergence for an inclination of 0°, 10°, and 20° using an outlet of 50°, quantity of 12 blades, breadth of 20mm, channel thickness of 15mm, and corner radius of 25mm	236
B.4	Convergence for an inclination of 0°, 10°, and 20° using an outlet of 50°, quantity of 14 blades, breadth of 20mm, channel thickness of 15mm, and corner radius of 25mm	237

B.5	Convergence for an inclination of 0° , 10° , and 20° using an outlet of 65° , quantity of 12 blades, breadth of 20mm, channel thickness of 15mm, and corner radius of 25mm	238
B.6	Convergence for an inclination of 0° , 10° , and 20° using an outlet of 65° , quantity of 14 blades, breadth of 20mm, channel thickness of 15mm, and corner radius of 25mm	239
B.7	Convergence for a breadth of 20mm, 30mm, and 40mm using an outlet of 50° , quantity of 14 blades, inclination of 0° , channel thickness of 15mm, and corner radius of 25mm	240
B.8	Convergence for a breadth of 20mm, 30mm, and 40mm using an outlet of 50° , quantity of 14 blades, inclination of 0° , channel thickness of 20mm, and corner radius of 25mm	241
B.9	Convergence for a corner radius of 25mm and 40mm using an outlet of 50° , quantity of 14 blades, inclination of 0° , breadth of 20mm, and channel thickness of 15mm	242

LIST OF TABLES

1.1	Classification of common fruits according to their climatic region of growth	4
1.2	Typical micro-organism growth rate at various temperatures	5
1.3	Respiration correlation coefficients for the experimental heat of respiration	6
1.4	Rate of carbon dioxide production due to respiration for fruits and vegetables	7
1.5	Optimal storage conditions for common fruits and vegetables in harsh climates	10
1.6	Compatibility for fruits and vegetables sharing optimal conditions for storage	12
1.7	Comparison between the typical properties of conventional refrigeration	14
2.1	Emissivity and absorptivity for insolation from the Sun for selected substances	40
2.2	Comparison between the typical characteristics of different types of batteries	59
2.3	Comparison between the shelf life using previous methods of storage and a Zeer Pot	63
2.4	Claimed performance of the Yuma under different environmental conditions	67
2.5	Claimed shelf life of selected fruits and vegetables using a Wakati One	69
5.1	Assessment of the importance of the criteria based on a weighting matrix	83
5.2	Evaluation of the Inlet concepts against the weighted criteria	85
5.3	Correlations for the properties of dry air, saturated water vapour, and saturated water	88
5.4	Typical properties of applicable materials which can be assumed to be constant	89
5.5	Configurations of the meshes with the skewness and aspect ratio metrics	104
5.6	Results at the positions of interest for each of the initial meshes	108
5.7	Results for outlet angles of 35°, 50°, and 65° using a quantity of 12 blades, inclination angle of 0°, breadth of 20mm, channel width of 15mm, and corner radius of 25mm	112
5.8	Results for quantities of 10, 12, and 14 blades using an outlet angle of 50°, inclination angle of 0°, breadth of 20mm, channel width of 15mm, and corner radius of 25mm	117
5.9	Results for inclination angles of 0°, 10°, and 20° using an outlet angle of 50°, quantity of 14 blades, breadth of 20mm, channel width of 15mm, and corner radius of 25mm	123
5.10	Results for breadths of 20mm, 30mm, and 40mm using an outlet angle of 50°, quantity of 14 blades, inclination of 0°, channel width of 15mm, and corner radius of 25mm	124
5.11	Results for a channel width of 20mm and breadths of 20mm, 30mm, and 40mm using an outlet angle of 50°, quantity of 14 blades, inclination of 0°, and corner radius of 25mm ..	131
5.12	Results for a corner radius of 40mm using an outlet angle of 50°, quantity of 14 blades, inclination angle of 0°, breadth of 20mm, and channel width of 15mm	132
5.13	Results comparing the wicking and distribution abilities of selected materials	137
5.14	Mechanical properties of ABS thermoplastic and polystyrene foam	143

6.1	Summary of the estimated electronic and material costs	160
6.2	Important measurements from 11 Feb. 2021 to 16 Feb. 2021	170
6.3	Evaporative cooling efficiency from 11 Feb. 2021 to 16 Feb. 2021	171
6.4	Important measurements from 17 Feb. 2021 to 22 Feb. 2021	175
6.5	Evaporative cooling efficiency from 17 Feb. 2021 to 22 Feb. 2021	175
6.6	Important measurements from 23 Feb. 2021 to 1 Mar. 2021	181
6.7	Mass and photographs of the avocados from 23 Feb. to 1 Mar. 2021	182
6.8	Mass and photographs of the baby marrows from 23 Feb. to 1 Mar. 2021	183
6.9	Mass and photographs of the bananas from 23 Feb. to 1 Mar. 2021	184
6.10	Mass and photographs of the bell peppers from 23 Feb. to 1 Mar. 2021	185
6.11	Mass and photographs of the cabbages from 23 Feb. to 1 Mar. 2021	186
6.12	Mass and photographs of the carrots from 23 Feb. to 1 Mar. 2021	187
6.13	Mass and photographs of the eggplants from 23 Feb. to 1 Mar. 2021	188
6.14	Mass and photographs of the granadillas from 23 Feb. to 1 Mar. 2021	189
6.15	Mass and photographs of the sweet corns from 23 Feb. to 1 Mar. 2021	190
6.16	Mass and photographs of the tomatoes from 23 Feb. to 1 Mar. 2021	191
7.1	Evaporative cooling efficiency from 2 Mar. 2021 to 5 Mar. 2021	206
A.1a	Additional optimal storage conditions for common fruits and vegetables	230
A.1b	Additional optimal storage conditions for common fruits and vegetables (continued)	231

LIST OF SYMBOLS

The general symbols used, with a description and relevant units, are represented as follows. Throughout the report, quantities are presented with convenient units for familiarity (for example, °C is used instead of K). All equations and calculations presented in the report used the standard units given below. Due to conventions and a lack of available alternatives, several symbols have been associated with multiple descriptions and local context should be referred to when each symbol is used.

A	cross-sectional area, m ² ; surface area, m ² ;
a	speed of sound, m/s;
B	SST κ - ω blending function;
b	respiration correlation coefficient;
C	concentration, mol/m ³ ; heat capacity, J/K; SST κ - ω model auxiliary relation;
C_p	heat capacity at a constant pressure, J/K;
C_v	heat capacity at a constant volume, J/K;
c	mass specific heat capacity, J/kg/K; speed of light, 2.998×10^8 m/s;
c_p	mass specific heat capacity at a constant pressure, J/kg/K;
c_v	mass specific heat capacity at a constant volume, J/kg/K;
\bar{c}	molar specific heat capacity, J/mol/K;
\bar{c}_p	molar specific heat capacity at a constant pressure, J/mol/K;
\bar{c}_v	molar specific heat capacity at a constant volume, J/mol/K;
D	diameter, m; mass diffusivity, m ² /s;
E	elastic modulus, Pa; energy generated, J;
\dot{E}	rate of energy transfer, W;
F	force magnitude, N; SST κ - ω model blending function;
\vec{F}	force vector, N;
f	frequency, Hz; Moody or Darcy friction factor;
G	flux of electromagnetic radiation, W/m ² ; shear modulus, Pa;
g	gravitational acceleration, m/s ² ;
H	enthalpy, J; head rise, m; height, m;
h	mass specific enthalpy, J/kg; Planck's constant, 6.626×10^{-34} J.s;
\bar{h}	molar specific enthalpy, J/mol;
h_c	convection heat transfer coefficient, W/m ² /K;
\bar{h}_c	average convection heat transfer coefficient, W/m ² /K;
h_{fg}	mass specific heat of evaporation, J/kg;
\bar{h}_{fg}	molar specific heat of evaporation, J/mol;
h_m	convection mass transfer coefficient, m/s;
\bar{h}_m	average convection mass transfer coefficient, m/s;
h_r	radiation heat transfer coefficient, W/m ² /K;

I	current, A;
i	arbitrary placeholder or variable;
j	arbitrary placeholder or variable;
K	stiffness matrix, N/m;
k	stiffness, N/m; thermal conductivity, W/m/K;
L	characteristic dimension, m; length, m;
Le	Lewis number;
M	molar mass, kg/mol;
m	mass, kg;
\dot{m}	mass flow or transfer or production rate, kg/s;
Ma	Mach number;
n	design factor; mole, mol; proportional exponent; safety factor;
\dot{n}	mole flow or transfer or production rate, mol/s;
\hat{n}	perpendicular unit vector;
Nu	Nusselt number;
\overline{Nu}	average Nusselt number;
P	SST κ - ω model auxiliary relation; wetted perimeter, m;
p	pressure, Pa; volumetric force, N/m ³ ;
Pr	Prandtl number;
Q	heat transfer, J;
\dot{Q}	heat transfer rate, W;
R	mass specific gas constant, J/kg/K; Reynolds stresses, Pa;
\bar{R}	molar specific or universal gas constant, 8.314J/mol/K;
R_e	electrical resistance, ohm or Ω ;
R_t	thermal resistance, K/W;
r	radius, m;
s	specific entropy, J/K/kg; strain rate, m/m/s;
\vec{r}	radial directional or displacement vector, m;
Re	Reynolds number;
Sc	Schmidt number;
Sh	Sherwood number;
\overline{Sh}	average Sherwood number;
T	temperature, K; torque, N.m;
t	thickness, m; time, s; traction, N/m ² ;
U	internal energy, J; overall heat transfer coefficient, W/m ² /K;
u	displacement, m; mass specific internal energy, J/kg; parallel velocity, m/s;
\bar{u}	molar specific internal energy, J/mol;
\vec{u}	displacement vector, m; velocity of blade vector, m/s;

V	volume, m^3 ; voltage or electric potential difference, V;
\dot{V}	volumetric flow rate, m^3/s ;
\vec{v}	velocity of fluid vector, m/s;
W	width, m; work, J;
\dot{W}	work rate or power, W;
w	perpendicular velocity, m/s;
\vec{w}	relative velocity between blade and fluid vector, m/s;
x	displacement, m; position in parallel direction, m;
y	displacement, m; mole fraction, %; position in transverse direction, m;
Z	compressibility factor; intrinsic figure of merit, 1/K;
z	displacement, m; elevation or position in perpendicular direction, m;
α	absorptivity; Seebeck coefficient, V/K; thermal diffusivity, m^2/s ;
β	blade outlet angle, rad;
γ	heat capacity ratio; surface tension, N/m;
δ	boundary layer thickness, m; displacement, m; relative thickness, m;
ε	emissivity; slip coefficient, m; turbulence dissipation rate, m^2/s^3 ; strain, m/m;
ζ	virtual displacement, m;
η	mechanical, thermal, or electrical efficiency, %;
θ	angular displacement, rad; contact angle, rad; incident solar radiation angle, rad;
$\dot{\theta}$	angular velocity, rad/s;
κ	turbulence kinetic energy, m^2/s^2 ;
λ	wavelength, m;
μ	dynamic viscosity, kg/m/s or Pa.s or N.s/m ² ;
ν	kinematic viscosity, m^2/s ; Poisson's ratio;
ξ	coefficient of performance;
Π	Peltier coefficient, V;
ρ	density, kg/m ³ ;
σ	axial stress, Pa; Stefan-Boltzmann constant, $5.6704 \times 10^{-8} W/m^2/K^4$;
τ	shear stress, Pa;
υ	mass specific volume, m^3/kg ;
$\bar{\upsilon}$	molar specific volume, m^3/mol ;
ϕ	arbitrary placeholder or variable; relative humidity;
ψ	percentage difference, %;
ω	humidity ratio, kg_v/kg_a ; specific turbulence dissipation rate, m^2/s^3 ;

\square^*	normalised dimensionless	\square^n	numerical placeholder
\square_{1-9}	arbitrary placeholders	\square_1	initial state
\square_2	final state	\square_3	ideal state

∞	surroundings or free stream	$A-Z$	arbitrary placeholders
a	dry air or axial	abs	ABS material
avg	average	b	bending
bar	barrier	bck	back surface
bld	blade	CO_2	carbon dioxide
c	capillary	end	conduction
cnv	convection	$cold$	cold plate
con	concentration boundary layer	$cool$	cooling capacity
$csir$	CSIR Energy Centre	cut	cut-off
cv	control volume	D	diameter
dst	distance	ed	dynamic eddy viscosity
ele	electrical	equ	equivalent
evp	evaporation	ext	external
f	fluid film	fan	fan
fmt	front surface	g	saturated vapour state
gen	generated by system	h	effective hydraulic
hot	hot plate	hyd	hydraulic
i	arbitrary placeholder	in	incoming to system
ins	insulation	int	internal
j	arbitrary placeholder	L	characteristic length
$loss$	losses	m	bulk fluid mean
max	maximum	mch	mechanical
mst	moist air	mtr	motor
out	outgoing from system	pht	photon
ply	polystyrene material	prd	fruit or vegetable produce
r	transverse	rad	radiation
rmv	removed	res	respiration
s	hydrostatic or scale	shf	shaft
sta	static	str	stored in system
sun	sun	sur	surface
t	torsion	thm	thermal boundary layer
tot	total	v	vapour or water vapour
vel	velocity boundary layer	vol	volumetric
w	evaporated water	wet	wet-bulb
wll	wall	x	parallel direction
y	yield or transverse direction	z	perpendicular direction
$\kappa\omega$	SST κ - ω model	θ	tangential direction

1 INTRODUCTION

A reliable supply of food is an essential part of society and, for this to be accomplished, it is vital for the food to be preserved after harvesting through suitable storage, particularly in hot and dry regions which tend to be unfitting for fruits and vegetables. There are many challenges to overcome in achieving adequate preservation due to specific requirements for optimal storage conditions to delay decay, which is especially concerning in developing countries where resources are often limited. So, it was appropriate to establish an initial basis for the need of an affordable form of storage and infer if there are reasons for further investigation into the possible usefulness in developing countries.

1.1 BACKGROUND

Since the food security in both developed and developing countries is completely dependent on the global supply of food, there is an emphasis on the need to continuously maintain surplus food. However, based on their physiology, certain foods will rapidly deteriorate if the optimal storage conditions for preservation are not satisfied. So, the factors associated with food physiology and preservation needed to be examined to begin to discuss the potential of an affordable form of storage.

1.1.1 DEVELOPING COUNTRIES FOOD SECURITY

Currently, more than one-third or 1.6 billion tons of the food produced globally is lost to spoilage or wastage each year and this is projected to increase to as much as 2.1 billion tons by 2030 [1, 2]. In particular, people living in poor developing countries in Africa, Asia, and Latin America encounter the greatest negative impacts from this loss due to high levels of food insecurity, as seen in Figure 1.1 [1, 2]. Food insecurity is concerned with the unavailability of food and limited or uncertain ability of people to obtain sufficient food on a day-to-day basis and, because there are many inter-related aspects, there are many challenges to overcoming the food insecurity which affects 820 million people [3]. As a result, there are many cases of severe undernourishment in developing countries with a lack of viable solutions to control spoilage and wastage by preserving the available food which is harvested [2, 3].

Considering a healthy diet, fruits and vegetables form the most integral component as they provide a surplus of important nutritive requirements including minerals, vitamins, proteins, fats, carbohydrates, and fibre [1, 2]. So, because of their beneficial role but limited availability, it is crucial for the available fruits and vegetables to be preserved without spoilage or wastage after harvesting. Unfortunately, it is estimated that between 40% and 50% (up to 80% in extreme cases) of fruits and vegetables in developing countries are currently lost due to uncontrolled deterioration [2, 5, 6].

As outlined with the physiology of fruits and vegetables in Section 1.1.3, it is discouraged to store fruits and vegetables in the same space as meats, because these foods require incompatible storage

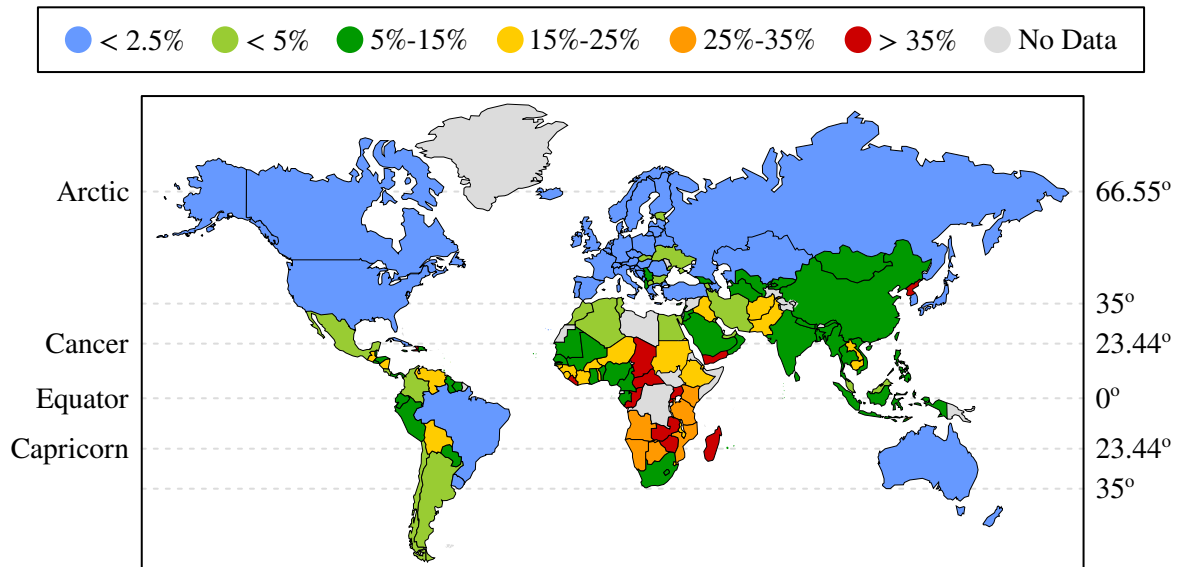


Figure 1.1: Estimations of the percentage of individuals in the total population of the respective countries classified as undernourished. The data was gathered based on three-year moving averages between 2016 and 2018 for undernourishment as the condition in which food consumption is insufficient to provide the amount of energy required to maintain a normal, active, and healthy life [4].

conditions and there is also an increased risk of cross-contamination from foreign micro-organisms [2, 7]. So, it is necessary to use independent storages to separately store fruits and vegetables apart from meats and, for the aim of this project, a focus was applied to fruits and vegetables due to their important role in a healthy diet, widespread relevance, and broad accessibility (although the prospect of meats in a healthy diet should not be disregarded without comprehensive consideration).

Also, up to 70% of the fruits and vegetables produced in developing countries are harvested through self-employment and subsistence farming on plots smaller than 0.02km² in rural areas [8, 9]. As opposed to commercial farming with production on a large-scale for multiple communities, subsistence farming is associated with production on a small-scale by family households or local clusters using primitive technologies with the aim of supplying sufficient food to satisfy the direct needs of the families or local clusters - if there is excess production, this is usually traded at markets as a supplementary benefit. This reveals that the current situation in developing countries is more inclined towards a compact and portable form of storage, rather than a large and fixed room or container for storage, where an internal volume of 50L is generally sufficient for the majority of subsistence farmers [10].

With regards to income and livelihood, there has been remarkable progress in combating poverty with the global percentage of people living in extreme poverty being 52.0% in 1981, 25.7% in 2005, and 9.2% in 2017, as expressed in Figure 1.2 with the change in poverty levels over time [9, 11, 12]. It was also reported in 2017 that approximately 0.689 billion people live on less than \$1.90/day, 1.805 billion people live on less than \$3.20/day, and 3.265 billion people live on less than \$5.50/day [12]. The majority of these people are concentrated in rural areas of Africa, South Asia, East Asia, Middle

East, and Latin America [9, 12]. Unfortunately, the recent SARS-CoV-2 pandemic is estimated to have had a significantly negative impact on reducing poverty, where it is estimated that 88 million to 115 million people are at risk of falling into extreme poverty [12]. It is also estimated that an additional 68 million to 132 million people are at risk of falling into extreme poverty by 2030 due to climate change [12]. Although there has been a decline in poverty, there are still many challenges to overcome.

The distribution of poverty is also dramatically emphasised by the gross domestic product per capita, where the lowest values were only \$782, \$984, \$1143, and \$1292 for Burundi, Central African Republic, Democratic Republic of the Congo, and Malawi respectively (excluding Syria and Venezuela) compared to the highest values of \$121293, \$101376, \$96491, and \$88241, for Luxembourg, Singapore, Qatar, and Ireland respectively for 2019 [13, 14]. This distribution of poverty highlights the disadvantages and lack of capital faced in developing countries. (These values have been adjusted for purchasing power parity to provide a measurement of the relative prices in different countries based on the purchase of a selection of goods to compare the absolute purchasing power of the currencies of these countries).

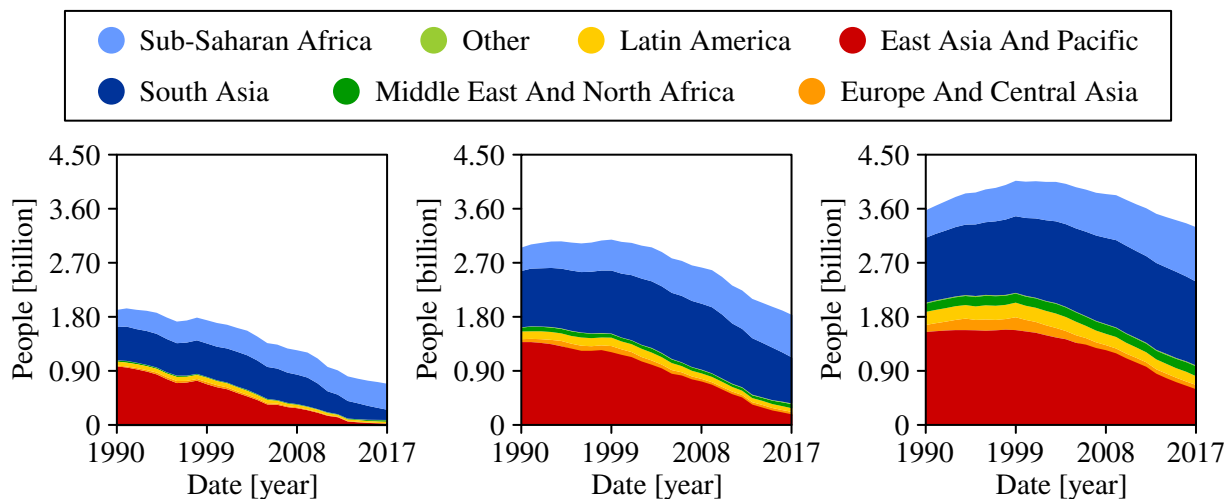


Figure 1.2: Assessment of the number of people living on less than \$1.90/day (left), less than \$3.20/day (centre), and less than \$5.50/day (right) in 2017 with stacking of the location distribution [12, 15].

1.1.2 GEOGRAPHICAL CONSIDERATIONS

As gathered from Figure 1.1, the developing countries with the highest food insecurity are situated primarily in Sub-Saharan Africa and partially in Asia and Latin America. When considering the environmental conditions, it is evident that these regions experience fairly harsh climates with conditions in Africa being the most extreme, where it is common to experience maximum air temperatures up to 45°C during the day with a low range of relative humidities below 60% during the day. An in-depth analysis of the expected environmental conditions in these regions is presented in Section 2.1.

Based on the climatic region of growth, it is possible to classify fruits and vegetables as tropical, sub-tropical, or temperate. A tropical region has a hot and wet climate and occurs around the Equator

between the Tropic of Cancer at 23.44°N and Tropic of Capricorn at 23.44°S (regions in which the Sun is directly overhead at least once during the solar year). A sub-tropical region occurs from the Tropic of Cancer to approximately 35°N and from the Tropic of Capricorn to approximately 35°S. A temperate region has a mild and diverse climate and occurs in the middle latitudes between the sub-tropics and the polar regions at approximately 66.55°N and 66.55°S. Due to their accustomed climate during growth, tropical and sub-tropical fruits and vegetables often lack the ability to adequately adapt to grow in low temperature environments, while temperate fruits and vegetables are generally more hardy and grow under a wider range of climates [7]. Table 1.1 shows some common fruits classified as tropical, sub-tropical, or temperate according to their climatic region of growth.

Table 1.1: Classification of common fruits according to their climatic region of growth [7].

Climatic Region	Example Fruits
Tropical	Banana, carambola, cashew apple, durian, granadilla, guava, longan, lychee, mango, mangosteen, papaya, pineapple, rambutan, sapodilla, and tamarind.
Sub-Tropical	Avocado, breadfruit, cherimoya, fig, grapefruit, jackfruit, kiwifruit, lemon, lime, mandarin, olive, orange, pomegranate, pummelo, and tangerine.
Temperate	Apple, apricot, blackberry, blueberry, chestnut, cranberry, grapes, nectarine, mulberry, peach, pear, plum, quince, raspberry, strawberry, and sweet cherry.

1.1.3 FRUIT AND VEGETABLE PHYSIOLOGY

From a botanical view, a fruit or vegetable is a living, respiring, and edible tissue which has been detached from its parent plant - a fruit contains the seed or its envelope while a vegetable does not [2, 16]. The physiology of fruits and vegetables can be evaluated through their observed quality based on odour, flavour, appearance, firmness, texture, and nutrient content [1, 7]. After a fruit or vegetable has been detached, the metabolic processes continue to occur during this post-harvest period which leads to the physiology of the fruit or vegetable changing through maturing and senescence processes [16, 17]. Eventually, the fruit or vegetable deteriorates to such an extent that it is considered unsuitable, or even unsafe, for consumption and it has seemingly spoiled and reached the end of its shelf life.

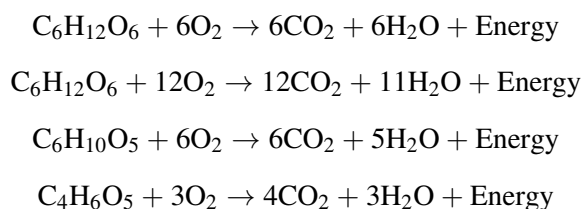
The rate at which quality deteriorates is dependent on the type of fruit or vegetable and storage conditions after harvesting, where the processes inducing the deterioration may be micro-biological, enzymatic, chemical, or physical [1, 7, 18, 19]. There is deterioration from micro-biological processes due to the growth of micro-organisms, where the optimal growth occurs between 20°C and 45°C, as seen in Table 1.2 - it is possible to differentiate between spoilage micro-organisms, which include bacteria, fungi, yeasts, moulds, phages, and protozoa; and pathogenic micro-organisms, which proliferate foodborne diseases [1, 7, 18, 19]. There are also enzymes naturally present in fruits and vegetables to aid in the ripening processes, but these enzymes will cause the fruits and vegetables to over-ripen and deteriorate if they are not consumed within their shelf life [7, 18]. A chemical process occurs when

the fruits and vegetables are exposed to and react with air which leads to oxidation with undesirable changes to the flavour, appearance, and nutrient content [18]. If the fruits and vegetables are exposed without a clean enclosure, there may also be physical damage from insects and pests directly eating the fruits and vegetables or indirectly spreading diseases by interacting with the fruits and vegetables [18]. Furthermore, the fruits and vegetables may undergo physical abuse with internal bruising and cracking in the peel, skin, or shell from bumps and vibrations if they are not safely housed in an enclosure designed for transportation [7, 18]. However, while each of these processes are concerning, the overriding priority is always to minimise or inhibit the growth of micro-organisms [19].

Table 1.2: Typical micro-organism growth rate at various temperatures, where each micro-organism has a minimum temperature below which growth is suppressed, optimal temperature at which there is peak and rapid growth, and maximum temperature above which growth is suppressed [1]. The majority of unwanted micro-organisms are mesophilic with peak growth from 20°C to 45°C.

Micro-Organism	Minimum Temp. [°C]	Optimal Temp. [°C]	Maximum Temp. [°C]
Psychrophiles	-3.7	10.8	20.1
Mesophiles	14.9	37.4	44.9
Thermophiles	43.0	68.2	80.1
Hyperthermophiles	66.5	90.7	105.6

The respiration process in fruits and vegetables involves the oxidation of energy-rich substrates, such as carbohydrates, sugars, starch, and organic acids, to molecularly simpler products with the exothermic production of energy - this transformation actually occurs through many metabolic processes with the participation of different enzymes, where the optimal temperature range for most enzymatic reactions is between 30°C and 40°C [2, 7]. Overall reactions common in many fruits and vegetables are the oxidation of glucose, sucrose, starch, or malate to produce carbon dioxide and water with the release of energy [2, 7, 16]. The water remains within the tissue, but the carbon dioxide escapes and accounts for mass losses in the range of 3% to 5% [2]. The chemical balances are respectively described as follows:



This presents a concern as the released energy contributes to heating which then increases the temperature of the surrounding air - approximately 40% to 60% of the released energy is dissipated as heat [2, 7]. As demonstrated in Figure 1.3, the rate of respiration varies based on the type of the fruits and vegetables and is also highly dependent on temperature, where the trend of van't Hoff's rule is generally observed - van't Hoff's rule states that the rate of a chemical reaction, such as respiration,

approximately doubles for each 10°C rise in temperature [2]. So, it is possible to measure the rate at which carbon dioxide is produced by a specific fruit or vegetable relative to the mass of the fruit or vegetable, which then allows for a reliable estimation of the rate at which heat is dissipated.

Based on these ideas, experimental correlations were developed by Becker and Fricke [20] and replicated in Equation 1.1 to estimate the production rate of carbon dioxide and Equation 1.2 to estimate the rate of heat dissipation from respiration assuming from the chemical reaction of sugar and oxygen that there is 2667kJ of heat generated for every 6mol of carbon dioxide produced. The necessary correlation coefficients are included in Table 1.3 for selected fruits and vegetables [2, 7]. Alternatively, a collection of production rates of carbon dioxide at various temperatures are listed in Table 1.4 for common fruits and vegetables. Also, since respiration is related to metabolic processes, the rate of respiration can often be an indicator of shelf life, where a higher respiration rate corresponds with a shorter shelf life and a lower respiration rate corresponds with a longer shelf life [2, 7].

$$\dot{m}_{CO_2} = 2.7778 b_1 m_{prd} (1.8T/K - 459.67)^{b_2} \times 10^{-10} \text{ kg}_{CO_2}/\text{kg}_{prd}/\text{s} \quad (1.1)$$

$$\dot{Q}_{res} = 10.7 \dot{m}_{CO_2} \times 10^6 \text{ J/kg}_{CO_2} = 2.9722 b_1 m_{prd} (1.8T/K - 459.67)^{b_2} \times 10^{-3} \text{ J/kg}_{prd}/\text{s} \quad (1.2)$$

Table 1.3: First and second respiration correlation coefficients for common fruits and vegetables for the experimental correlations for the heat of respiration in Equation 1.1 and Equation 1.2 [2, 7, 20].

Fruit / Vegetable	Correlation Coefficient		Fruit / Vegetable	Correlation Coefficient	
	b_1	b_2		b_1	b_2
Apple	5.6871×10^{-4}	2.5917	Lime	2.9834×10^{-8}	4.7329
Bell Pepper	3.5104×10^{-4}	2.7414	Onion	3.6680×10^{-4}	2.5380
Blueberry	7.2520×10^{-5}	3.2584	Orange	2.8050×10^{-4}	2.6840
Brussels Sprout	2.7238×10^{-3}	2.5728	Peach	1.2996×10^{-5}	3.6417
Cabbage	6.0803×10^{-4}	2.6183	Pear	6.3614×10^{-5}	3.2037
Carrot	5.0018×10^{-2}	1.7926	Plum	8.6080×10^{-5}	2.9720
Grapefruit	3.5828×10^{-3}	1.9982	Potato	1.7090×10^{-2}	1.7690
Grapes	7.0560×10^{-5}	3.0330	Sugar Beet	8.5913×10^{-3}	1.8880
Green Beans	3.2828×10^{-2}	2.5077	Strawberry	3.6683×10^{-4}	3.0330
Lemon	1.1192×10^{-2}	1.7710	Tomato	2.0074×10^{-4}	2.8350
Lima Beans	9.1051×10^{-4}	2.8900	Turnip	1.6524×10^{-4}	2.9039

In addition, fruits and vegetables are typically composed of 80% to 95% water and there is a concern for the loss of this water through transpiration. The processes of transpiration for a fruit or vegetable are driven by a difference in water vapour partial pressure between the surroundings and the surface of the fruit or vegetable and include the transport of water from the tissue and through the skin, evaporation of this water from the outer surface, and convective mass transport of the water to the surroundings [16,

Table 1.4: Experimental rate of carbon dioxide production due to respiration at various temperatures for common fruits and vegetables [2, 7, 16]. (*) Appropriate data could not be reliably sourced.

Fruit / Vegetable	Temperature [°C]					
	0	4 - 5	10	15 - 16	20 - 21	25 - 27
	CO ₂ Production Per Unit Total Mass [mgCO ₂ /kg _{prd} /hr]					
Apple	3 - 6	5 - 11	14 - 20	18 - 21	20 - 41	25 - 27
Avocado	*	*	20 - 40	*	80 - 120	*
Banana (green)	*	*	*	21 - 23	33 - 35	*
Banana (ripe)	*	*	21 - 39	25 - 75	33 - 142	50 - 245
Bell Pepper	*	*	10 - 20	*	40 - 80	*
Broccoli	19 - 21	32 - 37	75 - 87	161 - 186	278 - 320	*
Cabbage	4 - 6	9 - 12	17 - 19	20 - 32	28 - 49	49 - 63
Carrot	*	*	10 - 20	*	40 - 80	*
Cauliflower	16 - 19	19 - 22	32 - 36	43 - 49	75 - 86	84 - 140
Cucumber	*	*	23 - 29	24 - 33	14 - 48	19 - 55
Eggplant	*	*	10 - 20	*	40 - 80	*
Garlic	4 - 14	9 - 33	9 - 10	14 - 29	13 - 25	*
Grapes	1 - 2	3 - 6	8	10 - 12	*	25 - 30
Grapefruit	*	*	7 - 9	10 - 18	13 - 26	19
Green Beans	10 - 30	20 - 36	*	100 - 125	133 - 142	50 - 245
Lemon	*	*	11	10 - 23	19 - 25	20 - 28
Lime	*	*	*	6 - 10	7 - 10	15 - 45
Mango	*	10 - 12	*	45	75 - 151	120
Mushroom	28 - 44	71	100	*	264 - 316	*
Okra	*	52 - 59	86 - 95	138 - 153	248 - 274	138 - 362
Onion (dry)	3	3 - 4	7 - 8	10 - 11	14 - 19	27 - 29
Onion (green)	10 - 32	17 - 39	36 - 62	66 - 115	78 - 178	98 - 210
Orange	2 - 5	4 - 7	6 - 9	13 - 24	22 - 34	25 - 40
Papaya	4 - 6	*	15 - 32	20 - 40	*	39 - 58
Pear	47 - 75	79 - 98	*	*	349 - 556	*
Pineapple	*	2	4 - 7	10 - 16	19 - 29	28 - 43
Potato	*	3 - 9	7 - 10	6 - 12	8 - 16	*
Sweet Corn	30 - 51	43 - 83	104 - 120	151 - 175	268 - 311	282 - 435
Sweet Potato	*	*	14	20 - 24	*	*
Tomato (green)	*	5 - 8	12 - 18	16 - 28	28 - 41	35 - 51
Tomato (ripe)	*	*	13 - 16	24 - 29	24 - 44	30 - 42
Watermelon	*	3 - 4	6 - 9	*	17 - 25	*

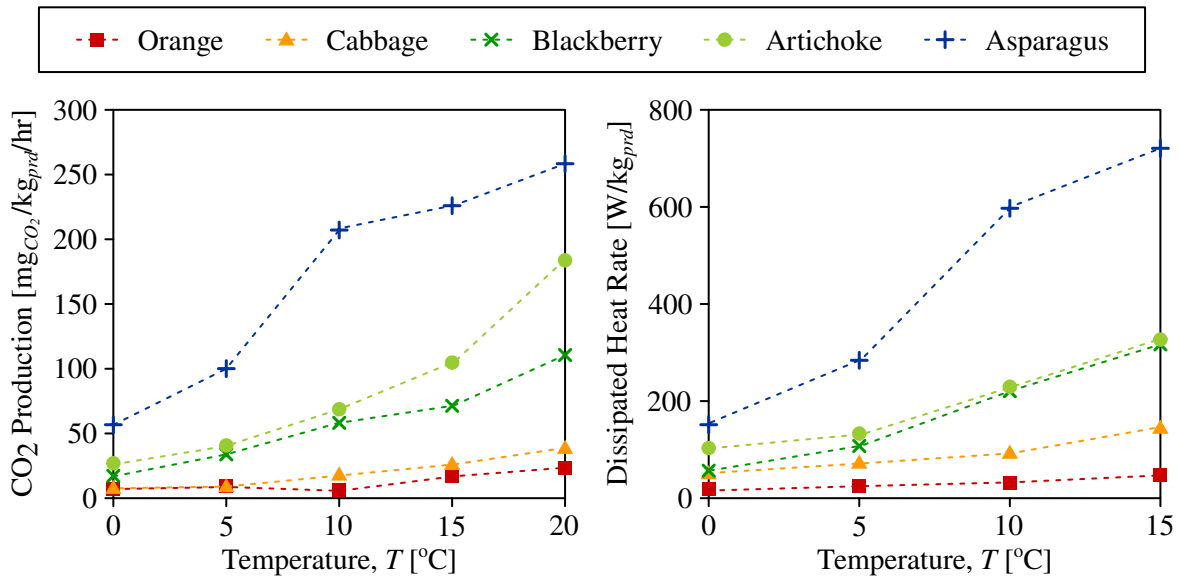


Figure 1.3: Examples of the effect of temperature on the rate of carbon dioxide production (left) and the rate of heat dissipation (right) due to respiration for selected fruits and vegetables [7].

20]. If transpiration is not managed, there can be significant implications with the prompting of wilting, mass losses, decreased crispness, and lower succulence with deteriorations in flavour, appearance, firmness, and texture - these symptoms usually become visible once 5% to 10% of the stored water has been lost [2, 7, 16, 20]. Naturally, there is also less water stored within the tissue as transpiration occurs and this biological stress induces accelerated maturing and senescence processes [2, 7].

There are epicuticular waxes on and cuticle layers in the skin of a fruit or vegetable which act as a barrier to restrict the water loss from the underlying tissue, as described in Figure 1.4, while also offering protection against excessive rain and sunburn from ultraviolet radiation and decreasing the susceptibility for attacks from fungi, pathogens, and pests [21]. During storage, the most effective method of retarding transpiration is by controlling the relative humidity and air movement such that a minimal amount of stored water is lost under the optimal conditions. A high relative humidity is generally required and one of the simplest means of achieving this is actually by decreasing the temperature. The rate of transpiration is directly proportional to the skin moisture transfer which, in

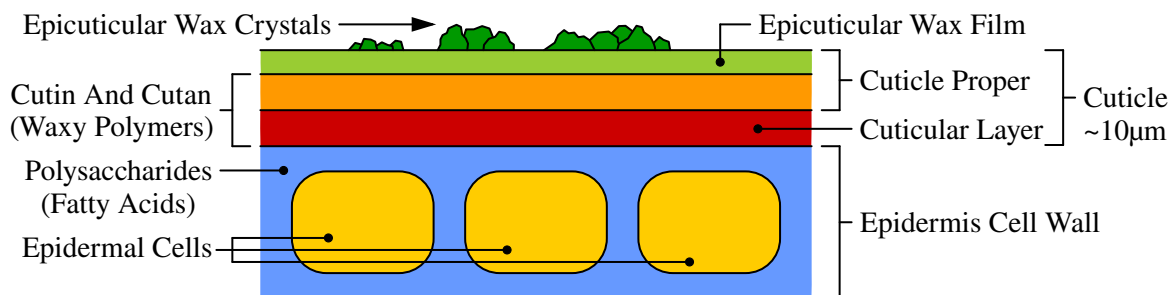


Figure 1.4: Microscopic structure of the skin of most fruits and vegetables with epicuticular waxes and cuticle layers acting as a barrier to restrict the water loss from the underlying tissue [21].

turn, can be related to the air movement, where a lower air movement within the storage corresponds with a lower skin moisture transfer and rate of transpiration [2, 7, 20]. In other words, it has been found that the skin moisture transfer increases at a logarithmic rate with increases in the air movement. For an explicit relationship, the skin moisture transfer can be seen as a transpiration coefficient which is equivalent to the reciprocal of the resistance to water loss through transpiration [7, 20].

1.1.4 FRUIT AND VEGETABLE PRESERVATION

Food preservation is essentially the method of maintaining food at a desired level of quality for as long as possible, such that the food remains in a suitable state for consumption [2, 7]. With regards to fruits and vegetables, this quality is related to retaining the physiology and nutrient content through controlling the temperature, relative humidity, air movement, light exposure, and atmospheric composition. In addition, it is vital to reduce the chances of contracting foodborne diseases by ensuring the storage environment is isolated, clean, and hygienic [1, 2, 7, 18]. For observations of quality, the *Color Atlas Of Postharvest Quality Of Fruits And Vegetables* by Nunes [21] can be used as a reference, as it provides visual comparisons of the degradation of several fruits and vegetables over time.

Among these factors contributing to preservation, temperature is definitively the most important and provides the most effective means of extending shelf life and limiting the loss of quality [1, 2, 7]. Temperature is able to affect preservation, because the rates of metabolic (micro-biological, enzymatic, and chemical), respiration, and transpiration processes decrease as the storage temperature is decreased and, correspondingly, this creates a decrease in the growth of micro-organisms with a delay in the rate of deterioration [1, 7, 18]. As seen in the samples in Figure 1.5 and Table 1.5, there is an optimal temperature range to store a given fruit or vegetable, where storage at temperatures above this range results in less effective preservation and storage at temperatures below this range results in irreversible chilling or freezing injuries. These injuries can result in pitting, browning, scalding,

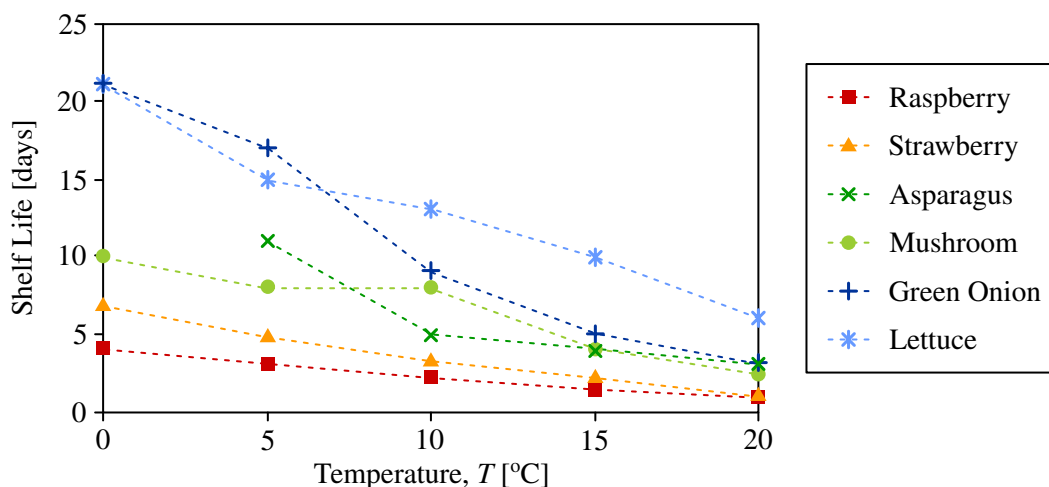


Figure 1.5: Examples of the effect of temperature on shelf life for selected fruits and vegetables [7]. These fruits and vegetables, except for asparagus, experience chilling injuries at very low temperatures.

Table 1.5: Optimal storage conditions for common fruits and vegetables with specific consideration for harvesting in harsh climates [1, 7, 16, 17]. Chilling injuries occur below the optimal temperature, while freezing injuries occur below the freezing point. (*) Appropriate data could not be reliably sourced.

Fruit / Vegetable	Temper. [°C]	Relative Humidity [%]	Optimal Shelf Life [weeks]	Freezing Point [°C]	Respiration Production	Respiration Sensitivity
Apple	-1 - 5	90 - 95	7 - 24	-1.5	High	Yes
Avocado	4.5 - 13	85 - 95	2 - 8	-0.9	High	Yes
Baby Marrow	6 - 10	90 - 95	1 - 2	-1.7	*	*
Banana	13 - 15	90 - 95	1 - 4	-0.8	Low	No
Bell Pepper	7 - 13	90 - 95	2 - 3	-0.7	None	No
Chilli Pepper	0 - 10	60 - 70	2 - 3	-0.7	None	Yes
Cucumber	7 - 12	90 - 95	2	-0.5	Low	Yes
Eggplant	8 - 12	90 - 95	1 - 2	-0.8	None	Yes
Granadilla	7 - 10	85 - 90	3 - 5	-0.9	*	*
Green Beans	3 - 7	95	1	-0.7	None	Yes
Guava	5 - 10	90	2 - 3	*	Medium	Yes
Leafy Greens	0 - 10	95 - 100	1 - 2	-0.6	None	Yes
Lemon	10 - 13	85 - 90	4 - 24	-1.4	Low	No
Lime	9 - 13	85 - 90	6 - 8	-1.6	Low	No
Mango	13	85 - 95	2 - 3	-1.4	Medium	Yes
Melon	7 - 13	85 - 90	2 - 4	-1.1	Low	Yes
Okra	7 - 10	90 - 95	1 - 2	-1.8	Low	Yes
Olives	6 - 10	85 - 90	4 - 6	-1.4	*	*
Orange	4 - 10	85 - 95	3 - 8	-0.8	Low	No
Papaya	7 - 13	85 - 90	1 - 3	*	Medium	Yes
Peas	4 - 5	95	1	-0.6	None	Yes
Pineapple	7 - 13	85 - 90	2 - 4	-1.1	Low	No
Plantain	13 - 15	90 - 95	1 - 5	-0.8	Low	No
Pomegranate	5 - 10	90 - 95	8 - 12	-3.0	None	No
Potato	4 - 12	90 - 95	20 - 32	-0.8	None	Yes
Pumpkin	12 - 15	50 - 70	8 - 12	-0.8	None	Yes
Squash	7 - 11	95	1 - 2	-0.5	None	Yes
Sweet Potato	13 - 15	85 - 95	16 - 28	-1.3	None	Yes
Tangerine	4 - 7	85 - 95	2 - 4	-1.1	Low	No
Tomato	9 - 14	85 - 95	1 - 3	-0.5	Medium	No
Watermelon	10 - 21	90	2 - 3	-0.4	None	Yes
Yam	15	70 - 80	8 - 28	-1.1	None	Yes

thawing, discolouration, darkening of the skin, changes in the flavour and texture, loss of ripening ability, and destruction of nutrient content [7]. The temperatures at which these injuries occur should be carefully avoided with a high safety threshold - this is particularly relevant to tropical and sub-tropical fruits and vegetables at temperatures below 12°C [1, 2, 7]. It is also desirable for the temperature to remain fairly constant, ideally within a range of 4°C but acceptably within a range of 8°C, as erratic fluctuations can cause rapid mass and water loss [2]. A more comprehensive list of optimal storage conditions for various fruits and vegetables is included in Table A.1 in Appendix A. (For supplement, the optimal temperature range for dry foods is usually from 10°C to 21°C with shelf lives extending for several months - including nuts, powdered milk, yeast, cereal grains, spices, jams, and flour [1]).

For the majority of fruits and vegetables, a high relative humidity above 85% is preferable for optimal preservation, otherwise there is a major risk of stored water being lost from the fruits and vegetables to the surrounding air, which would cause mass losses, shrivelling, and limping - although this introduces a minor risk of micro-organisms growing on the exposed surfaces [2, 7]. It is also crucial to maintain low air movement to reduce transpiration, although adequate circulation is still recommended to remove respiratory heat generated by the fruits and vegetables [2, 7, 20]. Moreover, a selection of fruits and vegetables are highly sensitive to light exposure from direct solar radiation, which can lead to colour distortions, oxidation of fats, and destruction of nutrient content due to the short-wave ultraviolet radiation which has excess energy to cause photochemical damage to cells [2, 18]. Unfortunately, it is often difficult to control the atmospheric composition to which the fruits and vegetables are exposed, unless specialised packaging with atmosphere modification or pressurisation are employed.

As a result of different optimal storage conditions, there is a concern for the compatibility of certain fruits and vegetables to be stored together. Overall, the main factors which determine compatibility are optimal temperature, optimal relative humidity, production of respiration products, sensitivity to respiration products, production of odours or flavours, and sensitivity to odours or flavours. Several collections of compatible groups are listed in Table 1.6. There may be overlaps between groups if slightly sub-optimal storage conditions are tolerable and, in a general sense, fruits and vegetables with low chilling temperatures are mostly compatible with fruits and vegetables with higher chilling temperatures (especially during short-term storage), but fruits and vegetables with high chilling temperatures are mostly incompatible with fruits and vegetables with lower chilling temperatures.

Apart from controlling the storage conditions and general hygiene through cleaning, there are also alternative processing techniques to accomplish food preservation, such as drying, curing, waxing, acidifying, blanching, surface coating, alcoholic fermenting, sterilizing, adding preservatives, adding anti-oxidants, controlling pH levels, high voltage electric discharging, and ionizing irradiation [1, 2, 7, 16, 19]. However, these techniques frequently present drawbacks with the loss of physiology and nutrient content in some form, applicability to specific types of food which usually exclude fruits and vegetables, and difficulties in implementing flexibly and affordably on a small-scale [1].

Table 1.6: Compatibility for fruits and vegetables sharing optimal conditions during storage [7, 17].

Temperature [°C]	Relative Humidity [%]	Fruits / Vegetables
0 - 2	90 - 95	Apple, apricot, beets, berries (except cranberries), cashew apple, cherries, coconut, grapes, horseradish, kohlrabi, leek, longan, loquat, lychee, mushroom, nectarine, orange, parsnip, peach, pear, plum, pomegranate, prune, quince, radish, rutabaga, and turnip.
0 - 2	95 - 100	Amaranth, anise, artichoke, asparagus, bean sprouts, bok choy, broccoli, brussels sprout, cabbage, carrot, cauliflower, celeriac, celery, sweet corn, daikon, endive, escarole, kiwifruit, grapes, leafy greens, lettuce, lo bok, mushroom, onion, parsley, parsnip, peas, pomegranate, raddichio, radish, rhubarb, rutabagas, salsify, scorzonera, spinach, turnip, water chestnut, and watercress.
5	90 - 95	Cactus leaves, cactus pear, caimito, cantaloupe, clementine, cranberries, lemon, lychee, kumquat, mandarin, orange, pepino tamarillo, tangelo, tangerine, ugli fruit, and yucca root.
10	85 - 90	Calamondin, chayote, cucumber, eggplant, haricot vert, horned melon, kiwano, legume beans, malanga, okra, olive, bell pepper, potato, pummelo, squash, tamarind, and taro root.
13 - 15	85 - 90	Atemoya, avocado, babaco, baby marrow, banana, bitter melon, black sapote, boniato, breadfruit, canistel, carambola, cherimoya, coconut, cucumber, feijoa, ginger, granadilla, grapefruit, guava, jaboticaba, jackfruit, langsat, lemon, lime, mango, mangosteen, melon, papaya, pineapple, plantain, potato, pumpkin, rambutan, santol, soursop, sugar apple, squash, tomatillo, and tomato.
18 - 21	85 - 90	Jicama, pear (for ripening), potato, sweet potato, tomato (mature green), watermelon, white sapote, and yam.

1.1.5 CONVENTIONAL REFRIGERATION

Currently, the most common conventional method of refrigeration is a vapour-compression cycle, but there are also systems which successfully implement a vapour-absorption cycle. Both of these cycles operate between a cold region and hot region, where heat is transferred to a refrigerant from the cold region and then from the refrigerant to the hot region, which allows for temperatures below -20°C to be maintained depending on the design specification. Unfortunately, these technologies are difficult and practically infeasible to implement on an extremely affordable, compact, and portable scale.

A vapour-compression cycle is based on a Carnot vapour-refrigeration cycle which operates using a refrigerant with a compressor, condenser, turbine, and evaporator. The refrigerant enters the evaporator as a liquid-vapour mixture and partly transitions from a saturated liquid to a saturated vapour as a result of heat transfer from the cold region to the refrigerant, while the temperature and pressure

of the refrigerant remain constant. The refrigerant then enters the compressor and is adiabatically compressed from the liquid-vapour mixture to a saturated vapour and the temperature increases from the temperature of the cold region to the temperature of the hot region with an accompanying increase in pressure. The refrigerant enters the condenser, where it changes from the saturated vapour to a saturated liquid as a result of heat transfer from the refrigerant to the hot region, while the temperature and pressure of the refrigerant remain constant. Finally, the refrigerant expands adiabatically through a turbine as a liquid-vapour mixture, where the temperature decreases from the temperature of the hot region to the temperature of the cold region with an accompanying decrease in pressure.

However, there are minor differences between a vapour-compression cycle and Carnot vapour refrigeration cycle. Firstly, instead of performing compression with a liquid-vapour mixture, it is more effective to heat the refrigerant to a saturated vapour state after the evaporator and perform compression with a superheated vapour, as this utilises dry compression instead of wet compression and avoids damages from liquid droplets. Secondly, the work generated by the turbine is sacrificed in favour of a simpler expansion or throttling valve, which allows for uncontrolled expansion of the refrigerant through an isenthalpic process. These departures are shown in the schematic in Figure 1.6.

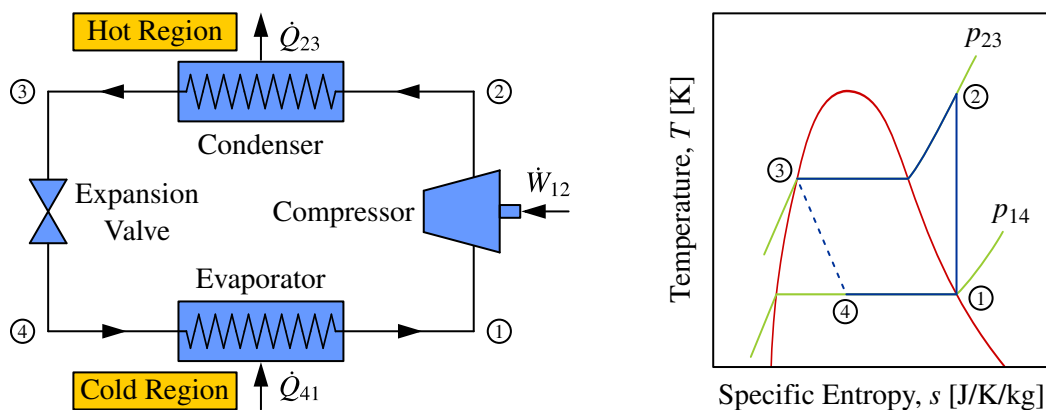


Figure 1.6: Schematic of a vapour-compression cycle (left) and depiction on a temperature against entropy diagram (right). The processes are assumed to be internally reversible at steady state and the area under a process line can be interpreted as the heat transfer per unit mass for the process.

A vapour-absorption cycle shares some characteristics with a vapour-compression cycle, but there are distinct differences in the compression stage. Instead of compressing the refrigerant as a superheated vapour between the evaporator and condenser, the refrigerant in a vapour-absorption cycle is absorbed as a saturated vapour by a subcooled liquid absorbent to form a mixture which is then pumped to the higher pressure. Because the average specific volume of the mixture is much less than the specific volume of the refrigerant as a superheated vapour, there is significantly less work required by the pump compared to the work required for a compressor in a vapour-compression cycle.

Although, it is also required for a means to separate the refrigerant from the mixture as a superheated vapour before it enters the condenser. This can be achieved through heat transfer from a hot body

which causes the refrigerant to transition to a superheated vapour while the absorbent remains as a subcooled liquid. So, a strong solution of the mixture enters a generator which receives heat transfer from a hot body and causes the refrigerant to exit the generator as a superheated vapour and a weak solution of the mixture to return to the absorber. A schematic of the processes is shown in Figure 1.7 with the relevant components (a rectifier could be included to remove any remaining traces of the absorbent and ensure that only the refrigerant as a superheated vapour enters the condenser).

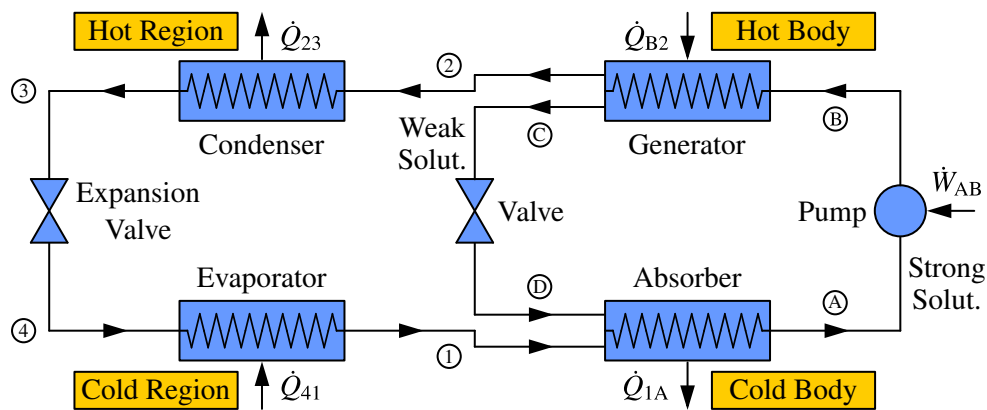


Figure 1.7: Schematic of a vapour-absorption cycle. Depending on the refrigerant and absorbent, the absorption may be exothermic and it would be appropriate for cooling to maintain a low temperature.

For a vapour-compression cycle, it is most common for either ammonia, R-134a, carbon dioxide, or hydrocarbons to be used as the refrigerant [24, 25]. For a vapour-absorption cycle, it is most common for either ammonia and water or water and lithium bromide to be used as the refrigerant and absorbent respectively [24, 26]. Due to environmental concerns, chlorofluorocarbons (CFCs) and hydrochlorofluorocarbons (HFCs) are avoided, although many of the environment-friendly alternatives compromise with other disadvantages related to toxicity, flammability, lower efficiency, or increased costs [24, 25]. This highlights another obstacle of conventional methods of refrigeration.

Table 1.7: Comparison between the typical properties of conventional refrigeration with the Dometic CFX3 40 for vapour-compression cycles and Dometic ACX 40 for vapour-absorption cycles [22, 23].

Conventional Refrigerator	External Size [mm]	Internal Volume [L]	Empty Mass [kg]	Min. Temperature [°C]	Power Required [W]	Cycle Refrigerant	Purchase Cost [€]
Dometic CFX3 40 (Compression Cycle)	694 × 398 × 500	40	18.7	-22 - 10	100	R134a	800
Dometic ACX 40 (Absorption Cycle)	508 × 444 × 500	40	15.0	$T_a - 30$	85	Ammonia Water	335

To provide examples of the typical properties of conventional refrigeration, the Dometic CFX3 40 and Dometic ACX 40 use a vapour-compression cycle and vapour-absorption cycle respectively and their specifications are listed in Table 1.7 [22, 23]. These units are aimed at being small-scale for transportation compared to larger and dedicated units like consumer refrigerators. However, their high mass from 15kg for an internal volume of only 40L makes them completely unsuitable as compact and portable solutions. Also, they have significant purchase costs over \$400 with up to 100W required for operation which makes them quite inappropriate as extremely affordable solutions.

1.1.6 PROMISING ALTERNATIVE TECHNOLOGIES

A promising technology which has been shown to provide encouraging performance for preserving fruits and vegetables is evaporative cooling. Briefly, the process of evaporative cooling involves utilising the phenomenon of evaporation, where the energy required to initiate evaporation is used to produce an overall cooling effect with the potential to achieve a temperature decrease of as much as 15°C under favourable conditions [2, 27]. The potential of evaporative cooling is maximised in dry regions with high temperatures above 25°C and low relative humidities below 50% [7].

It was estimated by Rao [2] that, although a difference in performance capacity is acknowledged, conventional refrigeration systems have a purchase cost up to four times greater and running costs between six to eight times greater than the costs for an evaporative cooling system. In this regard, the World Bank and the Food and Agriculture Organisation of the United Nations have advocated for evaporative cooling as an inexpensive alternative for the storage of fruits and vegetables [28, 29].

There are numerous self-constructed designs using evaporative cooling, such as the Zeer Pot, and there are a variety of commercial products which have recently been launched for the purpose of affordable refrigeration, such as the Bosch FreshBox and Fenik Yuma Cooler. But, these designs and products are reported to achieve a temperature decrease around only 10°C under optimal conditions, while the performance can decrease drastically under less ideal conditions. Moreover, the designs and products employ evaporative cooling passively with natural convection, which is completely dependent on the ambient environment and leads to erratic fluctuations in performance [30]. As a result, the adoption of small-scale evaporative cooling technologies among subsistence farmers is still low and its promotion requires evidence of its effectiveness to attain suitable storage conditions and preserve the quality of fruits and vegetables [31]. Therefore, since the current designs and products only used passive evaporative cooling with natural convection, there was potential to investigate the viability of active evaporative cooling with forced convection by developing a solution focused on this for increased and more predictable performance while remaining compact, portable, and affordable.

Likewise, the merits of a thermoelectric module are also worth examining as an emerging technology. A thermoelectric module is a form of solid-state refrigeration and uses the Peltier effect to create a

temperature difference between two plates through the conversion of electrical energy at a junction across two materials to induce one plate to decrease in temperature while the other plate increases in temperature. At peak performance, it is common to achieve a cooling effect up to 20°C below the ambient temperature at the cold plate, which corresponds with a heating effect up to 20°C above the ambient temperature at the hot plate [1]. Unfortunately, this striking performance comes at the expense of a very high power consumption often requiring a dedicated electricity supply.

Overall, the advantages of thermoelectric modules are that they do not require a refrigerant, have no moving parts, and can be manufactured in a variety of sizes, which aids in achieving very high reliability, compactness, lightness, noiseless operation, precise control, low maintenance, and long life [1, 24, 32, 33]. A thermoelectric module is also inexpensive and readily available, but they tend to have high inefficiencies which leads to the high power consumption and more overhead in order to achieve an effective temperature difference [1, 24, 33]. So, the prospect of a thermoelectric module is hindered with regards to extreme affordability, but it may be useful to complement evaporative cooling.

1.2 MOTIVATION

It is clear that there is always a need for an independent form of storage to extend the shelf life of fruits and vegetables by preventing spoilage and wastage. In developed countries, there are various options and alternative methods available to offer more than adequate solutions regardless of the conditions experienced, but the options in developing countries are considerably limited or virtually non-existent and the conditions experienced are often far from conducive to providing sufficient solutions [1, 2]. In essence, there are multiple barriers preventing developing countries from utilising the established technologies from developed countries to improve the preservation of fruits and vegetables.

A primary barrier experienced in developing countries is the lack of access to a reliable electricity supply, where national electricity grids are recurrently dysfunctional and personal fuel generators are expensive, large, disrupting, unsustainable, and present many health and environmental concerns [1, 2]. When fruits and vegetables are sold and bought at markets, there is a lack of infrastructure for preservation during storage as these markets regularly take place in the shade of tents, trees, or thatched roofs [2]. In addition, it is common to commute far distances by walking as the main mode of transportation and, when travelling to and from markets, this can leave fruits and vegetables exposed for extended periods of time, often in direct sunlight [1]. The settlements are also often quasi-permanent or informal, so it is unhelpful for possessions to be large and fixed in the event of an unplanned re-location, eviction, or other form of displacement [1]. There is also a lack of capital and individuals are unable to purchase existing hardware with high purchase costs and continuous operational costs [1]. Ultimately, a form of storage which is able to adapt to these barriers while successfully preserving fruits and vegetables would increase food supply and decrease food insecurity with subsequent positive effects, such as increasing the productivity, efficiency, and monetary savings of the population [1].

As further discussed in Section 2.7, there are no existing forms of storage for fruits and vegetables which are able to completely and affordably combat the situations and conditions in developing countries. This includes implementations of evaporative cooling, which only utilise natural convection, and conventional forms of refrigeration, which are too expensive on a small-scale. Thus, there is a definitive opportunity to provide a robust solution to demonstrate the viability of using evaporative cooling with forced convection to achieve a significant cooling effect and, as a consequence, aid in ensuring healthy societies with extensive and widespread benefits in economics, education, well-being, safety, and other social aspects due to the resulting improvements in the quality of life [1, 34].

Furthermore, although these are more specialised, there are also common situations in developed countries which require a compact and portable means for fruit and vegetable storage without an external electricity supply. These situations include various outdoor activities such as geologic prospecting, archaeological studying, road constructing, and recreational scenic spot outing. However, it was acknowledged that it is most likely for acceptable performance to be already achievable using expensive existing solutions since the significance of cost is less likely to be a prominent factor.

1.3 RESEARCH QUESTION

Thus, to investigate evaporative cooling with forced convection for the storage and preservation of fruits and vegetables in developing countries, a research question was proposed as follows:

Is it viable to employ evaporative cooling utilising forced convection to achieve a significant decrease in temperature and extension of the shelf life of common fruits and vegetables in high ambient temperatures and low to moderate ambient relative humidities, where a focus is applied to small-scale, portable, and off-grid applications while maximising affordability for use in developing countries?

1.4 INITIAL TASK STATEMENT

As a secondary outcome, a feasible prototype was to be developed to act as a guide in affirming whether the research question was successfully satisfied. The following description was established as the initial task statement, where the costs were based on accounting for maximum affordability in developing countries and creating a competitive solution compared to the existing commercial products:

Investigate a device which is capable of maintaining an enclosure at a temperature less than the ambient temperature by at least 11°C through the use of evaporative cooling with water and without the need for an external electricity supply. This device is intended to be used in developing countries, where there is a variety of climates, lack of infrastructure, and requirements for portability; and the aim of the device is to preserve fruits and vegetables for an extended period of time with an internal volume greater than 45L. Naturally, the device may employ internal electricity generation through

a photovoltaic system as a catalyst for improved convective and evaporative performance, but the additional cost of this enhancement must be minimised for the device to remain affordable with a standard cost less than €19 for the materials and less than €26 for the electronic components.

2 LITERATURE REVIEW

To establish a basis from which to progress towards the optimal investigation, it was crucial to source information to develop each of the aspects of the prototype. This involved describing and defining the environmental conditions expected during operation and investigating the ergonomics of the average user to ensure the scale was usable and comfortable. It was also necessary to examine and document theories, ideas, and mechanisms behind each aspect of the processes to supplement the succession of the analysis development. Finally, existing research, designs, and prototypes were reviewed and benchmarked to aid in the identification of and solutions to common issues and misconceptions. Although many of the concepts discussed are generally applicable to fruit and vegetable preservation, it should be noted that the information is presented primarily in relation to evaporative cooling.

2.1 ENVIRONMENTAL CONDITIONS

With regards to fruit and vegetable preservation, the most important and controllable factor is temperature followed by relative humidity and, so, it was necessary to analyse the environmental conditions for the regions in which it was expected for operation. Additionally, for the potential of evaporative cooling to be evaluated, it is also necessary to know the magnitude of the incoming solar radiation in these regions. Fortunately, the Earth Observing System Data and Information System (EOSDIS) from NASA's Langley Research Center and Jet Propulsion Laboratory [35, 36] provides historical data for various environmental conditions. This data has been captured by the Aqua satellite using its Moderate Resolution Imaging Spectroradiometer, Advanced Microwave Sounding Unit, Atmospheric Infrared Sounder, and Clouds and Earth's Radiant Energy System on a scale of 32km/px to 45km/px (for daily observations, there may be incomplete data due to orbital path and atmospheric disturbances).

For an estimation of the expected environmental conditions to be experienced, the average environmental conditions were considered for each month throughout 2019 on a global basis. Although considering a single year could appear to have a marginal distortion on accuracy, it was reasoned that the expected environmental conditions are continuously deviating from past historical averages as a result of climate change due to an increased amount of greenhouse gases in the atmosphere leading to increased temperatures and subsequent anomalies [37]. So, it was fair to claim that recent historical data provides a more accurate estimation than past historical data and, since it was the second hottest year on record, 2019 presented a prime example for expected environmental conditions in the future [37]. The scale of consideration as the average over each month was also acceptable as it presented a better indication of representative results, although an eight-day scale was also available and checked to ensure there were no extreme or outlying irregularities. Furthermore, it was not overly important for very precise values, as it was only necessary for an overview to provide expectations for benchmarking and safety factors could be applied to model for the possibility of unexpected exceptions.

2.1.1 TEMPERATURE AND RELATIVE HUMIDITY

The average surface air temperature during the day is shown in Figure 2.1. In Sub-Saharan Africa, this indicates high temperatures regularly above 30°C and up to 40°C during January to March and October to December, and similar conditions are also seen in the south-eastern parts of Asia. In North Africa and the Middle East, the temperatures are very extreme and in the range of 32°C to 45°C during April to September. With regards to Latin America, the conditions are less harsh throughout the year, but there are still periodic concerns when the temperature is fairly high at 34°C.

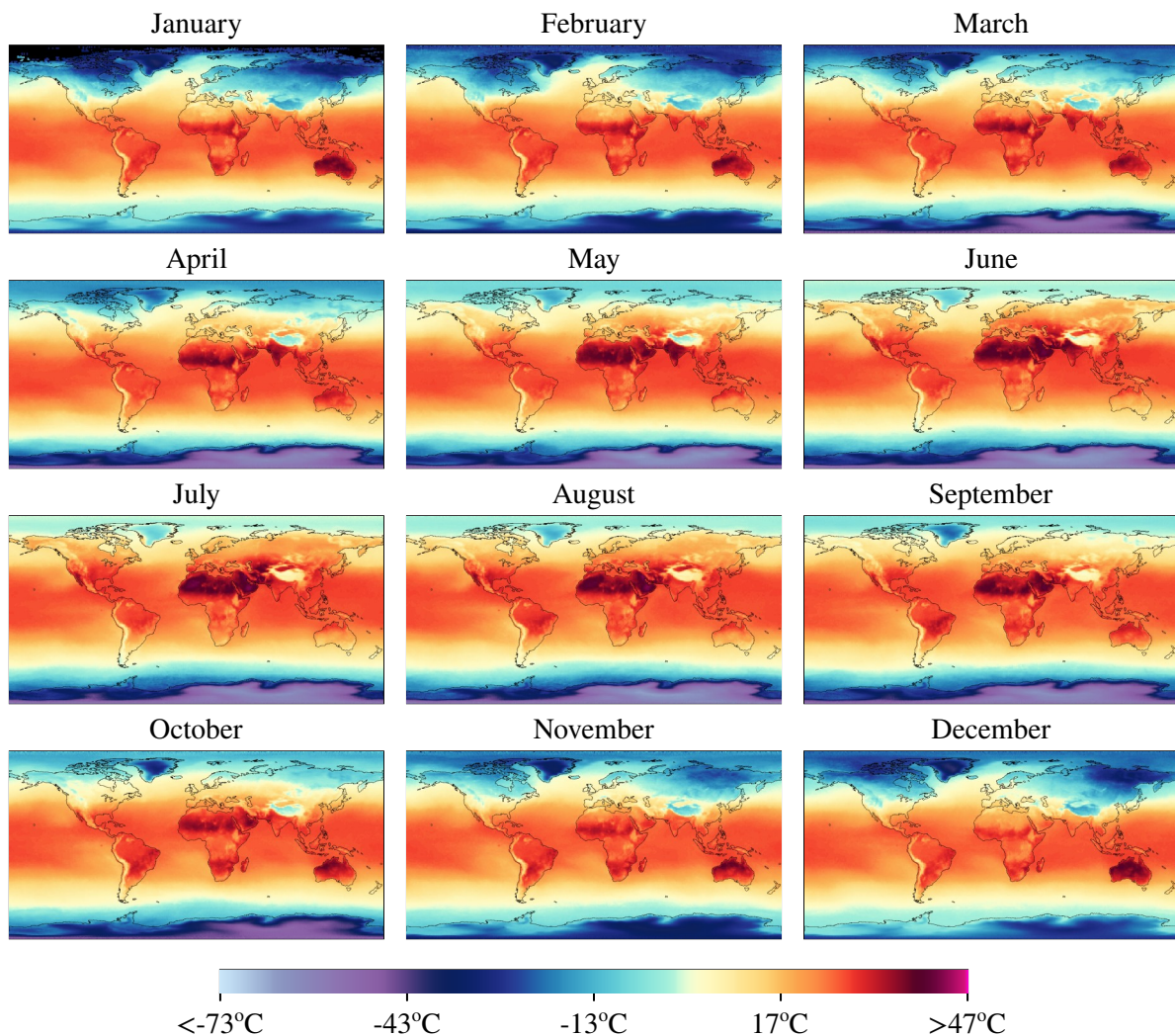


Figure 2.1: Average surface air temperature during the day for each month in 2019 [35].

The average surface relative humidity during the day, as derived from measurements of the air temperature and water vapour content of the atmosphere, is shown in Figure 2.2. In Sub-Saharan Africa, this indicates low relative humidity with consistent values below 65% throughout the year - this is particularly relevant to the southern areas with much lower values in a wider range of regions. In North Africa and the Middle East, the relative humidity is extremely minimal in the range of 0% to 30% throughout the year, as is expected given the desert climate and lack of water. Unlike with temperature,

the relative humidity in the south-eastern parts of Asia are not similar to Sub-Saharan Africa, but rather they appear to be similar to Latin America with mild values between 25% and 75% over the year. (The technical definition of relative humidity is discussed in Section 2.3).

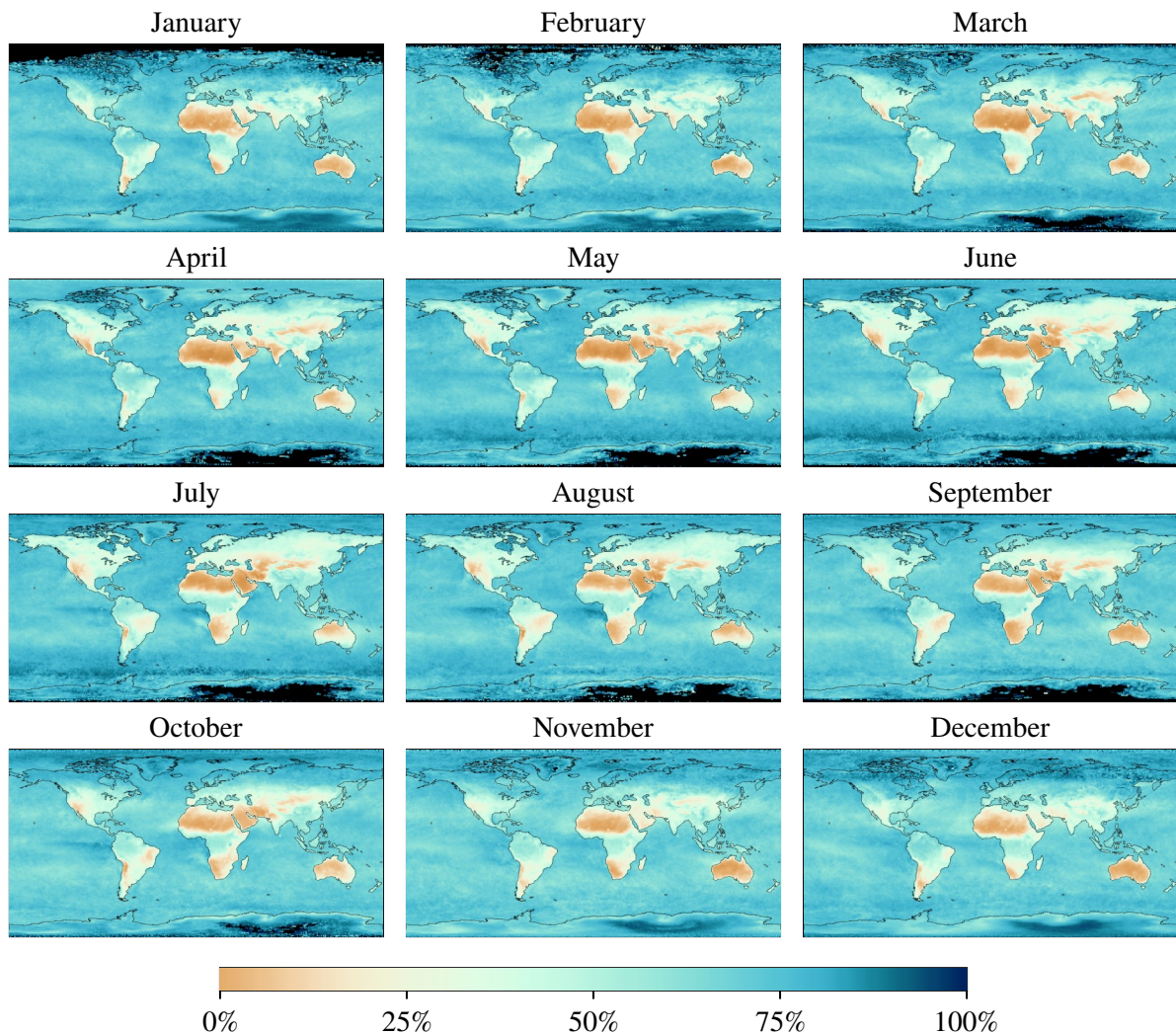


Figure 2.2: Average surface relative humidity during the day for each month in 2019 [35].

These conditions for temperature and relative humidity reveal the regions and times of year which are unfavourable for the preservation of fruits and vegetables and, notably, these regions correspond with the countries previously identified in Figure 1.1 where there is high and concerning food insecurity. The average surface air temperature and relative humidity during the night are respectively included in Figure A.1 and Figure A.2 in Appendix A and show less extreme conditions.

2.1.2 INCOMING SOLAR RADIATION

The incoming solar radiation or insolation or irradiation is a measure of the rate at which energy in the form of radiation is emitted from the Sun and incident on the surface of the Earth. This is shown in Figure 2.3, where the variation in intensity is clearly seen to be based on the tilt of the Earth and orbital cycle around the Sun. For tropical regions, the average intensity is fairly constant from 350W/m^2

to 450W/m^2 . For sub-tropical and temperate regions, there are polar opposites where the northern hemisphere experiences a maximum while the southern hemisphere experiences a minimum and the southern hemisphere experiences a maximum while the northern hemisphere experiences a minimum. In these regions, the maximum average intensity is approximately 420W/m^2 during April to September for the northern hemisphere or January to March and October to December for the southern hemisphere; and the minimum average intensity is approximately 140W/m^2 during January to March and October to December for the northern hemisphere and April to September for the southern hemisphere.

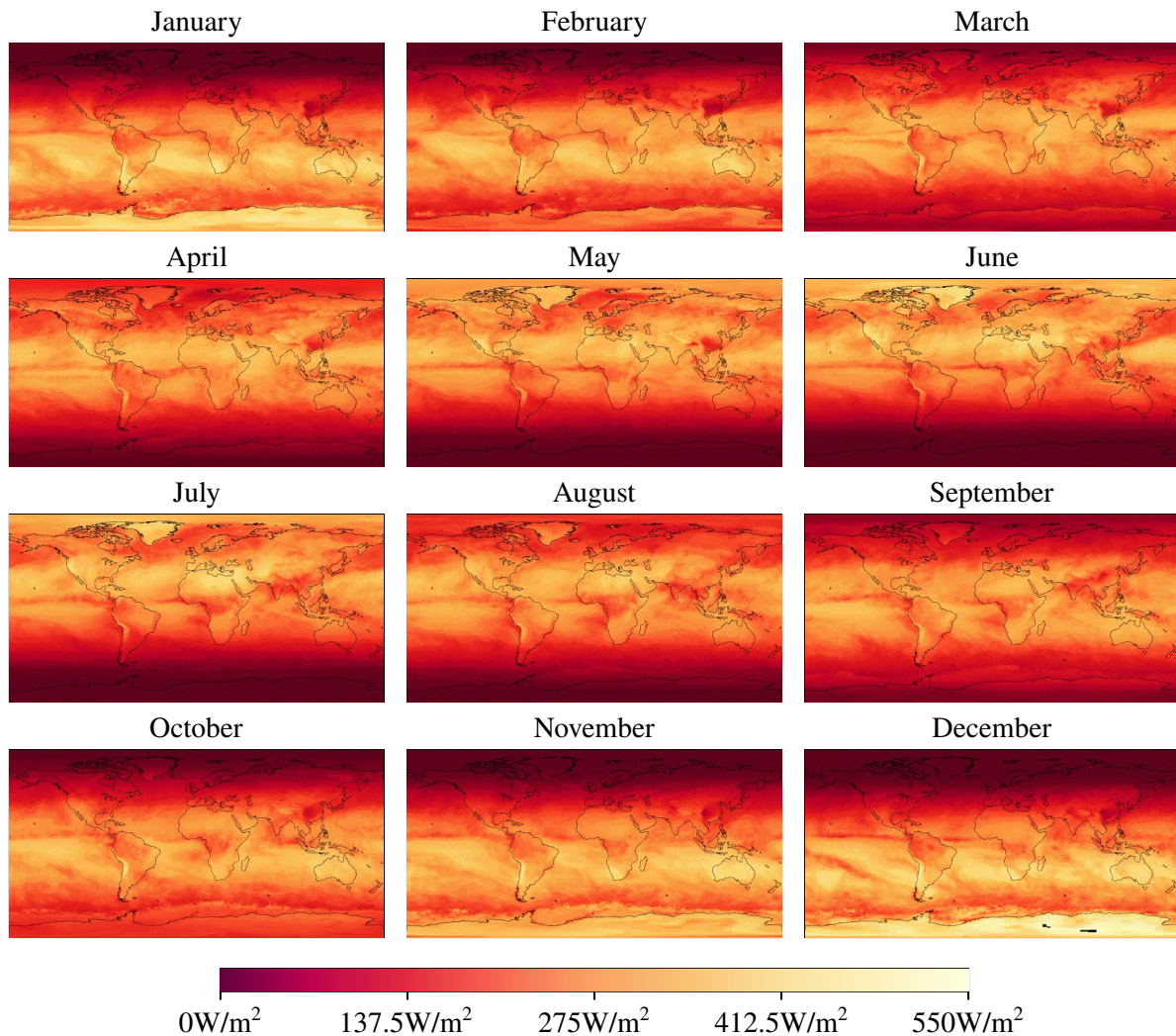


Figure 2.3: Average solar insolation during the day for each month in 2019 [36].

It should also be recognised that the maximum and minimum insolation in the northern and southern hemispheres align with the temperature conditions. In other words, maximum temperatures always occur with maximum insolation and minimum temperatures always occur with minimum insolation. The Southern African Universities Radiometric Network (SAURAN) publicly provides minute-averaged, hour-averaged, and day-averaged measurements of surface air temperature, relative humidity, wind speed and direction, direct normal insolation, diffuse horizontal insolation, and global horizontal insolation using Kipp & Zonen CMP11 pyranometers, Kipp & Zonen CHP1 pyrheliometers, and

It was also important to identify the mass an average male and female can lift, so the maximum mass of the design could be quantified based on an individual lifting the design with no external aid. Based on the definition of lifting as the act of manually grasping and raising an object of definable size, it was estimated by Mathesona et al. [41] that a male can comfortably lift up to 26.97kg while a female can comfortably lift up to 15.80kg for the 50th percentile individual between 15 years and 60 years.

2.3 PSYCHROMETRY

The analysis of systems involving dry air and water vapour is psychrometry or psychrometrics and this is essential in the design of thermodynamic processes involving the conditioning of dry air and controlling of the water vapour content. Initially, it was necessary to consider the energy and mass transfer relationships within the universe divided between a system and its surroundings. This is demonstrated through a control volume or open system, where the exchange of energy and mass is allowed, as opposed to a control mass or closed system where only the exchange of energy is allowed. Subsequently, the psychrometric applications were considered based on an ideal gas idealisation.

2.3.1 WORK, HEAT, AND ENERGY

The application of thermodynamics has been established over many centuries and is reliant on the definition of work and heat. Work is the amount of energy transferred by a mechanism through which the system can spontaneously exert forces on the surroundings or the surroundings can spontaneously exert forces on the system [24]. In addition, heat is the amount of energy transferred over the system boundary in a thermal process as a result of a temperature difference [24, 33]. This heat transfer is induced only as a result of a temperature difference between the system and its surroundings, where the process must always occur in the direction of decreasing temperature [24, 33]. (Conventionally, work done by the system on the surroundings is seen as positive, while work done by the surroundings on the system is seen as negative; and heat transferred to the system from the surroundings is seen as positive, while heat transferred to the surroundings from the system is seen as negative).

For a control volume with mass flow into and out of the system, the mass possesses internal, kinetic, and potential energies, where these energies are being exchanged from the surroundings to the system when the mass is incoming to the system and from the system to the surroundings when the mass is outgoing from the system [24]. Moreover, it is possible for the system to internally generate energy through chemical, electrical, or mechanical means, but this is often absent in simple thermodynamic systems. (Conventionally, transfer of these energies to the system from the surroundings is seen as positive, while transfer of these energies to the surroundings from the system is seen as negative).

As expressed in a general form in Equation 2.1, the conservation of energy or first law of thermodynamics states that energy cannot be created or destroyed but only transferred from one form to another,

where it is required for the total energy within the universe to always remain constant, such that energy is either released from the surroundings and stored by the system or released from the system and stored by the surroundings during a process. Thus, considering a rate balance while neglecting internal generation of energy, the rate of change of energy stored within the system must be equal to the sum of the heat transferred into the system, work done by the system, and rate at which energy is transferred with mass flow into and out of the system - this is described in Equation 2.2 [24].

$$\Delta E_{str} = E_{in} - E_{out} + E_{gen} \rightarrow \dot{E}_{str} = \dot{E}_{in} - \dot{E}_{out} + \dot{E}_{gen} \quad (2.1)$$

$$\dot{E}_{str} = \sum \dot{Q} - \sum \dot{W} + \sum \left(\dot{m} \left(u + \frac{v^2}{2} + gz \right) \right)_{in} - \sum \left(\dot{m} \left(u + \frac{v^2}{2} + gz \right) \right)_{out} \quad (2.2)$$

For the flow of a fluid, it is always required for a pressure difference between the inlets and outlets, where the fluid flows from a high pressure to low pressure. This pressure difference can be viewed as a resultant force acting on the fluid and moving through a distance and, so, there must be an accompanying component of work being performed. For simplification, it is possible to separate the components of work into the work from the flowing fluid and work from other influences affecting the system, which then allows for the convenient use of enthalpy as defined by Equation 2.3 [24]. (In accordance with the sign convention, the work done by the fluid at the inlet is negative with energy being transferred to the system from the surroundings, while the work done by the fluid at the outlet is positive with energy being transferred to the surroundings from the system).

Thus, the modified form of the rate balance is presented in Equation 2.4. At steady state, there is no change in stored energy and, so, the energy in the system must be constant - in other words, the rate of change of energy contained within the system must be zero, as shown in Equation 2.5 [24, 33].

$$H = U + pV \leftrightarrow h = \frac{H}{m} = \frac{\bar{h}}{M} = u + p\bar{v} \leftrightarrow \bar{h} = \frac{H}{n} = Mh = \bar{u} + p\bar{v} \quad (2.3)$$

$$\dot{E}_{str} = \dot{Q} - \dot{W}_{cv} + \sum \left(\dot{m} \left(h + \frac{v^2}{2} + gz \right) \right)_{in} - \sum \left(\dot{m} \left(h + \frac{v^2}{2} + gz \right) \right)_{out} \quad (2.4)$$

$$\text{Steady: } \dot{E}_{str} = 0 = \dot{Q} - \dot{W}_{cv} + \sum \left(\dot{m} \left(h + \frac{v^2}{2} + gz \right) \right)_{in} - \sum \left(\dot{m} \left(h + \frac{v^2}{2} + gz \right) \right)_{out} \quad (2.5)$$

In a similar manner, the conservation of mass states that the mass stored within a system is equal to the difference between the mass flow into and out of the system. This can be extended to the rate of change of mass, where a balance shows that the rate of change of mass stored within the system is equal to the difference between the mass flow rate into the system and the mass flow rate out of the system, as demonstrated by Equation 2.6. At steady state in Equation 2.7, there is no storage of mass and, so, the mass within the system must be constant - in other words, the rate of change of mass contained within the system must be zero, such that the mass flow rate into the system is equal to the mass flow rate out of the system. [24]. (Conventionally, mass flow to the system from the surroundings is seen as positive, while mass flow to the surroundings from the system is seen as negative).

$$m_{str} = \sum m_{in} - \sum m_{out} \rightarrow \dot{m}_{str} = \sum \dot{m}_{in} - \sum \dot{m}_{out} \quad (2.6)$$

$$\dot{m}_{str} = 0 \rightarrow 0 = \sum \dot{m}_{in} - \sum \dot{m}_{out} \quad (2.7)$$

It should be noted that the presented formulations for the conservation of energy and mass are considered with regards to one-dimensional flow. For this, it is necessary to assume that the flow is normal to the boundary at the inlets and outlets, while the intensive properties of the incoming and outgoing flow are uniform as bulk average values over each inlet or outlet cross-sectional area [24].

2.3.2 PRESSURE-VOLUME-TEMPERATURE RELATIONSHIPS

The state principle or postulate asserts that the required number of independent intensive properties to fix a state is equal to the sum of the relevant work and heat interactions between the system and surroundings [24]. For a simple thermodynamic system with pure substances or uniform mixtures of non-reacting substances, the only work interaction which can occur is associated with volume changes and the only heat interaction which can occur is associated with temperature differences. Thus, two independent intensive properties are required to fix the state for a simple thermodynamic system.

Usually, the considered intensive properties are pressure, specific volume, and temperature. As an example, the relationship between these properties are plotted using contours in Figure 2.5 for an arbitrary substance and reveal regions in which multiple phases can co-exist in equilibrium. In a one-phase region with a solid, liquid, or vapour phase, the state is fixed by any two properties of the pressure, specific volume, or temperature [24]. In a two-phase region with a liquid-vapour, solid-liquid, or solid-vapour mixture, the state is fixed by specific volume and either pressure or temperature, as pressure and temperature are no longer independent [24]. A three-phase region exists along the triple line as a solid-liquid-vapour mixture, but this is an uncommon occurrence in most systems.

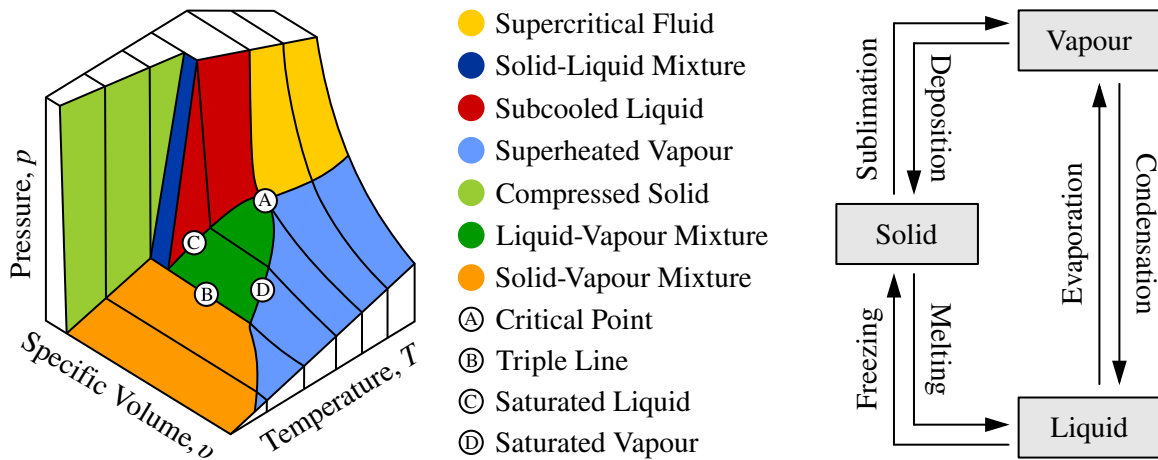


Figure 2.5: Relationship between pressure, specific volume, and temperature for an arbitrary substance which contracts during freezing (left) [24], and illustration of phase transition processes (right).

A state at which a phase transition begins or ends is a saturation state. The liquid-vapour dome is the region of the liquid-vapour states, where the saturated liquid and saturated vapour lines dictate the border. In this region, the quality is the ratio of the mass of saturated vapour to the total mass of the mixture, where a saturated liquid has a quality of zero and a saturated vapour has a quality of unity. The liquid or vapour saturation pressure is the pressure at which a liquid or vapour phase transition occurs. The liquid or vapour saturation temperature is the temperature at which a liquid or vapour phase transition occurs. The critical point is at the top of the liquid-vapour dome and represents the end point of equilibrium with the convergence of the saturated liquid and saturated vapour lines. The critical pressure and critical temperature occur at the critical point and respectively represent the maximum pressure and maximum temperature at which the liquid-vapour states can co-exist in equilibrium.

2.3.3 IDEAL GAS IDEALISATION

Firstly, the universal gas constant is defined when an arbitrary vapour is expanded such that the pressure can be extrapolated to zero [24]. This is described by Equation 2.8, where the limiting value from the ratio of the product of pressure and molar specific volume to temperature is labelled as the universal gas constant. It has been experimentally found that this value is common for all substances [24].

$$\lim_{p \rightarrow 0} \frac{p\bar{v}}{T} = \bar{R} = RM = 8.314\text{J/mol/K} \quad (2.8)$$

A compressibility factor can then be defined as the dimensionless ratio of the product of pressure and molar specific volume to the product of the universal gas constant and temperature, as given by Equation 2.9 [24]. When the pressure is small relative to the critical pressure or the temperature is large relative to the critical temperature, the compressibility factor becomes approximately equal to unity [24]. Thus, an ideal gas idealisation can be employed with the formation of the ideal gas equation of state in Equation 2.10. This idealisation is appropriate when considering a fluid with a slow-moving flow and allows for the fluid to be assumed as incompressible with a constant density [24, 33].

$$Z = \frac{p\bar{v}}{\bar{R}T} \rightarrow \text{Ideal Gas Idealisation: } \lim_{p \rightarrow 0} Z = 1 \quad (2.9)$$

$$pV = n\bar{R}T \leftrightarrow p\bar{v} = \bar{R}T \leftrightarrow pv = \frac{\bar{R}T}{M} \leftrightarrow pV = \frac{m\bar{R}T}{M} \quad (2.10)$$

To apply this to a mixture of various components, the Dalton model can be employed and it is assumed that each component behaves as an ideal gas as if it were alone at the particular temperature and volume of the overall mixture [24]. It follows that the individual components each exert a partial pressure and the sum of these partial pressures is equal to the pressure of the overall mixture [24]. This is based on the concept of an ideal gas as consisting of molecules which exert negligible intermolecular forces on one another and whose volume is negligible relative to the volume of the overall mixture and, in the absence of significant intermolecular forces, the behaviour of each component is unaffected by the presence of the other components. An analytical representation is given by Equation 2.11.

Alternatively, the Amagat model can be used which also views the components individually, but it is assumed that each component behaves as an ideal gas as if it were alone at the particular temperature and pressure of the overall mixture [24]. It follows that the individual components each occupy a partial volume and the sum of these partial volumes is equal to the pressure of the overall volume, as demonstrated in Equation 2.12 [24]. However, the Amagat model is usually less useful than the Dalton model, because it is more common to deal with partial pressures rather than partial volumes.

$$p = \sum_{i=1}^j p_i \rightarrow p_i = \frac{n_i \bar{R}T}{V} = \frac{m_i \bar{R}T}{M_i V} \rightarrow \frac{p_i}{p} = \frac{n_i}{n} = \frac{m_i}{m} \frac{M}{M_i} = y_i \quad (2.11)$$

$$V = \sum_{i=1}^j V_i \rightarrow V_i = \frac{n_i \bar{R}T}{p} = \frac{m_i \bar{R}T}{M_i p} \rightarrow \frac{V_i}{V} = \frac{n_i}{n} = \frac{m_i}{m} \frac{M}{M_i} = y_i \quad (2.12)$$

It is also appropriate to define the heat capacity in Equation 2.13 as a measure of the amount of heat needed to provide a system with a unit change in temperature relative to the current temperature [24]. For a fluid, the heat capacity can be considered with association to a fixed volume within the limits of a container, where heat transfer causes a change in internal energy; or with association to a fixed pressure without the limits of a container, where heat transfer causes work and a change in internal energy, as represented through enthalpy. For generalisation, the specific heat capacity can be considered as the heat capacity on a mass or molar basis. Applying the ideal gas idealisation, these relationships are simplified in Equation 2.14 with the heat capacity ratio while assuming constant heat capacity.

$$C = \frac{\delta Q}{\delta T} \text{ with } C_v = \frac{\delta U}{\delta T} \text{ and } C_p = \frac{\delta H}{\delta T} \leftrightarrow c = \frac{C}{m} = \frac{\bar{c}}{M} \leftrightarrow \bar{c} = \frac{C}{n} = Mc \quad (2.13)$$

$$\gamma = \frac{C_p}{C_v} = \frac{c_p}{c_v} = \frac{\bar{c}_p}{\bar{c}_v} \rightarrow C_v = \frac{\Delta U}{\Delta T} = \frac{n\bar{R}}{\gamma - 1} \text{ and } C_p = \frac{\Delta H}{\Delta T} = \frac{n\bar{R}\gamma}{\gamma - 1} \rightarrow C_p - C_v = n\bar{R} \quad (2.14)$$

2.3.4 PSYCHROMETRIC APPLICATIONS

For distinction, dry air refers to a mixture of approximately 78% nitrogen, 21% oxygen, 0.9% argon, 0.04% carbon dioxide, and small amounts of other gases, while moist air refers to a mixture of dry air and water vapour in which the dry air may actually be treated as if it were an independent component because it is much more numerous than the water vapour [24]. In most situations, it is acceptable to consider the moist air as an ideal gas using the Dalton model, as presented in Equation 2.15.

$$p = \frac{m\bar{R}T}{MV} = p_a + p_v \text{ with } p_a = \frac{m_a \bar{R}T}{M_a V} = y_a p \text{ and } p_v = \frac{m_v \bar{R}T}{M_v V} = y_v p \quad (2.15)$$

There is a limit to the amount of water vapour which can be contained in moist air and, when the partial pressure of the water vapour corresponds to the saturation pressure of water vapour at the current temperature, the moist air is said to be saturated and cannot contain more water vapour. The composition of moist air can be described through the humidity ratio and relative humidity based on

the relationship between the amount of dry air and amount of water vapour. The humidity ratio or specific humidity is defined as the ratio of the mass of water vapour to the mass of dry air and it can be manipulated as done in Equation 2.16 to be directly represented in terms of the water vapour partial pressure and moist air pressure [24]. The relative humidity is defined as the ratio of the mole fraction of water vapour to the mole fraction of water vapour in saturated moist air at the current temperature and it can be manipulated, as done in Equation 2.17, to be the ratio of the water vapour partial pressure to the saturated water vapour partial pressure at the current temperature [24].

It should also be noted that, if the pressure remains constant, the capacity of moist air to contain water vapour is decreased if the temperature is decreased or increased if the temperature is increased. This is evident from the inverse implications of changing temperature at a constant pressure, because the saturated water vapour partial pressure decreases as the temperature decreases or increases as the temperature increases. From a different perspective, a low relative humidity indicates a high capacity to contain additional water vapour, while a high relative humidity indicates a low capacity to contain additional water vapour. This influence on capacity of moist air to contain water vapour can be inferred through the original definition of the relative humidity, where the relative humidity correspondingly increases as the temperature is decreased or decreases as the temperature is increased.

$$\omega = \frac{m_v}{m_a} = \frac{n_v}{n_a} = \frac{M_v p_v}{M_a p_a} = 0.622 \frac{p_v}{p - p_v} = 0.622 \frac{\phi p_{v,g}}{p - \phi p_{v,g}} \quad (2.16)$$

$$\phi = \frac{y_v}{y_{v,g}} = \frac{n_v}{n_{v,g}} = \frac{m_v}{m_{v,g}} = \frac{p_v}{p_{v,g}} = \frac{\omega p}{p_{v,g}(0.622 + \omega)} \quad (2.17)$$

For understanding, it is necessary to define the dry-bulb and wet-bulb temperatures. The dry-bulb temperature is the temperature of the air measured by a thermometer exposed to the air but shielded from radiation and moisture (usually reported as the ambient temperature). The wet-bulb temperature

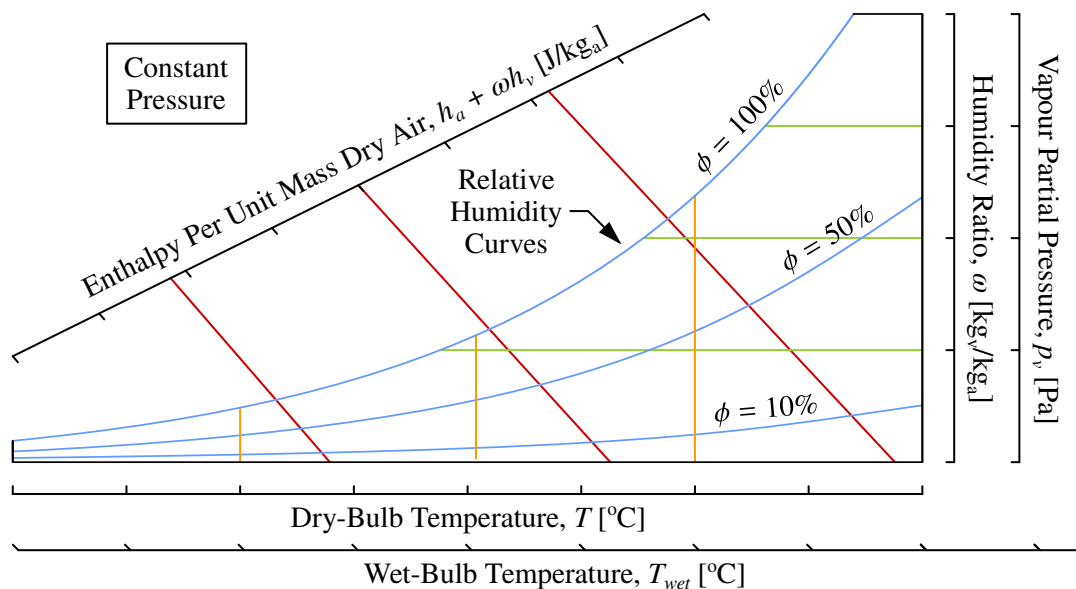


Figure 2.6: Example of a psychrometric chart with axes for reading various properties.

is the temperature of the air measured by a thermometer constantly enclosed in a water-soaked material over which air is freely passed. Essentially, the dry-bulb measurement is only concerned with the dry air, while the wet-bulb measurement experiences effects from evaporative cooling based on the relative humidity in the moist air. As a result, the wet-bulb temperature is less than the dry-bulb temperature, unless the relative humidity is 100% in which case the dry-bulb and wet-bulb temperatures are equal.

The properties of moist air and respective relationships at a constant pressure can be illustrated graphically on psychrometric charts, with an example markup seen in Figure 2.6. On these charts, there is an abscissa of the dry-bulb temperature, ordinate of the humidity ratio, ordinate of the water vapour pressure, diagonal of the mixture enthalpy per unit mass of dry air, contours of constant relative humidity, and lines of constant wet-bulb temperature. However, it should be noted that the properties on a psychrometric chart are specific to a region depending on altitude and atmospheric pressure.

2.3.5 AIR AND WATER PROPERTIES

For the development of the analysis in Chapter 5, various properties of moist air, dry air, and water vapour were required and reliably sourced from the published data in *Fundamentals Of Engineering Thermodynamics* by Moran et al. [24] and *Air-Cooled Heat Exchangers And Cooling Towers - Thermal-Flow Performance Evaluation And Design* by Kröger [42]. Psychrometric charts from the CSIR [43, 44] for sea level with an atmospheric pressure of 101.32kPa and an altitude of 1700m with an atmospheric pressure of 82.50kPa were also available, which provided a graphical means to confirm the analytical calculations. An example of these psychrometric charts is included in Appendix A.

2.4 HEAT TRANSFER

Expanding on the definition of heat, the heat transfer rate is concerned with the rate of energy transfer over the system boundary in a thermal process as a result of a temperature difference. The heat transfer processes can be classified into conduction, convection, and radiation. As there is reliance on heat transfer from the enclosure to the surroundings, the heat transfer processes needed to be understood.

2.4.1 CONDUCTION

Conduction is defined as the transfer of heat between parts of a body or separate contacting bodies at different temperatures, without significant bulk or macroscopic motion of portions of the body or bodies [33]. Essentially, conduction may be viewed as the transfer of energy from the more energetic to the adjacent less energetic molecules of the body or bodies due to various molecular interactions and diffusion through random molecular motion between the molecules [33]. This occurs in fluids through collisions and the transfer of kinetic energy between molecules as a result of random translational and rotational microscopic motions without bulk motion, while this occurs in solids due to lattice vibrations of molecules and the possible translational migration of free electrons [33].

The rate of conductive heat transfer is governed by Fourier's law. For a one-dimensional form in Equation 2.18, this states that the conductive rate of heat transfer through a cross-sectional area is directly proportional to this area normal to the direction of heat transfer and the temperature difference in the respective direction, with the constant of proportionality being the thermal conductivity of the body or bodies which is dependent on the associated substance [33, 42]. The thermal conductivity essentially provides a measure of the ability of the substance to conduct heat. A simplification of the process of conduction is outlined in Figure 2.7 with a depiction of conduction through a plane wall.

$$\dot{Q}_{cnd} = -kA \frac{\partial T}{\partial x} \rightarrow \text{Steady: } \dot{Q}_{cnd} = -kA \frac{dT}{dx} \rightarrow \text{Constant } k: \dot{Q}_{cnd} = -kA \frac{T_2 - T_1}{x_2 - x_1} \quad (2.18)$$

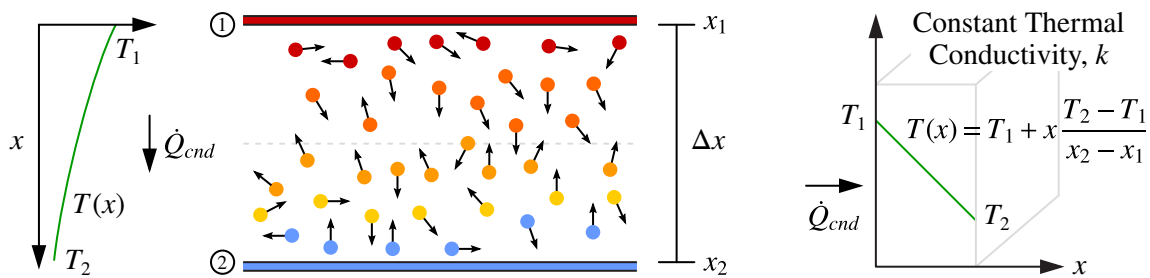


Figure 2.7: Simplification of the process of conduction considering molecular interactions (left), and temperature distribution for a one-dimensional conduction through a simple plane wall (right).

The thermal conductivity is generally dependent on the free electrons and lattice vibrations in solids or mean free path and molecular speed in fluids and varies as a function of temperature, as is shown in Figure 2.8 for selected solids and fluids [33]. Broadly and if a minor loss of accuracy is tolerable, a constant value can be assumed for most substances for temperatures between 0°C and 50°C.

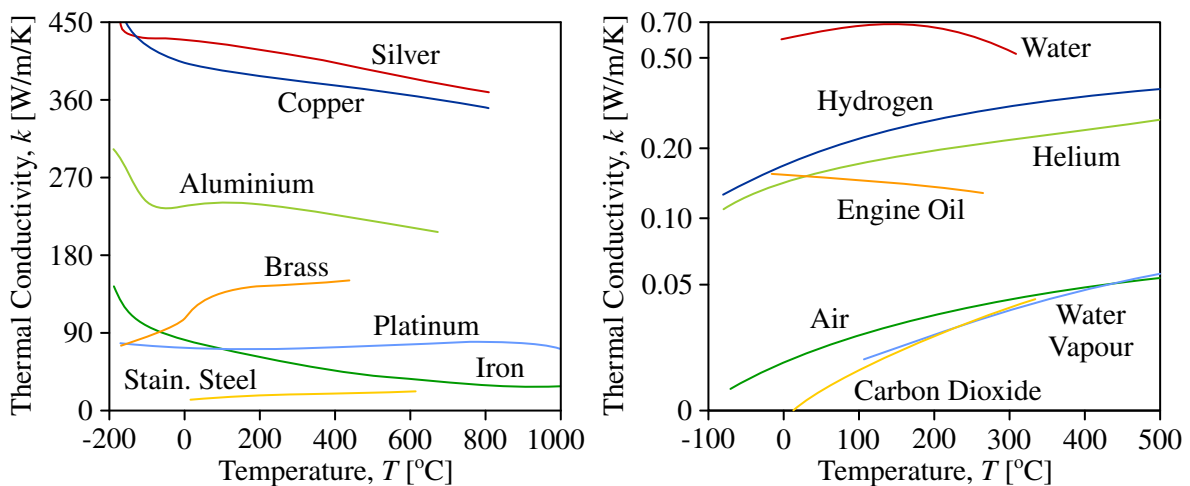


Figure 2.8: Variation in thermal conductivity with temperature for solids (left) and fluids (right) [33].

When considering the response to a temperature change, it is useful to define the thermal diffusivity in Equation 2.19 as the ratio of the thermal conductivity to the product of the density and mass specific heat capacity of the substance. This provides a measure of the ability of the substance to either rapidly

or sluggishly diffuse heat, where a greater thermal diffusivity implies higher effectiveness in conduction than heat storage (with heat rapidly diffusing through the substance) or a lesser thermal diffusivity implies higher effectiveness in heat storage than conduction (with heat slowly diffusing through the substance). In a sense, thermal diffusivity is the measure of thermal inertia [33].

$$\alpha = \frac{k}{\rho c_p} \quad (2.19)$$

2.4.2 CONVECTION

Convection is defined as the transfer of heat between a surface and a fluid in motion. So, in addition to energy transfer due to various molecular interactions and diffusion through random molecular motion between the molecules in the fluid, energy is also transferred by the bulk motion of the fluid where a macroscopic number of molecules move collectively in a similar manner [33, 42]. Thus, the primary mechanism of convection is actually conduction with the inclusion of bulk motion [33]. Although less common, it should be noted that advection refers to the heat transfer only due to the bulk motion.

The rate of convective heat transfer is governed by Newton's law of cooling. This states that the convective rate of heat transfer is directly proportional to the surface area and temperature difference between the surface and free stream temperature of the fluid, with the constant of proportionality being the convection heat transfer coefficient which is dependent on temperature, conditions in the thermal boundary layer, nature of the flow, and other fluid properties. Any study of convection ultimately reduces to a study of the means by which the convection heat transfer coefficient may be determined, which is typically based on dimensional analysis and experimental correlations as opposed to analytical procedures, because analytical models often rely on many assumptions since there are a multiplicity of fluid properties (such as density, viscosity, thermal conductivity, and heat capacity), surface geometries, and flow conditions for which to account [33, 42]. This is expressed in Equation 2.20.

$$\dot{Q}_{cnv} = h_c A (T_{sur} - T_\infty) \quad (2.20)$$

2.4.2.1 ANALYTICAL CONSIDERATIONS

To understand the processes of convection, consider a fluid flowing over a flat isothermal surface at a different temperature. A velocity boundary layer is formed near the surface due to collisions between the fluid molecules and surface, where the fluid velocity is reduced to zero at the surface with adjacent layers of increasing velocity until the free stream velocity - this is known as the no-slip condition [33]. Similarly, there is a region of the fluid near the surface, which is the thermal boundary layer, in which the temperature varies from the temperature of the surface until the free stream temperature [33].

Since the no-slip conditions dictates that the fluid velocity is zero at the surface, the heat transfer must be purely conduction at the surface and there is an enhanced resistance to heat transfer due to viscous

effects. In other words, the contribution from various molecular interactions and diffusion through random molecular motion is greater than the contribution from the bulk motion, where the contribution from the bulk motion increases farther from the surface as the fluid velocity increases [33]. This is analytically derived in Equation 2.21 and reveals that the effects of heat transfer penetrate farther into the free stream with an increased convection heat transfer coefficient as the thermal boundary layer grows - although, as mentioned, this derivation is not inherently useful for applications as the temperature difference within the thermal boundary layer is difficult to model [33].

$$\dot{Q}_{cnv} = -kA \left. \frac{\partial T}{\partial z} \right|_{z=0} = h_c A (T_{sur} - T_\infty) \rightarrow h_c = \frac{-k(\partial T / \partial z|_{z=0})}{T_{sur} - T_\infty} \quad (2.21)$$

When considering a fluid flowing over a surface where a phase change may occur, there is the development of a concentration boundary layer which shares characteristics with velocity and thermal boundary layers [33]. Due to the transfer of a species from the phase change, a concentration difference forms and the concentration varies from an increased concentration near the surface until the free stream concentration [33]. This is specifically applicable to evaporation with air as the flowing fluid and water as the species undergoing a phase change, where the concentration of water vapour in the air can increase as the air flows over a surface of water and evaporation occurs.

The rate at which a species is transferred by various molecular interactions and diffusion through random molecular motion can be described through an approximation of Fick's law in Equation 2.22, which is analogous to Fourier's law using the mass diffusivity as the constant of proportionality [33]. For water vapour diffusing in air between 0°C and 50°C, the mass diffusivity is approximately 0.253cm²/s [45]. With the idea that there is a lack of bulk motion directly at the surface due to the velocity boundary layer, the species transfer rate at the surface can be analytically derived in Equation 2.23 using a relationship between the species transfer rate and concentration difference on a molar basis, which is analogous to Newton's law of cooling and defines the convection mass transfer coefficient [33]. As with the convection heat transfer coefficient and thermal boundary layer, the convection mass transfer coefficient is dependent on the conditions of the concentration boundary layer.

As an alternative, Fick's law and the species transfer rate can be expressed on a mass basis. This is given in Equation 2.24 and Equation 2.25 respectively. The convection mass transfer coefficient is compatible with the species transfer rate on either a molar or mass basis without modification.

$$\dot{n}_{cnv} = -DA \frac{\partial C}{\partial z} \quad (2.22)$$

$$\dot{n}_{cnv} = -DA \left. \frac{\partial C}{\partial z} \right|_{z=0} = h_m A (C_{sur} - C_\infty) \rightarrow h_m = \frac{-D(\partial C / \partial z|_{z=0})}{C_{sur} - C_\infty} \quad (2.23)$$

$$\dot{m}_{cnv} = -DA \frac{\partial \rho}{\partial z} \quad (2.24)$$

$$\dot{m}_{cnv} = -DA \left. \frac{\partial \rho}{\partial z} \right|_{z=0} = h_m A (\rho_{sur} - \rho_\infty) \rightarrow h_m = \frac{-D(\partial \rho / \partial z|_{z=0})}{\rho_{sur} - \rho_\infty} \quad (2.25)$$

The flow within the boundary layers may be laminar or turbulent, where a laminar flow is characterised by ordered behaviour in which the adjacent layers of the fluid can be imagined to slide relative to one another, while a turbulent flow is characterised by chaotic behaviour in which there are unpredictable local fluctuations in the magnitude and direction of velocity [33]. The transition from laminar flow to turbulent flow results due to a triggering mechanism and corresponds with a transitional regime characterised by local regions of regular and irregular flow [33]. The triggering mechanism may result from the interaction of unsteady flow structures which develop naturally or small disturbances which originate from fluctuations in the free stream or surface geometry and roughness. These regions are characterised in Figure 2.9 with the velocity, thermal, and concentration boundary layers.

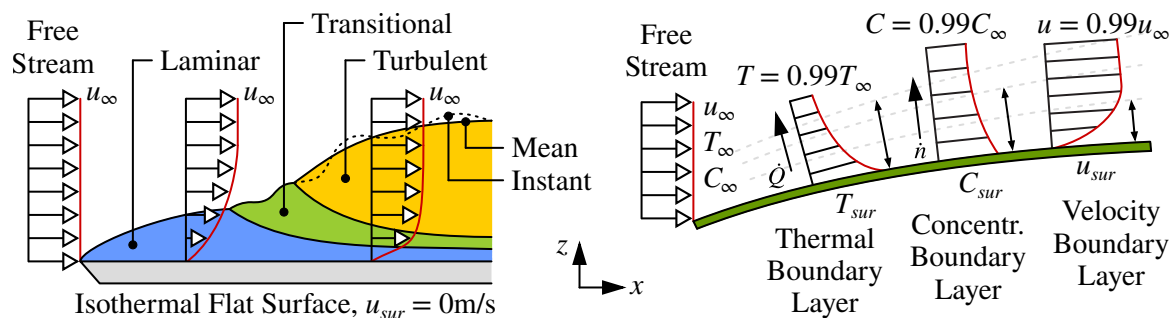


Figure 2.9: Velocity boundary layer and laminar, transitional, and turbulent regimes for a fluid flowing over a flat surface (left) and development of the velocity, thermal, and concentration boundary layers for a fluid flowing over an arbitrary surface with a surface temperature which is greater than the free stream temperature and surface concentration greater than the free stream concentration (right) [33].

The flow can be classified as laminar, transitional, or turbulent through the dimensionless Reynolds number in Equation 2.26, which provides a measure of the ratio of the inertial forces to the viscous forces in the boundary layers. A low Reynolds number suggests that there are primary contributions from viscous forces with minimal inertial forces and indicates laminar flow, while a high Reynolds number suggests that there is a predominance of inertial forces over viscous forces and indicates turbulent flow. The rate of convective heat transfer is directly related to the Reynolds number, since the nature of the resistance to heat transfer in the thermal boundary layer is dependent on whether the flow is laminar or turbulent [33]. This is also the case for the species transfer rate and ultimately suggests that the convection heat and mass transfer coefficients strongly depend on the free stream velocity, since this is recognised as the most susceptible parameter of the Reynolds number [33].

The dynamic viscosity in the definition of the Reynolds number is a measure of the resistance to deformation at a given rate from the movement of adjacent layers of the fluid. The kinematic viscosity can then be defined as the ratio of the dynamic viscosity to density and can be interpreted as the momentum diffusivity. Also, the characteristic dimension in the definition of the Reynolds number is a representation of the relative scale of the system, which is typically the length for a flat surface, diameter a circular duct, or effective hydraulic diameter for a non-circular duct (defined in Section 2.4.2.2).

$$\text{Re}_L = \frac{u_\infty \rho L}{\mu} = \frac{u_\infty L}{\nu} \quad \text{with } \nu = \frac{\mu}{\rho} \quad (2.26)$$

Subsequently, to estimate the convection heat transfer coefficient, the convective heat transfer may be classified according to the nature of the flow. This includes forced convection, which occurs when the flow is caused by external means (usually requiring an input of work); and free or natural convection, which occurs when the flow is induced by buoyancy forces due to density differences caused by temperature variations in the fluid [33]. It is also possible for mixed convections with a combination of forced and free convection for the local regions in a flow. Furthermore, a flow may be external without constraints to the volume of the flow or internal with constraints to the volume of the flow [33].

This also introduces the notion that the convection coefficients may not be identical for the local regions in a flow, as recognised for an external flow around an arbitrary shaped body or an internal flow in a duct with significant viscous effects [33]. Thus, for consideration of the global flow, the average convection coefficients can be defined as an accumulation of the local regions. This is shown in Equation 2.27 to Equation 2.29 for the convection heat and mass transfer coefficients.

$$\bar{h}_c = \frac{1}{A} \int_A h_c dA \rightarrow \dot{Q}_{cnv} = \bar{h}_c A (T_{sur} - T_\infty) \quad (2.27)$$

$$\bar{h}_m = \frac{1}{A} \int_A h_m dA \rightarrow \dot{n}_{cnv} = \bar{h}_m A (C_{sur} - C_\infty) \quad (2.28)$$

$$\bar{h}_m = \frac{1}{A} \int_A h_m dA \rightarrow \dot{m}_{cnv} = \bar{h}_m A (\rho_{sur} - \rho_\infty) \quad (2.29)$$

The significance of the Reynolds number is seen through analytical consideration of the motion and physical processes of the fluid in the boundary layers. Fundamentally, the conservation of mass, momentum, energy, and species must be satisfied for each point at which there exists velocity, temperature, and concentration differences [33]. Through simplifying assumptions in two-dimensions, Bergman et al. [33] presents the mass conservation for continuity of incoming and outgoing flow as given by Equation 2.30, momentum conservation relating to the velocity boundary layer as given by Equation 2.31, energy conservation relating to the thermal boundary layer as given by Equation 2.32, and species conservation relating to the concentration boundary layer as given by Equation 2.33.

$$\frac{\partial u}{\partial x} + \frac{\partial w}{\partial z} = 0 \quad (2.30)$$

$$u \frac{\partial u}{\partial x} + w \frac{\partial u}{\partial z} = -\frac{1}{\rho} \frac{\partial p}{\partial x} + \nu \frac{\partial^2 u}{\partial z^2} \quad (2.31)$$

$$u \frac{\partial T}{\partial x} + w \frac{\partial T}{\partial z} = \alpha \frac{\partial^2 T}{\partial z^2} + \frac{\nu}{c_p} \left(\frac{\partial u}{\partial z} \right)^2 \quad (2.32)$$

$$u \frac{\partial C}{\partial x} + w \frac{\partial C}{\partial z} = D \frac{\partial^2 C}{\partial z^2} \quad (2.33)$$

These equations can then be normalised through dimensionless parameters to establish the presence of similarity parameters from dimensionless forms of the conservation equations. Formally, these

similarity parameters conform with the definitions of the Reynolds number, Prandtl number, and Schmidt number, which respectively correspond with the velocity, thermal, and concentration boundary layers [33]. From the conservation equations, the Reynolds number is uncoupled from the Prandtl number and Schmidt number, but the Prandtl number and Schmidt number are inherently dependent on the Reynolds number [33]. The Prandtl number is defined in Equation 2.34 as the ratio of the kinematic viscosity or momentum diffusivity to the thermal diffusivity. The Schmidt number is defined in Equation 2.35 as the ratio of the kinematic viscosity or momentum diffusivity to the mass diffusivity. In addition, the Lewis number is defined as the ratio of the Schmidt number to the Prandtl number and provides a gauge of the rates of growth of the thermal and concentration boundary layers through a comparison between the thermal and mass diffusivities, as shown in Equation 2.36 [33, 42].

$$\text{Pr} = \frac{v}{\alpha} = \frac{c_p \mu}{k} = \frac{\delta_{vel}}{\delta_{thm}} \quad (2.34)$$

$$\text{Sc} = \frac{v}{D} = \frac{\mu}{\rho D} = \frac{\delta_{vel}}{\delta_{con}} \quad (2.35)$$

$$\text{Le} = \frac{\text{Sc}}{\text{Pr}} = \frac{\alpha}{D} = \frac{k}{\rho c_p D} = \frac{\delta_{thm}}{\delta_{con}} \quad (2.36)$$

By considering the formulation of the convection heat and mass transfer coefficients, dependent dimensionless parameters can be developed in Equation 2.37 and Equation 2.38 as the dimensionless temperature difference at the surface, known as the Nusselt number, and dimensionless concentration difference at the surface, known as the Sherwood number, respectively [33, 42]. Moreover, since the average convection heat and mass transfer coefficients are obtained by integrating over the surface of a body, the same principles can be applied to these parameters to accumulate averages over the surface of the body [33]. In a descriptive sense, the average Nusselt number provides a measure of the convection heat transfer occurring at the surface and it is a function of the Reynolds number and Prandtl number, while the average Sherwood number provides a measure of the convection mass transfer occurring at the surface and it is a function of the Reynolds number and Schmidt number [33].

This is useful as it allows for the convection heat and mass transfer coefficients to be described in terms of a minimal set of dimensionless parameters, rather than a comprehensive set of dimensional parameters, and these dimensionless parameters may be determined analytically, numerically, or experimentally. Additionally, because the parameters are dimensionless and independent of scale, it allows for results obtained for a surface experiencing certain convective conditions to be universally applied to geometrically similar surfaces experiencing entirely different convective conditions [33].

$$\text{Nu}_L = + \left. \frac{\partial T^*}{\partial z^*} \right|_{z^*=0} \quad \text{with } T^* = \frac{T - T_{sur}}{T_\infty - T_{sur}} \quad \text{and } z^* = \frac{z}{L} \rightarrow \text{Nu}_L = \frac{h_c L}{k} \rightarrow \bar{\text{Nu}}_L = \frac{\bar{h}_c L}{k} \quad (2.37)$$

$$\text{Sh}_L = + \left. \frac{\partial C^*}{\partial z^*} \right|_{z^*=0} \quad \text{with } C^* = \frac{C - C_{sur}}{C_\infty - C_{sur}} \quad \text{and } z^* = \frac{z}{L} \rightarrow \text{Sh}_L = \frac{h_m L}{D} \rightarrow \bar{\text{Sh}}_L = \frac{\bar{h}_m L}{D} \quad (2.38)$$

Within the presented model it should be noted that it has been assumed that there is an ideal gas idealisation, body forces are negligible, flow is incompressible with a constant density, flow is non-reacting, viscous dissipation is negligible, there is no energy generation, there is no species generation, pressure gradient in the boundary layers can be approximated as the free stream pressure gradient, and differences in momentum, energy, and species are negligible in the flow direction [33, 42]. This is reasonable and acceptable for most flows since steady flow can be realistically expected, boundary layers are very thin, compressibility effects only become a concern for Mach numbers above approximately 0.3 (as detailed in Equation 2.39), and velocity, temperature, and concentration variations are much larger in the normal direction than those variations in the flow direction [33].

$$\text{Ma} = \frac{u_\infty}{a} \text{ with } a = \sqrt{\gamma RT} \text{ and } \gamma = \frac{c_p}{c_v} \rightarrow \text{Incompressible: } \text{Ma} \lesssim 0.3 \text{ or } u_\infty \lesssim 0.3a \quad (2.39)$$

2.4.2.2 INTERNAL FLOWS

For an internal flow with a duct, the boundary layers are unable to develop without eventually being constrained and there is the formation of an entrance region and fully developed region, shown in Figure 2.10, which occurs due to viscous effects from the surfaces constraining volume of the flow. The characteristic dimension used for the Reynolds number, Nusselt number, and Sherwood number is the effective hydraulic diameter in Equation 2.40, which provides a first approximation for ducts of non-circular cross-section [33, 42]. Also, because the velocity and temperature vary over the cross-section, a mean velocity and temperature need to be considered since there is no well-defined free stream [33]. In the entrance region, the convection heat transfer coefficient varies but these variations diminish as the boundary layers develop and, eventually in the fully developed region, the convection heat transfer coefficient approaches a constant value with minimal variation [33].

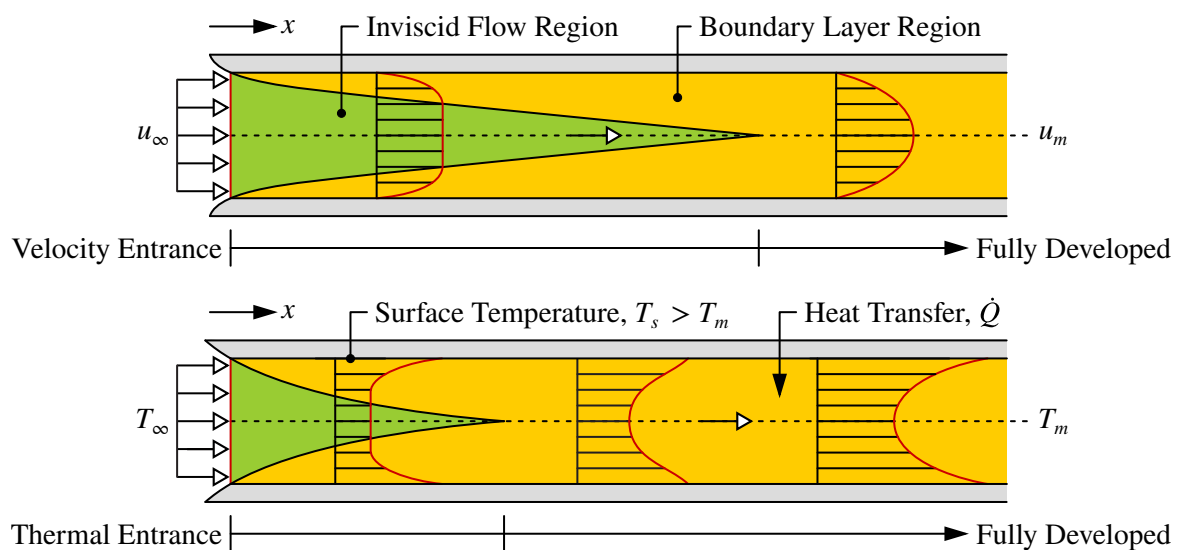


Figure 2.10: Velocity boundary layer (top) and thermal boundary layer (bottom) development for a flow within a circular duct, where the surface temperature is greater than the flow temperature [33].

$$D_h = \frac{4A}{P} \rightarrow \text{Re}_{D_h} = \frac{u_m \rho D_h}{\mu} = \frac{u_m D_h}{\nu} \text{ with } u_m = \frac{\dot{m}}{\rho A} \quad (2.40)$$

To predict the convective properties for a flow in a duct of circular cross-section with smooth surfaces, several experimental correlations have been developed for fully developed flow under turbulent conditions. For small to moderate temperature differences, the local Nusselt number may be obtained from the Dittus-Boelter correlation in Equation 2.41 with the range over which it has been experimentally confirmed to be accurate [33, 46, 47]. Alternatively, if the flow is characterised by large variations in properties due to large temperature differences, the correlation proposed by Sieder and Tate [48] may be considered from Equation 2.42 as a more suitable option [33, 42]. For improved accuracy, Equation 2.43 was developed by Gnielinski [49] and can be combined with an approximation for the Moody or Darcy friction factor developed by Petukhov [50] for smooth surfaces [33, 42].

With regards to the level of accuracy, the Dittus-Boelter and Sieder-Tate correlations can produce errors up to 25% depending on the flow conditions, while the Gnielinski correlation produces errors up to only 10% depending on the flow conditions [33, 42]. Basically, the further the flow deviates from the conditions and range of validity, the less accurate the results from the correlation will be.

Although these correlations were originally developed for ducts of circular cross-section, they can still be applied for ducts of non-circular cross-section using the effective hydraulic diameter for an acceptable first approximation. However, it should be noted that the convection heat transfer coefficient will vary around the periphery, approaching zero at sharp corners, and must be viewed as an average over the perimeter [33]. Additionally, since the entrance region is usually short for turbulent flow, the local Nusselt number found for fully developed flow can be assumed to be equal to the average Nusselt number over the length of the duct when the ratio of the length to the effective hydraulic diameter is approximately greater than 60 - this assumption generally produces an error of less than 15% [33].

$$\text{Nu}_D = \frac{h_c D}{k} = 0.023 \text{Re}_D^{0.8} \text{Pr}^n \text{ with } n = 0.4 \text{ for } T_m < T_s \text{ or } n = 0.3 \text{ for } T_m > T_s \quad (2.41)$$

$$\left[0.6 \lesssim \text{Pr} \lesssim 160 \text{ and } \text{Re}_D \gtrsim 10^4 \text{ and } \frac{L}{D} \gtrsim 10 \right]$$

$$\text{Nu}_D = \frac{h_c D}{k} = 0.027 \text{Re}_D^{0.8} \text{Pr}^{0.333} \left(\frac{\mu}{\mu_{sur}} \right)^{0.14} \quad (2.42)$$

$$\left[0.7 \lesssim \text{Pr} \lesssim 16.7 \times 10^3 \text{ and } \text{Re}_D \gtrsim 10^4 \text{ and } \frac{L}{D} \gtrsim 10 \right]$$

$$\text{Nu}_D = \frac{h_c D}{k} = \frac{0.125 \text{Pr} f (\text{Re}_D - 1000)}{1 + 4.49 f^{0.5} (\text{Pr}^{0.667} - 1)} \text{ with } f = (0.790 \ln(\text{Re}_D) - 1.64)^{-2} \quad (2.43)$$

$$\left[0.5 \lesssim \text{Pr} \lesssim 2000 \text{ and } 3000 \lesssim \text{Re}_D \lesssim 5 \times 10^6 \text{ and } \frac{L}{D} \gtrsim 10 \right]$$

Even though Equation 2.41 to Equation 2.43 apply directly to smooth surfaces, it may be tolerable to apply these correlations as broad approximations for rough surfaces, but the convection heat transfer

coefficient tends to be under-predicted since the heat transfer coefficient actually increases as the roughness of the surfaces increases [33]. Also, if there is transitional flow with a Reynolds number from 2300 to 4000, these correlations are still somewhat effective as initial approximations, but caution should be applied as the convection heat transfer coefficient tends to be over-predicted [33].

2.4.3 RADIATION

Radiation is defined as the transfer of heat from electromagnetic energy emitted by matter due to its finite or non-zero temperature [33]. Fundamentally, the emission derives from changes in the electron configurations of the constituent molecules and is propagated or transported by photons, which are classified as packets of electromagnetic energy, in either the presence or absence of a material medium [33]. A single body emitting and absorbing radiation to and from the surroundings is shown in Figure 2.11 with a spectrum of the electromagnetic energy received from the Sun for extraterrestrial and surface air mass coefficients, which define the proportion of atmosphere through which insolation following a direct path length at a certain zenith angle must pass before reaching the surface.

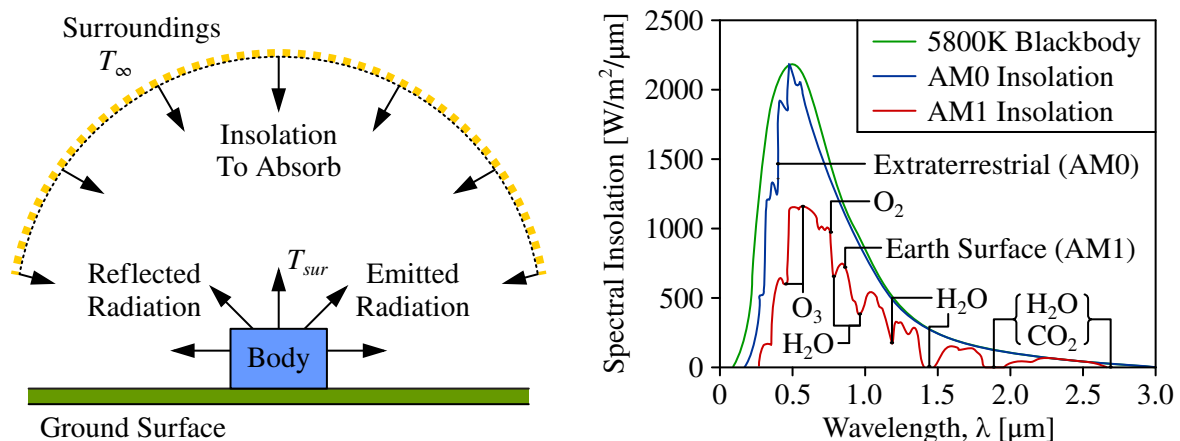


Figure 2.11: Example of a single body emitting and absorbing radiation to and from the surroundings (left), and spectrum of the electromagnetic energy received from the Sun as insolation considering an extraterrestrial air mass coefficient of 0 and surface air mass coefficient of 1.0 (right) [33].

The rate of radiative heat transfer is governed by the Stefan-Boltzmann law. This states that the radiative rate of heat transfer from a surface is directly proportional to the emissivity, surface area, and fourth power of the temperature of the surface, with the constant of proportionality being the Stefan-Boltzmann constant [33]. The emissivity is a measure of the ability or efficiency of the surface of a body to emit electromagnetic energy relative to ideal conditions - in other words, the emissivity is a ratio of the actual radiation emitted to the ideal radiation emitted by a black-body [33, 51].

This is indicated in Equation 2.44, but it is also necessary to balance the resultant radiative heat transfer with the absorbed electromagnetic energy which has been emitted by surrounding bodies. This can be accounted for through the absorptivity as a measure of the ability or efficiency of the surface of

a body to absorb electromagnetic energy relative to ideal conditions [33, 51]. Considering a single body and its surroundings, the surroundings can be seen to act as a black-body with an emissivity of unity and an expression of the heat transfer can be acquired in Equation 2.45, assuming the emissivity and absorptivity are equivalent as is the case for a gray-body, and further simplified in Equation 2.46 using the radiation heat transfer coefficient - it is also supposed that there is no internal transmission of electromagnetic energy which only becomes a concern when the body has a degree of transparency [33]. It should be noted that, if the absorptivity is less than unity, the remaining portion of incident electromagnetic energy is reflected by the surface without contributing to heat transfer [33, 51].

$$\dot{Q}_{rad} = -\epsilon\sigma AT_{sur}^4 \quad (2.44)$$

$$\dot{Q}_{rad} = \alpha\sigma AT_{\infty}^4 - \epsilon\sigma AT_{sur}^4 = -\epsilon\sigma A(T_{sur}^4 - T_{\infty}^4) \text{ with } \epsilon \approx \alpha \quad (2.45)$$

$$\dot{Q}_{rad} = -h_r A(T_{sur} - T_{\infty}) \text{ with } h_r = \epsilon\sigma(T_{sur} + T_{\infty})(T_{sur}^2 + T_{\infty}^2) \quad (2.46)$$

The emissivity and absorptivity for selected substances and surface finishes at 27°C are given in Table 2.1. However, these values are aimed to be only tolerable for the temperatures between 0°C and 50°C with insolation emitted by the Sun, because the emissivity and absorptivity may vary slightly based on the temperature of the surface and frequency, wavelength, and angle of the insolation [33, 51]. The ratio of the absorptivity to emissivity is also listed, where a small value is desirable if the surface is intended to dissipate heat and a large value is desirable if the surface is intended to store heat.

Table 2.1: Emissivity and absorptivity for insolation from the Sun for selected substances [33, 51].

Surface Material	ϵ	α	α/ϵ
Aluminium, Anodised	0.84	0.14	0.17
Aluminium, Dull	0.20	0.42	2.10
Aluminium, Polished	0.03	0.09	3.00
Chromium	0.08	0.24	3.00
Clay, Light	0.90	0.22	0.24
Clay, Porcelain	0.92	0.50	0.54
Glass, Smooth	0.92	*	*
Iron, Polished	0.26	0.64	2.46
Iron, Galvanised	0.13	0.65	5.00
Paint, Black, General	0.86	0.96	1.12
Paint, Black, Flat/Matte	0.97	0.97	1.00

Surface Material	ϵ	α	α/ϵ
Paint, White, General	0.89	0.39	0.44
Plastic, General, Black	0.87	0.96	1.10
Plastic, General, White	0.90	0.21	0.28
Plastic, Polypropylene	0.97	*	*
Plastic, PTFE	0.92	*	*
Plastic, PVC	0.91	*	*
Rubber, Foam	0.90	0.65	0.72
Rubber, Natural, Hard	0.91	0.65	0.71
Rubber, Natural, Soft	0.86	0.65	0.76
Stain. Steel, Dull	0.21	0.50	2.38
Stain. Steel, Polished	0.75	0.78	1.04

With regards to the spectrum of insolation in Figure 2.11, the Sun initially emits electromagnetic energy as an approximate black-body at 5800K [33]. As the insolation propagates towards the Earth, the flux of electromagnetic energy decreases due to the increasing spherical area through which it passes. At the edge of the atmosphere, the flux of electromagnetic energy has decreased by a factor based on the

inverse square law and equal to the square of the ratio of the radius of the Sun to the distance between the Sun and Earth [33]. Additionally, a departure from a normal zenith angle at which the insolation is received also decreases the flux of electromagnetic energy as the insolation is spread over an increased area on the surface. In this case, a solar constant can be defined as the flux of electromagnetic energy incident on a horizontal surface at the edge of the atmosphere when the Earth is at a mean distance from the Sun [33]. This results in a value of approximately 1368W/m^2 received by the flat two-dimensional cross-sectional area of the Earth or an average of approximately 684W/m^2 when spread evenly over the hemispheric three-dimensional surface area of the Earth (varies based on elliptical orbit of the Earth around the Sun) [33]. The propagation of insolation is portrayed in Figure 2.12.

However, as the insolation propagates through the atmosphere, there is a degrading effect on its magnitude, spectral distribution, and directional distribution due to absorption and scattering by the constituents of the atmosphere [33]. The absorption prevents a portion of insolation from reaching the surface and, as exhibited in Figure 2.11, the effect of absorption is primarily from oxygen, ozone, water vapour, carbon dioxide, and dust particles. The scattering also prevents a portion of insolation from reaching the surface and the effect of scattering occurs as a result of the re-direction of the insolation by gas molecules through Rayleigh scattering (ratio of the effective particle diameter to the wavelength of the radiation is much less than unity and provides for nearly uniform scattering in all directions) or dust particles through Mie scattering (ratio of the effective particle diameter to the wavelength of the radiation is approximately unity and is concentrated in the direction of the incident rays) [33]. The effect from cloud coverage can drastically decrease the insolation received on the surface by over 50% to 95% for clouds ranging from cirrus, stratus, cumulus, and nimbus respectively.

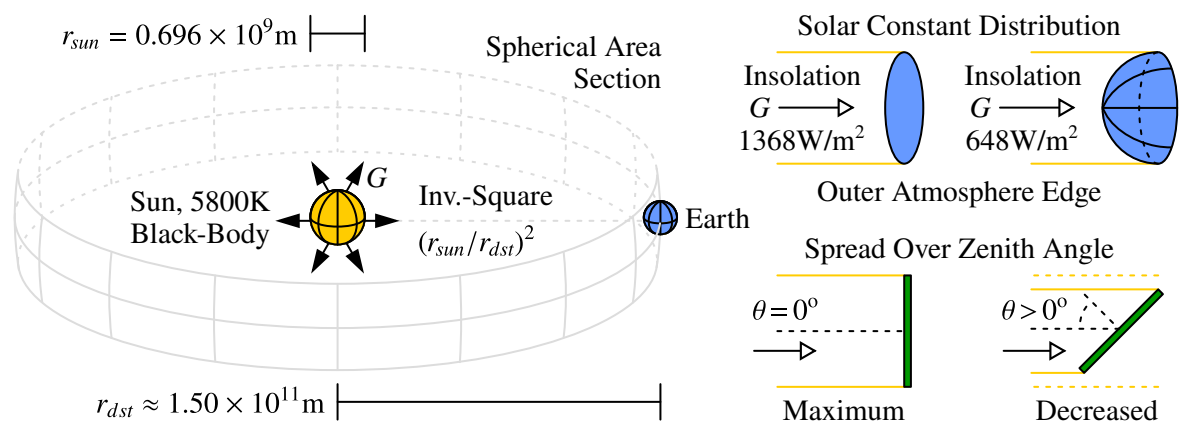


Figure 2.12: Propagation and distribution of insolation from the Sun through space towards the Earth.

2.4.4 RESISTANCE AND OVERALL HEAT TRANSFER

When a point is at a constant temperature, the total heat transfer to and from that point must be in equilibrium whether there are steady state or transient conditions [33, 42]. Thus, the overall sum of the rates of heat transfer through conduction, convection, and radiation must be equal to zero. This can be

given as the heat transfer rate balance expressed in Equation 2.47 and can equally be extended to an infinitesimally thin surface of a medium which encloses no mass or volume.

$$\sum \dot{Q}_i = 0 \rightarrow \dot{Q}_{in} - \dot{Q}_{out} = 0 \rightarrow \dot{Q}_{cnd} + \dot{Q}_{cnv} + \dot{Q}_{rad} = 0 \quad (2.47)$$

For systems only involving conduction and convection, the thermal resistance can be defined in Equation 2.48 as the ratio of the thermal potential difference or temperature difference to the heat transfer rate [33, 42]. In series, the thermal resistances are equivalently combined additively and, in parallel, the thermal resistances are equivalently combined with reciprocals additively. In a sense, a thermal circuit can be constructed, where heat transfer and thermal resistance are analogous to charge and electrical resistance respectively. The overall heat transfer coefficient can also be defined in Equation 2.49 as a representation of the combination of the thermal resistance and associated area.

$$R_t = \frac{\Delta T}{\dot{Q}} \rightarrow R_{t,cnd} = \frac{L}{kA} \text{ and } R_{t,cnv} = \frac{1}{hA} \text{ and } R_{t,rad} = \frac{1}{h_r A} \quad (2.48)$$

$$U = \frac{1}{R_t A} \rightarrow \dot{Q} = UA\Delta T \quad (2.49)$$

2.5 EVAPORATIVE COOLING

As mentioned, the process of evaporative cooling relies on using the energy required to initiate evaporation to produce an overall cooling effect. This process can be modelled by considering the heat transfer processes between the components of the system and the psychrometric properties of the moist air as it flow through the system. To maximise performance, the components of the system need to be specifically optimised to induce peak evaporation and a high forced air flow.

2.5.1 BASIC PROCESS MODEL

The heat of evaporation or enthalpy of vaporisation or latent heat of vaporisation is defined as the amount of heat which must be transferred to a liquid to transition a quantity of the substance into a vapour [24, 33]. The heat of evaporation exists due to the change in internal energy which occurs during the phase transition and is dependent on pressure and temperature until the critical point, but it is acceptable to assume a constant heat of evaporation for small pressure and temperature ranges. With regards to water, the heat of evaporation is relatively high, where a large amount of heat is required for the phase transition and it can be found from the difference between the enthalpy at the saturated liquid and saturated vapour states, as shown in Equation 2.50. The mass specific heat of evaporation is plotted in Figure 2.13 for selected substances, where it is seen that a constant value of 2442kJ/kg can be assumed for water for temperatures between 0°C and 50°C at atmospheric pressure [24].

$$\Delta h_{fg} = h_g - h_f \leftrightarrow \Delta \bar{h}_{fg} = \bar{h}_g - \bar{h}_f \quad (2.50)$$

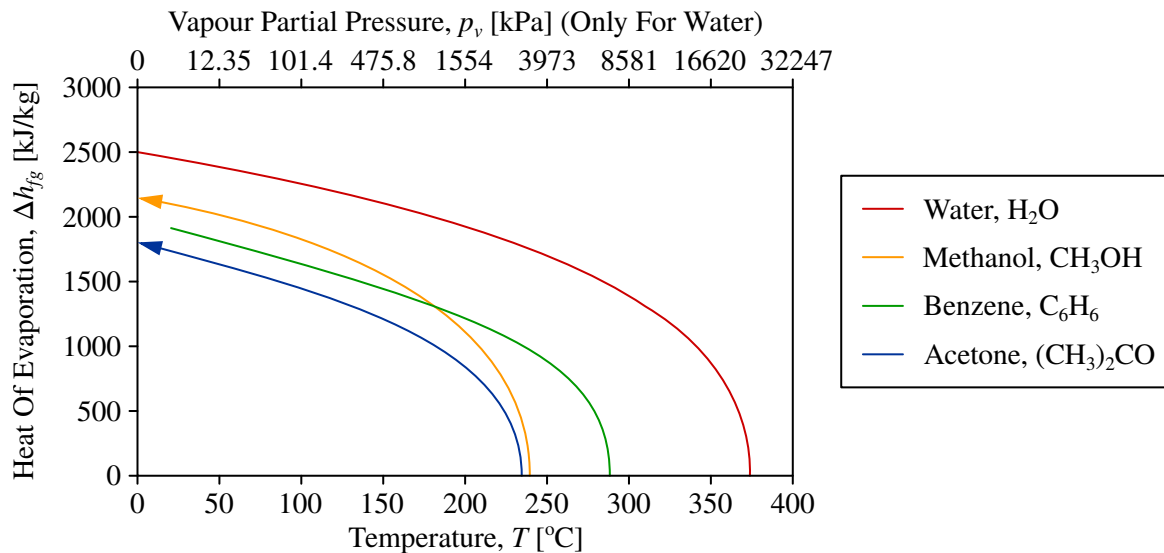


Figure 2.13: Variation in heat of evaporation for changes in temperature for selected substances [24].

So, the principle of evaporative cooling is based on using the energy of an air flow to evaporate water from a source through convective processes, such that there is heat and mass transfer between the air flow and water, as demonstrated in Figure 2.14. The source is typically a pad soaked in water over or through which air is allowed to flow. Considering the water in the pad, evaporation is able to occur because the water molecules near the surface experience collisions with the air molecules which increases their internal energy above the requisite heat of evaporation to overcome the relatively strong hydrogen bonds, other intermolecular forces, and vapour partial pressure of the atmosphere [33]. As a result, the average internal energy of the water is decreased which corresponds with a decrease in the temperature of the water and, subsequently, a decrease in the temperature of the pad since there are interactions between the pad and water to reach an equilibrium temperature [33].

Before considering the air, it should be noted that there are sensible heat and latent heat components. The sensible heat component is associated with heat transfer which results in a change in temperature, such as with changes in internal energy [33]. The latent heat component is associated with heat transfer which does not result in a change in temperature, such as during a phase transition [33]. Now considering the air, the internal energy transferred from the air molecules during the collisions with

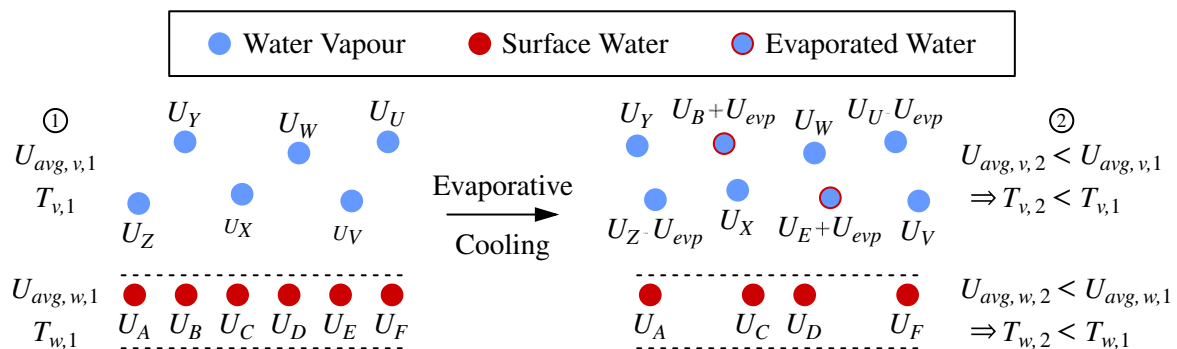


Figure 2.14: Simplification of the process of evaporative cooling considering molecular interactions.

the water molecules causing evaporation results in a decrease in sensible heat which corresponds with a decrease in the temperature of the air [33]. Moreover, there is an increase in the latent heat due to the water vapour transferred from the pad which corresponds with an increased relative humidity of the air (it should be emphasised that this does not increase the average internal energy of the water vapour, since these additional molecules have a minimum internal energy just above the requisite heat of evaporation) [33]. When neglecting other forms of energy transfer and due to the conservation of energy, it is required for the loss in sensible heat to be equal to the gain in latent heat.

A graphic of the arrangement of the system is illustrated in Figure 2.15, where the air flow can be achieved through free convection from natural winds or forced convection from a fan. If the surface of the pad is considered as the system at steady state, the heat transfer rate balance is given in Equation 2.51 with no other heat transfer, such that the sensible heat in Equation 2.52 is equal to the latent heat in Equation 2.53 on a mass basis. The heat of evaporation is evaluated at the surface temperature. The water vapour density at the surface is associated with saturated conditions at the surface temperature.

$$\sum \dot{Q}_i = 0 \rightarrow \dot{Q}_{cnv} = \dot{Q}_{evp} \quad (2.51)$$

$$\dot{Q}_{cnv} = h_c A (T_m - T_{sur}) \quad (2.52)$$

$$\dot{Q}_{evp} = \dot{m}_w \Delta h_{fg} = h_m A (\rho_{v,sur} - \rho_{v,m}) \Delta h_{fg} \text{ with } \rho_{v,sur} = \rho_{v,g,sur} \text{ at } T_{sur} \quad (2.53)$$

For further evaluation, it is first necessary to recall that the Prandtl number provides a measure of the relative effectiveness of momentum and energy transport in the velocity and thermal boundary layers, while the Schmidt number provides a measure of the relative effectiveness of momentum and species transport in the velocity and concentration boundary layers [33]. Hence, as long as the boundary conditions are analogous, the profiles of the thermal and concentration boundary layers must be of the same functional form and, for this reason, the relationships of heat and species transfer for a particular geometry are actually interchangeable [33, 52]. This implies that the result for the transfer of species can be found using the result from the heat transfer by substituting the Nusselt number with the Sherwood number and the Prandtl number with the Schmidt number - conversely, the heat transfer could be found from the transfer of species [33, 52]. Thus, the convection heat and mass transfer

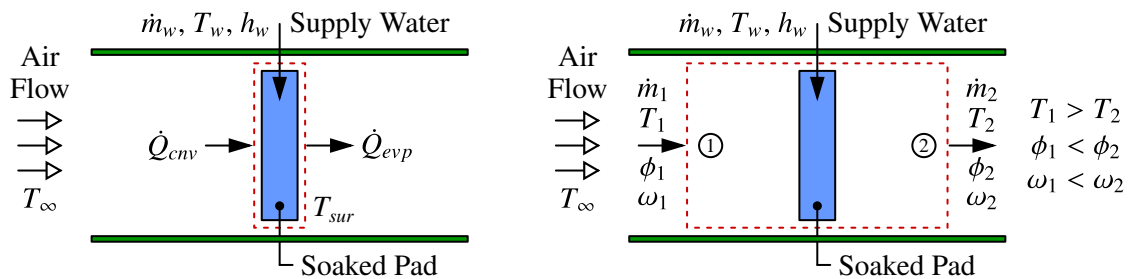


Figure 2.15: Illustration of evaporative cooling with moist air flow through a soaked pad, with considerations for the surface of the pad as the system (left) and air flow as the system (right).

coefficients can be directly related through Equation 2.54. A proportional exponent is applied to the Prandtl number and Schmidt number as Bergman et al. [33] reported that the Nusselt number and Sherwood number are respectively proportional to these parameters. The proportional exponent must be positive, less than one, and typically has a value of one-third for most applications [33, 53].

For accuracy in the relation of the convection heat and mass transfer coefficients, the properties for the density, mass specific heat capacity, and Lewis number should be evaluated at the film or arithmetic mean temperature of the thermal boundary layer [33]. As expressed in Equation 2.55, the film temperature is simply an average of the surface and free stream temperatures.

$$\frac{\text{Nu}_L}{\text{Pr}^n} = \frac{\text{Sh}_L}{\text{Sc}^n} \rightarrow \frac{h_c}{h_m} = \frac{k_a}{D_{a,v}} \frac{\text{Pr}^n}{\text{Sc}^n} = \frac{k_a}{D_{a,v}} \frac{1}{\text{Le}^n} = \rho_a c_{p,a} \text{Le}^{1-n} \quad \text{with } 0 < n < 1 \quad (2.54)$$

$$T_f = \frac{T_{sur} + T_m}{2} \quad (2.55)$$

Thus, the magnitude of the overall cooling effect can be determined with Equation 2.56. For easier evaluation, this can be simplified to Equation 2.57 by applying the relationships from the ideal gas idealisation, so that vapour densities can be evaluated through vapour partial pressures and temperatures.

$$T_m - T_{sur} = \Delta h_{fg} \left(\frac{h_m}{h_c} \right) (\rho_{v,g,sur} - \rho_{v,m}) = \frac{\Delta h_{fg}}{\rho_a c_{p,a} \text{Le}^{1-n}} (\rho_{v,g,sur} - \rho_{v,m}) \quad (2.56)$$

$$T_m - T_{sur} = \frac{M_w \Delta h_{fg}}{\bar{R} \rho_a c_{p,a} (\alpha_a / D_{a,v})^{0.667}} \left(\frac{p_{v,g,sur}}{T_{sur}} - \frac{p_{v,m}}{T_m} \right) \quad (2.57)$$

If the flow of moist air between an inlet and outlet is considered as the system at steady state, the applicable aspects to consider are the properties of the incoming and outgoing moist air flow. Based on the conservation of mass and adopting the Dalton model, the dry air can be considered individually and, therefore, its mass flow rate must remain constant between the inlet and outlet since there are no changes to the amount of dry air, while the water vapour can also be considered individually, but its mass flow rate at the outlet must be greater than the mass flow rate at the inlet due to the addition of water vapour through evaporation. This is assessed in Equation 2.58 and Equation 2.59 for the dry air and water vapour respectively, where the mass flow rate of the evaporated water can be expressed in terms of the mass flow rate of the dry air and the difference in the humidity ratio at the outlet and inlet.

$$\dot{m}_{a,in} = \dot{m}_{a,out} \rightarrow \dot{m}_{a,1} = \dot{m}_{a,2} = \dot{m}_a \quad (2.58)$$

$$\dot{m}_{v,in} = \dot{m}_{v,out} \rightarrow \dot{m}_{v,1} + \dot{m}_w = \dot{m}_{v,2} \rightarrow \omega_1 \dot{m}_a + \dot{m}_w = \omega_2 \dot{m}_a \rightarrow \dot{m}_w = \dot{m}_a (\omega_2 - \omega_1) \quad (2.59)$$

With regards to the conservation of energy, there is no resultant heat transfer or work performed and it can reasonably be assumed that the changes in kinetic and potential energies are negligible [24]. Thus, the rate balance can be readily evaluated to Equation 2.60 and further simplified to Equation 2.61, where it is supposed that the water vapour can be evaluated as a saturated vapour and the evaporated water can be evaluated as a saturated liquid [24]. The specific enthalpy of the evaporated water is

usually much less than the specific enthalpy of the dry air and water vapour, which leads to the moist air effectively maintaining a nearly constant enthalpy and wet-bulb temperature [24].

$$0 = \sum (\dot{m}h)_{in} - \sum (\dot{m}h)_{out} \rightarrow 0 = (\dot{m}_a h_a + \dot{m}_v h_v)_1 - (\dot{m}_a h_a + \dot{m}_v h_v)_2 + \dot{m}_w h_w \quad (2.60)$$

$$0 = (h_a + \omega h_{g,v})_1 - (h_a + \omega h_{g,v})_2 + (\omega_2 - \omega_1) h_{f,w} \text{ with } h_v \approx h_{g,v} \text{ and } h_w \approx h_{f,w} \quad (2.61)$$

An example of the changes in the properties of the moist air flow are depicted on the psychrometric chart in Figure 2.16, where the ideal conditions for best performance include a low relative humidity below 50%. These conditions are associated with a large difference between the dry-bulb and wet-bulb temperatures of at least 10°C [24]. Theoretically, the system is limited to achieving a relative humidity of 100% and the corresponding dry-bulb and wet-bulb temperature at this point and, thus, an efficiency for an evaporative cooling system can be defined in Equation 2.62 as a measure of the degree to which the wet-bulb temperature is approached [2, 27, 52]. This efficiency tends to be between 60% and 100% depending on the configuration of the system with either direct or indirect cooling [2, 27].

$$\eta_{evp} = \frac{T_1 - T_2}{T_1 - T_3} \times 100\% \quad (2.62)$$

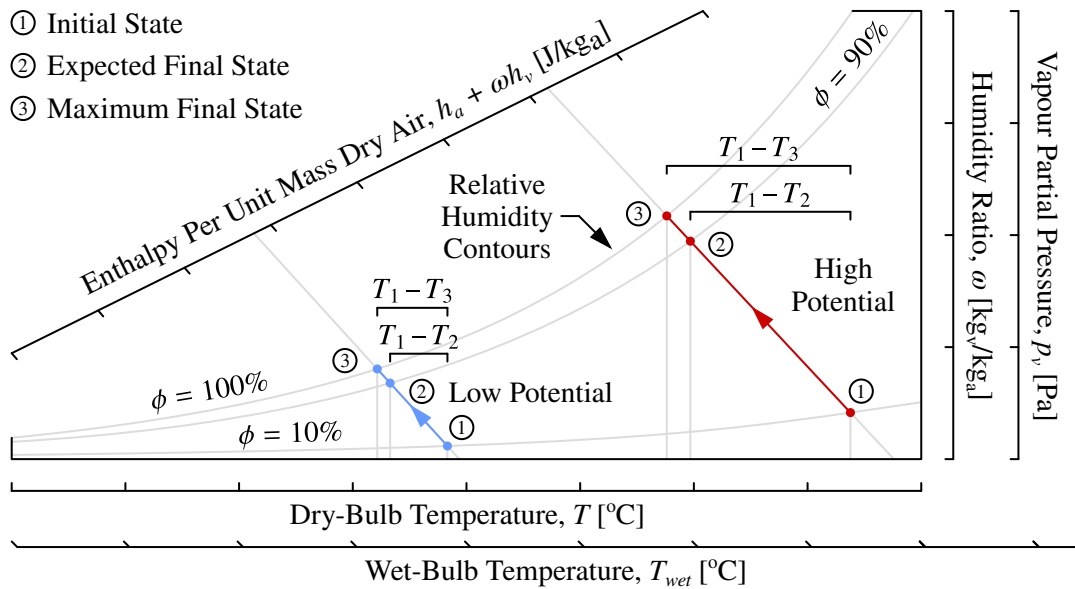


Figure 2.16: Example of a psychrometric chart for moist air undergoing an evaporative cooling process with a demonstration of high potential with a large overall cooling effect and low potential with a small overall cooling effect - in each case, the relative humidity is significantly increased.

Overall, evaporative cooling presents an opportunity to achieve considerable cooling while requiring no work input for natural convection, minimal work input for forced convection, low equipment requirements, little maintenance, negligible operating costs, and minor operating supplies. This allows for an affordable system compared to conventional refrigeration. The accuracy of this model is governed by the alignment of the actual system with the underlying assumptions, which is often fairly acceptable

for preliminary analysis - in other words, the error in the results increases the further the actual system varies from the underlying assumptions. For a more complex model, possibly incorporating other forms of heat exchange, the presented model has been introduced in sufficient detail and as an appropriate base to be adapted to build a more in-depth and accurate model for design development.

2.5.2 CONVENTIONAL COOLING PADS

Firstly, it should be noted that there is an alternate method of deploying evaporative cooling through spraying a mist or fog into the moist air flow. This allows for better evaporation for an improved cooling effect with an increased efficiency [2]. However, it is also required for a significant work input and additional equipment to increase the pressure and flow rate of the water to create the mist or fog, as opposed to using natural flow due to gravity to soak a pad. Basically, a soaked pad offers a higher performance-to-cost ratio and is a more suitable option for the current circumstances [2].

For the construction of the pad, there have been numerous materials investigated and experimented on in several studies to gauge relative performance for the best evaporation and cooling effect while remaining affordable and using local materials. The overarching criteria for the material is that it is able to store large amounts of water and maintain a uniform distribution of this water [54]. Although the methods of implementing evaporative cooling may differ, some of the common materials include jute, hessian, balsa, palm, luffa, cotton, and straw fabrics; aspen, pine, fir, cedar, red wood, spruce, and other wood wools; plain and etched glass fibres; porous ceramics and stones; copper, bronze, and galvanised steel screenings; expanded and corrugated papers; and various synthetic polymer woven cloths, microfibres, and foams such as polyester, polyethylene, and polyamide [54, 55, 56, 57].

There are also commercial pads available which primarily include deviations of CELdek, which consists of impregnated and corrugated cellulose paper sheets at different flute angles which have been bonded together and designed to allow for the through-flow of air with a low pressure drop; and GLASdek, which is constructed from premium inorganic and ceramic materials with cross-flutes and the aim of offering maximum efficiency for maximum cooling with a through-flow of air [58, 59, 60]. A collection of samples of some of the listed materials is seen in Figure 2.17.

As mentioned, there have been several studies comparing different materials to gauge relative performance, but it is difficult to compile an absolute ranking of materials since the configuration of the systems, operating equipment, and environmental conditions may have been different in each case. In some cases, there was a focus on cooling buildings and personal spaces as opposed to cooling for fruits and vegetables. So, the results of the most useful studies are presented qualitatively for a general sense of relative performance, although comparisons between studies is not necessarily reliable.

Manuwa and Odey [55] compared latex foam, jute, charcoal, and miscellaneous wood shavings, and it was found that there was a very marginal overall difference in performance with a ranking of jute,



Figure 2.17: Selected samples of common materials used for convectional pads [58, 59, 60, 61].

wood shavings, latex foam, and charcoal from best to worst. Olosunde, Igbeka, and Olurin [28] tested jute, cotton, and hessian with a ranking respectively in this order, although the jute was prone to mould formation. Guo [57] found that cotton offered superior performance over linen and wool. Jain and Hindoliya [62] investigated using coconut coir and palash fibres as replacements for aspen wool and khus fibres, and it was concluded that the palash fibres performed noticeably better than the aspen wool and khus fibres, while the coconut coir performed better than the khus fibres and equally comparable to aspen wool. Al-Sulaiman [63] practically demonstrated that jute and luffa performed better than a reference commercial aspen wool, but date palm performed worse than the reference commercial aspen wool. Dhamneya, Rajput, and Singh [56] referred to a previous study and presented the ranking of performance as aspen wool, high density polythene foam, corrugated paper, and rigid cellulose from best to worst, where the overall difference in performance was minor but consistent. Xuan et al. [61] summarised the performance of pads constructed from GLASdek, CELdek, aluminium foil, porous ceramic, and polyvinyl chloride with the cooling efficiency decreasing respectively in this order. Finally, Liao and Chiu [64] evaluated the performance of coarse and fine fabrics of polyvinyl chloride sponge mesh in a wind tunnel, and it was reported that the fine fabric gave a slightly better cooling efficiency than the coarse fabric, although there was significantly less performance fluctuations for the coarse fabric compared to the fine fabric. It was also apparent that the inclusion of synthetic polymer woven cloths in the investigations were limited, but it could prove to be useful with a low cost.

An additional desirable characteristic is for the pad to remain fully saturated and distribute water from a supply reservoir at an equal rate to the rate at which it loses water through evaporation [57]. However, this is difficult to maintain without precise controlling equipment since the environmental conditions can vary widely. So, to ensure a maximum cooling effect and avoid the situation when the pad is unsaturated with dry regions, it is most practical to supply the pad at a slightly higher rate and collect the excess water in a surplus reservoir. If a pump is not used to recirculate the excess water, then it is

beneficial for the pad to have capillarity or capillary action properties, such that it is able to absorb and lift water from the surplus reservoir once the supply reservoir has been depleted [57].

Technically, capillarity is the ability of liquids to penetrate into fine pores with wettable walls and be displaced from those with non-wettable walls [65]. In fabrics, this action is often referred to as wicking and it is a result of a curved meniscus of the liquid formed in the capillary spaces between fibres in warp and weft directions, especially in the interstitial areas [65]. Thus, due to a pressure difference created by the surface tension across the curved meniscus, there are resultant forces acting on the liquid which drives the liquid into the capillary spaces [65]. The forces are governed by the properties of the liquid, liquid-surface interactions, and geometric configurations of the pore structure between the fibres [65]. A graphical explanation of capillarity is illustrated in Figure 2.18.

Considering water forming a column in a cylindrical tube due to capillarity, a hydrostatic equilibrium is achieved as the water rises with a force balance between the driving forces from the surface tension pressure difference and weight of the column of liquid. The surface tension pressure difference is derived from the Young-Laplace equation and is directly dependent on the surface tension and meniscus contact angle of the liquid-surface interface, as given by Equation 2.63 [65]. Thus, the force balance results in Equation 2.64 which can be manipulated to return the height to which the liquid rises or wicking height. So, if capillarity in fabrics is assumed to adhere to capillarity experienced in cylindrical tubes as a simplification, the property which determines the capillarity performance is only reliant on the capillary radii of the pores in the fabric when using the same liquid with each fabric.

$$p_c = \frac{2\gamma}{r} \cos(\theta) \quad (2.63)$$

$$\sum F_i = 0 \rightarrow \sum p_i = 0 \rightarrow p_c = p_s \rightarrow \frac{2\gamma}{r} \cos(\theta) = \rho g H \rightarrow H = \frac{2\gamma}{\rho g r} \cos(\theta) \quad (2.64)$$

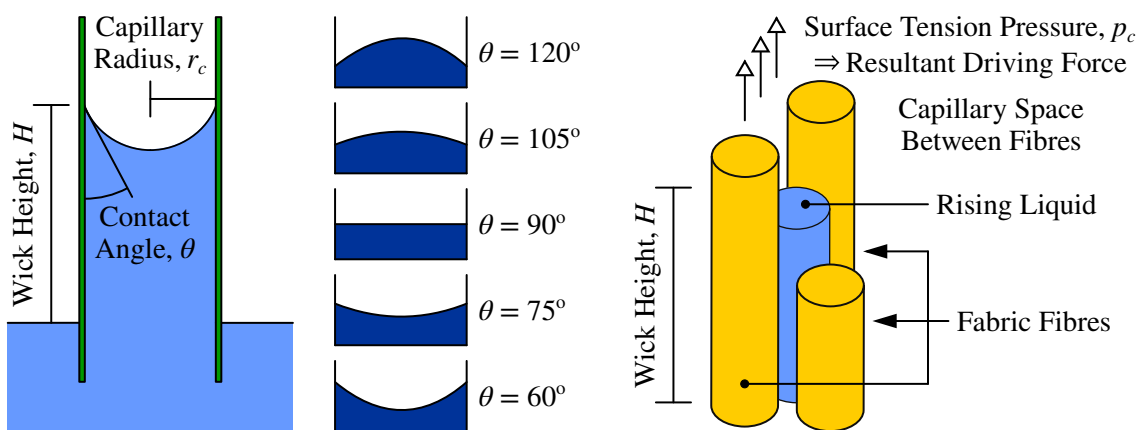


Figure 2.18: Cross-section of capillarity in a cylindrical tube with examples of different contact angles (left), and simplification of the process of capillarity between the fibres of a fabric (right).

Supposing capillarity in fabrics adheres to capillarity experienced in cylindrical tubes, Chatterjee and Singh [65] applied Lucas-Washburn dynamics from Equation 2.65, which traditionally describes

capillary flow in a bundle of parallel cylindrical tubes, to samples of polyester fabrics under multiple tensile loads with water as the liquid. This study related the rise of a liquid through capillarity to the density, viscosity, surface tension, and meniscus contact angle of the liquid and radius of the micro-capillaries (between fibres) and macro-capillaries (between strands of woven fibres) of the polyester fabrics. From the experimental results, it was discussed that the wicking height increased with increasing tensile load and it was reasoned that the tensile load caused a lateral elongation and radial compaction of the fibres which corresponds with a decrease in the capillary radius and leads to the development of a greater pressure within the capillary responsible for wicking, since the capillary pressure is inversely related to capillary radius; wicking height with a weft orientation was greater than the wicking height with a warp orientation for all of the samples and it was proposed that this occurs due to the difference in tension in the warp and weft directions during the formation of the fabric which creates differences in the capillary radius and disposition of the capillaries in the respective directions; and wicking height decreased as the weft strands density increased and it was suggested that the radial expansion of the fabric as the weft strands density increases is responsible, since there is a greater thickness which corresponds with a greater capillary radius and reduced pressure within the capillary responsible for wicking [65]. Notably, it was also seen that the rate at which the liquid rises before equilibrium will decrease as the capillary radius is decreased and distance risen is increased [65].

$$\frac{dL}{dt} = \frac{\sum p_i}{8\mu H} (r^2 + 4\epsilon r) \quad \text{with} \quad \sum p_i = p_c - p_s = \frac{2\gamma}{r} \cos(\theta) - \rho g H \quad (2.65)$$

2.5.3 FORCED AIR FLOW

The effect of a forced air flow allows for the air to be rapidly cleared once the local concentration of water vapour has increased from the evaporation of water vapour from the pad, such that new air is continuously introduced at the ambient relative humidity. This is achieved through turbomachines with air as the working fluid, where the rotation of a rotor with blades dynamically interacts with the fluid for the transfer of energy [66, 67]. In general, a pump is a turbomachine which transfers energy to the fluid with work being performed by the blades on the fluid, while a turbine is a turbomachine which transfers energy from the fluid with work being performed by the fluid on the blades [66, 67]. For the purpose of inducing a forced air flow, it is necessary to consider a fan as a form of pump.

A fan may induce an axial, radial, or mixed flow depending on the predominant direction of the air motion relative to the axis of the rotor as the air passes the blades. The transition of a turbomachine from an axial fan to a radial fan is illustrated in Figure 2.19 with mixed flow in-between. Typically, a predominantly axial flow has a very high flow rate, very high rotational speed, low pressure rise, small cross-sectional layout, large longitudinal-section layout, and high noise, while a predominantly radial flow has a moderate to high flow rate, moderate rotational speed, and moderate to high pressure rise, large cross-sectional layout, small longitudinal-section layout, and low noise [66, 67, 68].

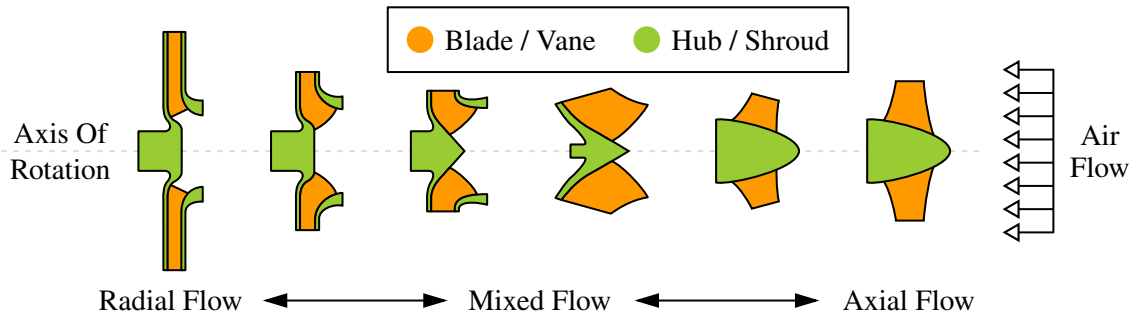


Figure 2.19: Difference in basic fan construction transitioning from radial flow to axial flow [66, 67].

2.5.3.1 PERFORMANCE CHARACTERISTICS

To clarify the analysis of fans, it can be assumed that the air is incompressible; there is one-dimensional and steady flow without turbulence or vorticity; the air flows smoothly along the surface of the blades such that the relative velocity between the blade and flow is parallel at the leading and trailing edges of the blades; for an axial flow, the flow enters and exits the blades at the same radial distance with no radial deviation; and, for radial-flow, the flow enters and exits the blades at the same axial distance with no axial deviation [66, 67]. This allows for the flow to be characterised using simplified approximations and idealised velocity triangles with the absolute velocity of the blades, absolute velocity of the flow, and relative velocity between the blade and flow, as shown in Figure 2.20. However, it should be kept in mind that the actual flow is very complex with compressible, three-dimensional, unsteady, and transient effects. Ultimately, an error up to 25% is realised with these assumptions [66, 67].

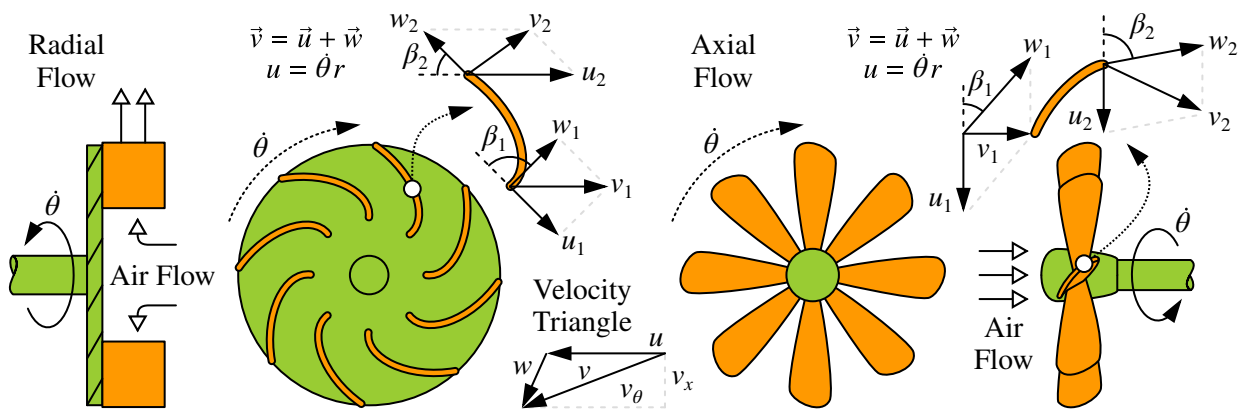


Figure 2.20: Velocity triangles along the fan blades for radial flow (left) and axial flow (right).

Considering a fan inducing an axial flow. The rotor can be seen to be driven at a constant angular velocity, such that the absolute velocity of a blade can be seen to be normal to the axis of rotation. The absolute velocity of the incoming flow can be seen to be parallel along the axis of rotation towards the blades. When the air encounters a blade, the air and blade must each experience opposite forces which change the direction of the flow with an increased absolute velocity and pressure through the performance of work by the blade on the air, since a force is translating through a displacement or, identically, a torque is translating through an angle [66, 67]. These observations can be equivalently

extended to a radial flow, but it should be recognised that a blade is usually curved and the blade velocity at the leading and trailing edges are not necessarily in the same direction [66, 67].

With the conservation of energy, mass, linear momentum for axial flow, and angular momentum for radial flow, it is possible to consider the fan as a control volume and derive the turbomachine equations which are given in Equation 2.66 and Equation 2.67 respectively for the torque and power transferred from the fan to the air flow [66, 67]. With this, the ideal pressure rise created by the fan can also be determined in Equation 2.68 in terms of head rise, which is a measurement of pressure in relation to the height difference for a column of fluid corresponding to the particular pressure exerted by the column of fluid, as outlined in Equation 2.69 [66, 67]. Again, this head rise can be seen as a maximum limit of performance since head losses may be suffered through irreversibilities from skin friction, flow separation, clearance flow, blade profile, shock losses, recirculation losses, vortex formation, and other three-dimensional hydraulic inefficiencies [66, 67]. For more accurate quantitative results, simulations and experimental measurements need to be prioritised in order to gain an understanding of the three-dimensional effects and actual performance. (Since work is being performed by the blade on the air, flow out of the system is seen as positive and flow into the system is seen as negative).

$$\sum(\vec{r} \times \vec{F}) = \int (\vec{r} \times \vec{v})\rho\vec{v} \cdot \hat{n} dA \rightarrow T = \dot{m}(r_2v_{\theta,2} - r_1v_{\theta,1}) \text{ with } \dot{m} = \dot{m}_1 = \dot{m}_2 = \rho\dot{V} \quad (2.66)$$

$$W_{fan} = T\theta \rightarrow \dot{W}_{fan} = T\dot{\theta} = \dot{m}(u_2v_{\theta,2} - u_1v_{\theta,1}) = \dot{m} \frac{(u_2^2 - u_1^2) + (v_2^2 - v_1^2) - (w_2^2 - w_1^2)}{2} \quad (2.67)$$

$$\dot{W}_{fan} = \rho g \dot{V} H_{fan} \rightarrow H_{fan} = \frac{\dot{W}_{fan}}{\rho g \dot{V}} = \frac{\dot{W}_{fan}}{\dot{m}g} = \frac{(u_2^2 - u_1^2) + (v_2^2 - v_1^2) - (w_2^2 - w_1^2)}{2g} \quad (2.68)$$

$$H_a = \left(\frac{p}{\rho g} + \frac{u_2v_{\theta,2} - u_1v_{\theta,1}}{g} + z \right)_2 - \left(\frac{p}{\rho g} + \frac{v^2}{2g} + z \right)_1 = H_{fan} - H_{loss} \quad (2.69)$$

For a radial fan, the profile of the blades can be backward-curved or forward-curved. As shown in Figure 2.21, backward-curved blades have an outlet angle less than 90° with air exiting primarily in the normal direction relative to the circumference and forward-curved blades have an outlet angle greater than 90° with air exiting primarily in the tangential direction relative to the circumference. However, forward-curved blades tend to suffer greater turbulent, unstable, and pulsating flow conditions with erratic stalling and choking, so backward-curved blades are preferred in most designs as they provide improved efficiency, adaptability, flow distribution, and long-term reliability without detrimental effects [68, 69, 70]. For emphasis, it was discussed by Frank and Darvish [71] that the maximum attainable efficiency for forward-curved blades is only 65%, while the maximum attainable efficiency for backward-curved blades is 85%, since the divergence of the flow is narrowed which produces less recirculation losses. Considering backward-curved blades, the inlet angle is normally in the range of 15° to 50° and the outlet angle is almost always in the range of 15° to 50° as well [66, 67, 72, 73].

For an axial fan, the profile of the blades is usually straight with a constant pitch between inlet and outlet angles in the range of 2° to 15° with lower values being more common to reduce the component

of radial flow [66, 67, 70]. The blades may also be curved backward or forward with different inlet and outlet angles, but these profiles may create a greater component of radial flow depending on the flow conditions [70]. These basic profiles are shown in Figure 2.21, but more complex designs with out-of-plane inclinations are usually pursued with optimisations to maximise efficiency. However, the design and performance prediction of a fan in general is a difficult task due to the high number of free geometric parameters and often needs to be approached iteratively with numerous designs, as acknowledged by Jansen and Kirschner [73], Zhou et al. [74], and Cheah et al. [75].

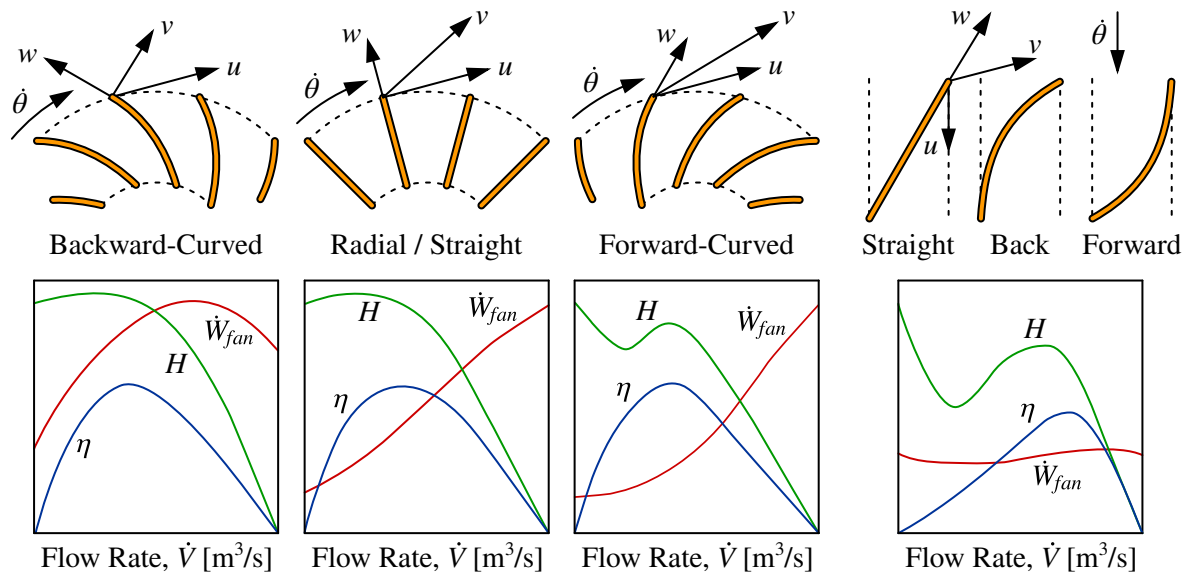


Figure 2.21: Comparison between the profile of blades along with the typical variation in work rate, head rise, and efficiency against flow rate for a radial fan (left) and axial fan (right) [66, 67, 68, 69].

2.5.3.2 DRIVING ELECTRIC MOTOR

To drive a small-scale fan creating a forced air flow, a brushed or brushless direct current motor is capable of achieving the desired performance and it is unnecessary to consider synchronous, induction, or other types of motors which require additional components to accommodate alternating current without explicit advantage. The physical difference between brushed and brushless motors, shown with the basic constructions in Figure 2.22, is the location of the coils, magnets, and delivery of current, where a brushed motor consists of permanent magnets creating a magnetic field as the stator to cause the rotation of excited coils as the rotor, while a brushless motor utilises the sequential excitation of coil pairs as the stator to create a rotating magnetic field to rotate a permanent magnet as the rotor. Traditionally, inexpensive ferrite magnets are used as the permanent magnets, but some motors use rare earth magnets for greater magnetic flux density to allow a smaller size for a given torque.

A brushed motor offers a high maximum speed, reduced costs, and simple control without a controller for fixed speed operation, but it may have a low efficiency, large size, high noise, arcing, dust residue, and substantial wear of the brushes leading to poor and irregular contact and reduced life expectancy.

A brushless motor usually has a high efficiency, compact size, good heat dissipation, low rotor inertia, and little wear for improved reliability and extended life expectancy, but it usually operates at a low maximum speed, has elevated costs, and requires complex control with precise timing and rotary encoders or Hall effect sensors to determine the position of the rotor. The life of a brushed motor is usually limited by its brushes, while the life of a brushless motor is only limited by its bearings.

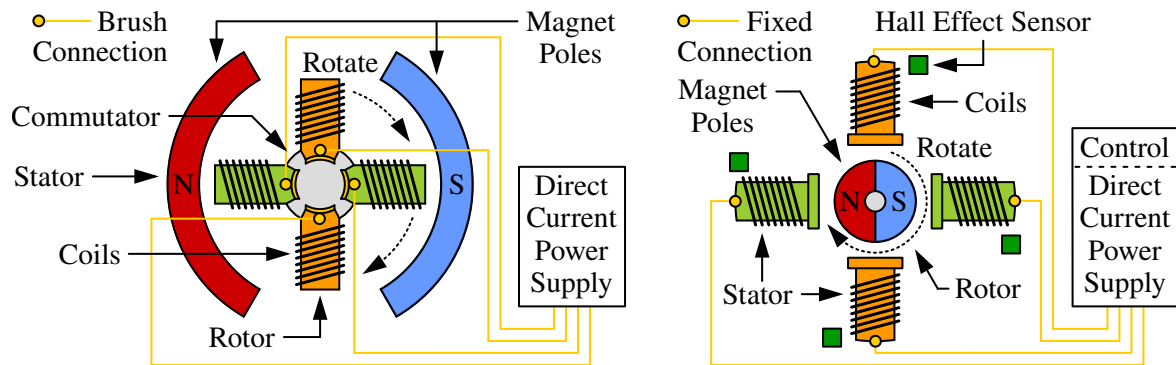


Figure 2.22: Comparison between the construction of brushed (left) and brushless (right) direct current motors. (A brushless motor can be inverted such that the stator is inside and the rotor is outside).

The motor essentially converts electrical energy into mechanical energy in the form of the rotation of the shaft of the rotor. The supplied power to the motor in Equation 2.70 is equal to the product of the current and voltage which can be further manipulated using Ohm's law. With regards to the efficiency in Equation 2.70, there are losses of energy due to heat, friction, and imbalanced loads which decrease the effectiveness of the conversion and reduce the magnitude of the useful mechanical energy which is generated. The efficiency for a brushed motor is typically lower between 65% and 80%, while the efficiency of a brushless motor is typically higher between 80% and 95%.

So, the overall efficiency of a fan is given by Equation 2.71 and can be seen to be dependent on the hydraulic inefficiencies, mechanical inefficiencies in the bearings and assembly, volumetric inefficiencies due to the leakage of flow, and electric inefficiencies in the motor [66, 67]. The mechanical and electric inefficiencies are fairly constant for most operating conditions, as shown in Figure 2.23, but the hydraulic and volumetric inefficiencies are directly dependent on the flow rate and, thus, the efficiency is a function of the flow rate and reaches a maximum value for a specific flow rate which is considered the operating condition. Examples of this relationship were included in Figure 2.21 for the various blade profiles with effects from friction and other losses shown in Figure 2.24.

An extension can be approached through the definition of the coefficient of performance for the overall system as the ratio of the heat transfer for a useful cooling effect to the work performed to achieve this cooling effect [24]. This is demonstrated in Equation 2.72. A general range for the coefficient of performance for evaporative cooling could not be reliably sourced, but a coefficient of performance from 11.1 up to 27.6 was reportedly calculated by Erens and Dreyer [52] for a temperature decrease of 5°C using an indirect evaporative cooler on a large scale for a room, while the coefficient of

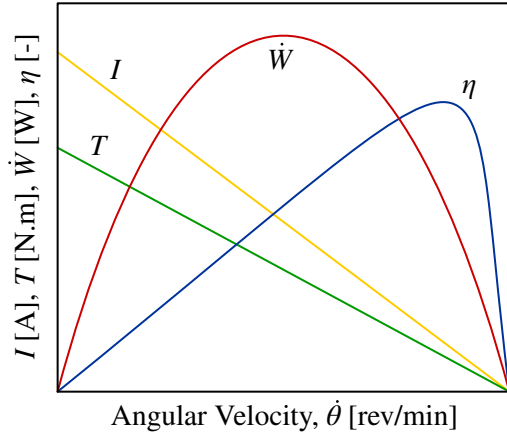


Figure 2.23: Typical variation in current, torque, power and efficiency for direct current motors.

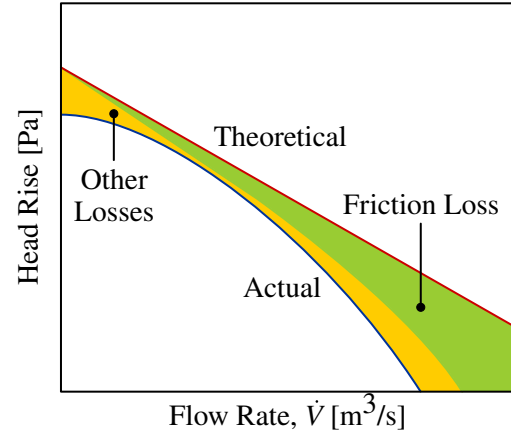


Figure 2.24: Effect of friction and other losses on the head rise over a fan with flow rate [67].

performance varied between 23 and 78 for Jin et al. [76] for external temperatures from 32°C to 40°C respectively using an indirect evaporative cooler to experimentally achieve a temperature difference up to 10°C for air conditioning. For comparison, a coefficient of performance around 2.69 to 8.0 is expected for a vapour-compression cycle and 0.47 to 1.70 is expected for a vapour-absorption cycle, although these cycles are aiming for a substantially greater temperature decrease [1, 77, 78, 79].

$$\dot{W}_{mtr} = IV = I^2 R_e = \frac{V^2}{R_e} \rightarrow \dot{W}_{shf} = T_{shf} \dot{\theta} = \eta_{mtr} \dot{W}_{mtr} \quad (2.70)$$

$$\dot{W}_{fan} = \eta_{hyd} \eta_{mch} \eta_{vol} \dot{W}_{shf} \rightarrow \dot{W}_{fan} = T_{fan} \dot{\theta} = \eta_{hyd} \eta_{mch} \eta_{vol} \eta_{mtr} \dot{W}_{mtr} \quad (2.71)$$

$$\xi = \frac{Q_{cool}}{W_{in}} = \frac{\dot{Q}_{cool}}{\dot{W}_{in}} \rightarrow \text{Evaporative Cooling: } \xi = \frac{Q_{cqv}}{W_{fan}} = \frac{\dot{Q}_{cqv}}{\dot{W}_{fan}} \quad (2.72)$$

2.6 SOLAR POWER AND PHOTOVOLTAIC SYSTEMS

The generation of solar power is associated with the conversion of energy from light into electrical energy using photovoltaic cells. This phenomenon is based on using an extrinsic semiconductor material which exhibits the photovoltaic effect with varying electrical characteristics, such as voltage, current, or electrical resistance, when the cell is exposed to light. The photovoltaic effect is ascribed to an incident photon of light being absorbed by a surface and causing an electron to be excited within the surface, assuming the photon of light has sufficient energy to overcome an energy barrier for the excitation of the electron to a higher energy state [80, 81]. As a result, an electric potential difference is produced by the separation of charge through diffusion [80, 81]. This is fundamentally similar to the photoelectric effect, except the photoelectric effect was originally developed and ascribed to an incident photon of light being absorbed by a surface and causing an electron to be emitted from the surface, instead of retaining the electron within the surface as a charge carrier as with the photovoltaic effect - principally, a photovoltaic cell is a form of a photoelectric cell [80]. In brief, the overall advantages of solar power and photovoltaic systems include a compact and lightweight configuration,

no operating costs, no dependency on the availability of fuels, low environmental impact with no emission of pollutants during operation (although there currently is minor pollution in the production of the cells), and form of renewable energy without the depletion of scarce resources.

2.6.1 PHOTOVOLTAIC EFFECT

For supplementary detail, a photon possesses energy due to its momentum and this is completely transferred as it is absorbed by the electron in a discontinuous process and, so, the number of electrons excited is directly proportional to the number of photons absorbed or the intensity of the incident light [51, 80]. Also, the energy of the photon must be sufficient to overcome the energy barrier for excitation of the electron, where the energy barrier is dependent on the characteristics of the material from which the surface is constructed [80, 81]. The energy of a photon is given by Equation 2.73 and is only dependent on the frequency of the incident light. Applying this to the energy barrier for a specific material, a cut-off frequency can then be defined below which no electrons are excited regardless of the intensity of the incident light. This can be adapted for a cut-off wavelength [51, 80].

$$E_{ph} = hf \rightarrow E_{ele} = E_{ph} - E_{bar} = hf - hf_{cut} \rightarrow f_{cut} = \frac{E_{bar}}{h} \rightarrow \lambda_{cut} = \frac{hc}{E_{bar}} \text{ with } \lambda = \frac{c}{f} \quad (2.73)$$

With the excitation of many electrons, the electric potential difference gives rise to the diffusion of these electrons as negative charge carriers which, in turn, leads to the generation of a direct current [80, 81]. Further inquiry into this generation of electric potential difference and current was unnecessary for the simple use of cells in an assembled configuration, as the overall performance can be sourced from the datasheet provided by suppliers of the cells, but it should be acknowledged that there is a saturation value for the maximum current which can be generated for the intensity of the incident light and further increasing the electric potential difference will not increase the current [80, 81]. (If cells were to be designed, Würfel [82] could be investigated with analysis for solid-state materials).

2.6.2 CONSTRUCTION AND PERFORMANCE

A cell is constructed from an extrinsic semiconductor material as a thin wafer with a positive electrode and negative electrode to form the electric poles. Considering inexpensive and reliable construction, these cells usually use mono-crystalline or multi-crystalline silicon with a single p-n junction [51, 81]. These designs use silicon as the primary material (doped with boron to form the p-type or acceptor layer and phosphorus to form the n-type or donor layer) with an energy barrier of 1.12eV which corresponds with a cut-off wavelength of 1.10 μ m, as shown in Figure 2.25 with the insolation from the Sun [51, 81]. There are other designs, such as cadmium-telluride thin-film cells or incorporating multiple p-n junctions with different doping materials for a range of energy barriers, but these designs are less available and either have a drastically reduced efficiency from 6% to 12% with a marginally lower cost or partially improved efficiency around 19% with a substantially higher cost [51, 81].

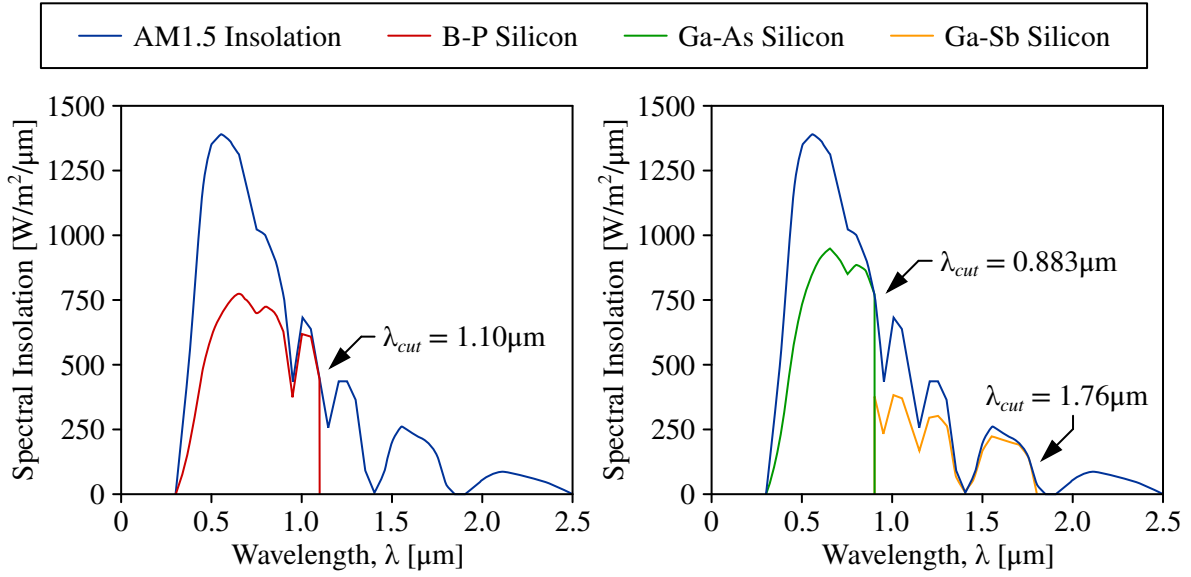


Figure 2.25: Performance of a single p-n junction with boron-phosphorus (left) and multiple p-n junction with gallium-arsenide and gallium-antimonide (right) for the spectrum of the electromagnetic energy received from the Sun as insolation considering a standard air mass coefficient of 1.5 [51, 81].

A mono-crystalline silicon cell consists of continuous silicon ingots formed from single crystals and cut to form a wafer. A multi-crystalline silicon cell consists of discrete silicon fragments formed from multiple crystals and melted to form a wafer. The efficiency of a cell is given by Equation 2.74 as the ratio of the generated power to the received electromagnetic energy and, in general for commercial cells, mono-crystalline silicon cells have a higher efficient between 13% and 19% compared to multi-crystalline cells with efficiencies between 11% and 15%, but multi-crystalline silicon cells are often more available, simpler to manufacture, and more inexpensive compared to mono-crystalline silicon cells [51, 81]. The life cycle is often comparable with a range well over 10 years without degradation in performance for both types [51, 81]. According to Hsu et al. [83] in their compilation of life cycle assessments, there is also a slight difference in the global warming potential, where mono-crystalline silicon cells have an average of 45 ± 20 g/kW/h of equivalent CO₂ emissions, while multi-crystalline silicon cells have an average of 55 ± 32 g/kW/h of equivalent CO₂ emissions - this accounts for the entire life cycle from the acquisition of the raw materials to the eventual disposal after operation. The typical construction of these cells with a single p-n junction is shown in Figure 2.26.

$$\eta_{ele} = \frac{\dot{E}_{max}}{GA} = \frac{IV}{GA} \quad (2.74)$$

A cell usually generates a voltage of approximately 0.6V with a current of approximately 340A/m² or power of approximately 200W/m² and can be connected in series or parallel to form panels or modules which can then be connected in series or parallel to form arrays, as included in Figure 2.26 [51, 81]. As is expected, if the panels are combined in series, the voltage is combined additively with a constant current and, if the cells are combined in parallel, the current is combined additively with a constant voltage. Unfortunately, when cells are connected in series, it is crucial for each cell to receive a similar

intensity of the incident light and avoid shading, otherwise there will be a substantial reduction in the current which is limited by the cell receiving the minimum intensity of the incident light [81].

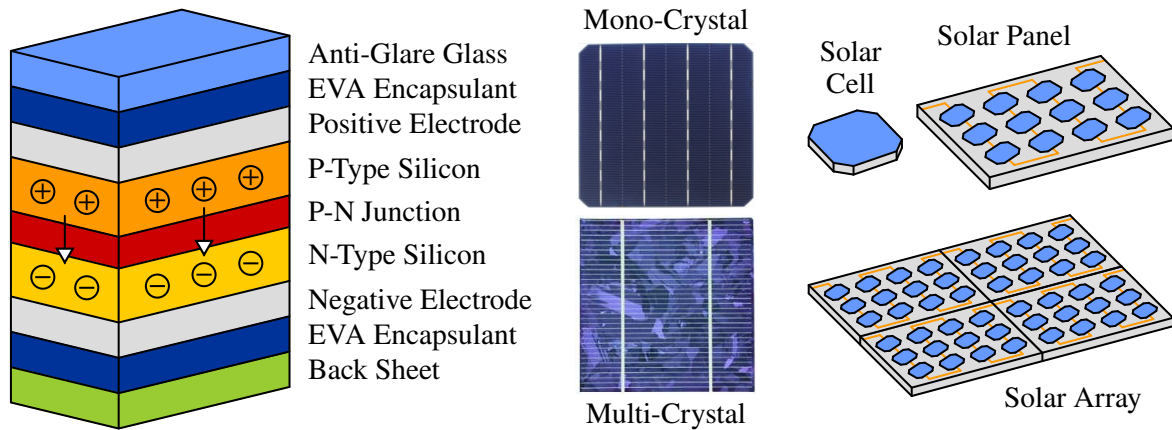


Figure 2.26: Construction of a photovoltaic cell (left), example of a mono-crystalline silicon cell and multi-crystalline silicon cell (centre), and set of a photovoltaic cell, panel, and array (right) [81].

It should also be noted that the temperature of the cell has an effect on its efficiency. For a general evaluation, the efficiency will decrease by 0.5% for each 1°C increase above 25°C when considering mono-crystalline or multi-crystalline silicon cells [51, 85]. Also, the performance is usually quoted as a maximum under standard conditions with 1000W/m² of incident light and an air mass coefficient of 1.5 at 25°C [51]. As a result, it is typical for the actual performance to be slightly lower than the quoted performance, especially at higher temperatures, so a practical safety factor should be considered. This is described in Figure 2.27, where the current slightly increases and voltage strongly decreases with temperature change; along with the behaviour as the intensity of incident light varies, where the current quasi-linearly increases and voltage slightly increases as the insolation increases [84].

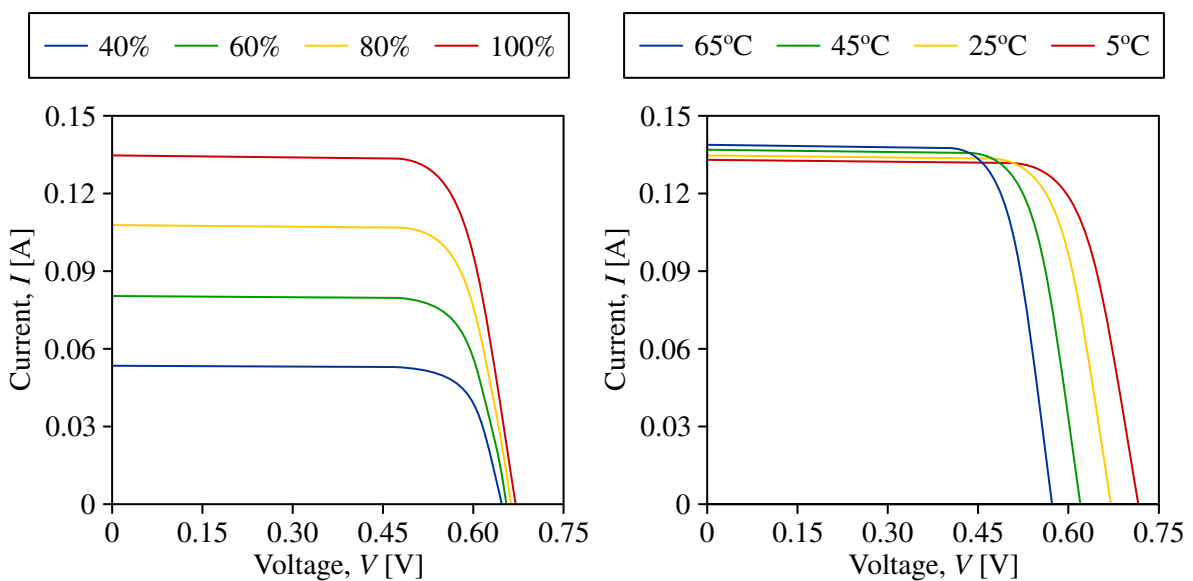


Figure 2.27: Variation in the current and voltage for changes in intensity of incident light (left), and variation in the current and voltage for changes in temperature (right) [51, 81, 84].

2.6.3 ENERGY STORAGE COMPONENTS

A complete solar power and photovoltaic system also includes a means of energy storage through a battery as an electro-chemical cell with an anode, cathode, and electrolyte, where the generated electrical energy from the source is stored as chemical energy within the battery during charging which can then be discharged as electrical energy. The electro-chemical process is facilitated by an oxidation-reduction reaction, where the most common types of reactions include lead-acid, nickel-cadmium, nickel-metal hydride, and lithium-ion batteries with their typical characteristics compared in Table 2.2. However, lead-acid and nickel-cadmium batteries should be avoided as they have steep performance degradation over time and serious health and environmental issues if mishandled, so it is preferable for nickel-metal hydride or lithium-ion batteries to be used for better performance, longer life, less environmental risk, and improved quality. The use of a rechargeable battery also requires the incorporation of a battery management system to monitor the voltage, state of charge, depth of discharge, state of power, and temperature to ensure safe operation by maintaining the cells at an equilibrium voltage and instituting over-charge, over-discharge, and short circuit protection.

Table 2.2: Comparison between the typical characteristics of lead acid, nickel-cadmium (Ni-Cd), nickel-metal hydride (Ni-MH), and lithium-ion (Li-Ion) batteries [85, 86, 87]. It should be noted that most characteristics are highly dependent on the temperature and stage in the life cycle of the battery.

Battery Type	Energy / Mass [W.hr/kg]	Energy / Volume [W.hr/L]	Energy / Cost [W.hr/\$]	Charge-Discharge Efficiency [%]	Self-Discharge Rate [%/month]	Cycle Durability [cycles]	Nominal Cell Voltage [V]	Operating Temperature [°C]	Toxicity And Environment Risk
Lead-Acid	30 - 50	80 - 90	4.0 - 7.1	65 - 95	3.0 - 20	< 700	2.0 / 2.1	-10 - 40	High
	Chemical Balance: $Pb + PbO_2 + 2H_2SO_4 \rightleftharpoons 2PbSO_4 + 2H_2O$								
Ni-Cd	40 - 85	50 - 150	1.6 - 3.3	60 - 70	5.0 - 15	< 2000	1.2	-20 - 50	High
	Chemical Balance: $Cd + NiO(OH) + 2H_2O \rightleftharpoons Cd(OH)_2 + 2NiO(OH)_2$								
Ni-MH	60 - 120	140 - 300	1.4 - 3.2	65 - 75	15 - 25	< 2000	1.2	-10 - 50	Low
	Chemical Balance: $MH + NiO(OH) \rightleftharpoons M + NiO(OH)_2$								
Li-Ion	90 - 250	250 - 690	1.5 - 5.0	80 - 90	0.5 - 5.0	< 1500	3.6 / 3.8	0 - 45	Low
	Chemical Balance: $Li_iC_6 + Li_{j-i}CoO_2 \rightleftharpoons LiCoO_2 + C_6$								

Alternatively, an electro-chemical capacitor with an anode and cathode separated by a dielectric or insulating material can act as a temporary reservoir in the system. A capacitor operates based on the

separation of charge, where a positive charge collects on the cathode while a negative charge collects on the anode to create an electric potential difference, such that this electric potential difference can be released during discharging. A capacitor usually has a specific energy between 0.5W.hr/kg and 12W.hr/kg, energy density of 5.0W.hr/L to 8.0W.hr/L, cost up to only 0.1W.hr/\$, charge/discharge efficiency from 90% to 95%, and cycle durability around 5×10^5 cycles [86]. The specific energy and energy density of a capacitor are significantly lower compared to a battery, because capacitors are only intended to provide a supply of energy for a short period of time on the scale of seconds to minutes. So, using an inline voltage regulator, a capacitor can aid in maintaining the voltage above a minimum value over short periods of time when the supply is intermittently disconnected or reduced. The construction and operation of a battery and capacitor are compared in Figure 2.28.

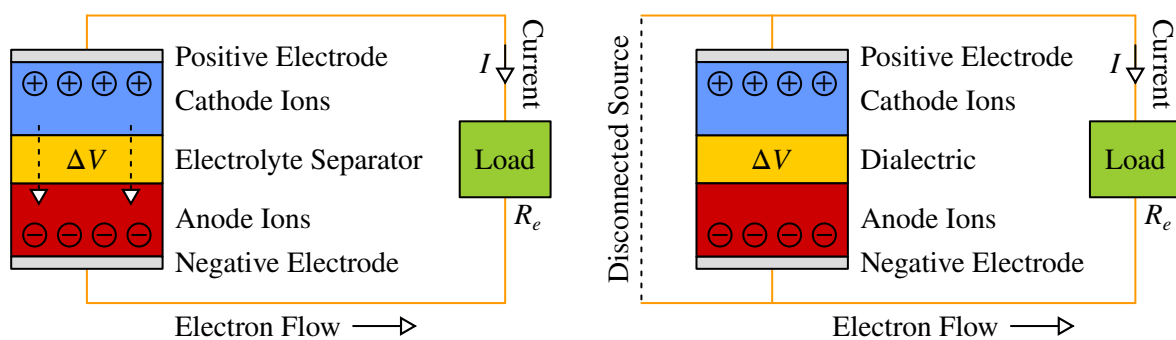


Figure 2.28: Construction of an electro-chemical battery (left) and electro-chemical capacitor (right) and operation during discharging (during charging, the electrons flow in the opposite direction).

2.7 EXISTING PRODUCTS

Although a majority of evaporative cooling implementations have been related to cooling buildings and personal spaces, there have been noteworthy attempts to create forms of storage for the preservation of fruits and vegetables using evaporative cooling. The first implementation of evaporative cooling for refrigeration was originally found in North Africa around 2500BC with a similar design to the modern Zeer Pot. There have been numerous iterations and designs over the years to explore the use of evaporative cooling for refrigeration (such as the coolgardie safe, bota bag, and charcoal cooler), but recent commercial products which demonstrate meaningful potential include the Bosch FreshBox and Fenik Yuma Cooler and these products are worth considering to recognise design similarities and competitive performance - although these products are not necessarily completely successful.

2.7.1 TRADITIONAL COOLER

A traditional cooler usually has a basic construction with an internal volume surrounded by walls formed from an external and internal layer of a synthetic polymer (such as polyethylene or polypropylene) with insulation in-between. It is most common for polyurethane foam to be used as the insulation with a composition consisting of up 98% air surrounded by walls of polyurethane, such that it can

be viewed in combination with a thermal conductivity of 0.10W/m/K to 0.30W/m/K contributed by the polyurethane and 0.0146W/m/K contributed by the air [88]. The foam may have an open-cell or closed-cell construction based on the pockets of air, where an open-cell construction has mostly partial pockets and tends to be flexible, while a closed-cell construction has mostly complete pockets and tends to be rigid. With regards to insulation, a closed-cell construction is primarily used as it usually has an improved performance over an open-cell construction and offers a reduced risk of water absorption - if water is absorbed into an open-cell construction, the open pockets will fill with water which increases the thermal conductivity and decreases the insulation potential [88, 89].

The molecular synthesis of polyurethane foam is complex with bonds between carbon, hydrogen, nitrogen, and oxygen atoms. The advantages of polyurethane foam are that it is readily available, simply manufactured and formed, lightweight with a density of 36kg/m³ to 470kg/m³, fairly inexpensive with an estimated cost from \$16/kg to \$17/kg, durable with a yield strength from 0.3MPa to 12MPa, and provides a very low thermal conductivity of 0.013W/m/K to 0.027W/m/K [88, 89]. The actual properties are highly dependent on the specified density, where a higher density generally has a higher cost, strength, and thermal conductivity compared to a lower density.

There are alternative materials used in other applications requiring insulation. These include polystyrene foam, polyethylene foam, polyisocyanurate foam, elastomeric foam, phenolic foam, nitrile rubber, cellular glass, bubble wrap, vacuum panels, cork, cellulose, aerogel, felt, cotton wool, fibreglass wool, or mineral wool. However, apart from polystyrene foam, these materials do not offer an attractive options when compared to polyurethane foam based on the combination of availability, manufacturing, mass, cost, durability, and thermal conductivity [88, 89]. A polystyrene foam has a simpler molecular synthesis in the form of carbon and hydrogen atoms with a closed-cell construction. This allows polystyrene foam to be readily available and inexpensive, although it is often pre-formed in sheets unless specifically manufactured for a complex shape. The density and strength of polystyrene foam are similar to that of polyurethane foam and it typically has an estimated cost of \$12/kg to \$15/kg but slightly higher thermal conductivity between 0.030W/m/K and 0.044W/m/K [88, 89].

The primary use of a traditional cooler is to chill beverages and it operates by placing the beverages within the internal volume along with ice. Similar to the evaporation of water, the melting of ice involves a transfer of energy through the heat of fusion or enthalpy of fusion or latent heat of fusion, which is defined as the amount of heat which must be transferred to a solid to transition a quantity of the substance into a liquid [33]. For ice, the mass specific heat of fusion is approximately 334kJ/kg for temperatures from 0°C to 50°C and allows for an equilibrium temperature just above 0°C [16, 33]. The performance is ultimately dependent on the wall thickness of the insulation which is usually dependent on the cost to purchase the cooler. An expensive cooler tends to have a wall thickness up to 50mm, while an inexpensive cooler usually has a thickness from 12mm - this is respectively seen based on the Yeti Tundra 45 with a list price of \$300 and Coleman 48 Quart with a list price of \$25 [90, 91].

However, there are critical disadvantages of using a traditional cooler. These include the need for a considerable amount of ice for operation, constant supply of ice for replenishment once melted, drainage and disposal of the melted water, reduced internal volume due to the space occupied by the ice, and increased mass from the melted water [16]. This introduces an operating cost to either make or purchase the ice. As a further note, to avoid the contents soaking in the melted water, it is necessary to divide the ice and contents by inconveniently placing one of them in a separate container.

2.7.2 ZEER POT

Found in many developing countries, a Zeer Pot or Pot-In-Pot Refrigerator or Clay Pot Cooler employs evaporative cooling through the use of an outer pot containing a lining of wetted sand and an inner pot to store fruits and vegetables. The outer pot is usually constructed from clay and has microscopic pores to allow the penetration of water from the wetted sand. The inner pot is also constructed from clay, but it is usually glazed to prevent the penetration of water from the wetted sand, and the internal volume can vary up to 100L [57, 10]. The type of sand is fairly irrelevant and simply needs to retain a uniform distribution of water, so it is usually sourced from a convenient local supply and can be replaced if it becomes contaminated [57]. A damp cloth or lid can be placed over the assembly to contain the cooling effect. Unfortunately, the total mass of the assembly is notable and it only provides a limited solution for portability since the pots are easily breakable. The cost to construct a Zeer Pot is estimated from \$10 to \$50 and there are no operating costs except for the water needed to wet the sand [10].

So, a Zeer Pot achieves evaporative cooling as the water from the wetted sand penetrates the outer pot and subsequently evaporates as air flows over the outer pot through natural convection. This results in the wetted sand decreasing in temperature, which then allows for heat to be transferred from the inner pot to the wetted sand. The effects on the air flow are not utilised for practical purposes. A schematic of the evaporative cooling process and an example of a Zeer Pot are seen in Figure 2.29. It should be emphasised that the design can be considered to be completely passive without an active means of cooling and the resulting cooling effect may be unreliable as it is completely dependent on the natural convection and, if there is insignificant natural convection, there will be no cooling effect.

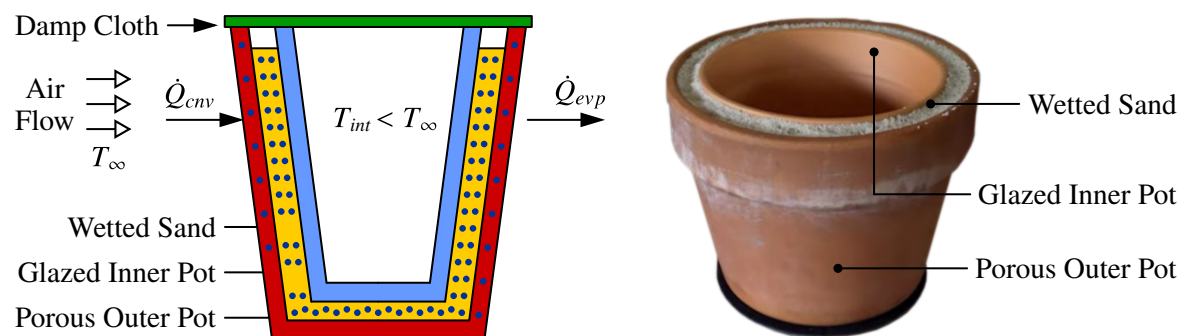


Figure 2.29: Cross-sectional schematic of the evaporative cooling process utilised by a Zeer Pot (left), and example of a regular assembly of a Zeer Pot without a damp cloth or lid (right) [10].

A study by Verploegen et al. [10] from the MIT D-Lab and World Vegetable Center evaluated the potential for non-electric evaporative cooling devices in the storage of fruits and vegetable in Bankass and Sikasso, Mali, with a focus on Zeer Pots and evaporative cooling chambers (an evaporative cooling chamber is similar to a Zeer Pot, but it is a large and dedicated structure and inapplicable as a compact and portable form of storage). In the investigation and experimentation, the crucial role of and need for the preservation of fruits and vegetables in society was acknowledged, and it was possible to achieve a temperature decrease of approximately 5°C to 8°C and relative humidity between 80% and 100%, which is realistic as a practical estimation based on ambient temperatures from 29°C to 37°C and relative humidity less than 40% - other factors which influence performance include the construction of the pot and air flow from the natural convection [10]. The corresponding results from the effects with regards to providing an extended shelf life for selected fruits and vegetables are shown in Table 2.3.

Table 2.3: Comparison between the shelf life of selected fruits and vegetables using previous methods of storage (woven basket, metal or plastic container, jar on wet sand, or sack) and a Zeer Pot [10].

Fruit / Vegetable	Dry Season Shelf Life [days]		Wet Season Shelf Life [days]	
	Previous	Zeer Pot	Previous	Zeer Pot
Cabbage	4 ± 2	8 ± 6	5 ± 3	9 ± 6
Cucumber	5 ± 3	9 ± 4	6 ± 4	13 ± 7
Eggplant	5 ± 3	10 ± 5	6 ± 3	12 ± 6
Hot Pepper	5 ± 2	9 ± 5	6 ± 3	11 ± 6
Tomato	4 ± 2	9 ± 4	6 ± 2	10 ± 5

Anyanwu [30] studied the use of a design similar to a Zeer Pot in Owerri, Nigeria. This design had the same arrangement as a Zeer Pot with an internal volume of 14L, but used coconut coir instead of sand as the wetted medium. When placed under shade with a fairly consistent natural wind up to 1.62m/s, it was reported that a maximum temperature decrease of 12°C was achievable with an ambient temperature of 38°C and relative humidity of 50% [30]. The overall results from the experimentation are reproduced in Figure 2.30 for the dry and wet seasons. Along with an identical sample outside of the enclosure, these results were obtained with a sample of fresh pumpkin and tomatoes inside of the enclosure to create realistic conditions accounting for the heat of respiration [30]. It was observed that, outside of the enclosure, the pumpkin and tomatoes showed initial signs of deterioration after 12hr and 32hr respectively and, inside of the enclosure, the pumpkin and tomatoes showed initial signs of deterioration after 60hr and 93hr respectively [30]. Overall, this illustrates the typical performance for evaporative cooling with natural convection, where the fluctuations in temperature within the enclosure are minimised between the day and night for more consistent diurnal and nocturnal conditions and improved prospects with regards to the short-term preservation of fruits and vegetables [30].

Although it is not directly relevant, Ambuko et al. [31] performed similar investigations with evaporative cooling chambers using silica waste and charcoal instead of sand in an attempt to decrease the twofold

to threefold deterioration of leafy greens for every 10°C increase in temperature. Their results provide a complement to the results presented by Verploegen et al. [10] and can be sourced for further detail, but the potential of evaporative cooling was ultimately highlighted for use in subsistence farming in rural areas since it is not required for a dependable form of energy to operate [31].

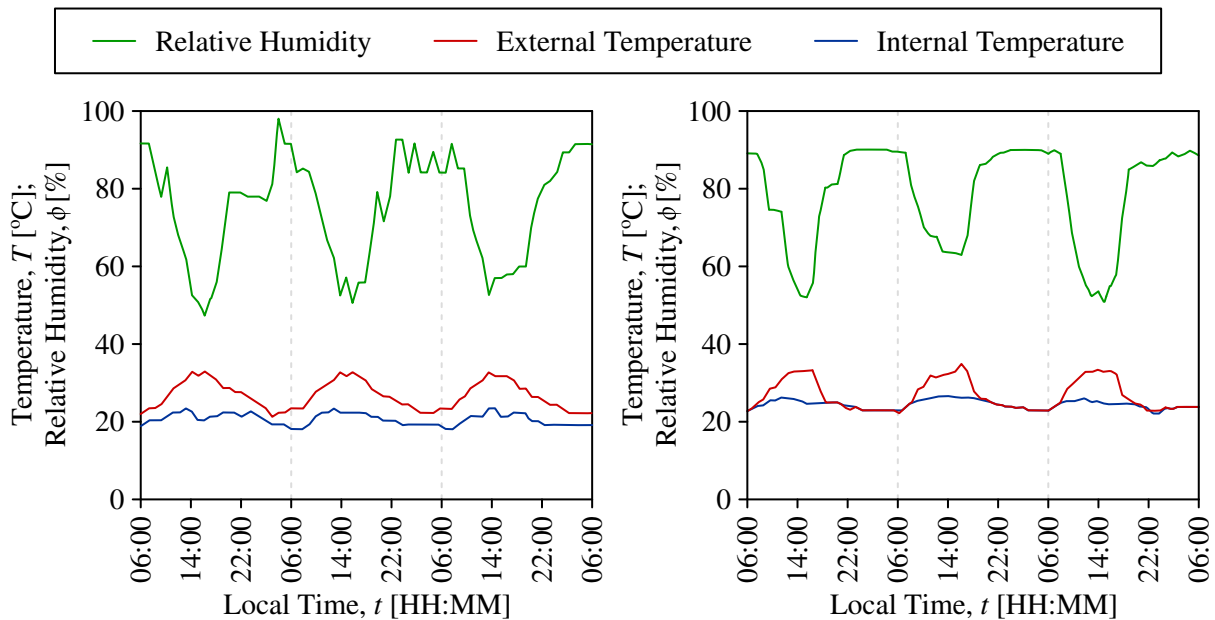


Figure 2.30: Representative results of the series of tests conducted in Owerri, Nigeria, during the dry (left) and wet seasons (right) by Anyanwu [30] for an evaporative cooling design similar to a Zeer Pot.

A modern product which mimics the design of a Zeer Pot is the MittiCool Clay Refrigerator, as seen in Figure 2.31. Instead of using sand, there is a built-in reservoir which houses up to 10L of water [92]. This water is then absorbed into the monolithic terracotta clay structure and exposed to an air flow in the same manner as the outer pot of a Zeer Pot, where it is claimed that a temperature decrease of 6°C to 8°C is achievable [92]. However, the MittiCool exhibits issues which include a possibility of the structure leaking due to its porosity, delay of 12hr as the water is absorbed before the cooling effect is perceivable, large mass of 20kg which reduces the potential as a portable solution, and fragile structure

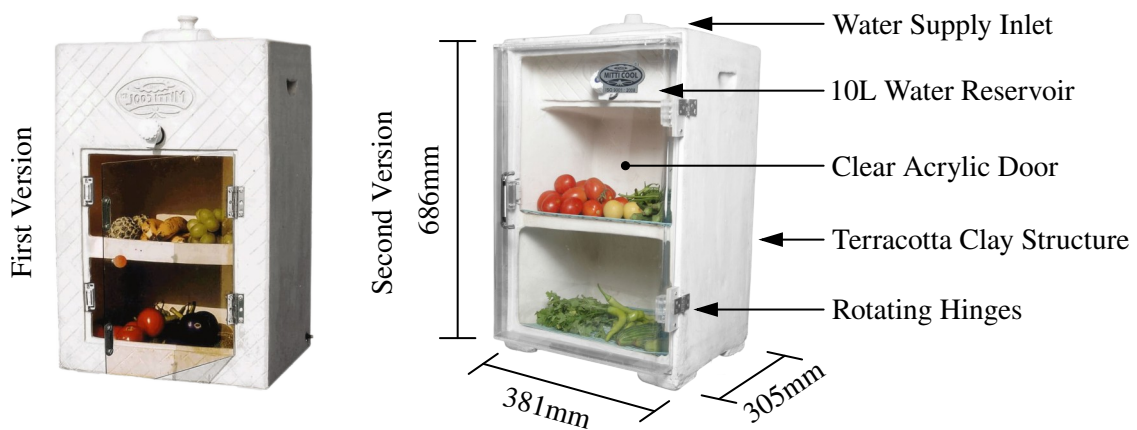


Figure 2.31: Graphic of a MittiCool with assemblies of the first (left) and second (right) versions [92].

which may fracture if mishandled [92]. The overall dimensions are 381mm by 305mm by 686mm with an internal volume of 50L [92]. The MittiCool is currently sold for \$130 in India [92].

2.7.3 BOSCH FRESHBOX

The FreshBox is a product recently developed by Bosch over two years and it is based on similar evaporative cooling principles as the Zeer Pot, with a focus for deployment in Lagos, Nigeria, and Mombasa, Kenya, during 2018 [93, 94]. Under optimal hot and dry conditions in the shade, the temperature within the FreshBox can be decreased by up to only 10°C with a corresponding increase in relative humidity compared to the environmental conditions [93, 94]. Other performance characteristics were not publicly available, but it was expected for the performance to decrease under less ideal environmental conditions. To achieve evaporative cooling, the FreshBox needs to be supplied with 1.4L/day to 2.0L/day of water [93, 94]. The dimensions of the FreshBox are 345mm by 628mm by 445mm with a mass of 6.4kg and internal volume of 43L [93, 94]. The cost to purchase a FreshBox is \$70 and, as with a Zeer Pot, there are no operating costs except for the supplied water [93, 94].

The assumed materials and assembly are shown in Figure 2.32. Although specific construction details are not available, it is presumed that the design utilises a fabric as a cooling pad situated between an internal aluminium wall and external synthetic polymer wall with slits acting as vents for air flow from natural convection. To maximise air flow, the external walls are likely to be open for ventilation, while the internal walls provide the structural support due to the high strength of aluminium - otherwise, a more inexpensive material could have been used for the internal walls, as discussed in Section 2.7.6. This obviously has an effect on costs, but it also does not provide any insulation for maintaining the temperature within the enclosure and cannot resist radiative heat transfer from insolation.

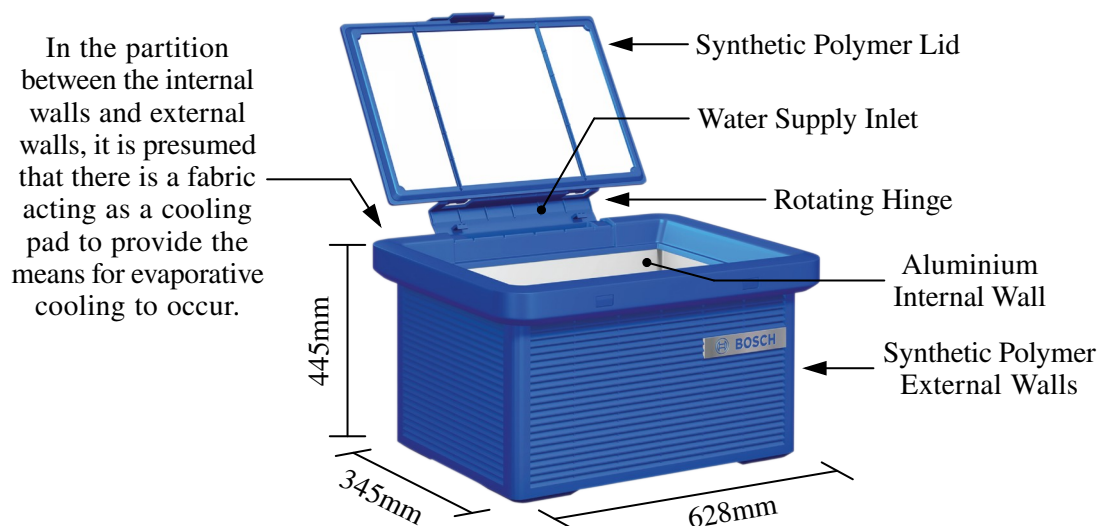


Figure 2.32: Graphic of a FreshBox with assumed materials and assembly for the construction [93].

The principle of this design is similar to the experimentation performed by Guo [57], where cotton, linen, and wool pads were soaked and used as a screen around a scaffolding frame to form an enclosure

in which fruits and vegetables were stored, although the enclosure was minimal with dimensions of 210mm in height with a 55mm radius for an enclosure volume of only 2.0L. The design was tested indoors using an external fan relying on an external electricity supply to create forced convection with air flow up to 6m/s, and it was possible to achieve a temperature of 11.9°C on average within the enclosure from an average ambient temperature of 23.1°C with a relative humidity between 37.4% and 48.1% [57]. These results are promising considering the low ambient temperature and average relative humidity, and it was estimated that the shelf life of fruits and vegetables could be extended by 5 days to 15 days [57]. For extension, the design was mounted to a car and, while the car was driven at 24.1km/hr, 48.2km/hr, and 72.4km/hr, the minimum temperatures within the enclosure were recorded as 22.8°C, 21.7°C, and 18.5°C respectively compared to the ambient temperature around 32°C with a relative humidity around 40% [57]. Given the unrealistic operating context, the second set of results are mostly redundant, but they do reinforce the idea that the cooling effect increases as the velocity of the air flow and convection heat transfer coefficient increase, which aligned with an increasing water consumption of 0.411L/hr at 24.1km/hr to 1.11L/hr at 48.2km/hr to 2.47L/hr at 72.4km/hr, as is expected if the convection heat and mass transfer coefficients are analogous [57].

2.7.4 FENIK YUMA COOLER

The Fenik Yuma Cooler or Evaptainer is also similar to a Zeer Pot, except it employs additional innovations and claims that it is able to achieve improved performance. Instead of a synthetic polymer creating a hard shell around the internal volume, a proprietary material called PhaseTek is substituted as a single wall to produce a large surface area around the internal volume of 60L [95, 96]. This material acts as a multi-layer membrane with a flexible bladder structure to absorb and retain water for an extended period of time [95, 96], and it was reasoned to be constructed of an outer hydrophobic membrane, which is water-proof but vapour permeable, and hydrophilic fabric to store the water between an inner thermoplastic polyurethane sheet. A similar multi-layer membrane was developed by Rothmaier et al. [97] for the purpose of a personal cooling garment and expanded upon by Yang, Cui, and Lan [54], where the membrane was constituted of dense layers of polyether-ester, which is a co-polymer of hydrophobic ester and hydrophilic ether allowing for water vapour to diffuse through the bulk polymer driven unidirectionally by the difference between the saturated water vapour partial pressure at the skin temperature and partial vapour of the surrounding air.

A total of 3.8L can be absorbed by the material with evaporation of approximately 0.5L/day and, since the material is flexible, the assembly can also be collapsed for more convenient portability [95, 96]. It is reported that it is possible to generate temperature decreases between 11°C and 17°C compared to the ambient temperature - other claims of performance under different environmental conditions are listed in Table 2.4 [95, 96]. However, the methodology of these claims was not disclosed and none of these claims have been verified. Overall, the mass of the Yuma is very low at 2.0kg and the dimensions are 457mm by 572mm with a collapsed height of 117mm or assembled height of 394mm [95, 96].

Table 2.4: Claimed performance of the Yuma under different environmental conditions [95, 96].

External Temper. [°C]	Relative Humidity [%]																
	2	5	10	15	20	25	30	35	40	45	50	55	60	65	70	75	80
	Internal Temperature [°C]																
23.9	12.2	12.8	13.9	14.4	15.0	16.1	16.7	17.2	17.8	18.3	18.9	19.4	20.0	20.6	21.1	21.7	22.2
26.7	13.9	14.4	15.6	16.7	17.2	17.8	18.9	19.4	20.0	20.6	21.7	22.2	22.8	23.8	24.4	24.4	25.0
29.4	16.1	16.7	17.2	18.3	19.4	20.0	21.1	21.7	22.2	22.8	23.3	23.9	24.4	25.0	26.1	27.2	
32.2	17.8	18.3	19.4	20.6	21.1	22.2	23.3	24.4	25.0	25.6	26.1	27.2	27.8	28.3	28.9	30.0	
35.0	19.4	20.0	21.1	22.2	23.3	24.4	25.6	26.1	27.2	27.8	28.9	29.4	30.6				
37.8	20.6	21.7	22.8	24.4	25.6	26.7	27.8	28.3	29.4	30.6	31.1						
40.6	22.2	23.3	25.0	26.1	27.2	28.9	30.0	31.1	31.7								
43.3	23.9	25.0	26.7	28.3	29.4	30.6	32.2	33.3									
46.1	25.6	26.7	28.3	30.0	31.7	32.8	34.4										
48.9	27.2	28.3	30.0	32.2	33.9	35.0											

After four years of development, the Yuma was launched in 2018 on an online crowdfunding platform to secure initial funding to begin large-scale production, where the aim was directed at consumers for recreational activities in developed countries [95, 96]. The lowest cost to purchase a unit during the fundraising stage was \$120 and the current list price is \$150, although it is not known whether this price would also apply after the funding period if it were to be deployed in developing countries [95, 96]. The Yuma is shown in Figure 2.33 in the collapsed and assembled configurations.

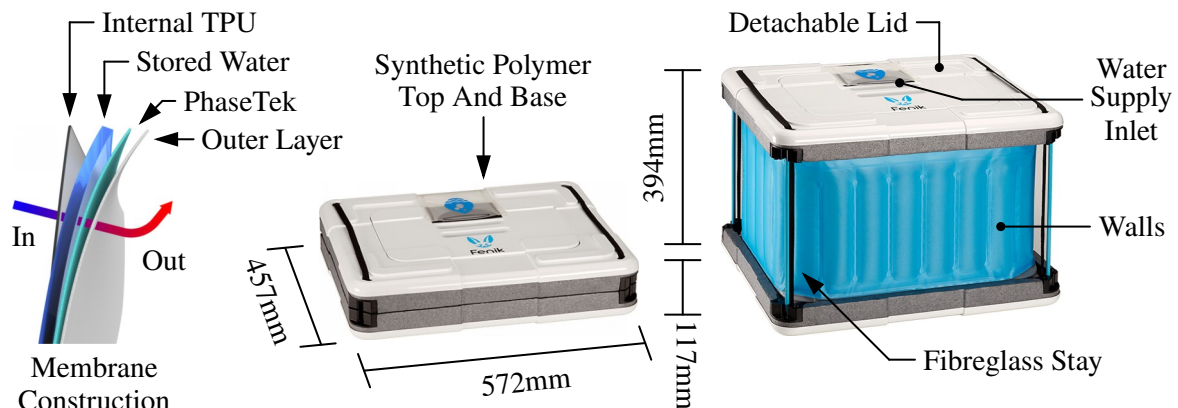


Figure 2.33: Graphic of the construction of the enclosing single wall of the Yuma (left), Yuma in the collapsed configuration (centre), and Yuma in the assembled configuration (right) [95, 96].

2.7.5 WAKATI ONE

The Wakati One pursues a different approach for the preservation of fruits and vegetables by using evaporative cooling to increase the relative humidity and ozone sterilisation and anti-oxidation to create a modified micro-climate within a tent structure made from an airtight fabric [98]. The processes

are achieved through ultrasonic evaporation to increase the relative humidity using approximately 0.2L/day to 0.4L/day of water and electric corona discharge to create the ozone with power supplied from a 10W solar panel [98]. The ultrasonic evaporator or humidifier consists of a diaphragm vibrating at an ultrasonic frequency to create water droplets and produce an extremely fine mist. The corona discharge operates by ionising the air around an electrically charged conductor which generates ozone and nitric oxide (can react with water vapour to form nitric acid) as a result - it should be noted that this can be toxic at high concentration levels. The temperature within the tent remains unchanged. The components are shown in Figure 2.34, where the tent is estimated to have a volume of 2m³.

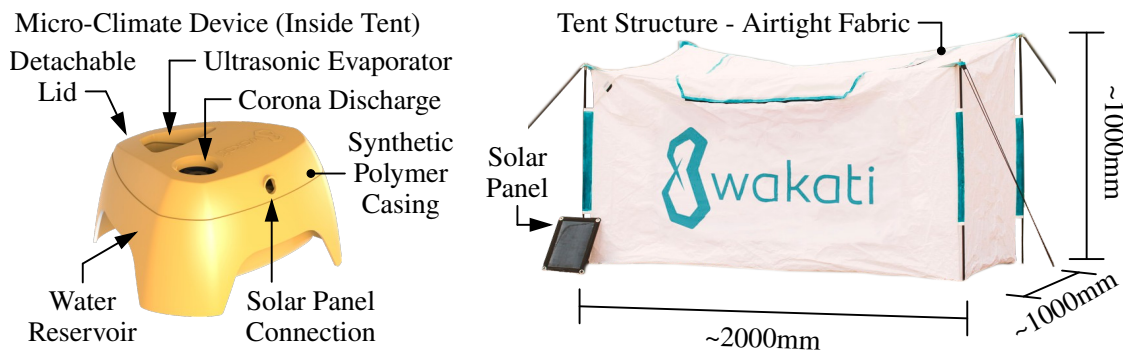


Figure 2.34: Graphic of a Wakati One with the micro-climate device (left) and assembly (right) [98].

Although it can be disassembled and relocated, the tent forms a dedicated structure and cannot be used to transport fruit and vegetables during storage, which was found to be a critical disadvantage in a study carried out by the World Vegetable Center in Arusha, Tanzania, where it was reasoned that subsistence farmers need a form of storage which allows for mobility to transport their produce to local markets [98]. This study found the Wakati One to be suitable for the short-term storage of fruits and vegetables up to 5 days, but there were major design flaws - it was recommended that the creation of ozone was redundant, as it does not perform consistently as a sterilisation agent at safe concentration levels and its effects on reducing oxidation were not observed; and it was recommended for an alternative method for initiating the evaporation using spray nozzles without the need for a solar panel, since the tent can be permanently located near a water supply to provide the necessary pressure [98].

There were prototypes of the Wakati One deployed for testing in 2014, where 105 units were distributed in Haiti, Uganda, and Afghanistan [99, 100]. The available results are shown in Figure 2.35 and

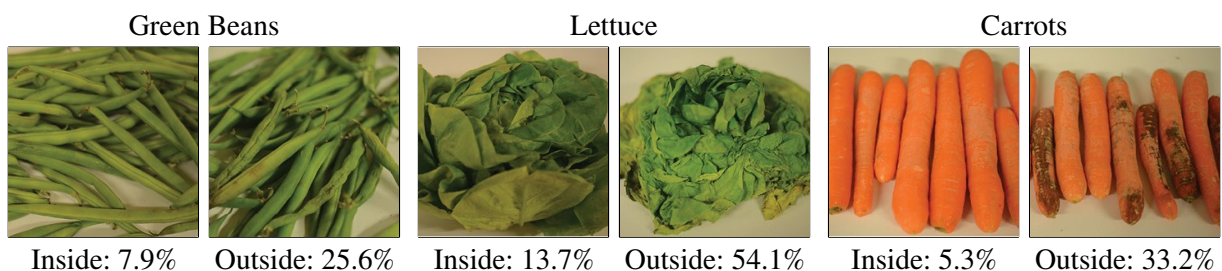


Figure 2.35: Photographs of selected vegetables which were stored inside and outside of the Wakati One at 27°C and respective mass losses of the samples which were measured after five days [99].

Table 2.5 with a 20% reduction in losses overall [99], although these results are assumed to vary depending on the environmental conditions. The sale price was expected to be around \$65 to \$100, but there have been no recent updates on the project and it appears to have been abandoned since 2017.

Table 2.5: Claimed shelf life of selected fruits and vegetables using a Wakati One [100].

Fruit / Vegetable	Shelf Life [days]	Fruit / Vegetable	Shelf Life [days]
Apple	30	Green Beans	12
Apricot	10	Mango	15
Banana	30	Okra	10
Carrot	10	Orange	10
Cucumber	10	Pear	25
Eggplant	10	Tomato	30
Grapes	40	Baby Marrow	10

2.7.6 BUILDING AIR CONDITIONING

For the air conditioning of buildings, evaporative cooling can be implemented through direct or indirect methods using forced convection. The direct method simply uses evaporative cooling to decrease the temperature and increase the relative humidity of a flow which is supplied to the conditioned space. The indirect method uses a heat exchanger, where there is an initial flow into which water is sprayed or a pad is soaked and an adjacent flow which is supplied to the conditioned space [52, 101, 102]. The psychrometric differences between direct and indirect methods are represented in Figure 2.36.

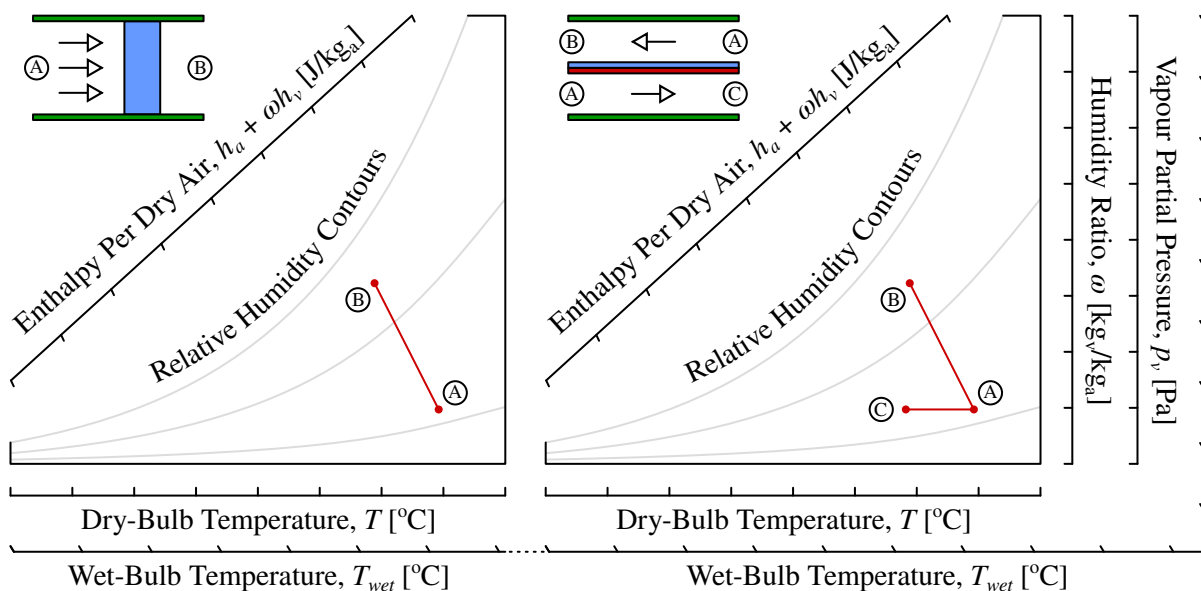


Figure 2.36: Comparison between direct (left) and indirect (right) evaporative cooling for buildings.

An interesting application of indirect evaporative cooling for cooling buildings is in wet surface heat exchangers, where there is an initial flow into which water is sprayed or a pad is soaked and an adjacent

flow which is supplied to the conditioned space [52, 101]. The flows are separated by a plate, where the water provided to the first flow collects on the plate to form a wet surface or film. This wet surface then produces evaporation within the first flow and decreases the temperature of the flow and, consequently, there is heat transfer from the second flow to the first flow - in a sense, the evaporation indirectly cools the second flow [52, 101]. This arrangement is represented in Figure 2.37.

Through experimental investigation, Pescod [102] proposed a design using polyvinyl chloride as the material for the plates and incorporated small protrusions to obtain encouraging results. It was also reasoned by Erens and Dreyer [52] that a synthetic polymer would be the ideal materials for the plate due to its low cost, low density, and corrosion resistance, although it tends to have very low thermal conductivity. However, since the plates can be extremely thin, the thermal conductivity is less concerning as the thermal resistance becomes relatively small in comparison to the thermal resistance from convection which is the governing resistance to heat transfer [52, 101]. This was also reinforced through practical experimentation by Gómez, González, and Martínez [103] with the use of 0.4mm panels of polycarbonate as the material for the plates to make the system light and inexpensive while avoiding the possibility of corrosion which may occur with metal plates. Although, it should be recognised that, as opposed to attempting to achieve a maximum temperature decrease and relative humidity increase, the ultimate objective for cooling buildings is to achieve comfort for the occupants with a temperature from 20°C to 26°C and relative humidity between 30% and 70% [52, 101, 104].

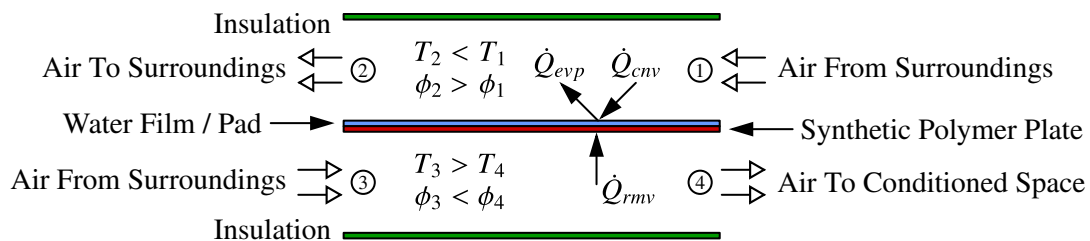


Figure 2.37: Arrangement of a wet surface heat exchanger with a counter-flow example [101].

Instead of directly wetting the surface, a thin fabric can be adhered against the candidate surface to aid in distributing and retaining the water. The irregular fibres also increase the wetted surface area, akin to a fractal in three-dimensional space, which increases the ability for evaporation, although it also introduces an additional thermal resistance to conduction through the surface [105, 106]. The results from Fancey et al. [105] indicated that textile fabrics (including several proprietary branded fabrics which are typically used for athletic clothing and were inferred to consist of polyester, spandex, and nylon since the specifications of their compositions were unavailable) performed well with regards to the wicking, distribution, and evaporation abilities, and it was argued that these fabrics offer favourable potential for use in wet surface heat exchangers due to their thinness and inexpensive cost. In addition to fabrics, Zhao, Liu, and Riffat [106] conducted a comparative study assessing metals, ceramics, zeolite, and carbon materials, and it was concluded that the thermal properties and capacity to retain water had little impact on the heat and mass transfer, as the majority of materials had an adequate thermal

conductivity and could retain an ample amount of water, but rather the most impactful characteristics were the cost, durability, formability, compatibility with other materials, and contamination risk.

2.8 THERMOELECTRIC COOLING

As mentioned in Section 1.1.6, a thermoelectric module is a form of solid-state refrigeration and uses the Peltier effect to create a temperature difference between two plates through the conversion of electrical energy. Although hinted by Lidorenko and Terekov in 1762, Volta in 1794, and Peters in 1810, Seebeck observed the phenomenon in 1821 of a current being induced in a closed circuit consisting of two dissimilar materials when a temperature difference was maintained at the junction of the materials [107]. In 1834, Peltier found the opposite phenomenon was also valid, where a temperature difference would be induced at a junction consisting of two dissimilar materials when a current was maintained in the closed circuit of the materials [107]. These fundamental principles are known as the Seebeck effect for the generation of an electric potential from a temperature difference and Peltier effect for the generation of a temperature difference from an electric potential.

A modern thermoelectric module replaces the dissimilar materials with semiconductors, where a variety of compounds are viable as the primary materials, such as bismuth telluride (most common), lead telluride, lanthanum telluride, cobalt arsenide, silicon germanium, magnesium silicide, and more complex compounds [32, 107, 108]. The capability of the material can be compared with the Seebeck coefficient as a measure of the induced electric potential in response to a temperature difference across the material - conversely, the Peltier coefficient could be considered with the opposite definition [107]. The construction and operation of a thermoelectric module is outlined in Figure 2.38, where p-type and n-type semiconductors are connected electrically in series and thermally in parallel with their sides contacting outer ceramic plates [24, 33]. In most cases, it is necessary to use a heat sink at the hot plate to ensure the thermoelectric module does not damage itself by overheating.

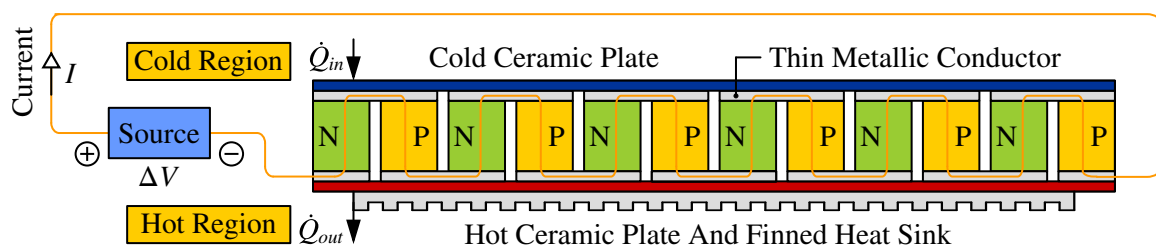


Figure 2.38: Illustration of a thermoelectric module with a temperature difference between two plates.

Combining the Seebeck coefficient, electrical resistance, and thermal conductivity, the intrinsic figure of merit can be defined in Equation 2.75 as a characterisation of the applicability of the material, which typically has a value of 0.0016/K for commercial thermoelectric modules with a typical Seebeck coefficient of 0.045V/K, electrical resistance of 2.55 Ω , and thermal conductivity of 0.495W/K [108, 109]. The maximum obtainable temperature difference between the cold plate and hot plate, as

physically limited by the material, can be estimated using Equation 2.76 and shows a difference of approximately 135°C for a typical intrinsic figure of merit and cold plate temperature of 20°C, although it is usually impractical to realistically achieve a temperature difference this high due to the excessive power requirements and heat sink for cooling at the hot plate. As the upper limit of performance, the maximum coefficient of performance which can be achieved by a thermoelectric module is limited by Equation 2.77 [108, 109]. Based on a typical intrinsic figure of merit, a maximum coefficient of performance of 0.7118 is obtained for a cold plate temperature of 20°C and hot plate temperature of 45°C. This low coefficient of performance highlights the inefficiencies of thermoelectric modules and it has been found that the coefficient of performance is almost always below 0.70 [1, 32, 108, 109].

$$Z = \frac{\alpha^2}{kR_{ele}} \text{ with } \Pi = \alpha T \rightarrow \text{Dimensionless: } ZT = \frac{\alpha^2 T}{kR_{ele}} = \frac{\alpha \Pi}{kR_{ele}} \quad (2.75)$$

$$\Delta T_{max} = (T_{hot} - T_{cold})_{max} \approx \frac{ZT_{cold}^2}{2} \quad (2.76)$$

$$\xi = \frac{T_{cold}}{T_{hot} - T_{cold}} \frac{\sqrt{1 + Z(T_{hot} + T_{cold})/2} - T_{hot}/T_{cold}}{\sqrt{1 + Z(T_{hot} + T_{cold})/2} + 1} \quad (2.77)$$

The applications of thermoelectric modules are widespread with uses in various industries including aerospace, telecommunications, electronic systems, military equipment, laser diodes, and medical devices, where these implementations usually focus on cooling rather than heating [1, 32]. Thermoelectric modules are also used for personal cooling, as innovated by Hara et al. [110] and Choi, Yun, and Whang [111]. A selection of applications with regards to research into refrigerated spaces include medicine storage by Field [112]; vaccine delivery by Buitendach, Jiya, and Gouws [113] and Gastelo-Roque and Morales-Acevedo [114]; blood transportation by Haynes, Puckett, and Monaghan [115]; air conditioning by Tipsaenporm et al. [116], Daghigh and Khaledian [117], and Shen et al. [118]; liquid chiller by Alomair et al. [119] and Chen et al. [120]; and domestic refrigerators by Mirmento, Syahrul, and Wirdan [121] and Min and Rowe [122]. There has also been a large focus on using thermoelectric modules for refrigeration with an emphasis on solar power and portability.

With specific attention, Dai, Wang, and Ni [109] investigated the use of a thermoelectric module in a compact and insulated refrigerator using a 12V thermoelectric module with up to 45W being supplied by two commercial solar panels of 0.4m² at 13% efficiency and a lead-acid battery of 100A.hr. As reported, the coefficient of performance varied between 0.20 and 0.50 during the experiment, where the cold plate temperature decreased below 10°C in 21.7min and maintained this for 3hr from an ambient temperature which varied between 24.7°C and 27.3°C [109]. The coefficient of performance was found to decrease as the temperature difference decreased, which demonstrated that an initial temperature decrease was feasible but further temperature decreases became more difficult [109].

The transient performance from Dai, Wang, and Ni [109] is shown in Figure 2.39 to represent typical expectations from a thermoelectric module. These results are largely in agreement with those presented

by Rahmen et al. [123], He et al. [124], and Abdul-Wahab et al. [125], who performed similar experiments with portable enclosures using photovoltaic systems. Rahmen et al. [123] used five TEC1-12706 thermoelectric modules to cool a miniature insulated enclosure of 0.635L with a photovoltaic system outputting 19W, such that the enclosure temperature was maintained around 17.5°C due to the cold plate which reached a minimum temperature of 10.2°C when the ambient temperature was approximately 30.1°C, while the hot plate increased to a maximum temperature of 39.3°C, to engender a coefficient of performance varying between 0.31 and 0.61. He et al. [124] investigated a large insulated enclosure of 125L for a scaled model of a room, where two TEC1-12703 thermoelectric modules of up to 3A at 12V, with a maximum of 36.3W output from the photovoltaic system, were able to decrease the temperature of the enclosure to a minimum of 16.6°C from the ambient temperature which increased from 21.7°C to 24.8°C, where the cold plates reached a minimum temperature of 9.6°C, while the hot plates reached a maximum temperature of 38.3°C, such that the coefficient of performance varied between 0.45 and 0.93 depending on the intensity of the insolation. On a smaller scale but higher power, Abdul-Wahab et al. [125] manufactured an insulated enclosure of 13.25L using ten ET-031-10-20-RS thermoelectric modules of up to 2.5A at 3.8V with a photovoltaic system designed to output up to 115.2W, where the enclosure experienced a temperature decrease from 27°C to 5°C in 44min and yielded a coefficient of performance of approximately 0.16.

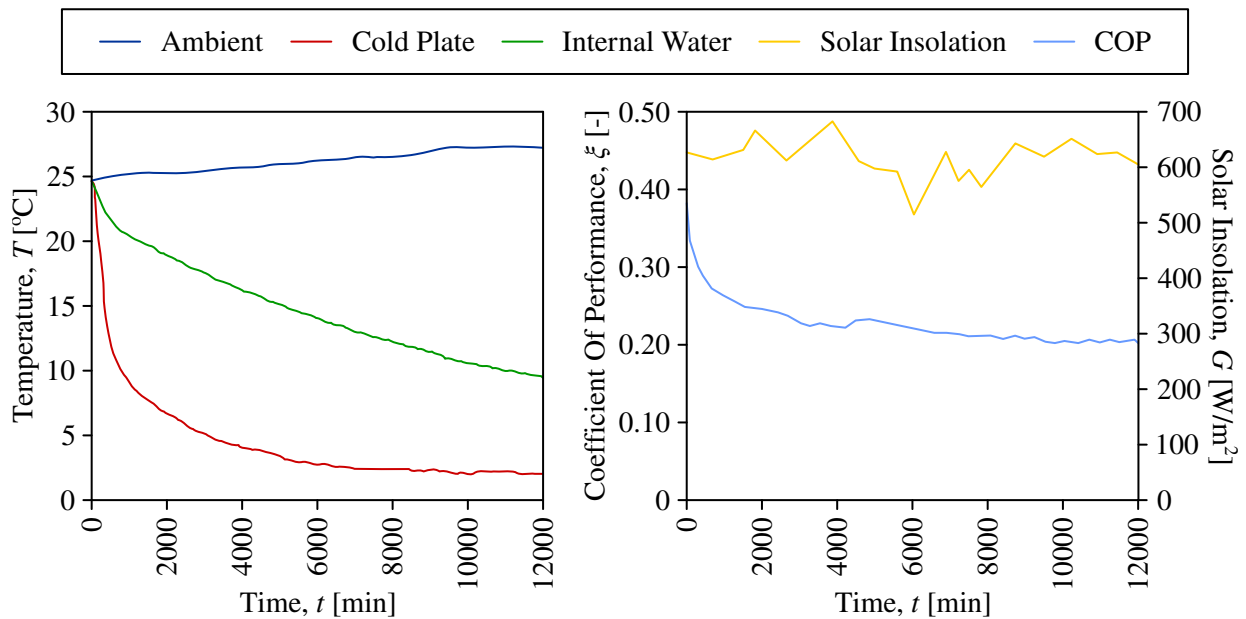


Figure 2.39: Variation of the results in the ambient temperature, cold plate temperature, and temperature of 500mL of water stored in the enclosure (left) and record of the intensity of insolation and coefficient of performance (right) from the experimental tests conducted by Dai, Wang, and Ni [109].

3 PROJECT OBJECTIVES

The primary objectives of the project were defined based on the desired outcomes as follows:

- Analytically predict the operating environmental conditions in which evaporative cooling with forced convection could achieve a temperature decrease of at least 11°C and relative humidity increase of at least 35% (up to a maximum of 100%) to examine the viability in developing countries which experience temperatures above 32°C and relative humidities below 50%.
- Numerically investigate the implementation of forced convection to achieve sufficient evaporative cooling for a temperature decrease of at least 11°C and relative humidity increase of at least 35% (up to a maximum of 100%) on a scale which is manually transportable by a single person and uses a self-contained photovoltaic system without relying on an external electricity supply.
- Practically compare several fabric materials, including different weaves with natural and synthetic fibres, to act as soaked pads for the evaporative cooling based on the ability to assist with evaporation, water wicking, water retention, water distribution, cost, and durability.
- Ensure the external structure has sufficient insulation to minimise the heat transfer effects when exposed to an insolation intensity of at least 420W/m², while also having adequate strength to stack multiple units on top of one another and withstand loads from manual transportation.
- Assemble a prototype for experimental optimisations by evaluating real-world performance under a variety of environmental conditions experienced in Johannesburg, South Africa, and compare the results with the desired specifications to achieve a temperature decrease of at least 11°C and relative humidity increase of at least 35% (up to a maximum of 100%), while aiming to maintain a manufacturing cost below €45 for affordability in developing countries.
- For supplement, perform enhancements by incorporating a thermoelectric module to complement the evaporative cooling for more consistent performance with temperature fluctuations minimised by 30% and compare the results based on the improvements relative to the cost increases.

In order to investigate these objectives, it was necessary to design a prototype to perform experimentation. For an optimal design assessing the most practical and realistic implementation, the objectives are further expanded in the description of the defined task statement and, for specific performance targets, quantitative and absolute requirements and constraints are listed in the desired specifications for success with criteria for comparing possible concepts during the analysis development.

3.1 DEFINED TASK STATEMENT

The following description was established as the final defined task statement:

For developing countries in Africa and other regions which frequently experience high temperatures above 32°C with low relative humidities below 50%, design a portable prototype with an enclosure

for the short-term storage of fruits and vegetables which is able to achieve an overall cooling effect using evaporative cooling for a temperature decrease of at least 11°C below the ambient temperature and relative humidity increase of at least 35% above the ambient relative humidity. The prototype should focus on preserving fruits and vegetables with optimal storage temperatures above 14°C and relative humidities above 85% in an attempt to extend the shelf life by more than 50% - examples of candidate fruits and vegetables include avocados, bananas, bell peppers, cucumbers, eggplants, granadillas, lemons, mangos, papayas, peppers, pineapples, potatoes, pumpkins, squashes, sweet potatoes, tomatoes, watermelons, and yams. The prototype should utilise a photovoltaic system to generate power for a fan which then induces a forced air flow for improved convective and evaporative performance. Finally, it is imperative for the prototype to be extremely affordable with a standard cost less than €19 for the materials and less than €26 for the electronic components.

3.2 DESIRED SPECIFICATIONS

In order to identify a clear gauge of success, the requirements, constraints, and criteria needed to be defined with consideration for the purpose of sub-systems. The requirements and constraints were essential and must be accomplished to judge whether the final prototype was successful. The criteria were used to guide the choices for and to distinguish between the possible solutions to the sub-systems. The sub-systems were organised into the external structure, internal structure, insulation, cooling pads, water supply reservoir, forced air flow, and photovoltaic system. Because the sub-systems were closely related, it was reasoned that it would be more practical to directly consider requirements, constraints, and criteria for the overall prototype, as opposed to considering each sub-system individually.

3.2.1 OVERALL REQUIREMENTS

The sub-systems and overall prototype needed to fulfil the following requirements:

- The design must utilise evaporative cooling for the short-term storage of fruits and vegetables, where the efficiency of this evaporative cooling is at least greater than 80%.
- The design must have an enclosure with an internal volume greater than 45L.
- The design must achieve a decrease in temperature of at least 11°C within the enclosure.
- The design must minimise temperature fluctuations, such that the temperature within the enclosure remains within a range of 8°C between the high and low temperatures during the day and night.
- The design must achieve an increase in relative humidity of at least 35% within the enclosure.
- The design must minimise relative humidity fluctuations, such that the relative humidity within the enclosure remains within a range of 25% between the high and low relative humidity during the day and night (although limited by a maximum relative humidity of 100%).
- The design must extend the shelf life by at least 50% of fruits and vegetables with optimal storage temperatures above 14°C and relative humidities above 85%, such as avocados, bananas,

bell peppers, cucumbers, eggplants, granadillas, lemons, mangos, papayas, peppers, pineapples, potatoes, pumpkins, squashes, sweet potatoes, tomatoes, watermelons, and yams.

- The design must store over 2L of water in the supply reservoir.
- The design must generate a forced air flow of at least 3m/s for the evaporative cooling, as this aligned with previous research and existing products as a conservative performance target.
- The design must only consider a photovoltaic system for internal power generation (in other words, the design must not require any form of external power supply or generation).
- The design must protect the contents from dirt, dust, splashes, corrosion, and pests.
- The design must have a standard cost of less than €19 for the materials.
- The design must have a standard cost of less than €26 for the electronic components.
- The design must have no operating costs, apart from the water for the evaporative cooling.

3.2.2 OVERALL CONSTRAINTS

The sub-systems and overall prototype needed to comply with the following constraints:

- The design must be able to operate at temperatures above 32°C without performance decline.
- The design must maintain functionality at temperatures between 0°C and 50°C.
- The design must be able to operate at relative humidities below 50% without performance decline.
- The design must maintain functionality at relative humidities between 0% and 100%.
- The design must maintain functionality at a standard atmospheric pressure of 101.325kPa with a variation up to 20%, which corresponds with altitudes over approximately 2000m.
- The design must be able to accommodate the heat of respiration from fruits and vegetables with optimal storage temperatures above 14°C and relative humidities above 85% without performance decline, where estimations show the heat of respiration to be equivalent to at least 1.0W.
- The design must have a mass less than 7.90kg for the structure to be carried by an average male or female between 15 years and 60 years (assuming the contents does not exceed 7.90kg for a maximum mass of 15.80kg, which would allow at least 50% of the mass to be for the contents).
- The design must have dimensions which accommodate carrying and manual transportation by a single male or female between the 5th and 95th percentiles and less than 60 years.
- The design must be able to fully operate when exposed to an average insolation intensity of 420W/m², where this insolation is utilised for operation by the photovoltaic system.
- The design must minimise the heat transfer effects from an insolation intensity of 420W/m².
- The design must be able to support at least 31.60kg applied over the top surface, as if two other fully loaded designs of 15.80kg each were stacked on top of it for a total of load of 310N, where the maximum permissible static deformation is no greater than 5mm.

- The design must be partially disassemblable to access the cooling pads for cleaning or replacement.
- The design must house the electronic components with a basic level of tamper-proofing.
- The design must be completely electrically insulated with no exposed circuitry.
- The design must operate autonomously without hindering or requiring input from the user.
- The design must operate in an environment-friendly manner without emissions during operation.
- The design must satisfy a thermal design factor of 1.2 and structural safety factor of 1.2 during the development to account for uncertainties and ensure the desired performance is achieved.

3.2.3 CONCEPT CRITERIA

The following criteria were used for conceptual evaluations and optimal development:

- The design needs to maximise the evaporation of water for maximum cooling.
- The design needs to be lightweight to reduce exertion while carrying.
- The design needs to be compact for improved comfort while carrying.
- The design needs to minimise the heat transferred from the surroundings.
- The design needs to perform consistently over its operating life.
- The design needs to be easy to maintain, repair, or replace.
- The design needs to operate silently with minimal noise.
- The design needs to be as efficient as possible.
- The design needs to be simple to manufacture and assemble.
- The design needs to be extremely cost effective and affordable.

4 PROJECT METHODOLOGY

As mentioned, if a relevant prototype aimed at investigating the objectives was able to achieve the specifications for success, then the objectives could be considered to be accomplished. The process of designing and testing a prototype to achieve the specifications was initialised through analytical and numerical analyses followed by experimentation with the prototype. The overall methodology used for the analysis development and practical experimentation is outlined as follows:

- Adopted an iterative design process with the successive improvement of the sub-systems of the design through analytical calculations, computational simulation, and practical experimentation.
 - The process initially involved conceptual evaluations to decide on the direction to follow for the design. These conceptual evaluations involved generating concepts and using the criteria to assess which concepts were most likely to be the most promising for further development.
 - Once the direction to follow for the design was established, further development could be engaged through analytical calculations for basic predictions, computational simulations for advanced optimisations, and practical experimentation for real-world results.
- Conducted analytical calculations for the psychrometry, air flow, heat transfer, and photovoltaic system. This involved applying the theories and ideas from Chapter 2, and it provided a means of comparison with and confirmation for the results from computational simulations.
 - The operating range of temperature and relative humidity in which the performance for the overall requirements can be achieved was evaluated for a preliminary assessment of the potential based on the psychrometry under the encountered environmental conditions.
 - The inception of the characteristics of the fan was proposed to estimate the required specifications to generate the air flow to create forced convection and enhance evaporative cooling.
 - The heat transfer through the external walls of the structure was examined for insulation purposes to prevent the penetration of heat from the insolation and surrounding air.
 - The specifications of the photovoltaic system were estimated based on the required power input to generate the forced convection, expected intensity of insolation, typical efficiencies of mono-crystalline and multi-crystalline silicon cells, and availability from local resellers.
- Executed computational simulations for the structure of the enclosure and forced air flow with high-performance computing hardware through finite element analysis (FEA) and computational fluid dynamics (CFD) respectively. This provided a baseline analysis before the prototyping and aided in reducing time inefficiencies which would have incurred if trial and error was pursued without prior analysis. The ANSYS Mechanical and ANSYS Fluent packages were used through the academic license of the University of the Witwatersrand (further information relating to the license is included in Appendix C with reference to the Collaboration Agreement).

- There was employment of the finite element method (FEM) using FEA to model and simulate the effects on the structure from applied loads through numerical techniques. Due to the low infrastructure environment and manual transportation, the enclosure could be subject to multiple loads applied to the external walls, where it would be imperative for endurance of these loads to ensure a long service life without repairs or replacement. This analysis entailed assessing the deformations and stresses from expected loads considering a reference case relative to desired safety factors with the loading from two other fully loaded enclosures stacked on top of it.
- There was employment of the finite volume method (FVM) using CFD to model and simulate the air flow through numerical techniques. This involved optimising the fan to produce the desired velocity as efficiently as possible, such that the required power input from the photovoltaic system would be minimised and the overall affordability would be maximised. The important factors to consider included whether the fan was axial or radial and variations of the blade characteristics, such as the outlet angle, quantity, inclination angle, breadth, channel width, and corner radius of the enclosure. The relevant measurements in relation to the convective heat and mass transfer included the velocity, induced turbulence, and pressure exerted on the driving and trailing surfaces of the blades which correspond with the resulting torque and power.
- Performed practical experimentation with the cooling pads, photovoltaic system, and overall prototype for continuous testing to confirm previous predictions and optimise the construction to meet the desired specifications. This involved sourcing materials from suppliers, manufacturing custom components, and sourcing common components from local resellers. A final prototype was constructed to evaluate and validate the real-world performance against the desired specifications. As mentioned, the experimentation was performed in Johannesburg, South Africa.
 - The fabrics which were available options for the cooling pads were compared using samples of each material with criteria based on their cost and abilities to wick, distribute, and retain water.
 - The necessary capacity for the energy storage in the photovoltaic system needed to be assessed to ensure operation during short periods of shading if there was cloud coverage or other obstructions to direct insolation. This surveyed a lower capacity for more affordability when minor inconsistencies in performance from shading were tolerable and higher capacity for more reliability to maintain performance when there may be extended periods of shading.
 - The performance evaluation of the final prototype involved continuously measuring the internal enclosure temperature and relative humidity, associated fluctuations in temperature and relative humidity, and differences compared to the ambient temperature and relative humidity.
 - The health of various fruits and vegetables throughout the day and over an extended period were monitored and compared against the health of the same fruits and vegetables stored in a regular box in the shade to highlight potential improvements in shelf life. The candidate fruits and vegetables which were locally available with almost ideal freshness included avocados, baby marrows, bananas, bell peppers, cabbages, carrots, eggplants, granadillas, sweet corns, and

- tomatoes. A sample was chosen from these fruits and vegetables specifically as their expected shelf lives were limited and deterioration would be visible over the testing period.
- There was also auxiliary assessment of the performance if the photovoltaic system was exposed to direct insolation while the enclosure was shaded, performance if the photovoltaic system and enclosure were exposed to the direct insolation, time to reach a steady state condition, and effect on the internal enclosure temperature and relative humidity if the top lid was opened.
 - A cost analysis was completed based on the chosen materials and electronic components to establish an estimated manufacturing cost. This manufacturing cost was applicable if there was to be the mass production of an equivalent final product when accounting for maximum affordability in developing countries and creating a competitive solution against existing products. (Although, it should be noted that the investment costs were not investigated).
- Incorporated a thermoelectric module into the system to complement the evaporative cooling. This required an increase in the specifications of the photovoltaic system to provide the necessary power input. The selected thermoelectric module with a heat sink and additional solar panels were installed in the prototype, such that the previous practical experimentation could be repeated for comparison based on the increase in performance relative to the increased cost.
 - The performance evaluation of the prototype with the thermoelectric module involved continuously measuring the internal enclosure temperature and relative humidity, associated fluctuations in temperature and relative humidity, and differences compared to the ambient temperature and relative humidity. A focus was applied to improving the consistency of the performance based on the effect on the fluctuations in temperature and relative humidity.

5 ANALYSIS DEVELOPMENT

The analysis development proceeded with an iterative process through successive consideration for the preliminary conceptual inception, basic initial predictions, optimisation of the air flow, cooling pad material, water supply layout, external insulation, and structural strength. The analysis evaluations involved various methods of investigation with analytical calculations based on theoretical and empirical relationships and numerical computations with CFD and FEA models and simulations. Ultimately, the aim of the analysis development was to optimise for the most promising prototype and provide an initial point of reference for the confirmation of the practical experimentation.

5.1 PROVISIONAL USER CONSIDERATIONS

The ergonomics of the enclosure were an intrinsic part of the development as they dictate the interactions with the user during general use and manual transportation. With regards to the basic shape, a box or cuboid with a rectangular profile and extruded length was the optimal choice, as it offered the most efficient form factor, robust structure with a high strength, stable mass distribution for suitable storage, and simple manufacturing without complex intricacies and with low material usage regarding the surface area per unit volume. A groove or lip could also be incorporated on either side as built-in handles to allow the user to carry the enclosure in front of them with extended arms. As the predominant aspect of ergonomics, it was necessary to consider the dimensions of the user in a comfortable carrying position to estimate the maximum size tolerable and appropriate ratios between the dimensions.

The applicable outlines are sketched in Figure 5.1 relative to the proportions for the torsos of an average male and female. For maximum comfort and minimum fatigue while carrying, the applicable ergonomic factors included a fixed and perpendicular bend at the elbow, free rotation in the shoulder, regular height above the pelvis but below the shoulders, and hands placed symmetrically along the

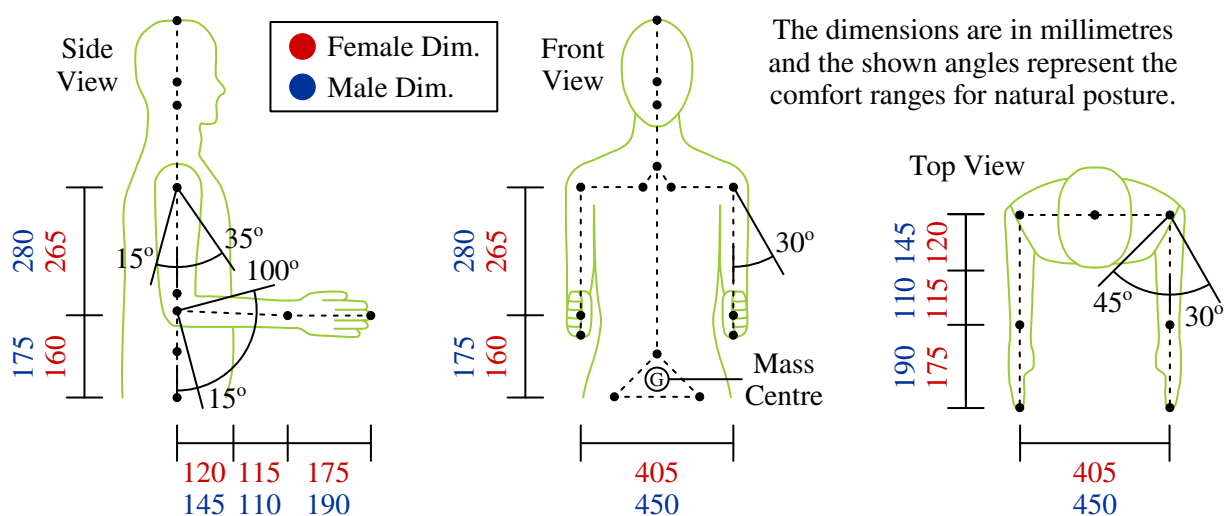


Figure 5.1: Proportions for the torso of an average male and female with extended arms [40].

sides and near the centre and middle, as depicted in Figure 5.2. Thus, since males and females needed to be accommodated, the enclosure can have a length in the front view up to 670mm, width in the side view up to 465mm, and height up to 455mm - these maximum values are limited by the dimensions of the average female with the dimensions of the average male being naturally compatible.

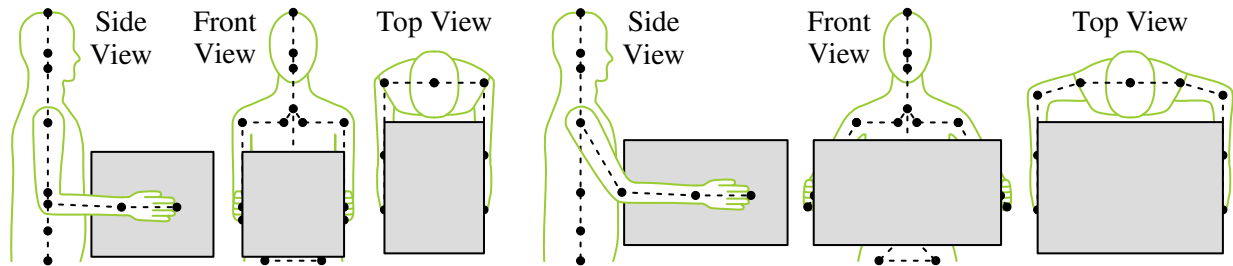


Figure 5.2: Examples for the torso of an average male and female carrying a box with the difference in ergonomics from the normal position for comfort (left) to the maximum position for comfort (right).

5.2 PRELIMINARY CONCEPT GENERATION

For the generation of preliminary concepts, the sub-systems were grouped based on function into the Inlet, which was related to the motor type, fan type, and cooling pad configuration; and Outlet, which was related to the channels and exhaust for the air flow. The remaining sub-systems were the photovoltaic system, water supply reservoir, external structure, and external insulation, although it was not required for a conceptual evaluation to be directly applied as these sub-systems could be decided based on the most practical implementations. Once the preliminary concepts were established, the groups could be integrated and issues with overlapping components could be resolved.

Because the importance of each criterion was not equal relative to the objectives, it was also necessary to use a weighting matrix to determine the order of importance or weight of the criteria, where each criterion was individually compared against the other criteria to decide which was the more relevant criterion in the comparison. With the weighted criteria, the best concepts could then be evaluated by scoring each preliminary concept against the criteria. The scoring levels are explained as follows:

- 0 = Does Not Comply
- 1 = Deficient
- 2 = Below Average
- 3 = Acceptable
- 4 = Good
- 5 = Perfect

5.2.1 CRITERIA WEIGHTING

The weighting matrix in Table 5.1 ranks the criteria which were to be used to evaluate the generated concepts. The upper-tier rankings included the maximisation of evaporation, minimisation of heat gains, and extreme affordability qualities for the concepts. The maximisation of evaporation was ranked as the most important criterion, because this was the utmost concern to generate a decrease

in temperature and increase in relative humidity for the preservation of fruits and vegetables. The criterion ranked second was the minimisation of heat gains, because this was directly associated with ensuring the evaporative cooling would be effective and achieve a substantial cooling effect. The next criterion was the cost effectiveness and affordability, which was ranked third since it was particularly essential in producing a successful product for widespread adoption in developing countries.

Table 5.1: Assessment of the importance of the criteria based on a weighting matrix. For the individual comparisons, it should be noted that, if X beats Y and Y beats Z, then X beats Z automatically.

Label	Criteria	Weighting Matrix Comparing Importance										Weight	Percent	Rank
		A	B	C	D	E	F	G	H	I	J			
A	Maximise Evaporation	A	A	A	A	A	A	A	A	A	A	10	18.2%	1st
B	Lightweight / Low Fatigue		B	B	D	B	B	B	B	B	J	7	12.7%	4th
C	Compact / High Comfort			C	D	C	C	C	C	C	J	6	10.9%	5th
D	Minimise Heat Gains				D	D	D	D	D	D	D	9	16.4%	2nd
E	Consistent Operation					E	E	E	E	E	J	5	9.1%	6th
F	Easy Maintenance						F	F	H	F	J	3	5.5%	8th
G	Minimal Noise							G	H	I	J	1	1.8%	10th
H	Efficient Operation								H	H	J	4	7.3%	7th
I	Simple Manufacturing									I	J	2	3.6%	9th
J	Cost Effective										J	8	14.5%	3rd

The middle-tier rankings included the weight, compactness, consistency, and efficiency of the concepts. A lightweight structure was ranked fourth, since this was crucial for avoiding user fatigue during manual transportation. Likewise, a compact structure was ranked fifth for comfort during manual transportation and functional storage when not in use, although it was motivated that a larger size would be more tolerable than a higher weight. The consistency in performance over time was ranked sixth, because this decreased uncertainty and allowed for the performance to be reliable and predictable. Subsequently, the need for efficient operation was ranked seventh, because an increased efficiency allowed for the same performance with more inexpensive and less specialised components.

The lower-tier rankings included the maintainability, manufacturing, and noise of the concepts. The ease of maintenance was ranked eighth, as it may be necessary to perform simple repairs or replace certain components in a modular fashion after wear has occurred from continuous use. Since it offered no performance advantages, the simplicity of manufacturing and assembling was ranked ninth, but it still carried relevance due to the need for rapid and low cost production. Finally, the criterion ranked tenth was the reduction of the noise during operation, because it was only preferable for convenience and user satisfaction and it was not valued over the other criteria related to performance. In the rankings, the highest criteria was weighted at 18.2%, while the lowest criteria was weighted at 1.8%.

5.2.2 INLET CONCEPTS

As mentioned, the Inlet could be divided into the motor type, fan type, and cooling pad configuration. For the motor type, the possible options included using a brushed motor or brushless motor and the most overriding criteria were the needs for integration and affordability while achieving the required performance. Since it was necessary for specific performance specifications, the motor type was only decided with the analysis based on the motors available from suppliers to meet the required specifications. For the fan type, the possible options included using a primarily radial fan or primarily axial fan. For the cooling pad configuration, it was decided to separate the configurations based on the application of evaporative cooling and, so, the possible options included using a bulk pad (such as aspen wool, corrugated paper, synthetic foam, or CELdek) through which air is allowed to flow or fabric pad (such as hessian, cotton, or polyester) over which air is allowed to flow. These options were combined alternately to form concepts labelled as the Radial Bulk, Radial Fabric, Axial Bulk, and Axial Fabric, which are shown in Figure 5.3 for illustrative comparison.

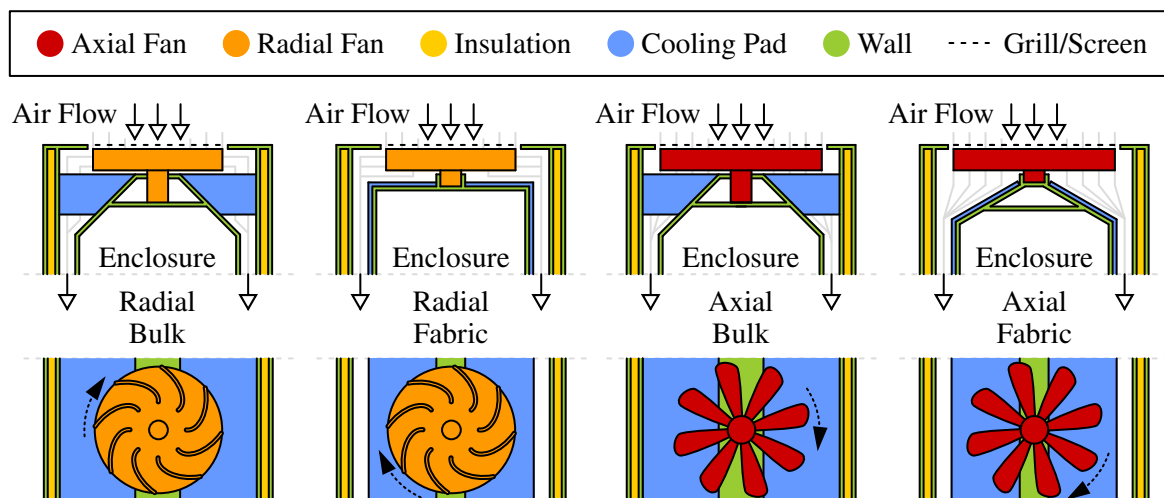


Figure 5.3: Illustration of the Inlet concepts for the combination of fan type and cooling pad configuration through cross-sections to show the relevant components in the top view (top) and front view (bottom). (These and other illustrations only present possible implementations of the general ideas).

The evaluation of the concepts against the weighted criteria is shown in Table 5.2. For the maximisation of evaporation, the fabric pads in the Radial Fabric and Axial Fabric were supposed to offer a larger area for increased evaporation over the bulk pads in the Radial Bulk and Axial Bulk. However, the bulk pads in the Radial Bulk and Axial Bulk were seen to act as insulation and minimise heat gained from the surroundings, while the fabric pads in the Radial Fabric and Axial Fabric offered little insulation as they would be required to be thin for optimal performance. With regards to cost effectiveness, a fabric pad was likely to be more inexpensive than a bulk pad and simpler walls for the enclosure required less material and manufacturing costs, where it was proposed that the Radial Fabric would be the most cost effective, followed by the Axial Fabric, and then the Radial Bulk and Axial Bulk.

In general, the fabric pads in the Radial Fabric and Axial Fabric would be lighter than the bulk pads in the Radial Bulk and Axial Bulk, where the bulk pads would also create a disproportionate mass distribution. Likewise, the axial fan and bulk pads required for the structure to be extended outwards, while the radial fan and fabric pads maximise compactness for optimal comfort during manual transportation, such that the Radial Fabric was the most compact and the Radial Bulk, Axial Bulk, and Axial Fabric were fairly enlarged. For consistency in performance, it was presumed that the performance of the Radial Fabric and Axial Fabric would remain fairly consistent, but dust and other particles could become embedded in the bulk pads of the Radial Bulk and Axial Bulk which would lead to declines in performance over time. Moreover, with regards to efficient operation, the bulk pads and bends to re-direct the flow would create major and minor resistance to the flow respectively which would require a much larger head rise from the fan and, based on this reasoning, the Radial Bulk with a bulk pad and bends was the most inefficient, Axial Bulk with a bulk pad was somewhat inefficient, Radial Fabric with bends was slightly inefficient, and Axial Fabric was the most efficient.

The Radial Fabric and Axial Fabric were seen to be simpler to maintain than the Radial Bulk and Axial Bulk, since the bulk pads could accumulate dust and other particles over time and require replacement by a compatible bulk pad with the same dimensions, but the fabric pads could be easily washed and, if necessary, an alternate locally available fabric could even be used as a replacement, although this

Table 5.2: Evaluation of the Inlet concepts against the weighted criteria.

Criteria	Total Weight	Max. Weighted Score	Rad. Bulk		Rad. Fabric		Axial Bulk		Axial Fabric	
			Score / 5	Weighted Score	Score / 5	Weighted Score	Score / 5	Weighted Score	Score / 5	Weighted Score
Maximise Evaporation	10	50	2	20	5	50	3	30	5	50
Lightweight / Low Fatigue	7	35	2	14	5	35	3	21	5	35
Compact / High Comfort	6	30	2	12	5	30	2	12	2	12
Minimise Heat Gains	9	45	5	45	2	18	5	45	2	18
Consistent Operation	5	25	3	15	4	20	3	15	4	20
Easy Maintenance	3	15	3	9	4	12	2	6	4	12
Minimal Noise	1	5	3	3	5	5	2	2	4	4
Efficient Operation	4	20	1	4	3	12	2	8	4	16
Simple Manufacturing	2	10	2	4	4	8	2	4	2	4
Cost Effective	8	40	2	16	5	40	2	16	4	32
Total Score		275		142		230		159		203
Percentage [%]		100		51.6		83.6		57.8		73.8

may negatively affect performance. For manufacturing simplicity, the Radial Fabric would have the least complex structure for the walls of the enclosure, but it may be more difficult to position and align the fabric pads compared to the bulk pads and, so, the Radial Bulk and Axial Bulk would be simpler to manufacture than the Axial Fabric. Finally, although difficult to judge, it was reasoned that the significant resistance to the flow from the bulk pads would likely require the fan to have a higher angular velocity for the larger head rise which would correspond with a higher noise level and, thus, the Radial Bulk and Axial Bulk would generate more disturbance, while the Axial Fabric was expected to be slightly louder than the Radial Fabric, since an axial fan is generally louder than a radial fan.

In total, the Radial Bulk achieved a score of 51.6%, Radial Fabric achieved a score of 83.6%, Axial Bulk achieved a score of 57.8%, and Axial Fabric achieved a score of 73.8%. Thus, this indicated that the Radial Fabric was the most promising to pursue into further analysis and development, although the potential and ideas of the Axial Fabric should not be completely disregarded.

5.2.3 OUTLET CONCEPTS

To account for the channels and exhaust for the air flow, the arrangement of the Outlet was considered with the walls and insulation forming the channels and exhaust. This primarily affects the area available for evaporation and the extent to which the enclosure would be isolated from the surroundings and insulation, which becomes especially important in maintaining the enclosure temperature if the fan were to pause operation for a short period of time. The most applicable concepts are illustrated in Figure 5.4 for the Straight Outer, with straight channels and insulation on the outer wall; Bent Inner, with bent channels and insulation on the inner wall; Bent Inner-Outer, with bent channels and insulation on the inner and outer walls; and Bent Outer, with bent channels and insulation on the outer wall.

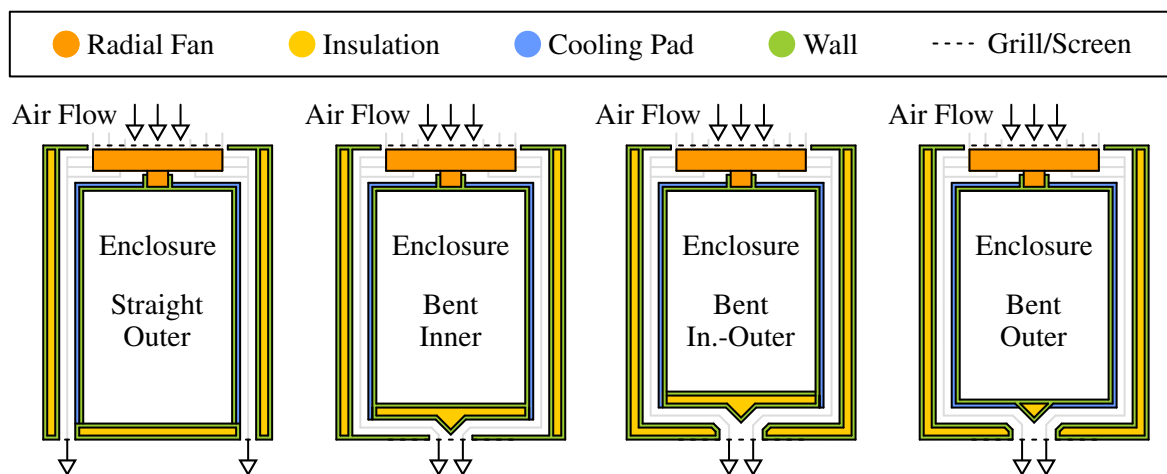


Figure 5.4: Illustration of the Outlet concepts for the combination of arrangement of the channels and exhaust for the air flow through a cross-section to show the relevant components in the top view.

Since the majority of the criteria are not significantly distinguishable between the concepts, the most appropriate arrangement was judged based on the maximisation of evaporation. Clearly, the Bent

Outer offered the largest area for evaporation. Although it may be slightly less space efficient than the Straight Outer and less insulated than the Bent Inner and Bent Inner-Outer, it still presented the best compromise for maximum performance while maintaining adequate compactness and insulation to isolate the enclosure from the surroundings and insulation. The Bent Outer was selected.

5.3 INITIAL ANALYTICAL ANALYSIS

An analytical analysis was performed for an initial estimation of the expected performance under various environmental conditions. The analysis focussed on determining the cooling effect from the evaporative cooling for a range of velocities for the air flow, convection heat transfer coefficients, convection mass transfer coefficients, and heat dissipation from the respiration of fruits and vegetables. Naturally, the analysis was based on underlying fundamental assumptions for acceptable simplification and implementation of the theoretical and empirical relationships mentioned in Chapter 2.

5.3.1 FUNDAMENTAL ASSUMPTIONS

To proceed with the analytical analysis, the following assumptions were accepted for the production of a realistic model while allowing for simplification but maintaining a suitable level of accuracy:

- The operation can be analysed at steady state without transient effects.
- The Dalton model is applicable and each component of the moist air behaves as an ideal gas as if it were alone at the particular temperature and volume of the overall mixture.
- The external walls are sufficiently insulated and there is no heat transfer with the surroundings.
- There is negligible work performed after the radial fan and between the inlet and outlet, apart from the innate work of the flow which is considered to be smooth.
- The changes in kinetic and potential energies are negligible.
- The external body forces (like gravitational effects) are negligible.
- The properties of the moist air can be evaluated at the film temperature as a simplified representation accounting for the effects from the thermal boundary layer.
- The properties of the evaporated water vapour can be evaluated at the saturated vapour state.
- The properties of the stored water can be evaluated at the saturated liquid state.
- The properties of the materials for the structure remain constant between 0°C and 50°C.
- The convection heat and mass transfer coefficients are analogous.
- The contact resistance at the interface between the cooling pad and wall is negligible.
- The channel geometry is uniform throughout and the walls are impervious to mass transfer.
- The air flow is fully developed in the velocity, thermal, and concentration boundary layers.
- The air flow is normal to the boundary at the inlets and outlets and the intensive properties of the flow are uniform as bulk average values over each inlet or outlet cross-sectional area.

Table 5.3: Correlations for the properties of dry air, saturated water vapour, and saturated water [42]. The correlations for dry air are valid between temperatures of -53°C and 107°C at standard atmospheric pressure of 101.325kPa . The correlations for saturated water vapour and water are valid between temperatures of 0°C and 107°C . (The necessary units for dimensional homogeneity are not displayed).

Density [kg/m^3]	$\rho_a = \frac{p_a}{287.08T} = \frac{352.95}{T} \quad (5.1)$
	$\rho_v = -4.06233 + 0.10277T - 9.76300T^2 \times 10^{-4} + 4.47524T^3 \times 10^{-6} - 1.00460T^4 \times 10^{-8} + 8.91549T^5 \times 10^{-12} \quad (5.2)$
	$\rho_w = (1.49343 \times 10^{-3} - 3.71640T \times 10^{-6} + 7.09782T^2 \times 10^{-9} - 1.90321T^6 \times 10^{-20})^{-1} \quad (5.3)$
Thermal Conductivity [$\text{W}/\text{m}/\text{K}$]	$k_a = -4.937787 \times 10^{-4} + 1.018087T \times 10^{-4} - 4.627937T^2 \times 10^{-8} + 1.250603T^3 \times 10^{-11} \quad (5.4)$
	$k_v = 1.3046 \times 10^{-2} - 3.756191T \times 10^{-5} + 2.217964T^2 \times 10^{-7} - 1.111562T^3 \times 10^{-10} \quad (5.5)$
	$k_w = -6.14255 \times 10^{-1} + 6.9962T \times 10^{-3} - 1.01075T^2 \times 10^{-5} + 4.74737T^4 \times 10^{-12} \quad (5.6)$
Mass Specific Heat Capacity [$\text{J}/\text{kg}/\text{K}$]	$c_{p,a} = 1.045356 \times 10^3 - 3.161783T \times 10^{-1} + 7.083814T^2 \times 10^{-4} - 2.705209T^3 \times 10^{-7} \quad (5.7)$
	$c_{p,v} = 1.3605 \times 10^3 + 2.31334T - 2.46784T^5 \times 10^{-10} + 5.91332T^6 \times 10^{-13} \quad (5.8)$
	$c_{p,w} = 8.15599 \times 10^3 - 2.80627T \times 10 + 5.11283T^2 \times 10^{-2} - 2.17582T^6 \times 10^{-13} \quad (5.9)$
Dynamic Viscosity [$\text{N}\cdot\text{s}/\text{m}^2$]	$\mu_a = 2.287973 \times 10^{-6} + 6.259793T \times 10^{-8} - 3.131956T^2 \times 10^{-11} + 8.150380T^3 \times 10^{-15} \quad (5.10)$
	$\mu_v = 2.562435 \times 10^{-6} + 1.816683T \times 10^{-8} + 2.579066T^2 \times 10^{-11} - 1.067299T^3 \times 10^{-14} \quad (5.11)$
	$\mu_w = 2.414 \times 10^{-5} \times 10^{247.8/(T-140)} \quad (5.12)$
Air-Water Mass Diffusivity [m^2/s]	$D_{a,v} = -1.28061 \times 10^{-4} + 1.61027T \times 10^{-6} - 7.14049T^2 \times 10^{-9} + 1.50971T^3 \times 10^{-11} - 1.16550T^4 \times 10^{-14} \quad (5.13)$
Specific Heat Evaporation [J/kg]	$\Delta h_{fg} = 3.4831814 \times 10^6 - 5.8627703T \times 10^3 + 12.139568T^2 - 1.40290431T^3 \times 10^{-2} \quad (5.14)$
Surface Tension [N/m]	$\gamma_w = 5.148103 \times 10^{-2} + 3.998714T \times 10^{-4} - 1.4721869T^2 \times 10^{-6} + 1.21405335T^3 \times 10^{-9} \quad (5.15)$
Vapour Partial Pressure [Pa]	$p_v = 611.21 \exp\left(\frac{T - 273.15}{T - 16.01} \left(18.678 - \frac{T - 273.15}{234.5}\right)\right) \quad (5.16)$

- The air flow has negligible compressibility effects, since the flow velocity is expected to be a minute fraction of the speed of sound, such that the flow is incompressible with a constant density.
- The cooling pad is completely wet with water and uniformly covers the area of the walls.
- The capillarity in the cooling pad adheres to capillarity experienced in cylindrical tubes.
- The water in the cooling pad is evenly distributed and continuously replenished with water at the same temperature, where the transfer of water within the pad has no effect on the heat transfer.
- The rate of heat dissipation from the respiration of fruits and vegetables is equally distributed between the channels and directly delivered to the walls of the internal enclosure.

Kröger [42] has compiled a list of correlations for selected properties of dry air, saturated water vapour, and saturated water for temperatures between 0°C and 107°C, such as the density, thermal conductivity, and specific heat capacity. The correlations were gathered from various reliable sources, which included the *Heat Transfer And Fluid Flow Data Book* by General Electric and *Handbook Of Fundamentals* by the ASHRAE [42]. The relevant correlations are summarised in Table 5.3 with Equation 5.1 to Equation 5.16. The remaining properties, like the thermal diffusivity and kinematic viscosity, could then be found from the listed properties based on the mentioned relationships.

The properties for applicable materials are listed in Table 5.4, with emphasis on density, yield strength, thermal conductivity, and cost. A range of metals are included, which were considered for the internal

Table 5.4: Typical ranges for the mechanical properties of applicable materials [126, 127]. (It should be noted that the cost values may be outdated, but represent a relative comparison between the materials).

Material	Density [kg/m ³]	Elastic Modulus [GPa]	Yield Strength [MPa]	Ultimate Strength [MPa]	Thermal Conduct. [W/m/K]	Cost [\$/kg]
Medium Carbon Steel	7800 - 7900	200 - 220	310 - 900	410 - 830	45 - 55	0.52 - 0.58
Stainless Steel	7600 - 8100	190 - 210	170 - 100	480 - 2200	12 - 24	5.9 - 6.5
Aluminium Alloys	2500 - 2900	68 - 82	30 - 500	58 - 550	76 - 240	2.1 - 2.3
Magnesium Alloys	1700 - 2000	42 - 47	70 - 400	190 - 480	50 - 160	3.1 - 3.4
Titanium Alloys	4400 - 4800	90 - 120	250 - 1200	300 - 1600	7 - 14	22 - 25
ABS Thermoplastic (TP)	1010 - 1210	1.1 - 2.9	19 - 51	28 - 55	0.19 - 0.34	2.4 - 2.7
Polyurethane TP	1100 - 1200	1.3 - 2.1	40 - 54	31 - 62	0.23 - 0.24	4.1 - 4.6
Polyvinyl Chloride TP	1300 - 1600	2.1 - 4.1	35 - 52	41 - 65	0.15 - 0.29	2.0 - 2.2
Polyethylene TP	940 - 960	0.62 - 0.90	18 - 29	21 - 45	0.40 - 0.44	2.1 - 2.3
Flex Low Density Foam	38 - 70	0.001 - 0.003	0.02 - 0.30	0.24 - 2.4	0.040 - 0.059	2.6 - 2.9
Flex High Density Foam	70 - 120	0.004 - 0.012	0.048 - 0.70	0.43 - 3.0	0.041 - 0.078	2.8 - 3.1
Rigid Low Density Foam	36 - 70	0.023 - 0.080	0.30 - 1.7	0.45 - 2.3	0.023 - 0.040	15 - 17
Rigid High Density Foam	170 - 470	0.20 - 0.48	0.80 - 12	1.2 - 12	0.034 - 0.063	15 - 17

walls, and a range of polymers are included, which were considered for the external and internal walls, along with the general properties of flexible and rigid foams with low and high densities for the insulation. This provided a means for high-level comparison between the materials to gauge which would be expected as the most suitable to investigate - although it should be recognised that the precise properties are dependent on the specific alloy, grade, or type of the material. Moreover, Ashby [126] has compiled several useful charts comparing various properties as a guide for material selection.

5.3.2 EVAPORATIVE COOLING EFFECT

For a prediction of the expected performance, the resulting cooling effect from the evaporation of water around the enclosure was investigated through an analytical analysis. This served as a basis for a proof of feasibility and provided a means for comparison against the practical experimentation in Chapter 6.

The internal layout for the development of the analytical analysis is detailed in Figure 5.5. The model elaborated in Section 2.5.1 was applied to determine the temperature of the enclosure for a range of external temperatures from 0°C to 50°C and relative humidities between 0% and 100%. However, for more accuracy, the additional heat from the respiration of fruits and vegetables was incorporated. With this addition, the heat transfer rate balance at the surface of the cooling pad is described by Equation 5.17 and expanded to give Equation 5.18, where the water vapour partial pressure of the air flow was related to the saturated water vapour partial pressure through the relative humidity. As mentioned, it was assumed that the insulation was sufficient to neglect heat transfer from the surroundings.

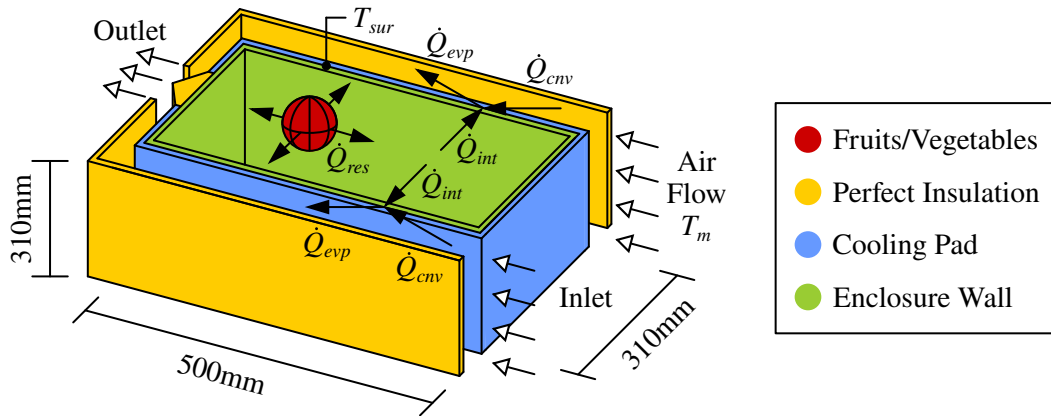


Figure 5.5: Internal layout for the analytical analysis without components for the forced air flow, external walls, or photovoltaic system. (The thickness of the channels for the air flow is exaggerated).

$$\sum \dot{Q}_i = 0 \rightarrow 2\dot{Q}_{cnv} + 2\dot{Q}_{int} = 2\dot{Q}_{evp} \rightarrow 2\dot{Q}_{cnv} + \dot{Q}_{res} = 2\dot{Q}_{evp} \quad (5.17)$$

$$T_m - T_{sur} = \frac{M_w \Delta h_{fg}}{\bar{R} \rho_a c_{p,a} (\alpha_a / D_{a,v})^{0.667}} \left(\frac{p_{v,g,sur}}{T_{sur}} - \frac{\phi p_{v,g,m}}{T_m} \right) - \frac{\dot{Q}_{res}}{2h_c A} \quad (5.18)$$

The rate of heat dissipation from respiration could be estimated using Equation 1.2. To gauge the magnitude of the resulting effects, various realistic scenarios were considered. For example, the heat

from respiration was equal to 1.431W when considering 2kg of bell peppers, 2kg of lemons, 2kg of onions, 2kg of peaches, and 2kg of pears; 1.116W when considering 6kg of potatoes and 4kg of tomatoes; and 1.323W when considering 2kg of apples, 2kg of cabbages, 1kg of carrots, 1kg of grapes, 1kg of limes, 2kg of oranges, and 1kg of plums. These common cases showed that the expected heat from respiration ranged up to about 1.5W. So, a heat transfer of 1.8W was considered for a conservative approximation using a safety factor of 1.2, in addition to already using a full storage of 10kg.

The cooling effect is increased as the velocity of the air flow increases due to the increase in the convection heat and mass transfer coefficients. To generate an expected estimation of performance, an average velocity of 3m/s was considered for the air flow. Also, the dimensions of the enclosure were initially considered to be 500mm in length, 310mm in width, and 310mm in height for an internal volume of 48.05L, while the channels for the air flow were considered to be 15mm thick. A slightly enlarged internal volume was used to give leeway to apply fillets and other enhancements for optimisations, ergonomics, and aesthetics. These dimensions affected the convection heat and mass transfer coefficients and area for the cooling pads, but their values were fairly arbitrary at this stage as the variation in the dimensions had a minor effect on the model compared to the effect from the variation in heat from respiration. In other words, the effect on the model from the variation in the velocity of the air flow or dimensions of the enclosure could be seen to be accounted for in the variation of the heat from respiration, while any effects from the infiltration of surrounding air into the enclosure or heat transfer through the enclosure walls could also be seen to be included in the extreme value.

This resulted in an effective hydraulic diameter of 46.38mm using Equation 2.40 and it was supposed that each of the cooling pads contacted an area of about 0.2400m². Found with Equation 2.26, the Reynolds numbers of the air flow ranged between 10665 and 7871 for film temperatures of 0°C and 50°C respectively, which indicated that the Reynold numbers were suitably above 2300 for a turbulent flow in a duct [66, 128]. This indicated that the Gnielinski correlation in Equation 2.43 could be used to estimate the convection heat transfer coefficient. The other conditions for the validity of the Gnielinski correlation were also satisfied with a Prandtl number from 0.7196 at 0°C to 0.7034 at 50°C and ratio of the length to the effective hydraulic diameter of 17.25. This was acceptable given that the Gnielinski correlation offered improved accuracy and both the Dittus-Boelter and Sieder-Tate correlations require a high Reynolds number above 10000 for validity. For acknowledgement, the Schmidt number was 0.7196 at 0°C to 0.7034 at 50°C, which resulted in a Lewis number of approximately unity for all temperatures and indicated that the heat transfer by convection was comparable to the mass transfer by diffusion, such that the temperature and concentration boundary layers coincide with each other.

With fully developed flow at 3m/s and the local Nusselt number being equal to the average Nusselt number, the average convection heat transfer coefficient was found to be between 16.26W/m²/K at 0°C and 14.71W/m²/K at 50°C. Through the assumed analogous relationship between the convection heat and mass transfer coefficients in Equation 2.54, the average convection mass transfer coefficient

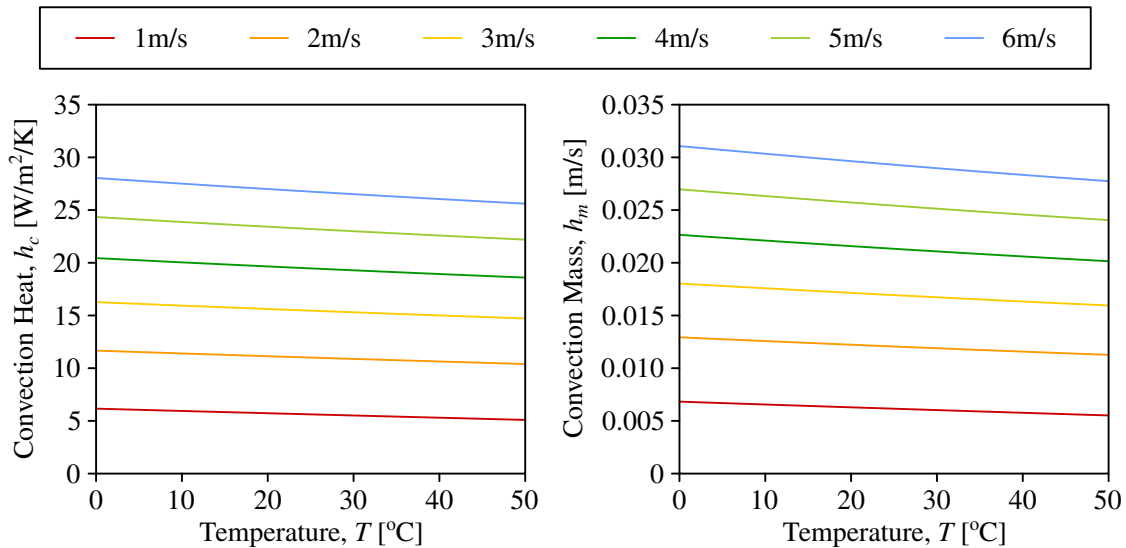


Figure 5.6: Variation of the convection heat transfer coefficient (left) and convection mass transfer coefficient (right) with temperature for a range of flow velocities up to 6m/s as contours.

corresponded with 0.01801m/s at 0°C and 0.01594m/s at 50°C. The nominal variation with temperature was somewhat expected since the properties of dry air and water vapour vary modestly between 0°C and 50°C. The variation with velocity was also computed in Figure 5.6 for a flow up to 6m/s and indicated that the coefficients increased considerably as the velocity increases, as expected from the experimentation performed by Guo [57], but caution must be maintained to avoid over-specifying components for marginal improvements with adverse effects on cost and other aspects.

Considering a range of external temperatures from 0°C to 50°C and relative humidities between 0% and 100%, numerical integration was performed to solve Equation 5.18 for the temperature within the

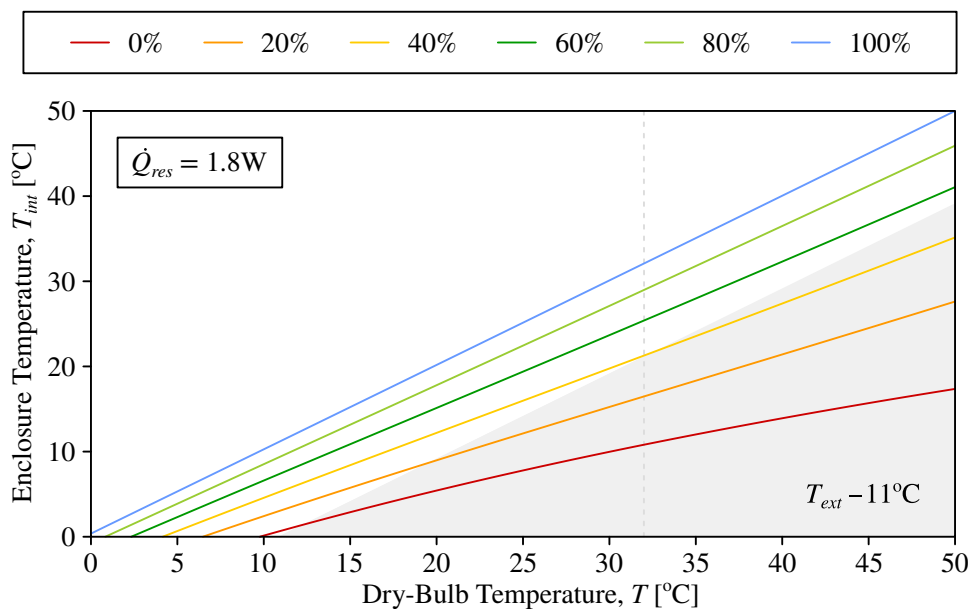


Figure 5.7: Variation in enclosure temperature with external temperature for a range of external relative humidities as contours and using a heat of respiration of 1.8W from the fruits and vegetables.

enclosure. The results are shown in Figure 5.7 using 1.8W for the heat of respiration. An envelope has also been drawn to highlight the region in which the temperature difference satisfies the requirements with a decrease equal to or greater than 11°C for external temperatures greater than 32°C. The minimum boundary of this requirement forms for an external relative humidity of 39.84%.

These overall results were promising and in line with the prospects presented experimentally by Verploegen et al. [10] and Anyanwu [30] in their respective investigations of Zeer Pots, while generally agreeing with the claims of the MittiCool Clay Refrigerator, Bosch FreshBox, and Fenik Yuma Cooler. It should also be noted that the volumetric flow rate was required to be 13.95L/s in each channel, which corresponds with a mass flow rate of approximately 0.01651kg/s in each channel, to achieve a flow of 3m/s. Furthermore, for a temperature difference of 11°C, the rate of evaporation from the pads is derived from Equation 2.53 to be approximately 0.1069L/hr and proportionally related to the temperature difference through the analogous convection heat and mass transfer coefficients.

5.3.3 AIR FLOW PROPERTIES

To predict the changes in the properties of the air flow between the inlet and outlet, it was necessary to explore the trends in the possible variation in these properties based on the efficiency of the evaporative cooling. Unfortunately, it is difficult to estimate the efficiency of the evaporative cooling without realistic results from practical experimentation. So, to provide an indication of the trends for different efficiencies, psychrometric charts were considered for an altitude of 0m with an atmospheric pressure of 101.32kPa and altitude of 1700m with an atmospheric pressure of 82.50kPa, which enabled efficiencies between 0% and 100% to be examined for inlet air with an external temperature from 0°C to 50°C and relative humidity of 0%, 30%, and 60%. The results are plotted in Figure 5.8 for an altitude of 0m and Figure 5.9 for an altitude of 1700m, where Equation 2.62 was used to determine the properties of the outlet air based on a constant wet-bulb temperature for the given properties of the inlet air.

As mentioned in Section 2.5, it was expected for an efficiency between 60% and 100% depending on the environmental conditions. At an altitude of 0m and for an efficiency of 60%, the predictions coincided with an outlet temperature and relative humidity of $20.5 \pm 0.5^\circ\text{C}$ and $34 \pm 2\%$ respectively, and, at an altitude of 1700m and for an efficiency of 60%, the predictions coincided with an outlet temperature and relative humidity of $20.0 \pm 0.5^\circ\text{C}$ and $32 \pm 2\%$ respectively for an inlet temperature of 32°C and relative humidity of 0%. For an inlet temperature of 32°C and relative humidity of 30% with an efficiency of 60%, the corresponding outcomes were an outlet temperature of $24.0 \pm 0.5^\circ\text{C}$ and relative humidity of $62 \pm 2\%$ at an altitude of 0m or an outlet temperature of $23.5 \pm 0.5^\circ\text{C}$ and relative humidity of $60 \pm 2\%$ at an altitude of 1700m. Likewise, for an inlet temperature of 32°C and relative humidity of 60% with an efficiency of 60%, a similar trend is seen with an outlet temperature of $27.5 \pm 0.5^\circ\text{C}$ and relative humidity of $84 \pm 2\%$ at an altitude of 0m or an outlet temperature of $27.0 \pm 0.5^\circ\text{C}$ and relative humidity of $80 \pm 2\%$ at an altitude of 1700m.

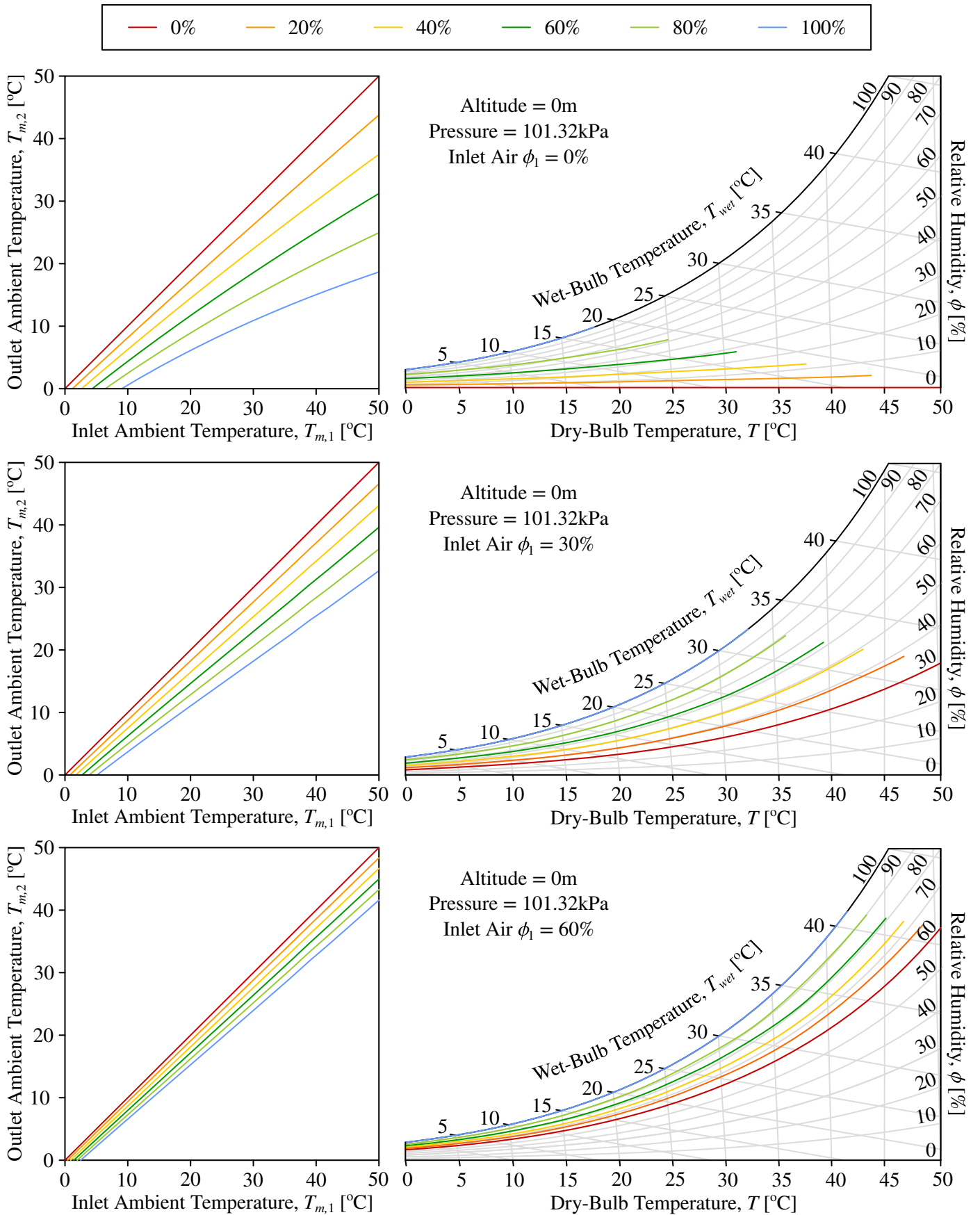


Figure 5.8: Variation in outlet temperature with inlet temperature for a range of efficiencies as contours and considering air with a relative humidity of 0% (top), 30% (middle), and 60% (bottom) at 0m.

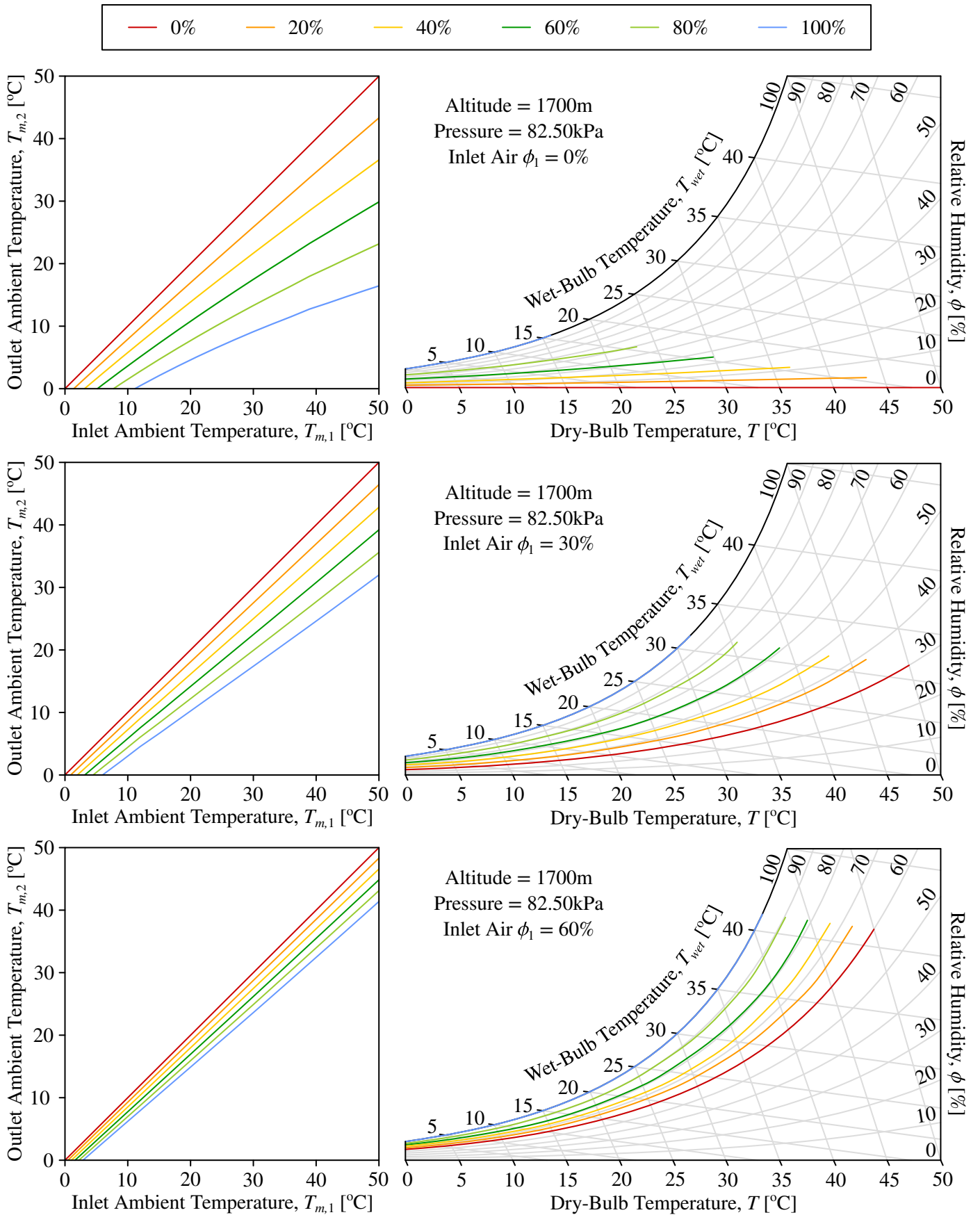


Figure 5.9: Variation in outlet temperature with inlet temperature for a range of efficiencies as contours and considering air with a relative humidity of 0% (top), 30% (middle), and 60% (bottom) at 1700m.

As expected, these predictions suggested that a significantly lower outlet temperature would be achievable for a low inlet relative humidity compared to the outlet temperature for a high inlet relative humidity. Assuming an efficiency of 60%, there was a useful decrease of approximately 44.98% for an inlet relative humidity of 0%, moderate decrease of approximately 29.60% for an inlet relative humidity of 30%, and unfavourable decrease of approximately 16.03% for an inlet relative humidity of 60%. There was also an indication that a higher altitude would have a marginally lower outlet temperature and relative humidity for the same inlet temperature and relative humidity at a lower altitude, but this effect appeared to be trivial compared to the effect from the actual properties of the inlet air.

5.4 FLOW SIMULATION ANALYSIS

A CFD simulation of the flow arising from the fan was useful as it allowed for multiple iterations of the design to be performed before finalising the design through practical experimentation. As mentioned in Section 2.5.3, backward-curved blades were the most promising profile to consider for a radial fan requiring high flow rate and maximum efficiency. However, the velocity distribution was expected to be very complex with dependence on numerous factors of the design and caution needed to be employed due to the curvature of the blades, rotation of the flow, and sensitivity to recirculation effects. Furthermore, even though an isothermal flow without heat transfer was considered, it was reasoned that minor heat transfer would not significantly affect the results, especially since it was expected for a temperature difference of only 11°C, such that it was justifiable to neglect any energy effects.

5.4.1 DESIGN INCEPTION

The design of the blades was focused on the development of the profile to guide and distribute the air flow through the channels. The primary criteria for the profile were that the blades were able to provide an acceptable distribution of relative velocity on both the driving and trailing surfaces in order to minimise the losses in performance from separation and boundary layer inefficiencies; the blades could be manufactured accurately and economically by means of automated procedures; and the blades must be sufficiently robust in order to ensure a long operational life without failure. Unfortunately, it was possible for situations in which these criteria were in conflict, such as a profile which offers an ideal velocity distribution but cannot be easily or affordably manufactured, so it was often necessary to compromise for the most reasonable arrangement [73]. So, because of this and the lack of explicit standardisation, an iterative design was adopted to develop the optimal profile through a trial and error process to obtain the most favourable accommodation between these criteria.

As depicted in Figure 5.10, a maximised diameter of 250mm was initially considered with blades extending from a central hub of 30mm in diameter. The blades were constructed as circular arcs with an outlet angle of 65° and tangency at the hub. Additionally, a constant width of 2mm was used with a constant in-plane breadth of 20mm without inclination, since the introduction of varying thickness or

out-of-plane inclination may increase the manufacturing complexity and cost to maintain tolerances. For the number of blades, the experimental recommendations from Pfeleiderer [129] in Figure 5.11 show that 12 blades corresponds with an outlet angle of 65° . This layout with a high outlet angle is similar to radial fans used in the cooling of processors in laptops which need to cycle a large amount of air while remaining compact, where it is even regular for forward-curved blades to be used, although the scale of these fans is slightly smaller with diameters around 80mm [130, 131].

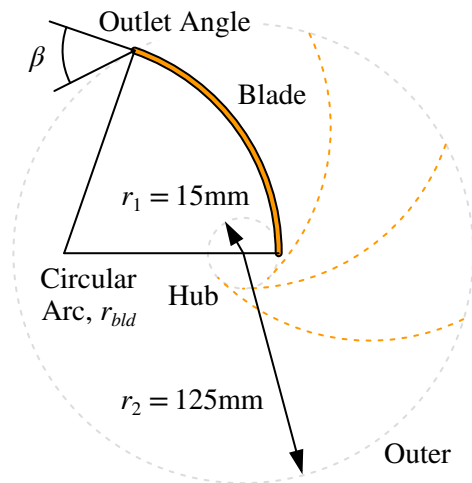


Figure 5.10: Geometry layout for the initial generation of the backward-curved blade profile.

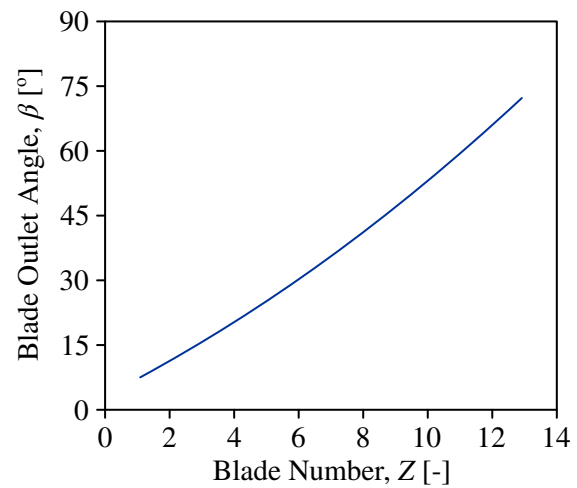


Figure 5.11: Experimental recommendations for the number of blades for the outlet angle [129].

Furthermore, Lee and Lim [132] investigated the optimal design of a centrifugal blower using a radial fan with a volute casing, which can be seen to be fairly similar to the proposed design except with a single outlet. They considered various profiles with s-shaped (combination of backward-curved followed by forward-curved), backward-curved, straight, and forward-curved blades, where the number of blades was also varied between 10 and 16 although this was seen to have a marginal effect [132]. Their analysis was conducted through a CFD simulation and complemented by practical experimentation in a certified test rig in a wind tunnel, where the results of each analysis were in consistent agreement [132]. In summary, it was concluded that forward-curved blades result in a slightly higher flow rate for the same angular velocity, but backward-curved blades require a significantly lower power for the same angular velocity [132]. For the same power, backward-curved blades offered a higher flow rate than forward-curved blades of more than 11.43%, which aptly reinforced the previous remarks and confirmed the use of a backward-curved blade profile for the maximisation of efficiency [132].

5.4.2 BASIC ANALYTICAL PREDICTIONS

Using velocity triangles with a total mass flow rate of 0.03302kg/s for an outlet velocity of 3m/s, this revealed that the angular velocity needed to be 227.7rev/min and, using Equation 2.66, it was required for a torque of 6.156mN.m. Based on the assumption that the pressure remains constant without significant changes in elevation, the head rise from Equation 2.68 was only dependent on the

velocities and, neglecting tangential swirl at the inlet, a head rise of 0.4529m or 5.262Pa emerged. The power could then be found to be approximately 0.1468W using Equation 2.67 in relation to the torque.

These results were reasonable, however the opening at the inlet and presence of bends downstream of the fan may lead to losses and irreversibilities. So, to account for hydraulic and volumetric inefficiencies, it was realistic to expect a higher angular velocity, torque, and power to be required with an increased head rise by up to 1.96 times to maintain the desired velocity of 3m/s in the channels [70]. This corresponded with an outlet velocity up to 4.2m/s, angular velocity of 318.8rev/min, torque of 12.07mN.m, head rise of 0.8876m or 10.31Pa, and power of 0.4028W. The expected velocity distribution through and points of separation within the passages of the backward-curved blades is shown in Figure 5.12 with the expected velocity distribution across bent and straight sections of the channels.

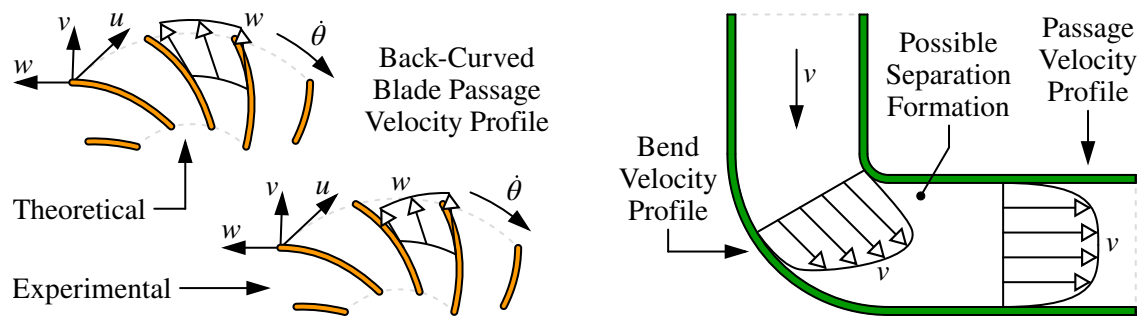


Figure 5.12: Expected distributions of the velocity profile through the passages of the backward-curved blades (left) and across bent and straight sections of the channels (right), where it is likely for separation to occur on the trailing surface of the blades and after the inner turn of a bend [70, 73, 129].

5.4.3 THEORETICAL BACKGROUND

As outlined by Wilcox [128], an incompressible, steady, and turbulent flow is described by the Navier-Stokes equations for the transportation of mass and momentum in Equation 5.19 and Equation 5.20 respectively when considering a Newtonian fluid. For practical evaluation, the Reynolds-averaged Navier-Stokes equations are defined in Equation 5.21 for mass and Equation 5.22 for momentum with the inclusion of the Reynolds stress, which is a stress tensor accounting for the net flux in momentum from turbulent fluctuations based on the Boussinesq hypothesis [128]. The Boussinesq hypothesis infers that momentum transfer caused by turbulent eddies can be modelled with an eddy viscosity, such that the Reynolds stress is proportional to the average strain rate, as given by Equation 5.23 [128].

To evaluate the Reynolds stress, it is necessary to assert assumptions based on findings from analytical and experimental results about the behaviour of the turbulent flow. So, a model of the turbulence can be constructed by decomposing the turbulent flow based on the time-averaged behaviour with rapid and random fluctuations about this average state, where the turbulence is then assumed to be stationary and constant on average over time, as illustrated in Figure 5.13 [128]. However, it should be noted that steady flows do not necessarily have a time scale, since the flow does not vary with time.

$$\frac{\partial u_i}{\partial x_i} = 0 \text{ with } u_i = (u, v, w) \text{ and } x_i = (x, y, z) \quad (5.19)$$

$$\rho \frac{\partial u_i}{\partial t} + \rho u_j \frac{\partial u_i}{\partial x_j} = -\frac{\partial p}{\partial x_i} + \frac{\partial}{\partial x_j} (2\mu s_{ji}) \text{ with } s_{ji} = \frac{1}{2} \left(\frac{\partial u_i}{\partial x_j} - \frac{\partial u_j}{\partial x_i} \right) \quad (5.20)$$

$$\frac{\partial \bar{u}_i}{\partial x_i} = 0 \text{ with } u_i = \bar{u}_i + u'_i \text{ and } \bar{u}_i = \int_t^{t+t_s} \frac{u_i}{t_s} dt \text{ for } t_1 \ll t_s \ll t_2 \quad (5.21)$$

$$\rho \frac{\partial \bar{u}_i}{\partial t} + \rho \bar{u}_j \frac{\partial \bar{u}_i}{\partial x_j} = -\frac{\partial \bar{p}}{\partial x_i} + \frac{\partial}{\partial x_j} (2\mu \bar{s}_{ji}) + \frac{\partial}{\partial x_j} (-\rho \overline{u'_j u'_i}) \text{ with } R_{ij} = -\rho \overline{u'_j u'_i} \quad (5.22)$$

$$R_{ij} = \rho \tau_{ij} = -\rho \overline{u'_i u'_j} = 2\mu_{ed} \bar{s}_{ij} - \frac{2}{3} \rho \kappa \delta_{ij} = 2\mu_{ed} \left(\frac{\partial \bar{u}_i}{\partial x_j} + \frac{\partial \bar{u}_j}{\partial x_i} \right) - \frac{2}{3} \rho \kappa \delta_{ij} \quad (5.23)$$

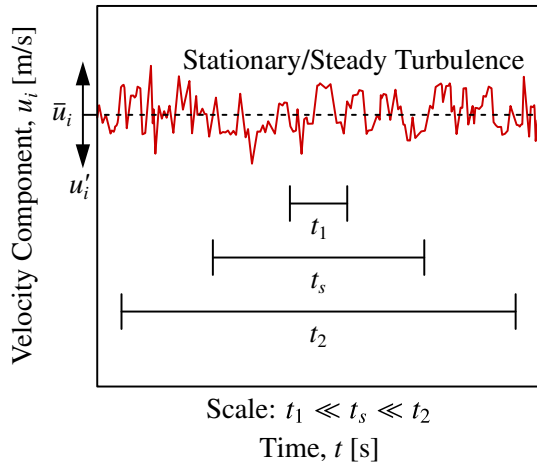


Figure 5.13: Example of random fluctuations in velocity about an average for turbulence [128].

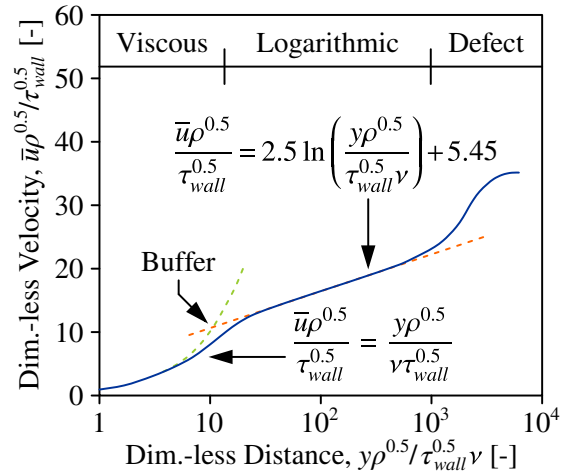


Figure 5.14: Typical characteristics of the velocity profile for a turbulent boundary layer [128].

The most common class of models used to close the Reynolds-averaged Navier-Stokes equations for turbulence have two additional transportation equations to account for history effects and represent the turbulent properties of the flow with a linear constitutive relationship. These derive from either the κ - ϵ model, which is associated with the turbulence kinetic energy and turbulence dissipation rate, or κ - ω model, which is associated with the turbulence kinetic energy and specific turbulence dissipation rate. Basically, the turbulence kinetic energy can be seen as the kinetic energy per unit mass of the turbulent fluctuations; the turbulence dissipation rate can be seen as the rate at which turbulence kinetic energy is converted into internal energy; and the specific turbulence dissipation rate can be seen as rate at which turbulence kinetic energy is converted into internal energy per unit volume. In a sense, the turbulence kinetic energy determines the energy in the turbulence, while the turbulence dissipation rate or specific turbulence dissipation rate determines the scale of the turbulence [128]. There are other classes of models for turbulence, which include algebraic or zero-equation and one-equation, but these models are often less reputable and applicable in fewer cases than the two-equation models [128].

The κ - ϵ model is a robust model and performs well for flow around complex features when the average pressure gradients are relatively small, although its reliability and accuracy does suffer in cases of large adverse pressure gradients and strong curvature of the flow [128]. Specifically, there has been the

construction of the standard κ - ε model developed by Launder and Sharma [133], re-normalised group κ - ε model developed by Yakhot and Orszag [134], and realisable κ - ε model developed by Shih et al. [135]. The κ - ω model is a broad model and performs well in predicting internal flow and effects due to recirculation and separation from large adverse pressure gradients with improved accuracy, although it may be very sensitive to the initial conditions and convergence may be problematic [128]. The major contributions towards the standard κ - ω model in its modern form have been from Wilcox [128, 136], while the shear stress transport κ - ω model has been proposed by Menter [137, 138] and uses the standard κ - ω model in the inner parts of the boundary layer and standard κ - ε model in the outer parts of the boundary layer and free stream with switching between the models being performed seamlessly by blending functions. The definition of the turbulence kinetic energy is given by Equation 5.24, where it is assumed that the turbulence is approximately isotropic, and the definitions of the turbulence dissipation rate and specific turbulence dissipation rate are given by Equation 5.25 [128].

$$\kappa = \frac{1}{2} (\overline{u'u'} + \overline{v'v'} + \overline{w'w'}) \text{ with } \overline{u'u'} \approx \overline{v'v'} \approx \overline{w'w'} \text{ (isotropic)} \rightarrow \kappa = \frac{1}{2} \overline{u_i'u_i'} \quad (5.24)$$

$$\varepsilon = -\frac{d\kappa}{dt} = 2 \frac{\mu}{\rho} \overline{s'_{ik}s'_{ik}} \approx \frac{\mu}{\rho} \overline{\frac{\partial u_i'}{\partial x_k} \frac{\partial u_i'}{\partial x_k}} \rightarrow \omega = \frac{\varepsilon}{\kappa\beta^*} \quad (5.25)$$

For modelling the flow through a radial fan and within narrow channels, it was reasoned that the shear stress transport κ - ω model would be the most suitable option. This was because it offers a balance between accuracy and solvability, where the standard κ - ω model provides improved performance for near-wall and low Reynolds number treatment and the standard κ - ε model is commonly used to model radial fans with full turbulence [130, 132, 139]. The associated dynamic eddy viscosity is given in Equation 5.26, and the additional transportation equations are shown in Equation 5.27 for the turbulence kinetic energy and Equation 5.28 for the specific turbulence dissipation rate [128, 137, 138].

$$\mu_t = \frac{\rho a \kappa}{\max(a\omega, \bar{s}B_2)} \text{ with } \bar{s} = \sqrt{2\bar{s}_{ij}\bar{s}_{ij}} \quad (5.26)$$

$$\rho \frac{\partial \kappa}{\partial t} + \rho \bar{u}_j \frac{\partial \kappa}{\partial x_j} = P_\kappa - \rho \beta^* \kappa \omega + \frac{\partial}{\partial x_j} \left((\mu + \sigma_\kappa \mu_t) \frac{\partial \kappa}{\partial x_j} \right) \quad (5.27)$$

$$\rho \frac{\partial \omega}{\partial t} + \rho \bar{u}_j \frac{\partial \omega}{\partial x_j} = \frac{\gamma \rho}{\mu_t} P_\kappa - \rho \beta \omega^2 + \frac{\partial}{\partial x_j} \left((\mu + \sigma_\omega \mu_t) \frac{\partial \omega}{\partial x_j} \right) + 2\rho(1 - B_1) \frac{\sigma_\omega}{\omega} \frac{\partial \kappa}{\partial x_j} \frac{\partial \omega}{\partial x_j} \quad (5.28)$$

$$\left[\begin{array}{l} B_1 = \tanh \left(\min \left(\max \left(\frac{\sqrt{\kappa}}{\beta^* \omega y}, \frac{500\mu}{\rho \omega y^2} \right), \frac{4\rho \sigma_\omega \kappa}{C_{\kappa\omega} y^2} \right)^4 \right) \text{ and } B_2 = \tanh \left(\max \left(\frac{2\sqrt{\kappa}}{\beta^* \omega y}, \frac{500\mu}{\rho \omega y^2} \right)^2 \right) \\ P_\kappa = \min \left(\mu_t \frac{\partial \bar{u}_i}{\partial x_j} \left(\frac{\partial \bar{u}_i}{\partial x_j} + \frac{\partial \bar{u}_j}{\partial x_i} \right), 10\rho \beta^* \kappa \omega \right) \text{ and } C_{\kappa\omega} = \max \left(2\rho \frac{\sigma_\omega}{\omega} \frac{\partial \kappa}{\partial x_j} \frac{\partial \omega}{\partial x_j}, 10^{-10} \right) \\ \beta^* = 0.09 \text{ and } \beta = 0.0750B_1 + 0.0828(1 - B_1) \text{ and } \gamma = 0.5556B_1 + 0.4400(1 - B_1) \\ a = 0.31 \text{ and } \sigma_\kappa = 0.8500B_1 + 1.0000(1 - B_1) \text{ and } \sigma_\omega = 0.5000B_1 + 0.8560(1 - B_1) \end{array} \right]$$

Also, as mentioned in Section 2.4.2.1, it is always necessary to satisfy the no-slip condition near a surface with the subsequent effects forming the boundary layer and, so, a model of the profile can be

constructed through a viscous or linear sub-layer, buffer layer, and inertial or logarithmic layer, as shown in Figure 5.14 [128]. In the viscous sub-layer, the flow velocity varies linearly with distance from the wall; in the buffer layer, the inertial forces begin to dominate over viscous forces to produce turbulence; and, in the inertial layer, the flow is fully turbulent and the average flow velocity is logarithmically related to the distance from the wall. Since the viscous and buffer layers are very thin relative to the inertial layer, it can be computationally beneficial to employ an approximation by only considering the inertial layer with the formulation of empirical wall functions in this layer [128].

5.4.4 MODEL CONFIGURATION

For the CFD analyses, the simulations were setup and performed in ANSYS Fluent 2019 R3 installed on a Windows 10 x64 operating system, where the iterations were solved on an Intel Xeon E5-2690 using 8 cores, 16 threads, 8x32kB of primary cache, 8x256kB of secondary cache, 20MB of tertiary cache, base frequency of 2.90GHz, and turbo frequency of 3.80GHz with access to 24.4GB of system memory. To begin the pre-processing, the initial geometry and mesh needed to be prepared.

The geometry collectively described the domain in which the fluid flows and the limits of the geometry needed to be defined as boundary conditions. The geometry may be divided into parts to represent different regions within the domain. So, in the case of a radial fan with relative motion between the blades and bulk region, the bulk region could be considered as a stationary reference frame, while a region surrounding the blades could be set as a moving reference frame with a specific angular velocity. This essentially allowed for apparent unsteady flow, as considered from the stationary reference frame, to be viewed as steady flow with respect to the moving reference frame, while the effects from the resulting centrifugal and coriolis forces are included in the momentum equation.

Instead of using a moving reference frame, it would have been possible to use a mixing plane interface model or sliding mesh approach as alternative methods. However, these methods are either inherently simplified or explicitly used for unsteady flow and require greater computational effort and prolonged time to converge. This introduces a higher risk for other objectionable challenges to arise, such as requirements for the flow to be spatially averaged at the mixing plane interface, extrapolation to solve non-conformal interfaces between the stationary and sliding meshes if the elements of the meshes do not align, or a large number of time steps to resolve the transient motion and uncertain initial conditions (with a moving reference frame, the solutions at the interfaces between the meshes are simply solved using local velocity transformations between the reference frames and the model is steady with no time steps). Therefore, although a moving reference frame may be potentially less accurate, it was still the most preferable method for a reasonable approximation before practical experimentation.

The methodology for a moving reference frame is graphically described in Figure 5.15 with the parts making up the overall model. The part of the radial fan was constructed based on the mentioned geometry with the inclusion of a slight rib on the trailing surface for stability and the part of the

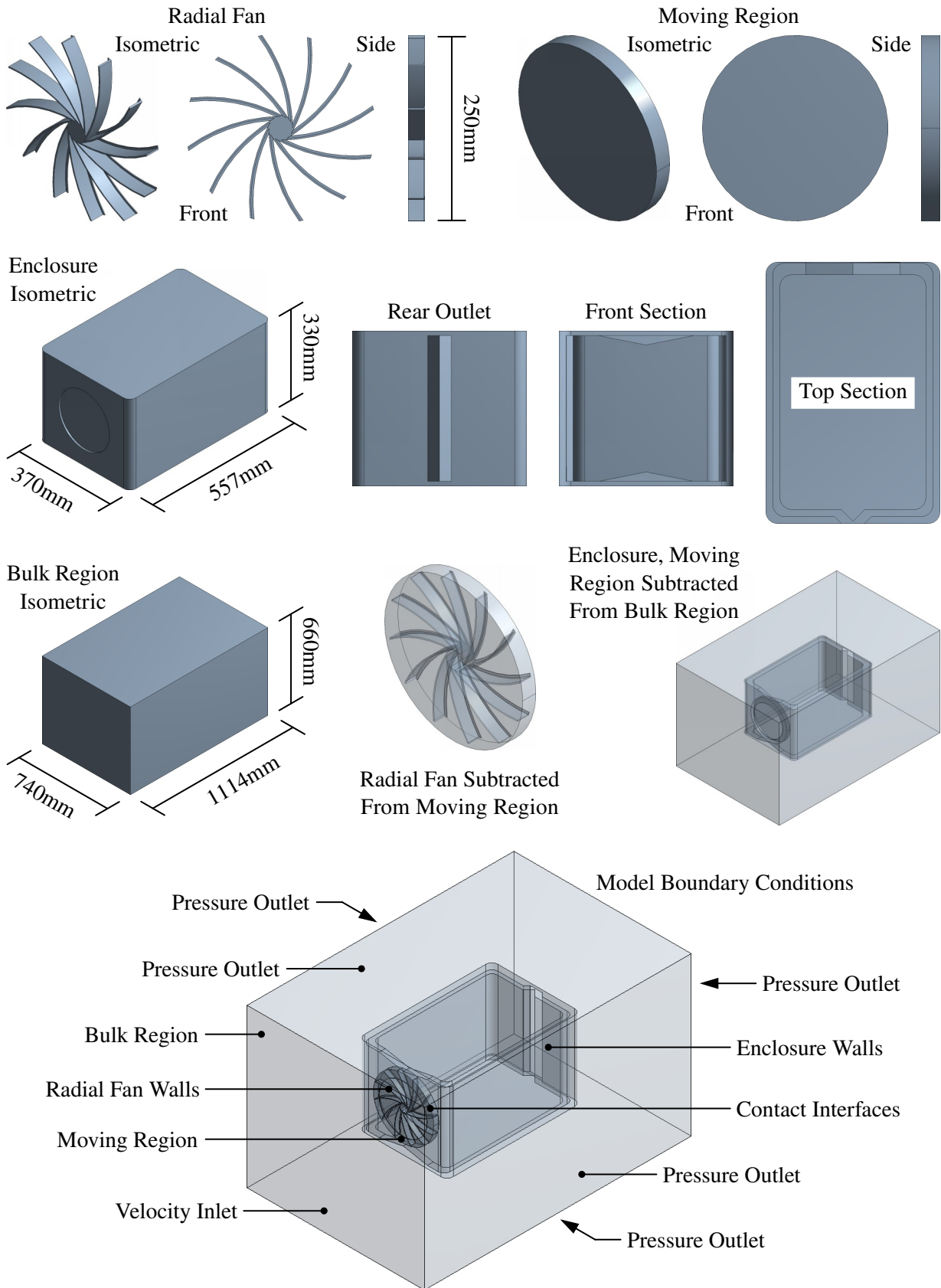


Figure 5.15: Parts for the radial fan and basic enclosure to construct the overall model for the CFD using a moving reference frame. The CAD model was generated using Autodesk Inventor Professional 2019 and ANSYS DesignModeler 2019 R3 for simulation in ANSYS Fluent 2019 R3.

basic enclosure was constructed to represent the walls on either side of the channels for the air flow. Subsequently, it was possible to use primitive boolean operations to modify these models into a bulk region to represent the fluid and a region surrounding the blades to represent the moving reference frame of the radial fan. This allowed for the fluid to form the domain of interest with the actual structure and surroundings represented through boundary conditions, where these boundary conditions were set for the driving surface as a velocity inlet with no incoming velocity or gauge pressure, trailing surface as a pressure outlet with no gauge pressure, surrounding surfaces as pressure outlets with tolerance for reverse flow, contact surfaces as interfaces between the bulk and moving regions, and remaining surfaces as walls for the radial fan and enclosure with the no-slip condition imposed.

To complete the pre-processing, a mesh needed to be generated to sub-divide the continuous geometry into discrete volumetric elements. The number of elements within the mesh governs the resolution of the solution up to the point where subsequent refinements of the mesh only have very marginal effects on the solution. In other words, it was necessary to perform a mesh independence analysis to confirm that the solution would subsist irrespective of the specific mesh used to find the solution.

5.4.5 BASE SETUP AND RESULTS

To achieve mesh independence with a compromise between accuracy and computation speed, a coarse mesh was created and iterations were performed by refining this mesh until the resulting properties throughout the flow had negligible changes between consecutive meshes. So, the mesh independence was confirmed based on an allowable tolerance for variations up to 2% between consecutive meshes using the conventional definition of percentage difference in Equation 5.29.

$$\psi = 2 \left| \frac{\phi_1 - \phi_2}{\phi_1 + \phi_2} \right| \times 100\% \quad (5.29)$$

In total, five meshes were generated ranging from 664759 nodes to 8593824 nodes, where the element size, adaptive resolution, adaptive transition, inflation layers, and refined sizing of critical regions were varied to refine the level of detail. The configuration of each mesh is summarised in Table 5.5 and labelled as rough, coarse, medium, fine, and detailed with respect to increasing levels of detail. In particular, the inflation layers were assigned to the internal walls of the channels to resolve the boundary layers and increased from 4 layers to 10 layers, while the element size was subsequently decreased around the blades and in the channels from 6mm to 2mm compared to the base element size of 10mm. As they are reliable for modelling turbulence, over 75% of the elements were tetrahedrals, which made up over 98% of the volume of the regions, with the remaining elements being wedges and pyramids. An evaluation of the skewness and aspect ratio of the elements, shown in Table 5.5, was used as a metric to judge the quality of the meshes, where a skewness minimised to 0 and aspect ratio minimised to 1 were desirable. It was seen that the quality of each of the meshes was satisfactory with an average skewness decreasing below 0.25 and aspect ratio maintained below 4.0. Examples

Table 5.5: Configurations of the initial meshes with the skewness and aspect ratio metrics.

Rough Mesh	Base Element Size: 10mm Adaptive Resolution: 7 Adaptive Transition: Fast Inflation Layers: 4 Refined Sizing: 6mm Elements: 664759 Nodes: 1254809 Compute Time: 2.58hr	<p>Skewness [-] Average: 0.293</p>	<p>Aspect Ratio [-] Average: 3.403</p>
Coarse Mesh	Base Element Size: 10mm Adaptive Resolution: 5 Adaptive Transition: Slow Inflation Layers: 4 Refined Sizing: 5mm Elements: 1262730 Nodes: 2191670 Compute Time: 6.96hr	<p>Skewness [-] Average: 0.256</p>	<p>Aspect Ratio [-] Average: 2.889</p>
Medium Mesh	Base Element Size: 10mm Adaptive Resolution: 7 Adaptive Transition: Slow Inflation Layers: 6 Refined Sizing: 4mm Elements: 2895387 Nodes: 4917428 Compute Time: 12.7hr	<p>Skewness [-] Average: 0.231</p>	<p>Aspect Ratio [-] Average: 3.109</p>
Fine Mesh	Base Element Size: 10mm Adaptive Resolution: 7 Adaptive Transition: Slow Inflation Layers: 6 Refined Sizing: 3mm Elements: 4562002 Nodes: 7923684 Compute Time: 23.2hr	<p>Skewness [-] Average: 0.227</p>	<p>Aspect Ratio [-] Average: 3.301</p>
Detailed Mesh	Base Element Size: 10mm Adaptive Resolution: 7 Adaptive Transition: Slow Inflation Layers: 10 Refined Sizing: 2mm Elements: 8593824 Nodes: 15551773 Compute Time: 77.9hr	<p>Skewness [-] Average: 0.223</p>	<p>Aspect Ratio [-] Average: 3.654</p>

of cross-sections through each of the meshes are shown in Figure 5.16. (The detailed mesh was the highest resolution before the mesh solver encountered errors due to a lack of system memory).

To judge convergence, the scaled residuals were monitored for the conserved parameters in the form of the conservation of mass, turbulence kinetic energy, turbulence dissipation rate, and three-dimensional velocities, such that it was possible to appropriately approach a solution to the Reynolds-averaged Navier-Stokes equations throughout the domain of the mesh. It is generally acceptable for the scaled residuals to decrease below 0.001 for satisfactory convergence, however this magnitude to which the scaled residuals decrease is based on the initialisation and can be misleading to simply apply as a universal criteria for convergence. For example, the scaled residuals will rapidly decay if the initial iterations are very inaccurate or only slightly decay if the initial iterations are very accurate, especially for the scaled residual for the continuity. Instead, the general trends of the scaled residuals should primarily be considered with the criteria for convergence requiring the scaled residuals to decay until they flatten without further changes, along with the area-weighted values for the mass flow rate, velocity, and pressure over several planes in the domain. The planes for the mass flow rate and velocity were positioned at the middle of the enclosure, 200mm upstream of the middle of the enclosure, 200mm downstream of the middle of the enclosure, and at the outlet of the enclosure. The planes for the pressure were set as the driving and trailing surfaces of the blades.

The solution setup was initialised using double-precision in parallel with a pressure-based solver and the air modelled at a constant density of 1.225kg/m^3 and dynamic viscosity of $1.7894 \times 10^{-5}\text{N}\cdot\text{s/m}^2$. The operating pressure and temperature were set as 101.325kPa and 25°C respectively and gravitational effects were neglected. As mentioned, the region surrounding the blades was set as a moving reference frame with an angular velocity of 318.8rev/min relative to the stationary bulk region. The coupled scheme was chosen as the method to solve the pressure-velocity coupling of the solution with the spatial discretisation for interpolation between elements using least squares cell based differencing for the gradient, second order central differencing for the pressure, second order upwind differencing for the momentum, first order upwind differencing for the turbulence kinetic energy, and first order upwind differencing for the specific turbulence dissipation rate. To control the solution, the pseudo-transient explicit relaxation factors regulate the extent by which properties change between iterations and the factors were set as 0.4 for the pressure, 0.4 for the momentum, 1.0 for the density, 0.6 for the turbulence kinetic energy, 0.6 for the specific turbulence dissipation rate, and 1.0 for the turbulent viscosity. Finally, the solution was initialised using uniform properties throughout the domain and the initial velocities relative to the motion of the reference frame for the specific regions.

The results at the positions of interest are listed in Table 5.6 for each mesh with the percentage difference for each result compared against the result from the subsequently refined mesh and result from the most detailed mesh. The changes in the scaled residuals and properties at the positions of interest are also included in Figure 5.17 and indicated suitable converge after approximately 1000 iterations with

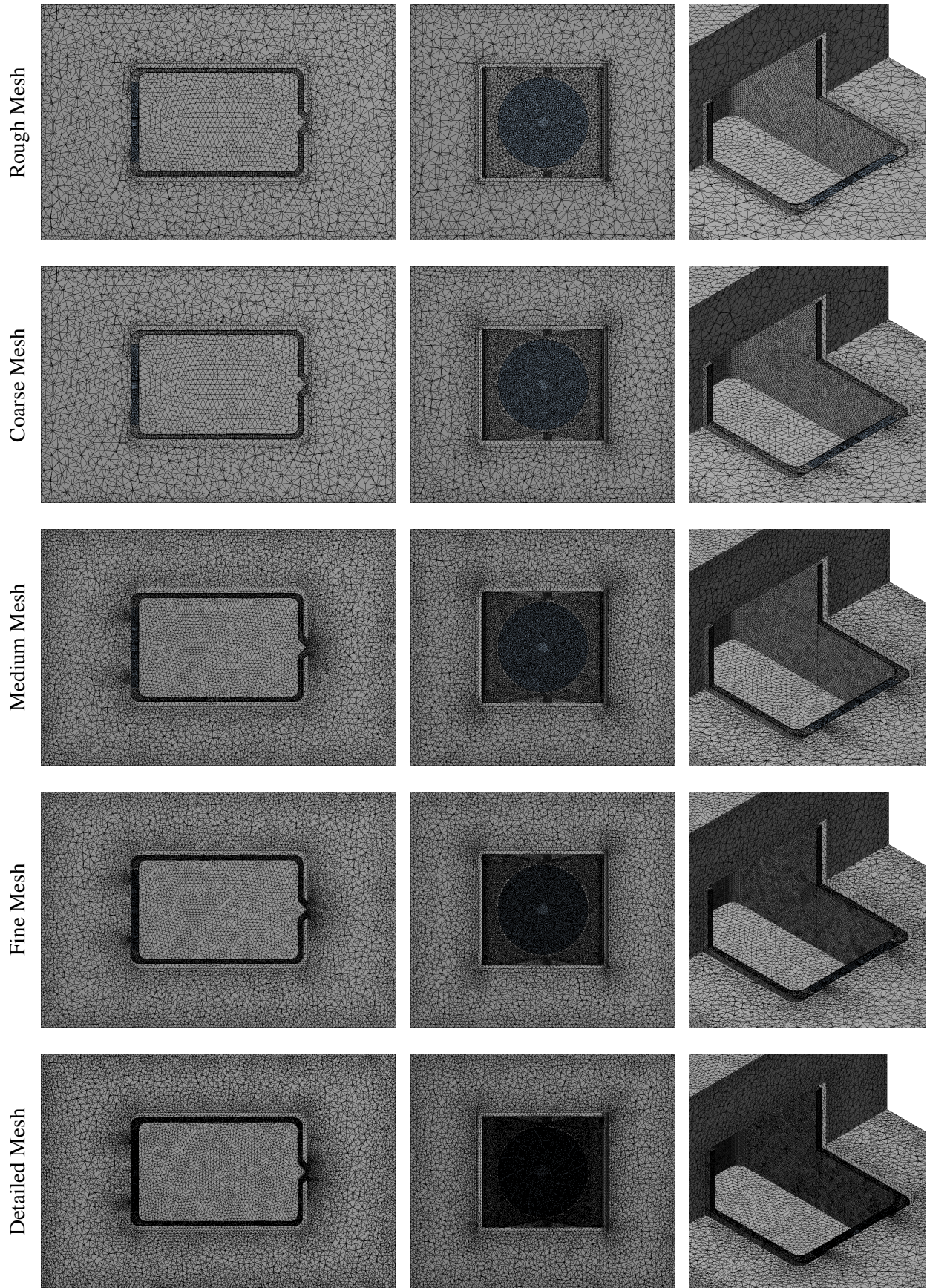


Figure 5.16: Examples of the initial meshes with cross-sections of the top, front, and isometric views.

the variation in the scaled residuals and properties flattening and approaching a steady value. These results indicated that a satisfactory mesh was obtained using the setup of the medium mesh, where the maximum variation between the medium mesh and fine mesh was only 1.02% and the maximum variation between the medium mesh and detailed mesh was only 1.69%. Specifically, the setup of the medium mesh used a base element size of 10mm, adaptive resolution of 7, slow adaptive transition, 6 inflation layers, and refined sizing of 4mm for a total of 2895387 elements. It should also be noted that the maximum variation between the fine mesh and detailed mesh was also below 2% at 1.63%, but the medium mesh was preferred as it was adequately accurate and had a computational time of only 12.7hr compared to 23.2hr for the fine mesh and 77.9hr for the detailed mesh.

Using the medium mesh, the contours of the velocity magnitude are plotted in Figure 5.18a on a plane through the centre of the model with the front, middle, back, and outlet planes and in Figure 5.18b in the region and on the surfaces of the radial fan. Notably, the free stream velocity was approximately 2.114m/s, while the average velocity through the middle plane was only 1.636m/s due to the clear viscous effects from the no-slip condition at the walls. For a visualisation of the flow, the streamlines after the radial fan are shown in Figure 5.18e with the plot displaying the variation in velocity and pressure along the streamlines, which showed prominent turbulence and mixing after the radial fan and around the first bend but more smooth and regular features were present towards the outlet.

These results were substantially less than the analytical predictions with a percentage difference of 34.64% between the free stream velocity and desired velocity or 58.84% between the average velocity and desired velocity. This was expected since the analytical predictions only made allowance for the irreversibilities from the bends for a maximum limit of performance without accounting for other more complex irreversibilities from viscosity, skin friction, flow separation, clearance flow, blade profile, shock losses, recirculation losses, vortex formation, and other three-dimensional hydraulic inefficiencies. On the contrary, before the irreversibilities became significant, the outlet velocity from the radial fan was approximately 4.159m/s, which was in line with the estimated velocity of 4.2m/s from the analytical predictions and aided in confirming the accuracy of the simulation with a percentage difference of only 0.98%. However, the air flow in the channels indicated that a greater angular velocity increased by about 1.85 times to 589.8rev/min would be required for the desired air flow of 3m/s.

Moreover, the contours of the static pressure are plotted in Figure 5.18c on a plane through the centre of the model with the front, middle, back, and outlet planes and in Figure 5.18d in the region and on the surfaces of the radial fan. With the difference in pressure across a blade, the torque and power could be calculated through Equation 5.30 and, using the average value of 1.014Pa for the driving surface and -1.871Pa for the trailing surface, it was predicted for a torque of 7.562mN.m and power of 0.2525W. Again, these results were substantially less than the analytical predictions with a percentage difference of 45.93%. Overall, with the average velocity at the middle plane and change in pressure across the channels, the useful power transferred by the flow was 0.06370W for an efficiency of 25.23%.

Table 5.6: Results at the positions of interest for each of the initial meshes and comparison with the percentage difference between the iterations. The uncertainty for each value is approximately $\pm 5\%$.

Property	Position	Rough Mesh			Coarse Mesh		
		Value	% Diff. Coarse	% Diff. Detailed	Value	% Diff. Medium	% Diff. Detailed
Velocity [m/s]	Front	1.702	0.82%	1.35%	1.716	1.14%	0.24%
	Middle	1.609	0.60%	0.50%	1.619	0.81%	0.86%
	Back	1.605	0.65%	0.48%	1.615	0.84%	0.85%
	Outlet	1.052	0.85%	2.21%	1.061	1.59%	1.16%
Mass Flow Rate [kg/s]	Front	0.01834	0.52%	0.28%	0.01844	0.67%	0.99%
	Middle	0.01828	0.66%	0.57%	0.01840	0.78%	0.84%
	Back	0.01828	0.66%	0.48%	0.01840	0.82%	0.87%
	Outlet	0.01875	0.90%	1.49%	0.01892	0.17%	0.45%
Total Pressure [Pa]	Driving	4.057	2.29%	4.27%	4.151	1.59%	2.91%
	Trailing	1.971	6.44%	6.49%	2.102	0.17%	1.58%
Static Pressure [Pa]	Driving	1.074	0.94%	4.87%	1.064	4.80%	4.68%
	Trailing	-1.851	1.09%	0.31%	-1.831	2.13%	1.91%
Torque [mN.m]		7.67	1.03%	1.56%	7.59	0.36%	0.46%
Power [W]		0.2560	1.03%	1.56%	0.2534	0.36%	0.46%

Property	Position	Medium Mesh			Fine Mesh		Detailed Mesh
		Value	% Diff. Fine	% Diff. Detailed	Value	% Diff. Detailed	Value
Velocity [m/s]	Front	1.736	0.61%	1.37%	1.725	0.76%	1.712
	Middle	1.632	0.92%	1.68%	1.617	0.76%	1.605
	Back	1.629	1.02%	1.69%	1.612	0.67%	1.601
	Outlet	1.078	0.23%	0.43%	1.075	0.21%	1.073
Mass Flow Rate [kg/s]	Front	0.01856	0.92%	1.52%	0.01839	0.61%	0.01828
	Middle	0.01855	0.87%	1.55%	0.01838	0.68%	0.01826
	Back	0.01855	1.00%	1.63%	0.01836	0.62%	0.01825
	Outlet	0.01895	0.42%	1.12%	0.01903	1.55%	0.01874
Total Pressure [Pa]	Driving	4.217	0.40%	1.33%	4.234	0.92%	4.273
	Trailing	2.099	0.22%	1.41%	2.104	1.63%	2.069
Static Pressure [Pa]	Driving	1.014	0.86%	0.12%	1.023	0.74%	1.015
	Trailing	-1.871	0.73%	0.22%	-1.857	0.51%	-1.867
Torque [mN.m]		7.56	0.17%	0.10%	7.55	0.07%	7.56
Power [W]		0.2525	0.17%	0.10%	0.2521	0.07%	0.2522

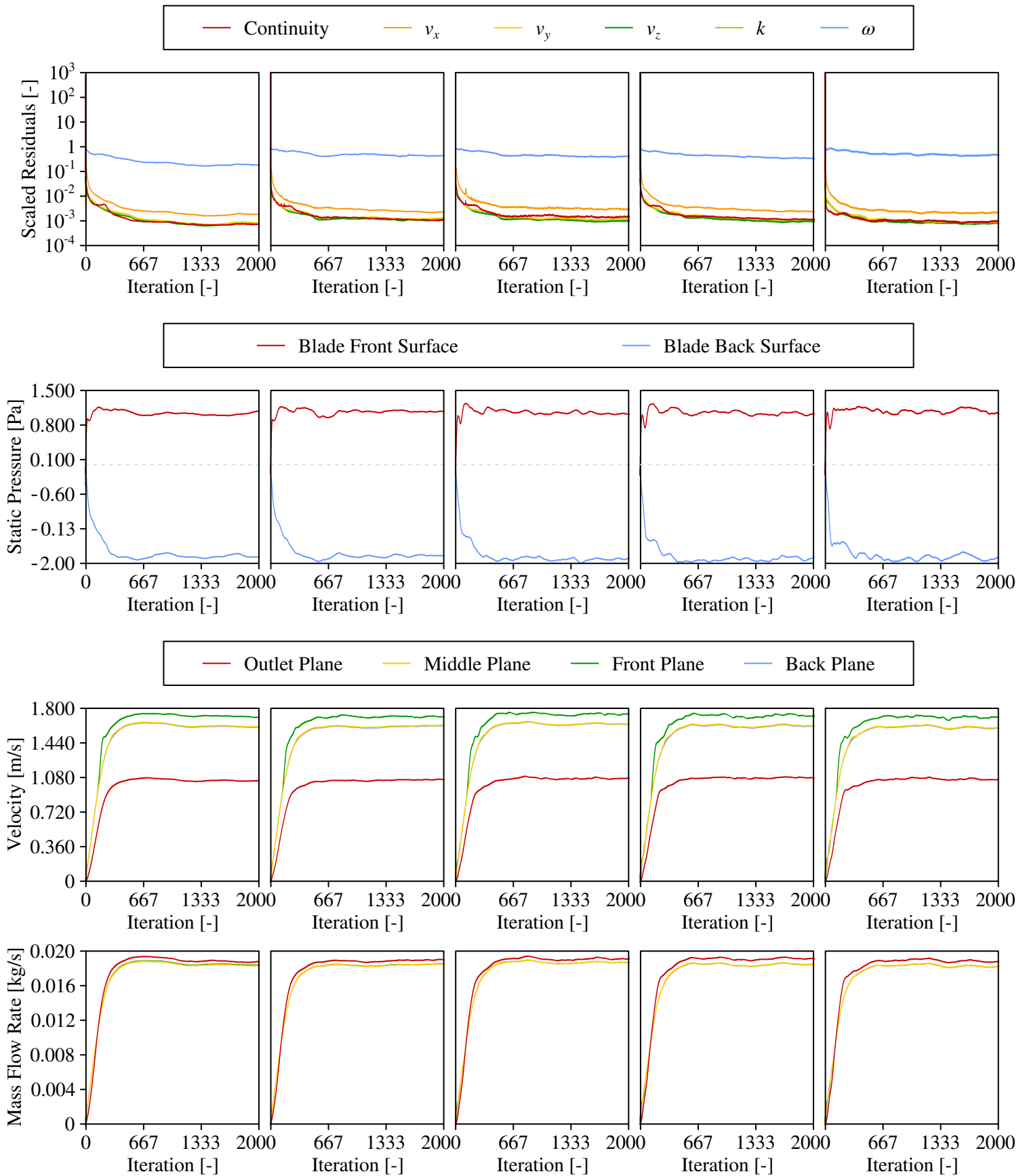


Figure 5.17: Changes in the scaled residuals and properties at the positions of interest for the initial meshes from the rough (first), coarse (second), medium (third), fine (fourth), and detailed (fifth).

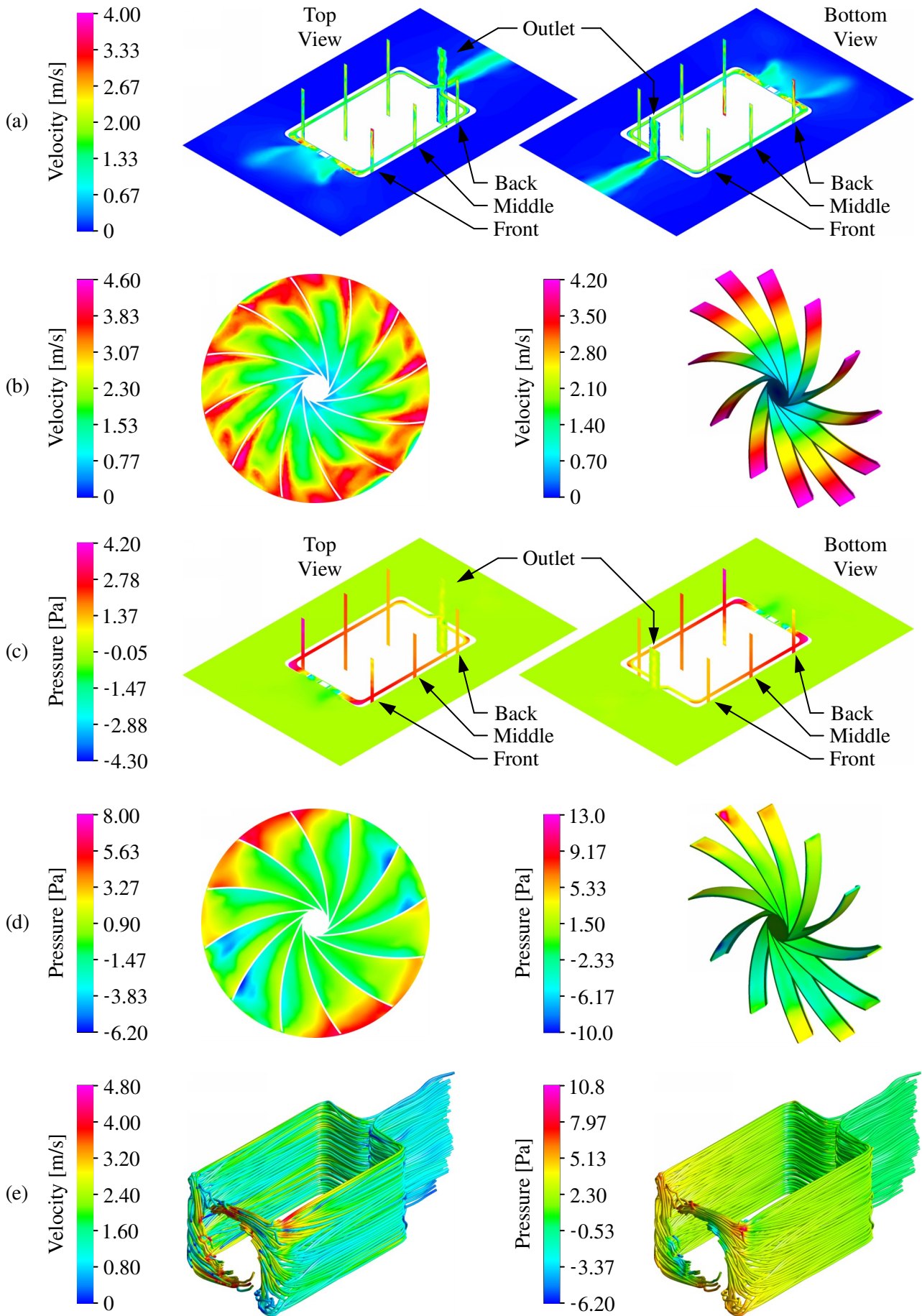


Figure 5.18: Velocity and pressure contours for the initial model considering the medium mesh.

$$\Delta p_{sta} = p_{fnt} - p_{bck} \rightarrow F_{bld} = \Delta p_{sta} A_{bld} \rightarrow F_{tot} = n F_{bld} \rightarrow T_{tot} = F_{tot} r \rightarrow W = T_{tot} \dot{\theta} \quad (5.30)$$

The results also showed that the maximum pressure of 12.87Pa was exerted on the driving surface of the blades at the top and bottom of the rotation when the air was forced to exit tangentially from the blades due to the walls. The minimum pressure of -10.07Pa was exerted on the trailing surface of the blades once they have passed the top and bottom points when the air exited in the normal direction relative to the circumference, as is typical for backward-curved blades. These regions of maximum and minimum pressure correspond with the regions of maximum velocity at the tips of the blades. By increasing the angular velocity to achieve the desired velocity through the channels, it was expected for there to be an impact on the pressure, torque, and power with an increased level of turbulence. This was investigated with the optimisation of the blades for the most efficient configuration.

5.5 FLOW OPTIMISATIONS

Building on the base setup and results, the performance of the radial fan was maximised with regards to efficiency by optimising the blades and varying the outlet angle, quantity, inclination angle, breadth, channel width, and corner radius of the enclosure. The model was also slightly adjusted, as shown in Figure 5.19, to include a grill at the inlet and outlet for a more realistic prediction with the expectation for an increase in losses and inefficiencies. It should be noted that the graphs which showed the convergence and agreement of the simulations are not presented here but included in Appendix B.

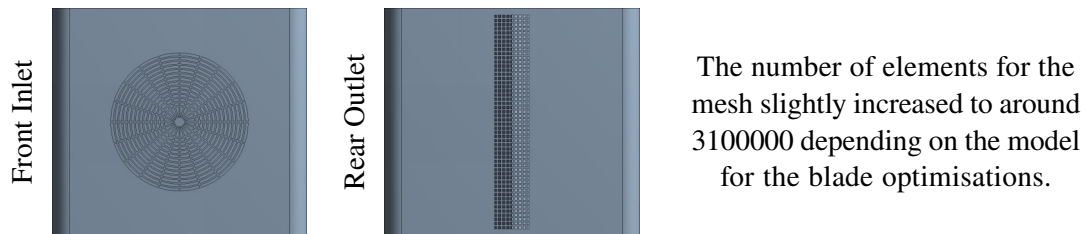


Figure 5.19: Modifications applied to the model to include a grill at the inlet and outlet.

5.5.1 BLADE OUTLET ANGLE

The outlet angles of 35°, 50°, and 65° were compared for the most optimal flow using the models in Figure 5.20. Using the prior settings but with the increased angular velocity of 589.8rev/min, the results are presented in Table 5.7 and the contours of the velocity magnitude and static pressure are plotted in Figure 5.21, Figure 5.22, and Figure 5.23 for the outlet angles of 35°, 50°, and 65° respectively. The intention of these modifications was to detect the effect of the outlet angle with a variation between more normal versus more tangential flow to provide the maximum efficiency for the radial fan.

The results show that, for the outlet angles of 35°, 50°, and 65°, the free stream velocity was approximately 2.877m/s, 2.935m/s, and 3.128m/s respectively, while the average velocity through the middle

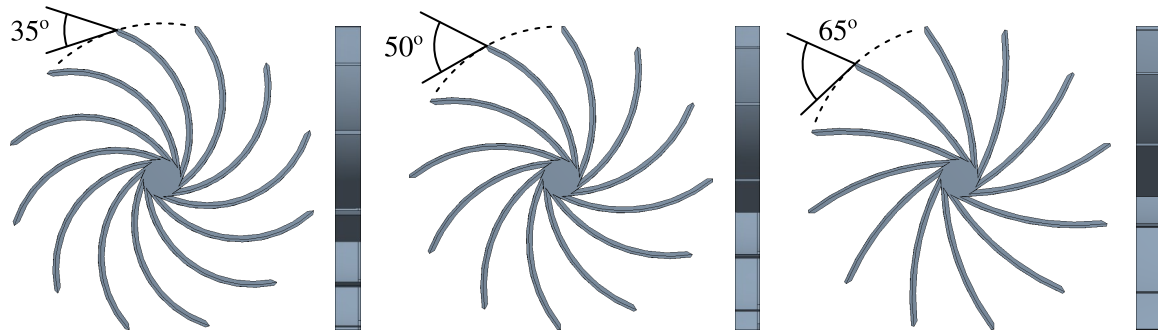


Figure 5.20: Example of the model with an outlet angle of 35° (left), 50° (centre), and 65° (right).

plane was 2.494m/s, 2.560m/s, and 2.659m/s respectively. These predictions were acceptable and in line with the desired velocity through the channels. Although, it was still recognised that the bends introduced notable irreversibilities and dramatically decreased the velocity, since the maximum outlet velocity from the radial fan was around 7.691m/s to 8.088m/s depending on the outlet angle.

It was also evident that the difference in pressure between the driving and trailing surfaces of the blades increased as the outlet angle increased, where the average difference was 36.0% larger for an outlet angle of 65° compared to an outlet angle of 35°. Also, from the contours, it was observed that a larger

Table 5.7: Results and comparisons with the percentage differences at the positions of interest for outlet angles of 35°, 50°, and 65° using a quantity of 12 blades, inclination angle of 0°, breadth of 20mm, channel width of 15mm, corner radius of 25mm, and angular velocity of 589.8rev/min.

Property	Position	Outlet 35°	Outlet 50°	Outlet 65°	% Diff. 35°-50°	% Diff. 50°-65°	% Diff. 35°-50°
Velocity [m/s]	Front	2.597	2.724	2.849	4.77%	4.49%	9.25%
	Middle	2.494	2.560	2.659	2.61%	3.79%	6.40%
	Back	2.492	2.553	2.648	2.42%	3.65%	6.07%
	Outlet	1.582	1.672	1.751	5.53%	4.62%	10.1%
Mass Flow Rate [kg/s]	Front	0.02770	0.02913	0.03024	5.02%	3.76%	8.77%
	Middle	0.02777	0.02919	0.03025	4.99%	3.57%	8.55%
	Back	0.02775	0.02918	0.03025	5.02%	3.60%	8.62%
	Outlet	0.02949	0.03100	0.03219	4.99%	3.77%	8.75%
Total Pressure [Pa]	Driving	10.67	11.56	12.97	7.94%	11.5%	19.4%
	Trailing	3.788	4.413	6.003	15.3%	30.5%	45.3%
Static Pressure [Pa]	Driving	2.256	1.998	2.143	12.1%	7.02%	5.14%
	Trailing	-4.563	-6.252	-7.671	31.2%	20.4%	50.8%
Torque [mN.m]		21.04	23.09	25.57	9.28%	10.2%	19.4%
Power [W]		1.299	1.426	1.579	9.28%	10.2%	19.4%
Volume [L]		0.09608	0.08817	0.08295	8.59%	6.10%	14.7%

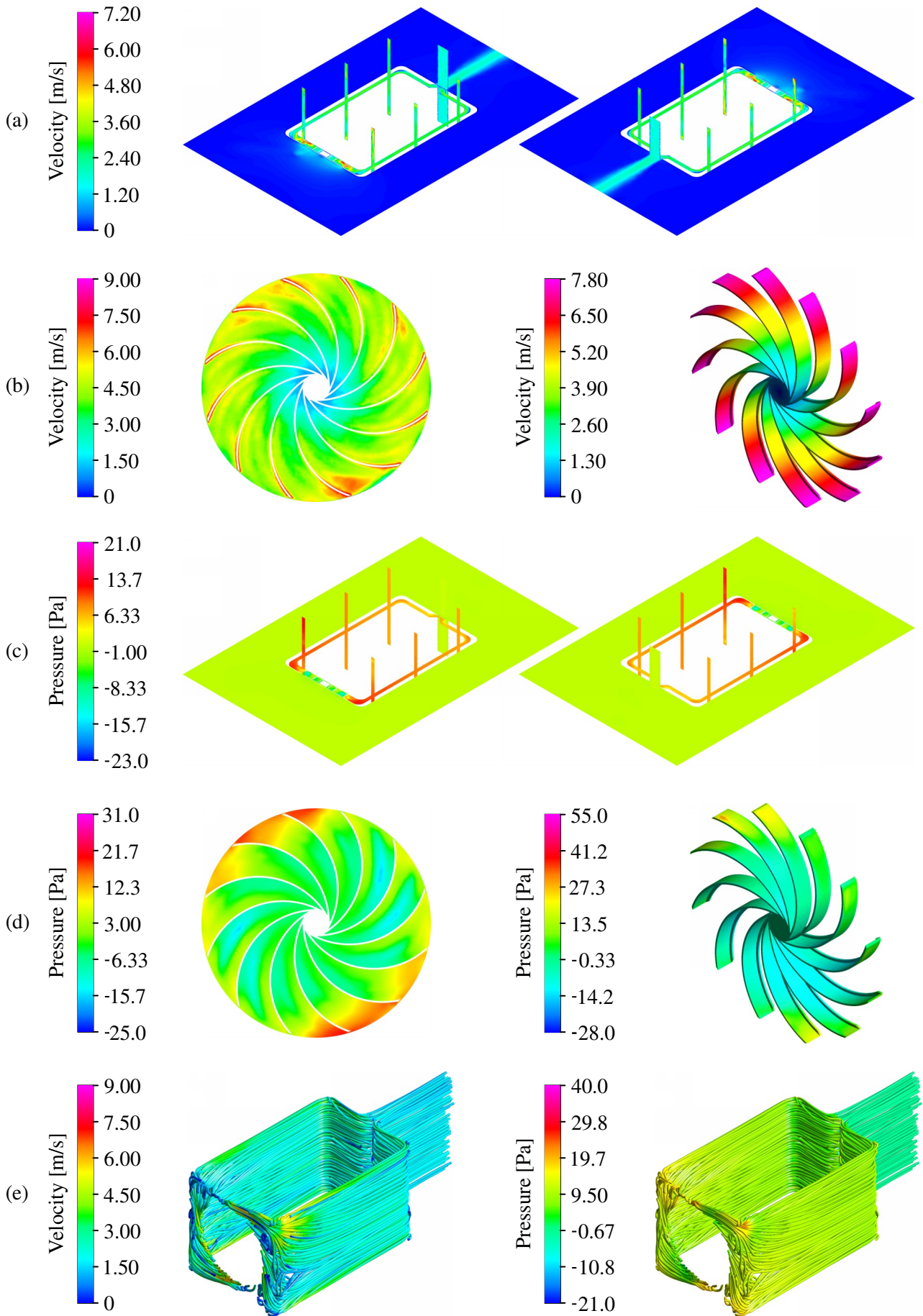


Figure 5.21: Contours for an outlet angle of 35° using a quantity of 12 blades, inclination of 0° , breadth of 20mm, channel width of 15mm, corner radius of 25mm, and angular velocity of 589.8rev/min.

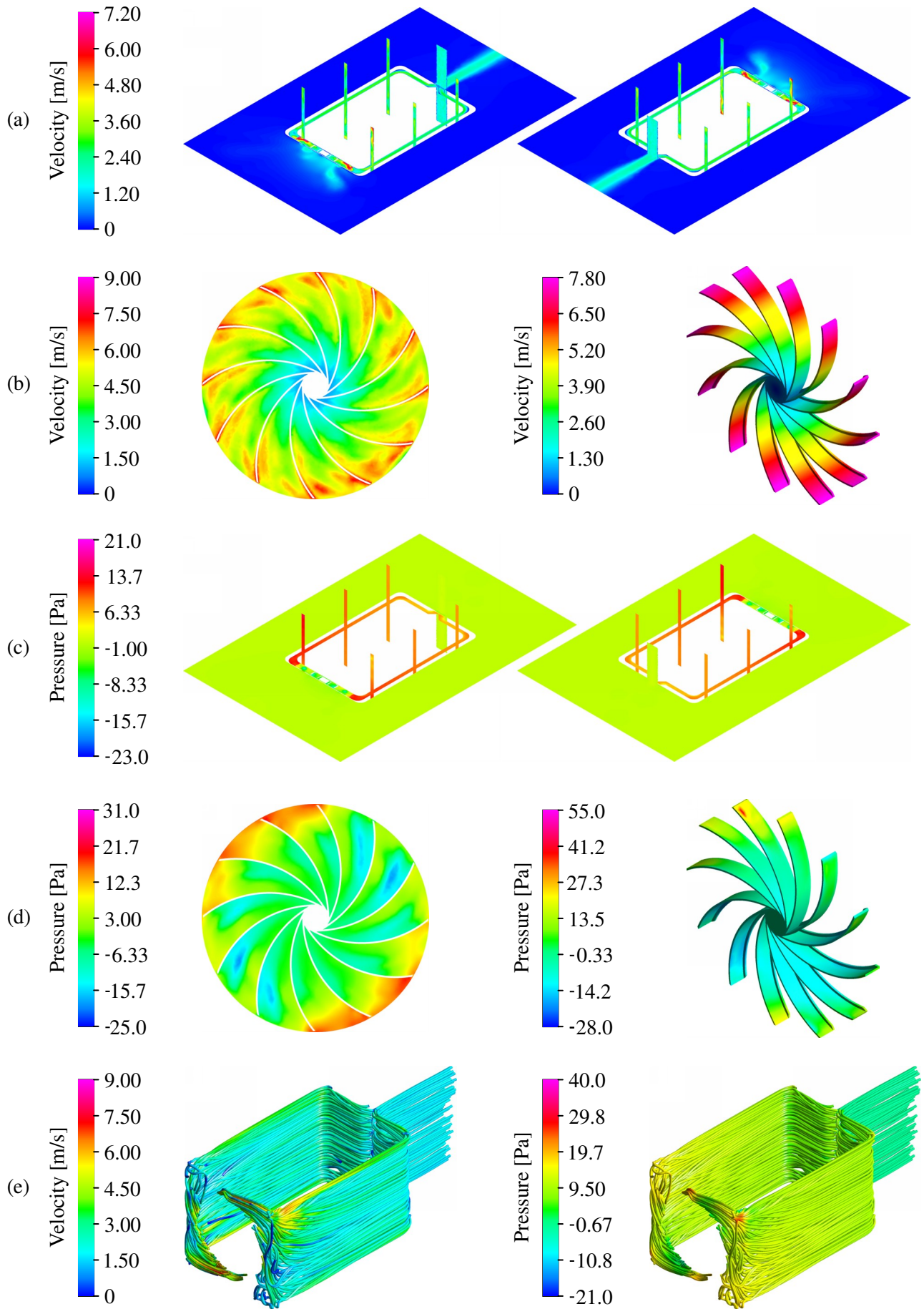


Figure 5.22: Contours for an outlet angle of 50° using a quantity of 12 blades, inclination of 0° , breadth of 20mm, channel width of 15mm, corner radius of 25mm, and angular velocity of 589.8rev/min.

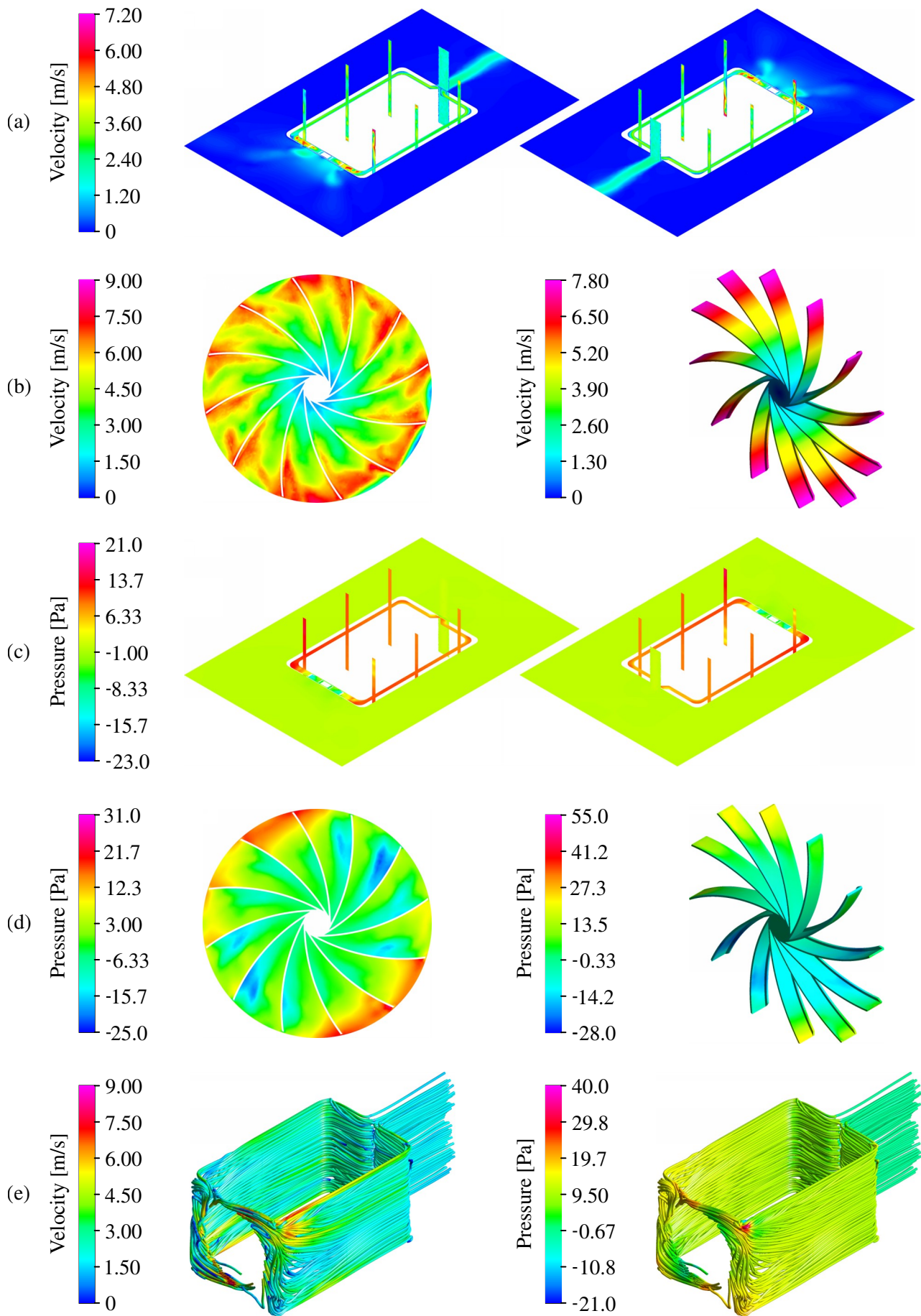


Figure 5.23: Contours for an outlet angle of 65° using a quantity of 12 blades, inclination of 0° , breadth of 20mm, channel width of 15mm, corner radius of 25mm, and angular velocity of 589.8 rev/min .

outlet angle equated to a decreased pressure on the trailing surface of the blades due to the longer blades aiding in reducing recirculation losses as well as the possibility of separation, although it was sensibly reasoned that the skin friction losses became greater as the length of the blades increased.

As a consequence, this increased difference in pressure contributed to a greater torque being required which corresponded with a greater power by up to 19.4% for an outlet angle of 65° compared to an outlet angle of 35°. This required power was significant but manageable with 1.299W, 1.426W, and 1.579W for the outlet angles of 35°, 50°, and 65° respectively. For differentiation by accounting for the resulting performance, the velocity produced per unit power was calculated as 1.919(m/s)/W, 1.795(m/s)/W, and 1.684(m/s)/W for the outlet angles of 35°, 50°, and 65° respectively.

There was an additional concern for the overall volume of the radial fan, where a greater volume would coincide with a higher mass and greater mass moment of inertia. This would imply a need for a greater torque, which was not accounted for in the results, and require a more powerful motor. There may also be a lesser concern for an increased cost for the materials during manufacturing. Assuming the cost was directly proportional to the volume, an outlet angle of 65° would have the lowest cost and an outlet angle of 35° would have the highest cost. The variation was substantial with a percentage difference of 14.7% between these outlet angles. An outlet angle of 50° offered the foremost resolution, where the velocity produced per unit volume was 29.04(m/s)/L, compared to a decrease of 11.1% to 25.96(m/s)/L for the outlet angle of 35° and increase of 9.88% to 32.05(m/s)/L for the outlet angle of 65°.

The general behaviour of a larger outlet angle producing an increased velocity in contrast to a smaller outlet angle was expected as the radial fan tended towards having straight or forward-curved blades. For the same reason, it was expected for a smaller outlet angle to require less power and produce a higher efficiency in contrast to a larger outlet angle. This indicated that an outlet angle of 35° would be the most optimal for the best performance. However, the increase in the volume correlating with an increase in the mass moment of inertia was considerable and, so, it was decided that an outlet angle of 50° would offer an acceptable compromise for performance based on the velocity produced per unit power and volume, where the outlet angle of 50° achieved 20.36(m/s)/W/L followed by the outlet angle of 65° with 20.29(m/s)/W/L and then the outlet angle of 35° with 19.98(m/s)/W/L.

5.5.2 BLADE QUANTITY COUNT

The quantities of 10, 12, and 14 blades were compared for the most optimal flow using the models in Figure 5.24. Repeating the simulations using the models of the 10 and 14 blades with the prior settings, the results are presented in Table 5.8 and the contours of the velocity magnitude and static pressure are plotted in Figure 5.25, Figure 5.22, and Figure 5.26 for the quantities of 10, 12, and 14 blades respectively. The intention of these modifications was to investigate the effect of the spacing and possible separation in the passages between the blades on the efficiency of the radial fan.

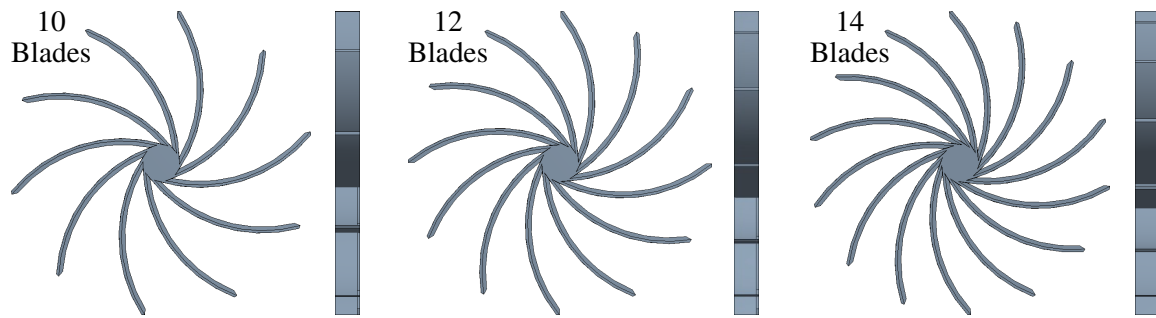


Figure 5.24: Example of the model with a quantity of 10 (left), 12 (centre), and 14 (right) blades.

For the quantities of 10, 12, and 14 blades, the results showed that the free stream velocity was approximately 2.711m/s, 2.935m/s, and 3.060m/s respectively, while the average velocity through the middle plane was 2.391m/s, 2.560m/s, and 2.658m/s respectively. Notably, the difference in pressure between the driving and trailing surfaces of the blades significantly decreased as the quantity increased, where the average difference varied from 9.058Pa for a quantity of 10 to 8.250Pa for a quantity of 12 to 7.436Pa for a quantity of 14. In a similar manner as with the outlet angle, this observation was reasoned to have occurred due to the increased number of blades aiding in reducing recirculation losses as well as reducing the possibility of separation, although the skin friction losses were expected to become mildly larger as the combined surface area of the blades increased with more blades.

Table 5.8: Results and comparisons with the percentage differences at the positions of interest for quantities of 10, 12, and 14 blades using an outlet angle of 50°, inclination angle of 0°, breadth of 20mm, channel width of 15mm, corner radius of 25mm, and angular velocity of 589.8rev/min.

Property	Position	Quantity 10	Quantity 12	Quantity 14	% Diff. 10-12	% Diff. 12-14	% Diff. 10-14
Velocity [m/s]	Front	2.578	2.724	2.852	5.51%	4.59%	10.1%
	Middle	2.391	2.560	2.658	6.83%	3.76%	10.6%
	Back	2.389	2.553	2.651	6.64%	3.77%	10.4%
	Outlet	1.557	1.672	1.732	7.12%	3.53%	10.6%
Mass Flow Rate [kg/s]	Front	0.02718	0.02913	0.03027	6.91%	3.86%	10.8%
	Middle	0.02717	0.02919	0.03024	7.17%	3.53%	10.7%
	Back	0.02717	0.02918	0.03024	7.13%	3.57%	10.7%
	Outlet	0.02901	0.03100	0.03226	6.63%	3.98%	10.6%
Total Pressure [Pa]	Driving	11.35	11.56	11.52	1.81%	0.30%	1.50%
	Trailing	4.000	4.413	5.095	9.80%	14.3%	24.1%
Static Pressure [Pa]	Driving	2.326	1.998	1.789	15.2%	11.0%	26.1%
	Trailing	-6.732	-6.252	-5.647	7.40%	10.2%	17.5%
Torque [mN.m]		25.35	23.09	20.81	9.34%	10.4%	19.7%
Power [W]		1.566	1.426	1.285	9.34%	10.4%	19.7%
Volume [L]		0.07586	0.08817	0.1004	15.0%	13.0%	27.9%

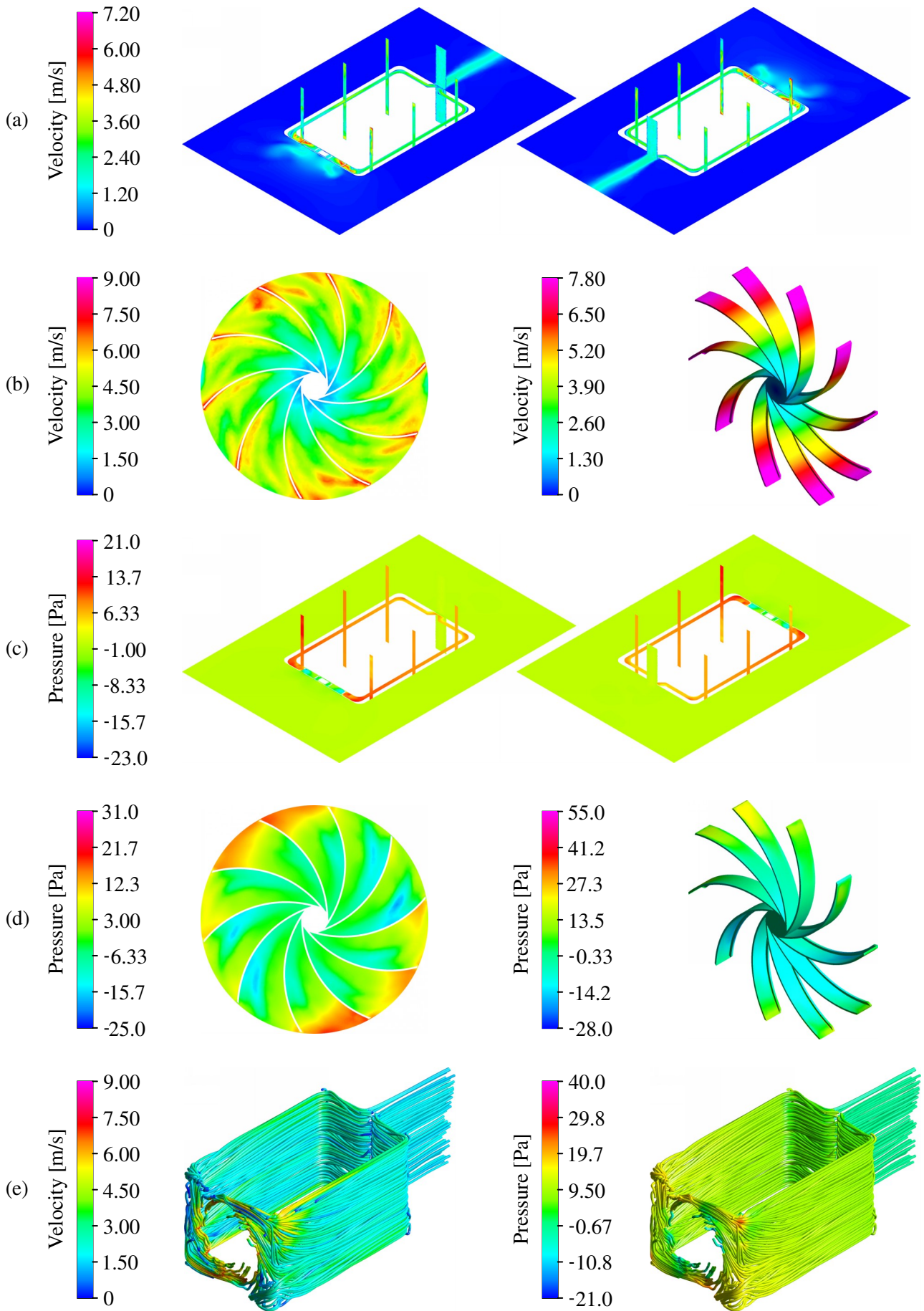


Figure 5.25: Contours for a quantity of 10 blades using an outlet angle of 50° , inclination of 0° , breadth of 20mm, channel width of 15mm, corner radius of 25mm, and angular velocity of 589.8rev/min.

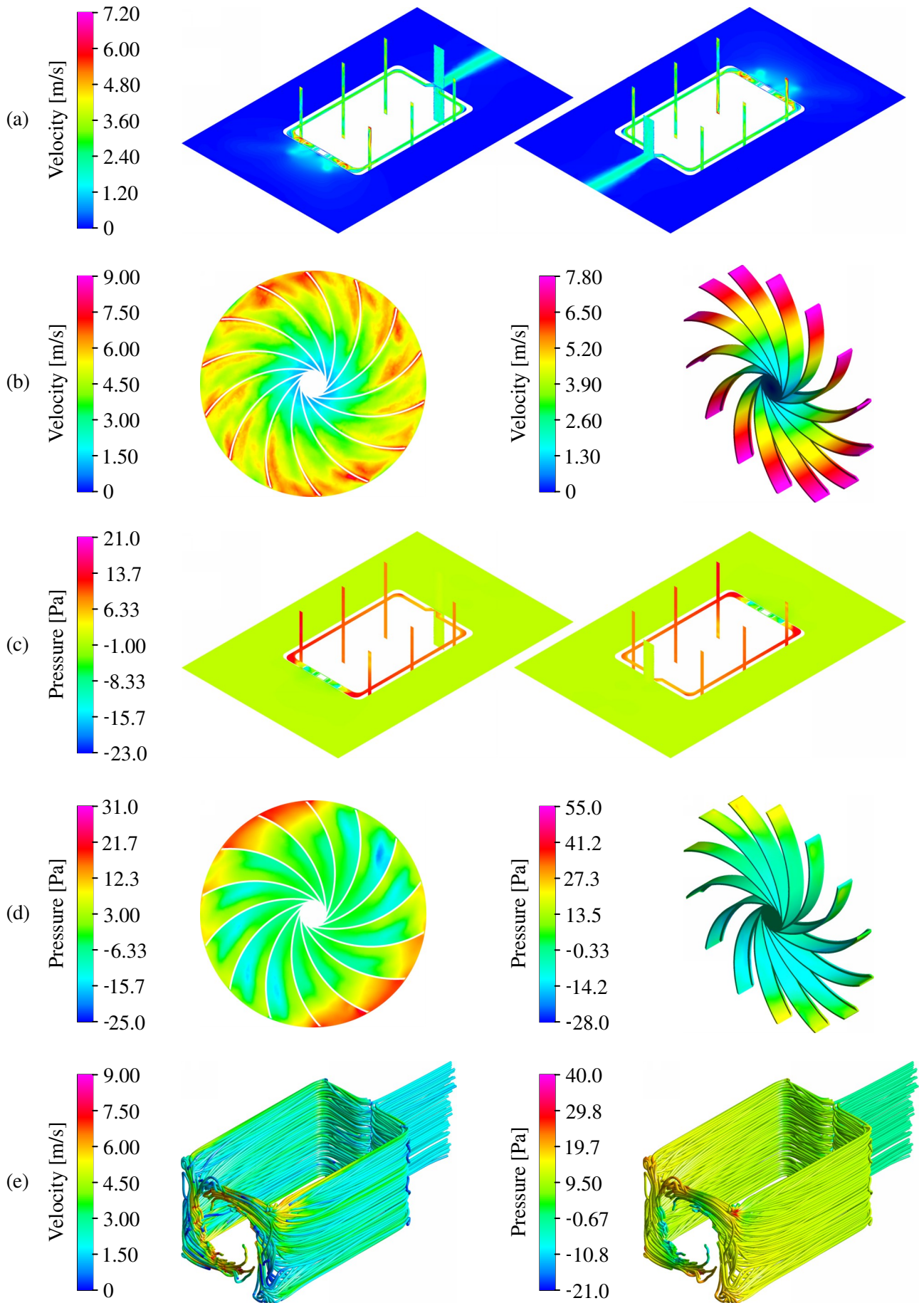


Figure 5.26: Contours for a quantity of 14 blades using an outlet angle of 50° , inclination of 0° , breadth of 20mm, channel width of 15mm, corner radius of 25mm, and angular velocity of 589.8rev/min.

Based on differences in pressure, the power required for the flow was 1.566W for a quantity of 10 blades, 1.426W for a quantity of 12 blades, and 1.285W for a quantity of 14 blades. This trend of decreasing power was likely due to the regions of low pressure trailing the blades which were more numerous but significantly decreased in magnitude for 14 blades compared to 10 and 12 blades. Correspondingly, the velocity produced per unit power was 1.527(m/s)/W, 1.795(m/s)/W, and 2.068(m/s)/W and, accounting for the volume of the radial fan, the velocity produced per unit volume was 23.81(m/s)/L, 29.04(m/s)/L, and 26.47(m/s)/L for the quantities of 10, 12, and 14 blades respectively.

With equal consideration for the power and volume, the velocity produced per unit power and volume was 15.21(m/s)/W/L for a quantity of 10 blades, 20.36(m/s)/W/L for a quantity of 12 blades, and 20.59(m/s)/W/L for a quantity of 14 blades, such that the percentage difference between the quantities of 10 and 12 blades was significant at 29.9%, but the percentage difference between the quantities of 12 and 14 blades was only 1.12%. Essentially, the choice of a quantity of 12 blades provided a smaller volume and increased power for a lower velocity, while the choice of a quantity of 14 blades provides a larger volume and decreased power for a higher velocity - in other words, a percentage difference of 13.0% in volume inversely corresponded with a percentage difference of 10.4% in power and 3.76% in velocity. Although the increase in volume was unfavourable, it was decided that the increase in efficiency and performance was more beneficial, while the low percentage difference between the quantities of 12 and 14 blades also indicated that there would be diminishing returns if the number of blades was increased further. So, a quantity of 14 blades was accepted to be optimal.

5.5.3 BLADE INCLINATION ANGLE

The inclination angles of 0°, 10°, and 20° were compared for the most optimal flow using the models in Figure 5.27. Repeating the simulations using the models of the 10° and 20° angles, the results are presented in Table 5.9 and the contours of the velocity magnitude and static pressure are plotted in Figure 5.26, Figure 5.28, and Figure 5.29 for the inclination angles of 0°, 10°, and 20° respectively. The intention of these modifications was to highlight the effect of introducing an axial component to the flow exiting the radial fan and whether this could increase the efficiency of the radial fan.

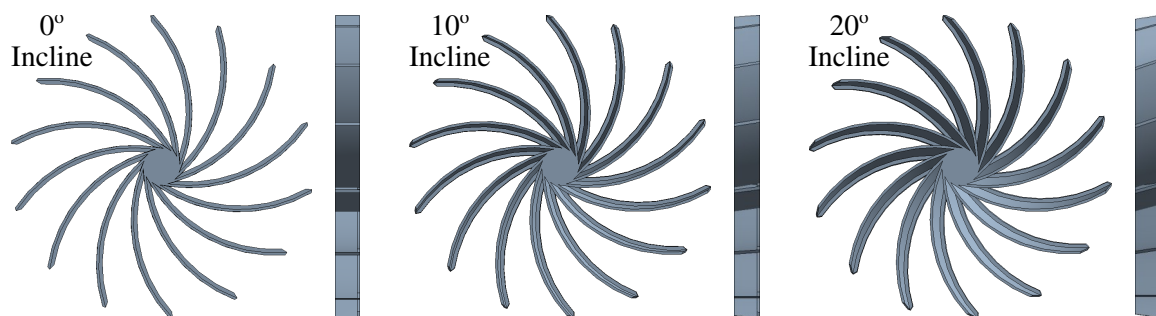


Figure 5.27: Example of the model with an inclination angle of 0° (left), 10° (centre), and 20° (right).

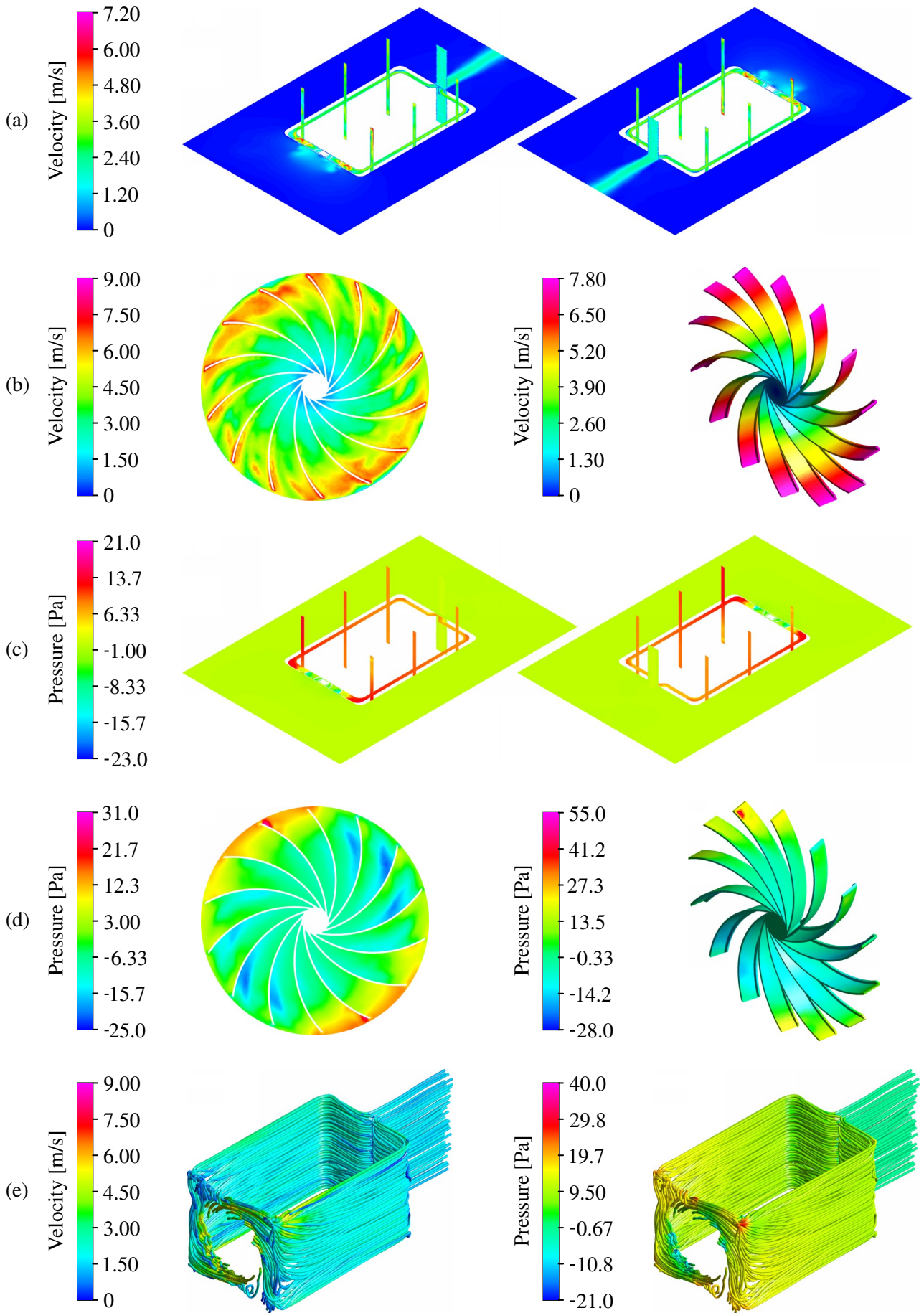


Figure 5.28: Contours for an inclination of 10° using an outlet angle of 50° , quantity of 14 blades, breadth of 20mm, channel width of 15mm, corner radius of 25mm, and angular velocity of 589.8rev/min.

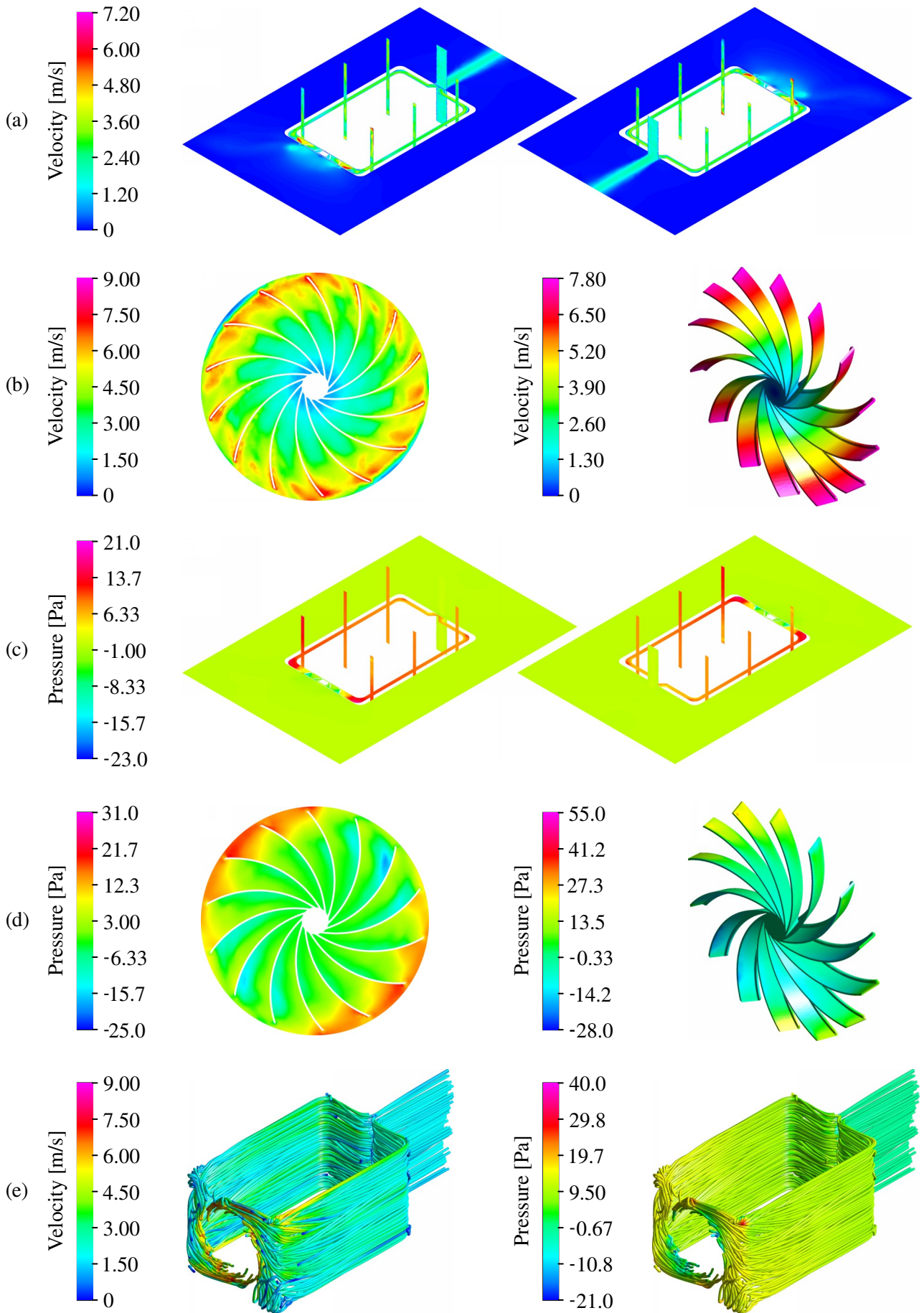


Figure 5.29: Contours for an inclination of 20° using an outlet angle of 50° , quantity of 14 blades, breadth of 20mm, channel width of 15mm, corner radius of 25mm, and angular velocity of 589.8rev/min.

Table 5.9: Results and comparisons with the percentage differences at the positions of interest for inclination angles of 0°, 10°, and 20° using an outlet angle of 50°, quantity of 14 blades, breadth of 20mm, channel width of 15mm, corner radius of 25mm, and angular velocity of 589.8rev/min.

Property	Position.	Incline 0°	Incline 10°	Incline 20°	% Diff. 0°-10°	% Diff. 10°-20°	% Diff. 0°-20°
Velocity [m/s]	Front	2.852	2.823	2.763	1.02%	2.15%	3.17%
	Middle	2.658	2.648	2.574	0.38%	2.83%	3.21%
	Back	2.651	2.636	2.572	0.57%	2.46%	3.03%
	Outlet	1.732	1.724	1.676	0.46%	2.82%	3.29%
Mass Flow Rate [kg/s]	Front	0.03027	0.03101	0.02927	2.42%	5.77%	3.36%
	Middle	0.03024	0.03075	0.02925	1.67%	5.00%	3.33%
	Back	0.03024	0.03076	0.02923	1.70%	5.10%	3.40%
	Outlet	0.03226	0.03204	0.03112	0.68%	2.91%	3.60%
Total Pressure [Pa]	Driving	11.52	11.94	11.93	3.58%	0.08%	3.50%
	Trailing	5.095	5.925	6.091	15.1%	2.76%	17.8%
Static Pressure [Pa]	Driving	1.789	2.412	2.850	29.7%	16.7%	45.7%
	Trailing	-5.647	-5.269	-4.681	6.93%	11.8%	18.7%
Torque [mN.m]		20.81	20.74	20.33	0.34%	1.97%	2.31%
Power [W]		1.285	1.281	1.256	0.34%	1.97%	2.31%
Volume [L]		0.1004	0.1012	0.1017	0.72%	0.57%	1.29%

In each of the simulations, the resulting flow was largely similar with a free stream velocity of approximately 3.060m/s for the inclination angle of 0°, 3.132m/s for the inclination angle of 10°, and 3.101m/s for the inclination angle of 20°. A similar trend was also observed when considering the average velocity, where the percentage differences remained within 3.50% at each of the positions of interest. There was a noticeable relationship arising with the pressure, where the pressure on the driving and trailing surfaces of the blades increased as the inclination angle increased. However, the difference in pressure remained within 2.5%, as seen in the similar torque and power required for each inclination angle. Although the deviation was minimal, it was also found that the velocity produced per unit power and volume was 20.59(m/s)/W/L, 20.44(m/s)/W/L, and 20.15(m/s)/W/L for the inclination angles of 0°, 10°, and 20° respectively. This was fairly expected given the path of the channels, where the introduction of an axial component to the flow exiting the radial fan was unconstructive.

Therefore, there was no substantial evidence showing that an inclination angle would be beneficial, but rather it could actually have a detrimental effect. As an auxiliary check for verification, the same simulations were also performed using a quantity of 12 and 14 blades for outlet angles of 50° and 65°, where the results exhibited an identical trend with no perceivable advantages supporting the use of an inclination angle, as is included in Appendix B. Thus, the use of flat blades was preferred.

5.5.4 BLADE BREADTH

The breadth of the blades was increased from 20mm to 30mm and 40mm using the models in Figure 5.30. Repeating the simulations for each of the models, the results are presented in Table 5.10 and the contours of the velocity magnitude and static pressure are plotted in Figure 5.26, Figure 5.31, and Figure 5.32 for the breadths of 20mm, 30mm, and 40mm respectively. The intention of these modifications was to decide whether an increased breadth could increase the efficiency of the radial fan relative to the velocity of the flow since the angular velocity was maintained at 589.8rev/min.

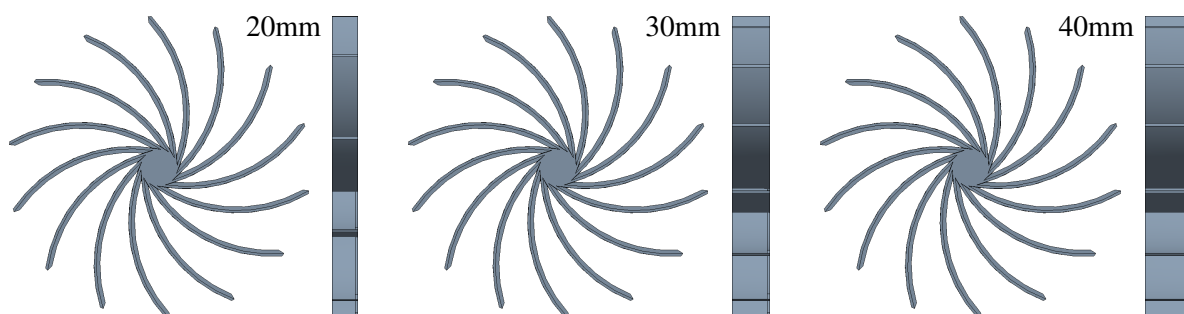


Figure 5.30: Example of the model with a breadth of 20mm (left), 30mm (centre), and 40mm (right).

Table 5.10: Results and comparisons with the percentage differences at the positions of interest for breadths of 20mm, 30mm, and 40mm using an outlet angle of 50°, quantity of 14 blades, inclination angle of 0°, channel width of 15mm, corner radius of 25mm, and angular velocity of 589.8rev/min.

Property	Position	Breadth 20mm	Breadth 30mm	Breadth 40mm	% Diff. 20-30mm	% Diff. 30-40mm	% Diff. 20-40mm
Velocity [m/s]	Front	2.852	3.176	3.270	10.8%	2.92%	13.7%
	Middle	2.658	2.954	3.046	10.5%	3.07%	13.6%
	Back	2.651	2.948	3.031	10.6%	2.78%	13.4%
	Outlet	1.732	1.907	1.977	9.62%	3.60%	13.2%
Mass Flow Rate [kg/s]	Front	0.03027	0.03366	0.03483	10.6%	3.42%	14.0%
	Middle	0.03024	0.03349	0.03476	10.2%	3.72%	13.9%
	Back	0.03024	0.03345	0.03472	10.1%	3.73%	13.8%
	Outlet	0.03226	0.03569	0.03685	10.1%	3.20%	13.3%
Total Pressure [Pa]	Driving	11.52	12.12	12.34	5.08%	1.77%	6.85%
	Trailing	5.095	5.591	5.649	9.28%	1.03%	10.3%
Static Pressure [Pa]	Driving	1.789	0.725	-0.401	84.6%	695%	315%
	Trailing	-5.647	-5.691	-5.902	0.78%	3.64%	4.42%
Torque [mN.m]		20.81	26.71	30.63	24.8%	13.6%	38.2%
Power [W]		1.285	1.650	1.892	24.8%	13.6%	38.2%
Volume [L]		0.1004	0.1454	0.1904	36.6%	26.8%	61.9%
Surface Area [mm ²]		2799	4198	5597	40.0%	28.6%	66.7%

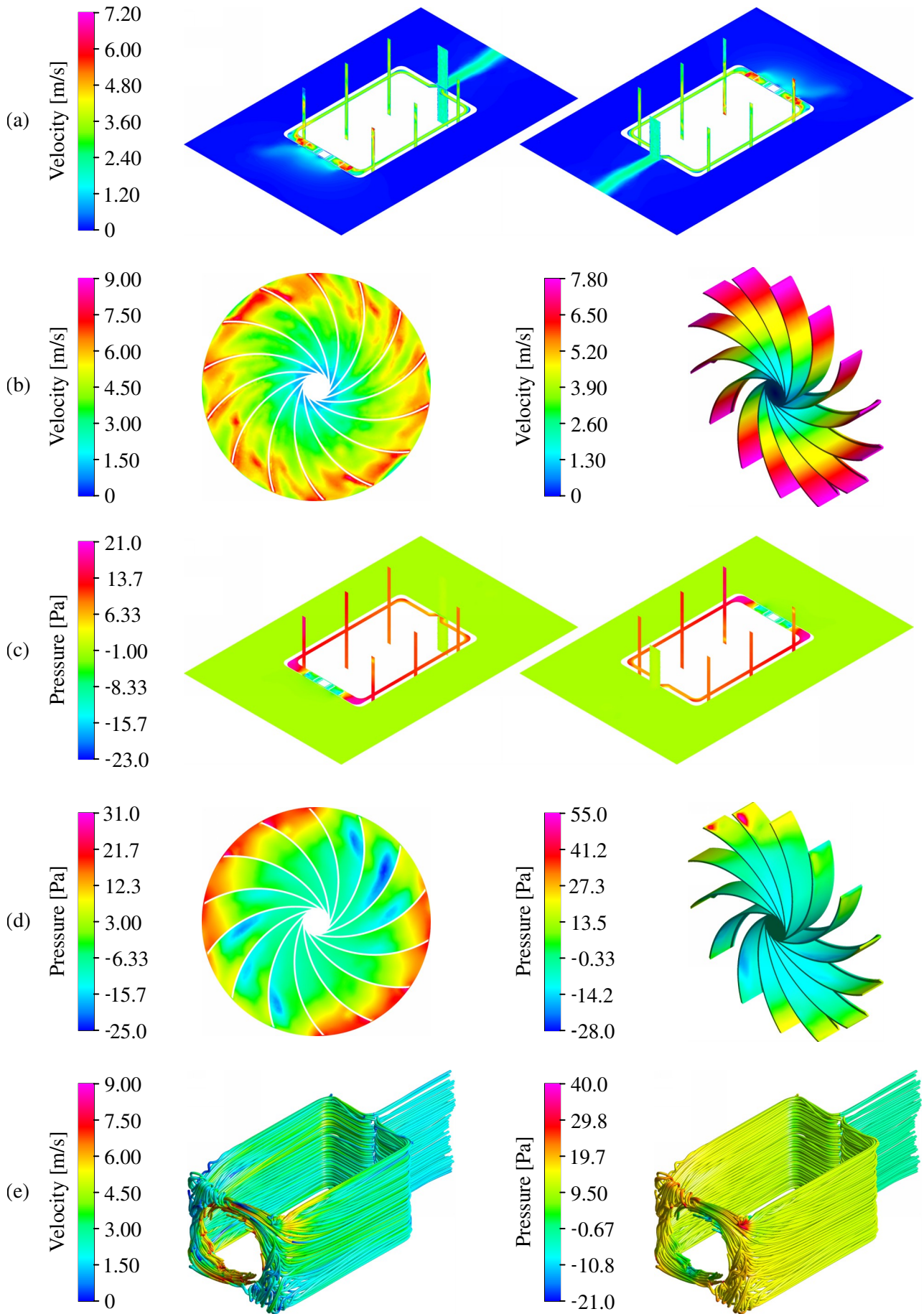


Figure 5.31: Contours for a breadth of 30mm using an outlet angle of 50° , quantity of 14 blades, inclination of 0° , channel width of 15mm, corner radius of 25mm, and angular velocity of 589.8rev/min.

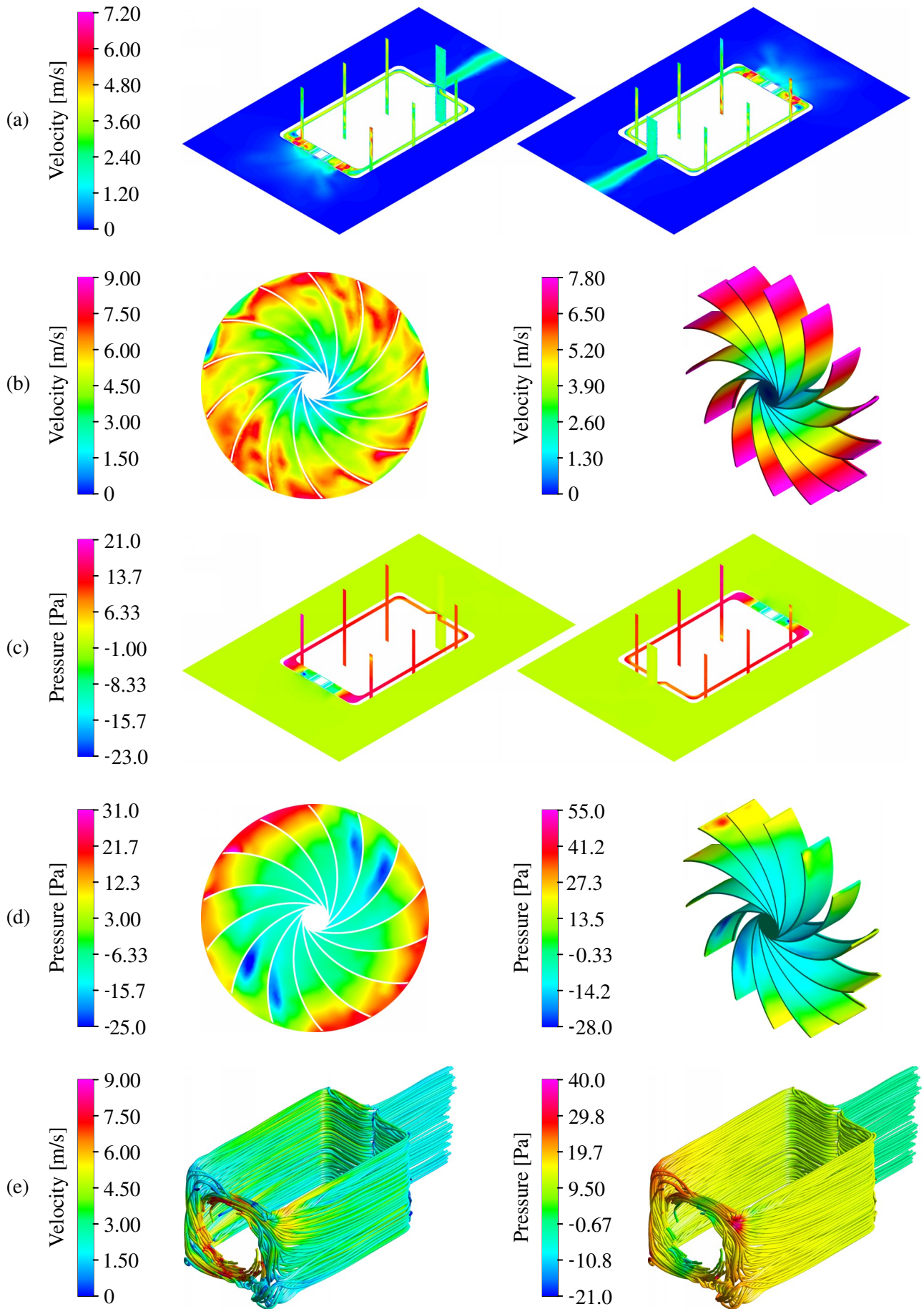


Figure 5.32: Contours for a breadth of 40mm using an outlet angle of 50° , quantity of 14 blades, inclination of 0° , channel width of 15mm, corner radius of 25mm, and angular velocity of 589.8 rev/min.

The results indicated that there would be an average velocity through the middle plane of 2.948m/s for a breadth of 30mm and 3.031m/s for a breadth of 40mm, compared to the corresponding velocity of 2.658m/s for a breadth of 20mm. There was a distinct increase in the free stream velocity from 3.060m/s to 3.428m/s to 3.705m/s for a breadth of 20mm, 30mm, and 40mm respectively - corresponding with appropriate percentage differences of 11.3%, 7.77%, and 19.1% respectively. So, as expected due to the increased mass flow rate, the velocity notably increased as the breadth increased.

However, the increase in the percentage difference between the surface areas was not favourably in accordance with the decrease in the percentage difference between the difference in pressure. In quantities, the percentage difference in the surface area between a breadth of 20mm and 30mm was 40.0% and the percentage difference in surface area between a breadth of 20mm and 40mm was 66.7%, but the percentage difference between in pressure between a breadth of 20mm and 30mm was only 12.5% and the percentage difference in pressure between a breadth of 20mm and 40mm was only 28.6%. This subsequently led to a velocity per unit power of 1.397(m/s)/W for a breadth of 30mm and 1.279(m/s)/W for a breadth of 40mm. Furthermore, the volume drastically increased as the breadth increased and led to a velocity per unit power and volume of only 16.67(m/s)/W/L for a breadth of 30mm and only 13.25(m/s)/W/L for a breadth of 40mm. Thus, although it resulted in a lower velocity, a breadth of 20mm had the most preferable characteristics, where it would be more effective to increase the angular velocity, rather than increasing the breadth, if a higher velocity was desired.

5.5.5 CHANNEL WIDTH

The width of the channels was slightly increased from 15mm to 20mm, while again reviewing a breadth for the blades of 20mm, 30mm, and 40mm, to compare the most optimal flow. Repeating the simulations for each of the adjusted models, the results are presented in Table 5.11 and the contours of the velocity magnitude and static pressure are plotted in Figure 5.33, Figure 5.34, and Figure 5.35 using the increased width of the channels for the breadths of 20mm, 30mm, and 40mm respectively. The intention of these modifications was to examine the impact from the increase in the width of the channels, specifically at the bends, after the radial fan compared against the previous results.

Because the channel width was increased while the mass flow rate remained the same, it was expected for the velocity to decrease if the breadth remained 20mm. This was realised with a percentage difference of 20.5% from 2.658m/s to 2.164m/s for the average velocity through the middle plane and percentage difference of 14.1% from 3.060m/s to 2.657m/s for the free stream velocity. There was an almost negligible increase in the required power from 1.285W to 1.322W, which corresponded with a meaningful decrease in the velocity produced per unit power and volume to 16.30(m/s)/W/L from 20.59(m/s)/W/L as a result of the large decrease in velocity without a change in power.

With regards to the increased breadth, similar trends were observed with the increased channel width of 20mm as with the original channel width of 15mm. The average velocities through the middle

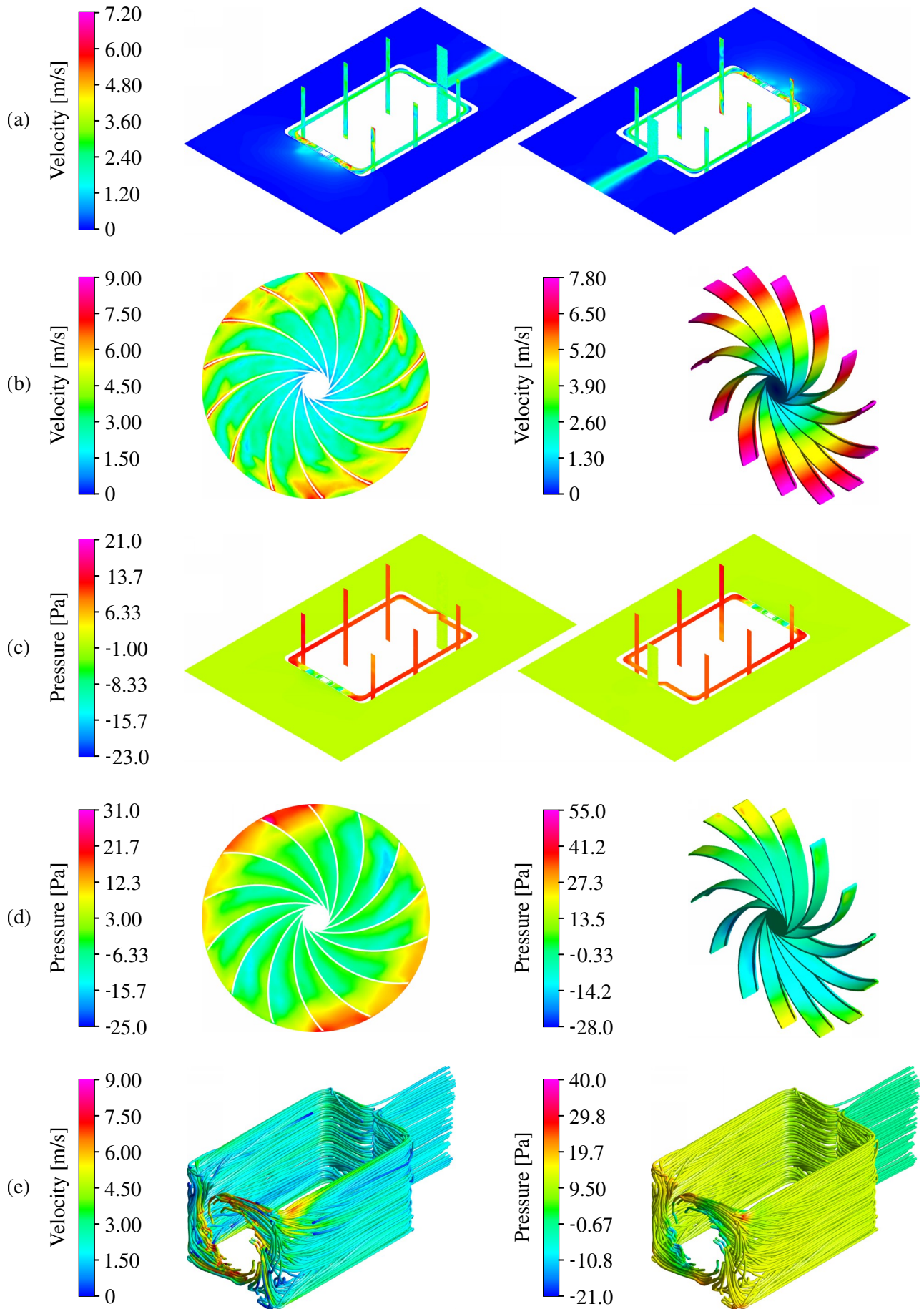


Figure 5.33: Contours for a channel width of 20mm and breadth of 20mm using an outlet angle of 50°, quantity of 14 blades, inclination of 0°, corner radius of 25mm, and angular velocity of 589.8rev/min.

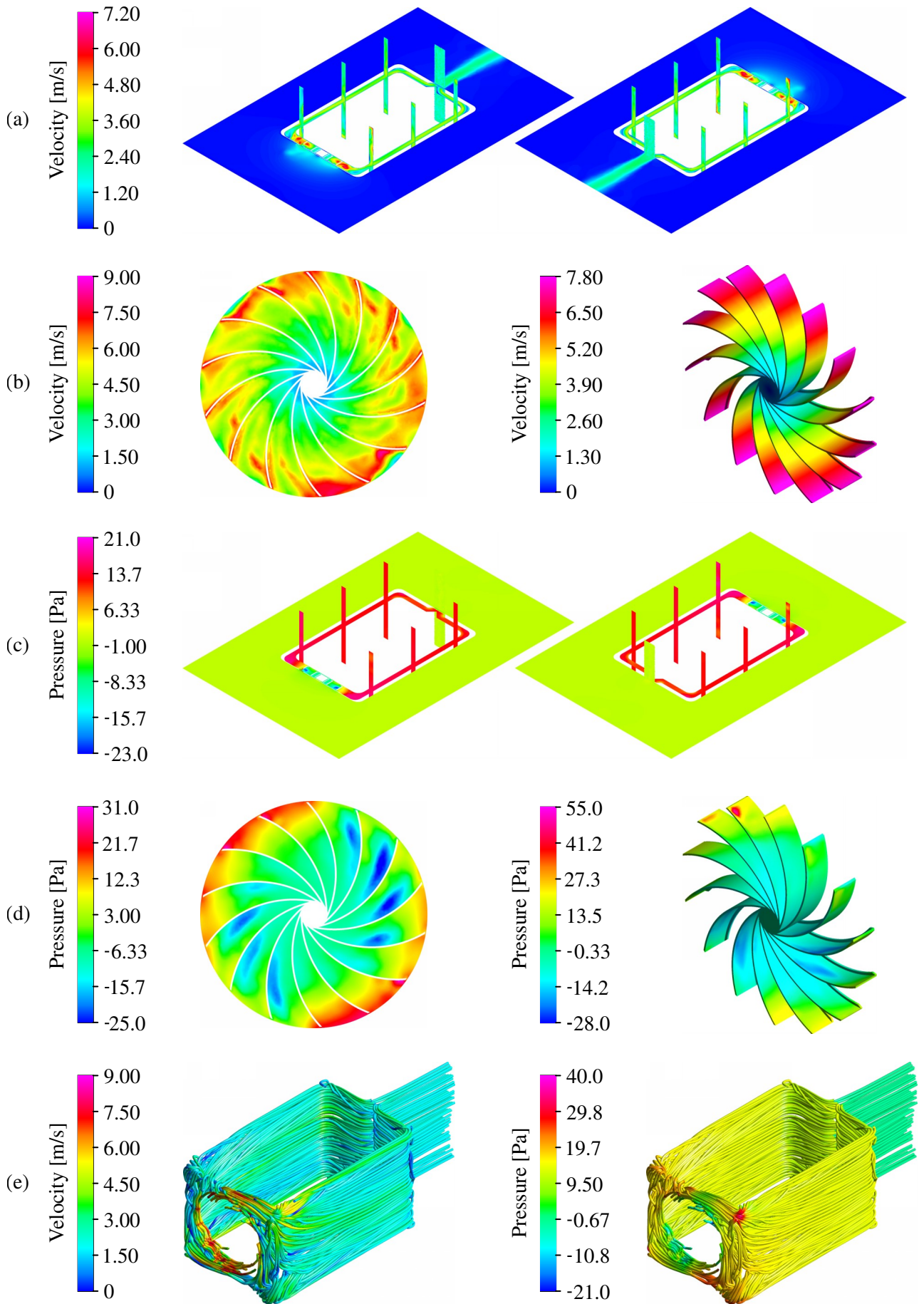


Figure 5.34: Contours for a channel width of 20mm and breadth of 30mm using an outlet angle of 50°, quantity of 14 blades, inclination of 0°, corner radius of 25mm, and angular velocity of 589.8rev/min.

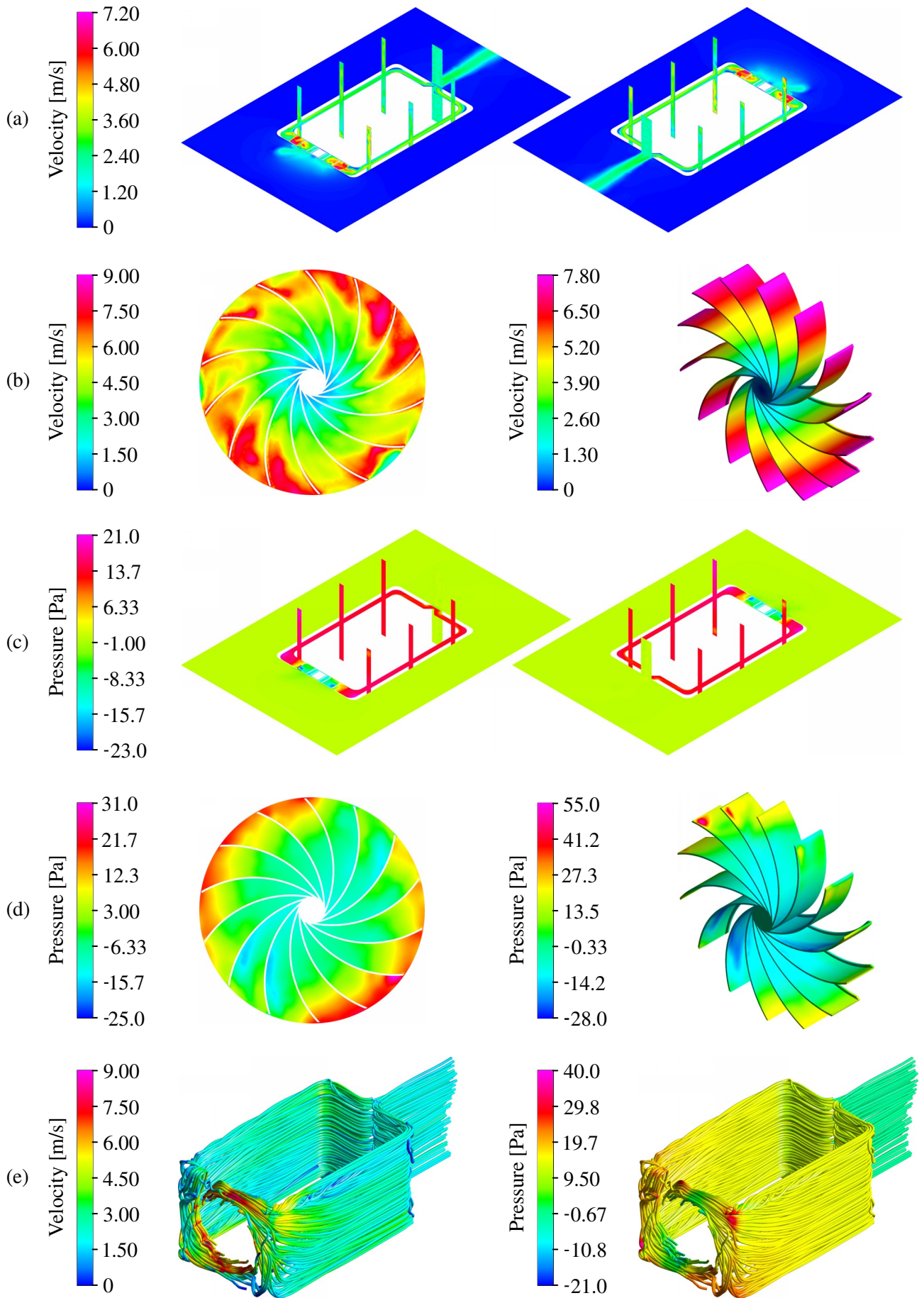


Figure 5.35: Contours for a channel width of 20mm and breadth of 40mm using an outlet angle of 50° , quantity of 14 blades, inclination of 0° , corner radius of 25mm, and angular velocity of 589.8rev/min.

Table 5.11: Results and comparisons with the percentage differences at the positions of interest for a channel width of 20mm and breadths of 20mm, 30mm, and 40mm using an outlet angle of 50°, quantity of 14 blades, inclination angle of 0°, corner radius of 25mm, and angular velocity of 589.8rev/min.

Property	Position	Breadth 20mm	Breadth 30mm	Breadth 40mm	% Diff. 20-30mm	% Diff. 30-40mm	% Diff. 20-40mm
Velocity [m/s]	Front	2.370	2.575	2.746	8.29%	6.43%	14.7%
	Middle	2.164	2.424	2.523	11.3%	4.00%	15.3%
	Back	2.151	2.407	2.500	11.2%	3.79%	15.0%
	Outlet	1.882	2.102	2.181	11.0%	3.69%	14.7%
Mass Flow Rate [kg/s]	Front	0.03276	0.03669	0.03818	11.3%	3.98%	15.3%
	Middle	0.03271	0.03657	0.03801	11.1%	3.86%	15.0%
	Back	0.03270	0.03655	0.03801	11.1%	3.92%	15.0%
	Outlet	0.03407	0.03822	0.03974	11.5%	3.90%	15.4%
Total Pressure [Pa]	Driving	11.21	11.50	11.65	2.55%	1.30%	3.85%
	Trailing	5.302	5.048	5.015	4.91%	0.66%	5.60%
Static Pressure [Pa]	Driving	1.619	0.349	-0.964	129%	427%	789%
	Trailing	-6.030	-6.401	-6.699	5.97%	4.55%	10.5%
Torque [mN.m]		21.41	28.10	31.93	27.1%	12.7%	39.5%
Power [W]		1.322	1.736	1.972	27.1%	12.7%	39.5%
Volume [L]		0.1004	0.1454	0.1904	36.6%	26.8%	61.9%
Surface Area [mm ²]		2799	4164	5568	39.2%	28.9%	66.2%

plane were acceptable at 2.424m/s and 2.523m/s for the breadths of 30mm and 40mm respectively. Likewise, the free stream velocities were prominent at 2.951m/s for a breadth of 30mm and 3.164m/s for a breadth of 40mm. The pressure over each surface decreased as the breadth increased with the difference in pressure between the driving and trailing surfaces of the blades decreased from 7.649Pa to 6.750Pa to 5.735Pa for a breadth of 20mm, 30mm, and 40mm respectively. However, the increased surface area of 4164mm² led to an excessive power of 1.736W for a breadth of 30mm and 5568mm² led to an unreasonable power of 1.972W for a breadth of 40mm. As expected, this resulted in poor values for the velocity per unit power and volume with only 9.605(m/s)/W/L for a breadth of 30mm and 6.721(m/s)/W/L for a breadth of 40mm. Thus, an increased channel width was detrimental.

5.5.6 CORNER BEND RADIUS

Using a blade outlet angle of 50°, blade quantity of 14, blade inclination angle of 0°, blade breadth of 20mm, and channel width of 15mm, the final optimisation which was performed was to consider the radius of the bends at the corners. This was expected to have an effect on the efficiency, since a sharper corner dramatically leads to more losses compared to a more rounded corner. To increase

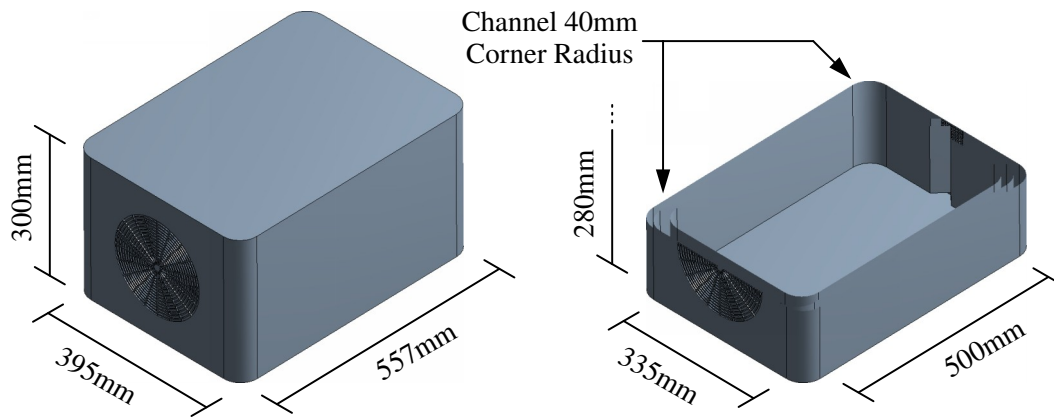


Figure 5.36: Example of the model with a corner radius of 40mm and modified dimensions.

the radius of the corners from 25mm to 40mm, it was also necessary to modify the dimensions of the internal enclosure to 500mm in length, 335mm in width, and 280mm in height to avoid interference with the radial fan, as seen in Figure 5.36. These changes resulted in an internal volume of 46.52L, which was still suitably above 45L to accommodate further inclusion of minor enhancements. An additional increase in the corner radius would affect ergonomics with an excessive width.

Repeating the simulations for modified model, the results are presented in Table 5.12 and the contours of the velocity magnitude and static pressure are plotted in Figure 5.37 for the increased corner radius

Table 5.12: Results and comparisons with the percentage differences at the positions of interest for a corner radius of 40mm using an outlet angle of 50°, quantity of 14 blades, inclination angle of 0°, breadth of 20mm, channel width of 15mm, and angular velocity of 589.8rev/min.

Property	Position	Radius 25mm	Radius 40mm	% Diff. 25-40mm
Velocity [m/s]	Front	2.852	2.842	0.35%
	Middle	2.658	2.639	0.72%
	Back	2.651	2.630	0.80%
	Outlet	1.732	1.754	1.26%
Mass Flow Rate [kg/s]	Front	0.03027	0.02727	10.4%
	Middle	0.03024	0.02721	10.5%
	Back	0.03024	0.02721	10.5%
	Outlet	0.03226	0.02920	9.96%
Total Pressure [Pa]	Front	11.52	11.51	0.09%
	Back	5.095	5.450	6.73%
Static Pressure [Pa]	Front	1.789	1.875	4.69%
	Back	-5.647	-5.124	9.71%
Torque [mN.m]		20.81	19.59	6.05%
Power [W]		1.285	1.210	6.05%

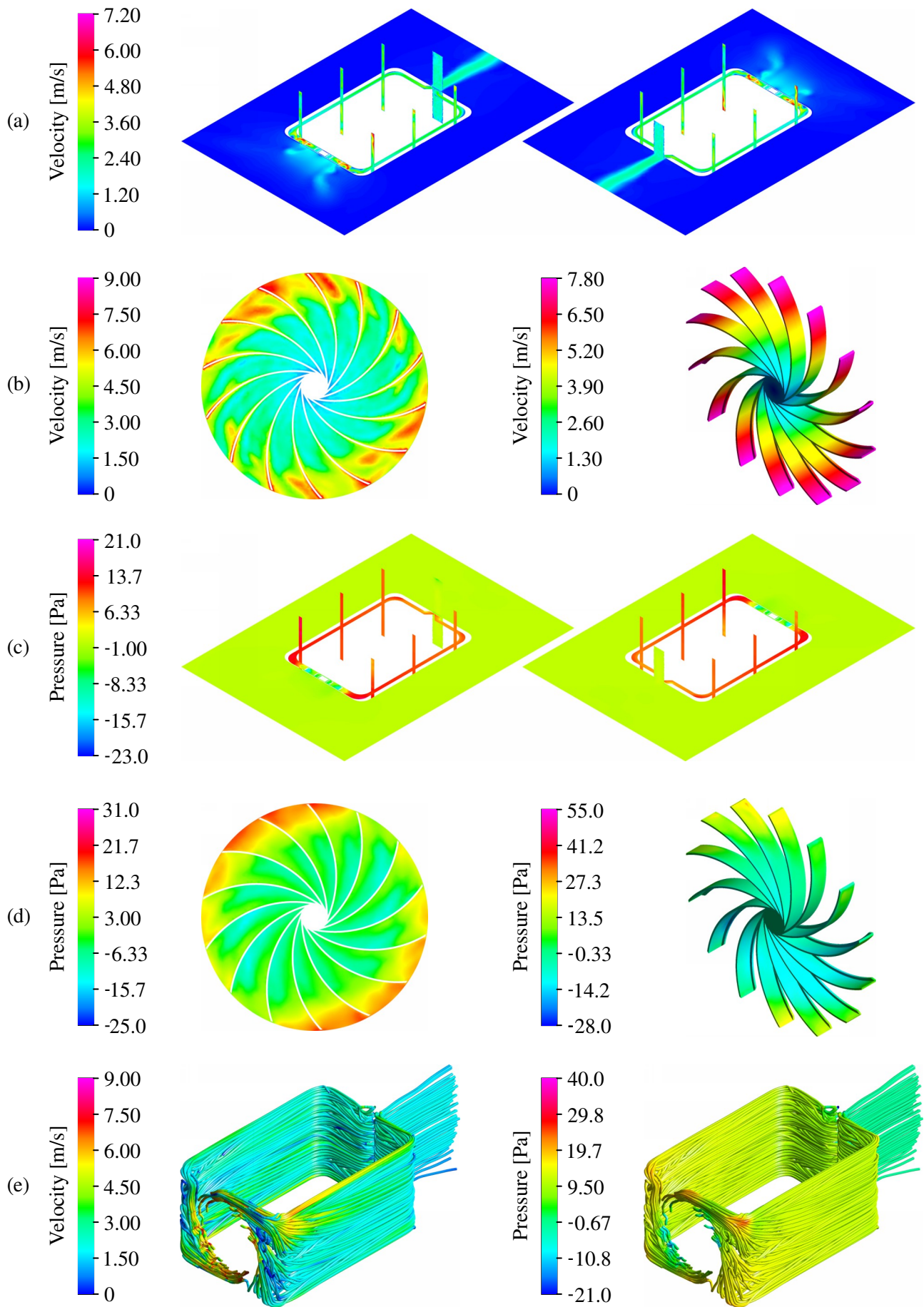


Figure 5.37: Contours for a corner radius of 40mm using an outlet angle of 50°, quantity of 14 blades, inclination of 0°, breadth of 20mm, channel width of 15mm, and angular velocity of 589.8rev/min.

of 40mm. There was a completely inconsequential effect on velocity with the average velocity through the middle plane being 2.639m/s and free stream velocity being 3.036m/s. However, there was a slight deviation in pressures, especially on the trailing surface of the blades, where the average pressure on the driving surfaces decreased with a percentage difference of 4.69% and average pressure on the trailing surfaces decreased with a percentage difference of 9.71%. Although the actual deviation in magnitude was minimal, the percentage difference in power was 5.34%, such that the velocity per unit power and volume was favourably increased from 20.59(m/s)/W/L to 21.72(m/s)/W/L. Thus, an increased corner radius was beneficial in terms of efficiency, but it did not have a distinguished effect on the velocity. It was decided that the corner radius of 40mm was suitable using the modified dimensions.

5.6 COOLING PAD

The cooling pad facilitated evaporation to induce the cooling effect. The water transfer properties from the cooling pad to the air flow were affected by characteristics such as the rudimentary material properties, fibre structures, weaving type and directions, and other microscopic features. The abilities of the material to wick, distribute, and retain water were the most crucial in ensuring that there would be sufficient water exposed to the air flow to maximise evaporation. This optimisation of the cooling pad through the detailed comparison of materials aimed to achieve the most efficient evaporation.

5.6.1 MATERIAL TYPES

It was required for the cooling pad to have a low cost, favourable wetted properties, and durability without tearing or ripping. Furthermore, it would be quite important for a simple process of cleaning the fabric rather than replacing it if it became contaminated, but there was also consideration for the benefit of the possibility of applying anti-microbial and anti-bacterial treatments to prevent contamination without affecting the properties of the material. Based on availability and for diversity, the materials which were investigated included cotton ring spun, cotton waffle weave, cotton canvas, cotton poplin, cotton-polyester, cotton-spandex, polyester, polyester-bamboo, spandex, viscose-spandex, linen, hessian, and kraft paper. A collection of samples of these materials is seen in Figure 5.38.

The cotton ring spun had a composition of cotton fibres, cost of R55.17/m², and mass of 200g/m² with the strands of cotton being twisted and thinned (rather than only twisted for regular strands) to make fine, elastic, and strong fibres. The cotton waffle weave had a composition of cotton fibres, cost of R110.3/m², and mass of 195g/m² with a specific weave resembling a three-dimensional waffle pattern for increased surface area. The cotton canvas had a composition of cotton fibres, cost of R66.67/m², and mass of 190g/m² with thicker fibres to build a sturdy and heavy weave. The cotton poplin had a composition of cotton fibres, cost of R55.17/m², and mass of 80g/m² with strands of cotton forming fine horizontal ribs in a plain weave and single knit. The cotton-polyester had a composition of cotton fibres and polyester thermoplastic (polyethylene terephthalate) fibres, cost of R26.31/m², and mass of 90g/m² with a very thin thickness and combination of properties from cotton and polyester. The

cotton-spandex had a composition of cotton fibres and elastane (polyether-polyurea copolymer) fibres, cost of R62.06/m², and mass of 155g/m² with an increase elasticity over ordinary cotton.

In addition, the polyester had a composition of polyester thermoplastic (polyethylene terephthalate) fibres, cost of R18.69/m², and mass of 65g/m² with some elasticity and hydrophobic strands (although there can be absorption between strands due to capillarity). The polyester-bamboo had a composition of polyester thermoplastic (polyethylene terephthalate) fibres and bamboo cellulose fibres, cost of R88.87/m², and mass of 145g/m² with a double-face construction for a balance between wicking and absorption in the semi-synthetic fibres. The spandex had a composition of elastane (polyether-polyurea copolymer) fibres, cost of R53.33/m², and mass of 220g/m² with exceptional elasticity and durability. The viscose-spandex had a composition of rayon fibres and elastane (polyether-polyurea copolymer) fibres cost of R55.17/m², and mass of 210g/m² with an involved fabrication process to form semi-synthetic fibres. The linen had a composition of flax fibres, cost of R185.7/m², and mass of 130g/m² with the selected sample having a thin weave for a reduced cost. The hessian had a composition of sisal fibres, cost of R24.17/m², and mass of 175g/m² with a rough texture and sparse spacing between thick strands. The kraft paper had a composition of lignocellulosic fibres, cost of R5.90/m², and mass of 50g/m² with a low elasticity before tearing and uniform in-plane properties without weaving.



Figure 5.38: Samples of the selected materials used for deciding the fabric of the cooling pad. (The hessian (similar to jute) was included previously in Figure 2.17 with examples of conventional pads).

5.6.2 PRACTICAL COMPARISON

To provide comparison, each of the materials was cut into strips of 90mm by 900mm and draped in the manner shown in Figure 5.39. This allowed for the ability to wick water to be tested along with the ability to distribute water and the ability to retain water. With regards to wicking, it was required to move the water over a height of at least 30mm before it advanced past the wall. With regards to distributing, it was imperative to measure the rate at which water dispersed through the pad before saturation. With regards to retaining water, it was useful to measure the amount of water retained by the pad once it was saturated. Subsequently, it was possible to recount this performance against the material costs per unit area to determine the most optimal material with regards to affordability.

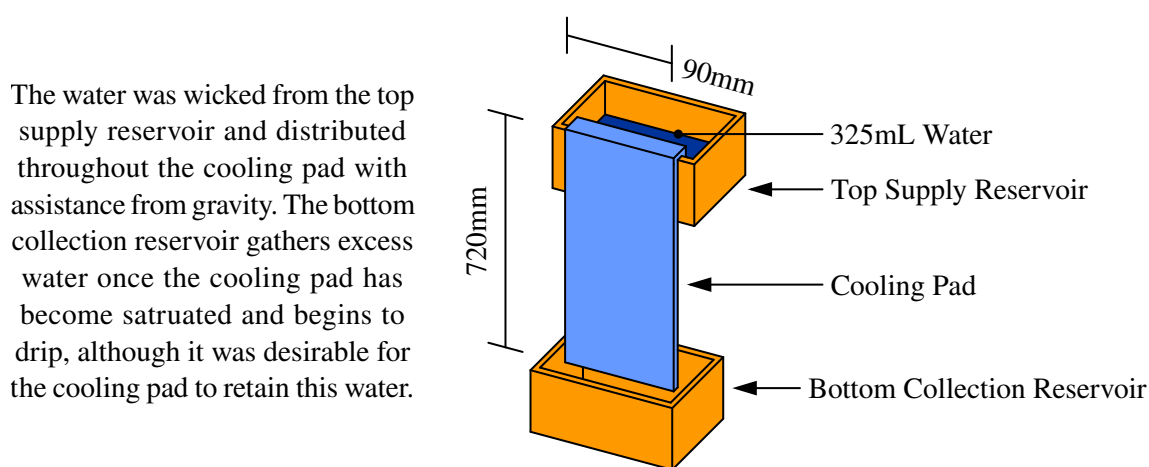


Figure 5.39: Practical test of the best material for wicking, distributing, and retaining water.

The top supply reservoirs were filled with approximately 325mL of water and each of the pads were draped into an individual reservoir above the bottom collection reservoirs. For a period of 180min, measurements were recorded at intervals of 20min for the mass of the top supply reservoir and mass of the bottom supply reservoir, which allowed for the mass of the water absorbed by the pad to be estimated by neglecting any evaporation. The approximate saturation of the pad was estimated by measuring the distance to which the water had dispersed up to saturation at a distance of 720mm and noting the mass of the water retained by the pad compared to the mass of the water retained by the pad once saturation was reached. Throughout the period, the temperature varied between $25.6 \pm 0.5^\circ\text{C}$ and $27.8 \pm 0.5^\circ\text{C}$ with the relative humidity ranging from $59.1 \pm 2\%$ to $66.9 \pm 2\%$. The results are presented in Table 5.13. It was assumed that any evaporation during the period was negligible.

The performance of the cotton-polyester and linen was extremely disappointing without any noticeable abilities for wicking and this was reasoned to be the case due to the thin weaves which had a significantly reduced density compared to the other materials. For the same reason, the cotton poplin also performed poorly with a saturation of only 25% after the period. The kraft paper was seen to readily absorb water, but it did not demonstrate wicking abilities, while it also became very fragile once wet and

Table 5.13: Results comparing the wicking, distribution, and retention abilities of selected materials for the cooling pad. (*) The material was completely wet and reached minimum saturation, although it was still able to absorb more water. It should be noted that the initial masses of the top supply reservoir and bottom collection reservoir have already been subtracted from the masses shown.

	0 Minutes				20 Minutes				40 Minutes				60 Minutes				80 Minutes			
	Top [g]	Pad [g]	Sat. [%]	Bot. [g]	Top [g]	Pad [g]	Sat. [%]	Bot. [g]	Top [g]	Pad [g]	Sat. [%]	Bot. [g]	Top [g]	Pad [g]	Sat. [%]	Bot. [g]	Top [g]	Pad [g]	Sat. [%]	Bot. [g]
Cot. Ring Spun	323	0	0	0	311	12	12	0	298	25	36	0	288	35	75	0	279	44	99	0
Cotton Waffle	325	0	0	0	303	22	11	0	299	26	23	0	295	30	33	0	291	34	47	0
Cotton Canvas	326	0	0	0	311	15	11	0	307	19	27	0	301	25	46	0	295	31	73	0
Cotton Poplin	326	0	0	0	322	4	3	0	321	5	6	0	320	6	9	0	319	7	11	0
Cot.-Polyester	323	0	0	0	321	2	0	0	320	3	0	0	320	3	0	0	319	4	0	0
Cotton-Spandex	328	0	0	0	307	21	12	0	300	28	30	0	292	36	54	0	289	39	77	0
Polyester	325	0	0	0	293	26	*	6	267	28	*	30	242	33	*	50	213	36	*	76
Poly.-Bamboo	329	0	0	0	317	12	4	0	308	21	26	0	297	32	84	0	286	39	97	0
Spandex	329	0	0	0	321	8	8	0	318	11	17	0	317	12	22	0	313	16	29	0
Visc.-Spandex	328	0	0	0	314	14	10	0	310	18	21	0	309	19	29	0	304	24	43	0
Linen	323	0	0	0	319	4	0	0	317	6	0	0	316	7	1	0	313	10	1	0
Hessian	325	0	0	0	309	16	3	0	307	18	12	0	302	23	31	0	294	31	44	0
Kraft Paper	328	0	0	0	327	1	0	0	326	2	0	0	325	3	0	0	325	3	0	0

	100 Minutes				120 Minutes				140 Minutes				160 Minutes				180 Minutes			
	Top [g]	Pad [g]	Sat. [%]	Bot. [g]	Top [g]	Pad [g]	Sat. [%]	Bot. [g]	Top [g]	Pad [g]	Sat. [%]	Bot. [g]	Top [g]	Pad [g]	Sat. [%]	Bot. [g]	Top [g]	Pad [g]	Sat. [%]	Bot. [g]
Cot. Ring Spun	268	51	*	4	259	52	*	12	248	54	*	21	237	55	*	31	231	56	*	36
Cotton Waffle	285	40	63	0	275	50	80	0	269	56	97	0	261	62	*	2	250	65	*	10
Cotton Canvas	287	39	99	0	281	42	*	3	275	43	*	8	268	45	*	13	261	46	*	19
Cotton Poplin	318	8	12	0	317	9	15	0	315	11	21	0	314	12	23	0	313	13	25	0
Cot.-Polyester	319	4	1	0	319	4	1	0	319	4	1	0	319	4	1	0	319	4	1	0
Cotton-Spandex	276	49	*	1	268	54	*	6	259	55	*	14	250	57	*	21	240	60	*	28
Polyester	189	39	*	97	167	44	*	114	147	47	*	131	131	48	*	146	113	52	*	160
Poly.-Bamboo	277	39	*	3	265	45	*	13	255	49	*	19	249	50	*	25	244	51	*	30
Spandex	309	18	36	2	304	23	41	2	299	24	57	6	293	28	61	8	285	32	66	12
Visc.-Spandex	302	26	50	0	299	29	63	0	293	35	72	0	289	39	83	0	285	43	92	0
Linen	313	10	1	0	313	10	2	0	312	11	2	0	309	14	3	0	309	14	3	0
Hessian	297	28	67	0	285	40	86	0	280	43	*	2	274	47	*	4	270	47	*	8
Kraft Paper	324	4	1	0	324	4	1	0	324	4	1	0	324	4	1	0	324	4	1	0

easily tore due to the cellulose bonds becoming compromised. The spandex was observed to have poor abilities for the water distribution, where it was prevalent for the water to spread in individual branches followed by a slower uniform distribution, as illustrated in Figure 5.40 against the other materials which exhibited more uniform distributions until saturation. This caused the spandex to drain into the bottom collection reservoir while its saturation was still estimated to be around only 36%. The viscose-spandex had a more uniform distribution than the spandex, but it dispersed very slowly and was unable to reach complete saturation with a saturation of only 92% after the period.

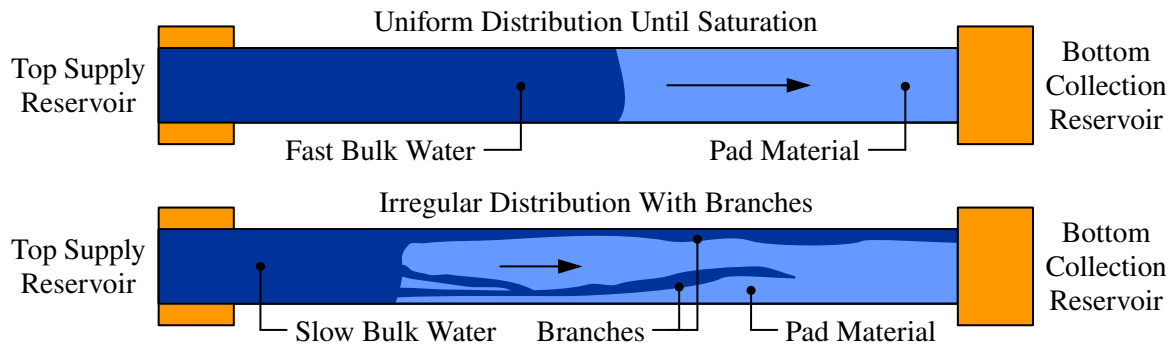


Figure 5.40: Illustration of the uniform distribution (top) observed for the majority of materials and irregular distribution with branches (bottom) observed for the spandex and partially polyester-bamboo.

The cotton waffle weave and cotton canvas displayed mediocre performance and were able to reach saturation in less than 160min and 120min respectively with the ability to retain a minimum of approximately 689g/m^2 and 467g/m^2 of water respectively once saturation was reached. However, when the cotton waffle weave and cotton canvas were compared against the remaining materials without considering performance, there were no perceivable advantages but there was an increased cost which was not warranted. A similar tendency was seen for the polyester-bamboo, which reached saturation in less than 100min and retained a minimum of approximately 433g/m^2 of water, but suffered a very high cost without justifiable improvements in performance. The hessian was able to reach saturation within 140min and retained a minimum of approximately 478g/m^2 of water. Compared to the cotton waffle weave, cotton canvas, and polyester-bamboo, the hessian was significantly more inexpensive, but its performance was only mediocre as the time until it was saturated was still prolonged.

The best performing materials were the cotton ring spun, cotton-spandex, and polyester. The cotton ring spun and cotton-spandex performed very similarly and were both able to reach saturation in less than 100min with the ability to retain a minimum of approximately 567g/m^2 and 544g/m^2 of water respectively. The cotton ring spun had a slight edge in performance over the cotton-spandex with a marginally decreased cost. The polyester dispersed very rapidly and was able to reach saturation in less than 20min. However, the polyester was slightly lacking in its ability to retain water with a minimum of approximately 289g/m^2 of water, although this increased to a more admissible value of 433g/m^2 after 100min. In any case, this was seen to be offset in favour of the very low cost for polyester.

Thus, accounting for the cost per unit area, polyester was accepted to be the most promising material with regards to distribution, but cotton ring spun was accepted to be the most promising material with regards to retention. So, both of the materials would be compared with regards to optimisation in the practical experimentation. It was acknowledged that polyester is derived from petroleum and irresponsible disposal can lead to harmful pollution, while cotton ring spun uses natural fibres which are biodegradable without an inherent impact on the environment, although the cultivation can be exploitative with negative environmental effects if inappropriately sourced [140].

5.7 WATER SUPPLY LAYOUT

The water supply needed to store at least 2L of water in a reservoir, as it was expected for this to provide enough water to operate for at least one day based on other existing products. It was also required for the layout to accommodate an opening of at least 200mm by 200mm to make allowance for the storage of large fruits and vegetables, such as pumpkin, cabbage, and watermelon. The proposed layout is shown in Figure 5.41 with an extruded height of 40mm for the surrounding walls, where a gap of 2mm was located surrounding the outer walls of the reservoir to allow for the cooling pad to be passed through and draped over these walls, as seen in the partial assembly in Figure 5.42.

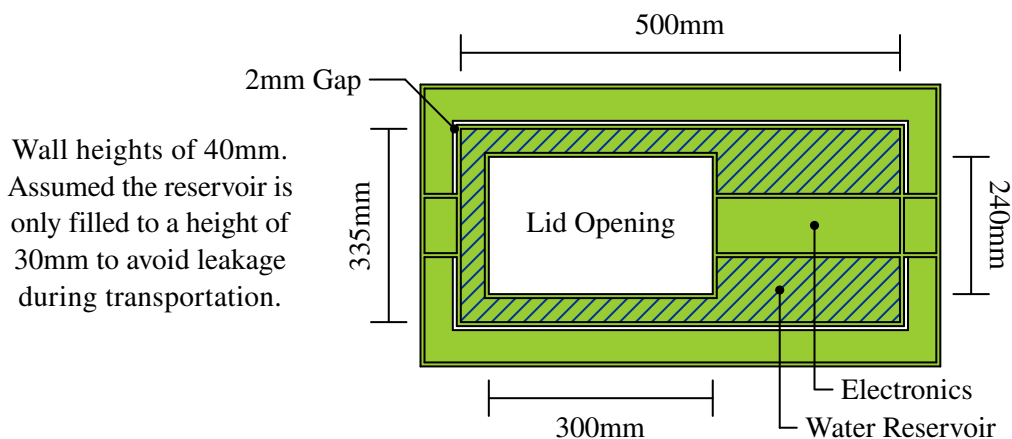


Figure 5.41: Representation of the dimensions of the water supply using a reservoir.

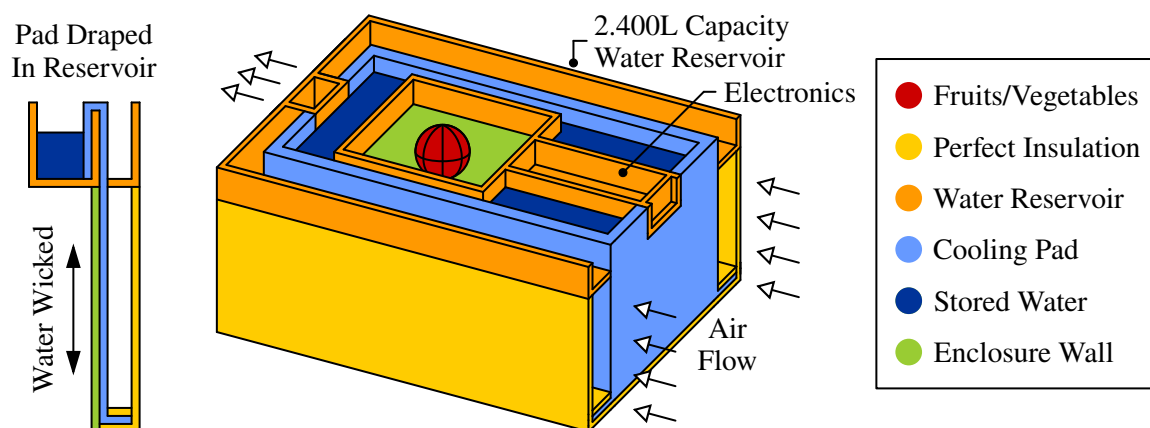


Figure 5.42: Layout of the water supply using a reservoir without components for the forced air flow.

This layout allowed for a surface area of 0.08001m^2 and total volume of approximately 2.400L, assuming the reservoir was only filled to a height of 30mm to avoid possible leakage from shocks during transportation - if the reservoir was filled to a maximum height of 40mm, the total volume would be 3.201L. With the pad easily wicking the water over the walls, gravity allowed for distribution throughout the pad. Before sewing the ends to form a loop, the dimensions of the pad were 380mm by 1800mm for a total surface area of 0.684m^2 . For polyester and based on the water distribution of $481.4\text{g}/\text{m}^2$ and cost of approximately $\text{R}18.69/\text{m}^2$, the pad was estimated to retain 0.3293L of water and cost $\text{R}12.78$. For cotton ring spun and based on the water distribution of $661.7\text{g}/\text{m}^2$ and cost of approximately $\text{R}55.17/\text{m}^2$, the pad was estimated to retain 0.4526L of water and cost $\text{R}37.74$.

5.8 EXTERNAL INSULATION

The aim of the external insulation was to inhibit the heat transfer from insolation and other sources of heat in the surroundings, such that the evaporative cooling and enclosure could be isolated. For the most constructive effect, insulation was embedded along the front, sides, top, bottom, and back with openings only for grills at the inlet and outlet regions, although it may be possible to reduce costs by substituting the insulation at the bottom for a sealed air cavity since it was not directly exposed to insolation. This involved a layer of insulation interposed between sheets making up the walls.

As the material of the walls, ABS was considered in the form of an opaque white thermoplastic with an approximate absorptivity of 0.21 and thermal conductivity of $0.265\text{W}/\text{m}/\text{K}$. A thickness of 1.2mm was considered, albeit this was fairly arbitrary since it was expected to have a relatively marginal effect on the heat transfer compared to the insulation. Furthermore, even though ABS was seen to be a promising option for the material of the walls, the choice was fairly arbitrary since the majority of candidate polymer materials had thermal conductivities in a similar range from $0.15\text{W}/\text{m}/\text{K}$ to $0.30\text{W}/\text{m}/\text{K}$ and this thermal conductivity was significantly greater than the thermal conductivity of the insulation. As the material of the insulation, polyurethane foam and polystyrene foam were considered with a constant thermal conductivity of $0.020\text{W}/\text{m}/\text{K}$ and $0.037\text{W}/\text{m}/\text{K}$ respectively to represent averages between the typical values. For the contact between the materials, it was assumed that the thermal contact resistance was negligible. The basic layout of the construction is shown in Figure 5.43.

From Figure 5.9 and as a representation of the most extreme environmental conditions, it was expected for a maximum temperature difference to occur with an efficiency of 100% when the relative humidity was 0%, such that the external air temperature was 50°C and the internal air temperature was 16.2°C . Based on Figure 2.3, it was expected for a maximum average insolation intensity of approximately $420\text{W}/\text{m}^2$, but, instead, the solar constant of $648\text{W}/\text{m}^2$ was chosen to be considered for a conservative analysis. It was also assumed that the temperature of the surroundings was equal to the temperature of the external surface, so as to exclude radiative heat transfer between the surroundings and external surface. Likewise, it was assumed that the external and internal air temperatures were negligibly

different from the temperatures of the external and internal surfaces respectively, so as to exclude meaningful convective heat transfer between the respective regions of air and surfaces.

As mentioned in Section 2.4, the conductive heat transfer is described by Equation 2.18 and radiative heat transfer is described by Equation 2.44, although it was not necessary to utilise the Stefan-Boltzmann law directly since the solar constant was applied instead. A surface heat transfer balance could then be performed on the external surface, where the radiative heat transfer to the surface was equal to the conductive heat transfer from the surface. This relationship is elaborated in Equation 5.31, where it was possible to solve for the required thickness of the insulation depending on the thermal conductivity.

$$\dot{Q}_{rad} = \dot{Q}_{cnd} \rightarrow \alpha GA = -A \frac{T_{int} - T_{ext}}{2t_{wll}/k_{wll} + t_{ins}/k_{ins}} \rightarrow t_{ins} = k_{ins} \left(\frac{T_{ext} - T_{int}}{\alpha G} - 2 \frac{t_{wll}}{k_{wll}} \right) \quad (5.31)$$

Proceeding with the designated variables and properties, 136.1 W/m^2 of insolation would be absorbed while the remaining 511.9 W/m^2 of insolation would be reflected by the external surface. Thus, it was required for the insulation to have a thickness of at least 4.787 mm for polyurethane foam or 8.855 mm for polystyrene foam, which corresponded with a thickness of at least 7.180 mm for polyurethane foam or 13.28 mm for polystyrene foam after the application of a safety factor of 1.5 to account for the uncertainties in the actual absorptivity of the external surface, thermal conductivities of the materials, and insolation. Overall, the calculations were fairly conservative, as required since the operation encapsulated a wide range of environmental conditions with a large scale of uncertainty.

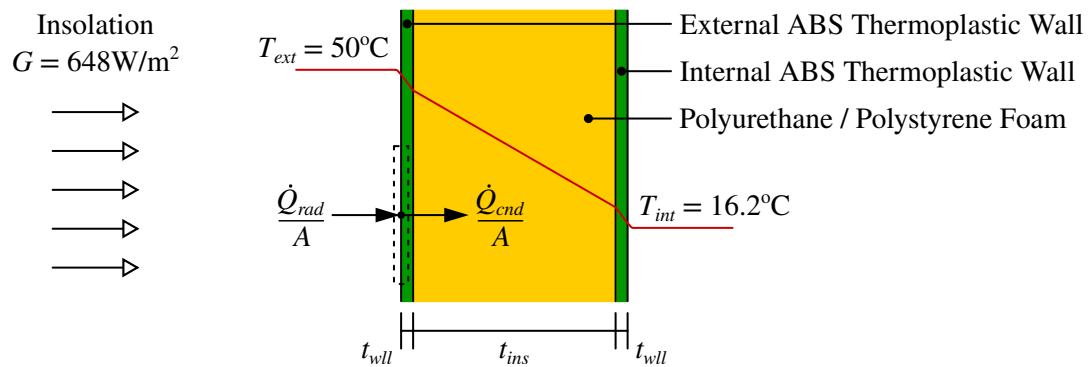


Figure 5.43: Basic layout of the insulation to minimise the effects from insolation.

5.9 STRUCTURAL STRENGTH

To ensure robustness, the strength of the structure was optimised through an FEA simulation using a linear analysis and steady state structural mechanics to assess the displacements, stresses, and safety from failure. This was also compared against analytical calculations, but it should be kept in mind that using analytical calculations involves creating an idealisation with assumptions for simplification to obtain a rough estimation of the solution. As mentioned, it was required for the enclosure to support at least 31.60 kg applied over the top surface, with a static deformation of less than 5 mm , as if two other

fully loaded enclosures of 15.80kg each were stacked on top of it. Similarly to the CFD simulations for the flow analysis, the expected temperature difference was only in the range of 11°C, so it was acceptable to neglect any energy effects and changes in mechanical properties due to heat transfer.

5.9.1 DESIGN INCEPTION

To satisfy the insulation implications from Section 5.8, a slab of polystyrene inserted between two sheets of ABS was considered for the external walls and a single sheet of ABS was considered for the internal walls around the enclosure. A composite of layers of polystyrene and ABS was also considered for the bottom underneath the enclosure and top plane above the water reservoir. ABS was chosen due to its balanced properties for environment resistance, dimensional stability, tensile strength, surface hardness, and rigidity, while also being very inexpensive due to its widespread availability with a safe rating for use in food processing. This layout is shown in Figure 5.44 with a cross-section.

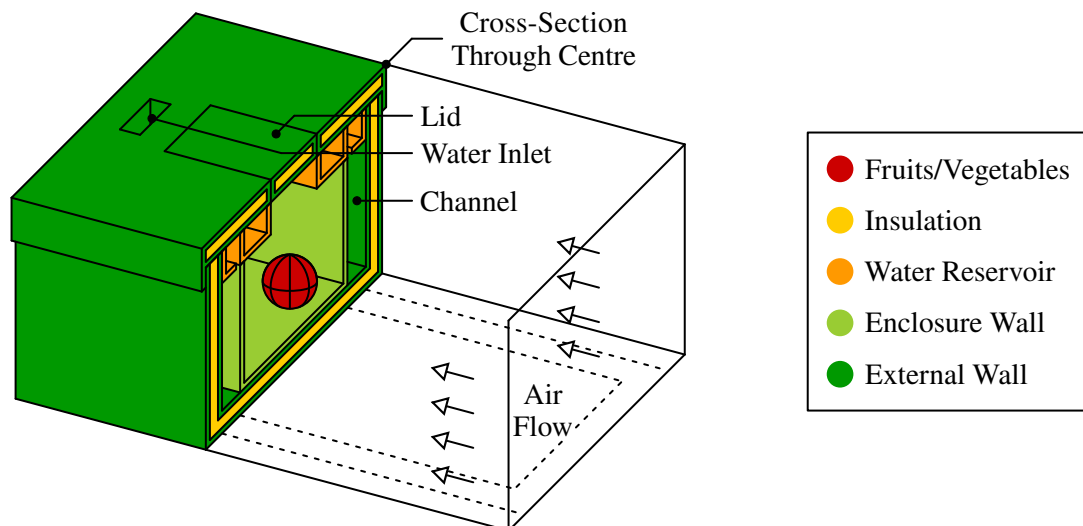


Figure 5.44: Layout of the structure through the centre of the enclosure without the cooling pad.

5.9.2 BASIC ANALYTICAL PREDICTION

A cross-section was considered at a plane through the middle of the enclosure. This plane intersected the external and internal walls which would primarily experience an axial displacement and stress when loaded. For the walls, the polystyrene was taken to have a thickness of 15mm, as this was the next available standard size above the required value for insulation, and the ABS was taken to have a thickness of 1.2mm, as this was deemed to be the thinnest standard size which was still rigid. The precise mechanical properties of the materials were sourced from ANSYS Granta EduPack 2021 and listed in Table 5.14. The composition of properties from the interposition of polystyrene and ABS can be seen to be based on the elastic modulus and cross-sectional area of each material in the simplified cross-section in Figure 5.45, such that the properties of the polystyrene contributed approximately 1.5% and ABS contributed approximately 98.5% of the overall composite elasticity. This was based on

the product of the respective elastic modulus and cross-sectional area as 7.399MPa for polystyrene and 494.3MPa for ABS for an equivalent composite elastic modulus of 501.7MPa. It was also assumed that the elastic behaviour was completely linear until yielding and the strength in tension and compression were equivalent, although the applicable loading was predominantly compressive.

Table 5.14: Mechanical properties of medium-impact injection-moulded ABS thermoplastic and high-density polystyrene foam. The properties were evaluated at 23°C and assumed to be constant.

Mechanical Property	Medium-Impact ABS Thermoplastic	High-Density Polystyrene
Density [kg/m ³]	1045	29.93
Poisson's Ratio	0.3986	0.2739
Elastic Modulus [MPa]	2390	9.328
Bulk Modulus [MPa]	3928	6.876
Shear Modulus [MPa]	854.4	3.661
Tensile Yield Strength [MPa]	41.37	0.224
Tensile Ultimate Strength [MPa]	44.27	0.380
Compressive Yield Strength [MPa]	41.37	0.224
Compressive Ultimate Strength [MPa]	44.27	0.380

The derived axial displacement and stress experienced by the external and internal walls is described by Equation 5.32 [141, 142]. Based on the requirement for the structure to support a load of 310N as if two other fully loaded enclosures were stacked on top of it, it was assumed that this load was equally and symmetrically distributed over the surface on which it was applied. Therefore, the basic arrangement of the loading for the external and internal wall is demonstrated in Figure 5.45 with the depiction of the cross-section. It should be noted that, if there was consideration for a combination of different types of loading, the cumulative stress could be evaluated through the equivalent or von Mises stress in Equation 5.33 to account for effects from axial, bending, shear, and torsion loads (relevant for the simulation) [141, 142]. The safety from failure could be judged using a safety factor specified through the distortion energy static failure theory defined in Equation 5.34 as the ratio of the applied stress to the yield strength [141, 142]. This theory predicts failure to occur when the strain energy, or energy stored due to the deformation, per unit volume exceeds the strain energy per unit volume for yielding, where a safety factor above unity implies safety but below unity implies failure.

$$k = \frac{EA}{L} = \frac{E_{ply}A_{ply} + E_{abs}A_{abs}}{L} \rightarrow \delta = \varepsilon L = \frac{F}{k} \rightarrow \sigma_a = \frac{F}{A} = \varepsilon \left(E_{ply} \frac{A_{ply}}{A} + E_{abs} \frac{A_{abs}}{A} \right) \quad (5.32)$$

$$\sigma_{equ} = \sqrt{(\sigma_a + \sigma_b)^2 + 3(\tau_r + \tau_t)^2} \quad (5.33)$$

$$n = \frac{\sigma_y}{\sigma_{equ}} \quad (5.34)$$

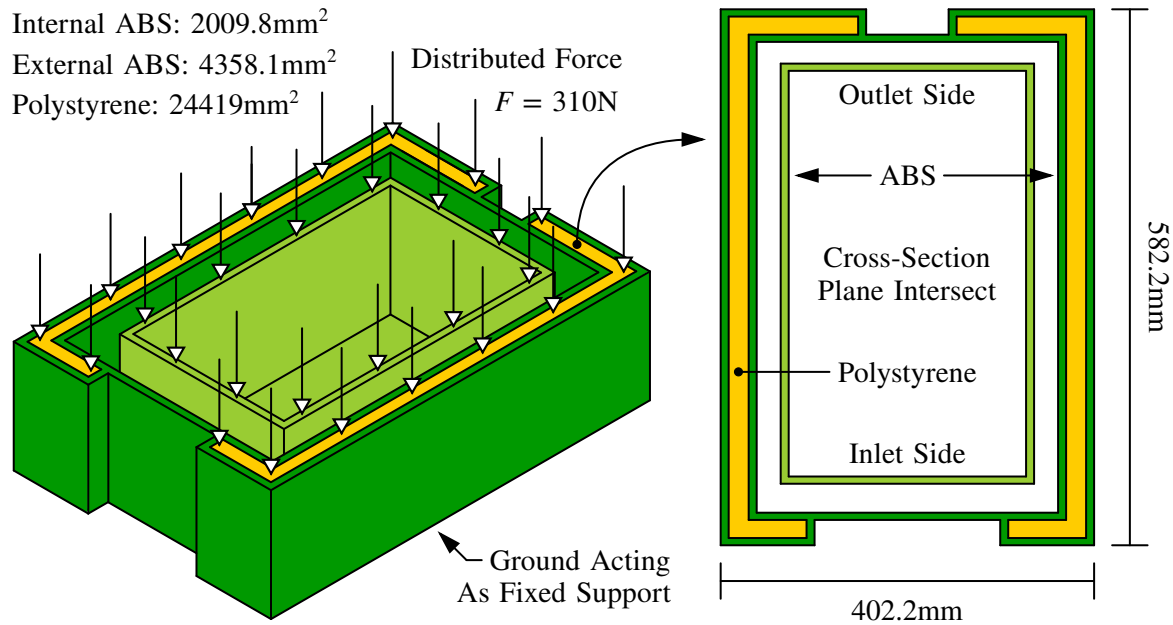


Figure 5.45: Simplified cross-section plane through the middle of the enclosure with a force of 310N.

Completing the calculations, there would be an expected displacement of 0.010mm and stress of 10.07kPa, which corresponded with a safety factor above 15 for both the polystyrene and ABS. If there was a sharp change in geometry, there would be a stress concentration which would amplify the calculated stress by a certain factor, but there were no meaningful stress concentrations to account for at the location of the plane relative to the type and direction of loading. For its purpose, this analysis was acceptable for conservative discretion to compare with the results from the simulation in order to judge the validity of the simulation. It was acknowledged that there was disregard for the possible bending within the structure, which would occur in two planes and be difficult to determine with simple calculations, so there was a likelihood of the actual displacement and stress being greater than the calculated displacement and stress. However, at the region of interest and with the relevant symmetric loading, the axial component was already expected to be significantly dominant over the bending component. It should also be emphasised that it was not expected for a large displacement or stress in this plane in any case, but there was more concern for a large displacement and stress near the regions for the lid and water reservoir, since the loading would have a significant bending component.

5.9.3 THEORETICAL BACKGROUND

A detailed account of the theoretical background of FEA is presented by Chen and Liu [143]. From fundamentals, a continuous solid is characterised by a finite number of volumetric elements and each element features a collection of nodes. Each node is characterised with a possible displacement in three directions and rotation about three axes for a maximum of six degrees of freedom which is reduced based on boundary conditions, such that the element features a total number of degrees of freedom equal to the sum of the non-zero degrees of freedom of each node. When there is an applied force at a

node in an element, it can be seen that there will be resulting displacements of the nodes and these displacements are related through the stiffness or elasticity of the element [143].

By connecting the individual elements, a model for the global structure can be derived. So, when there is an applied force at a node in an element, there are consequential displacements of each of the nodes in the entire structure, where these displacements are still related to the applied nodal forces and resulting internal forces at each node based on the stiffness of the material throughout the structure. The material is usually modelled as isotropic and linearly elastic, which introduces a minor modelling error as a real material is imperfect due to defects in the underlying microscopic structure [143].

This allows for the formation of a system of equations which states the relationship between the nodal displacements and nodal forces for the entire structure, where a vector of the nodal forces is equal to the dot product between a global stiffness matrix and vector of the nodal displacements, as simply expressed in Equation 5.35 for a two-dimensional structure of elements behaving as consecutive springs with only translational degrees of freedom [143]. The system can then be reduced through the application of known boundary conditions which restrict the displacements of certain nodes. The global stiffness matrix will be square, symmetric, banded, sparse, and have an order equal to the number of degrees of freedom and, for solvability, it is necessary for sufficient boundary conditions to prevent rigid body motion such that the number of unknown variables is equal to the number of equations [143]. The reduced system can then be solved for the displacements and internal forces based on a direct solution method, such as Gaussian elimination or lower-upper decomposition, or indirect solution method, such as Gauss-Seidel or conjugate gradient. Subsequently, strains and stresses throughout the structure can be calculated based on the displacements and internal forces [143].

$$\vec{F} = K \cdot \vec{u} \rightarrow \begin{bmatrix} F_1 \\ F_2 \\ F_3 \\ \vdots \\ F_n \\ F_{n+1} \end{bmatrix} = \begin{bmatrix} k_1 & -k_1 & 0 & \cdots & 0 & 0 \\ -k_1 & k_1+k_2 & -k_2 & \cdots & 0 & 0 \\ 0 & -k_2 & k_2+k_3 & \cdots & 0 & 0 \\ \vdots & \vdots & \vdots & \ddots & \vdots & \vdots \\ 0 & 0 & 0 & \cdots & k_{n-1}+k_n & -k_n \\ 0 & 0 & 0 & \cdots & -k_n & k_n \end{bmatrix} \cdot \begin{bmatrix} u_1 \\ u_2 \\ u_3 \\ \vdots \\ u_n \\ u_{n+1} \end{bmatrix} \quad (5.35)$$

However, this procedure of directly considering the applied forces, stiffnesses, and displacements is limited to simple applications for a static structure without body forces and it cannot be applied to more complex situations. As an alternative, the principle of virtual work can be employed to develop the global stiffness matrix with the assumption of small displacements leading to small strains. Essentially, there is direct consideration for the internal change in potential energy resulting when there is a displacement due to the elasticity and stiffness of the material and external change in potential energy resulting when there is a translation of an external force through a distance [143]. This method is more generalised and actually considered as the foundation of the FEM [143].

Considering the infinitesimal definitions, the strain can be expressed as Equation 5.36 and stress can be expressed as Equation 5.37 [143]. Applying the infinitesimal stress over an element due to an infinitesimal strain from a virtual displacement, an equilibrium condition must arise without a change in potential energy within the element, as illustrated in Figure 5.46 and given by Equation 5.38 [143]. Thus, considering the weak form to be only applicable in an element and not throughout the structure, the principle of virtual work can be derived in Equation 5.39 with the introduction of an external volumetric force and traction or stress across the surface at a normal orientation [143]. This can be interpreted as an equality between the internal virtual work, as the work done per unit volume by the actual stresses acting on the virtual strains, and external virtual work, as the work done by the body forces and boundary conditions [143]. To complete the solution, it would then be necessary for the discretisation and simplification of this formulation with a result for a static structure without body forces given in a form to that of a vector of the nodal forces being equal to the dot product between a global stiffness matrix and vector of the nodal displacements, as found with the previous method.

$$\varepsilon_{ii} = \frac{\partial u_i}{\partial x_i} \text{ and } \gamma_{ij} = \frac{\partial u_j}{\partial x_i} + \frac{\partial u_i}{\partial x_j} \text{ with } \gamma_{ij} = 2\varepsilon_{ij} \quad (5.36)$$

$$\sigma_{ii} = \frac{E}{(1+\nu)(1-2\nu)} ((1-\nu)\varepsilon_{ii} + \nu(\varepsilon_{jj} + \varepsilon_{kk})) \text{ and } \tau_{xy} = G\gamma_{ij} \text{ with } G = \frac{E}{2(1+\nu)} \quad (5.37)$$

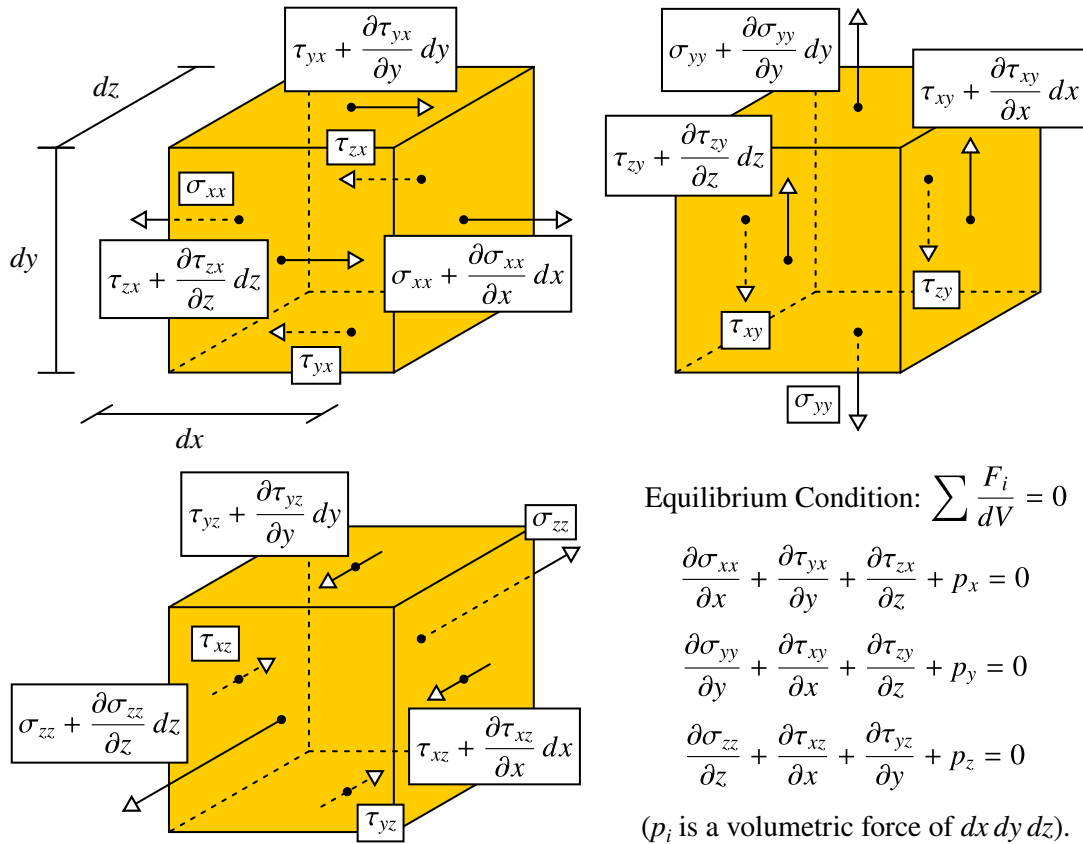


Figure 5.46: Illustration of the equilibrium conditions for an element and shown individually in each direction when an external force is applied and causes a strain and stress within the element.

$$\sigma_{ij,j} + p_i = 0 \rightarrow \frac{\partial \sigma_{ii}}{\partial x_i} + \frac{\partial \tau_{ij}}{\partial x_j} + \frac{\partial \tau_{ik}}{\partial x_k} + p_i = 0 \rightarrow \zeta = (\sigma_{ij,j} + p_i) \delta u_i = 0 \quad (5.38)$$

$$\int_V (\sigma_{ij,j} + p_i) \delta u_i dV = 0 \rightarrow \delta W_{int} = \int_V \sigma_{ij} \delta \epsilon_{ij} dV = \underbrace{\int_V p_i \delta u_i dV}_{\text{Volumetric}} + \underbrace{\int_S t_i \delta u_i dS}_{\text{Traction}} = \delta W_{ext} \quad (5.39)$$

With regards to accuracy, the field of displacements is constrained by a limited number of nodes which leads to a stiffening effect, where the model is stiffer than the real structure and displacements are generally smaller in magnitude than the exact values from an analytical analysis equivalent to using an infinite number of nodes [143]. Hence, the solution is a lower limit of the exact solution, but the solution will converge towards the exact solution from below as the number of elements and degrees of freedom increases [143]. To improve accuracy, like a higher resolution of elements in the mesh allows for a better approximation of the structure, a higher number of nodes in each element allows for a better interpolation of properties within the element. For linear elements, a minimum level of accuracy is achieved with first-order interpolation between displacements and constant interpolation between stresses. For quadratic elements, a higher level of accuracy is achieved with second-order interpolation between displacements and first-order interpolation between stresses. Generally, when considering a situation of similar computational effort, the use of higher-order elements is preferable over the option of more numerous lower-order elements for a more robust model.

5.9.4 MODEL CONFIGURATION

The model involved characterising the configuration with regards to the simplified geometry, contacts between the solids, required material properties, boundary conditions with supports and applied loads, meshing strategy, and chosen finite element properties. The simulations were setup and performed in ANSYS Mechanical 2021 R1 on the same system used for the CFD analysis. The software license only allowed for the use of up to 4 cores which affected the computation time, but the 24.4GB of system memory was the primary limitation for the size of the model, as with the CFD analysis.

The geometry modelled individual solids for each of the parts making up the domain, where a boolean operation was applied to split each of the solids in half along the longitudinal centreline plane for the application of reflective symmetry. The material properties assigned to the solids were characterised by those in Table 5.14 for polystyrene and ABS. The contacts between the solids were either set as bonded, for the walls as if they were physically joined with an adhesive or interlocking clips and there could not be tangential sliding or normal separation, or no separation, particularly for surfaces of the lid which could slide tangentially but general normal separation was constrained due to the geometry and loading. In each contact, the target surface was defined for the solid which was expected to be more rigid with a higher stiffness, while the contact surface was defined for the solid which was expected to be less rigid with a lower stiffness. For the boundary conditions relating the limits of the geometry to the surroundings, the bottom surface was set to be in contact with an incompressible ground surface through a displacement constraint to limit normal and transverse motion, while the surfaces along

the longitudinal centreline plane were set as symmetric interfaces due to the symmetric geometry, material, and loading. The symmetric interfaces act as displacement constraints, such that there cannot be motion normal to the longitudinal centreline plane, where the advantage of symmetry allows for the size of the model to be reduced or, equivalently, a more refined mesh can be generated for the model of the same size. Using these contacts and boundary conditions allowed for the contact area to remain constant for a linear analysis while maintaining a realistic approximation. The geometry, contacts, and boundary conditions are described in Figure 5.47 with an exploded view of the solids.

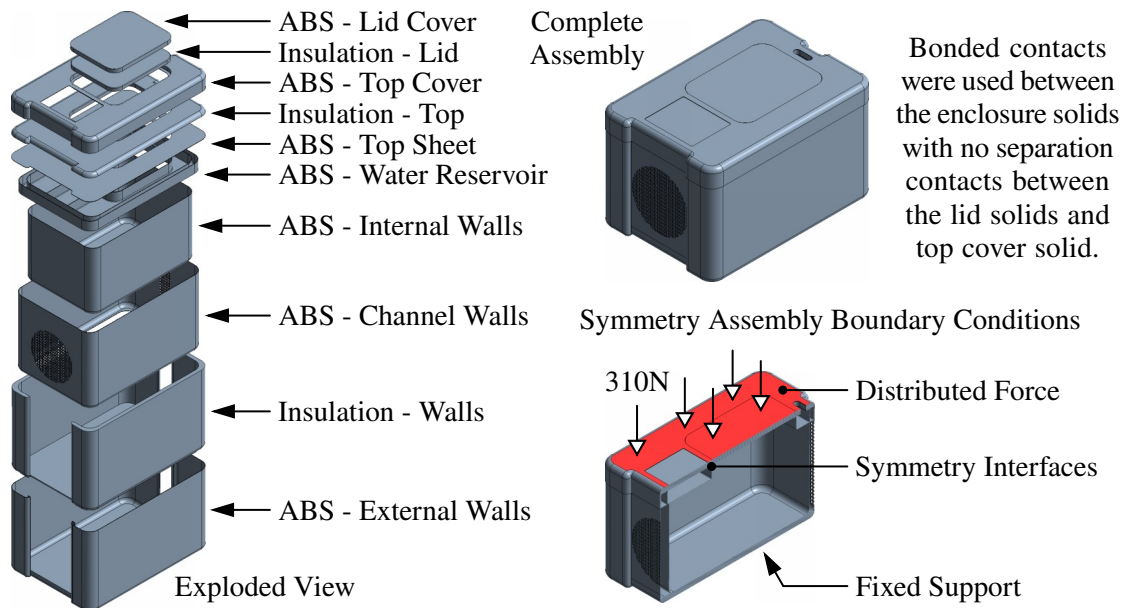


Figure 5.47: Parts for the structure to construct the overall model for the FEA. The CAD model was generated using Autodesk Inventor Professional 2019 for simulation in ANSYS Mechanical 2021 R1.

To sub-divide the continuous geometry into discrete volumetric elements, a mesh could be generated using a distribution of nodes. The formation of tetrahedral elements with linear and quadratic nodes are demonstrated in Figure 5.48. Based on the supports and applied load, this allowed for the response of each element to be evaluated individually, related between nodes, and then combined to formulate the total response of the structure. Again, it was still necessary to apply a mesh independence analysis to confirm that the solution subsists irrespective of the specific mesh used to find the solution.

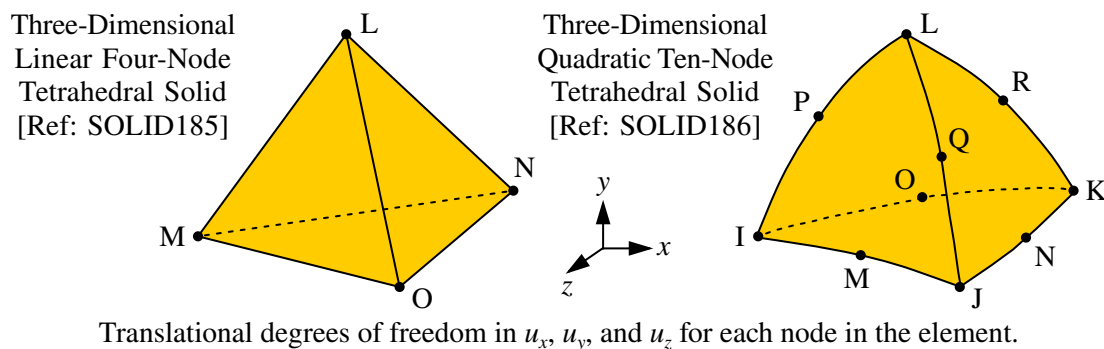


Figure 5.48: Example of a linear (left) and quadratic (right) tetrahedral element [144].

5.9.5 BASE SETUP AND RESULTS

Instead of generating a series of subsequently refined meshes as in the CFD simulations, the mesh independence was assessed through a convergence criteria, where the critical regions of an initial mesh were subsequently refined in iterations until the changes in properties were within an allowable tolerance of 2%. The considered properties were the maximum displacement and stress. To evaluate the relevance, only the critical regions were refined further and, after a sufficient resolution, other regions were less concerning and only needed to be represented with this resolution for the geometry and transmission of loads. This rational was based on Saint-Venant's Principle which enforces that the local stresses in one region do not directly affect the stresses elsewhere [142, 143]. The refinement was performed through the reduction in the element sizes in the critical regions, conventionally known as h-refinement as opposed to p-refinement which relates to increasing the order of the elements (which was not applicable since quadratic elements were already used). A maximum of 5 refinement iterations were allowed and a refinement depth of 1 was applied after each iteration.

The initial mesh featured an element size of 3mm, adaptive resolution of 2, and adaptive transition of fast for a total of 1110797 elements constituted by a total of 2178715 nodes. As a metric to judge the quality of the meshes, the skewness and aspect ratio were considered, where the average skewness was 0.523 and average aspect ratio was 2.83. This quality was relatively coarse, although passable for the initial mesh, and would be improved after each iteration with refinement. It was decided to only use tetrahedral elements through a patch conforming method to accurately follow the boundaries of the geometry. The element order was also chosen to be quadratic for a better representation of the geometry, improvement of the accuracy for the interpolation, and minimisation of the error from discretisation. Examples of cross-sections through the mesh are shown in Figure 5.49.

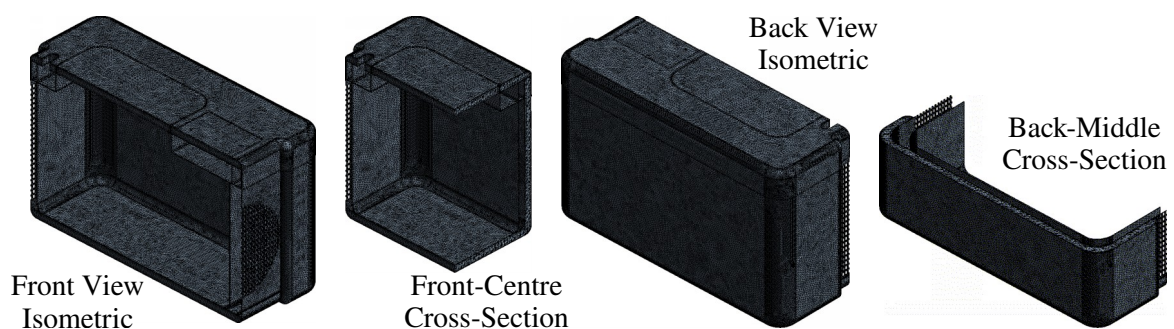


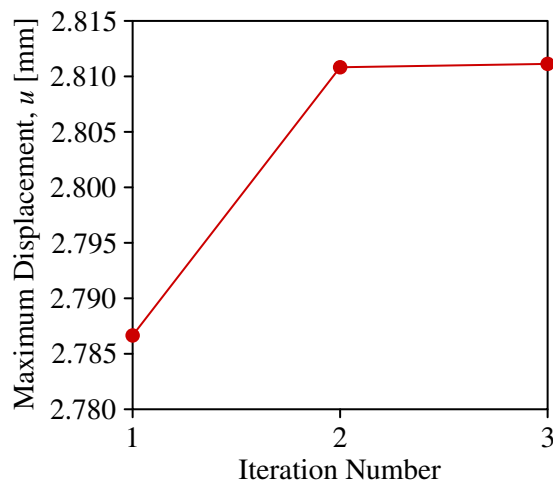
Figure 5.49: Examples of the initial mesh with cross-sections of various views.

The solution setup was initialised using an iterative solving method, since the model was fairly large and iterative solving methods are generally more suited to large models compared to and faster with less storage requirements than direct solving method. Due to the chosen materials and contacts, a linear analysis was used through the assumptions of the stress linearly relating to the strain from displacement and small displacements with these displacements having no impact the behaviour of the structure and no chances of stability failure through buckling. The applied force of 310N was uniformly distributed

over the top surfaces, excluding the indent for the solar panel, to emulate stacking. The relevant properties to monitor included the resulting displacement, equivalent stress, and safety factor.

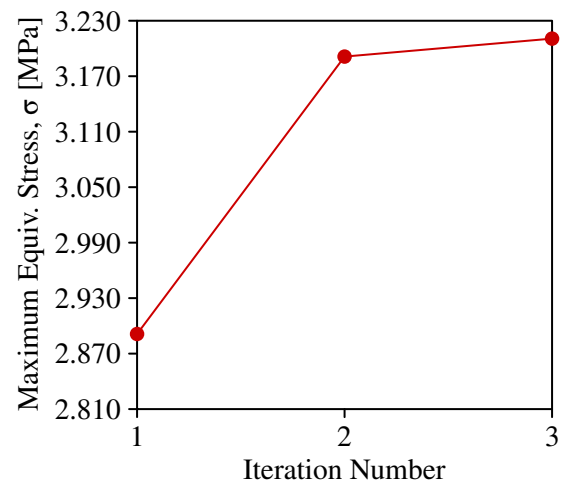
The maximum displacement and stress for each of the iterations are listed with graphs of the convergence in Figure 5.50 and Figure 5.51 respectively. The final mesh consisted of 1435618 elements constituted by 2703669 nodes with the change in maximum displacement between meshes developing from 0.863% to 0.010% and change in maximum stress between meshes developing from 9.85% to 0.642%. The final results after three iterations are shown in Figure 5.52 with contours of displacement and Figure 5.53 with contours of stress. Notably, the maximum displacement was 2.811mm at the centre of the lid, which was expected due to the lack of support allowing for increased bending compared to the edges. The maximum stress was 3.212MPa and located at the outer corner of the indent for the solar panel near a stress concentration due to the change in geometry. At the plane considered in the basic analytical predictions, the average displacement was 0.018mm and average stress was 12.26MPa, which respectively corresponded with a percentage difference of 57.1% and 19.6% with the analytically calculated displacement of 0.010mm and stress of 10.07MPa. As mentioned, it was expected for this prediction of the actual displacement and stress to be greater than the calculated displacement and stress due to the disregard for the possible stress concentrations and bending within the structure in the analytical calculations. The close alignment in magnitudes, calculated with Equation 5.40 to be within 13.6% and 8.17% for polystyrene and ABS respectively, reinforced the prospects for validity.

$$\psi = 2 \left| \frac{\log(\phi_1) - \log(\phi_2)}{\log(\phi_1) + \log(\phi_2)} \right| \times 100\% = 2 \left| \frac{\log(\phi_1/\phi_2)}{\log(\phi_1\phi_2)} \right| \times 100\% \quad (5.40)$$



#	Elements	Nodes	u [mm]	% Diff.
1	1110797	2178715	2.7867	-
2	1361421	2572628	2.8108	0.863%
3	1435618	2703669	2.8111	0.010%

Figure 5.50: Convergence of maximum displacement within 2% through refinement of the mesh.



#	Elements	Nodes	σ [MPa]	% Diff.
1	1110797	2178715	2.8921	-
2	1361421	2572628	3.1917	9.847%
3	1435618	2703669	3.2122	0.642%

Figure 5.51: Convergence of maximum stress within 2% through refinement of the mesh.

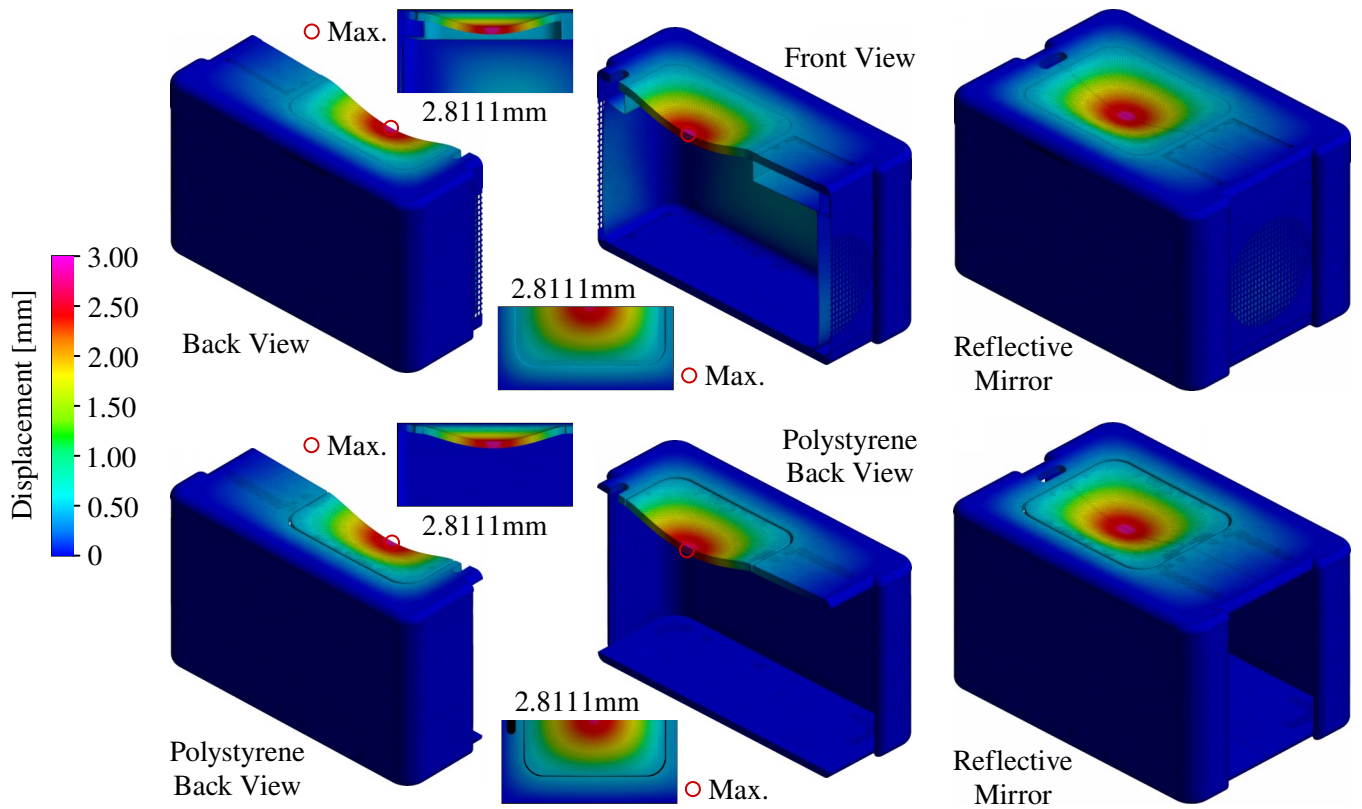


Figure 5.52: Contours of displacement with deformation scaled by a factor of 14, reflective mirroring to display the whole enclosure, views of the insulation in isolation, and highlights of the critical regions.

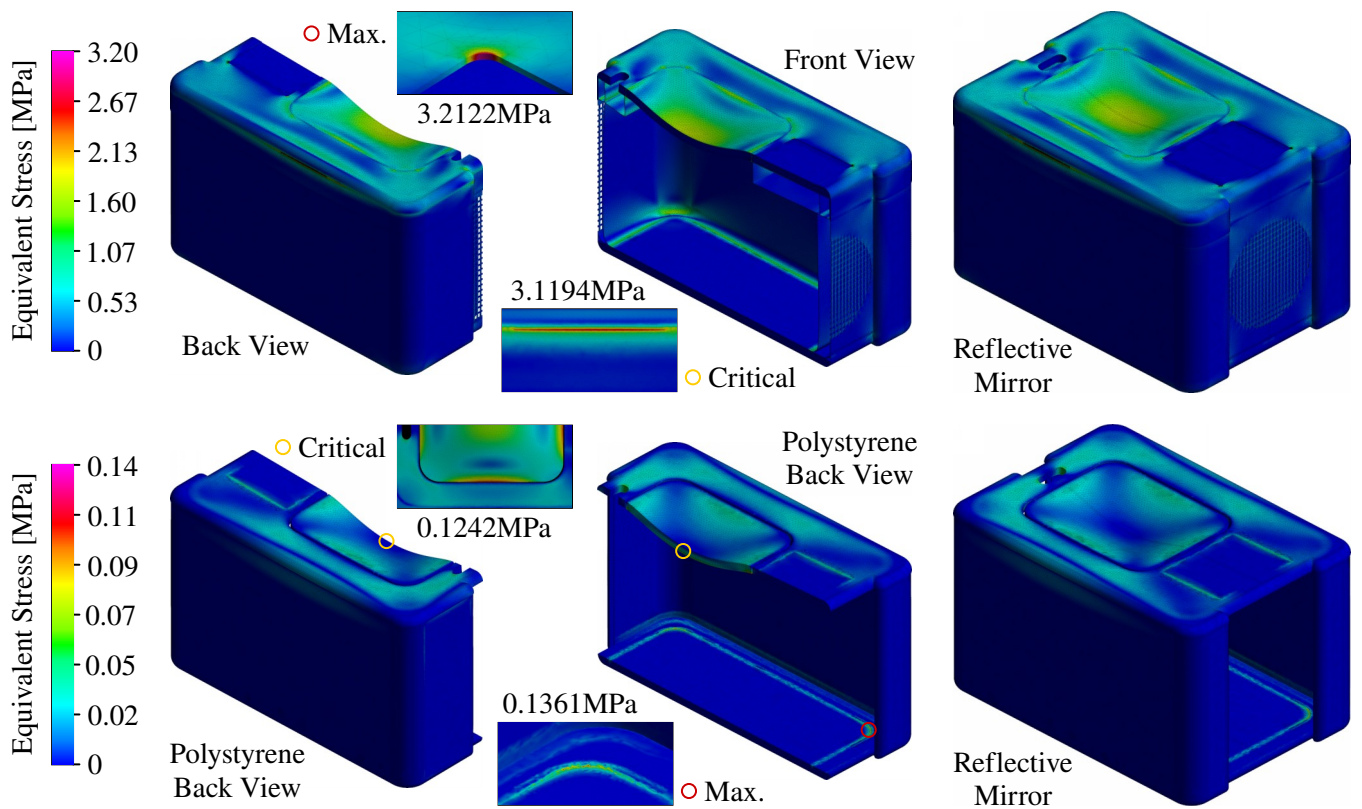


Figure 5.53: Contours of stress with deformation scaled by a factor of 14, reflective mirroring to display the whole enclosure, views of the insulation in isolation, and highlights of the critical regions.

To judge the safety since the polystyrene would fail at a lower yield strength of only 0.224MPa compared to the yield strength of ABS at 41.37MPa, the safety factor was evaluated with a preference for a value above 1.2 to guard against uncertainties and possible errors in the modelling and discretisation. The results are shown in Figure 5.54. The safety factor for the ABS was fairly high above 8.0 throughout the model, but the insulation experienced low safety factors at critical regions, as isolated in Figure 5.54. The minimum safety factor was 1.644 at the bottom corners, while other low safety factors below 2.0 occurred at the centre and edges of the lid, where the bending was severe with the largest displacements. Although the high safety factor of the ABS indicated that the thickness of the walls could be universally decreased from 1.2mm, this would result in a higher displacement of the composite of ABS and polystyrene which would lead to an unsafe stress experienced in the polystyrene as a consequence, while varying the thicknesses for the ABS and polystyrene to depend on the stress would also affect the insulation from heat transfer. Nevertheless, these results were still above the desired value of 1.2. Thus, the optimised strength of the structure was expected to be adequate to withstand the loading from two other fully loaded enclosures of 15.80kg each being stacked on top of it.

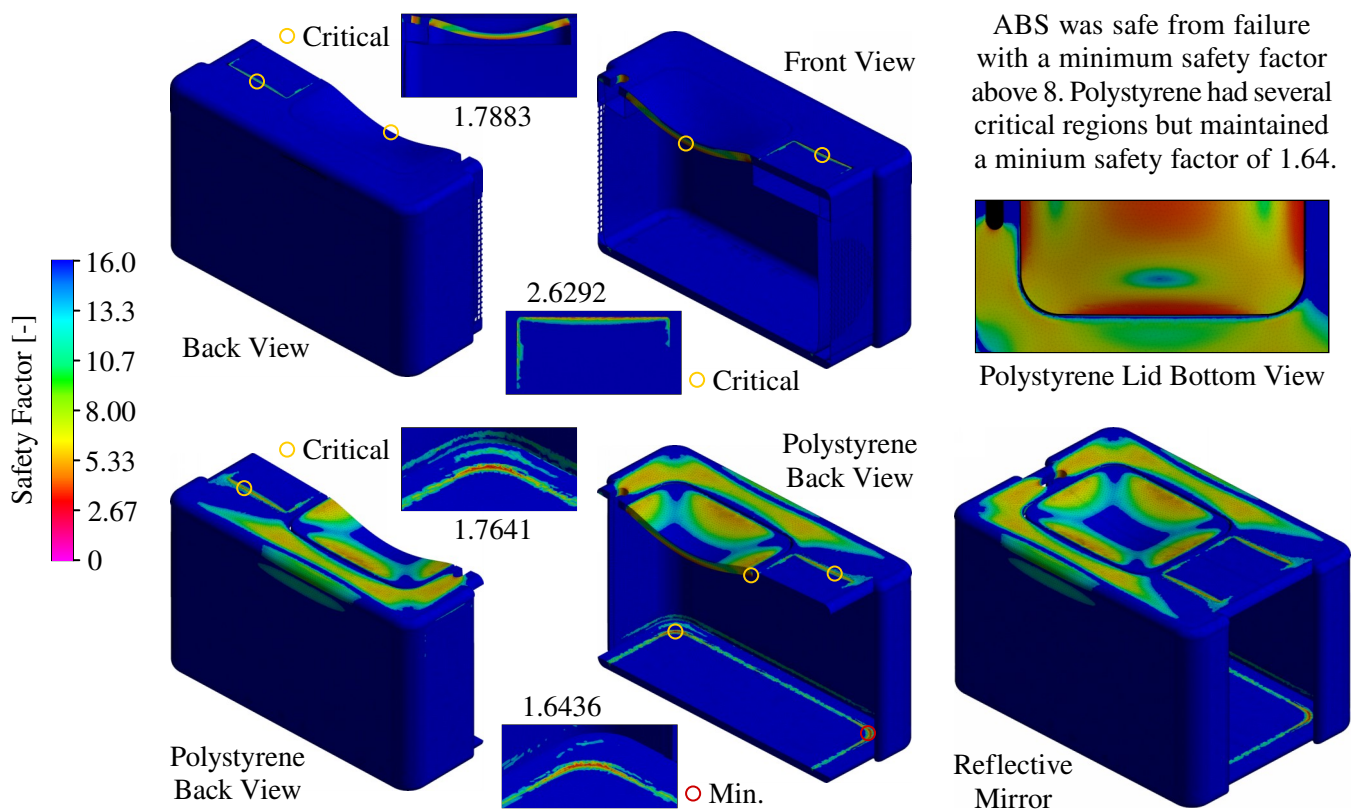


Figure 5.54: Contours of safety factor with deformation scaled by a factor of 14, reflective mirroring to display the whole enclosure, views of the insulation in isolation, and highlights of the critical regions.

6 PRACTICAL EXPERIMENTATION

The practical experimentation allowed for assessment of the predictions of the previous analysis and investigation of the research question into the viability to employ evaporative cooling for the extension of the shelf life of common fruits and vegetables. The construction of the prototype involved sourcing the appropriate electronic components and structural materials from local resellers and suppliers, where the overall cost of the electronic components and materials were also estimated. The tests with the prototype spanned three weeks and involved monitoring a variety of environmental conditions with considerations for the energy storage, insolation exposure, cooling pad materials, storage of fruits and vegetables, and discussion of performance in relation to previous research and existing products.

6.1 ELECTRONIC COMPONENTS

For the electronic components, it was necessary for a collection of photovoltaic cells forming a solar panel to convert electromagnetic energy into electrical energy, means of energy storage to collect excess electrical energy as chemical energy, motor to spin the radial fan, and solar power management module to receive the electrical energy from the solar panel and control the distribution between the energy storage and motor. These components were sourced from local suppliers based on availability and cost. The interactions between the components are illustrated with the schematic in Figure 6.1.

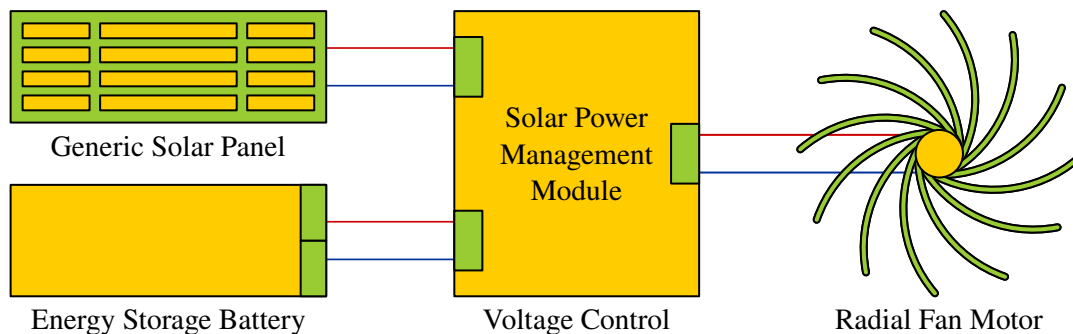


Figure 6.1: Interactions between the solar panel, battery, motor, and power management module.

6.1.1 SOLAR PANEL

Based on the flow simulation analysis, it was predicted for the radial fan to require power of approximately 1.210W. This would then be compounded due to the inefficiencies in the motor spinning the radial fan and, assuming a conservative efficiency of 60% for a brushless motor, the required power would be estimated to be at least 2.017W. As mentioned in Section 2.6, the standard conditions under which solar panels are rated for industry specification include a temperature of 25°C, insolation intensity of 1000W/m², and air mass coefficient of 1.5 [51]. The expected maximum average insolation intensity was approximately 420W/m² and, so, it was practical to apply a safety factor of 2.38 and anticipate a required power of at least 4.800W. The maximum average insolation intensity was considered since the

energy storage would provide extra power when the insolation intensity was insufficient. In addition, an air mass coefficient of 1.5 also corresponded with regions at approximately 48.2° in latitude, but a lower air mass coefficient around 1.0 to 1.2 would improve performance and could be presumed for regions between 0° and 25° in latitude depending on the time of year and altitude.

The chosen apparatus for prototyping was a generic solar panel integrating 60 individual mono-crystalline cells connected in sets on a printed circuit board with polyethylene terephthalate film for enhanced material stability, wear resistant, and non-toxicity. The rated power was 6.0W with an operating voltage of 12V and maximum current output of 0.50A. The dimensions were compact with a length of 200mm, width of 170mm, and height of 3mm for an overall power density of 176.5W/m² under standard conditions. The actual area occupied only by the cells was approximately 0.0375m² for a power density of 160W/m² and implied an efficiency of 16.0% when considering the 1000W/m² under standard conditions, which aligned with prospects for mono-crystalline silicon cells between 13% and 19%. The front and back photographs of the solar panel are included in Figure 6.2.

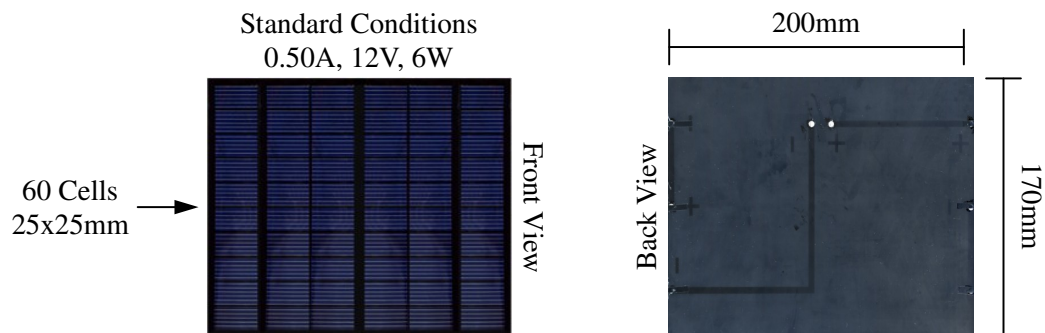


Figure 6.2: Front and back photographs of the 0.50A 12V 6.0W generic solar panel.

6.1.2 ENERGY STORAGE

An energy storage was required to provide power when the power output from the solar panel was inadequate due to shading or degraded insolation intensity. The most inexpensive and simple means of energy storage available was a lithium-ion battery. Based on Table 2.2, a lithium-ion battery was chosen over lead-acid, nickel-cadmium, and nickel-metal hydride batteries, because it was expected to offer superior performance durability and energy density relative to their cost and availability. As mentioned in Section 2.6.3, there was the possibility of using a high-capacity capacitor, but it was expected for long periods of gradual charging to be available when the solar panel operates abundantly due to excess insolation with shorter periods of gradual discharging when the solar panel operates deficiently due to obstructive shading. This diminished the primary advantage of a rapid rate of charging and discharging and escalated the inopportune disadvantages of a low energy density, low life cycle, high self-discharge rate, and progressive voltage loss compared to lithium-ion batteries.

A smaller 14500 battery with an operating voltage of 3.7V and lower capacity of 0.8A.hr was selected to test the performance under a limited backup power supply for short periods of time, such as operating

during shading due to clouds. A larger 26650 battery with an operating voltage of 3.7V and higher capacity of 5.0A.hr was selected to test the performance with a nearly inexhaustible backup power supply for extended periods of time, such as operating into the early evening. Assuming the batteries were fully charged with capacities of 2.96W.hr and 18.5W.hr, solar panel was completely shaded without assistance for charging, and steep current of 0.25A was continuously drawn at 12V, the lower capacity battery would last for approximately 59.2min, while the higher capacity battery would last for approximately 370min. The batteries and their standard dimensions are pictured in Figure 6.3.

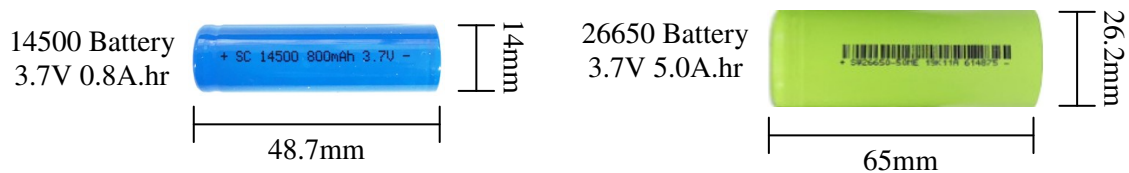


Figure 6.3: Photographs of the lithium-ion 14500 battery (left) and 26650 battery (right).

6.1.3 POWER MANAGEMENT MODULE

The power management module was required to deliver a regulated output, such that the solar panel continuously charged the battery to provide a reliable and consistent current and voltage to the connected load. The chosen power management module, shown in Figure 6.4, was the DFRobot Solar Power Manager SKU DFR0535 which allowed for a regulated output up to 0.5A at 12V, 0.5A at 9V, 1.5A at 5V, and 1.0A at 3.3V with the incorporation of a battery management system. The input from the solar panel for charging supported a voltage from 7V to 30V up to 20W with a charge efficiency of approximately 78% depending on the input - it was also possible to use a micro-USB connection for charging, in which case the charge efficiency was approximately 84% [145]. These inputs supported the charging of a lithium-ion battery at a voltage of 3.7V. The boost efficiency from the 3.7V of the battery to the output was between 82% and 96% depending on the output and load [145].

The battery management system allowed for charging up to 2.0A through a charge cycle utilising trickle, constant current, and constant voltage charging and featured multiple protection circuits with over-charge, over-discharge, reverse current, reverse connection, and overheating protection through

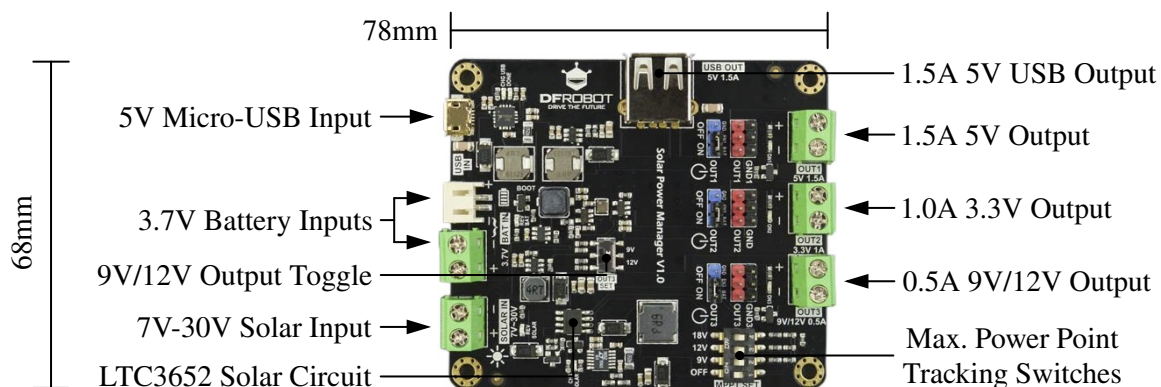


Figure 6.4: Photograph of the DFRobot Solar Power Manager SKU DFR0535.

a charging cut-off voltage of 4.2V and discharging cut-off voltage of 2.4V [145]. There was also protection at the output against short circuiting and overheating and at the input from the solar panel with backflow and reverse connection protection [145]. The outputs from the pin headers, terminals, or USB were regulated with an on-board high capacity aluminium electrolytic capacitor and multi-layer surface mounted ceramic capacitor to filter any residual distortions for stable performance [145].

The power management module also featured maximum power point tracking to maximise the efficiency of the solar panel by extracting the maximum power under all conditions. This is a technique which uses a control circuit to track the balance between the output of the solar panel, resulting from the current insolation intensity and solar panel temperature, and characteristics of the connected load with the aim of optimising the efficiency of power transferred by varying an auxiliary resistance [146]. In other words, the maximum power point tracking attempts to sample the output of the solar panel and apply an appropriate auxiliary resistance in conjunction with the connected load to obtain the maximum power for any given environmental conditions [84, 146]. This can be graphically identified in Figure 2.27 through the variation in the current and voltage under different situations, where the maximum power point occurs when the product of the current and voltage is at a maximum.

6.1.4 RADIAL FAN MOTOR

As reviewed in Section 2.5.3, the types of direct current motors include brushed and brushless configurations. However, apart from affordability, one of the overriding criterion for the motor was the integration through the profile or form factor to offer the most appropriate implementation. So, it was only possible to use a brushless motor as a brushed motor was not available in a compatible profile, which was acceptable as a brushless motor already offered more relevant advantages, given the operating requirements, at the expense of a slightly increased cost compared to a brushed motor.

A compact profile used in conventional fans was ideal, where the arrangement is inverted with an external rotor situated around the internal stator, such that it would be possible to mount the blades directly on the rotor without the need for a shaft. Unfortunately, it was not possible to directly source a suitable motor with this profile, so the foremost available option was to salvage a suitable motor from a conventional fan. The chosen fan was the Sunon MFC0251V2-0000-A99, as seen in Figure 6.5, which was initially designed to operate using a rated current of 0.25A at a rated voltage of 12V with a specific operating point at 2700rev/min \pm 10% for an air flow of 0.0439m³/s [147, 148]. The performance curve is shown in Figure 6.6 and indicated that the relationship between torque, relating to the static pressure, and angular velocity, relating to the flow rate, was fairly linear. This relationship was favourable as it was expected for the static pressure and torque to increase once fitted with the blades for the radial fan, while the angular velocity could decrease to about 600rev/min to generate the desired air flow.

With regards to the motor, it featured a single phase and four poles which implied that the internal position sensors reported signals based on the timing for the rotation demonstrated in Figure 6.7.

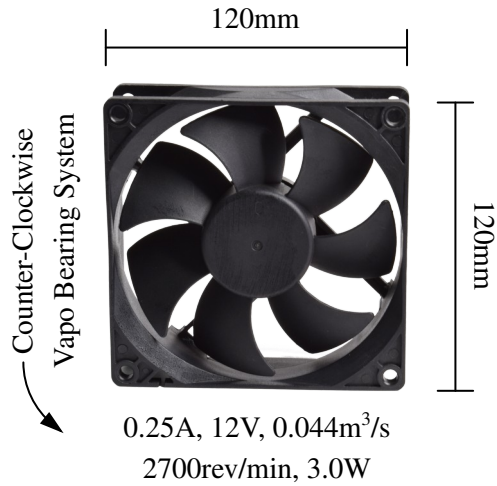


Figure 6.5: Photograph of the original axial Sunon MFC0251V2-0000-A99 before modifying.

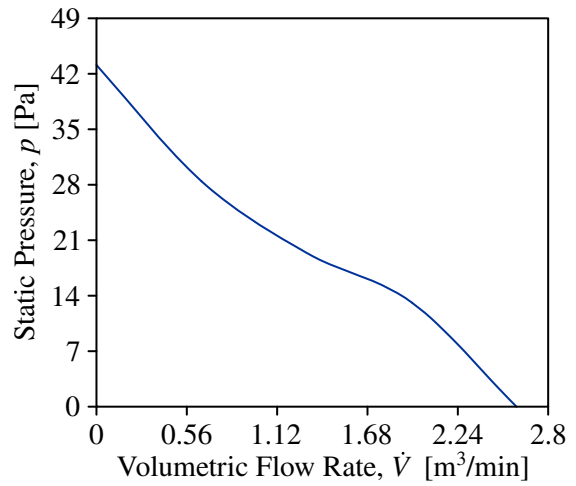


Figure 6.6: Performance curve for the original axial Sunon MFC0251V2-0000-A99 [147, 148].

The operating voltage range was between 4.50V and 13.8V with a drawn current up to 0.288A for a maximum power of 3.46W [148]. The motor also had an expected life of about 70000hr at 40°C with a relative humidity of 65% [148]. Moreover, there was protection from overheating to stop the motor if it was prevented from rotating and protection from an incorrect polarity connection, such that the direction of rotation was always counter-clockwise when viewed from the front [147, 148]. The hub contained a precise vapo-bearing system using magnetic levitation for improved stability to eliminate possible wobbling, while remaining dust-proof for improved life expectancy [147, 148].

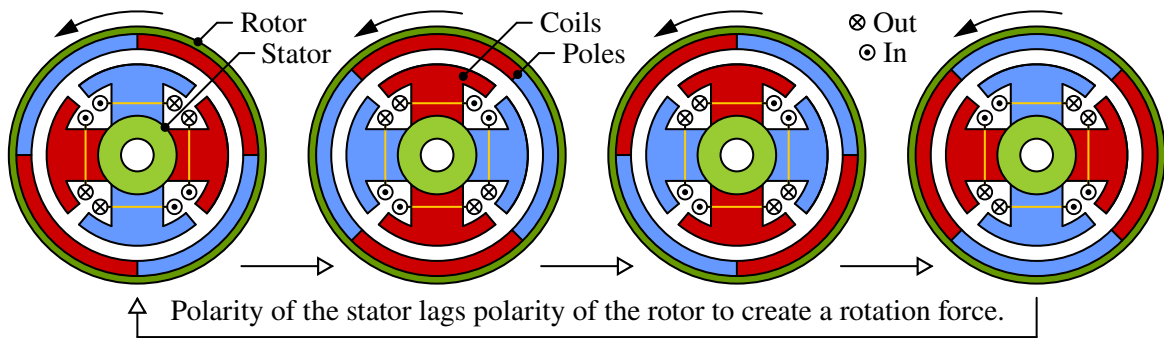


Figure 6.7: Timing for the polarity of the stator based on the rotational position of the rotor.

The angular velocity of the motor fitted with the blades for the radial fan was measured by connecting the motor to an external power supply up to 1.0A at 12V and using a slow-motion video camera to calculate the value. The camera was embedded in a Xiaomi Redmi Note 8 Pro featuring a Samsung Isocell GW1 S5KGW1 as the ultra-high 64Mpx 1/1.72" image sensor using Tetracell technology. The image sensor is a complementary metal-oxide-semiconductor sensor with a pixel size of 0.8 μ m and resolution up to 9280px by 6944px for photographs and 7680px by 4320px at 24fr/s for videos [149]. The camera also advertised a lens f-stop aperture of f/1.89, optical format of 9.21mm, focal length of 5.43mm or 26mm wide-angle equivalent, viewing angle of 68.8°, electronic rolling shutter, and phase-detection autofocus using paired masked pixels on the image sensor [149]. The images were

processed on-board the device with the MediaTek Helio G90T system-on-a-chip using a MT6785V/CC central processor, Mali-G76 3EEMC4 graphics processor, and 5.77GB of system memory [150]. The slow-motion video was recorded at a resolution of 1280px by 720px with 240fr/s. Analysing the frames of the slow-motion video, it was found that 1rev of the radial fan took 28.3fr or 0.118s on average from 20rev. Thus, it was estimated that the angular velocity was approximately 508.8rev/min, which was adequately in line with the expectations following from the analysis development.

6.2 STRUCTURE CONSTRUCTION

For an inexpensive but accurate prototype, the structure was constructed using ABS sheets and 3D printed parts through fused deposition modelling on a Creality CR-10S Pro. The 3D printed parts included the rounded corners for the air flow and blades for the radial fan, where a ring to connect the

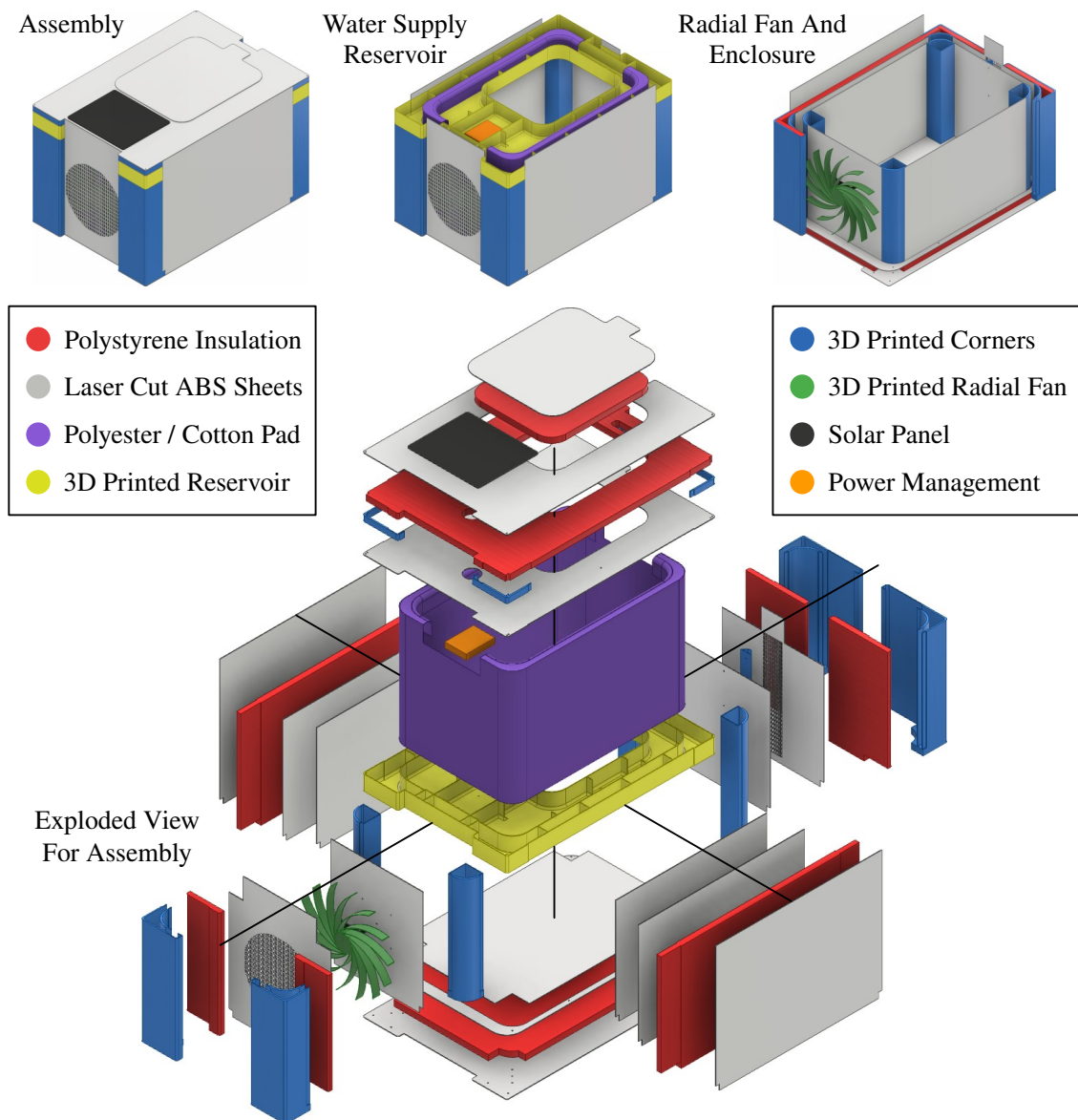


Figure 6.8: Rendering of the construction of the overall assembly with the exploded view.

blades was used for stability and to limit oscillations rather than the ribs which were initially included in the CFD simulations. The polystyrene insulation was then inserted and joined to the ABS sheets using Pattex High Tack, which is a multi-purpose adhesive compatible with a wide range of surfaces. The total mass of the construction was 6.623kg with 5.819kg from the structure, 0.387kg from the insulation, 0.377kg from the electronic components, and 0.0445kg for the cooling pad of polyester or 0.137kg for the cooling pad of cotton ring spun. A rendering of the overall assembly, cutaway sections, and exploded view is shown in Figure 6.8. A collection of photographs of the final construction for prototyping is shown in Figure 6.9 with the electronic components installed.

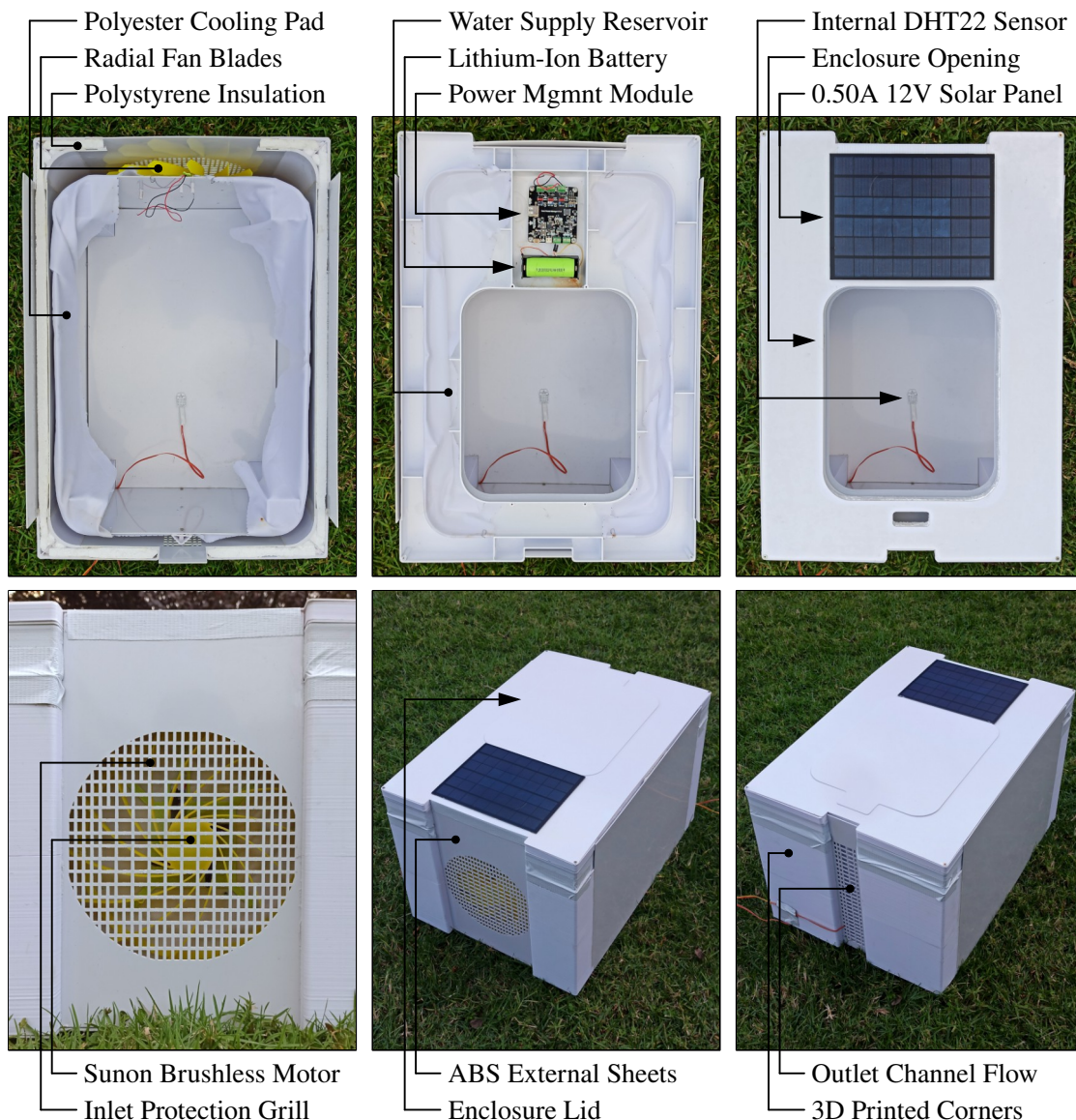


Figure 6.9: Photographs of the construction of the assembled prototype for practical experimentation.

6.3 COST ANALYSIS

To ensure the performance of the prototype was an accurate reflection of a product which could be manufactured at an extremely affordable cost, a cost analysis was performed based on the prototype

for the electronic components and materials of the structure. The costs for the electronic components were sourced from local resellers and can be seen as an upper limit for the estimation. The costs for the materials of the structure were determined through the typical cost per unit mass found from various sources and can be seen to be premised on an order of magnitude or ratio budget estimation using similar historical cost data with an expected accuracy within 20% [151]. Although highly volatile, the exchange rate between the South African Rand and Euro was discretionally taken to be €1 = R17.93 as of 1 Jan. 2021 (in 2020, the exchange rate varied between €1 = R15.96 to €1 = R20.78) [152]. A summary of the costs is presented in Table 6.1 with separation of the electronic and material costs.

Table 6.1: Summary of the estimated electronic and material costs with various configurations.

Item		Battery Configuration [R]			Battery Configuration [€]		
		None	Low	High	None	Low	High
Electronic	Generic Solar Panel 6W	168	168	168	9.37	9.37	9.37
	Generic 14500 Battery 0.8A.hr	0	34	0	0	1.90	0
	Generic 26650 Battery 5.0A.hr	0	0	158	0	0	8.81
	Sunon MFC0251V2 Fan Motor	130	130	130	7.25	7.25	7.25
	Voltage Management Module	0	68	68	0	3.79	3.79
	Sub-Total	298	400	524	16.61	22.30	29.21
Material	5.819kg ABS at R32.8/kg	191			10.65		
	0.387kg Polystyrene at R49.4/kg	19			1.06		
	Cotton / Polyester Cooling Pad	38			2.12		
	Sub-Total (without Safety Factor)	248			13.83		
	Sub-Total (with Safety Factor)	298			16.62		
Overall Total (with Safety Factor)		596	698	822	33.23	38.92	45.83

6.3.1 ELECTRONIC COSTS

The generic solar panel had a retail cost price of R168, which equated to approximately R28/W. The 14500 battery with a capacity of 0.8A.hr had a retail cost price of R34, which equated to approximately R42.5/(A.hr), while the 26650 battery with a capacity of 5.0A.hr had a retail cost price of R158, which equated to approximately R31.6/(A.hr). The radial fan motor had a retail cost price of R130 for the original Sunon MFC0251V2-0000-A99 axial fan, but this may decrease by as much as 20% if it were to be possible to only purchase the motor or a similar motor separately. Although it was not thoroughly scrutinised, there may also be a possibility of assessing the Sunon EEC0251B1-0000-A99 for a retail cost price of R136, as it operates at a rated current of 0.451A and rated voltage of 12V with a specific operating point at 3100rev/min±10% for an air flow of 0.0509m³/s [147].

With particular attention, the DFRobot Solar Power Manager SKU DFR0535 had a retail cost price of R495. This was very high and would be unsuitable for a production unit. However, it was chosen as

it offered expandability and convenience for the practical experimentation. Using the results of the practical experimentation, a more affordable power management module could be selected based on more concentrated specifications. It could reasonably be expected for this power management module and any other auxiliary components to have a retail cost price between R40 and R159.

For example, the Waveshare Solar Management Module 16120, included in Figure 6.10, accommodates a regulated output up to 1.0A at 5V and also supports maximum power point tracking with an input from the solar panel at a voltage from 6V to 24V at a charge efficiency of approximately 78% [153]. Since this power management module only outputs at a voltage of 5V, it could then be coupled with a boost voltage regulator to balance the drawn power against the angular velocity of the radial fan. The MT3608 regulator, included in Figure 6.11, is common and inexpensive with an acceptable input voltage from 2V to 24V and adjustable output voltage from 2V to 28V with a maximum output current of 2A [154]. A disadvantage of using a boost voltage regulator would be a slightly decreased efficiency, where the boost efficiency of approximately 86% from the Waveshare Solar Management Module 16120 would be compounded by the MT3608 regulator with an efficiency from 34% to 93% depending on the output [153, 154]. The Waveshare Solar Management Module 16120 has a retail cost price of R139, but there are other more inexpensive power management modules available, such as the TP4056 for R20, J5019 for R48, MH-CD42 for R48, and CN3065 for R98, although these may have less features and protections. The MT3608 regulator has a retail cost price of R20.

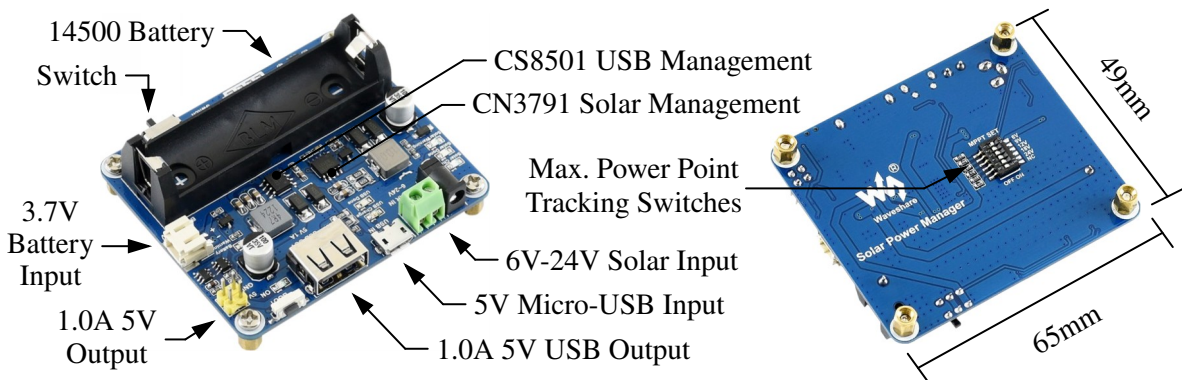


Figure 6.10: Top and bottom photographs of the Waveshare Solar Management Module 16120.

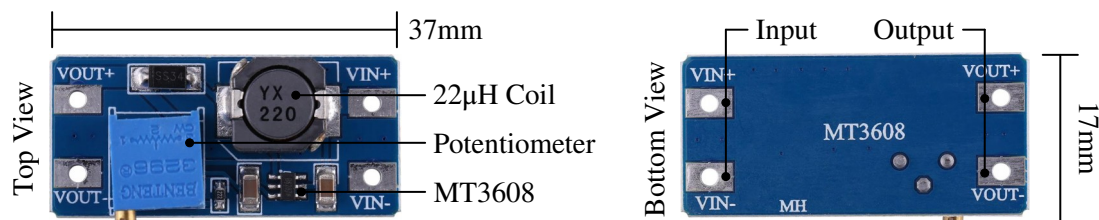


Figure 6.11: Top and bottom photographs of the MT3608 regulator.

Thus, assuming the retail cost prices from local resellers were an upper limit for the estimation, the cost price for the electronics with the 26650 battery was estimated to be less than R524 or approximately €29.21 and the cost price for the electronics with the 14500 battery was estimated to be less than R400

or approximately €22.30. If it was imperative for extreme affordability and inconsistent performance was tolerable, the motor could be connected directly to the solar panel without a battery or power management module and the cost price for the electronics without a battery or power management module was estimated to be less than R298 or approximately €16.61. These costs may be further reduced by up to 10% through bulk ordering and economies of scale for mass manufacturing [151].

6.3.2 MATERIAL COSTS

The cost per unit mass is approximately R32.8/kg for ABS and R49.4/kg for polystyrene, as sourced from the upper limits in ANSYS Granta EduPack 2021 and broadly with local suppliers. As mentioned in Section 6.2, it would be required for approximately 5.819kg of ABS for the structure and 0.387kg of polystyrene for the insulation, which led to a cost of R191 for the structure and R19 for the insulation. As mentioned in Section 5.7, the cost for the cooling pad would be approximately R13 for polyester or R38 for cotton ring spun. Since there may be adjustments before a final product, a safety factor of 1.2 could provide an estimation while allowing for possible modifications. Thus, the standard material cost was estimated to be less than R248 or approximately €13.83 before the application of the safety factor or less than R298 or approximately €16.62 after the application of the safety factor. The investment costs for manufacturing, labour, and equipment were not investigated, but these costs would be distributed over each unit produced and dramatically diminish per unit as the number of units increased through mass manufacturing. However, to remain below €19, these investment costs would need to be distributed up to 12.52% of the standard material cost with up to €2.38 per unit.

6.4 MONITORING EQUIPMENT

The monitoring of the temperature and relative humidity was essential in measuring the performance of the prototype to determine if it was successful in fulfilling the requirement to achieve a temperature decrease of at least 11°C and relative humidity increase of at least 35%. This required precise sensors to constantly measure the external and internal temperatures and relative humidities, microcontroller to process the signals from the sensors, and laptop to store the received data.

6.4.1 PROPERTIES MEASUREMENT

To monitor the temperature and relative humidity, two DHT22 (also known as RHT03 or AM2302) composite sensors were chosen and installed for their accuracy, stability, and cycle endurance. The first sensor was placed internally in the enclosure towards the rear beneath the lid. The second sensor was placed externally outside in the shade to prevent direct insolation but permit exposure to scattered and reflected insolation and natural convection in the surroundings. This allowed for a measure of the internal changes in the enclosure resulting from the evaporative cooling, which could be aggregated against the external changes to quantify the cooling effect and if it was substantial.

The DHT22 sensor is shown in Figure 6.12 with the installation locations in Figure 6.13 and was able to precisely measure temperature with an accuracy of $\pm 0.5^{\circ}\text{C}$, sensitivity of 0.1°C , repeatability of $\pm 0.2^{\circ}\text{C}$, and range from -40°C to 80°C ; and relative humidity with an accuracy of $\pm 2\%$, sensitivity of 0.1% , repeatability of $\pm 1\%$, and range from 0% to 99.9% [155]. The temperature was measured using a high-precision negative temperature coefficient sensor, where a thermistor or thermal resistor made from powdered metallic oxides is encapsulated in a ceramic impermeable material, such that the temperature of the thermistor affects the resistance in an inverse fashion which can then be converted into a measurement of temperature based on a calibrated relationship [155]. The relative humidity was measured using a capacitive moisture sensor, where a moisture holding substrate made from a hygroscopic dielectric material is interposed between a pair of electrodes, such that the amount of water vapour absorbed by the substrate affects the capacitance between the electrodes which can then be converted into a measurement of relative humidity based on a calibrated relationship [155]. The temperature and relative humidity sensors had already been compensated in an accurate calibration chamber with the calibration coefficient being saved in non-volatile one time programmable memory.

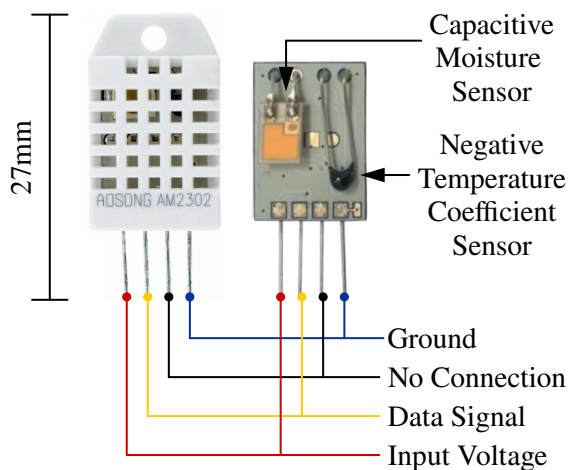


Figure 6.12: Photographs of the DHT22.

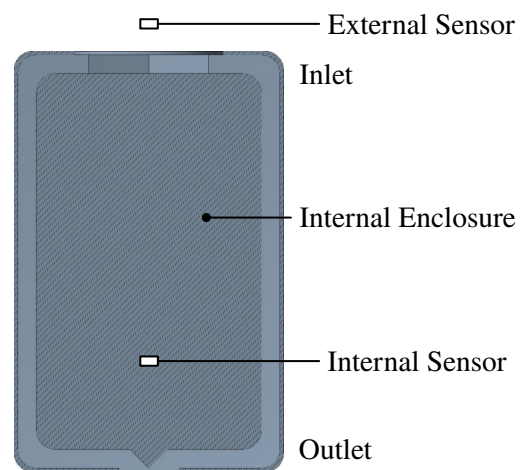
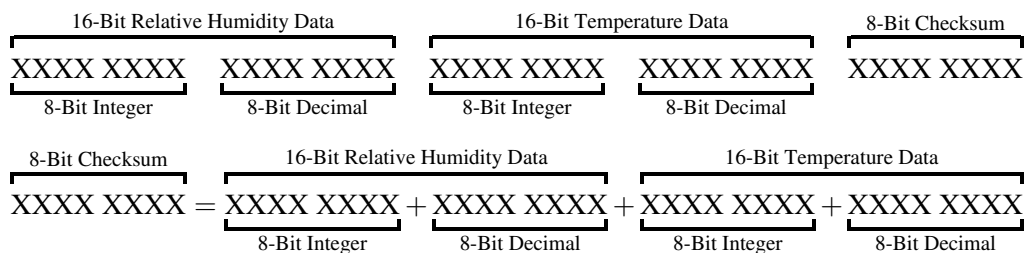


Figure 6.13: Locations of the DHT22.

The DHT22 sensor draws between 1.0mA and 1.5mA and required connections for a source between 3.3V and 6.0V , ground at 0V , and digital output signal for communication with a microcontroller via a one-wire bus for low-speed data and signalling over a single interface [155]. This communication from the DHT22 sensor to microcontroller was comprised of integer and decimal parts for the temperature and relative humidity with a checksum to confirm successful transmission, as described as follows:



6.4.2 MICROCONTROLLER AND DATA

The chosen microcontroller was an Arduino Uno Revision 3 based around the Microchip 8-Bit ATmega328P at a clock speed of 16MHz with 2kB of static random-access memory, 1kB of electrically erasable programmable read-only memory, and 32kB of programmable flash memory [156]. The Arduino Uno offered a regulated 5V supply up to approximately 0.4A and was equipped with six analog input pins and fourteen digital input/output pins for communication with external sensors. The Arduino Uno was programmed using the Arduino Integrated Development Environment and powered over USB from an HP Notebook 14-AN013NR to which serial communication data was transferred. The connections of the microcontroller to the DHT22 sensors are laid out in Figure 6.14.

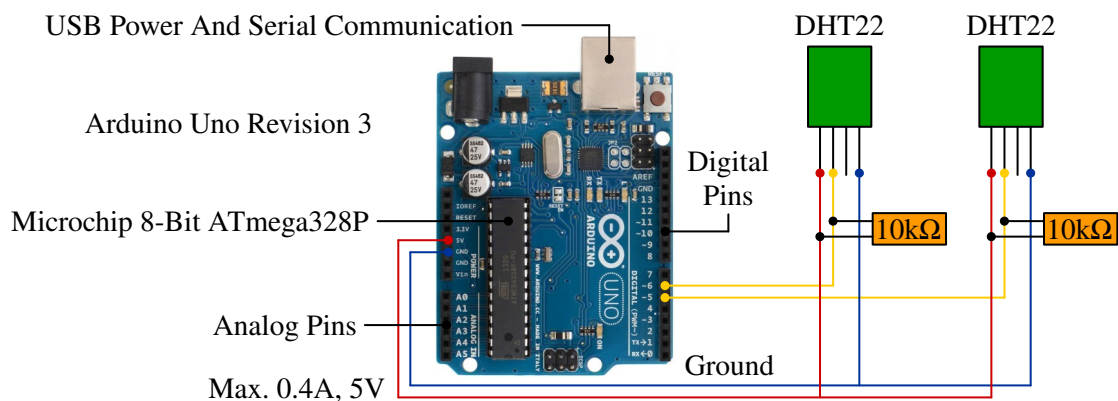


Figure 6.14: Photograph and connections of the Arduino Uno Revision 3 for recording data. A 10k Ω resistor was connected between the supply voltage and data pin as a pull-up resistor to reduce noise.

6.5 DATA AND RESULTS

The practical experimentation using the prototype allowed for realistic implementation and accurate evaluation of the performance through various tests considering the cooling pad and influences from fruits and vegetables. Before the tests were performed, the energy storage was considered to confirm the viability of the 14500 battery and 26650 battery to act as adequate means of energy storage for the radial fan during operation. This involved measuring the time for which the batteries could independently power the radial fan through the power management module without support from the solar panel.

For the tests, the cotton ring spun and polyester were each considered over a period of six days, where the enclosure was shaded from direct insolation (with only the solar panel exposed) for three days and exposed to direct insolation for three days in each of the two tests - during these tests, the internal enclosure was empty and the supply reservoir was filled each morning. The test was then repeated for a third iteration for seven days with a sample of fruits and vegetables within the internal enclosure, while an identical sample of fruits and vegetables were stored in a regular box to compare the changes in health and possible extension of shelf life. In this test, the health of the fruits and vegetables was

based on the appearance, firmness, texture, and mass loss. As mentioned, the temperature and relative humidity were monitored within the enclosure and in the surroundings using DHT22 sensors. It should be emphasised that the uncertainty of these sensors was $\pm 0.5^{\circ}\text{C}$ and $\pm 2\%$.

Throughout the tests, the cloud coverage was qualitatively viewed with satellite photographs of the regions in Gauteng, South Africa, while data was accessed through the SAURAN as an indication of the received insolation. Although a variety of environmental conditions would contribute to exploring the versatility of the enclosure, it was still predominantly desirable for an external temperature above 32°C and relative humidity below 50% with minimal cloud coverage and average insolation around $420\text{W}/\text{m}^2$ to judge performance under the expected environmental conditions during operation. As mentioned, there were measurements of the temperature and relative humidity internally within the enclosure towards the rear beneath the lid and externally outside in the shade.

The views of the regional cloud coverage were sourced from satellite photographs accessed from the EUMETSAT Meteosat-11 at 08:00, 12:00, and 16:00. The EUMETSAT Meteosat-11 is a spin-stabilised geostationary satellite at an orbit of 36000km over Europe and Africa to capture imagery with a high rate spinning enhanced visible and infrared imager every 15min with 12 spectral bands and a resolution of 3km for weather forecasting and climate monitoring [157]. The data on the received insolation was collected from the CSIR Energy Centre in Pretoria, South Africa, for the direct normal insolation, diffuse horizontal insolation, and global horizontal insolation, which were averaged between 07:00 to 09:00, 11:00 to 13:00, and 15:00 to 17:00. Although the distance between the test location and CSIR Energy Centre was approximately 48km, it was the nearest source of appropriate data for reference and presented a quantitative overview to complement the satellite photographs of the cloud coverage. The most relevant measurement of insolation was the global horizontal insolation as it resembled the manner in which the solar panel would function under realistic operation.

6.5.1 ENERGY STORAGE FACTORS

To compare the use of the 14500 battery and 26650 battery, the batteries were fully charged, connected to the power management module with only the radial fan, and allowed to operate until completely discharged. The 14500 battery had an open-circuit voltage of 4.16V at the start and 2.81V once discharged, while the 26650 battery had an open-circuit voltage of 4.14V at the start and 2.83V once discharged. With the radial fan connected, the voltage across the 14500 battery was 3.16V at the start and 2.39V once discharged, while the voltage across the 26650 battery was 3.27V at the start and 2.47V once discharged. The 14500 battery lasted 57.85min until the radial fan stopped the first time. The 26650 battery lasted 304.6min until the radial fan stopped the first time. It should be emphasised that these tests considered the period until the radial fan stopped the first time and did not account for the radial fan restarting due to a battery recovery effect, which occurs when the usable charge has not diffused evenly around the battery and may be depleted at the terminals but not internally.

These results were in line with the expectations outlined based on the rated capacity of the 14500 battery to be 2.96W.hr and 26650 battery to be 18.5W.hr. They also indicated that both batteries would offer acceptable performance as long as the periods of shading were less than about 1hr, although this was conservative as it would still be possible for the solar panel to supply reduced power if there was cloud coverage or other obstructions to direct insolation. Thus, both batteries were adequate for operation throughout the day with regards to the expected environmental conditions. The 26650 battery was used for further experimentation for a gauge of the upper limit of performance and to apply the primary focus towards the abilities of the evaporative cooling using forced convection.

6.5.2 COTTON RING SPUN RESULTS

The cotton ring spun test was completed between 11 Feb. 2021 and 16 Feb. 2021 with the enclosure being shaded from insolation from 11 Feb. 2021 to 13 Feb. 2021 and exposed to insolation from 14 Feb. 2021 to 16 Feb. 2021. The cloud coverage experienced during this period is presented in Figure 6.15 with the measured properties of insolation. The conditions during the mornings and middays were fairly clear with only thin and sparse clouds when present, but there was detrimental cloud coverage in the afternoons from 12 Feb. 2021 to 15 Feb. 2021 unfortunately. There was also meaningful rainfall in the evening on 14 Feb. 2021 and in the afternoon and evening on 15 Feb. 2021.

The measured external and internal temperatures are plotted in Figure 6.16 based on a moving average with a period of 1hr in an attempt to smooth local and erratic fluctuations in the measurements. Likewise, the measured external and internal relative humidities are plotted in Figure 6.17 based on a moving average with a period of 1hr. The differences between the external and internal measurements are plotted in Figure 6.18 for the temperature and Figure 6.19 for the relative humidity with highlights of the intervals of particular interest under which the appropriate environmental conditions were experienced with a temperature above 32°C and relative humidity below 50%.

Reading from the important measurements in Table 6.2, the maximum external temperatures recorded were 28.5°C on 11 Feb. 2021, 27.3°C on 12 Feb. 2021, 29.7°C on 13 Feb. 2021, 33.4°C on 14 Feb. 2021, 33.6°C on 15 Feb. 2021, and 33.2°C on 16 Feb. 2021. Meanwhile, the maximum internal temperatures recorded were maintained at 24.1°C on 11 Feb. 2021 (affected by initial conditions), 21.5°C on 12 Feb. 2021, 21.0°C on 13 Feb. 2021, 21.9°C on 14 Feb. 2021, 23.7°C on 15 Feb. 2021, and 19.5°C on 16 Feb. 2021. The external relative humidity tended to vary very widely by decreasing below 50%, as low as 35.2%, during the day and increasing above 65%, as high as 94.9%, during the night. The internal relative humidity remained conveniently above 80% with fluctuations of less than 20% after the first day in the wake of improving from the initial conditions.

The maximum difference between the external and internal temperature was 6.0°C on 11 Feb. 2021, 8.3°C on 12 Feb. 2021, 9.3°C on 13 Feb. 2021, 13.2°C on 14 Feb. 2021, 10.9°C on 15 Feb. 2021, and 13.7°C on 16 Feb. 2021. The maximum difference between the external and internal relative humidity

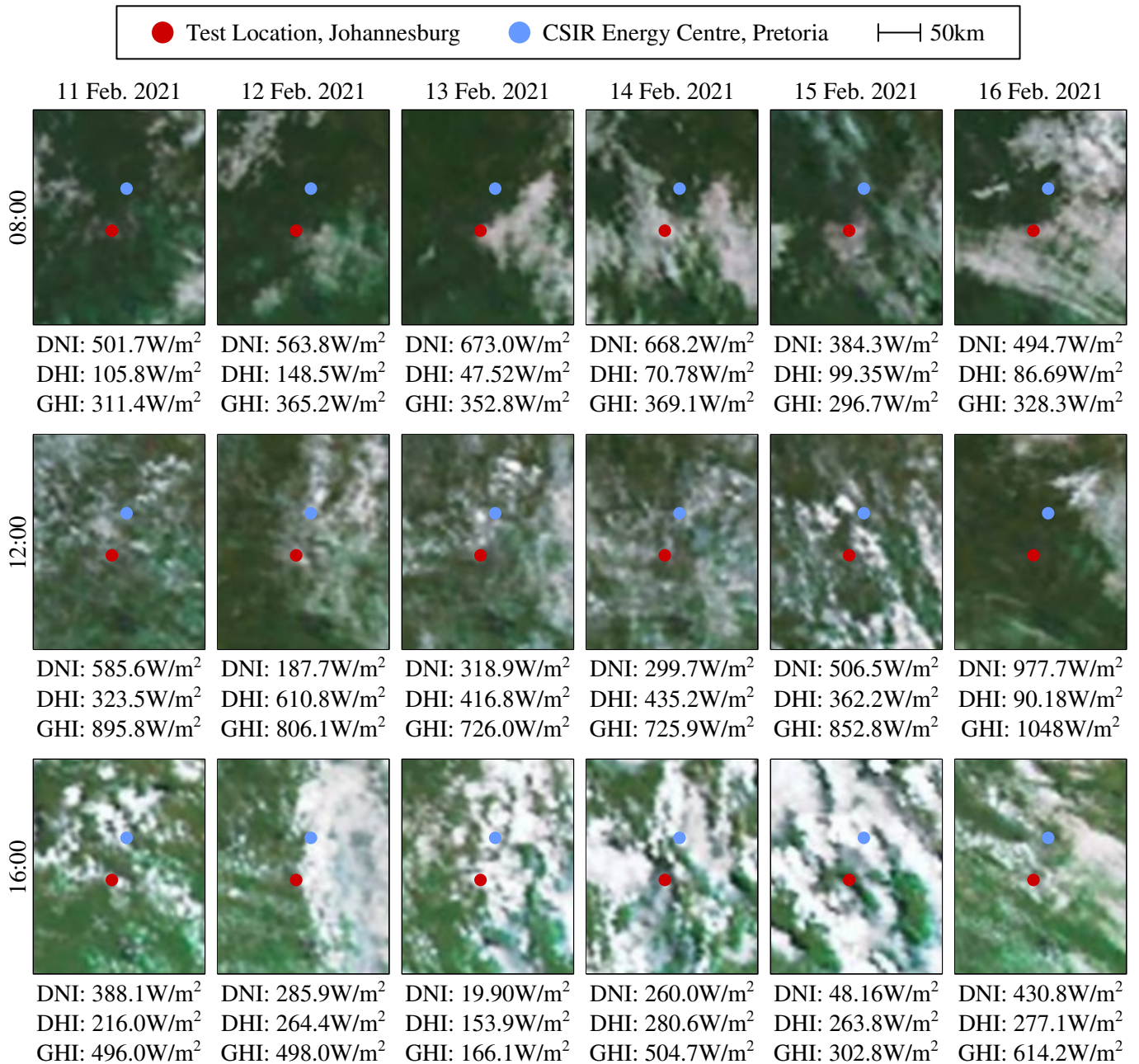


Figure 6.15: Satellite photographs of Gauteng, South Africa, retrieved from the EUMETSAT Meteosat-11 [158] to show the cloud coverage and measurements of insolation intensity in Pretoria, South Africa, retrieved from the SAURAN [38, 39] between 11 Feb. 2021 and 16 Feb. 2021 throughout the day.

was 40.8% on 11 Feb. 2021, 39.2% on 12 Feb. 2021, 39.7% on 13 Feb. 2021, 60.1% on 14 Feb. 2021, 50.9% on 15 Feb. 2021, and 55.7% on 16 Feb. 2021. These differences were most prevalent during the day and became immaterial during the night. During the periods these differences were above 11°C and 35%, the external temperature was above 32°C and external relative humidity was below 50%.

The maximum fluctuations in external temperature throughout the day ranged from 10.2°C on 11 Feb. 2021, 9.1°C on 12 Feb. 2021, 9.7°C on 13 Feb. 2021, 15.8°C on 14 Feb. 2021, 17.6°C on 15 Feb. 2021, and 19.2°C on 16 Feb. 2021. The maximum fluctuations in internal temperature throughout

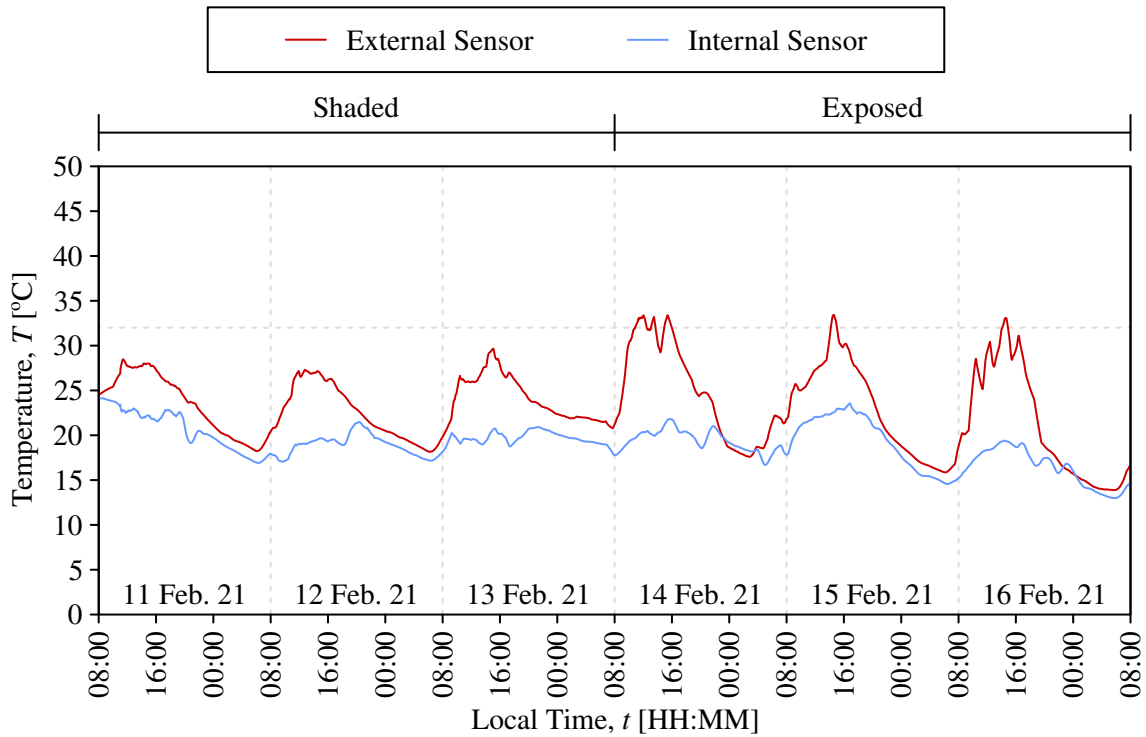


Figure 6.16: Measurements of temperature based on a moving average with a period of 1hr using cotton ring spun as the cooling pad without fruits and vegetables stored in the enclosure during a shaded period from 11 Feb. 2021 to 13 Feb. 2021 and exposed period from 14 Feb. 2021 to 16 Feb. 2021.

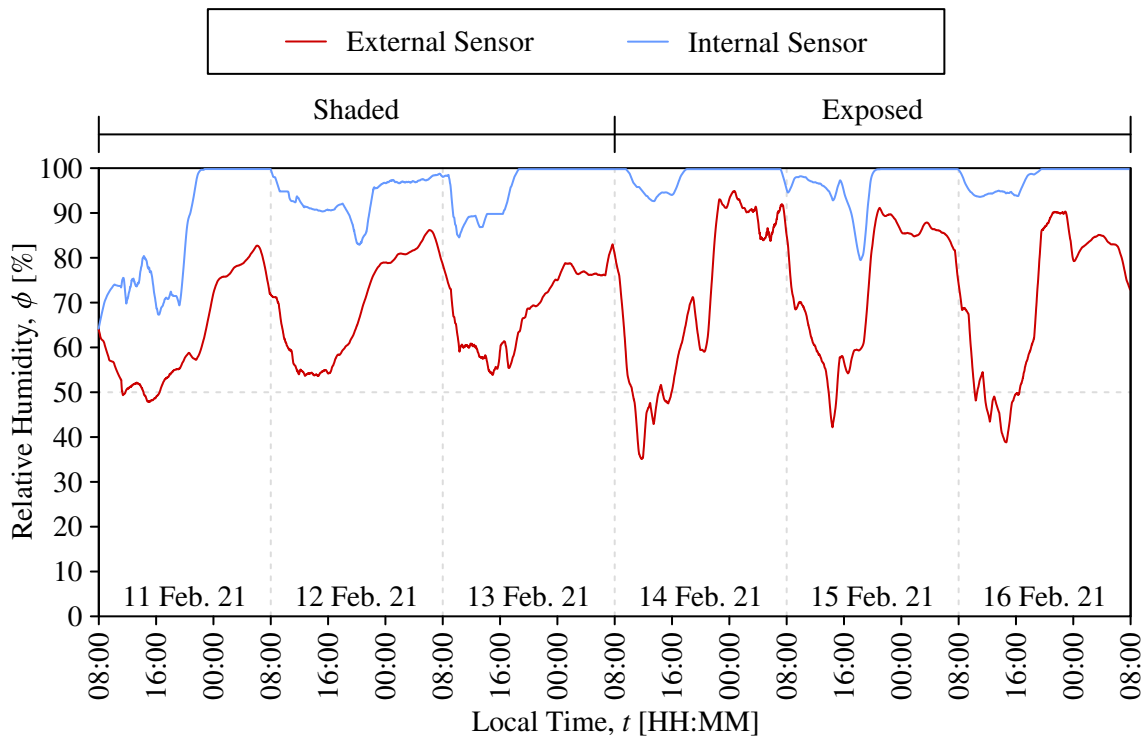


Figure 6.17: Measurements of relative humidity based on a moving average with a period of 1hr using cotton ring spun as the cooling pad without fruits and vegetables stored in the enclosure during a shaded period from 11 Feb. 2021 to 13 Feb. 2021 and exposed period from 14 Feb. 2021 to 16 Feb. 2021.

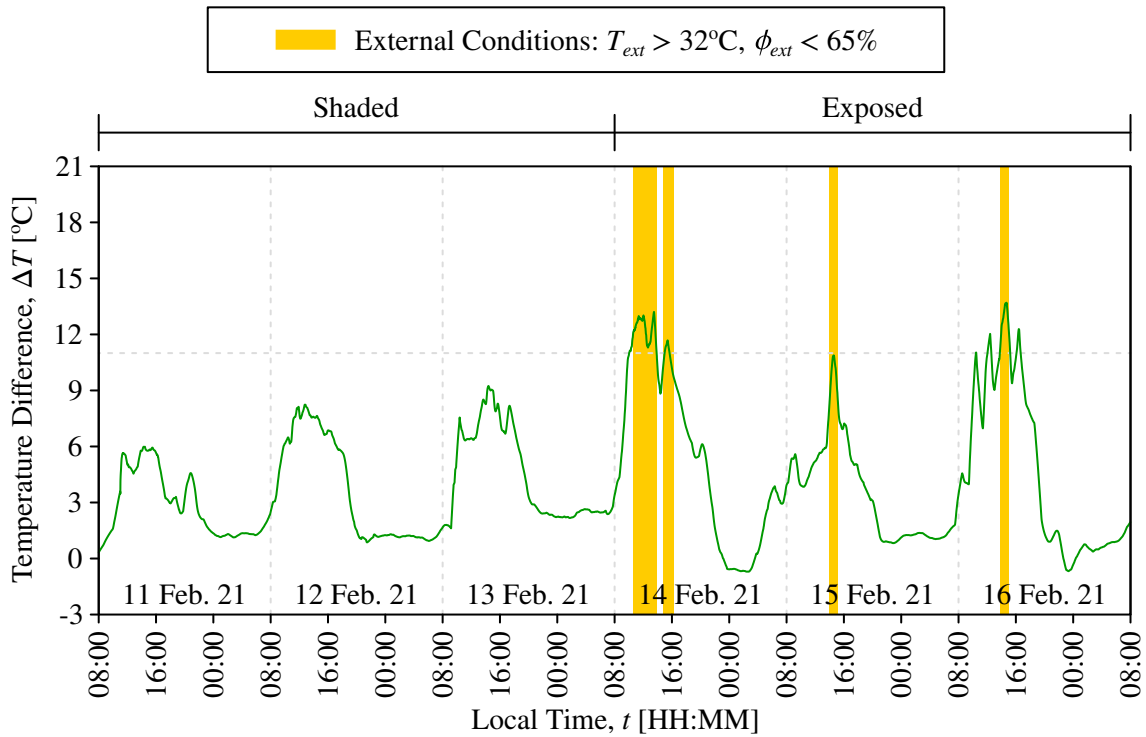


Figure 6.18: Differences in temperature based on a moving average with a period of 1hr using cotton ring spun as the cooling pad without fruits and vegetables stored in the enclosure during a shaded period from 11 Feb. 2021 to 13 Feb. 2021 and exposed period from 14 Feb. 2021 to 16 Feb. 2021.

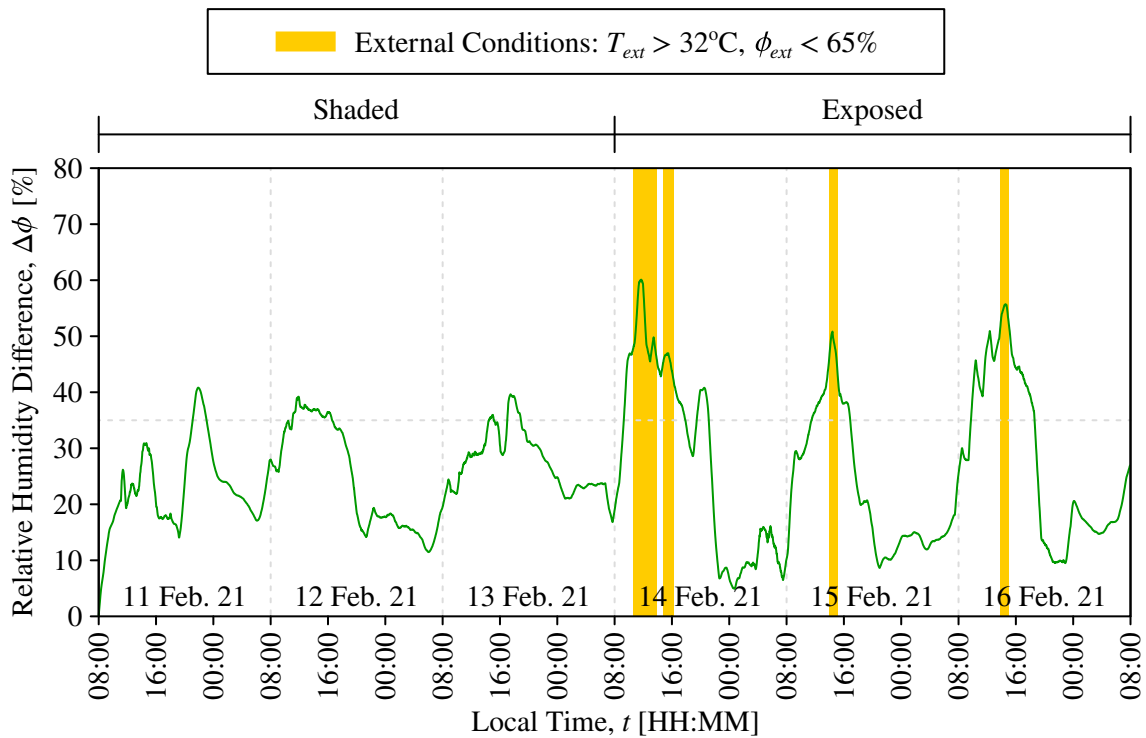


Figure 6.19: Differences in relative humidity based on a moving average with a period of 1hr using cotton ring spun as the cooling pad without fruits and vegetables stored in the enclosure during a shaded period from 11 Feb. 2021 to 13 Feb. 2021 and exposed period from 14 Feb. 2021 to 16 Feb. 2021.

the day were minimised to 7.2°C on 11 Feb. 2021 (affected by initial conditions), 4.4°C on 12 Feb. 2021, 3.1°C on 13 Feb. 2021, 5.1°C on 14 Feb. 2021, 9.0°C on 15 Feb. 2021, and 6.4°C on 16 Feb. 2021. Considering the entire period, the maximum fluctuation in external temperature was up to 19.5°C, while the maximum fluctuation in internal temperature was up to 11.0°C (affected by initial conditions). The reduced fluctuations within the enclosure were seen to be a result of the evaporative cooling reducing the temperature and insulation preventing heat transfer from the surroundings, which were both effective during the day while converging to the external temperature during the night.

The efficiency of the evaporative cooling could be calculated using Equation 2.62 based on the difference between the external and internal temperatures at a given time. This also required the determination of the wet-bulb temperature, which was found using the psychrometric chart in Appendix A for an altitude of 1700m with an atmospheric pressure of 82.50kPa. For a circumscribed point of reference, the efficiency was determined for each day at the maximum external temperature. The processed results are included in Table 6.3, where the efficiency was regularly over 90%.

In the final values for the efficiency, it was acknowledged that there was a sizeable propagation of uncertainty from the sensor accuracies of $\pm 0.5^\circ\text{C}$ and $\pm 2\%$ as well as the difference in characteristics for the psychrometric chart, constructed for an altitude of 1700m with an atmospheric pressure of 82.50kPa, compared to the actual conditions at the test location with an altitude of approximately 1569m and unmeasured atmospheric pressure - although the atmospheric pressure was measured at the CSIR Energy Centre at an altitude of approximately 1377m. Unfortunately, due to the unmeasured atmospheric pressure, the propagated uncertainty could not be precisely investigated, but it was conservatively reasoned to be within $\pm 5\%$, since the atmospheric pressure at the CSIR Energy Centre averaged 85.5kPa and was expected to decrease at the higher altitude of the test location.

Table 6.2: Important maximum and minimum measurements and differences of the internal and external temperatures and relative humidities from 11 Feb. 2021 to 16 Feb. 2021. (The internal temperature and relative humidity on 11 Feb. 2021 may have been affected by initial conditions).

Measurement	11 Feb. 2021	12 Feb. 2021	13 Feb. 2021	14 Feb. 2021	15 Feb. 2021	16 Feb. 2021
Max. External Temperature [°C]	28.5	27.3	29.7	33.4	33.6	33.2
Max. Internal Temperature [°C]	24.1	21.5	21.0	21.9	23.7	19.5
Max. Difference Temperature [°C]	6.0	8.3	9.3	13.2	10.9	13.7
Max. Difference Relative Humidity [%]	40.8	39.2	39.7	60.1	50.9	55.7
Max. Fluctuations Ext. Temperature [°C]	10.2	9.1	9.7	15.8	17.6	19.2
Max. Fluctuations Int. Temperature [°C]	7.2	4.4	3.1	5.1	9.0	6.4

Table 6.3: Evaluation of the evaporative cooling efficiency at the maximum external temperature from 11 Feb. 2021 to 16 Feb. 2021. Measurements from the CSIR Energy Centre are included. (The internal temperature and relative humidity on 11 Feb. 2021 may have been affected by initial conditions).

Date	Time	External		Internal		Wet-Bulb		CSIR Energy Centre		
		Temperature [°C]	Humidity [%]	Temperature [°C]	Humidity [%]	Temperature [°C]	Efficiency [%]	Temperature [°C]	Humidity [%]	Pressure [kPa]
11 Feb. 2021	15:07	28.5	48.1	22.1	76.9	19.7	72.7%	28.3	47.6	86.0
12 Feb. 2021	12:52	27.3	53.9	19.9	91.5	19.5	94.9%	26.9	53.3	85.7
13 Feb. 2021	14:38	29.7	53.7	21.8	89.9	21.2	92.9%	28.1	54.1	85.6
14 Feb. 2021	11:58	33.4	35.6	20.9	94.8	20.3	95.4%	31.5	52.3	85.4
15 Feb. 2021	14:29	33.6	42.8	22.6	92.9	22.2	96.5%	30.9	50.9	85.2
16 Feb. 2021	14:42	33.2	36.6	21.4	94.5	20.6	93.7%	33.4	38.8	85.3

6.5.3 POLYESTER RESULTS

The cotton ring spun was replaced by the polyester at 7:40 on 17 Feb. 2021. The polyester test was completed with the enclosure being shaded from insolation from 17 Feb. 2021 to 19 Feb. 2021 and exposed to insolation from 20 Feb. 2021 to 22 Feb. 2021. The cloud coverage is included in Figure 6.20 with the measured insolation. The conditions were mostly clear with optimal temperatures above 32°C and relative humidities below 50% during each of the days, until 22 Feb. 2021 on which it inaptly rained heavily throughout the day. The measured external and internal temperatures and relative humidities are plotted in Figure 6.21 and Figure 6.22 respectively based on a moving average with a period of 1hr. The differences between the external and internal measurements are plotted in Figure 6.23 for the temperature and Figure 6.24 for the relative humidity with highlights of the relevant intervals under which the external temperature was above 32°C and external relative humidity was below 50%.

In Table 6.4, the maximum external temperatures recorded were 33.3°C on 17 Feb. 2021, 33.9°C on 18 Feb. 2021, 34.4°C on 19 Feb. 2021, 33.8°C on 20 Feb. 2021, 34.3°C on 21 Feb. 2021, and 23.4°C on 22 Feb. 2021. Meanwhile, the maximum internal temperatures recorded were comparatively 22.1°C on 17 Feb. 2021, 22.8°C on 18 Feb. 2021, 23.4°C on 19 Feb. 2021, 21.7°C on 20 Feb. 2021, 21.6°C on 21 Feb. 2021, and 20.7°C on 22 Feb. 2021. The external relative humidity remained very low below 50%, as low as 21.8%, for the majority of the period, but sporadically rose up to 82.4% during the night and 95.0% when it rained. The internal relative humidity remained above 65% with the maximum fluctuation reaching up to 35% when the external relative humidity was at a minimum.

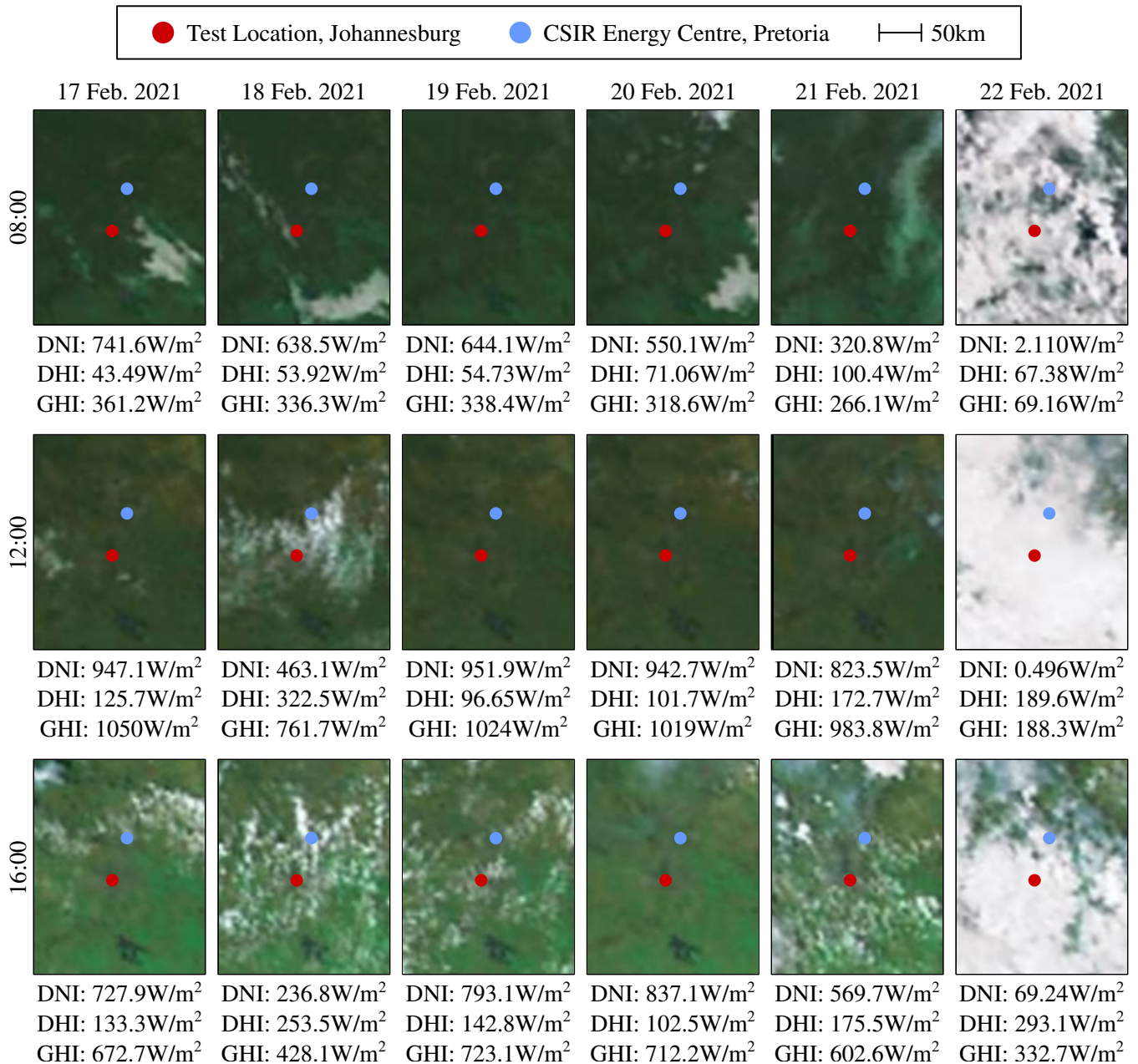


Figure 6.20: Satellite photographs of Gauteng, South Africa, retrieved from the EUMETSAT Meteosat-11 [158] to show the cloud coverage and measurements of insolation intensity in Pretoria, South Africa, retrieved from the SAURAN [38, 39] between 17 Feb. 2021 and 22 Feb. 2021 throughout the day.

The maximum difference between the external and internal temperature was 13.5°C on 17 Feb. 2021, 12.8°C on 18 Feb. 2021, 13.1°C on 19 Feb. 2021, 13.2°C on 20 Feb. 2021, 15.3°C on 21 Feb. 2021, and 4.7°C on 22 Feb. 2021. The maximum difference between the external and internal relative humidity was 64.1% on 17 Feb. 2021, 53.3% on 18 Feb. 2021, 53.8% on 19 Feb. 2021, 67.9% on 20 Feb. 2021, 65.1% on 21 Feb. 2021, and 30.0% on 22 Feb. 2021. As previously, these differences were diminished during the night due to the reduced capacity for evaporative cooling since the external temperature decreased and external relative humidity increased. When these differences were above 11°C and 35%, the external temperature was above 32°C and external relative humidity was below 50%.

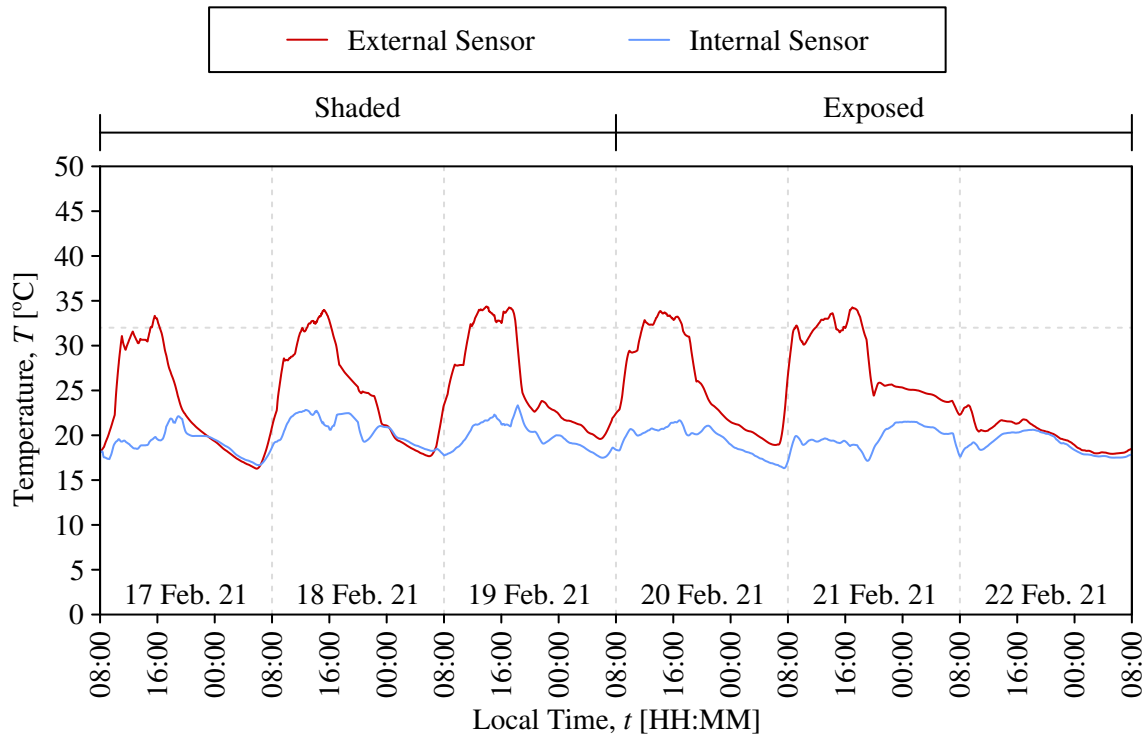


Figure 6.21: Measurements of temperature based on a moving average with a period of 1hr using polyester as the cooling pad without fruits and vegetables stored in the enclosure during a shaded period from 17 Feb. 2021 to 19 Feb. 2021 and exposed period from 20 Feb. 2021 to 22 Feb. 2021.

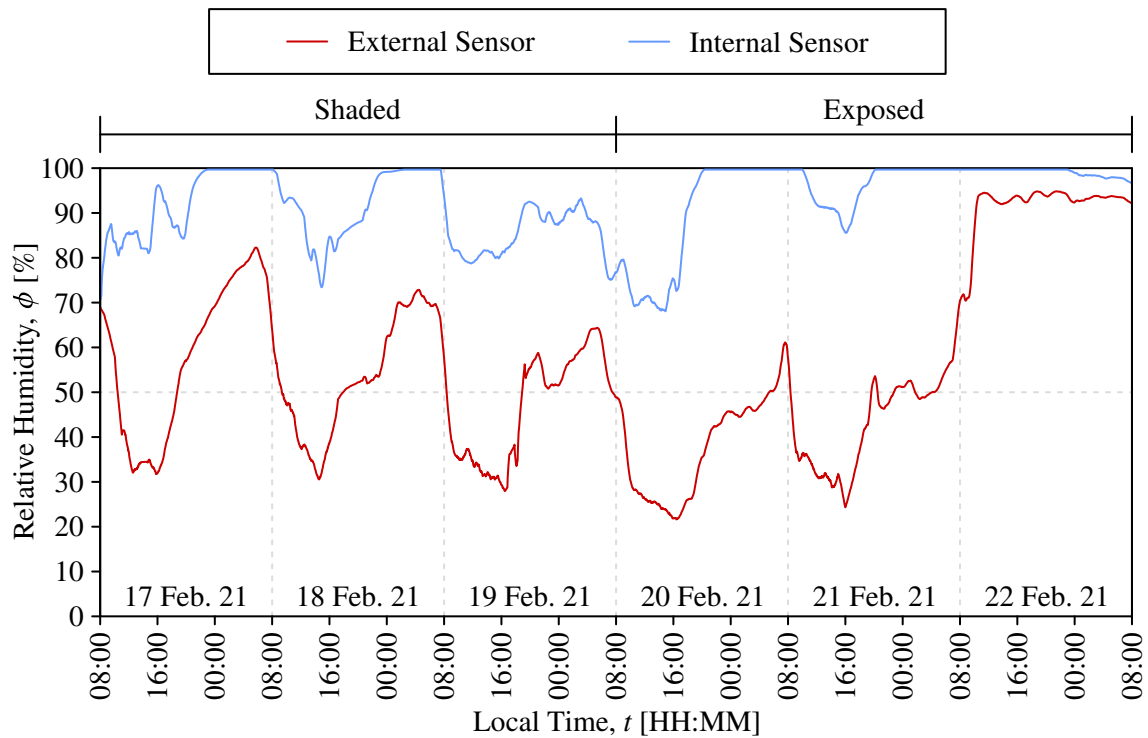


Figure 6.22: Measurements of relative humidity based on a moving average with a period of 1hr using polyester as the cooling pad without fruits and vegetables stored in the enclosure during a shaded period from 17 Feb. 2021 to 19 Feb. 2021 and exposed period from 20 Feb. 2021 to 22 Feb. 2021.

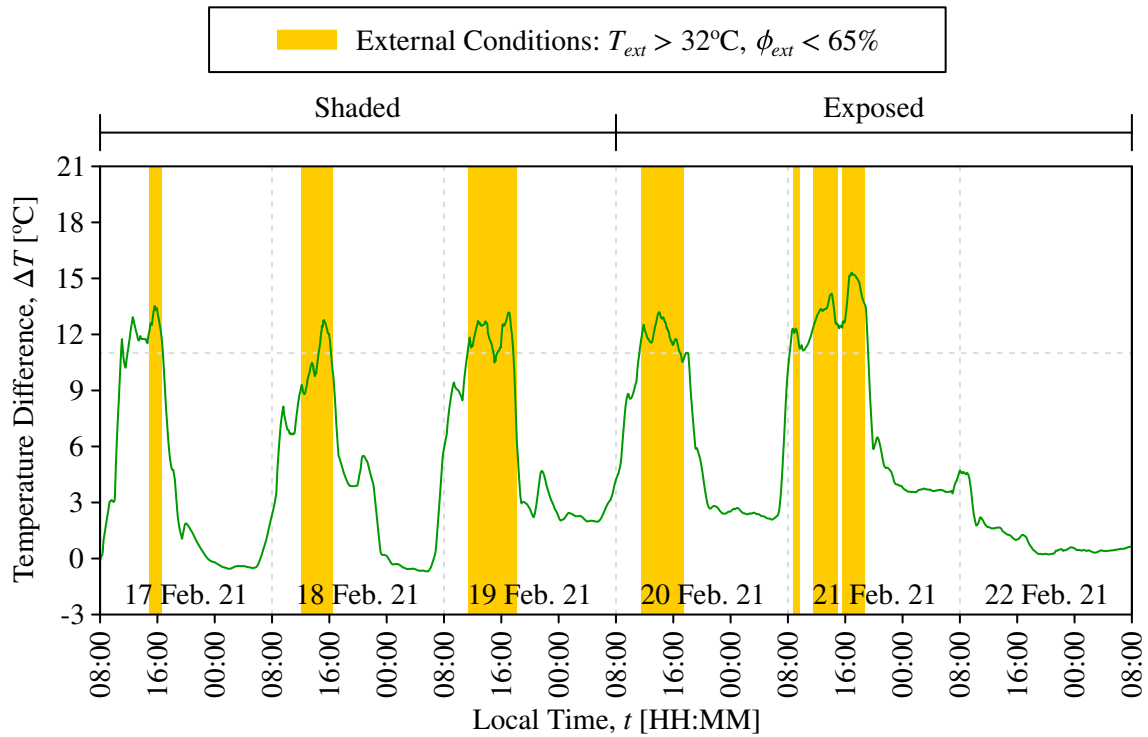


Figure 6.23: Differences in temperature based on a moving average with a period of 1hr using polyester as the cooling pad without fruits and vegetables stored in the enclosure during a shaded period from 17 Feb. 2021 to 19 Feb. 2021 and exposed period from 20 Feb. 2021 to 22 Feb. 2021.

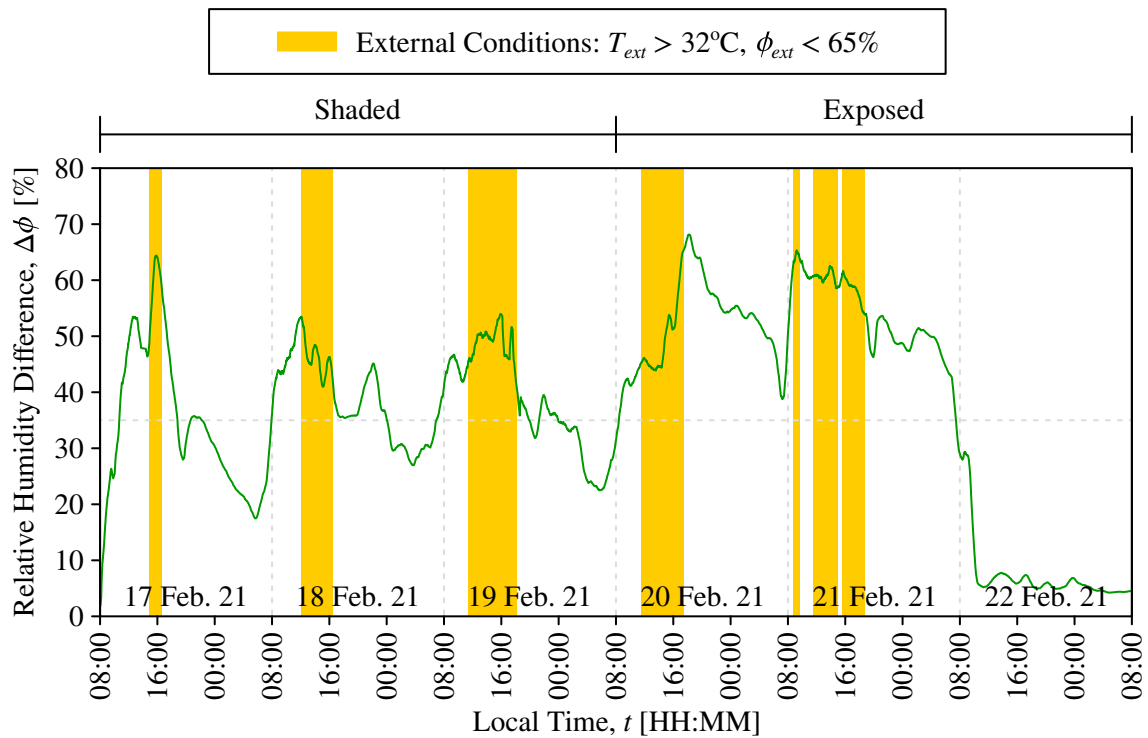


Figure 6.24: Differences in relative humidity based on a moving average with a period of 1hr using polyester as the cooling pad without fruits and vegetables stored in the enclosure during a shaded period from 17 Feb. 2021 to 19 Feb. 2021 and exposed period from 20 Feb. 2021 to 22 Feb. 2021.

Table 6.4: Important maximum and minimum measurements and differences of the internal and external temperatures and relative humidities from 17 Feb. 2021 to 22 Feb. 2021.

Measurement	17 Feb. 2021	18 Feb. 2021	19 Feb. 2021	20 Feb. 2021	21 Feb. 2021	22 Feb. 2021
Max. External Temperature [°C]	33.3	33.9	34.4	33.8	34.3	23.4
Max. Internal Temperature [°C]	22.1	22.8	23.4	21.7	21.6	20.7
Max. Difference Temperature [°C]	13.5	12.8	13.1	13.2	15.3	4.7
Max. Difference Relative Humidity [%]	64.1	53.3	53.8	67.9	65.1	30.0
Max. Fluctuations Ext. Temperature [°C]	17.0	16.3	14.7	14.9	11.9	5.4
Max. Fluctuations Int. Temperature [°C]	5.5	5.0	5.8	5.3	4.6	3.1

Table 6.5: Evaluation of the evaporative cooling efficiency at the maximum external temperature from 17 Feb. 2021 to 22 Feb. 2021. Measurements from the CSIR Energy Centre are included.

Date	Time	External		Internal		Wet-Bulb		CSIR Energy Centre		
		Temperature [°C]	Humidity [%]	Temperature [°C]	Humidity [%]	Temperature [°C]	Efficiency [%]	Temperature [°C]	Humidity [%]	Pressure [kPa]
17 Feb. 2021	15:38	33.3	32.1	20.4	95.4	19.7	94.9%	32.3	37.5	85.7
18 Feb. 2021	15:09	33.9	32.9	21.5	87.9	20.2	90.5%	33.1	40.0	85.8
19 Feb. 2021	13:58	34.4	29.5	21.7	82.8	20.0	88.2%	33.9	26.7	85.8
20 Feb. 2021	14:21	33.8	24.1	21.0	76.6	18.1	81.5%	34.0	18.4	85.7
21 Feb. 2021	17:05	34.3	31.2	20.9	90.1	20.4	96.4%	32.8	26.2	85.8
22 Feb. 2021	10:19	23.4	71.3	19.4	99.9	19.3	97.6%	24.7	66.3	86.3

The maximum fluctuations in external temperature throughout the day ranged from 17.0°C on 17 Feb. 2021, 16.3°C on 18 Feb. 2021, 14.7°C on 19 Feb. 2021, 14.9°C on 20 Feb. 2021, 11.9°C on 21 Feb. 2021, and 5.4°C on 22 Feb. 2021. The maximum fluctuations in internal temperature throughout the day were minimised to 5.5°C on 17 Feb. 2021, 5.0°C on 18 Feb. 2021, 5.8°C on 19 Feb. 2021, 5.3°C on 20 Feb. 2021, 4.6°C on 21 Feb. 2021, and 3.1°C on 22 Feb. 2021. Considering the entire period, the maximum fluctuation in external temperature was up to 18.1°C, while the maximum fluctuation in internal temperature was only 6.9°C. The nearly identical environmental conditions and performance during the shaded period from 17 Feb. 2021 to 19 Feb. 2021 compared against the indistinguishable environmental conditions and performance during the exposed period from 20 Feb. 2021 to 21 Feb.

2021 (excluding 22 Feb. 2021 due to rain) demonstrated the capability of the insulation to isolate the enclosure from heat transfer from the surroundings and insolation. The ability of the insulation to mitigate heat transfer was also adversely underscored during the night on 17 Feb. 2021 and 18 Feb. 2021 when the external temperature was marginally lower than the internal temperature.

The efficiency of the evaporative cooling is presented in Table 6.5 for each day at the maximum external temperature. The efficiencies were moderately high with the lowest of the considered efficiencies being 81.5% on 20 Feb. 2021, although the external relative humidity at this time was at a low of 24.1% and corresponded with a very high difference to the wet-bulb temperature at 18.1°C, which still allowed for a temperature difference of 12.8°C from the external temperature of 33.8°C to the internal temperature of 21.0°C. The result for the last day was inhibited by the rain throughout the day, but the efficiency was still high, although the difference in temperature was only 4.0°C.

6.5.4 FRUITS AND VEGETABLES RESULTS

To account for effects from respiration and transpiration from the fruits and vegetables which would be imminent during operation, a sample of several candidate fruits and vegetables were selected and stored within the enclosure for seven days between 23 Feb. 2021 and 1 Mar. 2021 with the enclosure exposed to insolation throughout the whole period. An identical sample was also stored in the shade in the surroundings within a regular open box, where the fruits and vegetables were only exposed to ventilation from natural convection. The samples are photographed in Figure 6.25. Since its results were partially inhibited due to the cloud coverage in the afternoons during its test, the cotton ring spun replaced the polyester at 7:40 on 23 Feb. 2021 and was reused as the material for the cooling pad to provide additional verification of its potential as a prospective material.

The candidate fruits and vegetables which were available for each sample included one avocado, three baby marrows, three bananas, two bell peppers, one cabbage, four carrots, two eggplants, three granadillas, one sweet corn, and two tomatoes. These fruits and vegetables were chosen as they offered a large range of optimal storage conditions from 0°C for carrots to 15°C for bananas with a relative

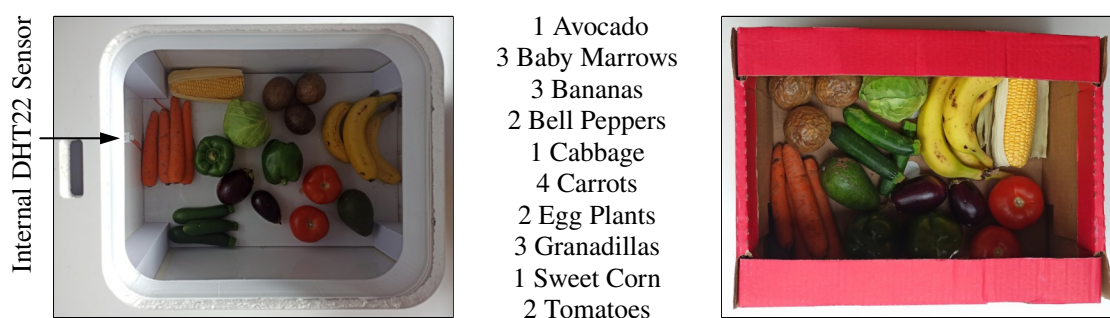


Figure 6.25: Photographs of the identical samples of fruits and vegetables stored internally in the enclosure (left) and externally in the surroundings (right) between 23 Feb. 2021 and 1 Mar. 2021.

humidity above 85% for all of the fruits and vegetables. The health of the fruits and vegetables were monitored based on their appearance and mass between 12:00 and 13:00 each day. This also allowed for the opportunity to investigate the response to an interruption when the lid of the enclosure was left open for 1hr and subsequent time needed to recover to steady state from the inevitable increase in temperature and decrease in relative humidity once the lid was re-applied to the enclosure.

The cloud coverage throughout the monitoring period is shown in Figure 6.26. The conditions were mostly mild during the mornings and middays but slightly inhibited during the afternoons. Specifically, the conditions on 23 Feb. 2021, 27 Feb. 2021, 28 Feb. 2021, and 1 Mar. 2021 were imperfect but still satisfactory, while the conditions from 24 Feb. 2021 to 26 Feb. 2021 were partly insufficient. As with the other tests, the temperature and relative humidity were measured within the enclosure, with the recorded results plotted in Figure 6.27, and externally in the surroundings, with the recorded results plotted in Figure 6.28. The differences in temperature and relative humidity between the external and internal sensors are found in Figure 6.29 and Figure 6.30 respectively with indication of the periods under which there was an external temperature above 32°C and relative humidity below 50%.

From Table 6.6, the maximum external temperatures recorded were 32.2°C on 23 Feb. 2021, 30.2°C on 24 Feb. 2021, 28.4°C on 25 Feb. 2021, 30.5°C on 26 Feb. 2021, 29.1°C on 27 Feb. 2021, 33.5°C on 28 Feb. 2021, and 26.8°C on 1 Mar. 2021. Meanwhile, the maximum internal temperatures recorded were maintained at 20.1°C on 23 Feb. 2021, 22.2°C on 24 Feb. 2021, 21.8°C on 25 Feb. 2021, 22.0°C on 26 Feb. 2021, 22.4°C on 27 Feb. 2021, 22.5°C on 28 Feb. 2021, and 18.8°C on 1 Mar. 2021. The external relative humidity varied below 50%, as low as 32.8%, during the day and above 65%, as high as 100%, during the night, while the internal relative humidity remained at 100% due to the additional influence from the transpiration and respiration of the fruits and vegetables, apart from when the enclosure was opened at which point there were momentary fluctuations down to a relative humidity of 65%.

The maximum difference between the external and internal temperature was 12.2°C on 23 Feb. 2021, 10.1°C on 24 Feb. 2021, 9.0°C on 25 Feb. 2021, 11.4°C on 26 Feb. 2021, 9.9°C on 27 Feb. 2021, 16.1°C on 28 Feb. 2021, and 10.0°C on 1 Mar. 2021. The maximum difference between the external and internal relative humidity was 50.9% on 23 Feb. 2021, 46.2% on 24 Feb. 2021, 40.6% on 25 Feb. 2021, 36.0% on 26 Feb. 2021, 49.5% on 27 Feb. 2021, 67.1% on 28 Feb. 2021, and 55.5% on 1 Mar. 2021. Although seldom, during the periods these differences were above 11°C and 35%, the external temperature was above 32°C and external relative humidity was below 50%.

The maximum fluctuations in external temperature throughout the day ranged from 13.9°C on 23 Feb. 2021, 9.7°C on 24 Feb. 2021, 11.8°C on 25 Feb. 2021, 16.1°C on 26 Feb. 2021, 13.6°C on 27 Feb. 2021, 17.7°C on 28 Feb. 2021, and 11.1°C on 1 Mar. 2021. The maximum fluctuations in internal temperature throughout the day occurred when the enclosure was opened and were minimised to 2.7°C on 23 Feb. 2021, 5.1°C on 24 Feb. 2021, 5.2°C on 25 Feb. 2021, 6.9°C on 26 Feb. 2021, 7.4°C on

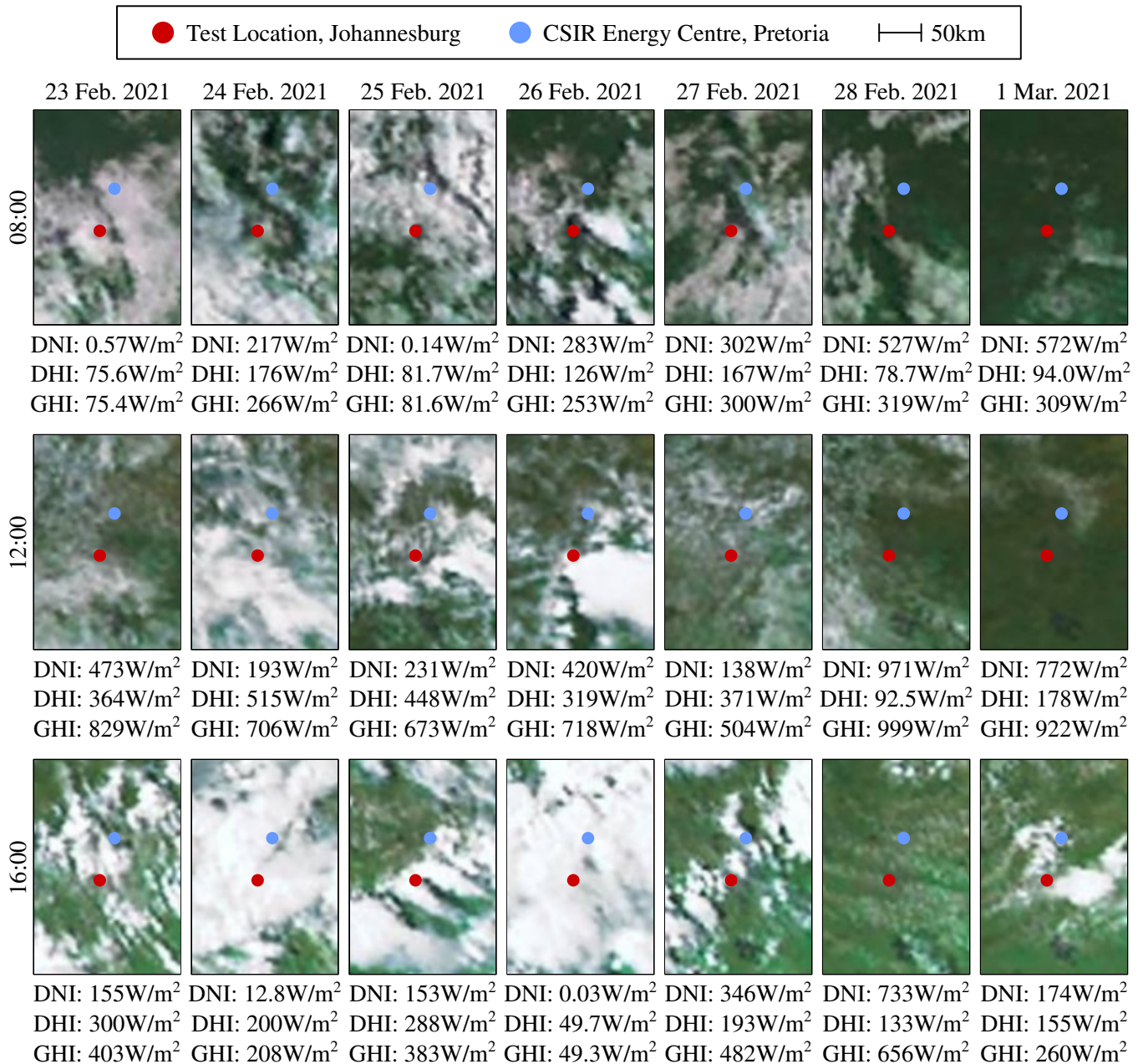


Figure 6.26: Satellite photographs of Gauteng, South Africa, retrieved from the EUMETSAT Meteosat-11 [158] to show the cloud coverage and measurements of insolation intensity in Pretoria, South Africa, retrieved from the SAURAN [38, 39] between 23 Feb. 2021 and 1 Mar. 2021 throughout the day.

27 Feb. 2021, 9.6°C on 28 Feb. 2021, and 6.0°C on 1 Mar. 2021. Considering the entire period, the maximum fluctuation in external temperature was up to 19.0°C, while the maximum fluctuation in internal temperature was up to 9.7°C. The elevated fluctuations in internal temperature and relative humidity were a direct result of opening the enclosure between 12:00 and 13:00, where sharp peaks in temperature and sharp troughs in relative humidity were triggered almost immediately after the interruptions with subsequent recoveries over the following 1hr to 2hr. The efficiency of the evaporative cooling was not calculated as there was discontinuous influences from opening the enclosure and extrinsic effects from the respiration and transpiration of the fruits and vegetables.

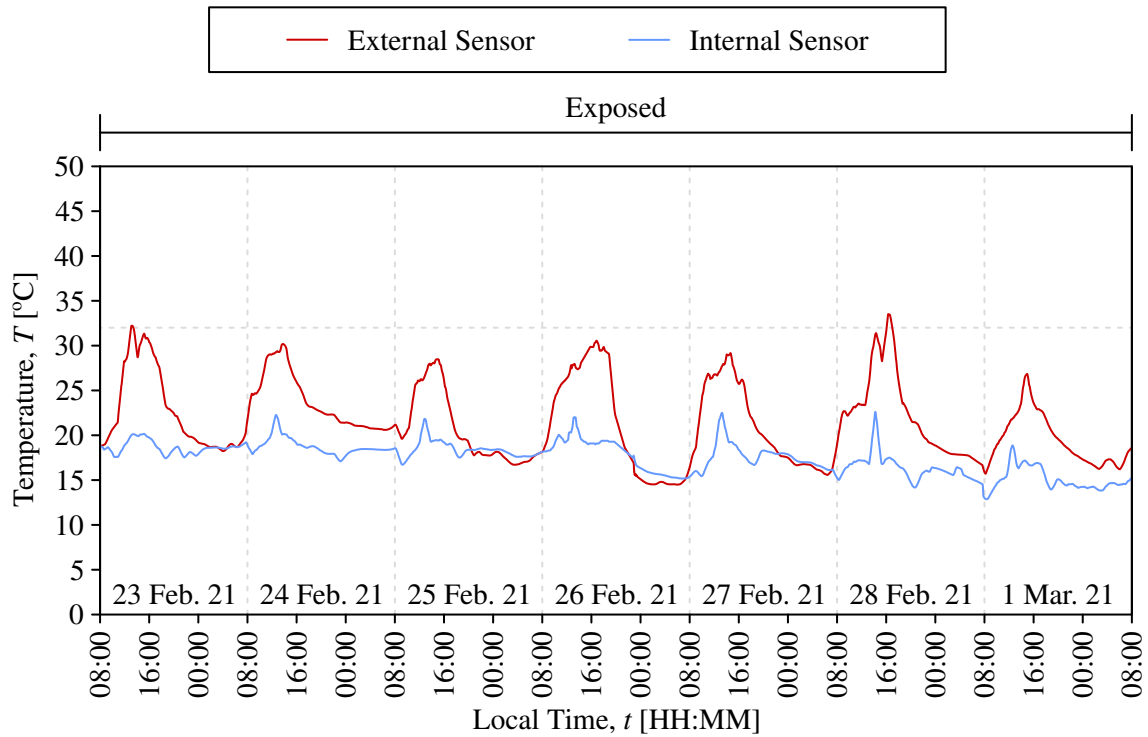


Figure 6.27: Measurements of temperature based on a moving average with a period of 1hr using cotton ring spun as the cooling pad with fruits and vegetables stored in the enclosure during an exposed period from 23 Feb. 2021 to 1 Mar. 2021. The enclosure was opened from 12:00 to 13:00 each day.

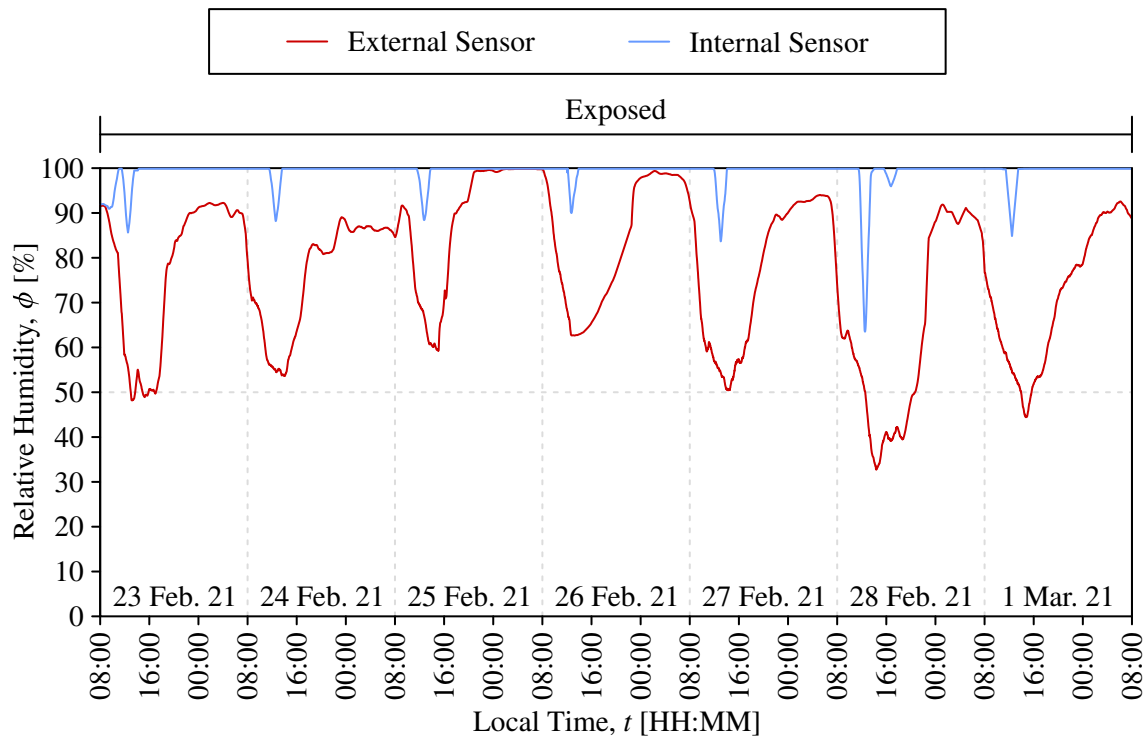


Figure 6.28: Measurements of relative humidity based on a moving average with a period of 1hr using cotton ring spun as the cooling pad with fruits and vegetables stored in the enclosure during an exposed period from 23 Feb. 2021 to 1 Mar. 2021. The enclosure was opened from 12:00 to 13:00 each day.

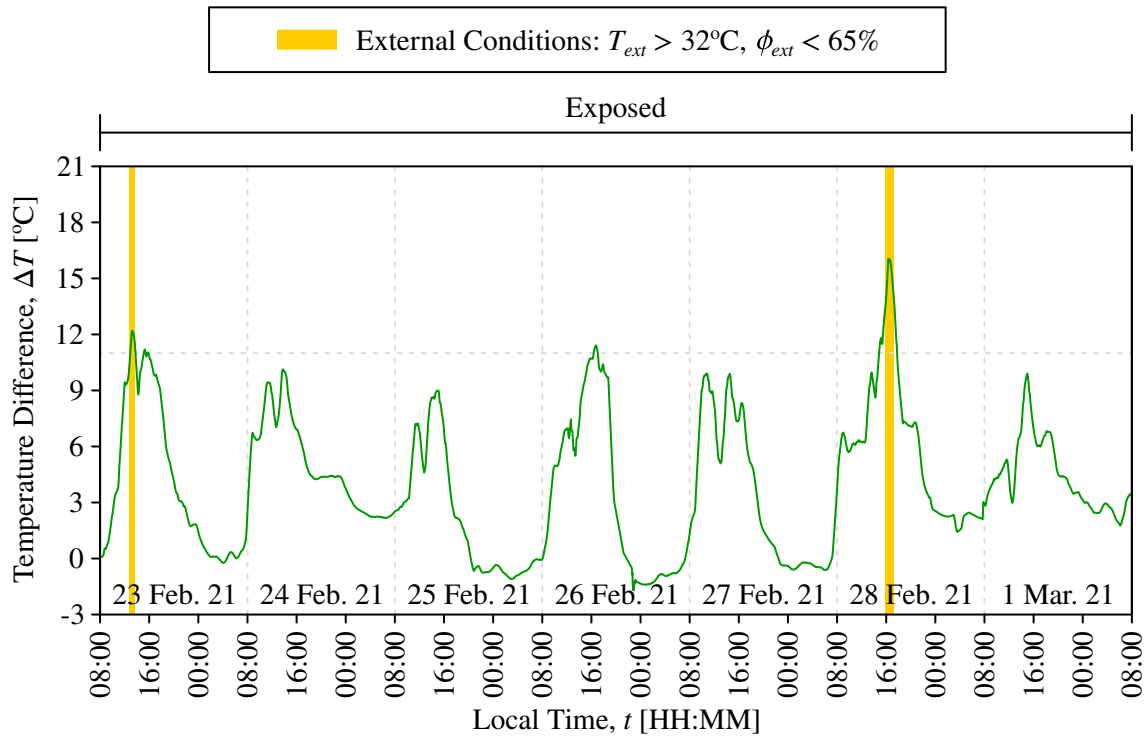


Figure 6.29: Differences in temperature based on a moving average with a period of 1hr using cotton ring spun as the cooling pad with fruits and vegetables stored in the enclosure during an exposed period from 23 Feb. 2021 to 1 Mar. 2021. The enclosure was opened from 12:00 to 13:00 each day.

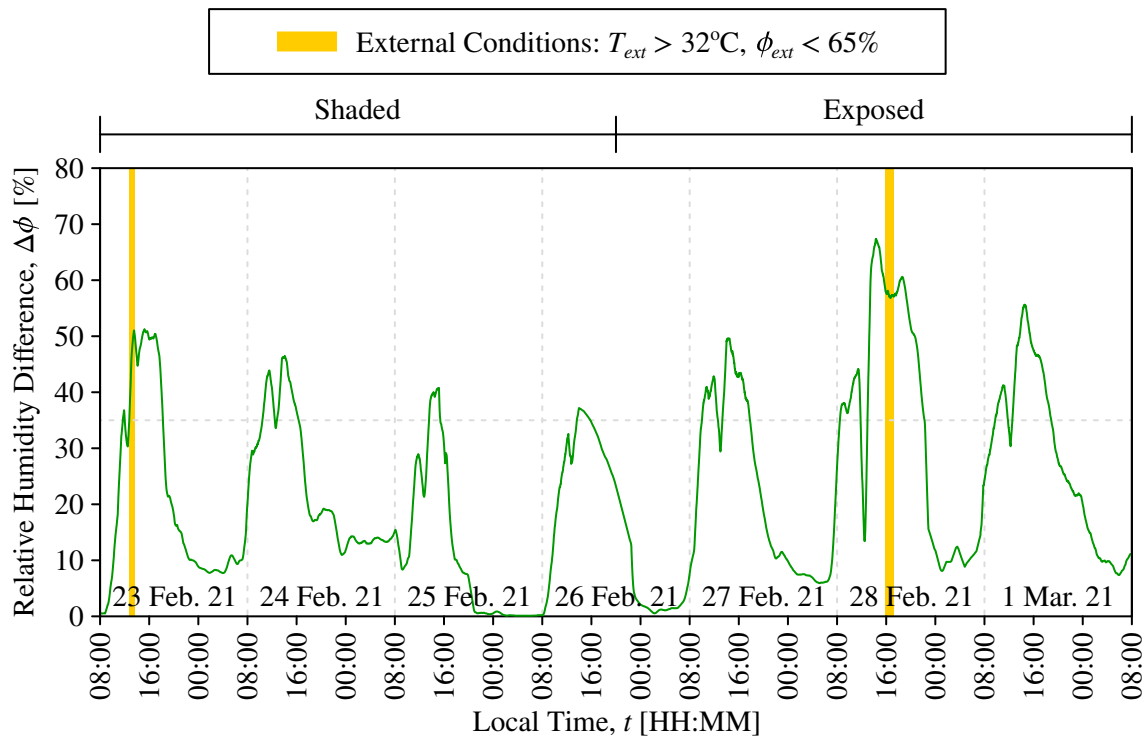


Figure 6.30: Differences in relative humidity based on a moving average with a period of 1hr using cotton ring spun as the cooling pad with fruits and vegetables stored in the enclosure during an exposed period from 23 Feb. 2021 to 1 Mar. 2021. The enclosure was opened from 12:00 to 13:00 each day.

Table 6.6: Important maximum and minimum measurements and differences of the internal and external temperatures and relative humidities from 23 Feb. 2021 to 1 Mar. 2021.

Measurement	23 Feb. 2021	24 Feb. 2021	25 Feb. 2021	26 Feb. 2021	27 Feb. 2021	28 Feb. 2021	1 Mar. 2021
Max. External Temperature [°C]	32.2	30.2	28.4	30.5	29.1	33.5	26.8
Max. Internal Temperature [°C]	20.1	22.2	21.8	22.0	22.4	22.5	18.8
Max. Difference Temperature [°C]	12.2	10.1	9.0	11.4	9.9	16.1	10.0
Max. Difference Relative Humidity [%]	50.9	46.2	40.6	36.0	46.5	67.1	55.5
Max. Fluctuations Ext. Temperature [°C]	13.9	9.7	11.8	16.1	13.6	17.7	11.1
Max. Fluctuations Int. Temperature [°C]	2.7	5.1	5.2	6.9	7.4	9.6	6.0

The photographs and measurements of the mass of the fruits and vegetables for each day are included from Table 6.7 to Table 6.16 for the avocados, baby marrows, bananas, bell peppers, cabbages, carrots, eggplants, granadillas, sweet corns, and tomatoes respectively. The percentage of the mass loss on a certain day was also determined relative to the mass on the previous day and mass on the initial day. This percentage loss was calculated with Equation 6.1. Based on the appearance and mass loss, a judgement of the quality of the fruits and vegetables was performed for each day using a rating for the shelf life as either healthy, degraded, or expired. As mentioned, the *Color Atlas Of Postharvest Quality Of Fruits And Vegetables* by Nunes [21] contained visual comparisons for the degradation of several fruits and vegetables over time and was used to augment and justify the judgements of quality (available for the bell peppers, cabbages, eggplants, granadillas, sweet corns, and tomatoes).

$$\psi = \frac{\phi_1 - \phi_2}{\phi_1} \times 100\% \quad (6.1)$$

The optimal storage conditions for avocados were a temperature of 4.5°C to 13°C and relative humidity of 90% to 95% with a sensitivity to respiration products. At the beginning of the test, each of the avocados were firm and at similar final stages of becoming ripe for consumption. The avocado stored externally in the surroundings reached a degraded quality after five days with the development of darkened discolouration, blemishes, and soft feel, especially when touched at the patches of discolouration and blemishes. The avocado stored internally in the enclosure remained healthy throughout the period and maintained a consistent colour while only declining slightly and uniformly in firmness.

The optimal storage conditions for baby marrows were a temperature of 6°C to 10°C and relative humidity of 90% to 95% (appropriate data could not be reliably sourced for the sensitivity to respiration products). The baby marrows stored externally in the surroundings began to reveal underlying scars as the skin became proportionately more rough and less moist, while they also withered from the loss of water and became discoloured with a slightly duller and darker colour. This rough texture may have

Table 6.7: Measurements of the mass, with percentage difference, and photographs of the avocados stored externally in the surroundings and internally in the enclosure from 23 Feb. 2021 to 1 Mar. 2021.


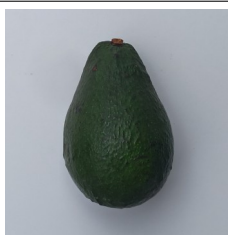

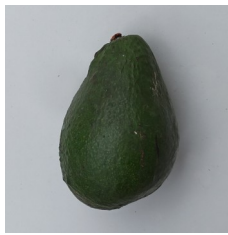



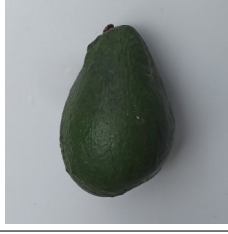

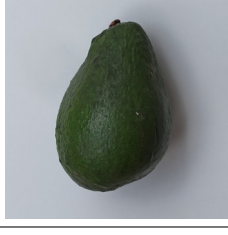
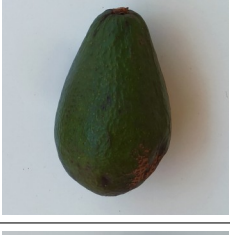
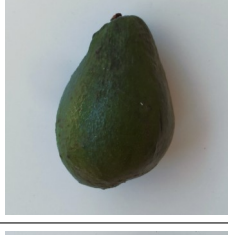
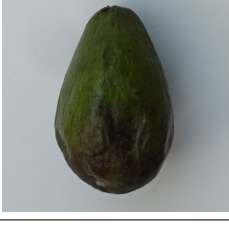

	External Avocado		Internal Avocado	
23 Feb. 2021	Mass: 160g Quality: Healthy		Mass: 172g Quality: Healthy	
24 Feb. 2021	Mass: 157g Previous: 1.63% Quality: Healthy		Mass: 170g Previous: 0.93% Quality: Healthy	
25 Feb. 2021	Mass: 155g Previous: 1.84% Initial: 3.44% Quality: Healthy		Mass: 169g Previous: 0.59% Initial: 1.51% Quality: Healthy	
26 Feb. 2021	Mass: 153g Previous: 1.10% Initial: 4.50% Quality: Healthy		Mass: 169g Previous: 0.24% Initial: 1.74% Quality: Healthy	
27 Feb. 2021	Mass: 152g Previous: 0.85% Initial: 5.31% Quality: Healthy		Mass: 169g Previous: 0.27% Initial: 2.01% Quality: Healthy	
28 Feb. 2021	Mass: 151g Previous: 0.66% Initial: 5.94% Quality: Degraded		Mass: 168g Previous: 0.33% Initial: 2.33% Quality: Healthy	
1 Mar. 2021	Mass: 149g Previous: 0.93% Initial: 6.81% Quality: Degraded		Mass: 168g Previous: 0.24% Initial: 2.56% Quality: Healthy	

Table 6.8: Measurements of the mass, with percentage difference, and photographs of the baby marrows stored externally in the surroundings and internally in the enclosure from 23 Feb. 2021 to 1 Mar. 2021.











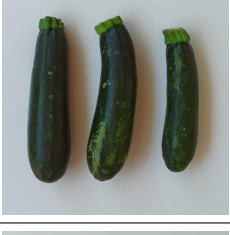
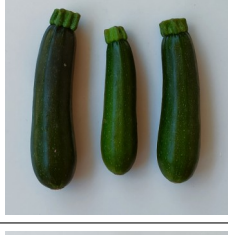


	External Baby Marrows		Internal Baby Marrows	
23 Feb. 2021	Mass: 178g Quality: Healthy		Mass: 178g Quality: Healthy	
24 Feb. 2021	Mass: 166g Previous: 6.74% Quality: Healthy		Mass: 176g Previous: 1.12% Quality: Healthy	
25 Feb. 2021	Mass: 159g Previous: 4.22% Initial: 10.7% Quality: Healthy		Mass: 174g Previous: 1.14% Initial: 2.25% Quality: Healthy	
26 Feb. 2021	Mass: 154g Previous: 2.89% Initial: 13.2% Quality: Degraded		Mass: 172g Previous: 1.15% Initial: 3.37% Quality: Healthy	
27 Feb. 2021	Mass: 150g Previous: 2.85% Initial: 15.7% Quality: Degraded		Mass: 170g Previous: 1.45% Initial: 4.78% Quality: Healthy	
28 Feb. 2021	Mass: 144g Previous: 4.00% Initial: 19.1% Quality: Degraded		Mass: 167g Previous: 1.59% Initial: 6.29% Quality: Healthy	
1 Mar. 2021	Mass: 133g Previous: 7.64% Initial: 25.3% Quality: Expired		Mass: 164g Previous: 1.68% Initial: 7.87% Quality: Degraded	

Table 6.9: Measurements of the mass, with percentage difference, and photographs of the bananas stored externally in the surroundings and internally in the enclosure from 23 Feb. 2021 to 1 Mar. 2021.








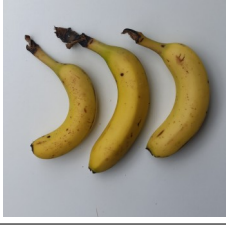
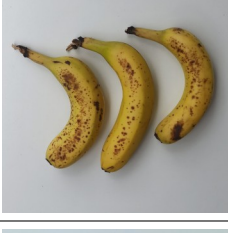

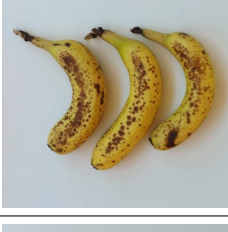
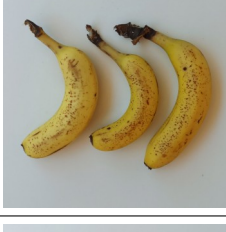


	External Bananas		Internal Bananas	
23 Feb. 2021	Mass: 446g Quality: Healthy		Mass: 406g Quality: Healthy	
24 Feb. 2021	Mass: 437g Previous: 1.93% Quality: Healthy		Mass: 404g Previous: 0.49% Quality: Healthy	
25 Feb. 2021	Mass: 430g Previous: 1.69% Initial: 3.59% Quality: Healthy		Mass: 402g Previous: 0.50% Initial: 0.99% Quality: Healthy	
26 Feb. 2021	Mass: 424g Previous: 1.40% Initial: 4.93% Quality: Healthy		Mass: 400g Previous: 0.45% Initial: 1.43% Quality: Healthy	
27 Feb. 2021	Mass: 419g Previous: 1.27% Initial: 6.14% Quality: Healthy		Mass: 398g Previous: 0.52% Initial: 1.95% Quality: Healthy	
28 Feb. 2021	Mass: 412g Previous: 1.58% Initial: 7.62% Quality: Degraded		Mass: 396g Previous: 0.53% Initial: 2.46% Quality: Healthy	
1 Mar. 2021	Mass: 401g Previous: 2.79% Initial: 10.2% Quality: Expired		Mass: 393g Previous: 0.88% Initial: 3.33% Quality: Healthy	

Table 6.10: Measurements of the mass, with percentage difference, and photographs of the bell peppers stored externally in the surroundings and internally in the enclosure from 23 Feb. 2021 to 1 Mar. 2021.











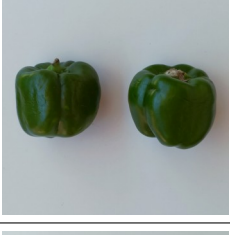
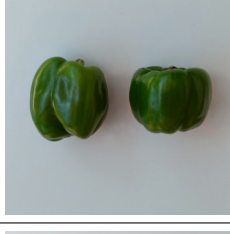


	External Bell Peppers		Internal Bell Peppers	
23 Feb. 2021	Mass: 246g Quality: Healthy		Mass: 240g Quality: Healthy	
24 Feb. 2021	Mass: 240g Previous: 2.44% Quality: Healthy		Mass: 239g Previous: 0.38% Quality: Healthy	
25 Feb. 2021	Mass: 237g Previous: 1.08% Initial: 3.50% Quality: Healthy		Mass: 238g Previous: 0.46% Initial: 0.83% Quality: Healthy	
26 Feb. 2021	Mass: 235g Previous: 1.01% Initial: 4.47% Quality: Healthy		Mass: 237g Previous: 0.50% Initial: 1.33% Quality: Healthy	
27 Feb. 2021	Mass: 232g Previous: 1.23% Initial: 5.65% Quality: Degraded		Mass: 236g Previous: 0.30% Initial: 1.63% Quality: Healthy	
28 Feb. 2021	Mass: 228g Previous: 1.77% Initial: 7.32% Quality: Degraded		Mass: 235g Previous: 0.47% Initial: 2.08% Quality: Healthy	
1 Mar. 2021	Mass: 222g Previous: 2.63% Initial: 9.76% Quality: Degraded		Mass: 233g Previous: 0.68% Initial: 2.75% Quality: Healthy	

Table 6.11: Measurements of the mass, with percentage difference, and photographs of the cabbages stored externally in the surroundings and internally in the enclosure from 23 Feb. 2021 to 1 Mar. 2021.

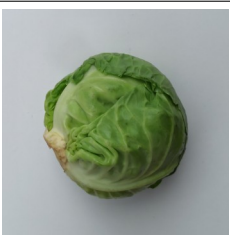









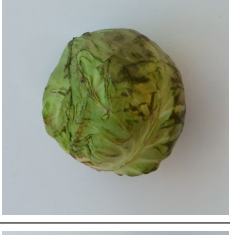
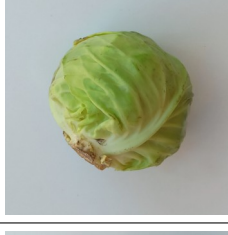


	External Cabbage		Internal Cabbage	
23 Feb. 2021	Mass: 176g Quality: Healthy		Mass: 154g Quality: Healthy	
24 Feb. 2021	Mass: 164g Previous: 6.82% Quality: Healthy		Mass: 151g Previous: 1.69% Quality: Healthy	
25 Feb. 2021	Mass: 159g Previous: 3.05% Initial: 9.66% Quality: Degraded		Mass: 148g Previous: 1.95% Initial: 3.60% Quality: Healthy	
26 Feb. 2021	Mass: 155g Previous: 2.83% Initial: 12.2% Quality: Expired		Mass: 146g Previous: 1.52% Initial: 5.06% Quality: Healthy	
27 Feb. 2021	Mass: 151g Previous: 2.52% Initial: 14.4% Quality: Expired		Mass: 145g Previous: 1.09% Initial: 6.10% Quality: Healthy	
28 Feb. 2021	Mass: 146g Previous: 3.39% Initial: 17.3% Quality: Expired		Mass: 143g Previous: 1.11% Initial: 7.14% Quality: Healthy	
1 Mar. 2021	Mass: 141g Previous: 2.96% Initial: 19.8% Quality: Expired		Mass: 140g Previous: 1.89% Initial: 8.90% Quality: Degraded	

Table 6.12: Measurements of the mass, with percentage difference, and photographs of the carrots stored externally in the surroundings and internally in the enclosure from 23 Feb. 2021 to 1 Mar. 2021.















	External Carrots		Internal Carrots	
23 Feb. 2021	Mass: 332g Quality: Healthy		Mass: 307g Quality: Healthy	
24 Feb. 2021	Mass: 303g Previous: 8.73% Quality: Healthy		Mass: 303g Previous: 1.17% Quality: Healthy	
25 Feb. 2021	Mass: 281g Previous: 7.26% Initial: 15.4% Quality: Degraded		Mass: 300g Previous: 1.02% Initial: 2.18% Quality: Healthy	
26 Feb. 2021	Mass: 260g Previous: 7.47% Initial: 21.7% Quality: Degraded		Mass: 297g Previous: 1.03% Initial: 3.19% Quality: Healthy	
27 Feb. 2021	Mass: 239g Previous: 8.08% Initial: 28.0% Quality: Degraded		Mass: 294g Previous: 1.08% Initial: 4.23% Quality: Healthy	
28 Feb. 2021	Mass: 208g Previous: 13.0% Initial: 37.3% Quality: Expired		Mass: 287g Previous: 2.38% Initial: 6.51% Quality: Degraded	
1 Mar. 2021	Mass: 174g Previous: 16.4% Initial: 47.6% Quality: Expired		Mass: 277g Previous: 3.48% Initial: 9.77% Quality: Degraded	

Table 6.13: Measurements of the mass, with percentage difference, and photographs of the eggplants stored externally in the surroundings and internally in the enclosure from 23 Feb. 2021 to 1 Mar. 2021.


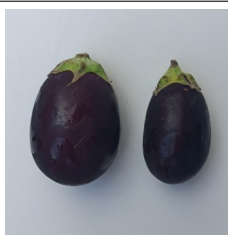








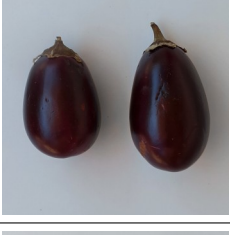
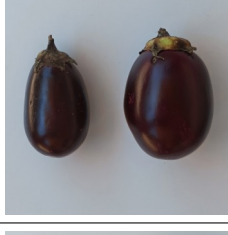

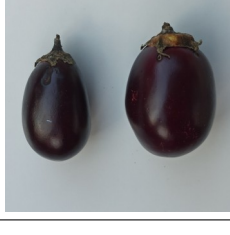
	External eggplants		Internal eggplants	
23 Feb. 2021	Mass: 120g Quality: Healthy		Mass: 134g Quality: Healthy	
24 Feb. 2021	Mass: 117g Previous: 2.50% Quality: Healthy		Mass: 133g Previous: 0.67% Quality: Healthy	
25 Feb. 2021	Mass: 115g Previous: 2.14% Initial: 4.58% Quality: Healthy		Mass: 132g Previous: 0.83% Initial: 1.49% Quality: Healthy	
26 Feb. 2021	Mass: 113g Previous: 1.66% Initial: 6.17% Quality: Healthy		Mass: 131g Previous: 0.76% Initial: 2.24% Quality: Healthy	
27 Feb. 2021	Mass: 111g Previous: 1.78% Initial: 7.83% Quality: Healthy		Mass: 130g Previous: 0.69% Initial: 2.91% Quality: Healthy	
28 Feb. 2021	Mass: 109g Previous: 1.81% Initial: 9.50% Quality: Degraded		Mass: 129g Previous: 0.85% Initial: 3.73% Quality: Healthy	
1 Mar. 2021	Mass: 107g Previous: 1.47% Initial: 10.8% Quality: Degraded		Mass: 128g Previous: 0.78% Initial: 4.48% Quality: Healthy	

Table 6.14: Measurements of the mass, with percentage difference, and photographs of the granadillas stored externally in the surroundings and internally in the enclosure from 23 Feb. 2021 to 1 Mar. 2021.















	External Granadillas		Internal Granadillas	
23 Feb. 2021	Mass: 226g Quality: Healthy		Mass: 202g Quality: Healthy	
24 Feb. 2021	Mass: 217g Previous: 3.77% Quality: Healthy		Mass: 200g Previous: 1.04% Quality: Healthy	
25 Feb. 2021	Mass: 210g Previous: 3.67% Initial: 7.30% Quality: Healthy		Mass: 197g Previous: 1.50% Initial: 2.52% Quality: Healthy	
26 Feb. 2021	Mass: 202g Previous: 3.39% Initial: 10.4% Quality: Degraded		Mass: 195g Previous: 0.96% Initial: 3.47% Quality: Healthy	
27 Feb. 2021	Mass: 196g Previous: 3.41% Initial: 13.5% Quality: Degraded		Mass: 194g Previous: 0.72% Initial: 4.16% Quality: Healthy	
28 Feb. 2021	Mass: 185g Previous: 5.37% Initial: 18.1% Quality: Degraded		Mass: 192g Previous: 0.83% Initial: 4.95% Quality: Healthy	
1 Mar. 2021	Mass: 168g Previous: 9.19% Initial: 25.7% Quality: Expired		Mass: 190g Previous: 0.94% Initial: 5.84% Quality: Degraded	

Table 6.15: Measurements of the mass, with percentage difference, and photographs of the sweet corns stored externally in the surroundings and internally in the enclosure from 23 Feb. 2021 to 1 Mar. 2021.



















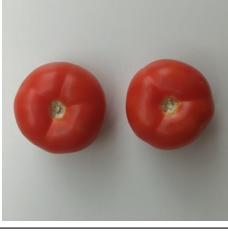

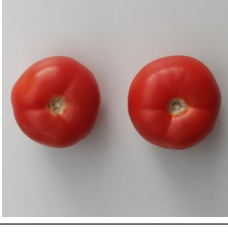

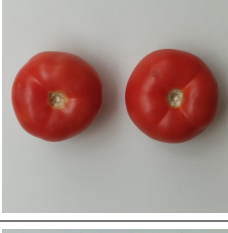

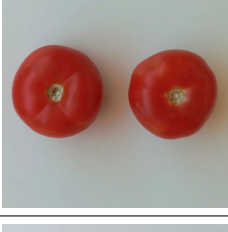
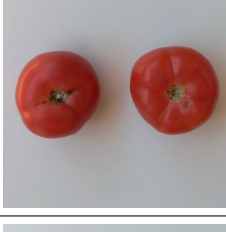


	External Corn		Internal Corn	
23 Feb. 2021	Mass: 220g Quality: Healthy		Mass: 205g Quality: Healthy	
24 Feb. 2021	Mass: 209g Previous: 4.91% Quality: Healthy		Mass: 201g Previous: 1.95% Quality: Healthy	
25 Feb. 2021	Mass: 199g Previous: 4.88% Initial: 9.55% Quality: Degraded		Mass: 197g Previous: 1.99% Initial: 3.90% Quality: Healthy	
26 Feb. 2021	Mass: 190g Previous: 4.52% Initial: 13.6% Quality: Expired		Mass: 194g Previous: 1.52% Initial: 5.37% Quality: Degraded	
27 Feb. 2021	Mass: 179g Previous: 5.79% Initial: 18.6% Quality: Expired		Mass: 192g Previous: 1.29% Initial: 6.59% Quality: Degraded	
28 Feb. 2021	Mass: 169g Previous: 5.59% Initial: 23.1% Quality: Expired		Mass: 189g Previous: 1.10% Initial: 7.61% Quality: Degraded	
1 Mar. 2021	Mass: 162g Previous: 4.14% Initial: 26.4% Quality: Expired		Mass: 187g Previous: 1.06% Initial: 8.59% Quality: Expired	

Table 6.16: Measurements of the mass, with percentage difference, and photographs of the tomatoes stored externally in the surroundings and internally in the enclosure from 23 Feb. 2021 to 1 Mar. 2021.

	External Tomatoes		Internal Tomatoes	
23 Feb. 2021	Mass: 296g Quality: Healthy		Mass: 298g Quality: Healthy	
24 Feb. 2021	Mass: 293g Previous: 0.88% Quality: Healthy		Mass: 298g Previous: 0.20% Quality: Healthy	
25 Feb. 2021	Mass: 292g Previous: 0.48% Initial: 1.35% Quality: Healthy		Mass: 297g Previous: 0.27% Initial: 0.47% Quality: Healthy	
26 Feb. 2021	Mass: 290g Previous: 0.65% Initial: 1.99% Quality: Healthy		Mass: 296g Previous: 0.20% Initial: 0.67% Quality: Healthy	
27 Feb. 2021	Mass: 289g Previous: 0.52% Initial: 2.50% Quality: Healthy		Mass: 296g Previous: 0.13% Initial: 0.80% Quality: Healthy	
28 Feb. 2021	Mass: 287g Previous: 0.55% Initial: 3.04% Quality: Healthy		Mass: 296g Previous: 0.10% Initial: 0.90% Quality: Healthy	
1 Mar. 2021	Mass: 286g Previous: 0.52% Initial: 3.55% Quality: Healthy		Mass: 295g Previous: 0.24% Initial: 1.14% Quality: Healthy	

been a primary result of the erosion of epicuticular waxes on the skin, which consist of hydrophobic organic compounds and assist in restricting the water loss through transpiration. The baby marrows stored internally in the enclosure sustained their bright colour and were less vulnerable to mass loss, although they did become degraded after the sixth day as the colour dulled and mass loss increased.

The optimal storage conditions for bananas were a temperature of 13°C to 15°C and relative humidity of 90% to 95% with no sensitivity to respiration products. The bananas were momentarily unripe for consumption on the first day and featured green parts on the peel which were still in the process of turning yellow. The bananas stored externally in the surroundings became ripe around the third or fourth day until the sixth day at which point the decay became inadmissible with extreme bruising and browning of the peel through over-ripening. On the seventh day, the body was also very tender at the brown areas in particular and almost inedible for consumption. The bananas stored internally in the enclosure also became ripe around the fourth day but remained ripe up to and after the seventh day without detrimental browning of the peel yet, although the body was beginning to soften.

The optimal storage conditions for bell peppers were a temperature of 7°C to 13°C and relative humidity of 90% to 95% with no sensitivity to respiration products. The quality of bell peppers can be indicated from their stiff flesh and bright skin colour. The flesh of the bell peppers stored externally in the surroundings were initially stiff, but developed noticeable wrinkles and cracks towards the end of the period with a more flaccid and compromised flesh around the fifth day. These effects were fairly expected since the bell peppers were hollow and had thin walls with a limited capacity to store water. The bell peppers stored internally in the enclosure almost did not change in appearance and appeared as healthy on the last day as they did initially on the first day. The colour change after the period was indifferent between the bell peppers and mostly indistinguishable compared to the initial quality.

The optimal storage conditions for cabbages were a temperature of 0°C and relative humidity of 95% to 100% with a sensitivity to respiration products. At the beginning of the period, both of the cabbages felt dense, moist, and smooth with bushy leaves. The cabbage stored externally in the surroundings began to have a very dry feel and rough texture towards the end of the period with degradation from severe browning and loosening of the leaves and wilting at the edges of the exposed leaves after only two days. The leaves of the cabbage stored internally in the enclosure were still relatively healthy without discolouration and only experienced minimal browning and wilting by the last day, while still feeling dense, moist, and smooth due to the comparatively high amount of water retained.

The optimal storage conditions for carrots were a temperature of 0°C and relative humidity of 98% to 100% with a sensitivity to respiration products. The carrots stored externally in the surroundings and internally in the enclosure were highly adversely affected. The carrots stored externally in the surroundings exhibited elevated levels of shrivelling and became limp with an immediate decrease in size due to the substantial mass loss from the second day and rapid deterioration in appearance from the fourth day. The carrots stored internally in the enclosure performed partially better and maintained

a solid body, while only succumbing to a degraded appearance on the sixth day with a detrimental mass loss by the seventh day. There was the formation of black spots on the carrots, but these were deemed to be surface lesions from spoilage micro-organisms, such as bacteria, fungi, yeasts, moulds, phages, and protozoa, so the carrots may still be edible if the spots were removed.

The optimal storage conditions for eggplants were a temperature of 8°C to 12°C and relative humidity of 90% to 95% with a sensitivity to respiration products. The health of the eggplants was impressive during the entire period with tolerable mass losses, where the cuticle layers covering the epidermis were successful in acting as a barrier to regulate the loss of water. However, the eggplants stored externally in the surroundings showed signs of pitting with the initial formation of sunken cavities by the fourth day and serious trauma by the seventh day. The eggplants stored internally in the enclosure did not display defects and preserved their rigid feel, glossy sheen, and smooth texture even after the last day, since there were no irregularities to jeopardise the strength of the walls.

The optimal storage conditions for granadillas were a temperature of 7°C to 10°C and relative humidity of 85% to 90% (appropriate data could not be reliably sourced for the sensitivity to respiration products). The skin of the granadillas was initially hard, mostly even, and innocuously discoloured in some regions. The granadillas stored externally in the surroundings experienced an onset of excessive withering from the fourth day with defined crinkling throughout the skin and minor shrinkage as a result of an unchanged surface area but increased unevenness. The granadillas stored internally in the enclosure were able to preserve their hard and mostly even skin until the seventh day when there were inevitable signs of withering from the formation of creases. It should be noted that, although the skin crinkled to an unmarketable degree, the internal juices and pulp are often still permissible for consumption.

The optimal storage conditions for sweet corns were a temperature of 0°C and relative humidity of 90% to 98% with no sensitivity to respiration products. These conditions were stringent and inflexible, as the sweet corn stored externally in the surroundings was dried after two days and expired on the fourth day. This dryness impacted the kernels which dented or collapsed soon after the start of the period with some eventually becoming blackened. The sweet corn stored internally in the enclosure was also affected by dryness and rapidly lost water, but it was able to last until the seventh day before appearing expired with the kernels beginning to become tough and desiccated. The husk around the sweet corn stored externally in the surroundings was initially bright green and fresh but became completely dry and perished after the second day, while the husk around the sweet corn stored internally in the enclosure remained tight-fitting but became dry and pale towards the sixth day.

The optimal storage conditions for tomatoes were a temperature of 9°C to 14°C and relative humidity of 85% to 95% with no sensitivity to respiration products. The changes in appearance for the tomatoes were very minimal for all of the tomatoes stored externally in the surroundings and internally in the enclosure as well. There were partial damages at the point where the body attached to the original stem on one of the tomatoes stored internally in the enclosure, but this was seen to be due to a flaw

during growth and the actual pericarp remained crisp and plump with marginal mass loss. Overall, the tomatoes kept their plumpness and health throughout the period and even after the last day.

6.6 DISCUSSION

The prototype featured an internal volume of 46.52L and was tested based on the short-term storage of fruits and vegetables. As a source for evaporative cooling, the prototype featured a supply reservoir of 2.400L of water and produced a forced air flow which was simulated to be at least 3m/s - unfortunately, the actual velocity of the air flow within the channels could not be measured. The air flow was generated by a radial fan, using a motor with a maximum power of 3.46W, which received power from a completely independent photovoltaic system encompassing internal power generation through a 6.0W solar panel, such that there were no operating costs apart from the water for the evaporative cooling. The total mass of the prototype was 6.623kg with dimensions of 585mm by 405mm by 360mm to be carried by an average and unaided male or female less than 60 years. The performance of the prototype was evaluated with regards to the temperature change, temperature fluctuations, relative humidity change, relative humidity fluctuations, evaporative cooling efficiency, recovery from being opened for an extended period, and extension of the shelf life of fruits and vegetables.

Throughout the period for testing and when it was not raining, the intervals of cloud coverage were as expected and slightly obstructed the insolation when present, but the measured insolation at the CSIR Energy Centre still reported an average direct normal insolation of 479.4W/m², 688.1W/m², and 456.9W/m² and average global horizontal insolation of 842.4W/m², 837.8W/m², and 764.4W/m² between 11:00 and 13:00 during the cotton ring spun, polyester, and fruits and vegetables tests respectively. These values, specifically the global horizontal insolation, were still above the assumed direct normal insolation of 420W/m² used when estimating the required specifications for the photovoltaic system. Again, it was acknowledged that the test location was in Johannesburg, South Africa, while the CSIR Energy Centre was located at a distance of approximately 48km in Pretoria, South Africa. However, the CSIR Energy Centre was the nearest source of appropriate data for reference and, as further support, the satellite photographs from the EUMETSAT Meteosat-11 did not display a significant difference in cloud coverage between each of the locations for the majority of the days.

The environmental conditions were partially disappointing during the cotton ring spun test, where the maximum external temperature was below 30°C for the first three days and erratically above 32°C for the last three days. Although disappointing, the results were still useful to assess the performance under sub-optimal conditions. The environmental conditions were mostly optimal during the polyester test, where the maximum external temperature consistently reached over 32°C on each day except the last day. The results from the polyester test could be viewed as the most accurate indication of performance under the expected environmental conditions. The environmental conditions were imperfect but still satisfactory during the fruits and vegetables test, where the maximum external

temperatures consistently reached 30°C and occasionally reached 32°C, although it would have been preferable for regular temperatures above 32°C. In each test, the external relative humidity was readily below 50% for the vast majority of the days. Overall, the environmental conditions were sufficient to evaluate the potential of employing evaporative cooling utilising forced convection to achieve a significant decrease in temperature and extension of the shelf life of common fruits and vegetables.

When the external temperature was above 32°C and external relative humidity was below 50%, the internal temperature was decreased by at least 11°C in 83.2% and internal relative humidity was increased by at least 35% in 100% of the periods under which these environmental conditions were present for the cotton ring spun test. Considering the polyester test as a more consistent assessment since the frequency of the periods was higher, the internal temperature was decreased by at least 11°C in 81.7% and internal relative humidity was increased by at least 35% in 100% of the periods under which the external temperature was above 32°C and external relative humidity was below 50%. Although scarce in the fruits and vegetables test, the internal temperature was decreased by at least 11°C in 98.7% of the periods under which the external temperature was above 32°C and external relative humidity was below 50%. The relative humidity during the fruits and vegetables test remained at 100%, apart from when the enclosure was opened, which was presumed to be due to the respiration and transpiration from the fruits and vegetables. When the enclosure was opened for 1hr between 12:00 and 13:00, the temperature recovered after approximately 2.11hr after 12:00 on average, while the relative humidity recovered after approximately 2.17hr after 12:00 on average.

These temperature decreases of 11°C and relative humidity increases of 35% were primarily a direct result of the active impact from the evaporative cooling, as well as the passive impact of the insulation acting to prevent acute radiative heat transfer even though the enclosure was exposed to direct normal, scattered, and reflected insolation. As presented with the analytical predictions of the evaporative cooling effect in Figure 5.7, this performance was expected for the candidate environmental conditions when achieving the desired air flow of at least 3m/s for which the radial fan was modelled. Furthermore, the average evaporative cooling efficiency calculated at the maximum external temperature was 91.0% for the cotton ring spun test and 91.5% for the polyester test. The general expectation for the efficiency of evaporative cooling was between 60% and 100%. Correspondingly, an efficiency inclined towards the upper limit was anticipated due to the moderately low average external relative humidity of 44.1% for the cotton ring spun test and 37.9% for the polyester test, which indicated that there was surplus capacity for a cooling effect, such that the internal relative humidity approached 100%.

With regards to the material of the cooling pad, it was found that cotton ring spun offered the best ability to retain water with approximately 661.7g/m², while the polyester offered the best ability to distribute water with saturation in less than 20min. Unfortunately, the performance of the cotton ring spun could not be as extensively tested at external temperatures above 32°C as the performance of the polyester. However, the efficiency of the evaporative cooling which was achieved using the cotton

ring spun under sub-optimal conditions indicated that it would still offer performance equivalent to the polyester for external temperatures above 32°C. The distinguishing factor between the cotton ring spun and polyester became the cost, where the polyester was 197% more affordable at R18.69/m² than the cotton ring spun at R55.55/m². So, the polyester was the most appealing and optimised option for the material of the cooling pad, but it was speculated that the polyester may be even more attractive if it had a higher mass around 100g/m² instead of 65g/m² to increase its ability to retain water at the expense of a slightly higher cost. Since it is synthetic rather than organic, polyester also offered moderate resistance to mildew, but anti-microbial and anti-bacterial treatments would still be advisable.

The recurrent results for a temperature decrease over 11°C under optimal environmental conditions indicated improved performance over a Zeer Pot using natural convection, as Verploegen et al. [10] found that a Zeer Pot could only achieve a temperature decrease between approximately 5°C and 8°C under effectively optimal environmental conditions with an external temperature from 29°C to 37°C and external relative humidity below 40%. A similar indication of improvement could be presumed over the MittiCool Clay Refrigerator which claimed to achieve a temperature decrease of 6°C to 8°C, while having a delay of 12hr before the cooling was perceivable, large mass of 20kg with a monolithic construction, fragile structure made from terracotta clay, and substantial cost of \$130 [92].

Comparing the results against the performance of the Bosch Freshbox and Fenik Yuma Cooler, the performance was moderately improved over the Bosch Freshbox which claimed to achieve a maximum temperature difference only up to 10°C and mostly equivalent to the Fenik Yuma Cooler which claimed to achieve a maximum temperature difference from 11°C to 17°C [93, 94, 95, 96]. However, the performance of the Bosch Freshbox and Fenik Yuma Cooler were only valid when there was natural convection to facilitate the evaporative cooling and their performance would be highly degraded if the natural convection was minimal or absent and capabilities for evaporation were compromised. Moreover, neither the Bosch Freshbox or Fenik Yuma Cooler featured forms of dedicated insulation and, as a consequence, their performance would be highly degraded if exposed to direct insolation. There were also widespread advantages for better durability, since the Bosch Freshbox was only constructed from a thin shell made from a synthetic polymer and the walls of the Fenik Yuma Cooler were a multi-layer membrane with concerns for robustness due to its flexible nature. Furthermore, the costs for the electronic components and materials were estimated to be between R596 or €33.23 and R822 or €45.83 depending on the configuration of the electronic components, whereas the MittiCool Clay Refrigerator had a cost of \$130, Bosch Freshbox had a cost of \$70, and Fenik Yuma Cooler had a cost of \$150, although this was comparing the suggested retail selling prices. Unfortunately, there was no documentation of the performance with regards to the effect on the internal relative humidity for the Zeer Pot, MittiCool Clay Refrigerator, Bosch Freshbox, and Fenik Yuma Cooler.

In addition, the results with regards to fluctuations in temperature portrayed a similar trend to those presented by Anyanwu [30] for an evaporative cooling design similar to a Zeer Pot used for a series of

tests undertaken in Owerri, Nigeria. The highlights of the investigation from Anyanwu [30] were a construction with two layers of clay either side of coconut coir, constant shading without exposure to direct insolation, and natural convection with a wind up to 1.62m/s. As seen in Figure 2.30, Anyanwu [30] was able to significantly reduce the internal fluctuations in temperature to within 5.5°C during a day, while the external fluctuations in temperature remained below a maximum of 13°C during a day. The average maximum internal fluctuations in temperature were 5.8°C, 4.9°C, and 6.1°C during a day during the cotton ring spun, polyester, and fruits and vegetables (affected by opening the enclosure) tests respectively, while the average maximum external fluctuations in temperature were 13.6°C, 13.4°C, and 13.7°C during a day during the cotton ring spun, polyester, and fruits and vegetables tests respectively. This showed a broad consensus between the results from the practical experimentation and Anyanwu [30] and, overall, these general similarities provided an ancillary confirmation for the prospects of consistent diurnal and nocturnal conditions suitable for the improved short-term preservation of fruits and vegetables with temperature fluctuations contained to a range within 8°C.

Considering the results from the storage of fruits and vegetables, the superior appearance and lower mass loss of the internal fruits and vegetables compared to the external fruits and vegetables were seen to be a direct result of the decreased temperature and increased relative humidity within the enclosure. This decreased temperature and increased relative humidity favoured a slowing of the maturing processes with a reduced rate of ripening, such that the shelf life was extended before senescence processes began to occur with over-ripening. Based on the judgements of quality of the candidate fruits and vegetables, the internal sample was healthier than the external sample for every fruit and vegetable, where the internal sample remained healthy for approximately 88.3% longer than the external sample on average with a maximum of 200% for the cabbage and minimum of 40% for the avocado, bananas, and eggplants (excluding the tomatoes which were healthy in both samples for the entire period). There was an average mass loss of 5.52% for the internal sample and 18.6% for the external sample between the first and last days, which equated to an increase of 3.37 times for the mass loss of the external sample relative to the internal sample. The cabbage, carrots, and sweet corn were the most susceptible to deterioration because of their low optimal storage temperature.

The specific fruits and vegetables which are often, although not necessarily optimally, stored between 10°C and 20°C with a relative humidity above 85% included the avocado, baby marrows, bananas, bell peppers, eggplants, granadillas, and tomatoes. On average for these fruits and vegetables, the internal sample remained healthy for approximately 65.8% longer than the external sample, while the average mass loss was still impressive with 3.99% and 13.2% respectively for the internal and external samples between the first and last days. The majority of mass loss occurred through the loss of water due to transpiration and respiration. The compounded loss of water each day led to continuous biological stresses developing through rapid cellular breakdown, loss of membrane integrity, and removal of epicuticular waxes, which resulted in the ability of the outer flesh and inner tissues to retain water to

become further compromised and accelerate subsequent deterioration. Since the external sample was more easily subjected to losses of water compared to the internal sample, it rapidly suffered severe symptoms from the increased dryness and degenerated in appearance as a consequence.

The decay between the same fruits and vegetables stored within the same sample was mostly indifferent, as each of the fruits and vegetables had a similar quality at the beginning of the period without any major damages or defects. An abnormal difference would have only been expected if a fruit or vegetable had a preliminary damage or defect, such as a bruise, crack, or puncture, which would have contributed to an increased rate of decay with symptoms developing sooner through a heightened and contradictory susceptibility to deterioration. Although the low-level scope was unnecessary to explore, Nunes [21] goes on to suggest that the mass loss during storage may be further influenced due to various effects from molecular composition, biological structure, ratio of surface area to volume, internal cross-sections, cultivation methods, sugar content, starch content, vitamin and mineral content, membrane lipid content, electrolyte leakage, acidity levels, pigment concentration, and lipoxygenase activity. Unfortunately, there was no consideration for the internal properties of the fruits and vegetables throughout the period, such as changes in odour, flavour, and nutrient content.

Thus, the investigation of a prototype utilising evaporative cooling was successful in realising a temperature decrease of more than 11°C and relative humidity increase of more than 35% at an average of 82.6% during the periods when the environmental conditions were above 32°C in temperature and below 50% in relative humidity. There was also successful minimisation of the temperature and relative humidity fluctuations within the required ranges of 8°C and 25% respectively during a day for smooth transitions between diurnal and nocturnal intervals. In turn, the mass loss in a sample of ten candidate species of fruits and vegetables stored within the enclosure was minimised to an average of 5.52% compared to the stark mass loss of 18.6% for an identical sample of fruits and vegetables stored in the surroundings. Consequently, this resulted in a drastic extension of the shelf life of the sample stored within the enclosure, where an average improvement of 88.3% was found compared to the sample stored in the surroundings. With regards to extreme affordability for viability in developing countries, the material costs were estimated to be approximately €16.62 after applying a safety factor of 1.2, while the electronic components costs were estimated to be €29.21 for a configuration with a high capacity battery, €22.30 for a configuration with a low capacity battery, and €16.61 for a configuration with no battery. Therefore, the distribution of a low-cost product utilising evaporative cooling could prove to be a very effective resource for the short-term storage of fruits and vegetables in small-scale, portable, and off-grid applications - specifically in developing countries, where households and subsistence farmers could store their harvest with better quality and marketability for longer periods to ultimately improve communities and societies through the reduction of food insecurity.

7 PERFORMANCE ENHANCEMENT

The prototype was optimised with the incorporation of a thermoelectric module to enhance the performance. This also required the expansion of the photovoltaic system to support the additional power requirements from the thermoelectric module. The primary objective of this enhancement was to improve the consistency in performance by reducing the fluctuations in internal temperature and relative humidity, following which the improvements could then be compared against the increases in cost for the additional components. The test with the modified prototype spanned four days and involved investigating and monitoring a variety of environmental conditions for comparison.

7.1 ELECTRONIC COMPONENTS

For the enhancements, the additional components included a thermoelectric module and two solar panels to increase the power output to account for the thermoelectric module. Due to the high power requirements of the thermoelectric module, the thermoelectric module was connected directly in parallel to the two additional solar panels and operated separately from the original solar panel, lithium-ion battery, power management module, and radial fan motor. In this way, the performance of the thermoelectric module would be directly dependent on the intensity of insolation. The interactions between these components are illustrated with the schematic in Figure 7.1.

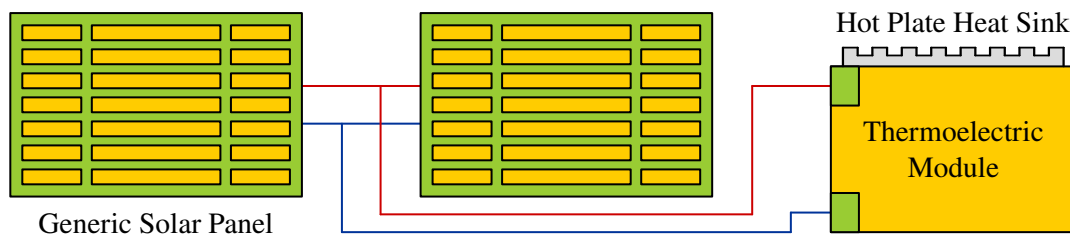


Figure 7.1: Interactions between the additional solar panels and thermoelectric module.

7.1.1 ADDITIONAL SOLAR PANELS

In addition to the original generic solar panel, two more generic solar panels integrating 36 individual mono-crystalline cells connected in series on a high strength printed circuit board with polyethylene terephthalate lamination for enhanced material stability, wear resistant, and non-toxicity. Individually, the rated power was 3.5W with an operating voltage of 6.0V and maximum current output of 0.5833A. The dimensions were fairly compact with a length of 160mm, width of 160mm, and height of 3mm for an overall power density of 136.7W/m^2 under standard conditions. The actual area occupied only by the cells was approximately 0.01954m^2 and implied an efficiency of 17.9% under standard conditions, which aligned with prospects for mono-crystalline silicon cells between 13% and 19%. Together in parallel, the rated power was 7.0W with an operating voltage of 6.0V and maximum current output of 1.167A. The front and back photographs of the solar panel are included in Figure 7.2.

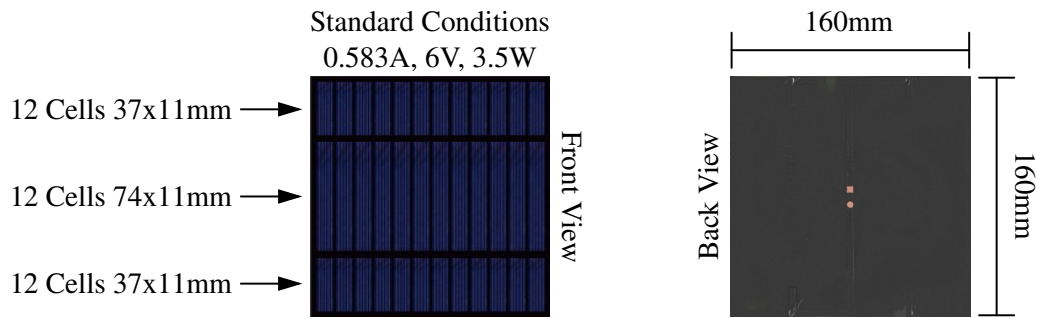


Figure 7.2: Front and back photographs of the 0.5833A 6V 3.5W generic solar panel.

7.1.2 THERMOELECTRIC MODULE

The chosen thermoelectric module was the TEC1-12706 which was capable of reaching temperatures ranging from -30°C to 70°C between the plates [159]. The operating voltage range was between 0V and 15.4V with a drawn current up to 6.4A for a maximum power around 80W [159]. The electrical resistance varied between 1.98Ω and 2.30Ω depending on the temperature difference between the plates. The thermoelectric module used bismuth telluride as the semiconductor with 127 couples of p-n junctions, while the ceramic plates were blank (not metallised) and constructed from aluminium oxide [159]. The expected life was about 200000hr, where it was mandatory for the maximum temperature to remain below 138°C at which point the bismuth tin soldering would begin to melt.

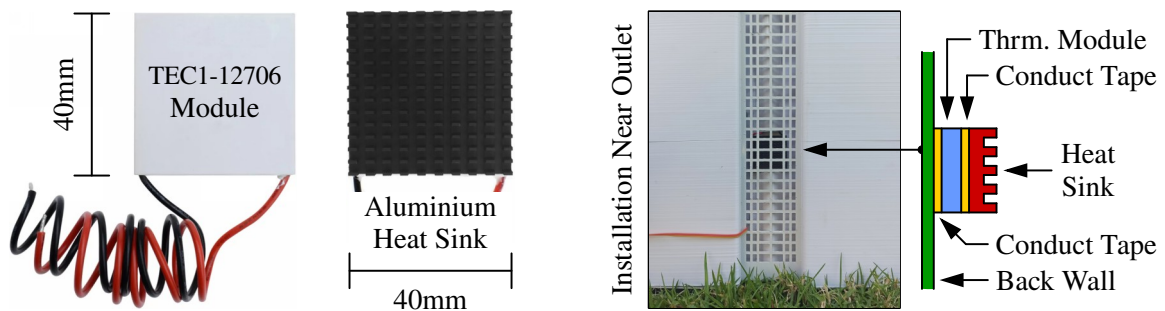


Figure 7.3: Front photographs of the TEC1-12706 thermoelectric module (left) with the finned aluminium heat sink (centre) and installation location on the back wall of the internal enclosure (right).

The thermoelectric module was fairly large with dimensions of 40mm by 40mm and a height of 3.8mm [159]. An aluminium heat sink was selected to cool the hot plate with matching dimensions of 40mm by 40mm and 140 equally-spaced fins of 6mm in height for a thermal resistance of 13.8K/W . The thermoelectric module was positioned on the back wall of the internal enclosure, where the heat sink was able to intercept the air flow at the outlet to optimise cooling as effectively as possible. To maximise the efficiency of the heat transfer, thermally conductive tape was used as an adhesive between the back wall and thermoelectric module and between the thermoelectric module and heat sink. The photographs of the thermoelectric module are shown in Figure 7.3 with the finned heat sink and installation location. The contours of the relationships between the current, voltage, temperature difference, cooling capacity, and coefficient of performance are plotted in Figure 7.4.

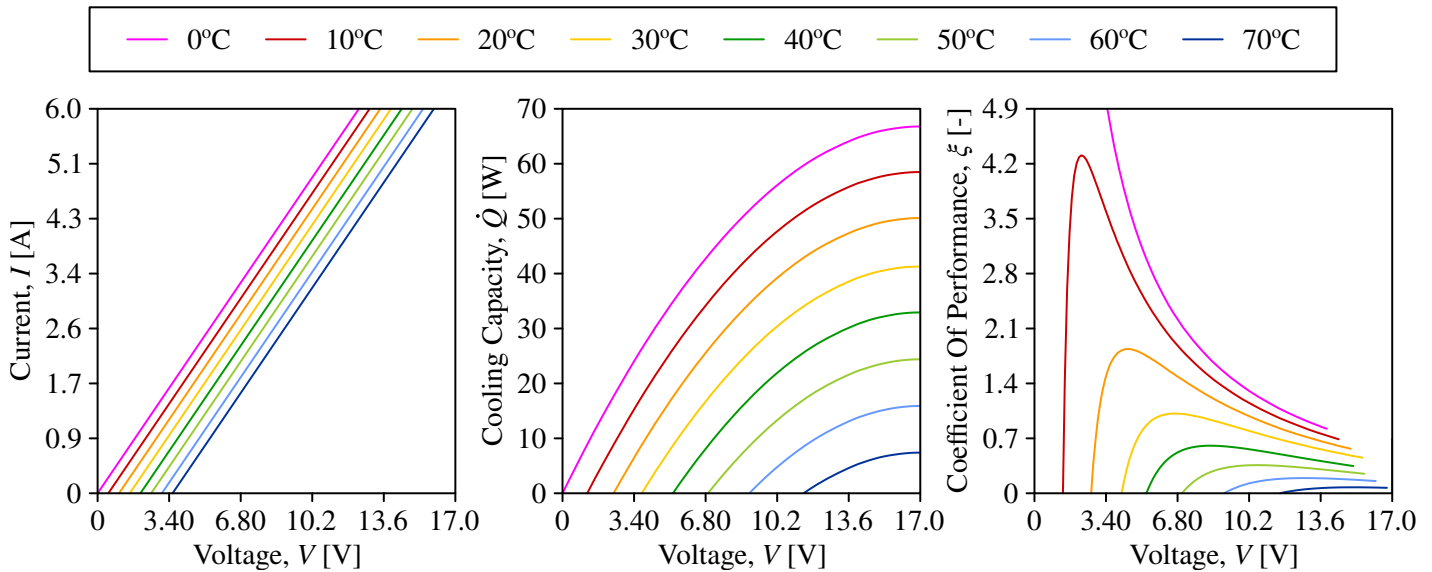


Figure 7.4: Performance curves for the TEC1-12706 thermoelectric module with variation in current and voltage (left), cooling capacity and voltage (centre), and coefficient of performance and voltage (right) for changes in the temperature difference between the hot and cold plates, when the hot plate had a temperature of 50°C and was mounted on a heat radiator to control the temperature [159].

7.2 COST ANALYSIS

To quantify the possibility of increased performance relative to the increased costs, a cost analysis was performed based on the additional components incorporated in the prototype for enhancement. The generic solar panels each had a retail cost price of R135 for a total of R270, which equated to approximately R39/W and was slightly less cost efficient than the original solar panel. The TEC1-12706 thermoelectric module had a retail cost price of R65. This accumulated to a total of R335 or approximately €18.68 for the additional components. As mentioned, the exchange rate between the South African Rand and Euro was discretionally taken to be €1 = R17.93 as of 1 Jan. 2021.

7.3 DATA AND RESULTS

Repeating the practical experimentation allowed for an evaluation of the performance of the prototype with the thermoelectric module to assess possible improvements in performance. The tests were completed from 2 Mar. 2021 to 5 Mar. 2021. The temperature and relative humidity were monitored with the same equipment and at the same positions as previously used. The cloud coverage was still examined with satellite photographs of the regions in Gauteng, South Africa, from the EUMETSAT Meteosat-11, while data was once again accessed through the SAURAN as an indication of the received insolation. The cloud coverage experienced is shown in Figure 7.5 with the measured insolation.

The measured external and internal temperatures and relative humidities are plotted in Figure 7.6 and Figure 7.7 respectively based on moving averages with a period of 1hr in an attempt to smooth

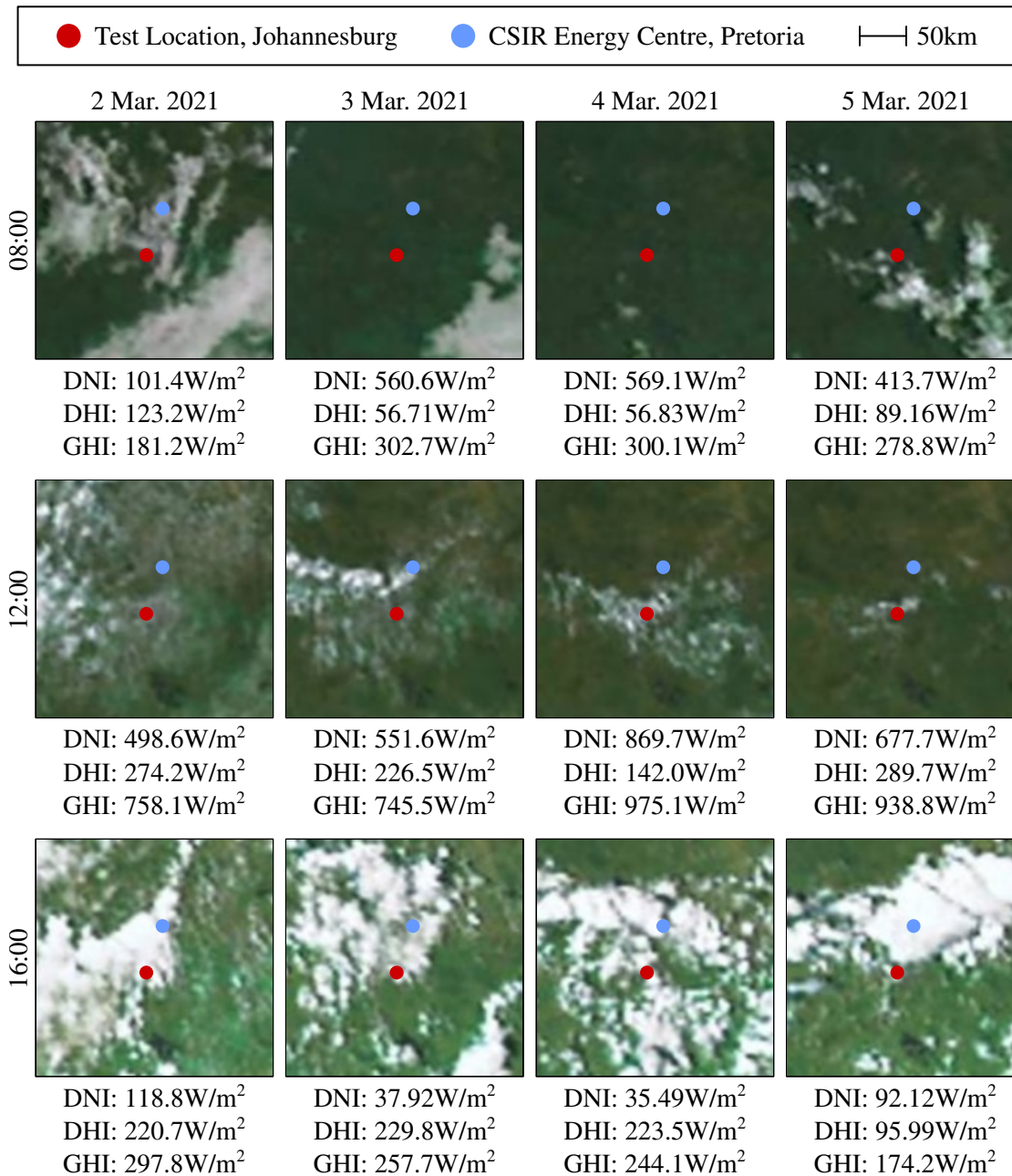


Figure 7.5: Satellite photographs of Gauteng, South Africa, retrieved from the EUMETSAT Meteosat-11 [158] to show the cloud coverage and measurements of insolation intensity in Pretoria, South Africa, retrieved from the SAURAN [38, 39] between 2 Mar. 2021 and 5 Mar. 2021 throughout the day.

local and erratic fluctuations in the measurements. The differences between the external and internal measurements are plotted in Figure 7.8 for the temperature and Figure 7.9 for the relative humidity with highlights of the intervals of particular interest under which the appropriate environmental conditions were experienced with a temperature above 32°C and relative humidity below 50%.

The maximum external temperatures recorded were 28.8°C on 2 Mar. 2021, 28.7°C on 3 Mar. 2021, 33.3°C on 4 Mar. 2021, and 34.2°C on 5 Mar. 2021. Meanwhile, the maximum internal temperatures recorded were comparatively only 22.3°C on 2 Mar. 2021, 19.6°C on 3 Mar. 2021, 20.0°C on 4 Mar.

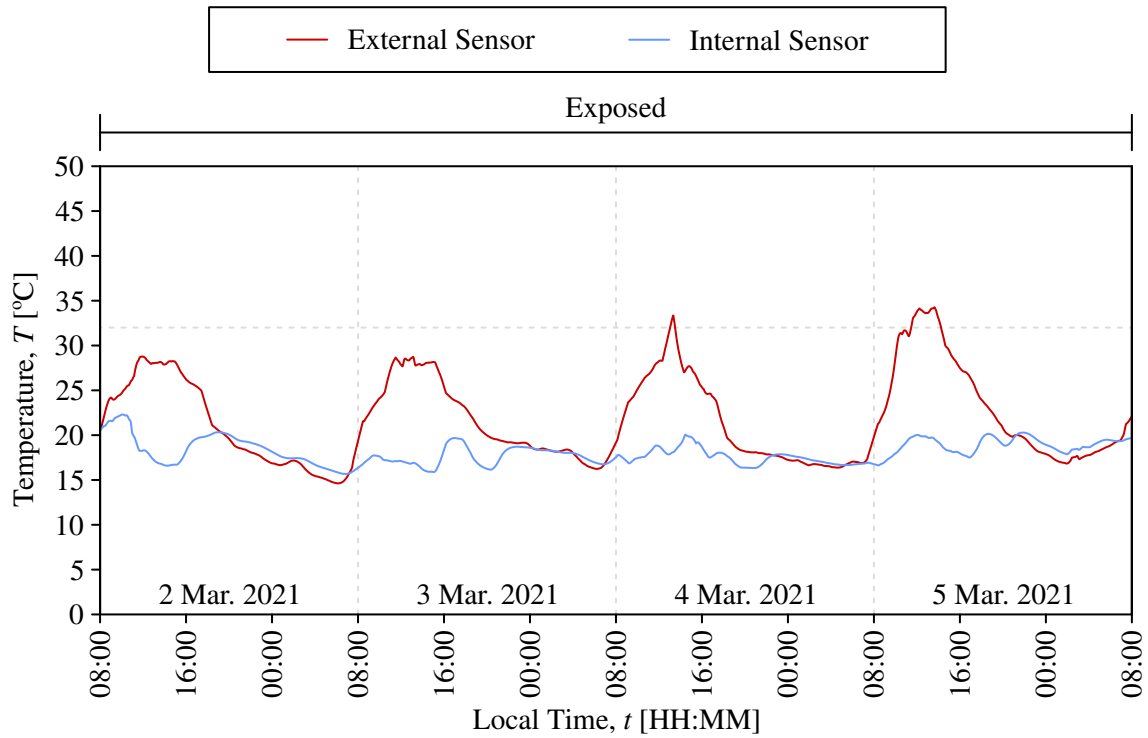


Figure 7.6: Measurements of temperature based on a moving average with a period of 1hr using a thermoelectric module for enhancement and cotton ring spun as the cooling pad without fruits and vegetables stored in the enclosure during an exposed period from 2 Mar. 2021 to 5 Mar. 2021.

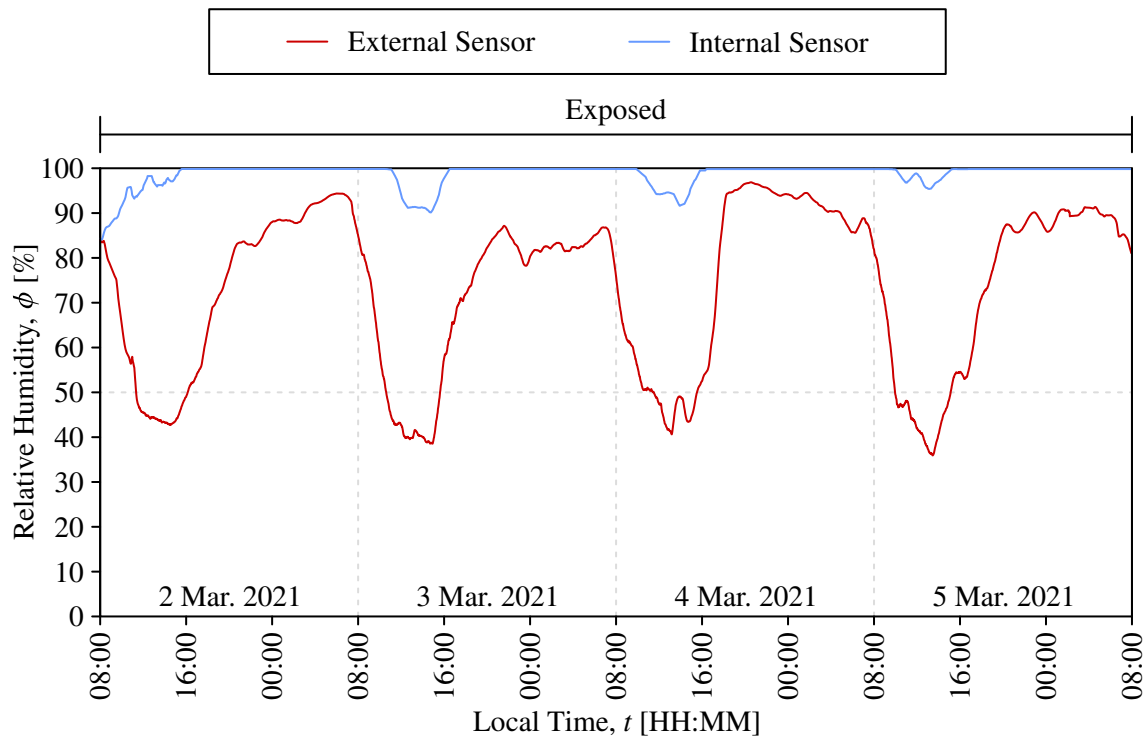


Figure 7.7: Measurements of relative humidity based on a moving average with a period of 1hr using a thermoelectric module for enhancement and cotton ring spun as the cooling pad without fruits and vegetables stored in the enclosure during an exposed period from 2 Mar. 2021 to 5 Mar. 2021.

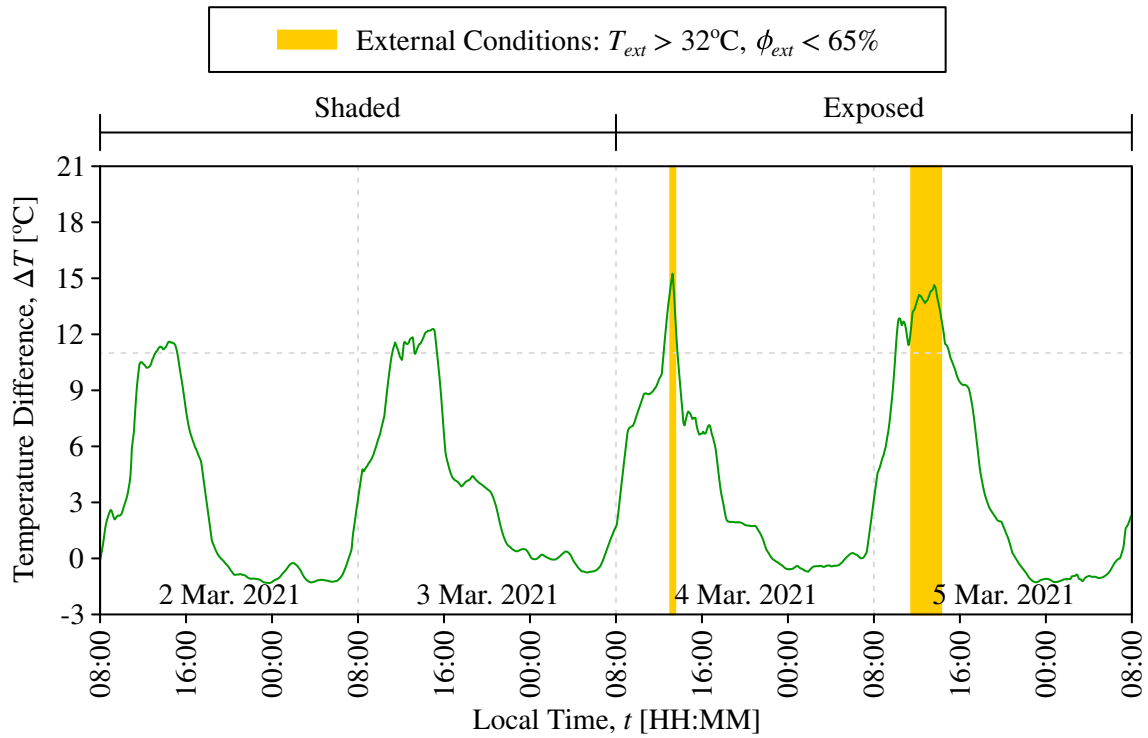


Figure 7.8: Differences in temperature based on a moving average with a period of 1hr using a thermoelectric module for enhancement and cotton ring spun as the cooling pad without fruits and vegetables stored in the enclosure during an exposed period from 2 Mar. 2021 to 5 Mar. 2021.

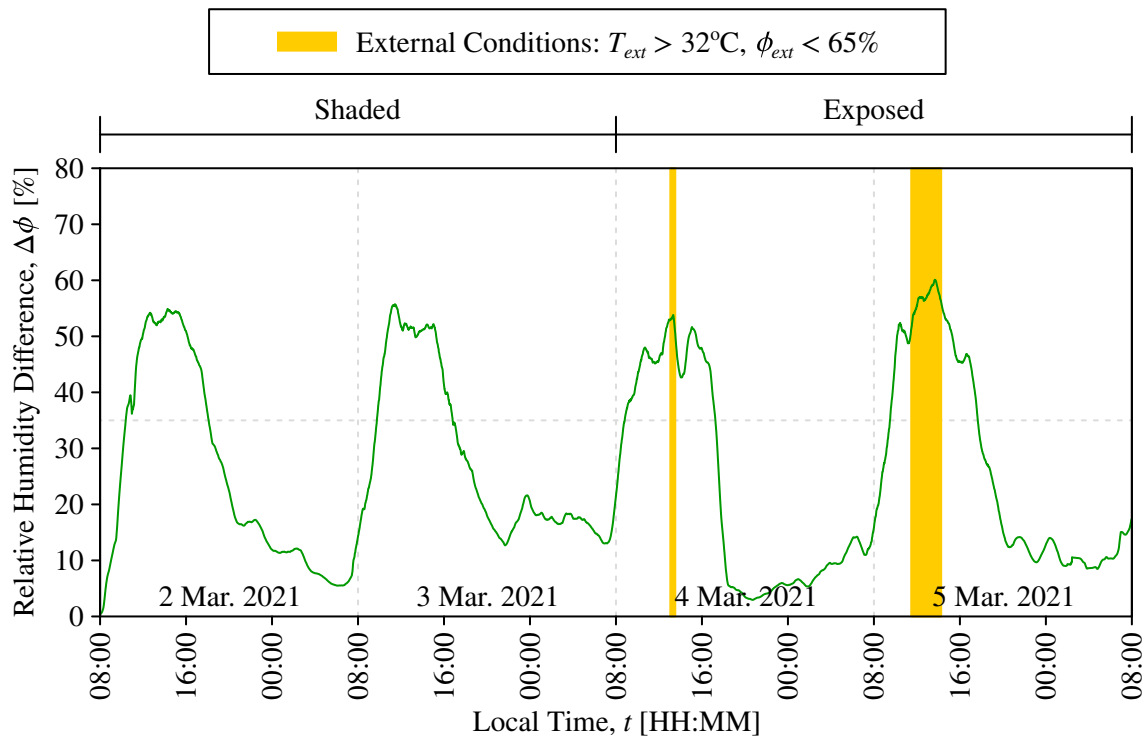


Figure 7.9: Differences in relative humidity based on a moving average with a period of 1hr using a thermoelectric module for enhancement and cotton ring spun as the cooling pad without fruits and vegetables stored in the enclosure during an exposed period from 2 Mar. 2021 to 5 Mar. 2021.

2021, and 20.3°C on 5 Mar. 2021. The external relative humidity tended to regularly vary by decreasing below 50%, as low as 36.0%, during the day and increasing above 80%, as high as 97.1%, during the night. The internal relative humidity remained above 80% (affected by initial conditions) and then 90% with the maximum fluctuation reaching up to only 15.8% (affected by initial conditions) and then 9.8% during the day when the external relative humidity was at a minimum.

The maximum difference between the external and internal temperature was 11.6°C on 2 Mar. 2021, 12.3°C on 3 Mar. 2021, 15.3°C on 4 Mar. 2021, and 14.6°C on 5 Mar. 2021. The maximum difference between the external and internal relative humidity was 54.8% on 2 Mar. 2021, 55.7% on 3 Mar. 2021, 53.8% on 4 Mar. 2021, and 60.1% on 5 Mar. 2021. As previously, these differences were diminished during the night due to the reduced capacity for evaporative cooling since the external temperature decreased and external relative humidity increased, while the power supplied to the thermoelectric module was interrupted until morning. Interestingly, on 2 Mar. 2021 and 3 Mar. 2021, these differences were over 11°C and 35% even though the external temperature was not above 32°C, although the external relative humidity was below 50%, which indicated the influence contributed by the thermoelectric module. On 4 Mar. 2021 and 5 Mar. 2021, the external temperature was above 32°C and external relative humidity was below 50% when these differences over 11°C and 35% occurred, as expected from the discussion of the results from the previous practical experimentation.

The maximum fluctuations in external temperature throughout the day ranged from 14.2°C on 2 Mar. 2021, 12.5°C on 3 Mar. 2021, 17.0°C on 4 Mar. 2021, and 17.5°C on 5 Mar. 2021. The maximum fluctuations in internal temperature throughout the day were minimised to 6.6°C on 2 Mar. 2021 (affected by initial conditions), 3.8°C on 3 Mar. 2021, 3.7°C on 4 Mar. 2021, and 3.6°C on 5 Mar. 2021. Considering the entire period, the maximum fluctuation in external temperature was up to 19.6°C, while the maximum fluctuation in internal temperature was only 6.6°C (affected by initial conditions). The capability of the insulation to isolate the enclosure from heat transfer from the surroundings and insulation was so effective that, during the night on each of the days, the ability of the insulation to mitigate heat transfer was actually adversely underscored when the external temperature was marginally lower than the internal temperature, although this was only by up to 1.3°C on 2 Mar. 2021, 0.8°C on 3 Mar. 2021, 0.7°C on 4 Mar. 2021, and 1.3°C on 5 Mar. 2021 and it did not cause a concern since the periods were relatively short and the temperatures were already below 20°C.

Using Equation 2.62 and for each day at the maximum external temperature, the apparent efficiency of the evaporative cooling is presented in Table 7.1. This apparent efficiency can be viewed as the efficiency of the evaporative cooling as if the entire cooling effect was produced only due to the evaporative cooling. With regards to relevance, this allows for the impact contributed by the thermoelectric module to be distinguished by comparing this apparent efficiency against the efficiencies found in the previous practical experimentation. The results indicated very high apparent efficiencies and even exceeded 100% with a minimum of 115% on 3 Mar. 2021 and maximum of 134% on 4

Mar. 2021. An excess of 100% was expected, since there was a thin layer of condensation repeatedly observed on the back surface near the position of the thermoelectric module throughout the days.

Table 7.1: Evaluation of the apparent evaporative cooling efficiency at the maximum external temperature from 2 Mar. 2021 to 5 Mar. 2021. Measurements from the CSIR Energy Centre are included.

Date	Time	External		Internal		Wet-Bulb		CSIR Energy Centre		
		Temperature [°C]	Humidity [%]	Temperature [°C]	Humidity [%]	Temperature [°C]	Efficiency [%]	Temperature [°C]	Humidity [%]	Pressure [kPa]
2 Mar. 2021	12:01	28.8	44.6	18.5	95.5	21.5	127%	26.1	44.1%	86.3
3 Mar. 2021	13:04	28.7	39.9	16.9	91.3	18.4	115%	28.0	29.9%	86.1
4 Mar. 2021	13:14	33.3	40.7	18.2	94.4	22.1	134%	32.8	37.2%	85.9
5 Mar. 2021	13:33	34.2	36.1	19.3	96.0	21.8	120%	33.4	38.0%	86.0

7.4 DISCUSSION

A thermoelectric module was added to the prototype with the inclusion of two additional solar panels connected directly to the thermoelectric module. The chosen thermoelectric module was the TEC1-12706, which required up to 6.4A at up to 15.4V with dimensions of 40mm by 40mm, and each of the solar panels provided 3.5W from 0.5833A at 6V. The cold plate was positioned on the back wall of the internal enclosure with a finned aluminium heat exchanger mounted against the hot plate to increase the heat transferred to the air flow at the outlet. In total, the additional components had a cost of approximately €18.68. As with the previous practical experimentation, the performance of the prototype was tested with regards to the temperature decrease, temperature fluctuations, relative humidity increase, relative humidity fluctuations, and evaporative cooling efficiency.

Fortunately, there were mostly clear conditions and no rain throughout the period for testing, although there were intervals of cloud coverage in the afternoons. The measured insolation at the CSIR Energy Centre reported an average direct normal insolation of 649.4W/m² and average global horizontal insolation of 854.4W/m² between 11:00 and 13:00. It was observed in the satellite photographs that the cloud coverage over the CSIR Energy Centre was mostly equal to the cloud coverage at the test location, apart from in the afternoons when it appeared to be greater over the CSIR Energy Centre than the test location which may have contributed to reduced measurements, especially on 5 Mar. 2021. The external temperatures were mild on 2 Mar. 2021 and 3 Mar. 2021 but more appropriate for the requirements on 4 Mar. 2021 and 5 Mar. 2021 with maximum temperatures above 32°C. The external relative humidity was readily below 50% for the vast majority of the days.

On 4 Mar. 2021 and 5 Mar. 2021, a temperature decrease over 11°C and relative humidity increase over 35% was achieved between the internal and external temperatures and relative humidities in 100% of the periods in which there was an external temperature above 32°C and external relative humidity below 50%. As mentioned, this difference reached a maximum of 15.3°C on 4 Mar. 2021 and 14.6°C on 5 Mar. 2021. Additionally, as long as the external relative humidity was below 50%, it was also possible to achieve these differences when the external temperature was as low as 28°C on 2 Mar. 2021 and 3 Mar. 2021, which demonstrated the underlying contribution from the thermoelectric module as this level of performance was not achieved in the previous practical experimentation.

The primary contribution from the thermoelectric module was seen in the fluctuations in the internal temperature, where the average internal fluctuation in temperature for a day was 4.4°C (including 2 Mar. 2021 which was adversely affected by initial conditions) relative to the average external fluctuation in temperature for a day at 15.3°C. This can be translated as the internal temperature fluctuating by 1°C for each 3.5°C fluctuation in the external temperature on average. This was contrasted against the previous practical experimentation, where, considering the cotton ring spun and polyester tests, the average internal fluctuation in temperature for a day was 5.8°C (including 11 Feb. 2021 which was adversely affected by initial conditions) and 5.0°C respectively relative to the average external fluctuation in temperature for a day at 13.6°C and 13.4°C respectively. For the cotton ring spun, this can be translated as the internal temperature fluctuating by 1°C for each 2.4°C fluctuation in the external temperature on average. For the polyester, this can be translated as the internal temperature fluctuating by 1°C for each 2.6°C fluctuation in the external temperature on average. In comparison, this can be seen as the thermoelectric module offering an improvement of 45.8% and 34.6% respectively in the internal temperature fluctuation per unit external temperature fluctuation. This was satisfactory in fulfilling the requirement for more consistent performance with temperature fluctuations minimised by 30%.

Moreover, the internal fluctuations in the relative humidity varied between 15.7% and 4.4% during a day with an average of 9.5% during a day throughout the period for testing, which was coupled to external fluctuations in the relative humidity between 56.3% and 48.6% during a day with an average of 53.0% during a day throughout the period for testing. This demonstrated an improvement of 41.7% over the cotton ring spun test, which realised an average internal relative humidity fluctuation of 16.3% during a day (average external relative humidity fluctuation of 42.8% during a day), and improvement of 53.4% over the polyester test, which realised an average relative humidity fluctuation of 20.4% during a day (average external relative humidity fluctuation of 39.9% during a day). Although it would be expected for less of an impact on the preservation of fruits and vegetables compared to temperature fluctuations, a more consistent relative humidity was still preferable and would slightly improve the shelf life of fruits and vegetables by reducing water losses through transpiration.

Based on the value for each day at the maximum external temperature, the average apparent efficiency was 124% compared to the average efficiency of 91.0% in the cotton ring spun test and average efficiency

of 91.5% in the polyester test. The definition of efficiency of the evaporative cooling in Equation 2.62 was based on the reasonable assumption that the dry-bulb temperature decreases proportionally to approach the wet-bulb temperature at a relative humidity of 100%, which was previously acceptable since the enclosure was sufficiently insulated and there were no other sources of heat. However, with the introduction of the thermoelectric module, this assumption was no longer accurate, since there could be a decrease in the dry-bulb temperature at a constant humidity ratio due to the thermoelectric module decreasing the sensible heat component without increasing the latent heat component. Thus, the presented efficiencies are apparent efficiencies and must only be viewed as the efficiency of the evaporative cooling as if the entire cooling effect was produced due to the evaporative cooling only. In this regard and since the averages of the efficiencies of evaporative cooling in the previous tests were consistent, the performance above the averages of 91.0% in the cotton ring spun test and 91.5% in the polyester test could be attributed to the assistance from the thermoelectric module.

Therefore, the thermoelectric module was successfully incorporated into the prototype to complement the evaporative cooling. There were impressive improvements in the form of a temperature difference of 11°C being achieved with external temperatures as low as 28°C, while the fluctuations in internal temperature were reduced by a factor of 1.85 and 1.53 respectively compared to the cotton ring spun and polyester tests. However, given the increased cost of approximately €18.68, it was judged that the advantages of the enhancements were questionable, as the extra cost would contribute to an increase of 83.8% over the previous electronic components costs with a low capacity battery and without the additional solar panels and thermoelectric module. Unfortunately, this would ultimately eliminate the original aim for extreme affordability and it was seen to be unsatisfactory in the context of the short-term storage of fruits and vegetables in developing countries.

8 CONCLUSIONS AND RECOMMENDATIONS

An investigation into the inherent aptitude of evaporative cooling utilising forced convection was performed with a principal focus applied to small-scale, portable, and off-grid applications. The primary intention was to show the capabilities of achieving a significant temperature decrease and extension of the shelf life of common fruits and vegetables when operating under high ambient temperatures and low to moderate ambient relative humidities. There was also consideration for extreme affordability to focus on potential adoption in developing countries. With the ultimate aim of answering the research question, the following conclusions could be summarised in relation to the objectives:

- Preliminary concepts for a design were initially generated to guide the most appropriate manner in which to analytically, numerically, and experimentally investigate evaporative cooling utilising forced convection. The scale of the concepts were 500mm by 310mm by 310mm with direct attention on the requirement for manual transportation by a single person. The final decision resembled a rectangular box or cuboid with external insulation, channels for the air flow, pads for the evaporative cooling, and an internal enclosure for the fruits and vegetables.
- Analytical calculations were performed to predict the operating environmental conditions in which evaporative cooling could successfully achieve a temperature decrease of at least 11°C and relative humidity increase of at least 35% (up to a maximum of 100%). The results indicated that it was expected for these criteria to be achieved when the environmental conditions consisted of an ambient temperature greater than 32°C and ambient relative humidity less than 39.84%. In the analysis, a heat transfer rate balance was considered between the latent and sensible heat transfer, where the convection was determined using the Gnielinski correlation for an air flow with an average velocity of 3m/s for an average convection heat transfer coefficient of 15.49W/m²/K and, through the assumed analogous relationship, convection mass transfer coefficient of 0.01696m/s. There was incorporation of heat transfer of 1.8W from the respiration of fruits and vegetables, which was higher than estimated by a safety factor of 1.2 for a conservative prediction. This analytical result was in agreement with experiments utilising evaporative cooling found in published literature.
- Numerical simulations were performed to investigate the implementation of forced convection to accomplish sufficient evaporative cooling to achieve the desired temperature decrease of 11°C and relative humidity increase of 35%, while accounting for a scale which was manually transportable by a single person and used a self-contained photovoltaic system without relying on an external electricity supply. The design considered a radial fan with backward-curved blades and the aim of generating an air flow of 3m/s and maximising efficiency by minimising the power to ultimately decrease the costs for the electronic components. For modelling the flow and motion, it was reasoned that the shear stress transport κ - ω model combined with a moving reference frame would be the most suitable option, because it offered a balance between accuracy and solvability for radial fans with full turbulence viewed as steady flow. Several CFD simulations were undertaken

in ANSYS Fluent 2019 R3 to vary and optimise the outlet angle, quantity, inclination angle, breadth, channel width, and corner radius of the enclosure. For the final proposed profile, the radial fan featured a diameter of 250mm, circular curvature, outlet angle of 50°, quantity of 14 blades, inclination angle of 0°, breadth of 20mm, channel width of 15mm, and corner radius of 40mm. The simulations predicted an average velocity of 2.639m/s and free stream velocity of 3.036m/s with angular velocity of 589.8rev/min, torque of 19.59mN.m, and power of 1.210W.

- Practical comparison was performed for several fabric materials to act as the cooling pad soaked in water for the evaporative cooling. The examined fabric materials included cotton ring spun, cotton waffle weave, cotton canvas, cotton poplin, cotton-polyester, cotton-spandex, polyester, polyester-bamboo, spandex, viscose-spandex, linen, hessian, and kraft paper. For optimisation, the performance of the fabric materials was judged based on their abilities to wick, distribute, and retain water and cost per unit area. The order of performance from worst to best was found to rank as the cotton-polyester, linen, cotton poplin, kraft paper, spandex, and viscose-spandex which performed poorly, followed by the cotton waffle weave, cotton canvas, polyester-bamboo, and hessian, and then the cotton ring spun, cotton-spandex, and polyester. The cotton ring spun and cotton-spandex performed similarly and demonstrated the most promising abilities to retain water, although the cotton ring spun was less expensive at R55.17/m² versus R62.06/m² for the cotton-spandex. The polyester demonstrated the most promising ability to distribute water rapidly and featured a low cost of R18.69/m². Although the polyester was accepted as the most successful, both the cotton ring spun and polyester were used for the prototype experimentation.
- Calculations of the necessary insulation were performed in order to isolate the enclosure and inhibit the heat transfer from insolation and other sources of heat in the surroundings. Interposed between two sheets of ABS with thicknesses of 1.2mm, the required thickness of polyurethane and polystyrene foams were calculated to be 7.112mm and 13.16mm respectively to maintain a temperature difference of 33.8°C with an insolation intensity of 648W/m² after the application of a safety factor of 1.5 to account for the uncertainties in the actual absorptivity of the external surface, thermal conductivities of the materials, and insolation. Using the interposition of ABS and polystyrene, numerical simulations were also performed to ensure that the construction was optimised with adequate strength to stack two additional enclosures on top of it for a total load of 310N. The FEA simulations were undertaken in ANSYS Mechanical 2021 R1 using a linear static analysis and indicated that it was expected for a maximum displacement of 2.811mm, maximum stress of 3.212MPa, and minimum safety factor of 1.644. These results were satisfactory as preliminary in preparation for the prototype experimentation. For the prototype experimentation, polystyrene was used due to its availability in sheets of a standard thickness of 15mm.
- Prototyping was performed to evaluate real-world performance under a variety of environmental conditions experienced in Johannesburg, South Africa, where the results were compared with the

desired specifications to achieve a temperature decrease of at least 11°C and relative humidity increase of at least 35% (up to a maximum of 100%), while aiming to maintain a manufacturing cost below €45 for affordability in developing countries. The electronic components included a generic 6.0W solar panel outputting 0.5A at 12V, 26650 lithium-ion battery with a capacity of 5.0A.hr at 3.7V, 14500 lithium-ion battery with a capacity of 0.8A.hr at 3.7V, DFRobot Solar Power Manager SKU DFR0535 to regulate the distribution, and motor from the Sunon MFC0251V2-0000-A99 operating at 0.25A at 12V for the radial fan. The total mass of the construction was 6.623kg; dimensions of the construction were 585mm by 405mm by 360mm; estimated costs for the electronic components were R524 or €29.21 with the 26650 battery, R400 or €22.30 with the 14500 battery, or R298 or €16.61 without a battery or power management module; and estimated costs for the materials were R298 or €16.62 after the application of a safety factor of 1.2. The prototyping was performed over a span of three weeks with monitoring of the internal and external temperature and relative humidity during tests when using the cotton ring spun, using the polyester, and storing fruits and vegetables, while the cloud coverage was observed with satellite photographs through the EUMETSAT Meteosat-11 and insolation intensity was accessed nearby in Pretoria, South Africa, through the SAURAN. Overall, the environmental conditions were seen to be acceptable as there were various periods with external temperatures above 32°C and external relative humidities below 65%, while the average global horizontal insolation was above 750W/m² between 11:00 and 13:00 in each of the tests. Due to the forced air flow, the evaporative cooling efficiency was regularly above 85% in the cotton ring spun and polyester tests for each day when the maximum external temperature occurred. The performance was very impressive, where the requirement for a temperature decrease of 11°C was achieved in 83.2% of the periods in the cotton ring spun test, 81.7% of the periods in the polyester test, and 98.7% of the periods (although scarce) in the fruits and vegetables test when the external temperature was above 32°C and external relative humidity was below 50%. An increase in relative humidity of 35% was achieved in all of the tests when the external temperature was above 32°C and external relative humidity was below 65%. Finally, the sample of fruits and vegetables stored within the enclosure had a superior appearance and lower mass loss compared to the sample of fruits and vegetables stored in the surroundings, where the internal sample remained healthy for approximately 88.3% longer than the external sample on average and there was an average mass loss of 5.52% for the internal sample and 18.6% for the external sample between the first and last days. From this experimentation, the results successfully demonstrated the potential of evaporative cooling utilising forced convection as an affordable alternative.

- Enhancements were performed with the incorporation of a thermoelectric module to complement the evaporative cooling for more consistent performance with temperature fluctuations minimised by at least 30%. The chosen thermoelectric module was the TEC1-12706 which had an operating voltage range between 0V and 15.4V with a drawn current up to 6.4A for a maximum power

around 80W and temperatures ranging between -30°C and 70°C . The photovoltaic system was expanded with two additional generic 3.5W solar panels each outputting 0.5833A at 6V which were connected in series directly to the thermoelectric module. The results showed an improved capability to provide a temperature decrease of at least 11°C in 100% of the periods when the external temperature was above 32°C and external relative humidity was below 50%. Remarkably, this decrease was achievable with external temperatures as low as 28°C while the external relative humidity remained below 50%. Furthermore, the temperature fluctuations were minimised to an average of 4.4°C , which could be interpreted as the internal temperature fluctuating by 1°C for each 3.5°C fluctuation in the external temperature on average. Compared to the previous tests with the internal temperature fluctuating by 1°C for each 2.4°C fluctuation in the external temperature on average for the cotton ring spun, the thermoelectric module offered an improvement of 45.8% in the internal temperature fluctuation per unit external temperature fluctuation. Likewise, compared to the previous tests with the internal temperature fluctuating by 1°C for each 2.6°C fluctuation in the external temperature on average for the polyester, the thermoelectric module offered an improvement of 34.6% in the internal temperature fluctuation per unit external temperature fluctuation. Ultimately, the incorporation of the thermoelectric module was successful, but, based on the extra cost of R335 or €17.93 for the thermoelectric module and additional solar panels, the cost for the electronic components would be increased by 83.8% over the configuration with a low capacity battery and this would unacceptably eliminate the original aim for an extremely affordable means of storing fruits and vegetables in developing countries.

Ensuing from the objectives and conclusions of this research and for further development, the following recommendations are proposed for the expansion of the research into the applicability of using evaporative cooling as a practical solution for the short-term storage of fruits and vegetables with a primary focus on portability, off-grid usage, and adoption in developing countries:

- Perform additional practical experimentation under extreme environmental conditions, such as in desert climates with higher temperatures and lower relative humidities, while also monitoring the changes to internal properties of the fruits and vegetables, such as flavour and nutrient content. There may also be consideration for the storage of other items, such as water and dry foods.
- Modify the design to develop a final and robust product orientated towards mass manufacturing. It would also be necessary to consider the investment costs for manufacturing, labour, and equipment relative to the projected costs for the materials and electronic components.
- Deploy several prototypes of the developed product to locals in the relevant locations for the most suitable operation, such as Nigeria, Kenya, India, and Yemen, and seek feedback from the locals on the performance and possible improvements compared to other options which are currently available to them for the storage of fruits and vegetables. This would be essential in determining if there are amalgamated humanitarian and commercial opportunities to pursue.

LIST OF REFERENCES

- [1] N. Aste, C. D. Pero and F. Leonforte. *Active Refrigeration Technologies For Food Preservation In Humanitarian Context*. Sustainable Energy Technologies and Assessments, Vol. 22, Pp. 150-160. ScienceDirect, Elsevier (Feb. 2017). ISSN: 2213-1388. DOI: 10.1016/j.seta.2017.02.014. URL: <https://www.sciencedirect.com/science/article/pii/S2213138817301121>.
- [2] C. G. Rao. *Engineering For Storage Of Fruits And Vegetables: Cold Storage, Controlled Atmosphere Storage, Modified Atmosphere Storage*. Academic Press, Elsevier (2015). ISBN: 978-0-12-803365-4. DOI: 10.1016/B978-0-12-803365-4.00049. URL: <https://www.sciencedirect.com/book/9780128033654/engineering-for-storage-of-fruits-and-vegetables>.
- [3] D. Beasley et al. *The State Of Food Security And Nutrition: Safeguarding Against Economic Slowdowns And Downturns*. World Food Programme of the United Nations (July 2019). URL: <https://docs.wfp.org/api/documents/WFP-0000106760/download/>.
- [4] D. Beasley et al. *Hunger Map 2019*. World Food Programme of the United Nations (Oct. 2019). URL: <https://docs.wfp.org/api/documents/WFP-0000108355/download/>.
- [5] National Research Council. *Postharvest Food Losses In Developing Countries*. National Academies Press (1978). ISBN: 978-0-309-33586-7. DOI: 10.17226/20028. URL: <https://www.nap.edu/catalog/20028/postharvest-food-losses-in-developing-countries>.
- [6] A. A. Kader. *Increasing Food Availability By Reducing Postharvest Losses Of Produce*. Acta Horticulturae, Vol. 682, Pp. 2169-2176. International Society for Horticultural Science (June 2005). ISSN: 2406-6168. DOI: 10.17660/ActaHortic.2005.682.296. URL: https://www.actahort.org/books/682/682_296.htm or <http://ucce.ucdavis.edu/files/datastore/234-528.pdf>.
- [7] M. S. Rahman et al. *Handbook Of Food Preservation*. 2nd Ed. CRC Press, Taylor & Francis Group (July 2007). ISBN: 978-1-57444-606-7. DOI: 10.1201/9781420017373. URL: <https://www.taylorfrancis.com/books/e/9780429191084>.
- [8] G. Rapsomanikis. *The Economic Lives Of Smallholder Farmers: An Analysis Based On Household Data From Nine Countries*. Food and Agriculture Organisation of the United Nations (Dec. 2015). URL: <https://www.fao.org/3/a-i5251e.pdf>.
- [9] G. S. Fields and P. N. Jefferson (Editor). *Poverty And Low Earnings In The Developing World*. Oxford Handbook of the Economics of Poverty, Oxford Handbooks (Dec. 2012). DOI: 10.1093/oxfordhb/9780195393781.013.0009. URL: <https://www.oxfordhandbooks.com/view/10.1093/oxfordhb/9780195393781.001.0001/oxfordhb-9780195393781-e-8>.
- [10] E. Verploegen, O. Sanogo and T. Chagomoka. *Evaporative Cooling Technologies For Improved Vegetable Storage In Mali*. MIT D-Lab, Massachusetts Institute of Technology, and World Vegetable Center, Mali (June 2018). URL: <https://d-lab.mit.edu/sites/default/files/in>

line-files/Evaporative%20Cooling%20Technologies%20for%20Improved%20Vegetable%20Storage%20in%20Mali%20-%20Evaluation%20Report_0.pdf and <https://d-lab.mit.edu/sites/default/files/inline-files/Evaporative%20Cooling%20Technologies%20for%20Improved%20Vegetable%20Storage%20in%20Mali%20-%20Appendix.pdf>.

- [11] S. Chen and M. Ravallion. *The Developing World Is Poorer Than We Thought, But No Less Successful In The Fight Against Poverty*. Quarterly Journal of Economics, Vol. 125, No. 4, Pp. 1577-1625. Oxford Academic (Nov. 2010). ISSN: 0033-5533. DOI: 10.1162/qjec.2010.125.4.1577. URL: <https://academic.oup.com/qje/article-abstract/125/4/1577/1916270>.
- [12] S. Freije-Rodríguez et al. *Poverty And Shared Prosperity 2020, Chapter 1: Monitoring Global Poverty*. World Bank (Oct. 2020). ISBN: 978-1-4648-1603-1. DOI: 10.1596/978-1-4648-1602-4. URL: <https://elibrary.worldbank.org/doi/abs/10.1596/978-1-4648-1602-4>.
- [13] International Comparison Program, World Development Indicators Database and Eurostat-OECD PPP Programme. *Gross Domestic Product Per Capita, PPP (International \$)*. World Bank (Jan. 2020). URL: <https://data.worldbank.org/indicator/NY.GDP.PCAP.PP.CD>.
- [14] World Economic Outlook Database. *Gross Domestic Product Per Capita, PPP (International \$)*. International Monetary Fund (Oct. 2020). URL: <https://www.imf.org/~media/Files/Publications/WEO/WEO-Database/2020/02/WEOOct2020all.ashx>.
- [15] W. Yang et al. *Rethinking Poverty: The World Social Situation 2010 - Chapter 2: Poverty: The Official Numbers*. Economic and Social Affairs, United Nations (Jan. 2010). ISBN: 978-92-1-130278-3. URL: <https://www.un.org/esa/socdev/rwss/docs/2010/chapter2.pdf>.
- [16] R. Wills and J. Golding. *Postharvest: An Introduction To The Physiology And Handling Of Fruits And Vegetables*. 6th Ed. University of New South Wales Press and Centre for Agriculture and Bioscience International (2016). ISBN: 978-1-78639-148-3. DOI: 10.1079/9781786391483.0000. URL: <https://www.cabi.org/nutrition/ebook/20163314760>.
- [17] American Society of Heating, Refrigerating, and Air-Conditioning Engineers. *2010 ASHRAE Handbook - Refrigeration (SI Edition)*. ASHRAE (2010). ISBN: 978-1-933742-82-3. URL: <https://app.knovel.com/web/toc.v/cid:kpASHRAE82/>.
- [18] J. Albrecht. *Food Storage*. University of Nebraska-Lincoln and US Department of Agriculture (Apr. 2007). URL: <https://extensionpublications.unl.edu/assets/pdf/ec446.pdf>.
- [19] G. W. Gould. *Methods For Preservation And Extension Of Shelf Life*. International Journal of Food Microbiology, Vol. 33, No. 1, Pp. 51-64. ScienceDirect, Elsevier (Sept. 1996). ISSN: 0168-1605. DOI: 10.1016/0168-1605(96)01133-6. URL: <https://www.sciencedirect.com/science/article/pii/0168160596011336>.
- [20] B. R. Becker and B. A. Fricke. *Transpiration And Respiration Of Fruits And Vegetables*. Science et Technique du Froid, Vol. 6, Pp. 110-121. International Institute for Refrigeration

- and American Society of Agricultural Engineers (1996). ISSN: 0151-1637. URL: <https://b.wiley.com/doi/10.1002/9780813802947>.
- [21] M. Nunes. *Color Atlas Of Postharvest Quality Of Fruits And Vegetables*. 1st Ed. Blackwell Publishing, John Wiley and Sons (May 2008). ISBN: 978-0-813-81752-1. DOI: 10.1002/9780813802947. URL: <https://onlinelibrary.wiley.com/doi/book/10.1002/9780813802947>.
- [22] Dometic Group. *CFX3 45 Operating Manual* (Feb. 2020). URL: https://www.dometic.com/assets/33/18/dometiccfx3_opm_4445103034_emea16_01_2020-02_73318.pdf.
- [23] Dometic Group. *Combicool ACX 40 Operating Manual* (Sept. 2017). URL: https://www.dometic.com/assets/35/41/operating%20manual_53541.pdf.
- [24] M. J. Moran et al. *Fundamentals Of Engineering Thermodynamics*. 9th Ed. Wiley, John Wiley and Sons (2018). ISBN: 978-1-119-39138-8. URL: <https://www.wiley.com/en-us/Fundamentals+of+Engineering+Thermodynamics%2C+9th+Edition-p-9781119391388>.
- [25] S. K. Kushwaha and A. C. Tiwari. *Evaporative Cooling Comfort In Agricultural Tractor Cabin*. Journal of the Brazilian Society of Mechanical Sciences and Engineering, Vol. 38, No. 3, Pp. 965-976. SpringerLink (Mar. 2016). ISSN: 1806-3691. DOI: 10.1007/s40430-015-0442-1. URL: <https://link.springer.com/article/10.1007/s40430-015-0442-1>.
- [26] P. Goyal et al. *Adsorption Refrigeration Technology - An Overview Of Theory And Its Solar Energy Applications*. Renewable and Sustainable Energy Reviews, Vol. 53, Pp. 1389-1410. ScienceDirect, Elsevier (Jan. 2016). ISSN: 1364-0321. DOI: 10.1016/j.rser.2015.09.027. URL: <https://www.sciencedirect.com/science/article/pii/S1364032115009971>.
- [27] A. Ial Basediya, D. V. K. Samuel and V. Beera. *Evaporative Cooling System For Storage Of Fruits And Vegetables - A Review*. Journal of Food Science and Technology, Vol. 50, No. 3, Pp. 429-442. SpringerLink (June 2013). ISSN: 0975-8402. DOI: 10.1007/s13197-011-0311-6. URL: <https://link.springer.com/article/10.1007/s13197-011-0311-6>.
- [28] W. Olosunde, J. Igbeka and T. Olurin. *Performance Evaluation Of Absorbent Materials In Evaporative Cooling System For Storing Fruits And Vegetables*. International Journal of Food Engineering, Vol. 5, No. 3, De Gruyter (July 2009). ISSN: 1556-3758. DOI: 10.2202/1556-3758.1376. URL: <https://www.degruyter.com/document/doi/10.2202/1556-3758.1376/html>.
- [29] G. J. Bom et al. *Evaporative Air-Conditioning: Applications For Environmentally Friendly Cooling*. World Bank (Mar. 1999). ISBN: 0-8213-4334-3. URL: <https://documents.worldbank.org/en/publication/documents-reports/documentdetail/717411468739217789/evaporative-air-conditioning-applications-for-environmentally-friendly-cooling>.
- [30] E. Anyanwu. *Design And Measured Performance Of Porous Evaporative Cooler For Preservation Of Fruits And Vegetables*. Energy Conversion and Management, Vol. 45, No. 13, Pp. 2187-2195. ScienceDirect, Elsevier (Aug. 2004). ISSN: 0196-8904. DOI: 10.1016/j.enconman.200

- 3.10.020. URL: <https://www.sciencedirect.com/science/article/pii/S0196890403003273>.
- [31] J. Ambuko et al. *Preservation Of Postharvest Quality Of Leafy Amaranth (Amaranthus spp.) Vegetables Using Evaporative Cooling*. Journal of Food Quality, Wiley, John Wiley and Sons, and Hindawi Publishing (Dec. 2017). ISSN: 0146-9428. DOI: 10.1155/2017/5303156. URL: <https://www.hindawi.com/journals/jfq/2017/5303156/>.
- [32] S. B. Riffat and X. Ma. *Thermoelectrics: A Review Of Present And Potential Applications*. Applied Thermal Engineering, Vol. 23, No. 8, Pp. 913-935. ScienceDirect, Elsevier (June 2003). ISSN: 1359-4311. DOI: 10.1016/S1359-4311(03)00012-7. URL: <https://www.sciencedirect.com/science/article/pii/S1359431103000127>.
- [33] T. L. Bergman et al. *Fundamentals Of Heat And Mass Transfer*. 8th Ed. Wiley, John Wiley and Sons (Dec. 2018). ISBN: 978-1-119-35388-1. URL: <https://www.wiley.com/en-us/Fundamentals+of+Heat+and+Mass+Transfer%2C+8th+Edition-p-9781119353881>.
- [34] W. Akpalu, A. K. Christian and S. N. A. Codjoe. *Food Access And Subjective Welfare In A Developing Country*. Journal of Behavioral and Experimental Economics, Vol. 73, Pp. 34-39. ScienceDirect, Elsevier (Jan. 2018). ISSN: 2214-8043. DOI: 10.1016/j.socec.2018.01.002. URL: <https://www.sciencedirect.com/science/article/pii/S2214804318300132>.
- [35] Earth Observing System Data and Information System (EODIS). *Earthdata Worldview - Surface Air Temperature And Surface Relative Humidity, During The Day, Monthly*. NASA (2020). URL: [https://worldview.earthdata.nasa.gov/?v=-285,-165,255,115&t=2019-01-03-T00%3A00%3A00Z&l=Coastlines,AIRS_L3_Surface_Relative_Humidity_Monthly_Day\(hidden\),AIRS_L3_Surface_Air_Temperature_Monthly_Day](https://worldview.earthdata.nasa.gov/?v=-285,-165,255,115&t=2019-01-03-T00%3A00%3A00Z&l=Coastlines,AIRS_L3_Surface_Relative_Humidity_Monthly_Day(hidden),AIRS_L3_Surface_Air_Temperature_Monthly_Day).
- [36] J. Allen and NASA Earth Observations (NEO). *Solar Insolation*. NASA (2020). URL: https://neo.sci.gsfc.nasa.gov/view.php?datasetId=CERES_INSOL_M&year=2019.
- [37] P. Taalas et al. *WMO Statement On The State Of The Global Climate In 2019*. World Meteorological Organization of the United Nations (Apr. 2020). ISBN: 978-92-63-11248-4. URL: https://library.wmo.int/doc_num.php?explnum_id=10211.
- [38] Southern African Universities Radiometric Network. *Solar Radiometric Data For The Public*. SAURAN (2020). URL: <https://sauran.ac.za/>.
- [39] M. J. Brooks et al. *SAURAN: A New Resource For Solar Radiometric Data In Southern Africa*. Journal of Energy in Southern Africa, Vol. 26, No. 1, Pp. 2-10. Scientific Electronic Library Online (SciELO) (Feb. 2015). ISSN: 2413-3051. URL: http://www.scielo.org.za/scielo.php?script=sci_arttext&pid=S1021-447X2015000100001.
- [40] A. R. Tilley and the Henry Dreyfuss Associates. *The Measure Of Man And Woman: Human Factors In Design*. Revised Ed. Wiley, John Wiley and Sons (Dec. 2001). ISBN: 978-0-471-09955-0. URL: <https://www.wiley.com/en-us/The+Measure+of+Man+and+Woman%3>

A+Human+Factors+in+Design%2C+Revised+Edition-p-9780471099550.

- [41] L. N. Mathesona et al. *Age And Gender Normative Data For Lift Capacity*. Work, Vol. 49, No. 2, Pp. 257-269. IOS Press (Mar. 2014). ISSN: 1051-9815. DOI: 10.3233/WOR-131671. URL: <https://content.iospress.com/articles/work/wor01671>.
- [42] D. G. Kröger. *Air-Cooled Heat Exchangers And Cooling Towers - Thermal-Flow Performance Evaluation And Design*. PennWell (2004). ISBN: 978-0-87814-896-7. URL: <https://app.knovel.com/web/toc.v/cid:kpACHECTT8/>.
- [43] National Mechanical Engineering Research Institute. *Psychrometric Chart 5, Sea Level, Barometric Pressure 101.32kPa*. Council for Scientific and Industrial Research (CSIR) (1981).
- [44] National Mechanical Engineering Research Institute. *Psychrometric Chart 12, Altitude 1700m, Barometric Pressure 82.50kPa*. Council for Scientific and Industrial Research (CSIR) (1982).
- [45] R. E. Bolz. *CRC Handbook Of Tables For Applied Engineering Science*. 2nd Ed. CRC Press, Taylor & Francis Group (1973). ISBN: 978-1-3152-1409-2. DOI: 10.1201/9781315214092. URL: <https://www.taylorfrancis.com/books/9781315214092>.
- [46] F. W. Dittus and L. M. K. Boelter. *Heat Transfer In Automobile Radiators Of The Tubular Type*. University of California Publications in Engineering, Vol. 2, No. 13, Pp. 443-461. University of California Press, Berkeley (Oct. 1930). Alternative Publication: *International Communications In Heat And Mass Transfer*, Vol. 12, No. 1, Pp. 3-22. ScienceDirect, Elsevier (1985). ISSN: 0735-1933. DOI: 10.1016/0735-1933(85)90003-X. URL: <https://www.science-direct.com/science/article/pii/073519338590003X>.
- [47] W. H. McAdams. *Heat Transmission*. 2nd Ed. McGraw-Hill and National Research Council (1942). URL: <https://archive.org/details/in.ernet.dli.2015.238768/page/n5/mode/2up>.
- [48] E. Sieder and G. Tate. *Heat Transfer And Pressure Drop Of Liquids In Tubes*. Industrial and Engineering Chemistry, Vol. 28, Pp. 1429-1435. American Chemical Society (1936). ISSN: 0019-7866. DOI: 10.1021/ie50324a027. URL: <http://pubs.acs.org/doi/10.1021/ie50324a027>.
- [49] V. Gnielinski. *New Equations For Heat And Mass Transfer In Turbulent Pipe And Channel Flow*. Engineering Research, Vol. 41, No. 1, Pp. 8-16. SpringerLink (1975). ISSN: 1434-0860. DOI: 10.1007/BF02559682. URL: <https://link.springer.com/article/10.1007/BF02559682>.
- [50] B. S. Petukhov. *Heat Transfer And Friction In Turbulent Pipe Flow With Variable Physical Properties*. Advances in Heat Transfer, Vol. 6, Pp. 503-564. Academic Press, Elsevier (Jan. 1970). ISSN: 0065-2717. DOI: 10.1016/S0065-2717(08)70153-9. URL: <https://www.science-direct.com/science/article/pii/S0065271708701539>.
- [51] D. Thorpe. *Solar Energy Pocket Reference*. 1st Ed. Routledge, Taylor & Francis (Nov. 2017). ISBN: 978-1-31575-176-4. DOI: 10.4324/9781315751764. URL: <https://www.taylorfrancis>

.com/books/9781315751764.

- [52] P. J. Erens and A. A. Dreyer. *Modelling Of Indirect Evaporative Air Coolers*. International Journal of Heat and Mass Transfer, Vol. 36, No. 1, Pp. 17-26. ScienceDirect, Elsevier (Jan. 1993). ISSN: 0017-9310. DOI: 10.1016/0017-9310(93)80062-Y. URL: <https://www.sciencedirect.com/science/article/pii/001793109380062Y>.
- [53] N. Gilani and A. H. Poshtiri. *Thermal Design Of Two-Stage Evaporative Cooler Based On Thermal Comfort Criterion*. Heat and Mass Transfer, Vol. 53, No. 4, Pp. 1355-1374. SpringerLink (Apr. 2017). ISSN: 1432-1181. DOI: 10.1007/s00231-016-1889-z. URL: <https://link.springer.com/article/10.1007/s00231-016-1889-z#citeas>.
- [54] Y. Yang, G. Cui and C. Q. Lan. *Developments In Evaporative Cooling And Enhanced Evaporative Cooling - A Review*. Renewable and Sustainable Energy Reviews, Vol. 113, Pp. 109230. ScienceDirect, Elsevier (July 2019). ISSN: 1364-0321. DOI: 10.1016/j.rser.2019.06.037. URL: <https://www.sciencedirect.com/science/article/pii/S1364032119304307>.
- [55] S. I. Manuwa and S. O. Odey. *Evaluation Of Pads And Geometrical Shapes For Constructing Evaporative Cooling System*. Modern Applied Science, Vol. 6, No. 6, Pp. 45-53. Canadian Center of Science and Education (May 2012). ISSN: 1913-1844. DOI: 10.5539/mas.v6n6p45. URL: <https://www.ccsenet.org/journal/index.php/mas/article/view/17377>.
- [56] A. K. Dhamneya, S. P. S. Rajput and A. Singh. *Thermodynamic Performance Analysis Of Direct Evaporative Cooling Systems For Increased Heat And Mass Transfer Area*. Ain Shams Engineering Journal, Vol. 9, No. 4, Pp. 2951-2960. ScienceDirect, Elsevier (Dec. 2018). ISSN: 2090-4479. DOI: 10.1016/j.asej.2017.09.008. URL: <https://www.sciencedirect.com/science/article/pii/S2090447917301260>.
- [57] X. Guo. *The Mechanics Of Fiber-Based Absorbent Evaporative Cooling (fbaEC) For Transport*. MOspace Repository, University of Missouri (Dec. 2016). URL: <https://mospace.umsystem.edu/xmlui/handle/10355/62511>.
- [58] Munters. *CELdek® 7060-15 Evaporative Cooling Pad - Product Data Sheet*. HumiCool Division, Munters Corporation AB (Feb. 2009). URL: https://www.munters.com/globalassets/inriver/resources/products/coolers--humidifiers/agh_prodsheet_celdek.pdf.
- [59] Munters. *CELdek® 7090-15 Evaporative Cooling Pad - Product Data Sheet*. HumiCool Division, Munters Corporation AB (Mar. 2011). URL: https://www.munters.com/globalassets/inriver/resources/products/coolers--humidifiers/1782-celdek-7090_15_gb.pdf.
- [60] Munters. *GLASdek® GX40 Evaporative Cooling Pad - Product Data Sheet*. HumiCool Division, Munters Corporation AB (Feb. 2020). URL: <https://www.munters.com/globalassets/inriver/resources/product-guide--glasdek-gx40.pdf>.
- [61] Y. M. Xuan et al. *Research And Application Of Evaporative Cooling In China - A Review, Part*

- I. Renewable and Sustainable Energy Reviews*, Vol. 16, No. 5, Pp. 3535-3546. ScienceDirect, Elsevier (June 2012). ISSN: 1364-0321. DOI: 10.1016/j.rser.2012.01.052. URL: <https://www.sciencedirect.com/science/article/pii/S1364032112000536>.
- [62] J. K. Jain and D. A. Hindoliya. *Experimental Performance Of New Evaporative Cooling Pad Materials*. *Sustainable Cities and Society*, Vol. 1, No. 4, Pp. 252-256. ScienceDirect, Elsevier (Dec. 2011). ISSN: 2210-6707. DOI: 10.1016/j.scs.2011.07.005. URL: <https://www.sciencedirect.com/science/article/pii/S2210670711000400>.
- [63] F. Al-Sulaiman. *Evaluation Of The Performance Of Local Fibers In Evaporative Cooling*. *Energy Conversion and Management*, Vol. 43, No. 16, Pp. 2267-2273. ScienceDirect, Elsevier (Nov. 2002). ISSN: 0196-8904. DOI: 10.1016/S0196-8904(01)00121-2. URL: <https://www.sciencedirect.com/science/article/pii/S0196890401001212>.
- [64] C.-M. Liao and K.-H. Chiu. *Wind Tunnel Modeling The System Performance Of Alternative Evaporative Cooling Pads In Taiwan Region*. *Building and Environment*, Vol. 37, No. 2, Pp. 177-187. ScienceDirect, Elsevier (Feb. 2002). ISSN: 0360-1323. DOI: 10.1016/S0360-1323(00)00098-6. URL: <https://www.sciencedirect.com/science/article/pii/S0360132300000986>.
- [65] A. Chatterjee and P. Singh. *Studies On Wicking Behaviour Of Polyester Fabric*. *Journal of Textiles*, Hindawi Publishing (Feb. 2014). ISSN: 2356-7678. DOI: 10.1155/2014/379731. URL: <https://www.hindawi.com/journals/jtex/2014/379731/>.
- [66] F. M. White. *Fluid Mechanics*. 8th Ed. McGraw-Hill Education (2015). ISBN: 978-0-07339-827-3. URL: <https://www.mhprofessional.com/9780073398273-usa-fluid-mechanics>.
- [67] P. M. Gerhart, A. L. Gerhart and J. I. Hochstein. *Munson, Young, And Okiishi's Fundamentals Of Fluid Mechanics*. 8th Ed. Wiley, John Wiley and Sons (Sept. 2016). ISBN: 978-1-119-08070-1. URL: <https://www.wiley.com/en-us/Munson%2C+Young+and+Okiishi%27s+Fundamentals+of+Fluid+Mechanics%2C+8th+Edition-p-9781119080701>.
- [68] J. Yu, T. Zhang and J. Qian. *Electrical Motor Products*. 1st Ed. Woodhead Publishing and ScienceDirect, Elsevier (Jan. 2011). ISBN: 978-0-85709-077-5. DOI: 10.1533/9780857093813.11. URL: <https://www.sciencedirect.com/book/9780857090775/electrical-motor-products>.
- [69] Eskom. *Fans Brochure - Blow The Lid On Ineffective Energy Usage* (Aug. 2010). URL: https://www.eskom.co.za/sites/idm/Documents/124538_Fans_Brochure.pdf.
- [70] M. Zumsteeg, S. Karadzhi and E. Rehmet. *Technical Handbook - Ventilation*. Systemair GmbH (July 2019). URL: https://www.systemair.com/fileadmin/user_upload/systemair-b2b/Local/Norway/Leaflets/Technical_Handbook_EN_2019-07_E2029_web_no.pdf.
- [71] S. Frank and M. Darvish. *Numerical Investigation On The Performance Characteristics Of Radial Fans With Forward Curved Blades By Means Of CFD*. STAR European Conference 2011, University of Applied Sciences HTW (Mar. 2011). URL: <https://mdx2.plm.automation>

[.siemens.com/sites/default/files/Presentation/26-berlin.pdf](https://www.siemens.com/sites/default/files/Presentation/26-berlin.pdf).

- [72] J. S. Anagnostopoulos. *CFD Analysis And Design Effects In A Radial Pump Impeller*. Transactions on Fluid Mechanics, Vol. 1, No. 7, Pp. 763-770 (Jan. 2006). ISSN: 1790-5087. URL: <https://worldses.org/journals/fluid/fluid-january2006.doc>.
- [73] W. Jansen and A. M. Kirschner. *Impeller Blade Design Method For Centrifugal Compressors*. Fluid Mechanics, Acoustics, and Design of Turbomachinery, Part 2, Pp. 537-563. NASA (Jan. 1974). URL: <https://ntrs.nasa.gov/search.jsp?R=19750003125>.
- [74] X. Zhou, Y. Zhang, Z. Ji and H. Hou. *The Optimal Hydraulic Design Of Centrifugal Impeller Using Genetic Algorithm With Boundary Vorticity Flux*. International Journal of Rotating Machinery, Hindawi Publishing (Aug. 2014). ISSN: 1542-3034. DOI: 10.1155/2014/845302. URL: <https://www.hindawi.com/journals/ijrm/2014/845302/>.
- [75] K. W. Cheah, T. S. Lee, S. H. Winoto and Z. M. Zhao. *Numerical Flow Simulation In A Centrifugal Pump At Design And Off-Design Conditions*. International Journal of Rotating Machinery, Hindawi Publishing (Apr. 2007). ISSN: 1542-3034. DOI: 10.1155/2007/83641. URL: <https://www.hindawi.com/journals/ijrm/2007/083641/>.
- [76] S. Jin et al. *Improved Indirect Evaporative Cooler Experimental Investigation*. Applied Energy, Vol. 256, ScienceDirect, Elsevier (2019). ISSN: 0306-2619. DOI: 10.1016/j.apenergy.2019.113934. URL: <https://www.sciencedirect.com/science/article/pii/S0306261919316216>.
- [77] I. Sarbu and C. Sebarchievici. *Review Of Solar Refrigeration And Cooling Systems*. Energy and Buildings, Vol. 67, Pp. 286-297. ScienceDirect, Elsevier (Dec. 2013). ISSN: 0378-7788. DOI: 10.1016/j.enbuild.2013.08.022. URL: <https://www.sciencedirect.com/science/article/pii/S0378778813005197>.
- [78] P. K. Bansal and A. Martin. *Comparative Study Of Vapour Compression, Thermoelectric, And Absorption Refrigerators*. International Journal of Energy Research, Vol. 24, No. 2, Pp. 93-107. Wiley, John Wiley and Sons (Feb. 2000). ISSN: 0363-907X. DOI: 10.1002/(SICI)1099-114X(200002)24:2<93::AID-ER563>3.0.CO;2-6. URL: [https://onlinelibrary.wiley.com/doi/10.1002/\(SICI\)1099-114X\(200002\)24:2%3C93::AID-ER563%3E3.0.CO;2-6](https://onlinelibrary.wiley.com/doi/10.1002/(SICI)1099-114X(200002)24:2%3C93::AID-ER563%3E3.0.CO;2-6).
- [79] A. Allouhi et al. *Solar Driven Cooling Systems: An Updated Review*. Renewable and Sustainable Energy Reviews, Vol. 44, Pp. 159-181. ScienceDirect, Elsevier (Apr. 2015). ISSN: 1364-0321. DOI: 10.1016/j.rser.2014.12.014. URL: <https://www.sciencedirect.com/science/article/pii/S1364032114010661>.
- [80] R. A. Serway and J. W. Jewett. *Physics For Scientists And Engineers With Modern Physics*. 10th Ed. Brooks/Cole CENGAGE Learning (2014). ISBN: 978-1-337-55329-2. URL: <https://www.cengage.co.uk/books/9781337553292/>.
- [81] L. Fraas and L. Partain. *Solar Cells And Their Applications*. 2nd Ed. Wiley, John Wiley and

- Sons (Aug. 2010). ISBN: 978-0-470-44633-1. URL: <https://www.wiley.com/en-us/Solar+Cells+and+Their+Applications%2C+2nd+Edition-p-9780470446331>.
- [82] P. Würfel and U. Würfel. *Physics Of Solar Cells, From Basic Principles To Advanced Concepts*. 3rd Ed. Wiley-VCH, John Wiley and Sons (Sept. 2016). ISBN: 978-3-527-41312-6. URL: <https://www.wiley.com/en-us/Physics+of+Solar+Cells%3A+From+Basic+Principles+to+Advanced+Concepts%2C+3rd+Edition-p-9783527413126>.
- [83] D. D. Hsu et al. *Life Cycle Greenhouse Gas Emissions Of Crystalline Silicon Photovoltaic Electricity Generation - Systematic Review And Harmonization*. Journal of Industrial Ecology, Vol. 16, No. S1, Pp. S122-S135. Wiley, John Wiley and Sons, and Yale University (Mar. 2012). ISSN: 0168-1605. DOI: 10.1111/j.1530-9290.2011.00439.x. URL: <https://onlinelibrary.wiley.com/doi/10.1111/j.1530-9290.2011.00439.x>.
- [84] Y. Wang et al. *Advanced Maximum Power Point Tracking Method For Photovoltaic Systems Using Variable Universe Fuzzy Logic Control Considering Temperature Variability*. Electronics, Vol. 7, No. 12, Multidisciplinary Digital Publishing Institute (2018). ISSN: 2079-9292. DOI: 10.3390/electronics7120355. URL: <https://www.mdpi.com/2079-9292/7/12/355>.
- [85] M. R. Patel. *Wind And Solar Power Systems - Design, Analysis, And Operation*. 2nd Ed. CRC Press, Taylor & Francis Group (July 2005). ISBN: 978-0-8493-1570-1. DOI: 10.1201/9781420039924. URL: <https://www.taylorfrancis.com/books/9780429114960>.
- [86] T. Reddy and D. Linden. *Linden's Handbook Of Batteries*. 4th Ed. McGraw-Hill (May 2010). ISBN: 978-0-07162-419-0. URL: <https://www.mhprofessional.com/9780071624190-usa-linden-handbook-of-batteries-4th-edition>.
- [87] I. S. Freitas Gomes, Y. Perez and E. Suomalainen. *Coupling Small Batteries And PV Generation: A Review*. Renewable and Sustainable Energy Reviews, Vol. 126, ScienceDirect, Elsevier (July 2020). ISSN: 1364-0321. DOI: 10.1016/j.rser.2020.109835. URL: <https://www.sciencedirect.com/science/article/pii/S1364032120301295>.
- [88] N. Gama, A. Ferreira and A. Timmons. *Polyurethane Foams: Past, Present, And Future*. Materials, Vol. 11, No. 10, Multidisciplinary Digital Publishing Institute (2018). ISSN: 1996-1944. DOI: 10.3390/ma11101841. URL: <https://www.mdpi.com/1996-1944/11/10/1841>.
- [89] M. Ashby. *Material Property Data For Engineering Materials*. 4th Ed. Cambridge University and Granta Design (Jan. 2016). URL: https://downloadfiles.grantadesign.com/pdf/booklets/Material_Property_Data_for_Engineering_Materials.pdf.
- [90] Yeti. *Tundra 45 Cooler*. Online (15th Apr. 2020). URL: https://www.yeti.com/en_US/hard-coolers/tundra-45-cooler/YT45.html (visited 16th Apr. 2020).
- [91] Coleman. *48 Quart Performance Cooler*. Online (2020). URL: <https://www.coleman.com/all-coolers/hard-coolers/48-quart-performance-cooler/> (visited 16th Apr. 2020).

- [92] MittiCool. *MittiCool Clay Refrigerator (50 Liter)*. Online (2019). URL: <https://mitticool.com/product/mitticool-clay-refrigerator50-liter/> (visited 13th Mar. 2020).
- [93] Bosch. *Products - FreshBox - FVB4290*. Online (2020). URL: <https://www.bosch-home.com.ng/productlist/fridges-and-freezers/freshbox/FVB4290> (visited 11th Mar. 2020).
- [94] BSH Home Appliances, Bosch. *FreshBox - BSH's Innovative Way To Keep Food Fresh Without Electricity For Rural Africa*. Online (2020). URL: <https://stories.bsh-group.com/en/freshbox-bshs-innovative-way-keep-food-fresh/> (visited 11th Mar. 2020).
- [95] Fenik. *Yuma 60L*. Online (2019). URL: <https://www.fenik.io/yuma> (visited 12th Mar. 2020).
- [96] Fenik. *The Fenik No-Ice Cooler, Yuma 60L*. Kickstarter. Online (15th Oct. 2019). URL: <https://www.kickstarter.com/projects/fenik/fenik-yuma-60l> (visited 12th Mar. 2020).
- [97] M. Rothmaier et al. *Design And Performance Of Personal Cooling Garments Based On Three-Layer Laminates*. *Medical and Biological Engineering and Computing*, Vol. 46, No. 8, Pp. 825-832. SpringerLink (June 2008). ISSN: 1741-0444. DOI: 10.1007/s11517-008-0363-6. URL: <https://link.springer.com/article/10.1007/s11517-008-0363-6>.
- [98] Wakati. *Product*. Online (2017). URL: <https://www.wakati.co/> (visited 29th Apr. 2020).
- [99] Wakati and A. Pauwels. *Wakati*. Online (2014). URL: <https://www.changemakers.com/nutrientsforall/competition/entries/new-entry-4> (visited 29th Apr. 2020).
- [100] Wakati. *Learn*. Online (2017). URL: <https://www.wakati.co/learn> (visited 29th Apr. 2020).
- [101] I. L. Maclaine-cross and P. J. Banks. *A General Theory Of Wet Surface Heat Exchangers And Its Application To Regenerative Evaporative Cooling*. *Journal of Heat Transfer*, Vol. 103, No. 3, Pp. 579-585. American Society of Mechanical Engineers (Aug. 1981). ISSN: 0022-1481. DOI: 10.1115/1.3244505. URL: <https://asmedigitalcollection.asme.org/heattransfer/article-abstract/103/3/579/413689/A-General-Theory-of-Wet-Surface-Heat-Exchangers>.
- [102] D. Pescod. *A Heat Exchanger For Energy Saving In An Air-Conditioning Plant*. *ASHRAE Transactions*, Vol. 85, No. 2, Pp. 238-251. ASHRAE (1979). ISSN: 0001-2505. URL: https://www.techstreet.com/ashrae/standards/de-2542-a-heat-exchanger-for-energy-saving-in-an-air-conditioning-plant?product_id=1853360.
- [103] E. Gómez, A. González and F. Martínez. *Experimental Characterisation Of Indirect Evaporative Cooling Prototype In Two Operating Modes*. *Applied Energy*, Vol. 97, Pp. 340-346. ScienceDirect, Elsevier (2011). ISSN: 0306-2619. DOI: <https://doi.org/10.1016/j.apenergy.2011.12.065>. URL: <https://www.sciencedirect.com/science/article/pii/S0306261911008610>.
- [104] American Society of Heating, Refrigerating, and Air-Conditioning Engineers. *Standard 55: Thermal Environmental Conditions For Human Occupancy*. ANSI/ASHRAE (2017). URL: https://www.techstreet.com/ashrae/standards/ashrae-55-2017?product_id=1994974.

- [105] K. S. Fancey et al. *Experimental Investigation On Performance Of Fabrics For Indirect Evaporative Cooling Applications*. Building and Environment, Vol. 110, Pp. 104-114. ScienceDirect, Elsevier (Dec. 2016). ISSN: 0360-1323. DOI: 10.1016/j.buildenv.2016.10.003. URL: <https://www.sciencedirect.com/science/article/pii/S036013231630395X>.
- [106] X. Zhao, S. Liu and S. B. Riffat. *Comparative Study Of Heat And Mass Exchanging Materials For Indirect Evaporative Cooling Systems*. Building and Environment, Vol. 43, No. 11, Pp. 1902-1911. ScienceDirect, Elsevier (Nov. 2008). ISSN: 0360-1323. DOI: 10.1016/j.buildenv.2007.11.009. URL: <https://www.sciencedirect.com/science/article/pii/S0360132307002338>.
- [107] C. Goupil (Editor). *Continuum Theory And Modeling Of Thermoelectric Elements*. 1st Ed. Wiley, John Wiley and Sons (Feb. 2016). ISBN: 978-3-527-41337-9. DOI: 10.1002/9783527338405. URL: <https://www.wiley.com/en-us/Continuum+Theory+and+Modeling+of+Thermoelectric+Elements-p-9783527413379>.
- [108] D. Zhao and G. Tan. *A Review Of Thermoelectric Cooling: Materials, Modeling, And Applications*. Applied Thermal Engineering, Vol. 66, No. 1, Pp. 15-24. ScienceDirect, Elsevier (May 2014). ISSN: 1359-4311. DOI: 10.1016/j.applthermaleng.2014.01.074. URL: <https://www.sciencedirect.com/science/article/pii/S1359431114000854>.
- [109] Y. J. Dai, R. Z. Wang and L. Ni. *Experimental Investigation And Analysis On A Thermoelectric Refrigerator Driven By Solar Cells*. Solar Energy Materials and Solar Cells, Vol. 77, No. 4, Pp. 377-391. ScienceDirect, Elsevier (June 2003). ISSN: 0927-0248. DOI: 10.1016/S0927-0248(02)00357-4. URL: <https://www.sciencedirect.com/science/article/pii/S0927024802003574>.
- [110] T. Hara et al. *Cooling Performance Of Solar Cell Driven, Thermoelectric Cooling Prototype Headgear*. Applied Thermal Engineering, Vol. 18, No. 11, Pp. 1159-1169. ScienceDirect, Elsevier (Nov. 1998). ISSN: 1359-4311. DOI: 10.1016/S1359-4311(98)00046-5. URL: <https://www.sciencedirect.com/science/article/pii/S1359431198000465>.
- [111] H. Choi, S. Yun and K. Whang. *Developing Temperature-Controlled Car-Seat System Utilizing Thermoelectric Device*. Applied Thermal Engineering, Vol. 27, No. 17, Pp. 2841-2849. ScienceDirect, Elsevier (Dec. 2007). ISSN: 1359-4311. DOI: 10.1016/j.applthermaleng.2006.09.004. URL: <https://www.sciencedirect.com/science/article/pii/S1359431106003073>.
- [112] R. L. Field. *Photovoltaic / Thermoelectric Refrigerator For Medicine Storage For Developing Countries*. Solar Energy, Vol. 25, No. 5, Pp. 445-447. ScienceDirect, Elsevier (Jan. 1980). ISSN: 0038-092X. DOI: 10.1016/0038-092X(80)90452-1. URL: <https://www.sciencedirect.com/science/article/pii/0038092X80904521>.
- [113] H. Buitendach, I. N. Jiya and R. Gouws. *Solar Powered Peltier Cooling Storage For Vaccines In Rural Areas*. Indonesian Journal of Electrical Engineering and Computer Science, Vol. 17, No. 1, Pp. 36-46. Institute of Advanced Engineering and Science (Jan. 2020). ISSN: 2502-4752.

DOI: 10.11591/ijeecs.v17.i1. URL: <http://ijeecs.iaescore.com/index.php/IJEECS/article/view/20237/13204> and <https://repository.nwu.ac.za/handle/10394/33508>.

- [114] J. Gastelo-Roque and A. Morales-Acevedo. *Design Of A Photovoltaic System Using Thermoelectric Peltier Cooling For Vaccines Refrigeration*. 2017 IEEE MIT Undergraduate Research Technology Conference, Institute of Electrical and Electronics Engineers (Nov. 2017). DOI: 10.1109/URTC.2017.8284211. URL: <https://ieeexplore.ieee.org/document/8284211>.
- [115] D. H. Haynes, D. H. Puckett and W. P. Monaghan. *Blood Storage And Transport Using A Portable Thermoelectric Refrigerator: Field Testing*. *Military Medicine*, Vol. 153, No. 2, Pp. 86-89. Oxford Academic (Feb. 1988). ISSN: 0026-4075. DOI: 10.1093/milmed/153.2.86. URL: <https://academic.oup.com/milmed/article-abstract/153/2/86/4846735>.
- [116] W. Tipsaenporm et al. *Improvement Of Cooling Performance Of A Compact Thermoelectric Air Conditioner Using A Direct Evaporative Cooling System*. *Journal of Electronic Materials*, Vol. 41, No. 6, Pp. 1186-1192. SpringerLink (Feb. 2012). ISSN: 1543-186X. DOI: 10.1007/s11664-012-1909-9. URL: <https://link.springer.com/article/10.1007/s11664-012-1909-9>.
- [117] R. Daghigh and Y. Khaledian. *Effective Design, Theoretical And Experimental Assessment Of A Solar Thermoelectric Cooling-Heating System*. *Solar Energy*, Vol. 162, Pp. 561-572. ScienceDirect, Elsevier (Mar. 2018). ISSN: 0038-092X. DOI: 10.1016/j.solener.2018.01.012. URL: <https://www.sciencedirect.com/science/article/pii/S0038092X18300252>.
- [118] L. Shen, F. Xiao, H. Chen and S. Wang. *Investigation Of A Novel Thermoelectric Radiant Air-Conditioning System*. *Energy and Buildings*, Vol. 59, Pp. 123-132. ScienceDirect, Elsevier (Apr. 2013). ISSN: 0378-7788. DOI: 10.1016/j.enbuild.2012.12.041. URL: <https://www.sciencedirect.com/science/article/pii/S0378778813000145>.
- [119] Y. Alomair et al. *Theoretical And Experimental Analyses Of Solar-Thermoelectric Liquid-Chiller System*. *International Journal of Refrigeration*, Vol. 56, Pp. 126-139. ScienceDirect, Elsevier (Aug. 2015). ISSN: 0140-7007. DOI: 10.1016/j.ijrefrig.2015.01.003. URL: <https://www.sciencedirect.com/science/article/pii/S0140700715000055>.
- [120] Y.-L. Chen et al. *Experimental Investigation On Thermoelectric Chiller Driven By Solar Cell*. *International Journal of Photoenergy*, Hindawi Publishing (June 2014). ISSN: 1110-662X. DOI: 10.1155/2014/102510. URL: <https://www.hindawi.com/journals/ijp/2014/102510/>.
- [121] M. Mirmanto et al. *Experimental Performances Of A Thermoelectric Cooler Box With Thermoelectric Position Variations*. *Engineering Science and Technology*, Vol. 22, No. 1, Pp. 177-184. ScienceDirect, Elsevier (Feb. 2019). ISSN: 2215-0986. DOI: 10.1016/j.jestch.2018.09.006. URL: <https://www.sciencedirect.com/science/article/pii/S2215098618307031>.
- [122] G. Min and D. Rowe. *Experimental Evaluation Of Prototype Thermoelectric Domestic Refrigerators*. *Applied Energy*, Vol. 83, No. 2, Pp. 133-152. ScienceDirect, Elsevier (Feb.

- 2019). ISSN: 0306-2619. DOI: 10.1016/j.apenergy.2005.01.002. URL: <https://www.sciencedirect.com/science/article/pii/S0306261905000085>.
- [123] S. M. A. Rahman et al. *Performance And Life Cycle Analysis Of A Novel Portable Solar Thermoelectric Refrigerator*. Case Studies in Thermal Engineering, Vol. 19, ScienceDirect, Elsevier (June 2020). ISSN: 2214-157X. DOI: 10.1016/j.csite.2020.100599. URL: <https://www.sciencedirect.com/science/article/pii/S2214157X19304599>.
- [124] W. He et al. *Theoretical And Experimental Investigation On A Thermoelectric Cooling And Heating System Driven By Solar*. Applied Energy, Vol. 107, Pp. 89-97. ScienceDirect, Elsevier (July 2013). ISSN: 0306-2619. DOI: 10.1016/j.apenergy.2013.01.055. URL: <https://www.sciencedirect.com/science/article/pii/S0306261913000640>.
- [125] S. A. Abdul-Wahab et al. *Design And Experimental Investigation Of Portable Solar Thermoelectric Refrigerator*. Renewable Energy, Vol. 34, No. 1, Pp. 30-34. ScienceDirect, Elsevier (Jan. 2009). ISSN: 0960-1481. DOI: 10.1016/j.renene.2008.04.026. URL: <https://www.sciencedirect.com/science/article/pii/S096014810800147X>.
- [126] M. Ashby. *Materials Selection In Mechanical Design*. 4th Ed. Butterworth-Heinemann, Elsevier (2011). ISBN: 978-1-85617-663-7. DOI: 10.1016/C2009-0-25539-5. URL: <https://www.sciencedirect.com/book/9781856176637/materials-selection-in-mechanical-design>.
- [127] M. Ashby. *Material Property Data For Engineering*. 4th Ed. Granta Design and Cambridge University (Jan. 2016). URL: <http://www.grantadesign.com/teachingresources/bokengen16/>.
- [128] D. C. Wilcox. *Turbulence Modeling For CFD*. 3rd Ed. DCW Industries (Nov. 2006). ISBN: 978-1-92872-908-2. URL: https://archive.org/details/turbulencemodeli00wilc_206/.
- [129] C. Pfleiderer. *Die Kreiselpumpen Für Flüssigkeiten Und Gase (Centrifugal Pumps For Liquids And Gases)*. 5th Ed. Springer-Verlag (1961). ISBN: 978-3-642-48170-3. DOI: 10.1007/978-3-642-48170-3. URL: <https://www.springer.com/gp/book/9783642481710>.
- [130] S.-C. Lin and M.-L. Tsai. *An Integrated Performance Analysis For A Backward-Inclined Centrifugal Fan*. Computers and Fluids, Vol. 56, Pp. 24-38. ScienceDirect, Elsevier (Mar. 2012). ISSN: 0045-7930. DOI: 10.1016/j.compfluid.2011.11.009. URL: <https://www.sciencedirect.com/science/article/pii/S0045793011003537>.
- [131] S.-C. Lin and C.-L. Huang. *An Integrated Experimental And Numerical Study Of Forward-Curved Centrifugal Fan*. Experimental Thermal and Fluid Science, Vol. 26, No. 5, Pp. 421-434. ScienceDirect, Elsevier (July 2002). ISSN: 0894-1777. DOI: 10.1016/S0894-1777(02)00112-7. URL: <https://www.sciencedirect.com/science/article/pii/S0894177702001127>.
- [132] Y.-T. Lee and H.-C. Lim. *Performance Assessment Of Various Fan Ribs Inside A Centrifugal Blower*. Energy, Vol. 94, Pp. 609-622. ScienceDirect, Elsevier (Dec. 2015). ISSN: 0360-5442. DOI: 10.1016/j.energy.2015.11.007. URL: <https://www.sciencedirect.com/science/article/pii>

i/S0360544215015303.

- [133] B. Launder and B. Sharma. *Application Of Energy-Dissipation Model Of Turbulence To Calculate Flow Near A Spinning Disc*. Letters in Heat and Mass Transfer, Vol. 1, No. 2, Pp. 131-137. ScienceDirect, Elsevier (Nov. 1974). ISSN: 0094-4548. DOI: 10.1016/0094-4548(74)90150-7. URL: <https://www.sciencedirect.com/science/article/pii/0094454874901507>.
- [134] V. Yakhot and S. A. Orszag. *Renormalization Group Analysis Of Turbulence*. Journal of Scientific Computing, Vol. 1, No. 1, Pp. 3-51. SpringerLink (Mar. 1986). ISSN: 1573-7691. DOI: 10.1007/BF01061452. URL: <https://link.springer.com/article/10.1007/BF01061452>.
- [135] T.-H. Shih et al. *A New k - ϵ Eddy Viscosity Model For High Reynolds Number Turbulent Flows*. Computers and Fluids, Vol. 24, No. 3, Pp. 227-238. ScienceDirect, Elsevier, and NASA (Mar. 1995). ISSN: 0045-7930. DOI: 10.1016/0045-7930(94)00032-T. URL: <https://www.sciencedirect.com/science/article/pii/004579309400032T>.
- [136] D. C. Wilcox. *Formulation Of The k - ω Turbulence Model Revisited*. AIAA Journal, Vol. 46, No. 11, Pp. 2823-2838. American Institute of Aeronautics and Astronautics (2008). ISSN: 0001-1452. DOI: 10.2514/1.36541. URL: <https://arc.aiaa.org/doi/10.2514/1.36541>.
- [137] F. R. Menter. *Two-Equation Eddy-Viscosity Turbulence Models For Engineering Applications*. American Institute of Aeronautics and Astronautics Journal, Vol. 32, No. 8, Pp. 1598-1605. American Institute of Aeronautics and Astronautics (Aug. 1994). ISSN: 0001-1452. DOI: 10.2514/3.12149. URL: <https://arc.aiaa.org/doi/10.2514/3.12149>.
- [138] F. R. Menter, M. Kuntz and R. Langtry. *Ten Years Of Industrial Experience With The SST Turbulence Model*. Turbulence, Heat, and Mass Transfer, Vol. 4, Begell House, Inc. (Oct. 2003). URL: <https://archive.org/details/tenyearsofindustrialexperiencewiththesst>.
- [139] L. Chunxi, W. S. Ling and J. Yakui. *The Performance Of A Centrifugal Fan With Enlarged Impeller*. Energy Conversion and Management, Vol. 52, No. 8, Pp. 2902-2910. ScienceDirect, Elsevier (Aug. 2011). ISSN: 0196-8904. DOI: 10.1016/j.enconman.2011.02.026. URL: <https://www.sciencedirect.com/science/article/pii/S0196890411001300>.
- [140] A. Usher. *Scoping Research On Labour And Social Issues In Global Cotton Cultivation*. Ergon Associates and BCI Steering Committee (Oct. 2006). URL: <https://www.evidensia.eco/resources/44/bci-scoping-research-on-labour-and-social-issues-in-global-cotton-cultivation/>.
- [141] R. C. Hibbeler. *Mechanics Of Materials*. 10th Ed. Pearson Prentice Hall (2017). ISBN: 978-0-13-431965-0. URL: <https://www.pearson.com/us/higher-education/product/Hibbeler-Mechanics-of-Materials-10th-Edition/9780134319650.html>.
- [142] R. G. Budynas and J. K. Nisbett. *Shigley's Mechanical Engineering Design*. 10th Ed. McGraw-Hill Education (Jan. 2014). ISBN: 978-0-07-339820-4. URL: <https://www.mhprofessional.com/9780073398204-usa-shigleys-mechanical-engineering-design>.

- [143] X. Chen and Y. Liu. *Finite Element Modeling And Simulation With ANSYS Workbench*. 2nd Ed. CRC Press, Taylor & Francis Group (Sept. 2018). ISBN: 978-1-3510-4587-2. DOI: 10.1201/9781351045872. URL: <https://www.taylorfrancis.com/books/9781351045872>.
- [144] F. Barlat and J. Lian. *ANSYS Mechanical APDL Element Reference*. ANSYS (Oct. 2012).
- [145] DFRobot. *Solar Power Manager SKU DFR0535*. Online (2020). URL: https://wiki.dfrobot.com/Solar_Power_Manager_SKU__DFR0535 (visited 10th Feb. 2021).
- [146] D. Freeman. *Introduction To Photovoltaic Systems Maximum Power Point Tracking*. Texas Instruments (Nov. 2010). URL: <https://www.ti.com/lit/an/slva446/slva446.pdf>.
- [147] Sunonwealth Electric Machine Industry. *DC Brushless Fan And Blower, 120x120x25mm Axial Fans* (Nov. 2012). URL: <http://www.mantech.co.za/datasheets/products/MFC0251V20000A99.pdf> and [https://www.sunon.com/MANAGE/Docs/WEBCONT/Files/290/SUNON%20DC%20Brushless%20Fan%20&%20Blower\(255-A\).pdf](https://www.sunon.com/MANAGE/Docs/WEBCONT/Files/290/SUNON%20DC%20Brushless%20Fan%20&%20Blower(255-A).pdf).
- [148] Sunonwealth Electric Machine Industry. *Specifications For Approval: 120x120x25mm Axial Fan MFC0251V2-000U-A99* (Jan. 2013). URL: http://portal.sunon.com.tw/pls/portal/sunon.ap.sunon_html_d_pkg.open_file?input_file_name=7264646F632F3230313430312F3137363539382F28443132303230383030472D3030292D322E706466.
- [149] Samsung. *Isocell GW1*. Online (26th Mar. 2021). URL: <https://www.samsung.com/semiconductor/minisite/isocell/mobile-image-sensors/isocell-bright-gw1/> (visited 10th July 2021).
- [150] MediaTek. *Helio G90 Series*. Online (7th June 2021). URL: <https://www.mediatek.com/products/smartphones/mediatek-helio-g90-series> (visited 11th July 2021).
- [151] D. R. Snaddon. *Firm Accountable Decisions: From Ideas To Business Plans*. 1st Ed. Picsie Press (Nov. 2009). ISBN: 978-0-620-45439-1. URL: https://books.google.co.za/books?id=3zI_swEACAAJ&dq=firm+accountable+decisions.
- [152] Bloomberg. *Currencies - Exchange Rate - Quote - EUR/ZAR*. Online (2021). URL: <https://www.bloomberg.com/quote/EURZAR:CUR> (visited 9th Feb. 2021).
- [153] Waveshare. *Solar Power Manager 16120 User Manual* (Feb. 2019). URL: https://www.waveshare.com/w/upload/6/6c/Solar_Power_Manager_user_manual_en.pdf.
- [154] Aerosemi Technology. *MT3608, High Efficiency 1.2MHz 2A Step Up Converter* (July 2012). URL: <https://www.mantech.co.za/datasheets/products/MT3608-180219A%5E1.pdf>.
- [155] Aosong (Guangzhou) Electronics. *AM2302, Digital Relative Humidity And Temperature Sensor* (Sept. 2013). URL: <https://akizukidenshi.com/download/ds/aosong/AM2302.pdf>.
- [156] Microchip. *ATmega328P, 8-Bit AVR Microcontroller With 32K Bytes In-System Programmable Flash* (Jan. 2015). URL: https://ww1.microchip.com/downloads/en/DeviceDoc/Atmel-7810-Automotive-Microcontrollers-ATmega328P_Datasheet.pdf.

- [157] EUMETSAT Data Services. *Meteosat Series*. European Organisation for the Exploitation of Meteorological Satellites (EUMETSAT). Online (2020). URL: <https://www.eumetsat.int/our-satellites/meteosat-series> (visited 18th Feb. 2021).
- [158] EUMETSAT Data Services, Meteosat-11. *EUMETView - Natural Colour Enhanced RGB, MSG, 0 Degree*. European Organisation for the Exploitation of Meteorological Satellites (EUMETSAT) (Feb. 2021). URL: <https://view.eumetsat.int/productviewer>.
- [159] Thermonamic. *Specification Of Thermoelectric Module: TEC1-12706* (Feb. 2017). URL: http://www.diyelectronics.co.za/store/index.php?controller=attachment&id_attachment=30 and <https://peltiermodules.com/peltier.datasheet/TEC1-12706.pdf>.
- [160] Earth Observing System Data and Information System (EODIS). *Earthdata Worldview - Surface Air Temperature And Surface Relative Humidity, During The Night, Monthly*. NASA (2020). URL: [https://worldview.earthdata.nasa.gov/?v=-285,-165,255,115&t=2019-01-03-T10%3A11%3A14Z&l=Coastlines,AIRS_L3_Surface_Relative_Humidity_Monthly_Night\(hidden\),AIRS_L3_Surface_Air_Temperature_Monthly_Night](https://worldview.earthdata.nasa.gov/?v=-285,-165,255,115&t=2019-01-03-T10%3A11%3A14Z&l=Coastlines,AIRS_L3_Surface_Relative_Humidity_Monthly_Night(hidden),AIRS_L3_Surface_Air_Temperature_Monthly_Night).

A ADDITIONAL RESOURCES

There were additional resources used to supplement the background, literature review, and analysis. A comprehensive list of optimal storage conditions for various fruits and vegetables was sourced from several references and is included in Table A.1. The average surface air temperature and relative humidity during the night are respectively included in Figure A.1 and Figure A.2 for each month throughout 2019 on a global basis. As an example, the psychrometric chart from the CSIR for an altitude of 1700m with an atmospheric pressure of 82.50kPa is included in Figure A.3.

B AUXILIARY DEVELOPMENT

The graphs which were used to show the convergence and agreement of the simulations for the flow optimisation in Section 5.5 are included in Figure B.1 to Figure B.9 for various iterations of the blade profile. Notably, although not directly included Section 5.5 but as an auxiliary check for verification, the blade inclination simulations were also performed using a quantity of 12 and 14 blades for outlet angles of 50° and 65°, where the results exhibited an identical trend with no perceivable advantages supporting the use of an inclination angle, as is seen in Figure B.4, Figure B.5, and Figure B.6.

C COLLABORATION DISCLAIMER

The dissemination, foreground intellectual property, and restrictions concerning third party rights resulting from the project belong to the University of the Witwatersrand, who have agreed to grant a license to Defy Appliances based on Section 10 of the terms and conditions set out in the Collaboration Agreement. With regards to funding in Section 7 of the terms and conditions set out in the Collaboration Agreement, it was agreed for Defy Appliances to cover the necessary expenses of the project - specifically, this included the tuition, training, and materials, manufacturing, and components for prototyping. A copy of the Collaboration Agreement may be obtained from the School of Mechanical, Industrial, and Aeronautical Engineering at the University of the Witwatersrand.

It should also be noted that the requisite knowledge, information, and resources to complete the project was acquired and evaluated through self-derived means in the form of published research, public online information, analytical calculations, computational simulations, and independent practical experimentation. Thus, there were no ethical risks or concerns for neither the University of the Witwatersrand nor Defy Appliances with no disturbance to, influence on, or collection of input data from human, animal, or environmental (plants, landforms, rivers, etc.) sources.

The author was employed by Defy Appliances as a Graduate Engineer during the completion of the project. As acknowledged, I am sincerely grateful to the University of the Witwatersrand and Defy Appliances for this opportunity. I have learnt from it and will carry it forward for the rest of my career.

Table A.1a: Optimal storage conditions for common fruits and vegetables with specific consideration for harvesting in harsh climates [1, 7, 16, 17]. Chilling injuries occur below the optimal temperature, while freezing injuries occur below the freezing point. (*) Appropriate data could not be reliably sourced.

Fruit / Vegetable	Temper. [°C]	Relative Humidity [%]	Optimal Shelf Life [weeks]	Freezing Point [°C]	Respiration Production	Respiration Sensitivity
Apple	-1 - 5	90 - 95	7 - 24	-1.5	High	Yes
Apricot	-0.5 - 0	90 - 95	1 - 3	-1.1	High	Yes
Artichoke	0 - 2	90 - 95	16 - 20	-2	None	No
Asparagus	2.5	95 - 100	2 - 3	-0.6	None	No
Avocado	4.5 - 13	85 - 95	2 - 8	-0.9	High	Yes
Baby Marrow	6 - 10	90 - 95	1 - 2	-1.7	*	*
Banana	13 - 15	90 - 95	1 - 4	-0.8	Low	No
Beetroot	0	98 - 100	2	-0.4	None	Yes
Bell Pepper	7 - 13	90 - 95	2 - 3	-0.7	None	No
Blueberry	-0.5 - 2	90 - 95	2 - 3	-1.3	Low	None
Broccoli	0	95 - 100	2	-0.6	None	Yes
Brussels Sprout	0	95 - 100	3 - 5	-0.8	None	Yes
Cantaloupe	2 - 3	90 - 95	2 - 4	-1.1	Medium	Yes
Carrot	0	98 - 100	3 - 4	-1.4	None	Yes
Cassava	0 - 5	85 - 90	4 - 8	*	*	*
Cherries	-1 - 0	90 - 95	1 - 2	-1.7	Low	No
Chilli Pepper	0 - 10	60 - 70	2 - 3	-0.7	None	Yes
Cranberry	2 - 6	90 - 95	8 - 16	-0.9	None	No
Cucumber	7 - 12	90 - 95	2	-0.5	Low	Yes
Eggplant	8 - 12	90 - 95	1 - 2	-0.8	None	Yes
Fig	-0.5 - 0	85 - 90	1	-2.4	Low	No
Ginger	13 - 18	65	24	*	None	No
Gooseberries	-0.5 - 0	90 - 95	-1.1	-1.1	*	*
Grapefruit	10 - 16	85 - 90	6 - 8	-1.1	Low	No
Grapes	-1 - 0	90 - 95	2 - 8	-2.7	Low	Yes
Granadilla	7 - 10	85 - 90	3 - 5	-0.9	*	*
Green Beans	3 - 7	95	1	-0.7	None	Yes
Guava	5 - 10	90	2 - 3	*	Medium	Yes
Kiwifruit	0	90 - 95	12 - 20	-0.9	High	Yes
Leafy Greens	0 - 10	95 - 100	1 - 2	-0.6	None	Yes
Lemon	10 - 13	85 - 90	4 - 24	-1.4	Low	No
Lime	9 - 13	85 - 95	6 - 8	-1.6	Low	No

Table A.1b: Optimal storage conditions for common fruits and vegetables with specific consideration for harvesting in harsh climates [1, 7, 16, 17]. Chilling injuries occur below the optimal temperature, while freezing injuries occur below the freezing point. (*) Appropriate data could not be reliably sourced.

Fruit / Vegetable	Temper. [°C]	Relative Humidity [%]	Optimal Shelf Life [weeks]	Freezing Point [°C]	Respiration Production	Respiration Sensitivity
Litchi	4 - 7	90 - 95	3 - 5	*	Medium	No
Mango	13	85 - 95	2 - 3	-1.4	Medium	Yes
Melon	7 - 13	85 - 90	2 - 4	-1.1	Low	Yes
Mushrooms	0	90	1 - 2	-0.9	None	Yes
Nectarine	-0.5 - 0	90 - 95	2 - 4	-0.9	High	None
Okra	7 - 10	90 - 95	1 - 2	-1.8	Low	Yes
Olives	6 - 10	85 - 90	4 - 6	-1.4	*	*
Onion	0 - 4	70	4 - 12	-0.8	None	No
Orange	4 - 10	85 - 95	3 - 8	-0.8	Low	No
Papaya	7 - 13	85 - 90	1 - 3	*	Medium	Yes
Passion Fruit	7 - 10	85 - 90	3 - 5	-0.9	*	*
Peas	4 - 5	95	1	-0.6	None	Yes
Peach	0	90 - 98	2 - 4	-0.9	High	Yes
Pear	-1 - 5 4.5	90 - 95	8 - 28	-1.6	High	Yes
Pineapple	7 - 13	85 - 90	2 - 4	-1.1	Low	No
Plantain	13 - 15	90 - 95	1 - 5	-0.8	Low	No
Plum	-0.5 - 0	90 - 95	2 - 5	-0.8	High	Yes
Pomegranate	5 - 10	90 - 95	8 - 12	-3.0	None	No
Potato	4 - 12	90 - 95	20 - 32	-0.8	None	Yes
Pumpkin	12 - 15	50 - 70	8 - 12	-0.8	None	Yes
Raspberry	-0.5 - 0	90 - 95	1	-0.9	Low	No
Spinach	0	95 - 100	2	-0.3	*	*
Squash	7 - 11	95	1 - 2	-0.5	None	Yes
Star Apple	3	90	3	-1.2	*	*
Strawberry	0	90 - 95	1	-0.8	Low	No
Sweet Corn	0	90 - 98	1	-0.6	None	No
Sweet Potato	13 - 15	85 - 95	16 - 28	-1.3	None	Yes
Tangerine	4 - 7	85 - 95	2 - 4	-1.1	Low	No
Tomato	9 - 14	85 - 95	1 - 3	-0.5	Medium	No
Turnip	0	95	16 - 20	-1.0	None	Yes
Watermelon	10 - 21	90	2 - 3	-0.4	None	Yes
Yam	15	70 - 80	8 - 28	-1.1	None	Yes

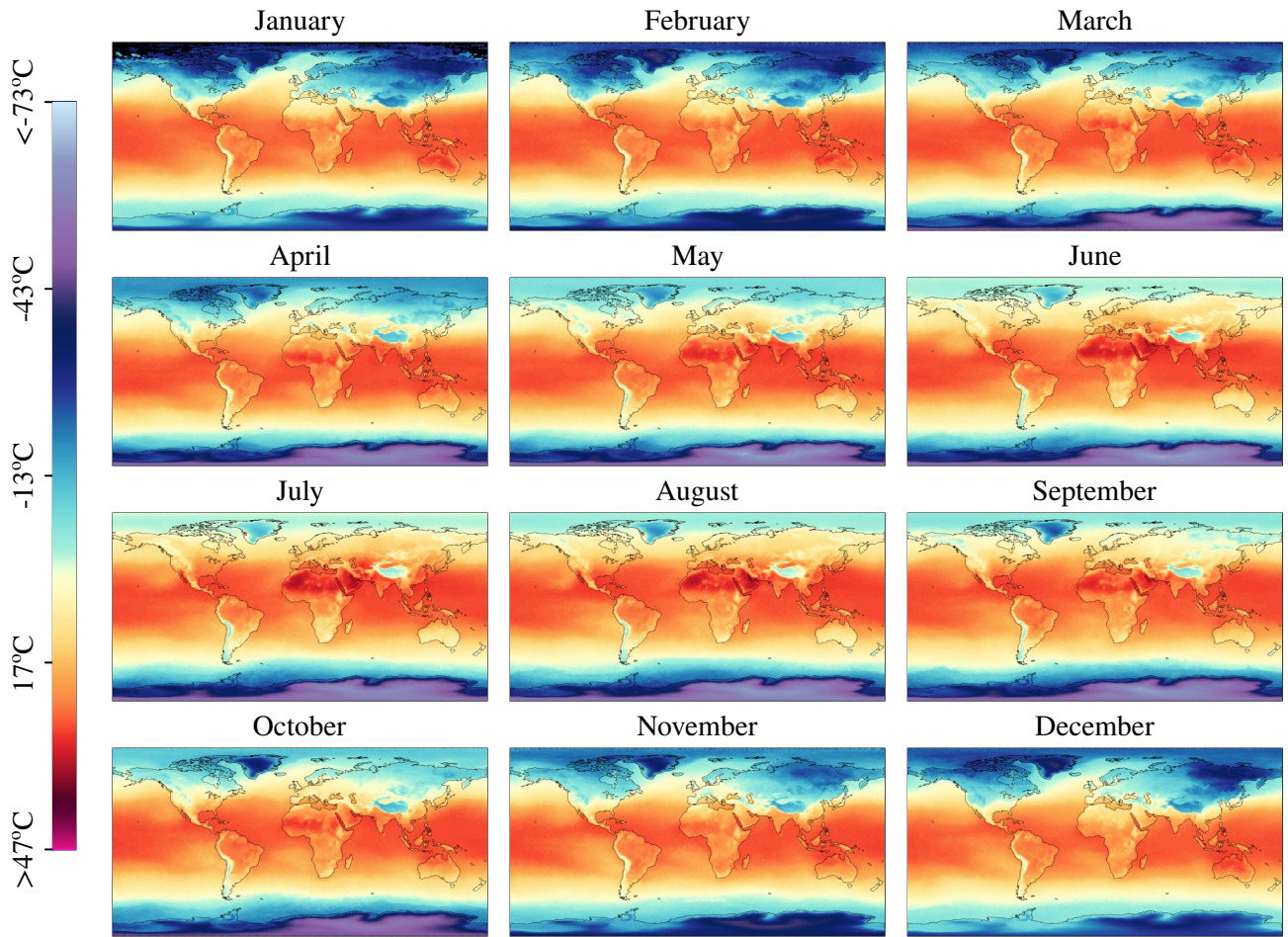


Figure A.1: Average surface air temperature during the night for each month in 2019 [160].

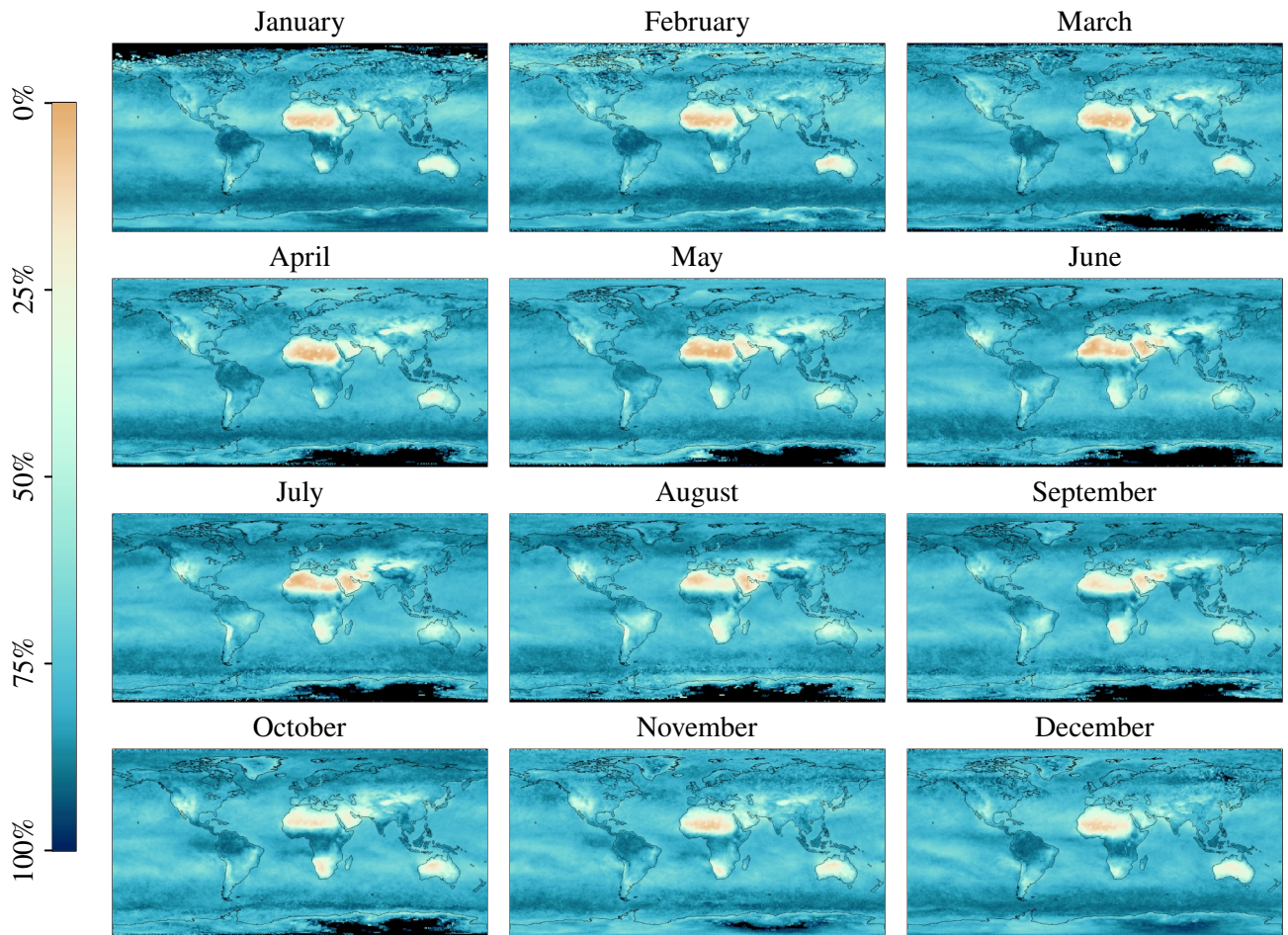


Figure A.2: Average surface relative humidity during the night for each month in 2019 [160].

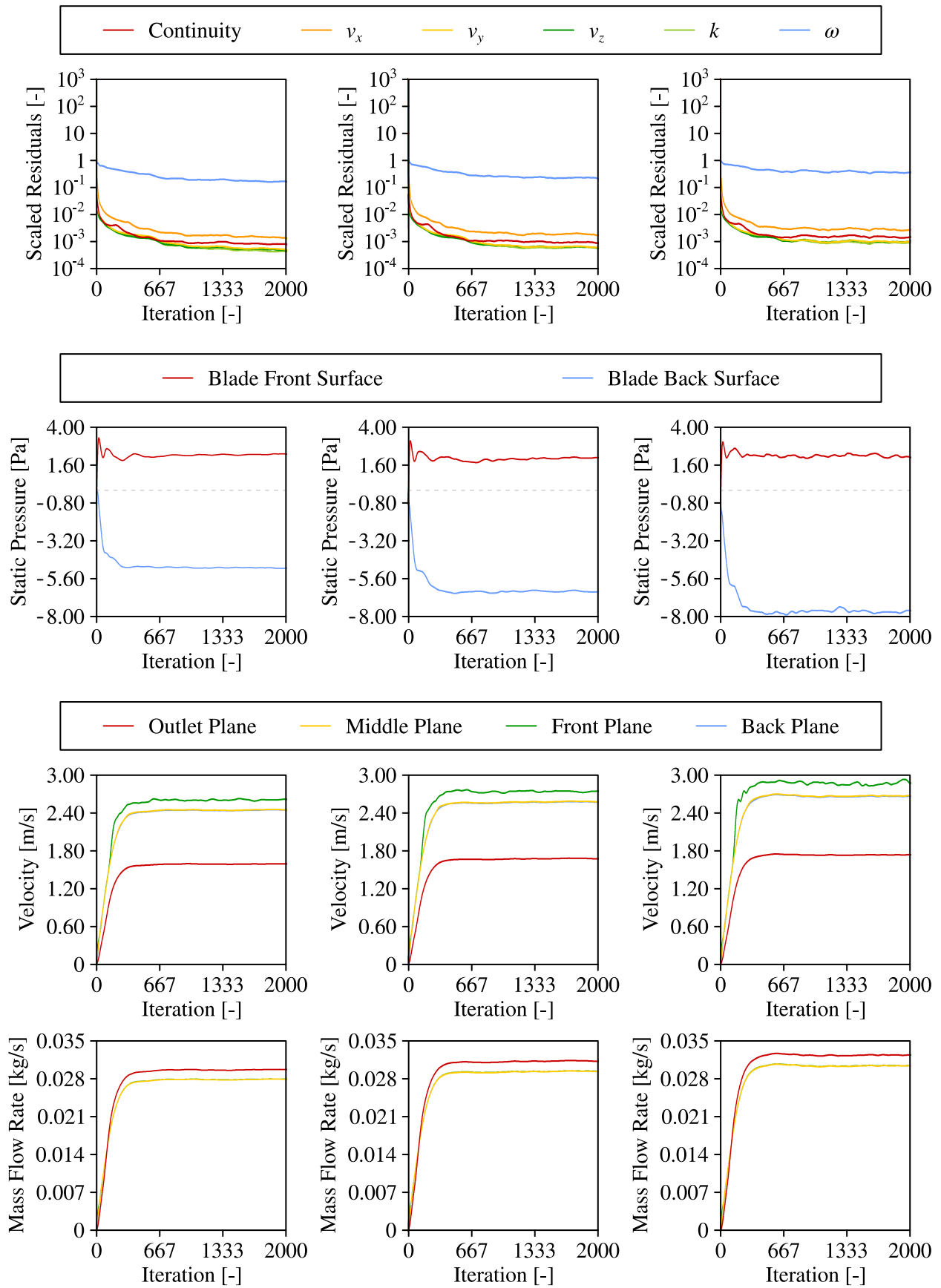


Figure B.1: Convergence of scaled residuals and properties at the positions of interest for an outlet angle of 35° (left), 50° (centre), and 65° (right) using a quantity of 12 blades, inclination of 0°, breadth of 20mm, channel thickness of 15mm, corner radius of 25mm, and angular velocity of 589.9rev/min.

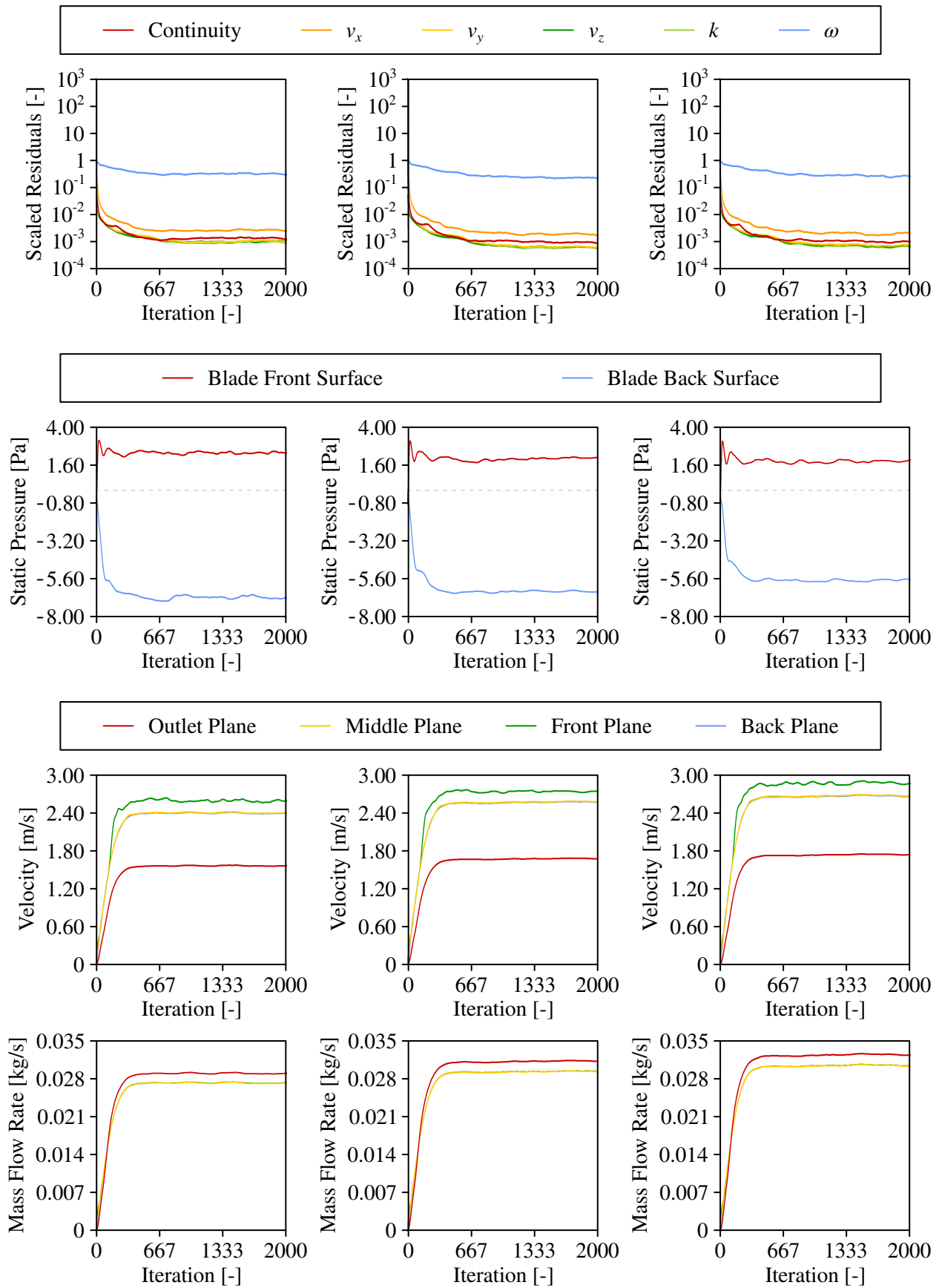


Figure B.2: Convergence of scaled residuals and properties at the positions of interest for a quantity of 10 (left), 12 (centre), and 14 (right) blades using an outlet angle of 50° , inclination of 0° , breadth of 20mm, channel thickness of 15mm, corner radius of 25mm, and angular velocity of 589.9rev/min.

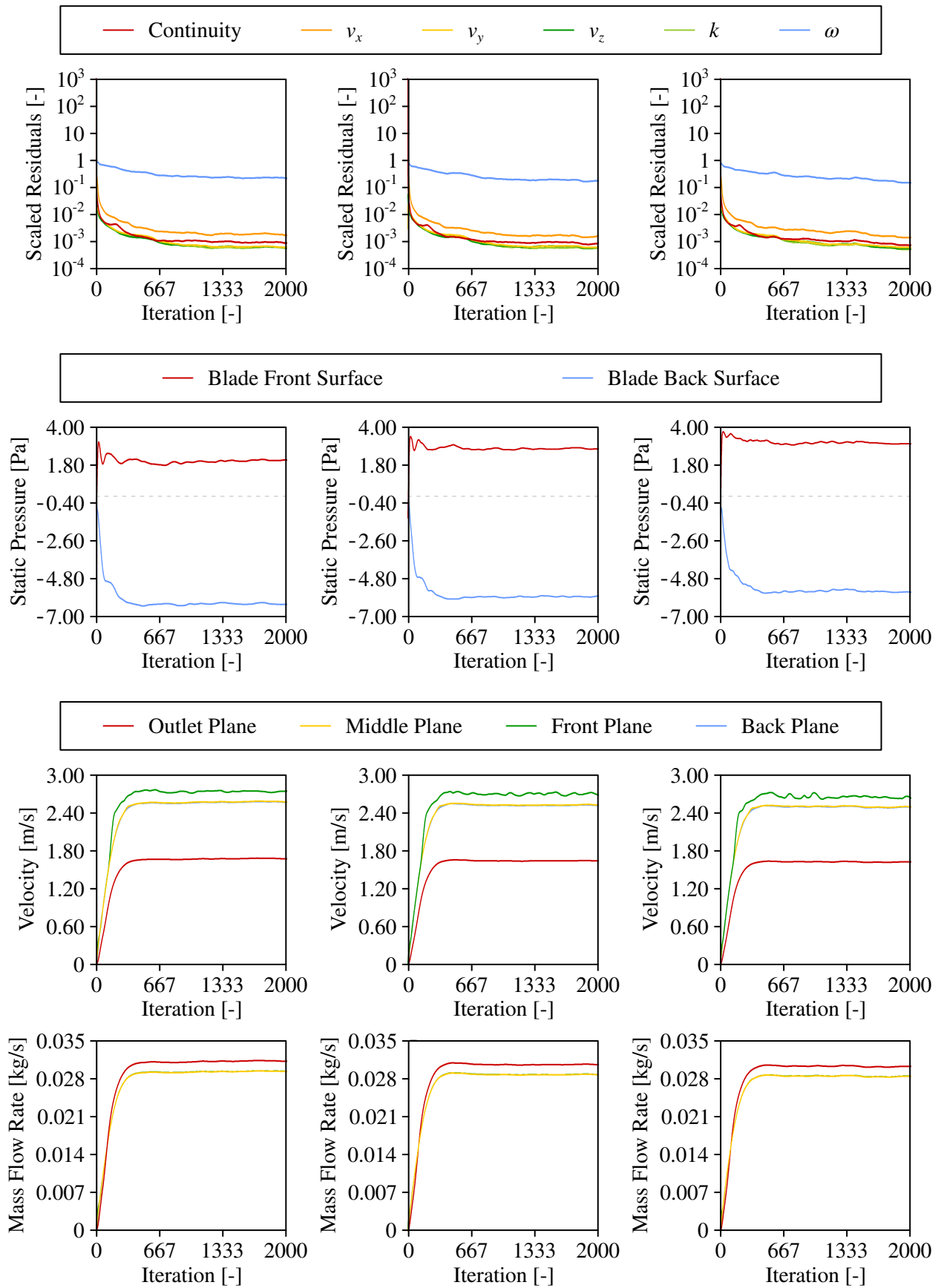


Figure B.3: Convergence of scaled residuals and properties at the positions of interest for an inclination of 0° (left), 10° (centre), and 20° (right) using an outlet angle of 50° , quantity of 12 blades, breadth of 20mm, channel thickness of 15mm, corner radius of 25mm, and angular velocity of 589.9rev/min.

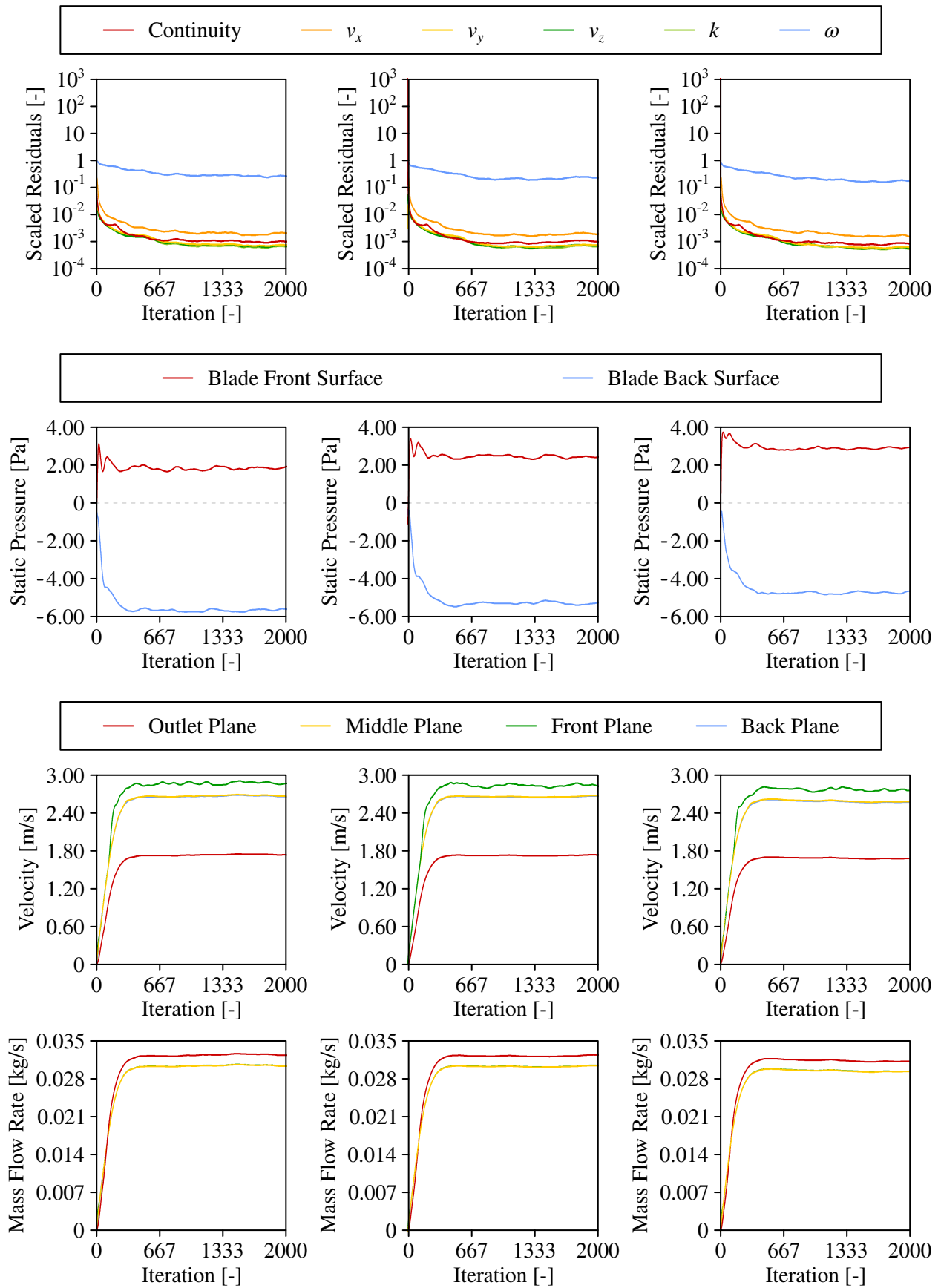


Figure B.4: Convergence of scaled residuals and properties at the positions of interest for an inclination of 0° (left), 10° (centre), and 20° (right) using an outlet angle of 50° , quantity of 14 blades, breadth of 20mm, channel thickness of 15mm, corner radius of 25mm, and angular velocity of 589.9rev/min.

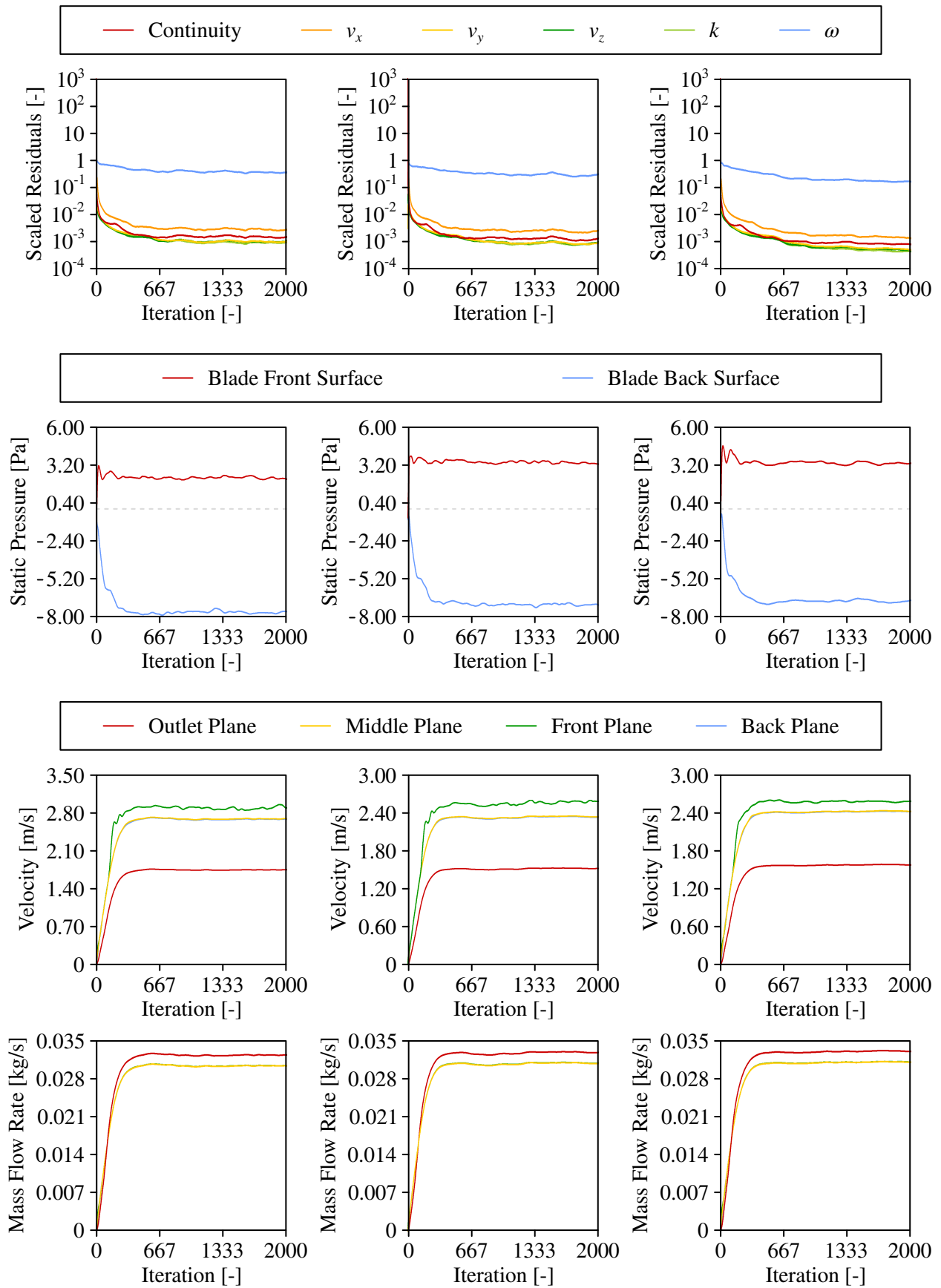


Figure B.5: Convergence of scaled residuals and properties at the positions of interest for an inclination of 0° (left), 10° (centre), and 20° (right) using an outlet angle of 65° , quantity of 12 blades, breadth of 20mm, channel thickness of 15mm, corner radius of 25mm, and angular velocity of 589.9rev/min.

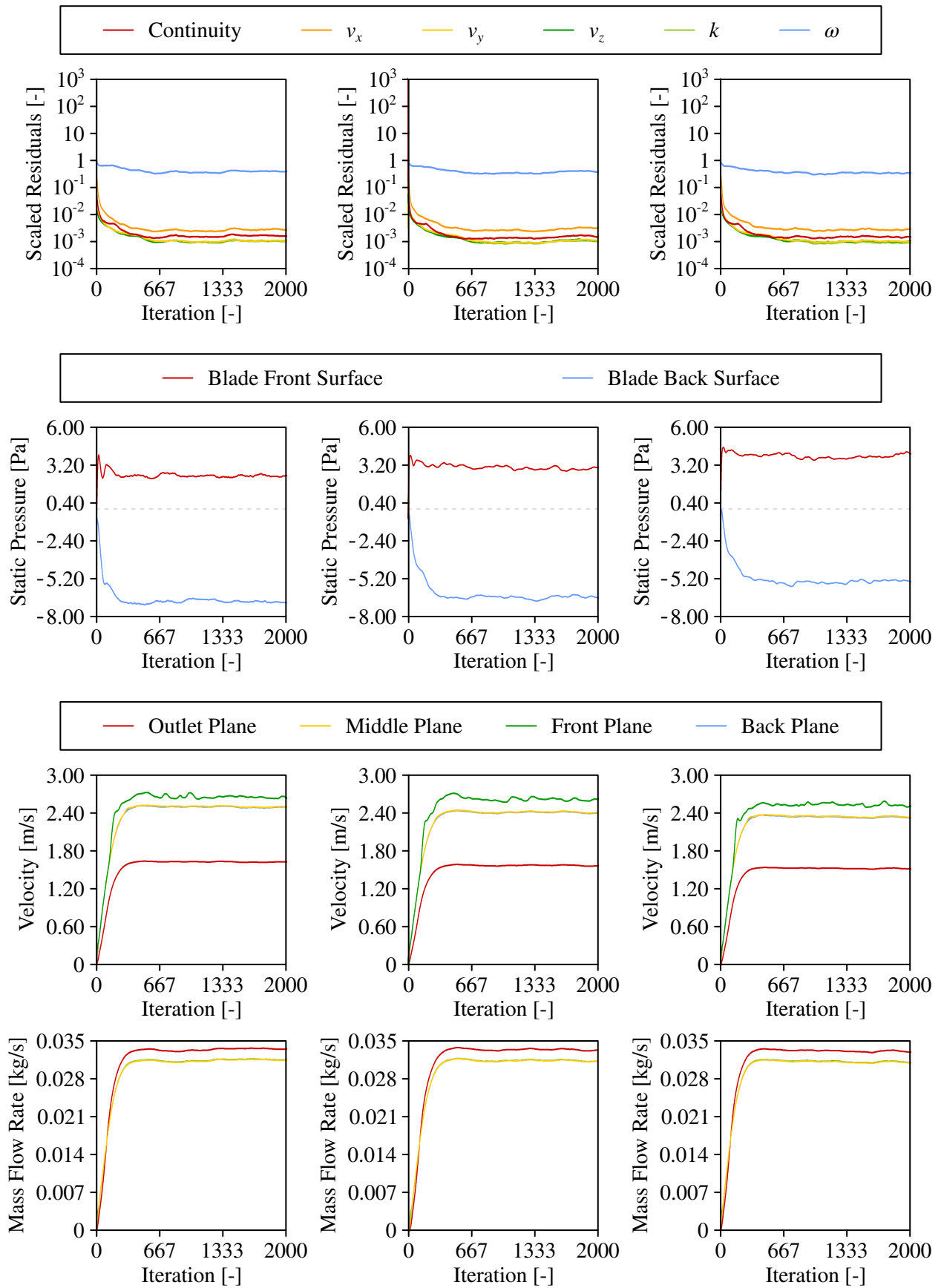


Figure B.6: Convergence of scaled residuals and properties at the positions of interest for an inclination of 0° (left), 10° (centre), and 20° (right) using an outlet angle of 65° , quantity of 14 blades, breadth of 20mm, channel thickness of 15mm, corner radius of 25mm, and angular velocity of 589.9rev/min.

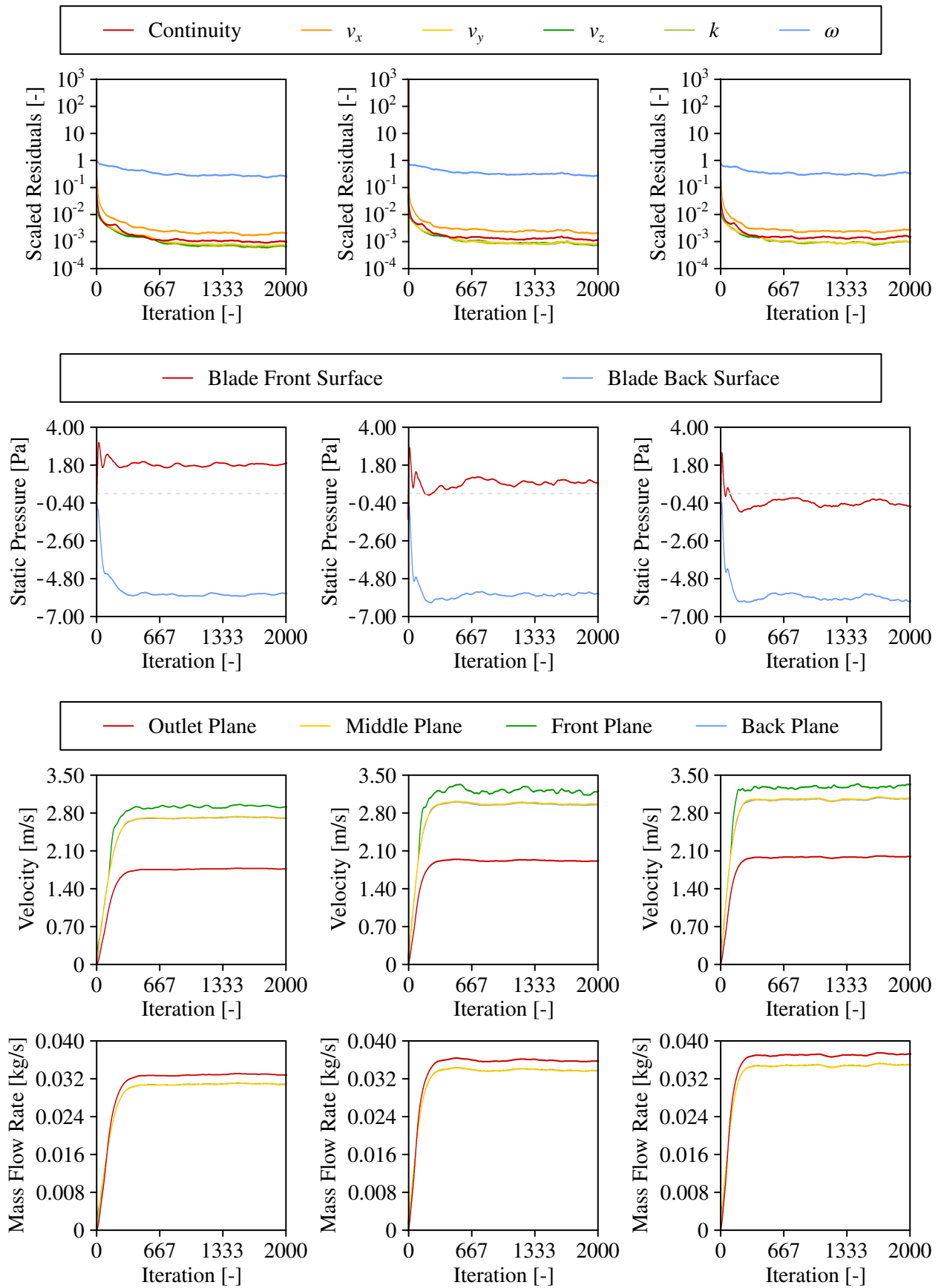


Figure B.7: Convergence of scaled residuals and properties at the positions of interest for a breadth of 20mm (left), 30mm (centre), and 40mm (right) using outlet angle of 50° , quantity of 14 blades, inclination of 0° , channel thickness of 15mm, corner radius of 25mm, and angular velocity of 589.9rev/min.

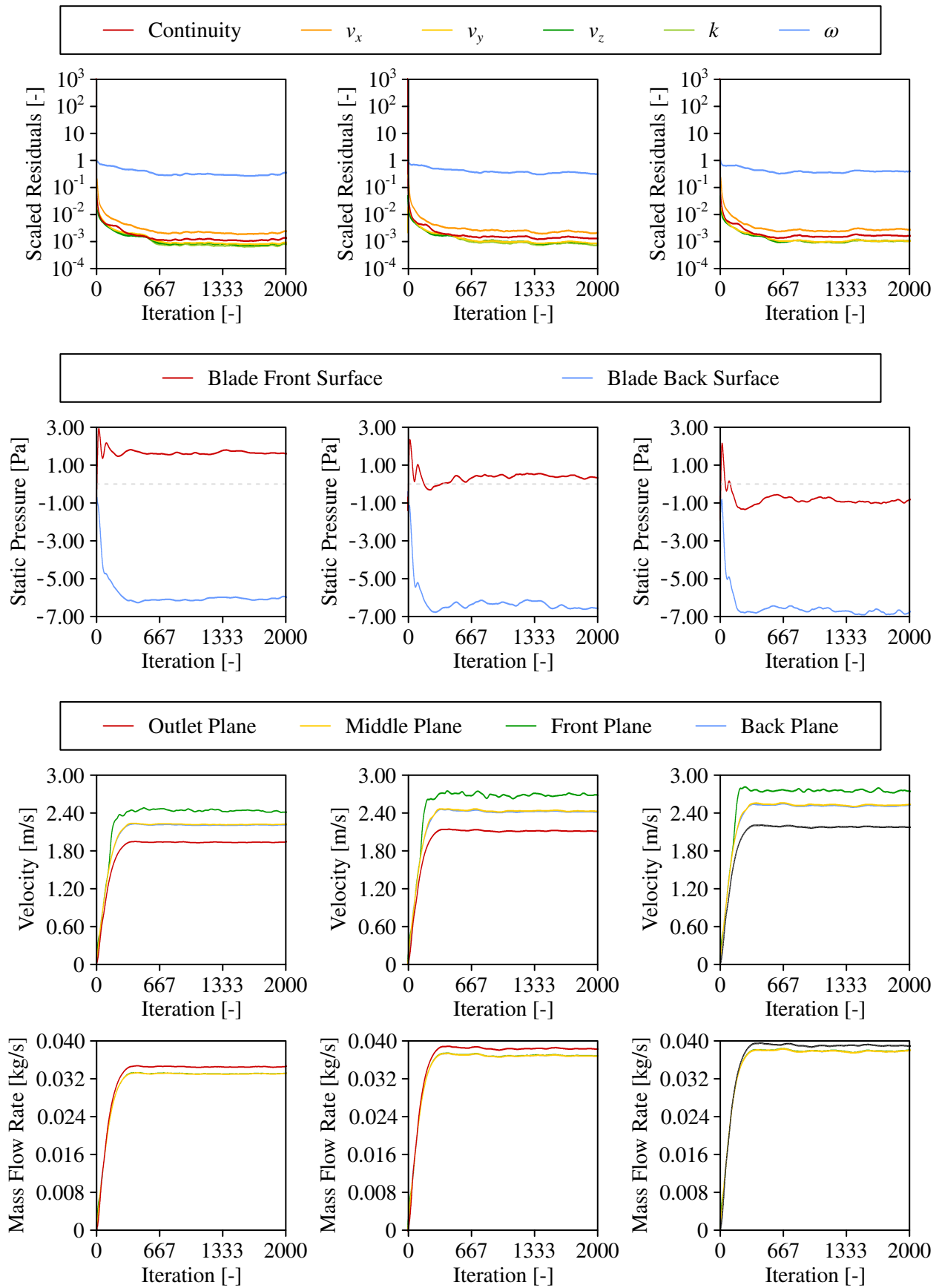


Figure B.8: Convergence of scaled residuals and properties at the positions of interest for a breadth of 20mm (left), 30mm (centre), and 40mm (right) using outlet angle of 50°, quantity of 14 blades, inclination of 0°, channel thickness of 20mm, corner radius of 25mm, and angular velocity of 589.9rev/min.

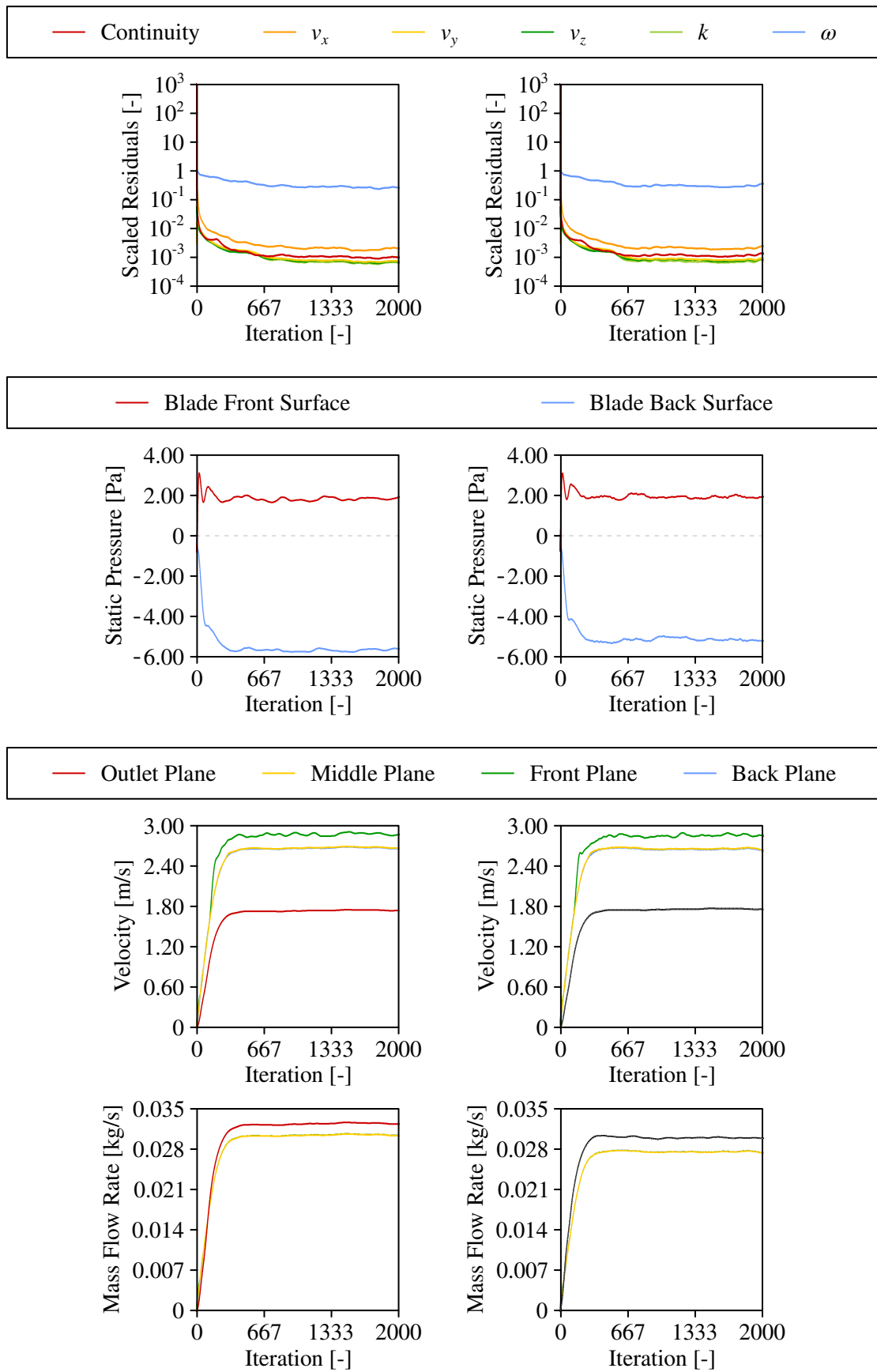


Figure B.9: Convergence of scaled residuals and properties at the positions of interest for a corner radius of 25mm (left) and 40mm (right) using an outlet angle of 50° , quantity of 14 blades, inclination of 0° , breadth of 20mm, channel thickness of 15mm, and angular velocity of 589.9rev/min.



07 June 2021

Re: Mr. Edward Rycroft (1478715)

Waiver letter number: HRECNMW21/06/06

To whom it may concern,

Mr. Rycroft is currently a registered Masters student at the School of Mechanical, Industrial, and Aeronautical Engineering at the University of the Witwatersrand, Johannesburg. This letter is to confirm that, at the time of writing, Mr. Rycroft does not need ethical clearance for his Masters study entitled 'Solar-Powered Evaporative Cooling For Fruits And Vegetables In Developing Countries'. This decision has been reached based upon a description of the project supplied by Mr. Rycroft to the University Human Research Ethics Committee (Non-Medical), which has been evaluated by the Chairs and Deputy Chairs. If, however, Mr. Rycroft changes the methods of data collection and analysis for this study, this decision may no longer be valid. If such changes take place, this should be communicated to the University Human Research Ethics Committee (Non-Medical) as soon as possible. This waiver letter is valid until 06 June 2024.

Please feel free to contact me should you require any further information.

Thank you.

Yours sincerely,
S Schoeman

Shaun Schoeman (Administrative Officer)

Solomon Mahlangu House, 10th Floor, Room 10004, Jorissen Street, Braamfontein, Johannesburg
Private Bag 3, Wits 2050

T + 27(0)11 717 1408 | E Shaun.Schoeman@wits.ac.za | hrec-medical.researchoffice@wits.ac.za

www.wits.ac.za/research/about-our-research/ethics-and-research-integrity/